MRI of the Spine

A Guide for Orthopedic Surgeons

William B. Morrison
John A. Carrino
Adam E. Flanders
Editors

Springer

MRI of the Spine

William B. Morrison
John A. Carrino • Adam E. Flanders
Editors

MRI of the Spine

A Guide for Orthopedic Surgeons

Springer

Editors
William B. Morrison
Division of Musculoskeletal Radiology
Thomas Jefferson University
Philadelphia, PA
USA

John A. Carrino
Department of Radiology and Imaging
Hospital for Special Surgery
New York, NY
USA

Adam E. Flanders
Division of Neuroradiology
Thomas Jefferson University
Philadelphia, PA
USA

ISBN 978-3-030-43626-1 ISBN 978-3-030-43627-8 (eBook)
https://doi.org/10.1007/978-3-030-43627-8

This Springer imprint is published by the registered company Springer Nature Switzerland AG
The registered company address is: Gewerbestrasse 11, 6330 Cham, Switzerland

For Binx and Boots
–William B. Morrison

Preface

MRI of the Spine is a book concept that arose from a spine imaging instructional course at the annual meeting of the American Academy of Orthopaedic Surgeons. The course has been the only dedicated radiology-based course at the AAOS meeting over the past decade, with radiology faculty and organizers. This unique arrangement reflects a need in the orthopaedic community, education on MR imaging, which has become an essential component of the diagnostic algorithm. Spine imaging incorporates degeneration, trauma, inflammatory conditions and infection, metabolic conditions, as well as dural and cord lesions, including neoplasia. An understanding of the MR imaging appearances of these conditions will assist the orthopaedist in understanding the nature and extent of the patient's condition. Following surgery and alteration of anatomy, MR imaging can be especially challenging to interpret. This is explored, with expected post-operative appearances and findings suggesting recurrent or new pathology. An understanding of methods for acquiring the images can also be helpful – what protocol to use and utility of contrast in different situations. To this end, we also provide tips for optimization of the MR imaging protocol. The editors and authors are musculoskeletal radiologists and neuroradiologists who work closely with surgeons in direct patient care. Our goal is to create a bridge between the radiologist and the orthopaedist, together using cutting-edge technology to better care for our patients.

Philadelphia, PA, USA
New York, NY, USA

William B. Morrison
John A. Carrino
Adam E. Flanders

Contents

Contributors

Kofi-Buaku Atsina, MD Department of Radiology, Thomas Jefferson University Hospital, Philadelphia, PA, USA

Laura W. Bancroft, MD, FACR University of Central Florida School of Medicine, Orlando, FL, USA

Florida State University School of Medicine, AdventHealth, Orlando, FL, USA

Richard D. Beegle, MD Department of Diagnostic Radiology, AdventHealth, Orlando, FL, USA

Andrew T. Cibulas, MD AdventHealth GME Radiology, Orlando, FL, USA

Mougnyan Cox, MD Hospital of the University of Pennsylvania, Philadelphia, PA, USA

Melissa Davis, MD, MBA Department of Radiology & Biomedical Imaging, Yale School of Medicine, New Haven, CT, USA

John V. Dennison, MD AdventHealth GME Radiology, Orlando, FL, USA

Vishal Desai, MD Thomas Jefferson University, Philadelphia, PA, USA

Sachin Dheer, MD Department of Radiology, Thomas Jefferson University Hospital, Jefferson Health, Philadelphia, PA, USA

Sean C. Dodson, MD Department of Diagnostic Radiology, AdventHealth, Orlando, FL, USA

Phan Q. Duy, BS Department of Radiology & Biomedical Imaging, Yale School of Medicine, New Haven, CT, USA

Jehan Ghany, MD Thomas Jefferson University, Philadelphia, PA, USA

Felix M. Gonzalez, MD Department of Radiology and Imaging Sciences, Emory University Hospital, Atlanta, GA, USA

Emory University Orthopaedics & Spine Center, Atlanta, GA, USA

Ricardo Hernandez, MS-III Philadelphia College of Osteopathic Medicine, Suwanee, GA, USA

Corey K. Ho, MD University of Colorado Anschutz Campus, Aurora, CO, USA

Ichiro Ikuta, MD Department of Radiology & Biomedical Imaging, Yale School of Medicine, New Haven, CT, USA

M. K. Jesse, MD University of Colorado Anschutz Campus, Aurora, CO, USA

Michele H. Johnson, MD Department of Radiology & Biomedical Imaging, Yale School of Medicine, New Haven, CT, USA

Ajit Karambelkar, MBBS, MD Thomas Jefferson University Hospital Philadelphia, Philadelphia, PA, USA

Karthik Krishnan, MS Weill Medical College of Cornell University, New York, NY, USA

Department of Radiology and Imaging, Hospital for Special Surgery, New York, NY, USA

Alexander Leyva, MD AdventHealth GME Radiology, Orlando, FL, USA

Prabath Kumar Mondel, MBBS, MD Philadelphia, PA, USA

Jack A. Porrino, MD Yale School of Medicine – New Haven Hospital, New Haven, CT, USA

Sophie C. Queler, BA Department of Radiology and Imaging, Hospital for Special Surgery, New York, NY, USA

Alessandra J. Sax, MD Department of Radiology, Thomas Jefferson University Hospital, Philadelphia, PA, USA

Kurt F. Scherer, MD University of Central Florida School of Medicine, Orlando, FL, USA

Florida State University School of Medicine, AdventHealth, Orlando, FL, USA

Darryl B. Sneag, MD Weill Medical College of Cornell University, New York, NY, USA

Department of Radiology and Imaging, Hospital for Special Surgery, New York, NY, USA

Monica Umpierrez, MD Department of Radiology and Imaging Sciences, Emory University Hospital, Atlanta, GA, USA

Philip K. Wong, MD Department of Radiology and Imaging Sciences, Emory University Hospital, Atlanta, GA, USA

Vahe M. Zohrabian, MD Department of Radiology & Biomedical Imaging, Yale School of Medicine, New Haven, CT, USA

MRI Protocol

1

Vishal Desai and Jehan Ghany

Introduction

Magnetic resonance imaging (MRI) is the mainstay for noninvasive evaluation of the spine, providing detailed anatomical assessment and excellent sensitivity for pathology, including degenerative disc disease, tumors, infection, bone marrow processes, spinal cord abnormalities, traumatic injuries, and compression fractures. Unlike other imaging modalities, MRI can evaluate the spinal cord, meninges, cerebrospinal fluid, marrow, and supporting structures in one routine study.

Advanced MR imaging can be obtained with additional sequences and/or with intravenous contrast to gather more information, help with troubleshooting, or assist in evaluating patients with prior spinal surgery with or without hardware. The high yield of MRI and the lack of ionizing radiation make it the imaging modality of choice for the spine in nearly all populations and for most indications.

V. Desai (✉) · J. Ghany
Thomas Jefferson University, Philadelphia, PA, USA
e-mail: vishal.desai@jefferson.edu; jehan.ghany@jefferson.edu

MRI Physics

To get a better understanding of the commonly performed MRI sequences and what information can be extracted from each, an overview of MRI physics is helpful [1]. MRI utilizes the body's natural magnetic properties for imaging, specifically the hydrogen nucleus due to its prevalence throughout the body in water and fat.

Magnetic Field

Hydrogen protons contain a net positive charge, providing them with their own magnetic spins and a local magnetic field. With the patient in the MRI scanner, a uniform magnetic field is applied to the protons in the slice or slab of interest, causing the randomly oriented protons to now align parallel to the external magnetic field, precess at a certain frequency, and contain a net magnetization in the longitudinal direction (Fig. 1.1).

RF Pulse

Next, a radiofrequency (RF) pulse or series of RF pulses is applied to the protons, dependent on the sequence and information desired. The energy from the RF pulse is absorbed by the protons, causing the net magnetization to tilt away from the longitudinal direction (Fig. 1.2).

W. B. Morrison et al. (eds.), *MRI of the Spine*, https://doi.org/10.1007/978-3-030-43627-8_1

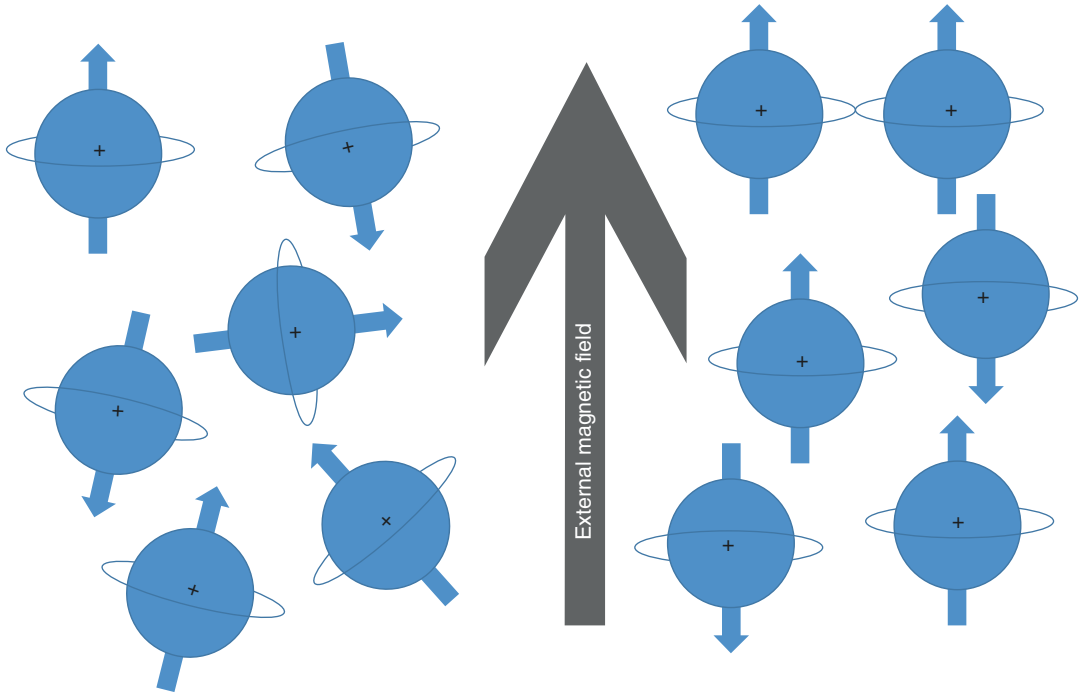

Fig. 1.1 With the application of an external magnetic field, the previously randomly oriented protons are now aligned and have a net magnetization

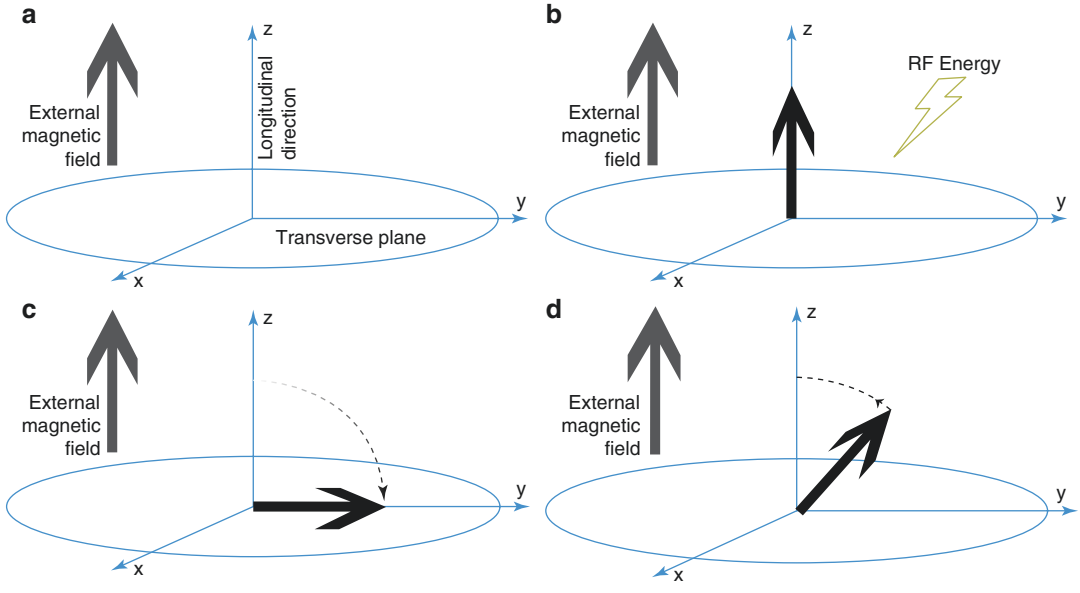

Fig. 1.2 After the protons are aligned by the external magnetic field (**a**), RF energy is applied by the scanner to tilt the protons into the transverse plane (**b**). As the protons move back to their lower energy state, the time to decay in the transverse plane and the time to relax to the longitudinal direction are related to the property of the tissues – T2 and T1, respectively (**c**, **d**). This provides important imaging characteristics

Again, the extent of this "tilt" depends on the RF pulse and can be manipulated to obtain different tissue characteristics.

Relaxation

As with any structure with high energy, there is a natural tendency toward a lower energy state. With MRI, this means the protons which were tilted and rotated by the RF pulse (high energy state) will realign with the magnetic field (low energy state). The time taken for a particular tissue to relax in the longitudinal direction is referred as the T1 relaxation rate. The time taken for transverse magnetization to decay to 37% of its initial value is referred to as the T2 relaxation rate (Fig. 1.2). Both T1 and T2 relaxation occur simultaneously based on the intrinsic properties of the excited tissue and its local environment.

As the tissues relax toward the lower energy states, RF energy is emitted and can be measured. The time from the delivery of the RF pulse and peak of the signal emitted (also known as an echo) is referred to as the "time to echo" (TE). The time interval between each excitation pulse is referred to as the "repetition time" (TR). These parameters (time, duration, and sequence of RF pulses) can be manipulated to create different types of images to characterize different structures and help answer the clinical question.

Image Formation

The last step is to translate the received signal into an image. The signal is received as frequency information, encoded with location information and intensity determined by the tissue characteristics and sequence parameters. Through Fourier transformation, this frequency information is converted into shades of gray in a matrix of pixels, which forms an image.

Image Quality

An optimal imaging protocol considers the clinical question and tailors the examination to answer it, with high yield sequences acquired in the minimum amount of time and with excellent quality to ensure diagnostic adequacy. Quality is determined by image resolution, image contrast, signal-to-noise ratio, and lack of artifacts. Fine-tuning imaging protocols are required to find the appropriate balance between resolution, contrast, signal, noise, and overall study time.

Resolution

Image resolution determines the ability to evaluate small structures or pathologies and can be regarded as the level of detail in the scan. A high-resolution image is able to distinguish between adjacent structures, whereas a low-resolution image would blur them together (Fig. 1.3). This depends on the size of the image pixel (or voxel for 3D sequences), which in turn depends on the matrix size, field of view, and slice thickness.

Increasing the matrix size increases the total number of pixels/voxels, which means a higher-resolution image but at the cost of more time and with less signal in each voxel. A larger field of view may be required to image the entire region of interest (such as the thoracic spine), but that means that each voxel now contains more area, decreasing spatial resolution. Similarly, increasing slice thickness covers more area, decreasing spatial resolution.

Signal-to-Noise Ratio

For any imaging modality, the goal is to obtain the highest amount of signal with the least amount of noise. For MRI, this often comes at the expense of spatial resolution, as more signal is obtained when the voxel size is larger (increased slice thickness, smaller matrix, and larger field of view). Additional strategies to increase signal and decrease noise

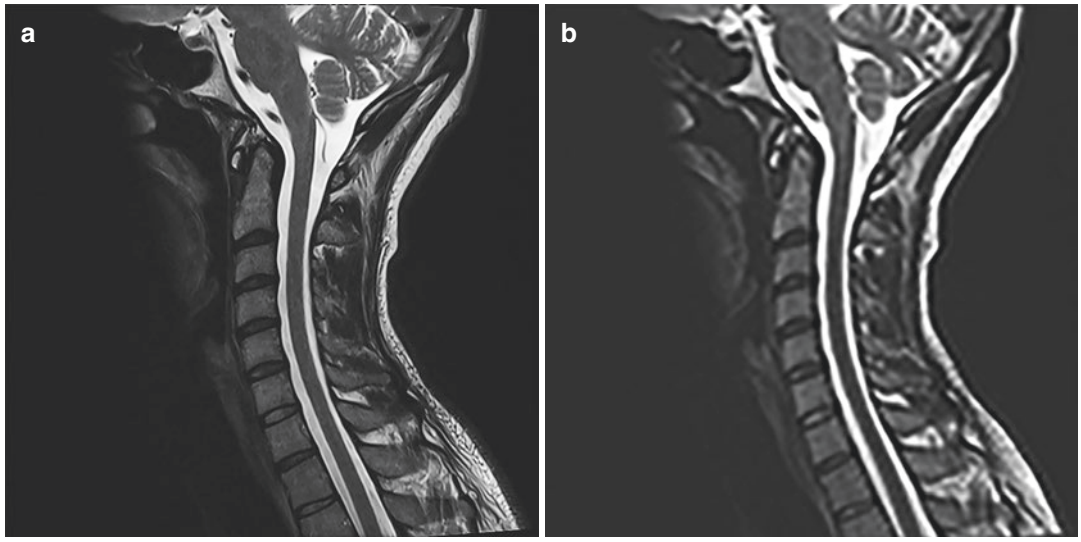

Fig. 1.3 An example of a high-resolution MRI image (**a**) compared to a low-resolution image (**b**), in which discerning small structures is difficult

without affecting spatial resolution include increasing the number of excitations (NEX) and utilizing RF coils. By increasing the NEX, more signal is received per acquisition and allows for averaging of the signal for a higher-quality, less noisy image.

Proper coil selection is a crucial but often overlooked concept in MR imaging. There are a wide variety and multiple configurations of coils available, including several optimized for spinal imaging. The coil should sit closely against the area of interest and should be the smallest size possible. RF coils serve as the "antenna" for the MR scanner. By optimizing the shape, size, and location of this antenna, the signal received back from the body part being imaged is greater, improving image quality.

Contrast

In order to detect pathology, the image must be able to display a difference, or contrast, in signal intensity between normal and abnormal tissue. MRI inherently has high contrast sensitivity and is adept at demonstrating differences in tissues in the body, both anatomy and pathology (Fig. 1.4).

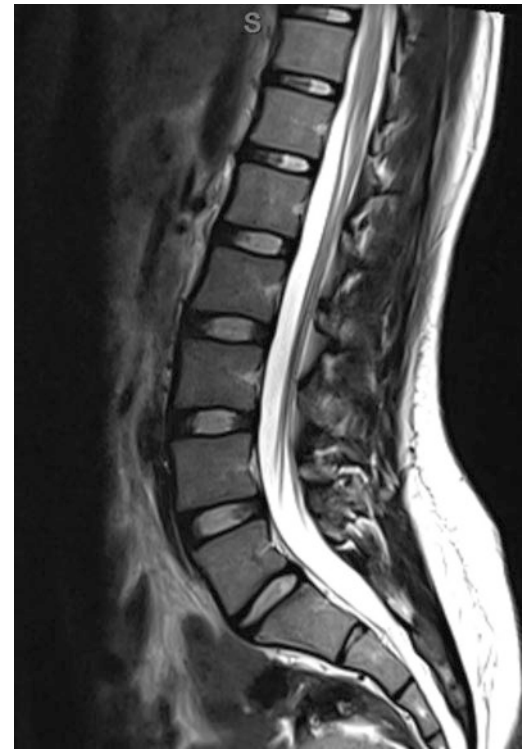

Fig. 1.4 An example of T2-weighted sequence demonstrating the excellent contrast resolution of MRI, with a clear distinction between CSF, fat, and soft tissues

Even though MRI has high contrast at baseline, the parameters must be optimized for each examination. By adjusting the TR and TE, the images can highlight tissue differences on T1-weighted, T2-weighted, and proton density sequences. More advanced sequences can evaluate and display other tissue characteristics if desired.

Field Strength

Besides intrinsic tissue contrast, several external factors can impact imaging quality, with one of the major ones being the primary property of the scanner – magnetic field strength. Magnetic field strength varies from 0.2 Tesla to 3 Tesla for clinical applications, with 1.5 Tesla the most commonly available and most commonly used. The higher the field strength, the better the contrast, the higher the resolution, and the higher the signal-to-noise ratio. This means that a stronger magnet improves overall image quality and thus diagnostic ability.

MRI scanners are available in both open and closed configurations. Open MRI scanners often have a lower field strength and several limitations, including a longer scan time which can predispose to motion artifact, poorer fat suppression, and a wider field of view to collect more signal. These limitations can contribute to lower-image quality compared to traditional scanners. As a result, open scanners should be reserved for claustrophobic and obese patients who may not fit in or cannot tolerate a closed system.

Artifacts

There are numerous artifacts that can impact image quality on MRI, which can be attributable to MR hardware and software, shielding of the MRI scanner room and magnetic field inhomogeneities, tissue heterogeneity, foreign bodies, patient motion, and physiologic motion [2] (Fig. 1.5).

Based on the type of artifact, solutions exist to remove or at least partially correct for the

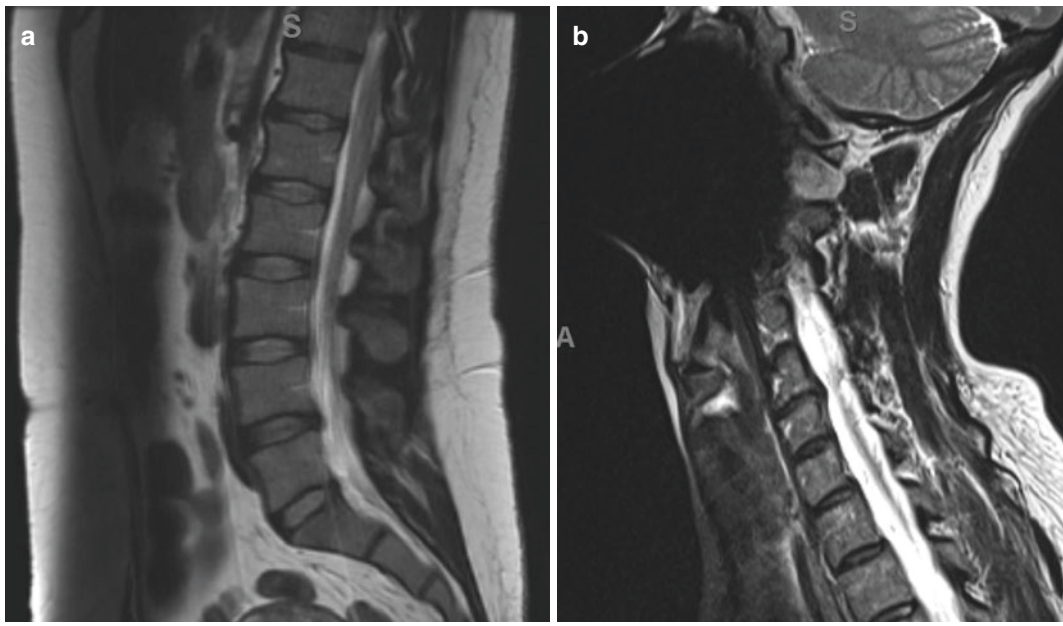

Fig. 1.5 (**a**) Motion artifact from the patient moving during image acquisition introduces blur and artifactual lines on the image. (**b**) Susceptibility artifact from dental hardware limits evaluation of the upper cervical spine

artifact to improve overall image quality. Artifacts could contribute to confusing imaging findings (pseudo-masses) or preclude diagnostic evaluation (extensive susceptibility artifact from hardware). While a full discussion on MRI artifacts is beyond the scope of this chapter, recognizing that they exist and factors contributing to them can be helpful in image optimization and study interpretation.

Routine Sequences

The routine imaging protocol for a spine MRI should include a T1-weighted sequence (excellent for evaluating anatomy and bone marrow), a T2-weighted sequence (for anatomy and pathology), and a fluid-sensitive sequence (excellent for detecting pathology). At the minimum, a spine protocol should contain sequences in both the sagittal and axial plane.

T1-Weighted Sequence

Sequences with T1 weighting evaluate differences in the T1 contrast of tissues. After excitation, tissues relax back to equilibrium at different rates based on its intrinsic characteristics. Relaxation in the longitudinal direction provides the T1 property of the tissue.

Physics

In general, T1-weighted imaging utilizes a short TR and short TE to maximize tissue contrast (Fig. 1.6). Fat, for instance, rapidly realigns from the longitudinal direction back to equilibrium, yielding a higher signal and thus appearing bright, or "hyperintense," on T1-weighted imaging. Conversely, water realigns slowly from the longitudinal direction, yielding less signal and thus appearing dark, or "hypointense," on T1-weighted imaging. Without a short TR, all of the protons would relax back to equilibrium yielding an image with equal intensity for all tissues; thus, a short TR is required for T1-weighted imaging to achieve tissue contrast.

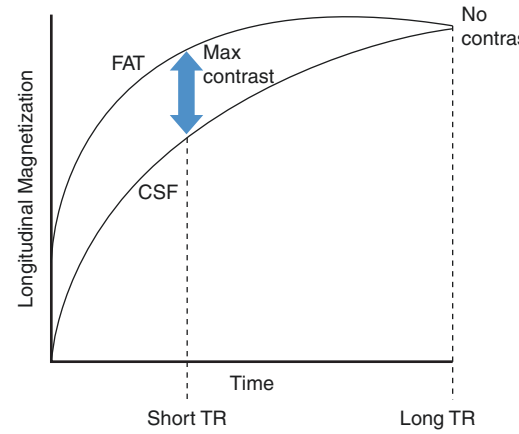

Fig. 1.6 A short TR and short TE maximize T1 tissue contrast

Practical Application

This sequence is universally utilized in nearly all MR imaging protocols, in part due to its very high signal-to-noise ratio, and is primarily used for evaluation of anatomy [3]. Due to the bright appearance of fat on this sequence, T1-weighted imaging is especially useful for evaluation of normal bone marrow in the spine. Normal marrow in adults is predominantly fatty (yellow marrow) and should appear hyperintense. Pathologic marrow, which can be seen with lymphoma, leukemia, metastases, infection, and other infiltrative process, results in hypointense marrow. A rule of thumb for spinal imaging is that normal bone marrow on T1-weighted imaging should be brighter than the disc space; otherwise this should raise a red flag for an infiltrative process (Fig. 1.7).

Besides fat, other structures that appear hyperintense on T1-weighted imaging include methemoglobin, melanin, slow-flowing blood, and proteinaceous fluid. T1-weighted imaging is also utilized after administration of IV contrast agents (such as gadolinium), which will be discussed separately.

T2-Weighted Sequence

T2-weighted imaging is another mandatory sequence for nearly all MR imaging and is useful for evaluating both anatomy and pathology. This

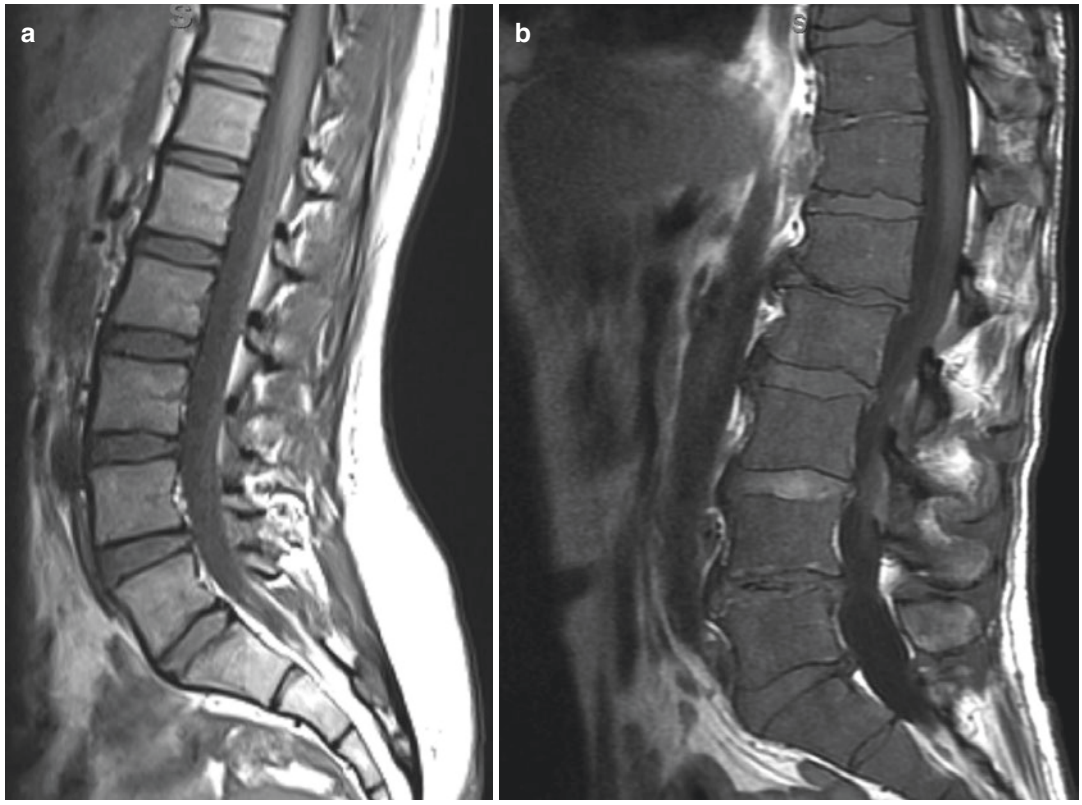

Fig. 1.7 (**a**) T1-weighted image demonstrating normal fatty bone marrow. (**b**) T1-weighted image in a different patient shows replacement of the normal fatty marrow. The vertebral body appears darker than the adjacent disk, a sign of a pathologic marrow process, which in this case was lymphoma

sequence evaluates differences in the T2 contrast of tissues, another inherent property (although it can be somewhat impacted by magnetic field inhomogeneities). Whereas T1-weighted imaging relies on relaxation in the longitudinal direction, T2-weighted imaging relies on decay in the transverse direction [3].

Physics

For T2-weighted imaging, long TR and TE times are required to accentuate differences in tissue contrast (Fig. 1.8). Water has a long T2 relaxation time, resulting in a hyperintense appearance on a T2-weighted image. Fat also appears bright on T2-weighted imaging.

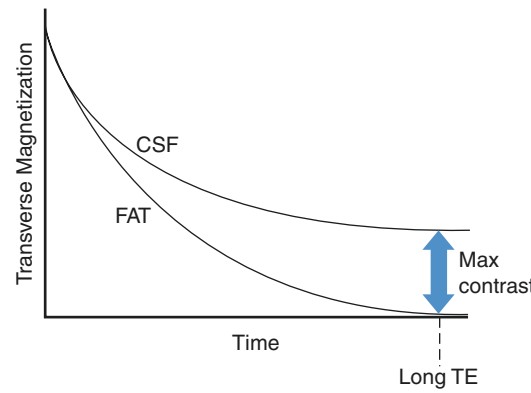

Fig. 1.8 A long TR and long TE maximize T2 tissue contrast

Practical Applications

For spine imaging, T2-weighted sequences allow excellent visualization of the cerebrospinal fluid (CSF) due to its high water content. As a result, loss of normal CSF space, such as in the case of a disc herniation narrowing the central canal or neural foramen, will be readily apparent on this sequence (Fig. 1.9).

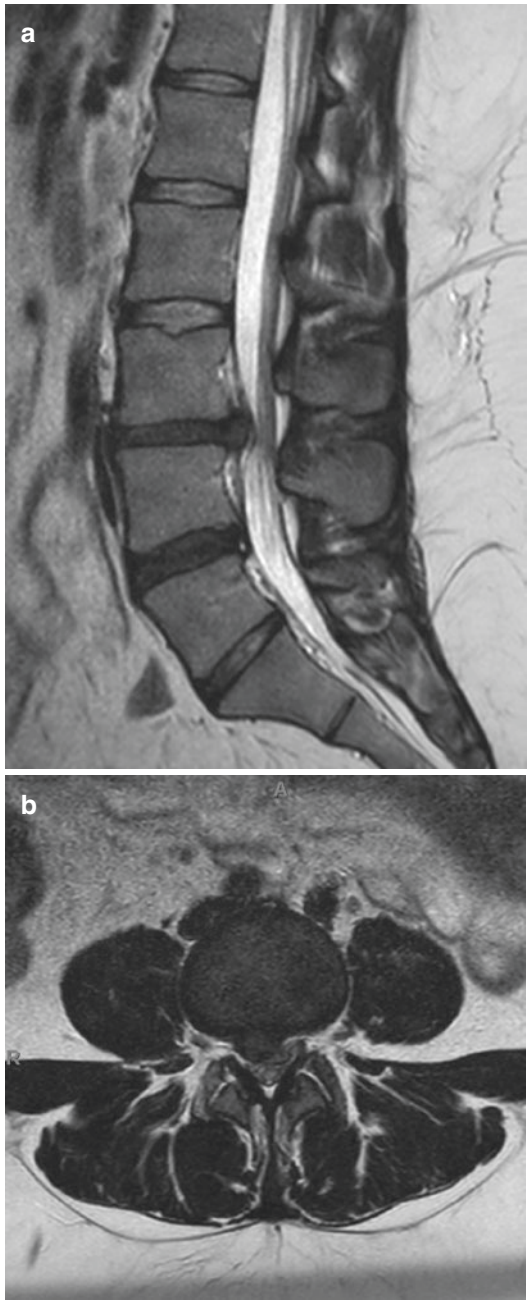

Fig. 1.9 T2-weighted imaging is excellent for evaluation of degenerative disc disease due to contrast in disc material, CSF, and nerve roots. There is a large disc extrusion seen on sagittal (**a**) and axial (**b**) T2-weighted sequences in this patient at the L3-L4 level

Most pathologic conditions – tumors, infections, inflammatory process – have a component of edema and as a result appear hyperintense on T2-weighted imaging. For instance, an epidural collection will generally appear bright or intermediate in signal on this sequence, perhaps with heterogeneity in the case of infection or blood products.

Fluid-Sensitive Sequence

While routine T2-weighted image will demonstrate fluid (and, as a result, most pathology) as hyperintense, fat also appears hyperintense which can make identifying and characterizing the abnormality difficult. Thus to get a truly fluid-sensitive sequence, different techniques can be applied to suppress the fat and highlight the presence of edema and pathologic tissues (Fig. 1.10).

Fat-Saturated T2-Weighted Sequence

The most commonly used technique to achieve a fluid-sensitive image is frequency-selective fat suppression. This method applies an RF pulse to the slice at the same resonance frequency of lipids to saturate all tissues with fat followed by a gradient pulse to nullify any signal from the lipid [4].

The advantage of this technique is that it can be applied to any sequence to suppress fat, including post-contrast imaging. However, it is highly susceptible to inhomogeneities in the magnetic field, which can lead to failure in fat suppression. Fat saturation techniques should not be used when metallic hardware is present in the area of interest (such as fixation devices in the spine) due to the resulting artifact.

STIR Sequence

An alternative and also commonly used sequence for fluid-sensitive imaging of the spine is short tau inversion recovery, or STIR. Since fat has such a short T1 relaxation time, shorter than most other tissues, its signal can be selectively nullified without impacting other tissues through the use of RF pulses [4].

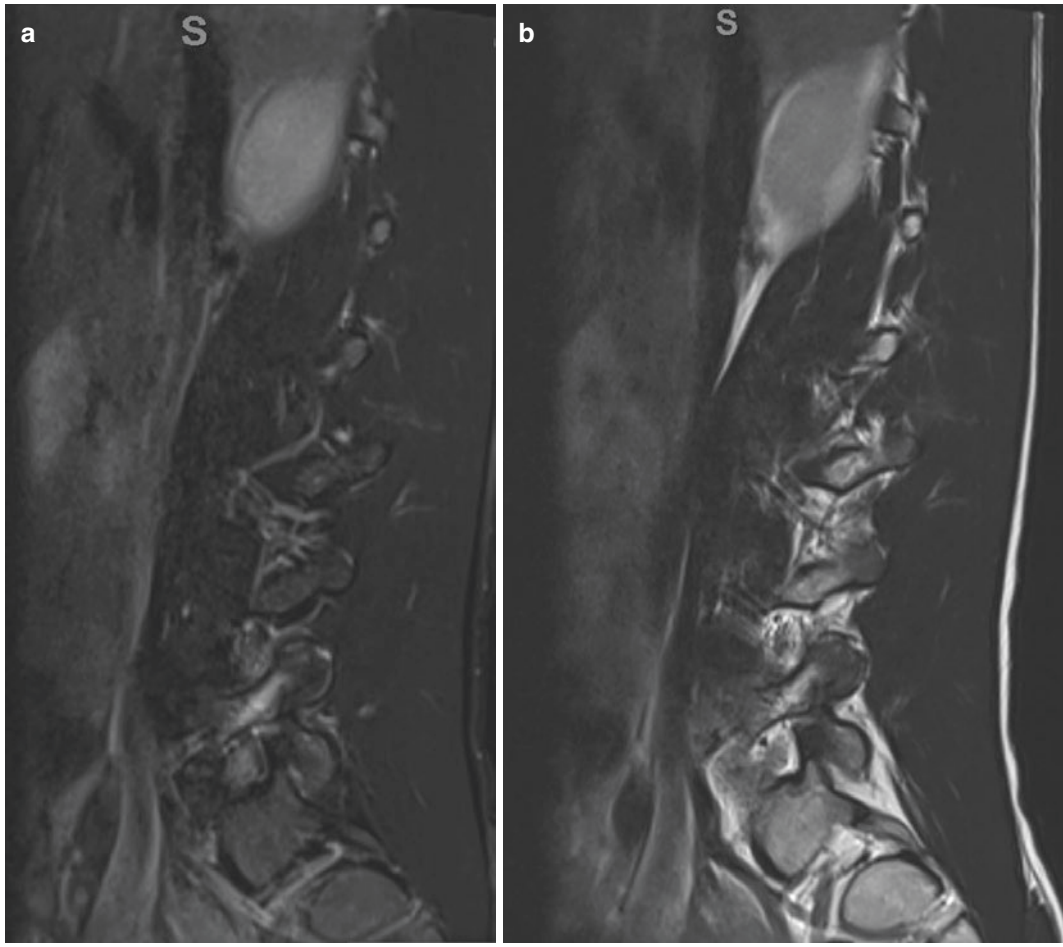

Fig. 1.10 Fluid-sensitive imaging (STIR, in this example) is helpful to highlight pathology, particularly edema, which in this case makes the pars interarticularis stress fracture readily apparent (**a**) compared to non-fat-suppressed imaging (**b**)

STIR imaging is significantly less susceptible to inhomogeneities in the magnetic field, leading to more uniform fat suppression. This is the preferred method for fluid-sensitive imaging in the presence of hardware. The only disadvantage is that the fat suppression is not selective for lipids but applies to any tissues with short T1, such as melanin, mucus, and, of particular interest in spine pathology, methemoglobin. For the same reason, STIR should not be used for post-contrast imaging, as the T1 relaxation properties of contrast are similar to fat and would result in signal loss of both.

Imaging Planes

Routine imaging of the spine should include T1-weighted, T2-weighted, and fluid sensitive (fat-saturated or STIR) sequences in the sagittal imaging plane. This combination allows for evaluation of the bone marrow, CSF, and for most pathologies. Axial imaging with at least T2-weighting should also be performed to allow for evaluation in more than one plane. Often, a T2-weighted sequence in an axial plane relative to the disc space is included to improve evaluation of degenerative disc disease (Fig. 1.11).

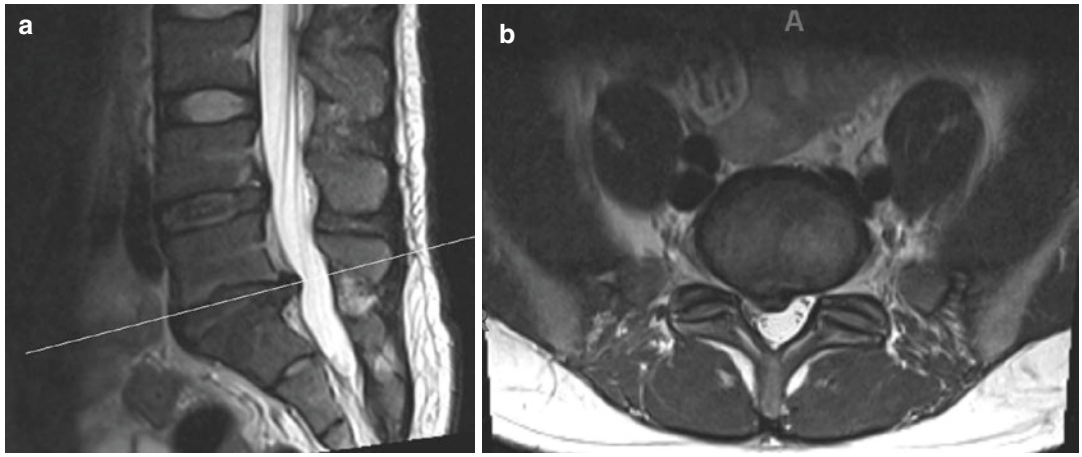

Fig. 1.11 Routine spinal imaging should include an axial T2-weighted sequence oriented to the disc spaces to improve evaluation of disc disease. The sagittal sequence demonstrating the correct plane selection (**a**) and resultant axial sequence through the disc space (**b**) are shown

Contrast

Contrast-enhanced MRI may be used to help identify and further characterize pathology, particularly neoplastic and inflammatory processes. Gadolinium-based contrast agents are the most commonly utilized and, for spinal imaging, are administered intravenously.

Physics

Gadolinium contrast is a paramagnetic agent, meaning that it contains unpaired electrons which results in a local magnetic field wherever the contrast is present. Pathologic conditions tend to have hypervascularity and as a result accumulate contrast after intravenous administration, referred to as "enhancement." The presence of gadolinium in these tissues alters the local magnetic field, resulting in "T1 shortening" or hyperintense appearance on T1-weighted imaging [5].

Practical Applications

Due to its impact on T1 imaging properties, the sequence of choice to complement contrast administration is a T1-weighted fat-saturated sequence. This allows enhancing pathology to appear bright while suppressing signal from lipids to avoid confusion.

The presence or absence of enhancement in addition to the pattern of enhancement can help determine benignity versus malignancy for certain lesions and help narrow the differential diagnosis for others. In spinal imaging, contrast is utilized for characterizing masses (in the spinal canal, soft tissues, or marrow), evaluating infection/inflammation, and assessing recurrent disc herniations or complications in the postoperative spine (Fig. 1.12).

Contrast Safety

Severe adverse reactions to gadolinium-based contrast agents, such as anaphylaxis, are relatively rare (1 in 100,000). Most reactions are self-limiting and include headaches, injection site pain, and nausea. Besides a history of prior severe adverse reaction, the only other relative contraindications include pregnancy and renal failure. Gadolinium-based contrast agents have been linked to nephrogenic systemic fibrosis in patients with renal failure and should be used cautiously in patients with eGFR <30 mL/min/1.73 m^2 [6].

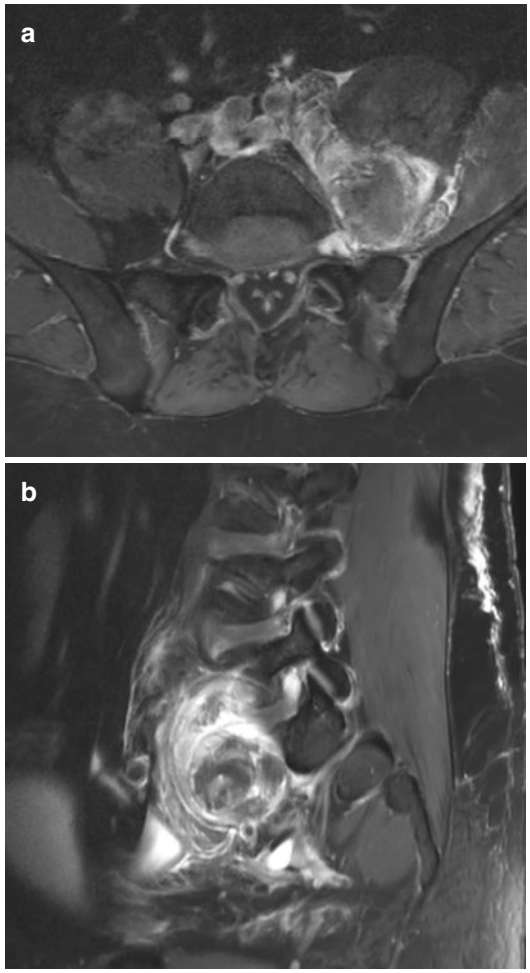

Fig. 1.12 Post-contrast axial (**a**) and sagittal (**b**) imaging of the lumbar spine demonstrates a large heterogeneous, enhancing mass inseparable from the enhancing left L5 nerve root, which was biopsy proven to be a nerve sheath tumor

Non-routine Sequences

Based on patient history, suspected pathology, or previous imaging findings, additional imaging sequences may be added to the routine protocol for better delineation and problem solving.

Proton Density Sequence

In proton density (PD)-weighted images, the signal intensity directly corresponds to the density of hydrogen atoms (protons) in the tissues. PD is considered an "intermediate" sequence, with a short TE and relatively long TR, producing imaging features of both T1 and T2 [3]. This sequence has a high signal-to-noise ratio, greater than both T1- and T2-weighted sequences. This sequence is commonly added to spinal imaging protocols to evaluate for demyelination, such as in multiple sclerosis, and has been shown to be more sensitive in that regard than T2-weighted imaging (Fig. 1.13) [7].

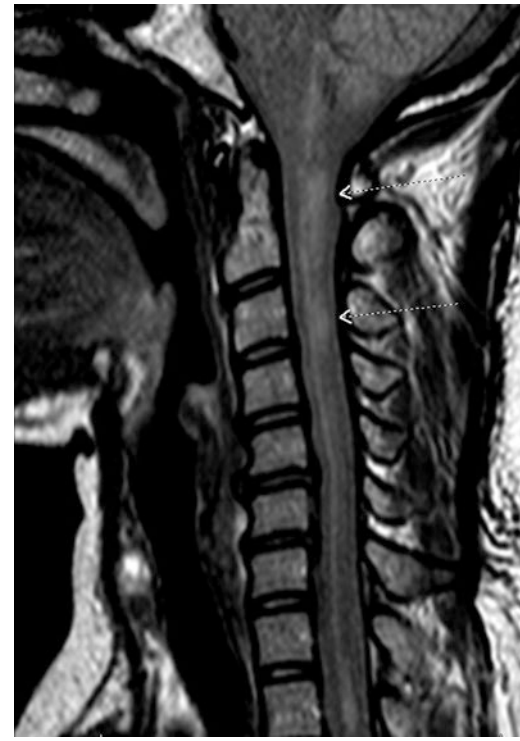

Fig. 1.13 Proton density imaging improves detection of demyelinating lesions in the spinal cord, as seen at the C2 and C3-C4 levels in this patient with multiple sclerosis

In-Phase and Out-of-Phase Imaging

In-phase and out-of-phase sequences, also referred to as chemical shift imaging, are paired sequences that assess for the presence of intralesional microscopic fat, a feature commonly regarded as a sign of benignity. Due to slight differences in resonance frequencies of protons in water versus fat, their spins are routinely "in phase" and "out of phase." These differences can be exploited by acquiring images at the same TR

but differing TE, such that when the spins are "in phase" the signal from fat and water within a voxel is additive and when "out of phase" is cancelled out.

As a result, if the tissue or lesion of interest contains both fat and water in the same voxel (such as edema or hematopoietic bone marrow), then there will be loss of signal (or dropout) on out-of-phase imaging relative to the in-phase sequence. If there is no signal dropout, then microscopic fat is not present suggesting neoplasia. This is particularly useful for osseous lesions in the spine, including evaluation of vertebral body compression fractures, since normal bone marrow should contain varying amounts of fat (Fig. 1.14). The dropout can be quantified using a region of interest (ROI) tool, found in nearly all image viewers, with a 20% drop from in-phase to out-of-phase commonly used as cutoff to maximize sensitivity and specificity [8].

False positives can occur with chemical shift imaging, such as in the presence of acute blood products, marrow fibrosis, sclerotic metastases, and fat-containing metastases which can all show loss of signal. Correlation with other sequences can help reduce misinterpretation.

Diffusion-Weighted Imaging

Diffusion-weighted imaging (DWI) is a powerful imaging sequence sensitized to the movement (diffusion) of water molecules. Any changes in the tissues or local environment that produce a barrier, such as ischemia, abscess, or tumor, will restrict diffusion. This can be utilized for MR imaging to help identify and characterize lesions. Gradient pulses are applied to the tissues of interest; protons that have not moved or have only minimally moved in between the pulses (restricted diffusion) will demonstrate the highest signal on the image.

DWI has revolutionized imaging of the brain for stroke and tumor evaluation and has more recently become routine for breast and body MRI. It is used much less frequently in spinal imaging due to artifact from the heterogeneous, complex anatomy (air, fluid, osseous, and soft

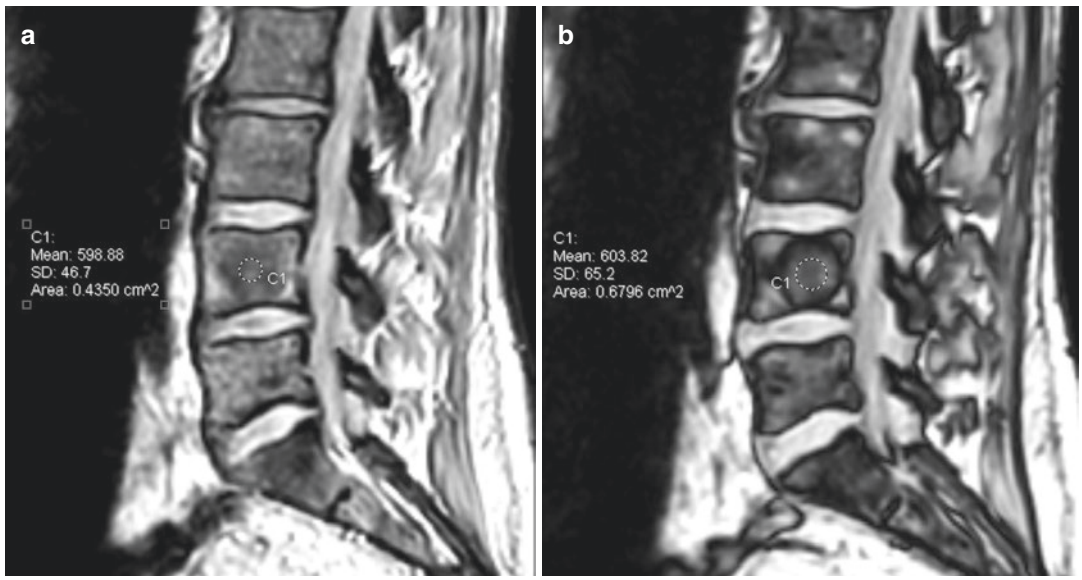

Fig. 1.14 In-phase (**a**) and out-of-phase (**b**) imaging is helpful to identify microscopic fat, a sign suggestive of a benign process. In this example, there is no drop in signal on out-of-phase imaging within the L4 lesion, which means there is no intralesional microscopic fat. This lesion was therefore deemed indeterminate and biopsy yielded a metastatic lesion

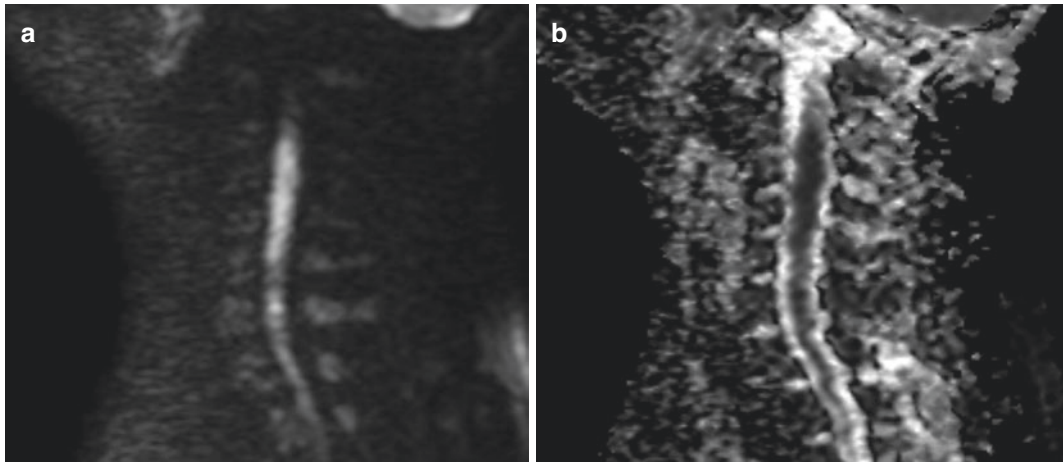

Fig. 1.15 Diffusion-weighted imaging (**a**) demonstrates increased signal within the expanded cervical cord in this young patient with sudden onset of paralysis, with low signal on the ADC map (**b**), highly suggestive of a cord infarct

tissues are all adjacent structures), motion artifact from breathing, and the relatively small size of the spinal cord for cord lesion characterization.

However, techniques to reduce these artifacts and obtain helpful diagnostic imaging have been created, and this sequence should be considered for troubleshooting indeterminate findings on routine imaging. Newer studies have shown DWI of the spine to be a useful adjunct for characterizing spinal cord lesions (infarcts, demyelination, myelomalacia, and tumors) in addition to intradural, epidural, and osseous lesions (Fig. 1.15) [9].

Advanced MRI Sequences

Dynamic Contrast-Enhanced Imaging

Dynamic contrast-enhanced (DCE) imaging acquires a series of MR images in succession after administration of intravenous contrast. This allows for characterization and quantification of the microvascular environment in the area of interest or "wash-in" and "wash-out" features of the lesion. A common feature among nearly all malignant processes is neoangiogenesis brought on by secretion of growth factors. Thus, DCE can help detect benign versus pathologic compression fractures, hypovascular and hypervascular masses, and the presence of residual or recurrent tumor post-treatment [10, 11].

Magnetic Resonance Angiography

Utilizing flow-related differences or contrast enhancement of vessels, magnetic resonance angiography (MRA) can help evaluate arteries and veins in and around the spine. This can assist in not only identifying dural arteriovenous fistulas and other vascular malformations but also in characterizing feeding and draining vessels (Fig. 1.16) [12–14]. Additionally, MRA can play an important role in preoperative planning to help identify the location of the artery of Adamkiewicz, critical spinal arteries, and veins to avoid inadvertent neurological damage.

Metal Artifact Reduction Sequence

For patients with spinal hardware, the MRI study must be optimized to minimize artifact from the hardware. This can be achieved using the methods discussed previously – avoid fat-saturation sequences, utilize STIR imaging, use low field strength magnets, obtain thinner slices, and adjust specific scan parameters such as bandwidth and matrix size. In addition, most vendors also include sequences with proprietary techniques to reduce metal artifact, such as MAVRIC (GE) and SEMAC (Siemens).

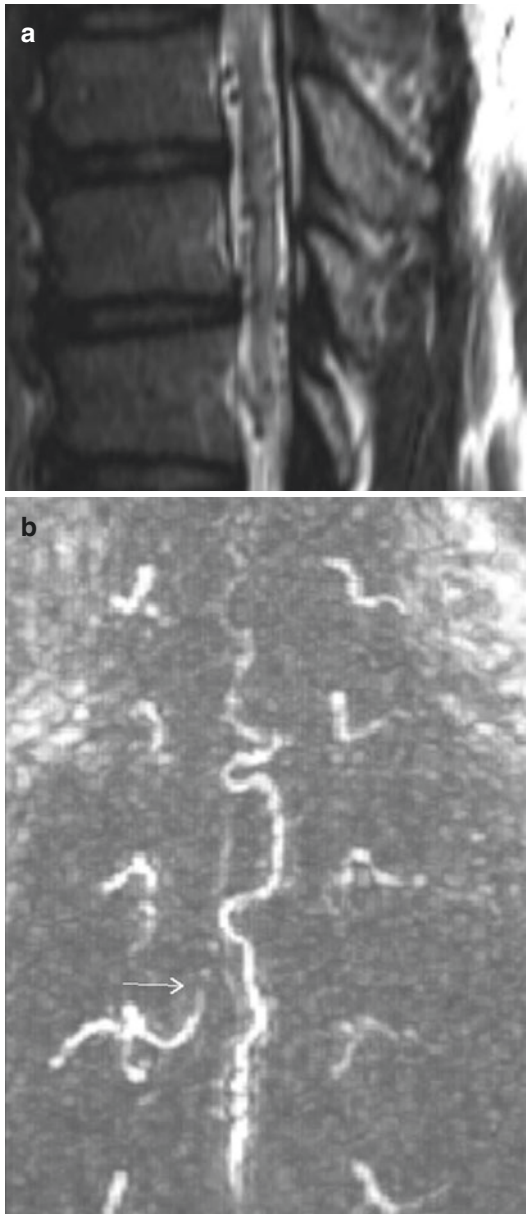

Fig. 1.16 Multiple flow voids are seen on T2-weighted imaging about the cord, a common finding for vascular lesions/anomalies (**a**). Magnetic resonance angiography confirms a dural arteriovenous fistula and identifies a possible feeding vessel (**b**)

Diffusion Tensor Imaging

Diffusion tensor imaging (DTI) is an extension of DWI, relying on movement of water molecules. DTI allows for detailed imaging of white matter tracts, as diffusion generally occurs in the path of least resistance (along the tracts, rather than perpendicular to them). DTI may be used to evaluate for cord damage in traumatic injury or in the integrity of and involvement of white matter in neoplastic processes [15, 16].

Functional MRI

Functional MRI (fMRI), originally utilized for brain imaging, has been adapted for use in the spine. Spinal fMRI depicts neural activity through changes in blood flow and blood oxygen levels about active gray matter. While still predominantly used for research purposes, fMRI clinically can be helpful in assessing areas of preserved and impaired function in spinal cord injury patients [17].

PET-MRI

While MRI is the imaging test of choice for evaluating bony and soft tissue anatomy and pathology in the spine, it does not provide physiologic information. The inclusion of positron emission tomography (PET) to MRI allows for high-spatial resolution imaging with soft tissue contrast *and* functional/physiological information. PET allows for assessment of metabolic activity of tissues through the administration of a radiotracer, most commonly 18F-fluorodeoxyglucose (18F-FDG). Tissues with high metabolic activity (most tumors, infection, inflammation) will have increased activity on PET imaging which can be overlaid on MRI for a detailed depiction. Often, the increased activity on PET precedes changes seen on MRI or CT allowing for earlier detection of pathology, such as metastatic disease.

Conclusion

MRI is crucial for evaluation of spinal anatomy and diagnosis of a broad spectrum of spinal pathologies. An understanding of basic MRI physics principles, routine imaging protocols, and techniques to optimize imaging quality is important for proper study interpretation, for knowing when to include more advanced sequences, and most importantly for ensuring the correct study is performed to answer the clinical question.

References

1. Pooley RA. Fundamental physics of MR imaging. Radiographics. 2005;25(4):1087–99. https://doi.org/10.1148/rg.254055027.
2. Morelli JN, Runge VM, Ai F, Attenberger U, Vu L, Schmeets SH, et al. An image-based approach to understanding the physics of MR artifacts. Radiographics. 2011;31(3):849–66. https://doi.org/10.1148/rg.313105115.
3. Bitar R, Leung G, Perng R, Tadros S, Moody AR, Sarrazin J, et al. MR pulse sequences: what every radiologist wants to know but is afraid to ask. Radiographics. 2006;26(2):513–37. https://doi.org/10.1148/rg.262055063.
4. Delfaut EM, Beltran J, Johnson G, Rousseau J, Marchandise X, Cotten A. Fat suppression in MR imaging: techniques and pitfalls. Radiographics. 1999;19(2):373–82. https://doi.org/10.1148/radiographics.19.2.g99mr03373.
5. Hao D, Ai T, Goerner F, Hu X, Runge VM, Tweedle M. MRI contrast agents: basic chemistry and safety. J Magn Reson Imaging. 2012;36(5):1060–71. https://doi.org/10.1002/jmri.23725.
6. Rogosnitzky M, Branch S. Gadolinium-based contrast agent toxicity: a review of known and proposed mechanisms. Biometals. 2016;29(3):365–76. https://doi.org/10.1007/s10534-016-9931-7.
7. Chong AL, Chandra RV, Chuah KC, Roberts EL, Stuckey SL. Proton density MRI increases detection of cervical spinal cord multiple sclerosis lesions compared with T2-weighted fast spin-echo. Am J Neuroradiol. 2016;37(1):180–4. https://doi.org/10.3174/AJNR.A4476.
8. Kenneally BE, Gutowski CJ, Reynolds AW, Morrison WB, Abraham JA. Utility of opposed-phase magnetic resonance imaging in differentiating sarcoma from benign bone lesions. J Bone Oncol. 2015;4(4):110–4. https://doi.org/10.1016/j.jbo.2015.10.001.
9. Tanenbaum LN. Clinical applications of diffusion imaging in the spine. Magn Reson Imaging Clin N Am. 2013;21(2):299–320. https://doi.org/10.1016/j.mric.2012.12.002.
10. Morales KA, Arevalo-Perez J, Peck KK, Holodny AI, Lis E, Karimi S. Differentiating atypical hemangiomas and metastatic vertebral lesions: the role of T1-weighted dynamic contrast-enhanced MRI. Am J Neuroradiol. 2018;39(5):968–73. https://doi.org/10.3174/AJNR.A5630.
11. Geith T, Biffar A, Schmidt G, Sourbron S, Dürr HR, Reiser M, Baur-Melnyk A. Quantitative analysis of acute benign and malignant vertebral body fractures using dynamic contrast-enhanced MRI. Am J Roentgenol. 2013;200(6):W635–43. https://doi.org/10.2214/AJR.12.9351.
12. Backes WH, Nijenhuis RJ. Advances in spinal cord MR angiography. Am J Neuroradiol. 2008;29(4):619–31. https://doi.org/10.3174/ajnr.A0910.
13. Saraf-Lavi E, Bowen BC, Quencer RM, Sklar EML, Holz A, Falcone S, et al. Detection of spinal dural arteriovenous fistulae with MR imaging and contrast-enhanced MR angiography: sensitivity, specificity, and prediction of vertebral level. AJNR Am J Neuroradiol. 2002;23(5):858–67.
14. Meckel S, Maier M, Ruiz DSM, Yilmaz H, Scheffler K, Radue E-W, Wetzel SG. MR angiography of dural arteriovenous fistulas: diagnosis and follow-up after treatment using a time-resolved 3D contrast-enhanced technique. AJNR Am J Neuroradiol. 2007;28(5):877–84.
15. Andre JB, Bammer R. Advanced diffusion-weighted magnetic resonance imaging techniques of the human spinal cord. Top Magn Reson Imaging. 2010;21(6):367. https://doi.org/10.1097/RMR.0B013E31823E65A1.
16. Sąsiadek MJ, Szewczyk P, Bladowska J. Application of diffusion tensor imaging (DTI) in pathological changes of the spinal cord. Med Sci Monit Int Med J Exp Clin Res. 2012;18(6):RA73–9. https://doi.org/10.12659/msm.882891.
17. Kornelsen J, Mackey S. Potential clinical applications for spinal functional MRI. Curr Pain Headache Rep. 2007;11(3):165–70. https://doi.org/10.1007/S11916-007-0186-4.

MRI in Spine Anatomy

2

Ajit Karambelkar

Embryology of the spine: Embryonically, the discs and the vertebrae develop from the notochord starting from the third week. The notochord then develops separately into the neural tube and somites. Somitogenesis is a process by which the paraxial mesoderm forms the somites [1]. The somites develop into the mesenchymal sclerotome ventrally and dermomyotome. The mesenchymal sclerotome contributes to building the vertebral column and ribs while the dermomyotome forms the paraspinal musculature and skin [2]. The early sclerotome divides into a ventral, central, dorsal, and lateral compartment, which will form the vertebral body, pedicle, neural arch, and the rib processes, respectively [3]. Further division in cranial and caudal half gives rise to adjacent vertebrae. The vertebral centra develop from the ventral sclerotome. This development occurs with the help of many positive and negative signals from the notochord, notably, positive signals from PAX1 expression [4].

The vertebral arch consists of lamina and pedicles. The ventral portion consisting of pedicles and the transverse processes originate from the central sclerotome, and the dorsal part of the pedicles, lamina, and the spinous process arise from the dorsal sclerotome [5]. The formation of the dorsal neural arch is related to the expression of the Msx 1 and Msx 2 genes [6]. The migration of the dorsal sclerotome cells over the roof plate of the neural tube requires PDGFR, TGF, and Zic 1 signaling pathway. Disruption of any of these pathways causes the failure of the dorsomedial closure of the bilateral vertebral lamina and results in spina bifida occulta-like phenotype [7–9]. Finally, vertebrae formation results from the unification of the cranial and caudal halves of the adjacent somites [10].

Notochord signals stimulate the ventral sclerotome which populates the perinotochordal space to form what is known as a perinotochordal sheath, which in turn provides mechanical support to the notochord. Subsequently, a pattern of dense and loose mesenchyme develops in the perinotochordal sheath. Loose mesenchyme gives rise to vertebral bodies, and highly proliferative cell population of dense mesenchyme gives rise to annulus fibrosus [11]. The notochord degenerates at the level of the vertebral bodies and eventually persists only at the level of the intervertebral discs to form the nucleus pulposus. At birth, the cells of the nucleus pulposus are the same as the cells of the notochord and later replaced by a smaller type of cells, capable of holding water and type II collagen together [12, 13].

The tendons of the back muscles originate from a sclerotomal subcompartment, the syndetome. The syndetome lies in the dorsolateral sclerotome in two separate portions at the cranial and caudal margin of the sclerotome, directly

A. Karambelkar (✉)
Thomas Jefferson University Hospital Philadelphia, Philadelphia, PA, USA
e-mail: Ajit.Karambelkar@jefferson.edu

W. B. Morrison et al. (eds.), *MRI of the Spine*, https://doi.org/10.1007/978-3-030-43627-8_2

beneath the myotome. Development of the vertebral ligaments which connect the adjacent bony elements is still unclear.

Basic Anatomy

Vertebrae: The typical human spine is composed of a total of 33 vertebrae, of which 5 lumbar-type and 23 presacral vertebrae are found in almost 90% of individuals. Two percent of individuals have four lumbar-type vertebrae, while 8% have six lumbar-type vertebrae with lumbarization of S1 [14].

C1 (atlas) is a bony ring. Posterior arch of the C1 is longer and carries a groove on the superior surface, which is occupied by horizontal V3 segments of the vertebral artery (Figs. 2.1, 2.2 and 2.3). The lateral masses bear the superior and inferior facets and articulate respectively with occipital condyles superiorly and superior articular facets of C2 inferiorly (Figs. 2.4 and 2.5).

C2 (axis) has dens or odontoid process that projects upward from the body of the C2. The odontoid process articulates with the posterior aspect of the anterior arch of C1 (Fig. 2.6). There are two superior articular facets which are just lateral to the dens to articulate with the inferior articular processes of the C1 (Fig. 2.5). The lateral mass has forward facing facet along undersurface, which articulates with the superior articular process of the C3.

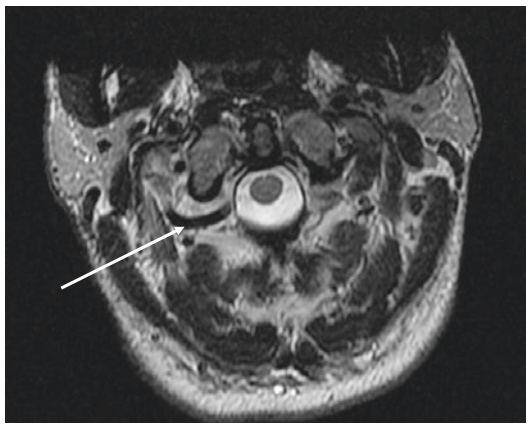

Fig. 2.1 Right vertebral artery

Subaxial, third to seventh, cervical vertebrae are morphologically similar having a central body with superior and inferior endplates, facets, and transverse processes as well as posterior neural arch. The dorsal neural arch is composed of lateral masses and lamina one on each side. The laminae fuse to give rise to the spinous process. Lateral masses of the cervical vertebra have on either side a foramen transversarium through which the vertebral artery transmits from C6 to C2 (Figs. 2.1 and 2.3). There may be more than one foramen transversarium on each side.

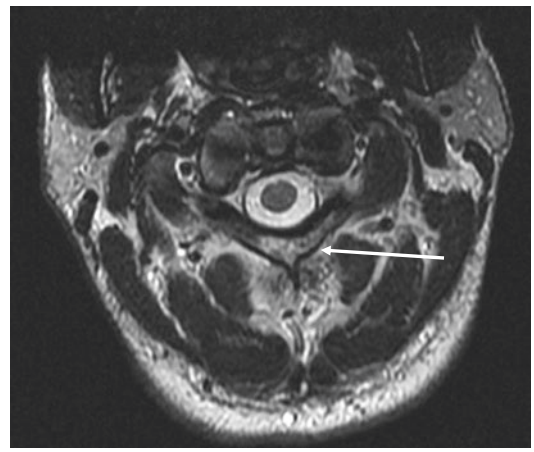

Fig. 2.2 Posterior arch of C1

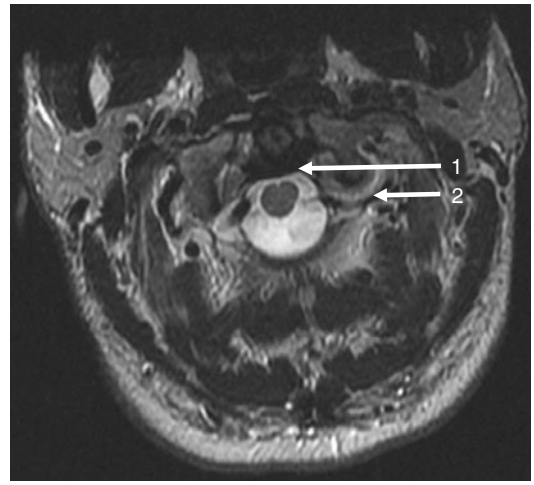

Fig. 2.3 1: Transverse ligament, 2: Vertebral artery

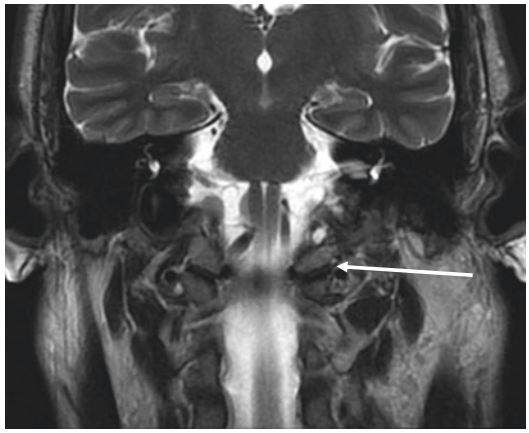

Fig. 2.4 Atlantooccipital joint

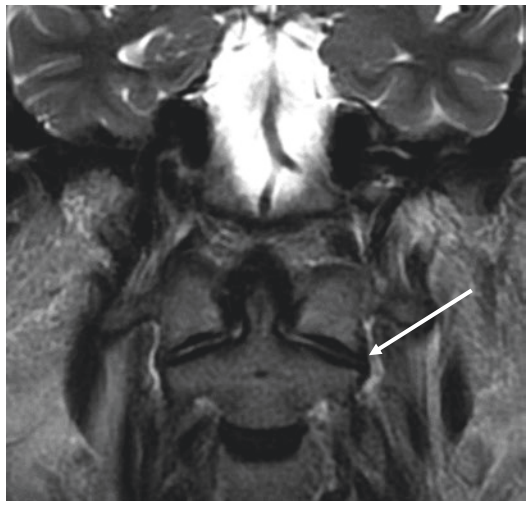

Fig. 2.5 Atlantoaxial joint

Uncinate Processes and Uncovertebral Joints Uncinate processes are at the posterolateral aspect of the superior endplate of the C3 to C7 vertebral bodies. The uncovertebral process is phylogenetic residua of the costovertebral joints in reptiles and birds [15] (Fig. 2.7). The medial surface of the uncovertebral process articulates with the inferior surface of the vertebral body above to form the uncovertebral joint. Uncovertebral joints evolve from rudimentary to mature joint and then degenerate over a lifetime. The distance between the uncinate process' upper margin and neural foramen is smallest at C5 and highest at C3 [16]. The uncovertebral articulation

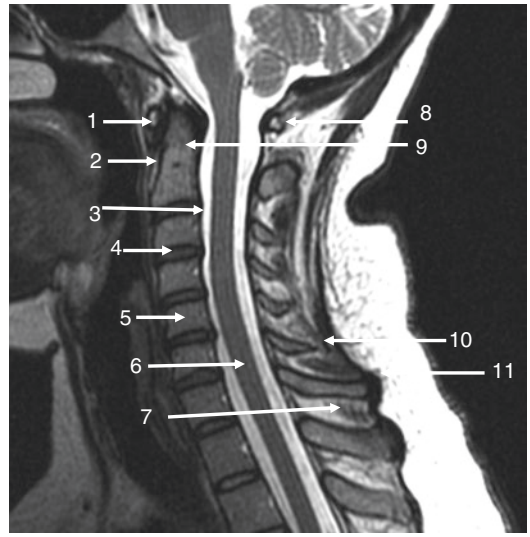

Fig. 2.6 1: Anterior arch of C1. 2: Anterior longitudinal ligament. 3: Posterior longitudinal ligament. 4: Disc. 5: Vertebral body. 6: Spinal cord. 7: Interspinous ligament. 8: Posterior arch of C1. 9: Dens. 10: Spinous process. 11: Supraspinous ligament

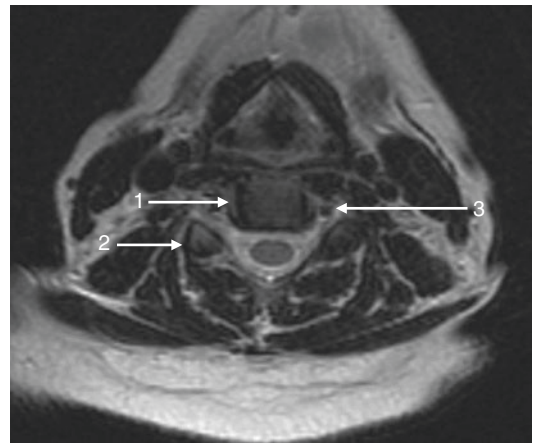

Fig. 2.7 1: Uncovertebral process. 2: Facet joint. 3: Vertebral artery

was found to contribute more than 60% of the stability of the spinal motion segment in extension at C3–C4 [17]. The uncovertebral joint forms the anteromedial margin of the neural foramen [16]. The nerve roots and lateral spinal cord are related to the posterior aspect of the uncovertebral joints. As the nerve roots pass through the intervertebral foramen, they are in the lower third

of the space with the apex of the uncovertebral process situated above each root. Intervertebral foramen at the cervical spine forms an angle of 45 ° with the coronal plane and extends forward from the vertebral channel [18, 19].

Thoracic and Lumbar Vertebrae The typical thoracic or lumbar vertebra has a body, posterior neural arch, facets and transverse processes on each side, and a single midline spinous process. The vertebral bodies increase in size inferiorly. The dorsal neural arch consists of pedicle and lamina. Two superior and inferior articular processes articulate with those of vertebra above and vertebra below, respectively, to form the facet joints (Fig. 2.8). The spinous process projects posteriorly and inferiorly from the vertebral arch and overlaps the inferior vertebra (Fig. 2.9).

The thoracic vertebrae have three facets on each side for the articulation of the ribs. Superior articular facets are directed postero-lateral and allow for rotation, flexion, and extension. The lumbar articular facets are vertical with the superior articular processes directed posteromedially with curved articular surface, which allows the movement in flexion and extension and lateral flexion but limits rotation [12].

Ligaments There are intrinsic and extrinsic types of ligaments supporting the craniocervical junction. MRI can demonstrate normal tectorial membrane and transverse ligaments. The ligaments are a low signal on T1 and T2 and better seen if there is surrounding blood and fluid. Alar ligaments have an oblique vertical course and insert on to the occipital condyles and adjacent superior aspect of the lateral mass of C1, although, in approximately one-third of individuals, it exclusively inserts on occipital condyles. Alar ligaments are not commonly seen on MRI, individually.

Transverse Ligament The transverse ligament is a vital component of the cruciform ligament, the largest, strongest craniocervical ligament (mean height/thickness 6–7 mm) [12]. The superior and inferior components of the cruciform ligament provide no significant craniocervical stability. The transverse ligament maintains stability at the craniocervical junction and divides

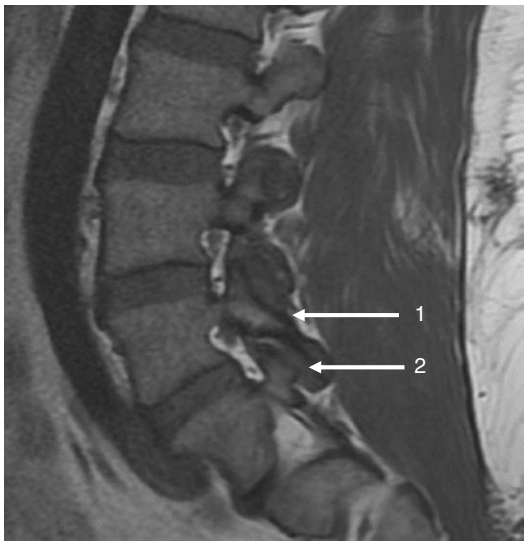

Fig. 2.8 1: Inferior articular facet of L4. 2: Superior articular facet L5

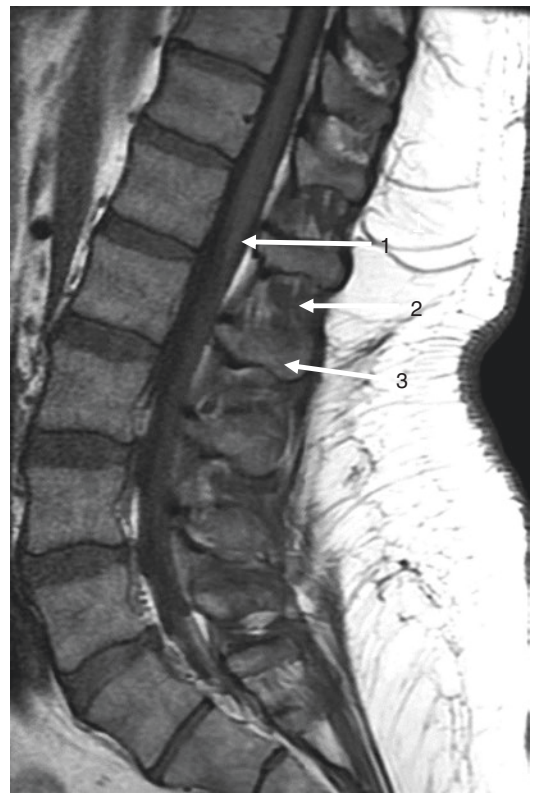

Fig. 2.9 1: Conus. 2: Interspinous ligament. 3: Spinous process

the ring of the atlas into an anterior compartment which houses the odontoid process and posterior chamber which contains the spinal cord and spinal accessory nerves. The transverse ligament fixes the odontoid process anteriorly against the posterior aspect of the anterior arch of C1 (Fig. 2.3). The transverse ligament attaches to the lateral tubercles of the atlas bilaterally, dorsal to the odontoid process of C2. Smooth gliding movement occurs between the odontoid process and the transverse ligament owing to the presence of synovial capsule and fibrocartilaginous surface [12].

There are several other ligaments in the cervical spine including anterior atlantooccipital membrane, anterior atlantoaxial membrane, anterior longitudinal ligament, posterior occipitoatlanto membrane, posterior atlantoaxial membrane, nuchal ligament, flaval ligaments, and interspinous and supraspinous ligaments (Figs. 2.1 and 2.2). Ligaments are a low signal on T1 and T2 and better seen when there is a contrast with the surrounding tissue such as blood or fluid or injured (Fig. 2.6).

Disc Intervertebral discs are located between the vertebral bodies and contribute about one-third of the height of the spinal column. The disc is made up of central gelatinous nucleus pulposus and the peripheral annulus fibrosus. The discs are attached to the bony endplates of the vertebral bodies with hyaline cartilage endplates (Fig. 2.10).

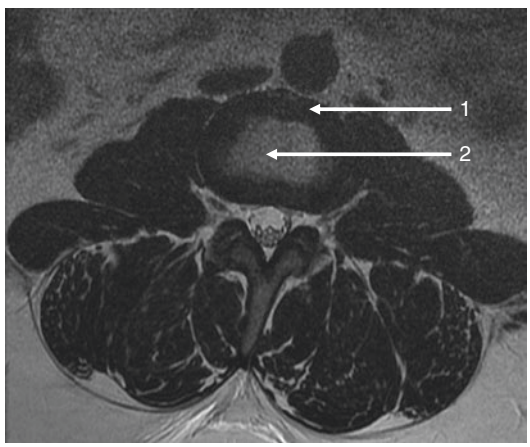

Fig. 2.10 1: Annulus fibrosus. 2: Nucleus pulposus

Nucleus pulposus provides spine mechanical flexibility and strength [20]. It bears the stresses on the spine and redistributes to the annulus fibrosus and the endplates. The cells of the nucleus pulposus express Fas ligand, which is responsible for the apoptosis of vascular endothelial cells. The vessel growth within the nucleus pulposus is weak due to suppression of the vascular endothelial growth factors [21, 22]. Therefore, the disc is mainly supplied from cartilaginous endplates via diffusion or gets blood supply from the vascularized annulus fibrosus [23]. Annulus fibrosus is a structure made up of collagenous tissue at the periphery of the nucleus pulposus. Cartilaginous endplates provide the mechanical barrier and transport nutrients for the disc.

Paraspinal Muscles The back muscles consist of smaller individual muscles arranged symmetrically in pairs separated by the spinous processes, interspinales muscles, and ligamentum nuchae. The paravertebral muscles consist of large muscles which extend from the base of the skull to the sacrum. The splenius capitis, semispinalis capitis, and longissimus capitis are the prime extensors of the head and neck. The splenius capitis arises from the C3 to T3 spinous processes and inserts on the superior nuchal line. The splenius cervicis arises from the T3 to T6 spinous processes and first three cervical transverse processes, respectively. Immediately deep to these muscles lie smaller semispinalis capitis and longissimus capitis. Levator scapulae, multifidus, and interspinales muscles are less bulky and located more centrally. Trapezius muscles are separated from the paraspinal muscles by fat. On cross-sectional imaging, the mid-cervical images demonstrate longissimus capitis and cervicis while the multifidus and semispinalis cervicis more medially (Figs. 2.11 and 2.12).

Splenius and semispinalis capitis, as well as cervicis muscles, lie deep to the trapezius muscles in the lower cervical spine. The paraspinal musculature may be the site for inflammatory or neoplastic processes and vascular malformations. The posterior elements such as lamina and the spinous processes of the vertebral body serve as the framework for the muscles of neck extension [24].

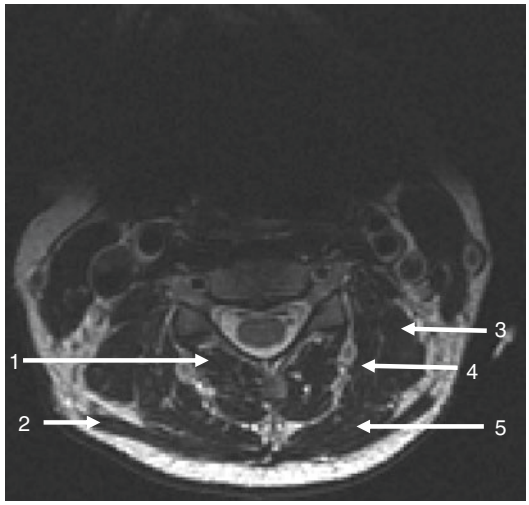

Fig. 2.11 1: Semispinalis cervicis. 2: Trapezius. 3: Levator scapulae. 4: Splenius capitis. 5: Semispinalis capitis

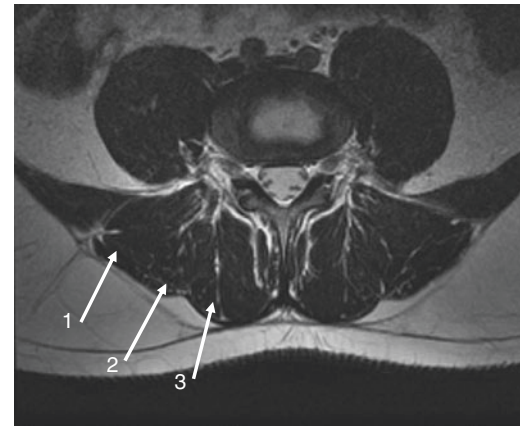

Fig. 2.12 1: Iliocostalis. 2: Longissimus. 3: Multifidus

The lower paraspinal muscles provide stabilization to the lumbar spine and act as an initiator for movement. The intersecting imaginary line passing through the transverse processes divides the paraspinal muscles into the anterior and posterior groups based on the imaginary plane passing through the transverse processes. Erector spinae group consists of multifidus medially and longissimus intermedius, and iliocostalis laterally (Fig. 2.12). They are also the primary extensors of the trunk at the lumbar spine. The multifidus has five fascicles arising from the spinous processes and laminae and attaches to the mammillary, accessory, and zygapophyseal processes and joint capsule and posterior superior iliac spine and sacrum. The multifidus maintains the stability of the lumbar spine. The superficial fibers are responsible for the spine orientation and the deep portion for intervertebral shear and torsion.

The longissimus muscles are slender and lie between the multifidus and the iliocostalis. The bundles of the longissimus arise from the accessory processes from L1 to L4 and extend to both the adjacent transverse processes, the mamillo-accessory ligament, and mammillary process. The bundle from L5 typically continues along the transverse process and over the accessory process to the mamillary process. The L1-L4 fascicles join the fascicle arising from the posterior surface of the L5 transverse process, which converges to form a common tendon of insertion, named as the lumbar intermuscular aponeurosis. The iliocostalis muscle arises from the tips of the transverse processes and the adjacent medial layer of the thoracolumbar fascia, which then inserts on the iliac crest lateral to the posterosuperior iliac spine. The erector spinae is supplied by lumbar dorsal rami which divide into medial, intermediate, and lateral branches. The medial branches provide the multifidus muscles. The intermediate branches supply the longissimus muscles. Lateral branches of L1-L4 supply the iliocostalis lumborum [25].

Prevertebral Soft Tissue Evaluation of the prevertebral soft tissues is difficult on radiographs and CT due to limited ability to differentiate the anatomical structures from the abnormal soft tissue pathologies such as hematoma, edema, or abscess. Increase in soft tissue thickness has been proved to be a good indicator of underlying ongoing pathology. Rojas et al. described the upper limits for normal cervical prevertebral soft tissue in cervical spine measuring 8.5 mm at C1, 6 mm at C2, 7 mm at C3, and 18 mm each at C6 and C7. Although the typical thickness does not exclude any underlying soft tissue injury or infection [26]. MRI can directly demonstrate the underlying pathology due to its better soft tissue resolution.

Spinal Epidural Space The spinal epidural space spans from the fusion of the spinal and periosteal layers of the dura at the foramen magnum to the sacrococcygeal membrane caudally (Fig. 2.6) [27]. Posterior longitudinal ligament, vertebral bodies, and the intervertebral discs form the anterior margin while the ligamentum flavum, capsules of the facet joints, and laminae are the posterior margin of the epidural space. Laterally, pedicles and intervertebral foramina form the lateral boundaries. Spinal epidural space is real space at the intervertebral level, and potentials are at the vertebral level as the dura fuses with the posterior longitudinal ligament and the annular ligament. Epidural space is most extensive, and posterior area measures 7.5 mm at the upper thoracic levels and 0.4 mm and 4–7 mm at cervical and lumbar levels, respectively (Fig. 2.13) [28].

Fat is the most prominent component of the epidural space. Dorsal epidural fat varies significantly in its thickness. Abundant dorsal epidural fat can accentuate the degenerative spinal canal narrowing.

The venous drainage of the epidural space is via Batson's plexus. It consists of external and internal venous plexus and enters intraosseous veins of the vertebral column [29]. There are two anterior and two posterior interconnecting longitudinal veins in these venous plexuses, and they connect with the various intracranial, cervical, intercostal, lumbar, and iliac veins [30]. Since the vertebral venous system is valveless, the root of infection and malignancy is commonly hematogenous. The dorsal epidural venous plexus varies larger in the dorsal and cervical region relative to the lumbar area.

Spinal Canal The bony spinal canal diameters measured with MRI are at L1 < 20 mm, L2 < 19 mm, L3 < 19 mm, L4 < 17 mm, L5 < 16 mm, and at S1 < 16 mm [31, 32].

Intervertebral foramen: Cervical neural foramen has three parts – medial area where there is ample space about the nerve root and related to ligamentum flavum posteriorly. Middle area is the narrowest with uncinate process anteriorly and posterior facet joints posteriorly. Cervical spinal ganglion, spinal nerve, and vertebral artery lie within the lateral portion and vertebral artery. The spinal ganglion lies between the vertebral artery and the posterior facet posteriorly. The axis of the cervical neural foramen is 45 ° forward to the sagittal plane and 20 mm in length [33].

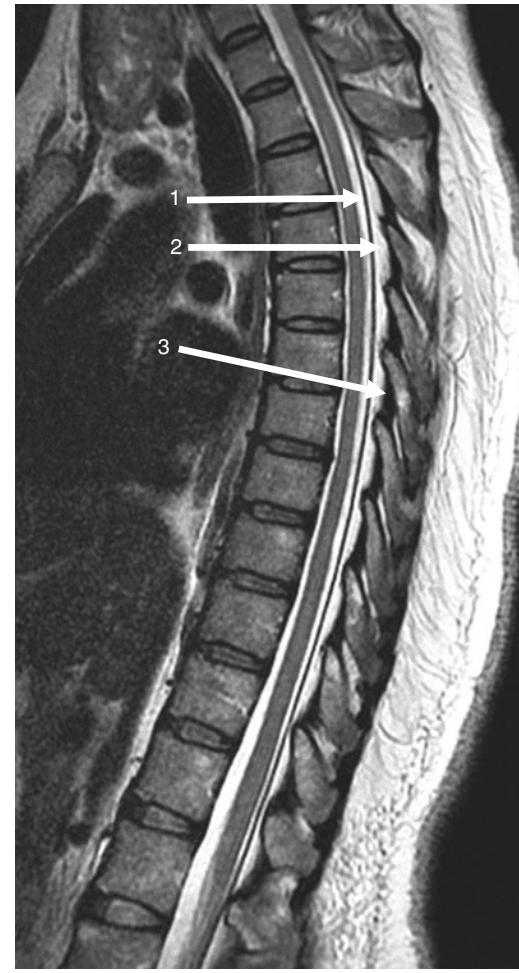

Fig. 2.13 1: Posterior dural margin. 2: Dorsal epidural space containing fat. 3: Ligamentum flavum

The cervical nerve is a confluence of the anterior and posterior root. The anterior root is thin and consists of four to seven rootlets from the anterior collateral sulcus of the spinal cord. The dorsal sensory root is threefold larger and consists of four to ten rootlets that penetrate the posterior collateral sulcus [34]. Each dorsal root ganglion lies at the periphery of the spinal

canal near the intervertebral foramen. Beyond the dorsal root ganglion, the ventral root combines with the dorsal root to form a spinal nerve (Fig. 2.14).

Lumbar foramen (Fig. 2.15) has a superior, rigid portion which carries the nerves and radiculomedullary arteries and the inferior dynamic portion which is affected by disc. The pedicle is posterior, and the posterior body is anterior to the superior part of the neural foramen. The disc is anterior, and the lamina is posterior to the inferior part of the neural foramen of the lumbar spine. The lumbar neural foramen is oval with a long vertical axis – the L5-S1 neural foramen in the most round but smaller to another lumbar foramen. Dorsal root ganglion fills most of the neural foramen. The size of the foramen is largest in maximum flexion as pedicles are most separated and disc convexity is minimum. In maximum extension, the size of the neural foramen is smaller by 20%, with disc protruding dorsally pedicles are closer together, and ligament flavum is pushed forward by the superior articular process of the vertebra below. During extension, there is no compression of the nerve root if the disc is preserved in height, but gets compressed with moderate size disc collapse of 4 mm, even with the absence of posterior articular osteophytes [35–37].

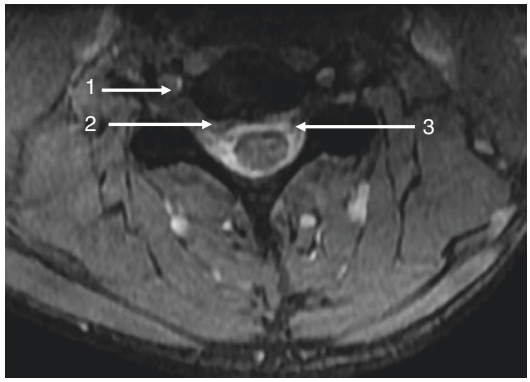

Fig. 2.14 1: Dorsal root ganglia. 2: Ventral nerve root. 3: Dorsal nerve root

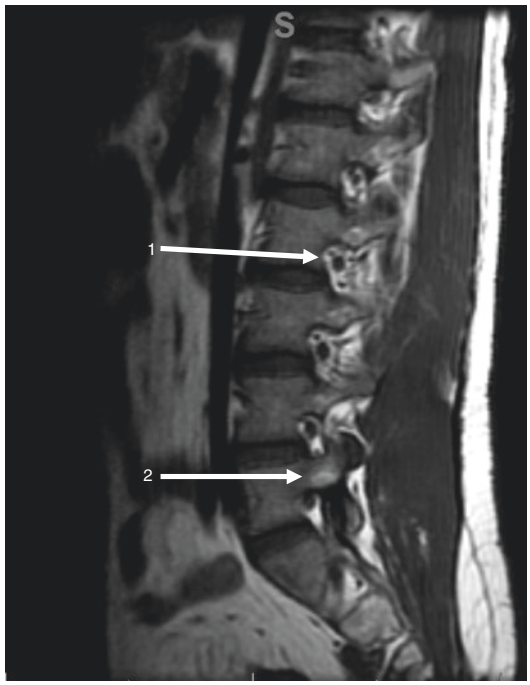

Fig. 2.15 1: Lumbar neural foramen. 2: Pedicle of L5 vertebral body

Nerve Roots The spine consists of 8 cervicals, 12 thoracic, 5 lumbar, 5 sacral, and 1 coccygeal paired spinal nerves. CT myelogram and MRI 3D T2 acquisition can demonstrate the course of the spinal nerves. C1 is the first sensory nerve and exists above the C1-C2 interval. C2 nerve exits through the C1-C2 and C3 nerve from C2-C3 so on till C8 nerve passes through the C8-T1. In the cervical spine, disc herniations affect the same numbered nerve root below the same numbered vertebra, for example, C5-C6 disc herniation affects C5 nerve root as it has flatter course compared to the lumbar nerves and located higher in the neural foramen. Cervical cord roots exit the spinal cord laterally corresponding to the vertebra, i.e., the C7 nerve root exits the neural foramen between the C6 and C7 and C8 between C7 and T1. The nerve roots are at the disc plane in the cervical spine and separated from the discs by the uncinate process.

Below C8, the nerve roots exit below the level of named vertebrae, such as T1 nerve passes through T1-T2 and T12 nerve passes between T12-L1.

Similarly, in the lumbar spine, L1 nerve root traverses below L1 vertebra and L5 nerve root

below L5 and above S1 vertebrae. There is one exiting and traversing nerve root at any lumbar disc level, for example, at L5-S1 disc level, there is an exiting L5 and traversing S1. The lumbar vertebrae are taller than thoracic and cervical region, developmentally. Hence, the exiting L5 nerve root is higher in location compared to the L5-S1 disc in neural foramen. Thus, the disc herniations often affect the S1 traversing nerve, which is at a lower level than the L5 exiting nerve at the same disc space.

The lumbosacral nerve roots come off the conus medullaris and course down the lumbar spinal canal. They separate from the cauda equina one level above the corresponding neural foramina. The lateral recess is the lateral most of the spinal canal, which is defined by pedicle laterally and zygapophyseal joint medially. The nerve root is traversing in the lateral recess and becomes exiting at the neural foramen, which is below that level, e.g., traversing L5 nerve root at L5 is exiting at L5-S1 neural foramen. The anterior root is narrow caliber and carries motor information. The cell bodies of sensory neurons lie in the dorsal root ganglion, near the neural foramen (Fig. 2.16).

The roots below the L1 occupy the spinal canal and resemble a horse's tail and hence are collectively termed as cauda equina. Since there is discordance between the levels of the myelomeres and corresponding numbered vertebrae, the lower roots are increasingly obliquely oriented. Hence, they are longer and thicker in the lumbosacral canal, relative to the upper portion of the body. Thus, the lumbar nerves increase in size from L1-2 to L5-S1, but the foramina decrease in size. Therefore, L5 roots, although thickest, have to traverse through the smallest foramen.

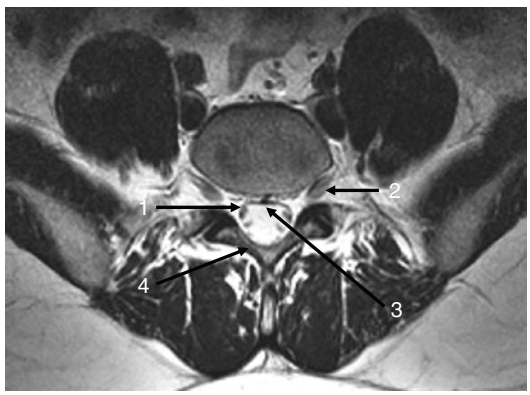

Fig. 2.16 1: Traversing nerve roots. 2: Dorsal root ganglia. 3: Anterior dural margin. 4: Lamina

Spinal cord develops from neurulation, canalization, and regressive differentiation. Neurulation is a progressive fusion of the lateral edges of the neural plate at the level of 3rd and 4th somite and then progresses cranially and caudally and starts at 3 weeks of embryonic age. The closure of the tube occurs at 23 and 26 days, respectively.

The spinal cord is about 45 cm in length spans from foramen magnum as an extension of the medulla oblongata and to the level first or second lumbar vertebra. The width ranges from 1.27 cm in cervical and lumbar regions and 64 mm in the thoracic region. The spinal cord has central H-shape gray matter and peripheral white matter. Gray matter: spinal cord has two symmetrical halves connected in midline via a commissure. The gray mater surrounds the central canal within the midline commissure – an imaginary line through the midcoronal divides into the anterior and posterior column.

The spinal cord has cervical and lumbar expansions at the level of attachment of the nerves. The conus is the inferior-most conical and caudal-most segment of the spinal cord. The conus terminates at a slightly lower level at L1-L2 in newborns and children to the age of 12 years [37]. Studies with MRI demonstrated that females could have longer cord and termination at L1-2 while that of males at T12-L1 [38]. Dural sac terminates at upper third S2 in men and middle third of S2 in women [39]. The conus medullaris ends most commonly at the lower level of the L1 followed by upper and intermediate levels of the L1. The location of the conus does not vary with the flexion or extension positions [40]. Conus ventricularis terminalis or fifth ventricle is a cystic cavity within the conus. It is considered as a regular step in the development of the spinal cord and may occur independently or as a part of Chiari malformation. The canalization and regressive differentiation process develop the conus medullaris and the filum terminale. The ventricularis terminalis develops from a second neural tube [41]. Inferiorly, the spinal

nerve roots and meninges occupy the lumbar spinal canal. Filum terminale is a fibrous extension of the spinal cord down to the coccyx.

The spinal cord has posterior median sulcus and anterior median fissure. Dorsal and ventral rootlets are attached laterally to the anterior median fissure. The segment of the spinal cord is called a myelomere to which a given pair of roots connects. The myelomeres are located above their corresponding vertebrae since the spinal cord does not span through most of the lumbar and sacral canal.

The spinal cord is anchored to the dura by the denticulate ligaments 20 or 21 pairs which decide the surgical landmark for the anterolateral segment of the spinal cord. The central canal spans from the fourth ventricle to the upper part of the filum terminale. Lipoma of the filum terminale is fat signal within the filum terminale (FTL) with >2 mm thickness, and studies proved that FTL is asymptomatic; however, most symptomatic patients had low conus. Variation in the width, length of the lipoma, and the distance from the symptomatic presentation does not correlate with symptoms. However, asymptomatic pediatric patients with low conus should be followed up, and treatment is beneficial for symptomatic patient with untethering (Fig. 2.17) [42].

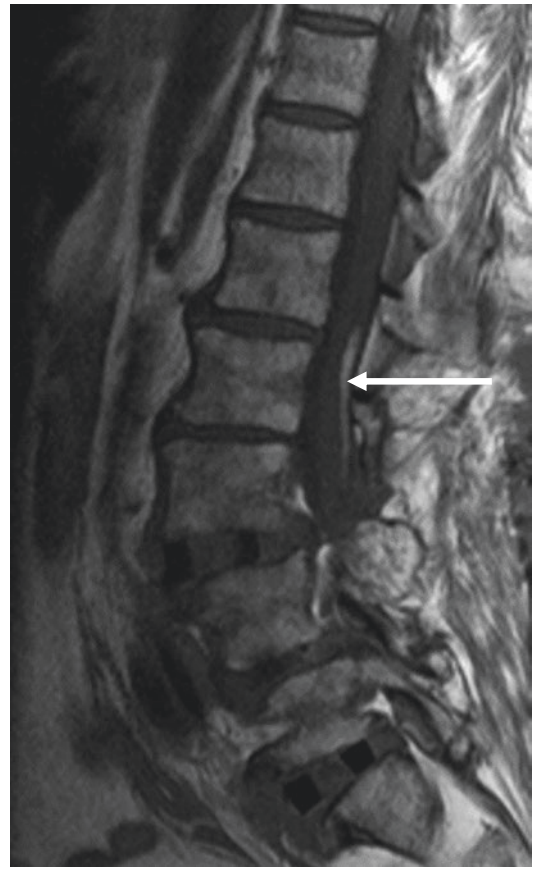

Fig. 2.17 Filum terminale lipoma

Segments There are a total of 31 spinal segments, including 8 cervical, 12 thoracic, 5 dorsal, and 1 coccygeal. They have paired dorsal and ventral roots and a pair of the spinal nerves except for the first cervical segment, which has only ventral root. The cervical and lumbar enlargements give off the branches to the upper and lower extremities, respectively.

The cord is divided into two halves by a deep anterior median fissure and a shallow posterior median sulcus the anterior fissure contains a double folded pia and floor is white commissure. The anterolateral sulcus is the exit of the ventral roots. The posterior median sulcus is the site of the posterior nerve root entry. Three funiculi separate the white matter of the cord, anterior, posterior, and lateral funiculus, which lies between the dorsal and ventral roots. Anterior funiculus lies between the anterior fissure and the ventral roots. Posterior funiculus lies between the posterior sulcus and the dorsal roots. Dorsal funiculus consists of fasciculus cuneatus and gracilis, which carry the signal for the position, vibration, and light touch. The fibers from lower extremity are positioned medially in the fasciculus gracilis. Subsequently, the lower extremity fibers are added laterally in the fasciculus cuneatus.

Pain pathway consists of a first-order neuron, which receives the information from peripheral sensory receptors to the dorsal funiculus. The second-order fiber extends from the dorsal funiculus after crossing to the contralateral side forming the medial lemniscus in the medulla. Ultimately, the medial lemniscus fibers terminate in ventral posterolateral nucleus of the thalamus [43].

Lateral funiculus contains spinocerebellar tracts which carry fibers transmitting the posi-

tion, sense, touch, and pressure sensing to the cerebellum. The lateral spinothalamic tract is located more medially in the lateral funiculus. It is a primary pain pathway transmitting pain and temperature sensation. The ventral spinothalamic tract is situated anterior to lateral spinothalamic tracts and carries the light touch and pressure sensation. The upper extremity fibers displace the lower extremity fibers laterally [43, 44].

The first-degree neuron of the spinothalamic pathway ends in the lamina I, II, or IV and V of the spinal cord gray matter. Here second-order neuron originates which crosses the midline and ascend the spinal cord to terminate in the ventroposterolateral nucleus of the thalamus. Collateral fibers from VPL connect to the reticular formation and periaqueductal gray at this level. Then the third-order neuron projects from the thalamus to the somatosensory cortex [45]. There are two primary pain pathways: medial attentional pathway and lateral discriminatory pathway. Nociceptive-specific neurons trigger the medial pathway. They pass from lamina I of the spinal horn to the mediodorsal and ventromedial nucleus of the thalamus and then to the anterior cingulate cortex, anterior insula, and amygdala. The neurons in the lateral system pass from lamina I and IV–VI of the dorsal horn to the ventroposterolateral nucleus of the thalamus to the primary somatosensory cortex [46].

The anterior root bundles constitute the motor output from the spinal cord. These anterior roots supply the striated muscles and the preganglionic autonomic motor fibers. After the joining of the ventral and dorsal roots, the nerve divides into smaller primary dorsal ramus and a broader ventral ramus. Dorsal ramus consists of a medial sensory branch and a lateral motor branch to supply the skin and the paraspinal muscles at the segmental level. The ventral ramus is longer and forms the brachial and lumbosacral plexuses and segmental branches to the intercostal nerves. The spinal nerve is formed by the dorsal/sensory root and ventral/motor root.

The dorsal root ganglion is distal dilation of the dorsal root just proximal to its joining with the ventral root to form the spinal nerves. There are no synapses within the dorsal root ganglion termed as pseudounipolar.

The spinal cord receives blood supply from multiple arteries from the aorta and its branches throughout the length, which traverse through the neural foramen. In the early embryonic period, each spinal nerve root has a radicular artery which divides in anterior and posterior branch supplying a spinal cord segment. Radicular arteries are branches of the vertebral arteries in the cervical spine. In the thoracic and lumbar spine, aorta gives off collateral arteries which divide into anterior and posterior end arteries. The anterior end arteries include intercostal or lumbar arteries (Fig. 2.18). The dorsal spinal arteries divide into a large artery supplying the posterior paraspinal muscles, and a smaller radicular artery goes to the neural foramen accompanying the spinal nerve. The radicular artery divides into the anterior and posterior artery. The radicular arteries measure 0.2–2 mm, with the anterior artery being broader than that of dorsal. Posterior radicular arteries lie behind the dorsal roots. There are three types of radicular arteries: radicular, radiculopial, and radiculomedullary arteries. Radicular arteries are

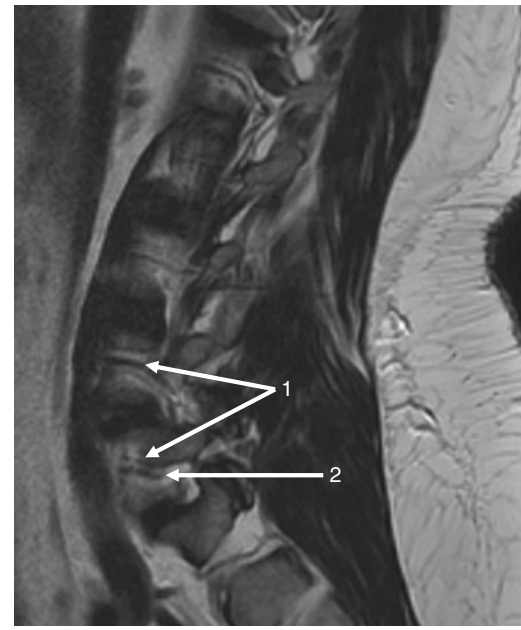

Fig. 2.18 1: Lumbar vein. 2: Lumbar artery

tiny and end at the roots before reaching the cord. The radiculopial arteries terminate at the pial plexus and supply the white matter of the anterolateral funiculi. The radiculomedullary arteries at the dorsolumbar junction provide blood supply to pial plexus and the gray and deep white matter of the spinal cord. The most important artery is the artery of Adamkiewicz, while the most common are the ninth and tenth dorsal arteries [46].

Intracranial vertebral arteries give off two anterior spinal arteries, which feed the upper cervical cord. Anterior radiculomedullary artery arises from the posterior dorsal spinal branch of the fourth or fifth left intercostal artery and feeds the 3–9 thoracic segments. Anterior radiculomedullary artery from the cervicointercostal trunk traverses along with the C7-T1 nerve roots and is the primary feeder for cervical enlargement and upper thoracic cord [47].

A thin anterior radiculomedullary artery feeds the 3–9 thoracic segment which arises from the posterior dorsal spinal branch of the fourth or fifth left intercostal artery in 80% of cases.

The radiculomedullary artery of the lumbosacral enlargement, artery of Adamkiewicz, feeds the lower thoracolumbar cord, and it arises from the left side in almost 85% of persons [48]. Venous drainage follows the arterial drainage.

Nerve Supply The ventral aspect of the cervical spine gets supplied by nerve plexus along the anterior longitudinal ligament contributed from the sympathetic trunk, rami communicantes, and sinuvertebral nerve (recurrent meningeal) and perivascular plexus [49–51]. The medial branches of the dorsal rami provide the dorsal cervical spine. These branches supply the zygapophyseal joints, ligamentum nuchae, ligamentum flavum, and a portion of the dura [51]. The vertebral nerve provides the small branches to the zygapophyseal and intervertebral joints. Medial branches of the posterior rami provide nerve supply to the thoracic spine [52].

The anterior lumbar spine is innervated from the anterior nerve plexus spinal nerve, sympathetic trunk, and the rami communicantes. Splanchnic nerves through sympathetic trunk also supply the ventral lumbar spine.

Dorsal innervation pathway is common in the cervical, lumbar, and thoracic spine. The posterior lumbar spine is innervated by posterior nerve plexus, with a notable contribution from sinuvertebral nerve through intervertebral foramen [53]. Lateral portions of the vertebral bodies receive innervation from the ventral and deep transverse and superficial oblique rami. Dorsal rami supply the lumbar zygapophyseal joints at the same levels [54, 55].

Meninges Dura, arachnoid, and pia cover the spinal cord from the outer to inner toward the cord. At the foramen magnum, the meningeal layer of the dura descends as the dural sleeve of the spinal cord. Epidural space lies between the dura and spinal canal and contains a layer of fat. Subdural space is the potential space within the arachnoid and pia mater.

Bone Marrow MRI is the best noninvasive imaging technique to evaluate bone marrow. It is essential to know the typical appearance of the bone marrow and its variations according to the age and physiological changes to distinguish from pathological conditions. The marrow is the main organ of hematopoiesis after 24 weeks of gestation. Red marrow is the active and predominant form of the marrow at the birth. Yellow marrow gradually replaces the red marrow, particularly in the spine, as the age progresses. The normal distribution of the red and yellow marrow varies according to the age and stabilizes to an adult pattern by the age of 25 years. Healthy marrow is composed of an intermixture of red hematopoietic marrow, yellow fatty marrow, and trabeculae in varying proportions based on the age and other factors; its usual appearance on MRI reflects this combination. Yellow marrow follows the signal intensity of subcutaneous fat on all pulse sequences. Red marrow demonstrates the intermediate signal on T1 and T2 and high in signal on STIR sequences showing higher signal than fat, saturated yellow marrow.

The signal intensity of the red marrow is higher than the skeletal muscles and intervertebral disc. The heterogeneous appearance of marrow is the most common as the fatty and red marrow are present in variable proportion in adults. When regions of marrow are as dark as, or darker than, a standard intervertebral disc or

adjacent muscle on the same image, pathology is almost certainly present [55].

Typically, in an adult, the red marrow is distributed centrally within the appendicular and axial skeletons. There are generally four typical patterns of fat and red marrow distribution in adult on T1-weighted (T1w) images. Linear areas of high-signal intensity parallel the basivertebral vein, in pattern 1. The remainder of the body is uniformly low in signal intensity on T1. The reduced signal intensity is from red marrow, which is observed in nearly half of those less than 20 years of age and rarely seen above 30 years of age.

In pattern 2, the conversion of the red to fatty marrow is at the periphery of the vertebral body. Bandlike and triangular regions of the high-signal intensity are along the anterior and posterior corners of the vertebral bodies and near the endplates. Degenerative disease can also have a similar appearance. Pattern 3 consists of Pattern 3a and has numerous indistinct high signal intensity foci. Pattern 3b consists of well-marginated regions of high-signal intensity ranging in size from 0.5 to 1.5 cm. In older individuals, more than 40, approximately 85%, show pattern 2, and about 75% show pattern 3 – combination of patterns 2, 3a, and 3b seen in a few cases. Marrow reconversion is a process that happens during times of stress in which the body requires increased blood cell production, such as in response to anemia [56].

References

1. Hubaud A, Pourquie O. Signalling dynamics in vertebrate segmentation. Nat Rev Mol Cell Biol. 2014;15(11):709–21.
2. Scaal M, Christ B. Formation and differentiation of the avian dermomyotome. Anat Embryol. 2004;208(6):411–24.
3. Christ B, Huang R, Scaal M. Formation and differentiation of the avian sclerotome. Anat Embryol. 2004;208(5):333–50.
4. Choi KS, Harfe BD. Hedgehog signaling is required for formation of the notochord sheath and patterning of nuclei pulposi within the intervertebral discs. Proc Natl Acad Sci U S A. 2011;108(23):9484–9.
5. Christ B, Huang R, Wilting J. The development of the avian vertebral column. Anat Embryol (Berl). 2000;202(3):179–94.
6. Monsoro-Burq AH, Le Douarin N. Duality of molecular signaling involved in vertebral chondrogenesis. Curr Top Dev Biol. 2000;48:43–75.
7. Pickett EA, Olsen GS, Tallquist MD. Disruption of PDGFRalpha-initiated PI3K activation and migration of somite derivatives leads to spina bifida. Development. 2008;135(3):589–98.
8. Wang Y, Serra R. PDGF mediates TGFbeta-induced migration during development of the spinous process. Dev Biol. 2012;365(1):110–7.
9. Aruga J, et al. Zic1 regulates the patterning of vertebral arches in cooperation with Gli3. Mech Dev. 1999;89(1–2):141–50.
10. Scaal M. Early development of the vertebral column. Semin Cell Dev Biol. 2016;49:83–91.
11. Huang R, et al. Function of somite and somitocoele cells in the formation of the vertebral motion segment in avian embryos. Cells Tissues Organs. 1996;155(4):231–41.
12. Waxenbaum JA, Futterman B. Anatomy, back, intervertebral discs. Treasure Island (FL): StatPearls Publishing; 2019.
13. Brent AE, Schweitzer R, Tabin CJ. A somitic compartment of tendon progenitors. Cell. 2003;113(2):235–48.
14. Paik NC, Lim CS, Jang HS. Numeric and morphological verification of lumbosacral segments in 8280 consecutive patients. Spine (Phila Pa 1976). 2013;38(10):E573–8.
15. Bland JH, Boushey DR. Anatomy and physiology of the cervical spine. Semin Arthritis Rheum. 1990;20(1):1–20.
16. Kocabiyik N, Ercikti N, Tunali S. Morphometric analysis of the uncinate processes of the cervical vertebrae. Folia Morphol (Warsz). 2017;76(3):440–5.
17. Kotani Y, et al. The role of anteromedial foraminotomy and the uncovertebral joints in the stability of the cervical spine. A biomechanical study. Spine (Phila Pa 1976). 1998;23(14):1559–65.
18. Ebraheim NA, et al. Quantitative anatomy of the cervical facet and the posterior projection of its inferior facet. J Spinal Disord. 1997;10(4):308–16.
19. Pesch HJ, et al. On the pathogenesis of spondylosis deformans and arthrosis uncovertebralis: comparative form-analytical radiological and statistical studies on lumbar and cervical vertebral bodies. Arch Orthop Trauma Surg. 1984;103(3):201–11.
20. Tubbs RS, et al. Ligaments of the craniocervical junction. J Neurosurg Spine. 2011;14(6):697–709.
21. Moon SM, et al. Evaluation of intervertebral disc cartilaginous endplate structure using magnetic resonance imaging. Eur Spine J. 2013;22(8):1820–8.
22. McCann MR, et al. Tracing notochord-derived cells using a Noto-cre mouse: implications for intervertebral disc development. Dis Model Mech. 2012;5(1):73–82.
23. Rodrigues-Pinto R, Richardson SM, Hoyland JA. An understanding of intervertebral disc development, maturation and cell phenotype provides clues to direct cell-based tissue regeneration therapies for disc degeneration. Eur Spine J. 2014;23(9):1803–14.

24. Chen S, et al. Meniscus, articular cartilage and nucleus pulposus: a comparative review of cartilage-like tissues in anatomy, development and function. Cell Tissue Res. 2017;370(1):53–70.
25. Mills MK, Shah LM. Imaging of the perivertebral space. Radiol Clin N Am. 2015;53(1):163–80.
26. Hu ZJ, Fang XQ, Fan SW. Iatrogenic injury to the erector spinae during posterior lumbar spine surgery: underlying anatomical considerations, preventable root causes, and surgical tips and tricks. Eur J Orthop Surg Traumatol. 2014;24(2):127–35.
27. Rojas CA, et al. Normal thickness and appearance of the prevertebral soft tissues on multidetector CT. Am J Neuroradiol. 2009;30(1):136–41.
28. Bromage PR. Epidural analgesia. Philadelphia/London: WB Saunders Company; 1978.
29. Nickalls RW, Kokri MS. The width of the posterior epidural space in obstetric patients. Anaesthesia. 1986;41(4):432–3.
30. Paksoy Y, Gormus N. Epidural venous plexus enlargements presenting with radiculopathy and back pain in patients with inferior vena cava obstruction or occlusion. Spine (Phila Pa 1976). 2004;29(21):2419–24.
31. Richardson J, Groen GJ. Applied epidural anatomy. BJA Edu. 2005;5(3):98–100.
32. Cheung JP, et al. Defining clinically relevant values for developmental spinal stenosis: a large-scale magnetic resonance imaging study. Spine (Phila Pa 1976). 2014;39(13):1067–76.
33. Cheung JP, Shigematsu H, Cheung KM. Verification of measurements of lumbar spinal dimensions in T1- and T2-weighted magnetic resonance imaging sequences. Spine J. 2014;14(8):1476–83.
34. Rabischong P. Anatomie fonctionnelle du rachis et de la moelle. In: Manelfe C, editor. Imagerie du rachis et de la moelle. Paris: Vigot; 1989. p. 109–34.
35. Revel M, et al. Variations morphologiques des trous de conjugaison lombaires lors de la flexion-extension et de l'affaissement discal. Rev Rhum Mal Osteoartic. 1988;5:361–6.
36. Panjabi MM, Takata K, Goel VK. Kinematics of lumbar intervertebral foramen. Spine. 1983;8(4):348–57.
37. Inufusa A, et al. Anatomic changes of the spinal canal and intervertebral foramen associated with flexion-extension movement. Spine. 1996;21(21):2412–20.
38. Van Schoor A-N, Bosman MC, Bosenberg AT. Descriptive study of the differences in the level of the conus medullaris in four different age groups. Clin Anat. 2015;28(5):638–44.
39. Demiryurek D, et al. MR imaging determination of the normal level of conus medullaris. Clin Imaging. 2002;26(6):375–7.
40. Nasr AY. Vertebral level and measurements of conus medullaris and dural sac termination with special reference to the apex of the sacral hiatus: anatomical and magnetic resonance imaging radiologic study. Folia Morphol (Warsz). 2016;75(3):287–99.
41. Liu A, et al. Level of conus medullaris termination in adult population analyzed by kinetic magnetic resonance imaging. Surg Radiol Anat. 2017;39(7):759–65.
42. Liccardo G, et al. Fifth ventricle: an unusual cystic lesion of the conus medullaris. Spinal Cord. 2005;43(6):381–4.
43. Cools MJ, et al. Filum terminale lipomas: imaging prevalence, natural history, and conus position. J Neurosurg Pediatr. 2014;13(5):559–67.
44. Fitzgerald MJT, Mtui E, Gruener G. Clinical neuroanatomy, and neuroscience. Edinburgh: Saunders/Elsevier; 2012.
45. Kulkarni B, et al. Attention to pain localization and unpleasantness discriminates the functions of the medial and lateral pain systems. Eur J Neurosci. 2005;21(11):3133–42.
46. De Ridder D, et al. Burst spinal cord stimulation for limb and back pain. World Neurosurg. 2013;80(5):642–649.e1.
47. Demondion X, et al. Radiographic anatomy of the intervertebral cervical and lumbar foramina (vessels and variants). Diagn Interv Imaging. 2012;93(9):690–7.
48. Thron AK. Vascular anatomy of the spinal cord: neuroradiological investigations and clinical syndromes. Wien/New York: Springer Science & Business Media; 1988.
49. Groen GJ, Baljet B, Drukker J. Nerves and nerve plexuses of the human vertebral column. Am J Anat. 1990;188(3):282–96.
50. Hartman J. Anatomy and clinical significance of the uncinate process and uncovertebral joint: a comprehensive review. Clin Anat. 2014;27(3):431–40.
51. Johnson GM. The sensory and sympathetic nerve supply within the cervical spine: review of recent observations. Man Ther. 2004;9(2):71–6.
52. Wozniak W, Grzymislawska M. Innervation of the human cervical and thoracic vertebrae at eight postovulatory weeks. Folia Morphol (Warsz). 2009;68(2):84–7.
53. Chua WH, Bogduk N. The surgical anatomy of thoracic facet denervation. Acta Neurochir. 1995;136(3–4):140–4.
54. Higuchi K, Sato T. Anatomical study of lumbar spine innervation. Folia Morphol (Warsz). 2002;61(2):71–9.
55. Bogduk N. Clinical anatomy of the lumbar spine and sacrum. Edinburgh: Churchill Livingstone; 1997.
56. Ricci C, et al. Normal age-related patterns of cellular and fatty bone marrow distribution in the axial skeleton: MR imaging study. Radiology. 1990;177(1):83–8.

MRI in Spine Trauma

3

Phan Q. Duy, Ichiro Ikuta, Michele H. Johnson, Melissa Davis, and Vahe M. Zohrabian

Demographics

Spine trauma is a major cause of morbidity and mortality worldwide. Approximately 80,000 spine fractures occur each year in the United States alone, with nearly half occurring in the cervical spine [1, 2]. Approximately 2% of blunt trauma patients will have a cervical spine fracture, although this number ranges from 1% to 3% in some series, and can reach as high as 5% [3–5]. The major cause of morbidity in this population is spinal cord injury (SCI). Primary injury refers to the immediate intracellular and extracellular effects of energy transfer, while secondary injury, which can be exacerbated by extrinsic factors, such as spinal axis instability, hypotension, and hypoxia, involves a complex cascade of pathophysiologic processes, beginning within seconds and lasting for weeks, which worsens the initial neurological damage. Injuries to the spinal axis can result in spine fractures with or without neurologic insult. Although the number of individuals who sustain SCI each year in the United States is far less than the number who sustain traumatic brain injury, SCI is devastating, and moreover, its financial costs are overwhelming. Due to the limited regenerative capacity of the central nervous system, SCI often results in permanent loss of function that profoundly affects quality of life, including, but not limited to, paralysis, loss of bladder and/or bowel control, and sexual dysfunction. In the United States alone, it has been estimated that approximately 18,000 new cases of SCI occur each year and that close to 300,000 people currently live with SCI, carrying a lifetime cost ranging from $1 to 5 million per person [6]. It is difficult to obtain an accurate estimate of the total number of SCIs since patients whose injuries are immediately fatal in the field are not included in these national statistics. Most spinal cord-injured patients are young male adults, between the ages of 16 and 30 years [6]. Leading etiologies of SCI include motor vehicle accidents, falls, acts of violence (e.g., gunshot wounds), and sports-related injuries [6].

Spine Clearance

Although the diagnosis of SCI is typically made on the basis of clinical history and neurological examination alone, imaging plays a large role in confirming and localizing the level of injury. Of paramount importance in the pre-hospital care of the trauma patient is the stabilization of airway, breathing, and circulation per advanced trauma life support (ATLS) protocols. During this primary survey, spine protection is critical, and

P. Q. Duy · I. Ikuta · M. H. Johnson · M. Davis
V. M. Zohrabian (✉)
Department of Radiology & Biomedical Imaging, Yale School of Medicine, New Haven, CT, USA
e-mail: duy.phan@yale.edu; ichiro.ikuta@yale.edu; michele.h.johnson@yale.edu; melissa.a.davis@yale.edu; vahe.zohrabian@yale.edu

W. B. Morrison et al. (eds.), *MRI of the Spine*, https://doi.org/10.1007/978-3-030-43627-8_3

manipulation of the spine, such as for airway management, should be avoided unless absolutely necessary until the spine can be cleared. The classic teaching has been that the cervical spine should be assumed to be injured in all blunt trauma patients who do not meet validated clinical decision rules, and appropriate fixation should be rapidly achieved through immobilization with a hard collar and supportive blocks on a backboard with straps in order to mitigate secondary injury. However, the risks of prolonged immobilization have taken center stage in the last several years as collars and backboards have been shown to potentially exacerbate spine injury [7–10], being associated with difficulties with airway management [11, 12], increased intracranial pressure [13–17], and pressure ulcers [18–22]. A growing number of studies have proposed alternate immobilization strategies that have omitted routine collar application and adopted more selective application criteria, though this is an area in which more evidence is needed [23–25].

Many prior studies have shown that there is an overwhelmingly small incidence of positive imaging findings in patients with spine trauma [26–28]. Furthermore, it has been shown that most detected injuries are non-threatening [26, 27, 29]. Clinical decision rules have been devised in order to determine those patients in whom spine imaging may be foregone. Derived from ample research and incorporating portions of a patient's history, clinical examination, and laboratory tests, these clinical decision rules are meant to efficiently triage patients and lend to earlier resuscitation. The best studied of these clinical decision rules is derived from the National Emergency X-Radiography Utilization Study (NEXUS) [27, 30]. A large, multicenter observational trial published in 2000, NEXUS relies on the following low-risk criteria: absence of midline cervical spine tenderness, absence of painful distracting injury, absence of intoxication, and absence of focal neurologic deficit in the setting of normal alertness. Those patients meeting all the above criteria are said to be at low-risk for cervical spine injury, and as such, imaging is said to be unnecessary (Box 3.1). The Canadian C-Spine Rule (CCR) is a more involved algorithm that is based on both high- and low-risk factors [31]. High-risk factors relate to advanced age, dangerous mechanism of injury, and presence of paresthesia in the extremities. If low-risk factors allow for the safe assessment, as well as successful completion, of neck range of motion, imaging is deemed unnecessary (Box 3.2). It is important to note that whereas the validation study for NEXUS included patients of all ages, CCR was limited to adult blunt trauma patients with GCS of 15. Comparison studies suggest that CCR may provide superior diagnostic accuracy when compared to NEXUS while minimizing the need for imaging [26, 32] (Box 3.3).

Although these clinical decision rules are well studied, there often remains reluctance by clinicians to discharge spine trauma patients without any imaging, especially the elderly and children. A prior study found that regardless of level of training, providers in the ED commonly imaged geriatric patients who met NEXUS low-risk criteria [33]. For example, in elderly patients, there may be issues relating to osteopenia, physical disability, comorbidity, dementia, and diminished pain perception, which may make application of the clinical decision rules more difficult. Furthermore, many elderly patients may have a GCS of 14 despite normal alertness. Several studies have shown that NEXUS performs comparably in the elderly as in younger patients, with sensitivities approaching 100% [34–37]. Others have proposed the use of modified NEXUS criteria, such as substituting baseline mental status for

Box 3.1: National Emergency X-Radiography Utilization Study (NEXUS)

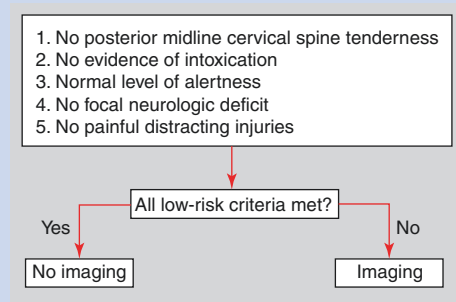

Adapted from Hoffman et al. [30]

Box 3.2: Canadian C-Spine Rule (CCR)

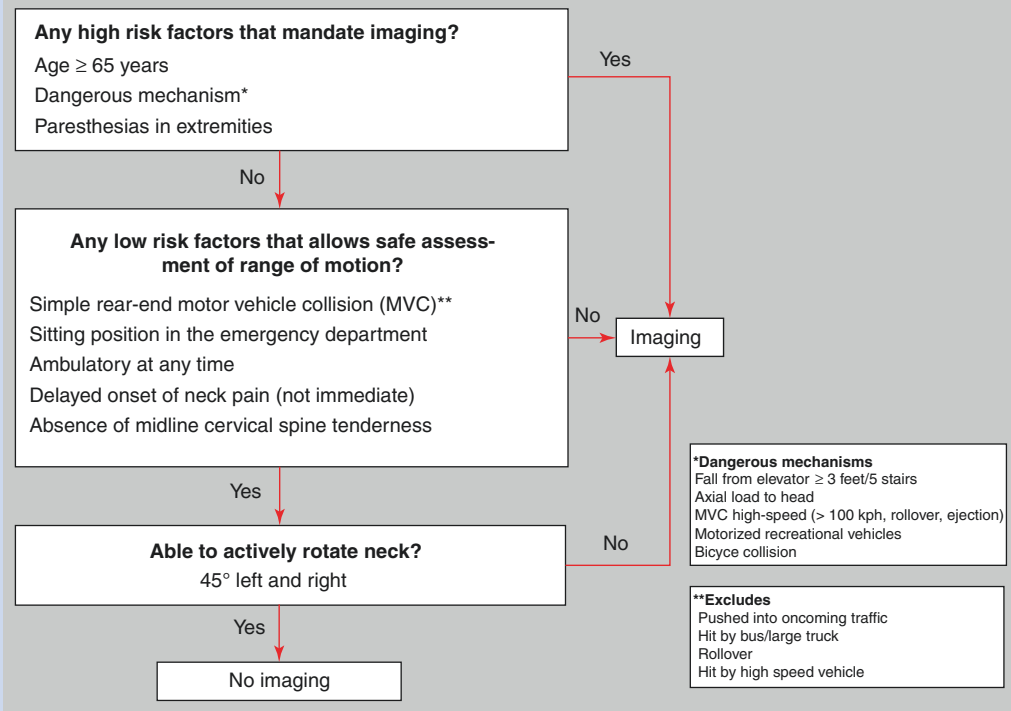

Adapted from Stiell et al. [31]

Box 3.3: NEXUS Versus CCR

	NEXUS	CCR
Sensitivity	90.70%	99.40%
Specificity	36.80%	45.10%
Imaging rate	66.60%	55.90%
Advantages	Simple to implement, can be widely applied in ED settings	Potentially better diagnostic accuracy with less imaging
Disadvantages	Potentially lower sensitivity in elderly populations	Some physicians uncomfortable with neck movement assessment

Adapted from Stiell et al. [26]

normal alertness and utilizing physical examination findings of trauma to the head or face as the only qualifying distracting injury [35]. In children, although the incidence of cervical spine injury is fortunately very low, applying clinical decision rules may prove challenging given diminished reliability of the clinical examination due to communication difficulties [38, 39]. In the NEXUS validation study, only four children younger than 9 years of age and none younger than 2 years of age were included in the cohort, although sufficient data on children aged 9–17 years allows it to perform reasonably well in older children. The CCR study did not include patients under the age of 16 years, and in a retrospective study of the CCR in patients younger than 10 years of age, a sensitivity of only 86% was achieved [40]. The Pediatric Emergency Care Applied Research Network (PECARN) identified eight high-risk factors with 98% sensitivity and 28% specificity for the absence of cervical spine injury in children aged 0–16 years, namely, altered mental status, focal neurologic deficits, complaints of neck pain, torticollis, sub-

stantial injury to the torso, predisposing conditions for cervical spine injury, high-risk MVC, and diving [41]. To date, unfortunately, no interdisciplinary standardized approach exists to clearing the cervical spine in pediatric patients.

Imaging Options

The armamentarium of imaging after spine trauma includes plain radiography, multidetector computed tomography (CT), and magnetic resonance imaging (MRI), each with its own advantages and disadvantages (Box 3.4). The current standard of care in those patients who fail clinical decision rules in clearing the cervical spine is high-quality 3 mm axial CT sections with sagittal and coronal reconstructions. CT has essentially supplanted plain radiography in the initial evaluation of spine trauma, except in pediatric patients where conventional radiographs still play a limited role due to concerns over radiation exposure. MRI remains the gold standard for diagnosing soft tissue injury, providing exceptional contrast resolution needed to display the internal architecture of the spinal cord, the relationship of the cord to surrounding structures, and the integrity of other spinal elements, such as nerve roots, intervertebral discs, ligaments, and muscles. Indeed, MRI informs outcome prediction and surgical intervention by enabling characterization of spinal cord hemorrhage, edema, compression, and transection. Many spine injury classification systems in place today employ MRI in the determination of spine stability.

For clearance of the thoracolumbar spine, the Eastern Association for the Surgery of Trauma (EAST) recommends CT in patients with back pain, tenderness on physical examination, neurologic deficits, altered mental status, intoxication, distracting injuries, or known/suspected high-energy mechanisms [42]. Evaluation of the entire spine by CT is recommended for blunt trauma patients with a known or suspected injury to the cervical or any other region of the spine. Awake patients with intact neurological and physical examinations and no complaints of thoracolum-

Box 3.4: Modalities for Spine Trauma Imaging

	Radiography	CT	MRI
Advantages	Rapid	Relatively rapid	Gold standard for spinal cord parenchyma, ligaments, discs, and nerve roots
		Soft tissue/ligamentous damage often inferred	
	Widely available	Excellent for bones, high spatial resolution	Advanced techniques for axonal integrity, prognosis after SCI
	Cost-effective	3D reformats in multiple planes	
	Optimal for gross fracture deformity	Can be obtained from CT C/A/P dataset	
		CTA for vascular imaging	
		Widely available	
Disadvantages	Overall, far less sensitive for fractures than CT	Ionizing radiation	Contraindications (e.g., pacemaker)
			Metallic artifacts (e.g., surgical hardware)
	Blind spots, especially at cervicothoracic junction		Longer exam times, motion artifact
	Ionizing radiation		Claustrophobia
		Poor contrast resolution compared to MRI	Less widely available, especially after hours
			Expensive

C/A/P chest, abdomen, and pelvis, *CTA* CT angiography, *SCI* spinal cord injury

bar spine pain may be cleared without imaging. In guidelines published by the American College of Radiology, MRI is recommended when physical examination or CT findings suggest neurologic involvement, especially posttraumatic myelopathy [43].

The current major controversy in cervical spine clearance is whether CT alone is sufficiently accurate at excluding injury, especially in those patients who are obtunded. Obtunded patients pose a particular difficulty given that a reliable clinical examination is not possible in those, for example, who are unconscious or altered (e.g., alcohol, drugs) [44]. Many institutions rely on MRI in clearing these patients, although some argue that MRI is over-utilized given that CT has been shown, in several studies, to be nearly 100% sensitive in excluding clinically significant injury [45–48]. Additionally, MRI is not without risk, as delayed collar removal has been shown to lead to complications [29, 49–52], including, but not limited to, pressure ulcer [18–22], pneumonia [50, 53], and venous thrombosis [50]. Moreover, MRI has been associated with morbidity relating to patient transport [49, 51]. A review of the literature demonstrates that even meta-analyses have been divergent on the topic of CT versus MRI, with some, for example, Panczykowski et al. (2011) [54], Raza et al. (2013) [55], and Badhiwala et al. (2015) [56], stating that CT alone is sufficient, while others, such as Muchow et al. (2008) [57], Schoenfeld et al. (2010) [58], Russin et al. (2013) [59], and James et al. (2014) [60], advocating for the use of MRI even in light of a negative CT. The reasons for such inconsistency in the literature are varied, although may relate, at least in part, to differences in the definitions of "obtunded," "clinically significant," or "unstable." For example, in a recent meta-analysis by Malhotra et al. (2017), a retrospective review of 23 studies (5,286 patients) found that although 16 unstable injuries were reported, only 11 were truly unstable based on the White and Panjabi and Denis three-column concept [61]. In 2015, EAST practice guidelines were published in an attempt to provide further guidance on cervical spine collar clearance in the obtunded patient [44]. A total of 12 single-center trials were reviewed, 8 of which were retrospective in design and only 1 of which was prospective (all, however, incorporating a low number of patients). In comparing CT to various adjunct studies, such as MRI, flexion-extension radiographs/CT, and clinical follow-up, CT was shown to have a 91% positive predictive value (PPV) for stable injury and 100% negative predictive value (NPV) for unstable injury. Given the weak evidence combined with high NPV of CT and costs/risks associated with MRI, EAST "conditionally recommends" cervical collar removal after a high-quality CT alone.

MRI-Specific Considerations

Although becoming more widespread, MRI remains a more limited resource than CT and its use in trauma protocols has not been standardized. It is accepted that MRI be performed within 48–72 hours of injury [62, 63], beyond which sensitivity for soft tissue edema and/or hemorrhage decreases; however, the potential risks associated with the transfer of a medically or neurologically unstable patient need to first be considered. In most cases, as long as appropriate precautions are adhered to and properly trained personnel are utilized, MRI can be performed with minimal risk. The potential harms in delaying surgical stabilization need to be weighed against the potential benefits of obtaining immediate information on spinal cord compression, spinal cord edema and/or hemorrhage, and discoligamentous injury. Moreover, regard must be given to the MRI compatibility of life-sustaining external devices, such as ventilators, ECG monitors, and intravenous medication pumps. The degradation of image quality due to ferromagnetic alloys in external fixation devices, as well as motion artifact (voluntary or involuntary), such as through movement of the head and neck caused by the ventilator, can make MRI technically challenging. Although ferrous femoral traction pins do not typically degrade images of the spine, tissue heating at contact points with the skin remains a concern.

In penetrating injury of the spine, retained ferrous objects in or around the spinal canal, such as bullets encased in steel, copper, or copper-nickel, may pose a safety concern given their potential for heating and/or migration when exposed to strong magnetic fields. In addition, ferrous materials can cause perturbations in local magnetic fields and result in image degradation. If metallic fragments are chronically embedded, it is assumed that sufficient scar tissue has formed that makes the risk for migration or dislodgement negligible. Special consideration is given to metallic foreign bodies in and around the orbits given that the visual apparatus may be secondarily injured. In unconscious patients in whom detailed clinical history is not available, radiologists are charged with reviewing prior radiographs and/or CT, or if not available, recommending they be performed so as to rule out the presence of ferrous materials in vital locations. If there is sufficient safety concern, MRI is foregone, and CT myelography is offered as the next step in the evaluation of spinal cord compression.

MRI Protocol

Conventional MRI tailored to provide a macrostructural view of the spine is comprised of a combination of different pulse sequences at different scan planes to highlight different tissue compositions (Box 3.5). An MRI pulse sequence is a set of parameters, such as time to echo (TE) and time to repetition (TR), which are programmed to change magnetic gradients to affect tissue contrast and spatial resolution. Conventional fast spin echo, turbo spin echo, and gradient echo (GRE) pulses are most commonly used. Tissues can be characterized by relaxation times - T1 (longitudinal relaxation time) and T2 (transverse relaxation time). T1-weighted images utilize a short TE and T2, whereas T2-weighted images utilize a longer TE and T2. T1-weighted and T2-weighted images can be further modified by fat attenuation, fluid attenuation, or contrast enhancement. On T1-weighted images, fluid/CSF appears dark or black, or low in signal intensity ("hypointense"), muscle appears gray, or intermediate in signal intensity, while fat appears bright or white, or high in signal intensity ("hyperintense"). On T2-weighted sequences, fluid/CSF appears white, muscle appears grey, and fat appears white. A proton density sequence shares features of both T1- and T2-weighted sequences, with fluid appearing white, muscle appearing gray, and fat appearing white. Fat suppression, achieved by either chemical fat saturation or short tau inversion recovery (STIR), nulls bright signal from fat and makes fluid or edema easier to detect on T2-weighted images. Additionally, susceptibility-sensitive sequences that are T2-weighted (T2∗ or T2 star GRE) cause blood products or calcium to stand out due to the resultant local magnetic field perturbations. Diffusion-weighted imaging (DWI) assesses the ease by which water molecules move in the extracellular space. As such, "restricted diffusion" refers to water moving around less easily, such as with increased cellularity (tumor) or cell swelling (ischemia), while "facilitated diffusion" refers to the opposite. A standard MRI in spine trauma should include, at the very least, sagittal T1-weighted, sagittal T2-weighted, sagittal STIR, and sagittal or axial T2∗-weighted sequences (Fig. 3.1). Additional high-resolution sagittal, axial, and coronal proton density images should be considered when injury to the craniocervical junction (CCJ) ligaments is suspected.

Box 3.5: MRI Spine Trauma Protocol Sequences

MRI sequence	Diagnostic purpose
T1-weighted	Anatomy, alignment, ligaments
T2-weighted	Spinal cord parenchymal damage, vascular flow voids (axial)
Proton density	Ligaments, especially CCJ
T2∗-weighted GRE	Blood products, calcium
STIR	Fluid/edema in bones and soft tissues

GRE gradient echo, *STIR* short tau inversion recovery, *CCJ* craniocervical junction

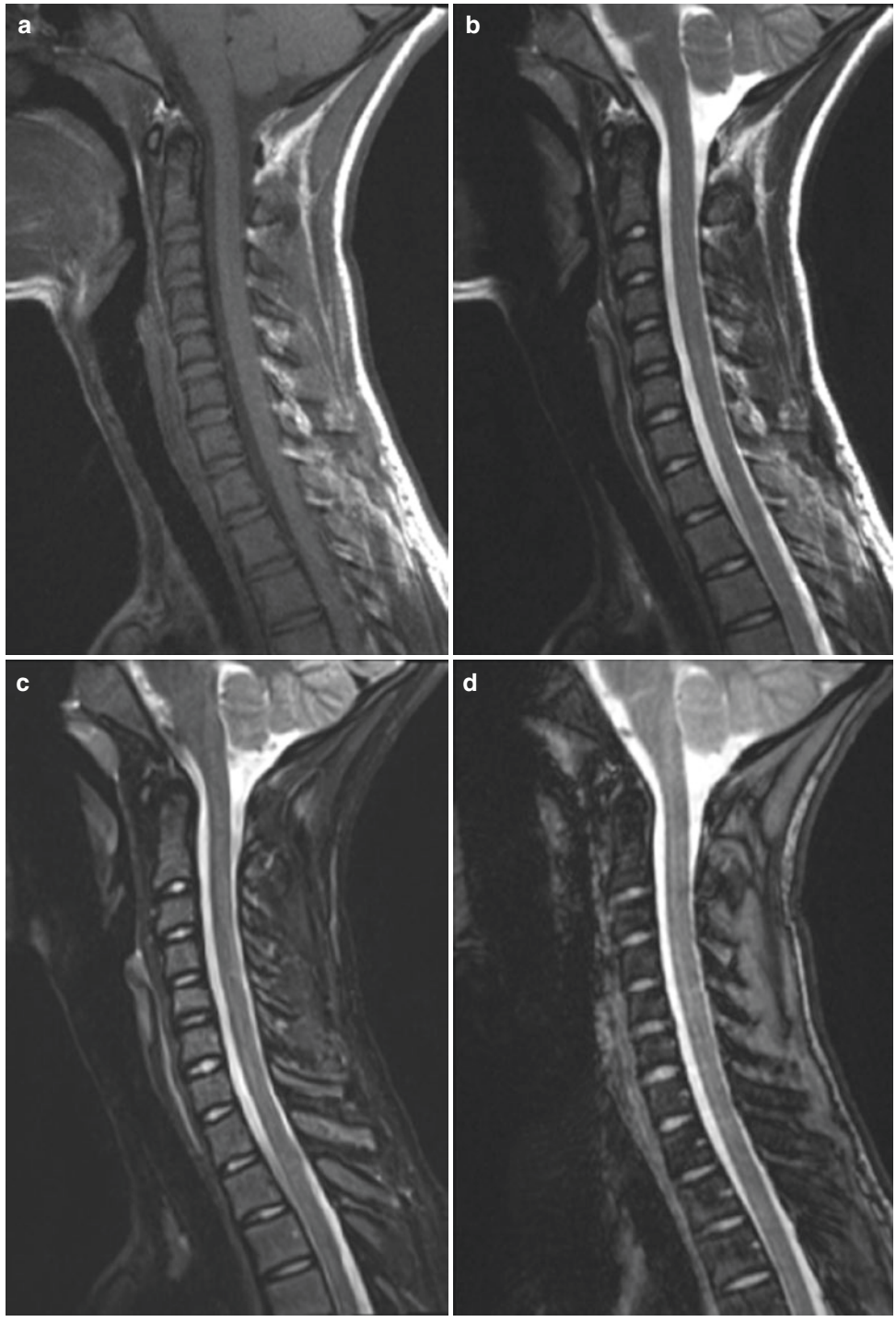

Fig. 3.1 Routine MRI spine trauma protocol. (**a**) Sagittal T1-weighted, (**b**) T2-weighted, (**c**) STIR, and (**d**) T2∗ GRE images of the normal cervical spine. Note that CSF is bright on all sequences, except on T1-weighted image where it is dark. Fat is bright on both T1- and T2-weighted images. STIR suppresses signal from fat in the dorsal soft tissues, allowing for the easier detection of edema. *STIR* short tau inversion recovery, *GRE* gradient echo

Fat-saturated techniques result in poor imaging quality when metallic fixation hardware is present. Modern MRI equipment makes it possible to interrogate the entire spine without repositioning the patient with combined head and spine surface array coils and moving MRI tables. When clinically warranted, additional imaging with two-dimensional (2D) time-of-flight (TOF) magnetic resonance angiography (MRA), three-dimensional (3D) TOF MRA, or contrast-enhanced MRA may be performed in order to interrogate the extracranial vasculature and exclude posttraumatic occlusion or dissection. There is no justifiable role for gadolinium contrast administration in routine spine trauma MRI.

MRI of Bony Injury

CT is very sensitive in the detection of osseous injuries after spine trauma, although MRI may play a complementary role. The major feature of osseous injury on MRI is marrow edema, appearing hyperintense on T2-weighted and STIR images and hypointense on T1-weighted images. MRI performs poorly in the detection of fractures at C1 and C2, including injuries to the posterior bony elements throughout the entire spine, given the small size, low proportion of medullary space, and complex geometry (Fig. 3.2). In older individuals, osteopenia and decreased vascularity of the odontoid may produce a false-negative result on fluid-sensitive STIR sequences (Fig. 3.3) [64]. MRI may sometimes demonstrate fractures as thin, T2-weighted/STIR hyperintense or T1-weighted hypointense bands traversing the vertebral bodies that may or may not interrupt the continuously hypointense cortical lines (Fig. 3.4). Displaced fractures are more readily detected given the involved deformity of the vertebral body and possibly thecal sac. MRI performs exquisitely well in the detection of osseous contusions or trabecular microfractures without fracture deformity or cortical failure, as

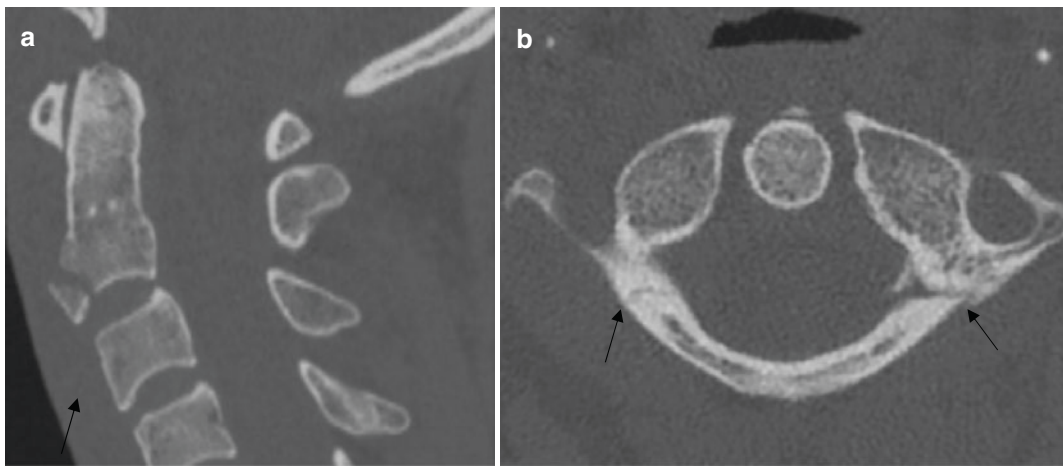

Fig. 3.2 (**a**) Sagittal CT demonstrates C2 teardrop fracture (black arrow). (**b**) Axial CT in same patient demonstrates bilateral C2 posterior arch fractures (black arrows) with extension into the transverse foramina (not shown here). (**c**) Corresponding sagittal STIR demonstrates very faint bright line (white arrow) corresponding to teardrop fracture without any appreciable bone marrow edema. There are secondary signs of injury, such as prevertebral and posterior paraspinal edema (red arrows). (**d**, **e**) Corresponding parasagittal T1-weighted and STIR images, respectively, demonstrate bony discontinuity (white arrows) compatible with posterior arch fractures, but no evidence of bone marrow edema

Fig. 3.3 (**a**) Sagittal CT in elderly patient demonstrates type 2 odontoid fracture with retropulsion and indentation of the thecal sac (white arrow). (**b**) Sagittal STIR in same patient demonstrates little, if any, bone marrow edema in C2. Note fluid signal in the predental interval (yellow arrow) and significant edema in the posterior soft tissues deep to the supraspinous ligament (red arrow) extending into the posterior atlantoaxial membrane (blue arrow)

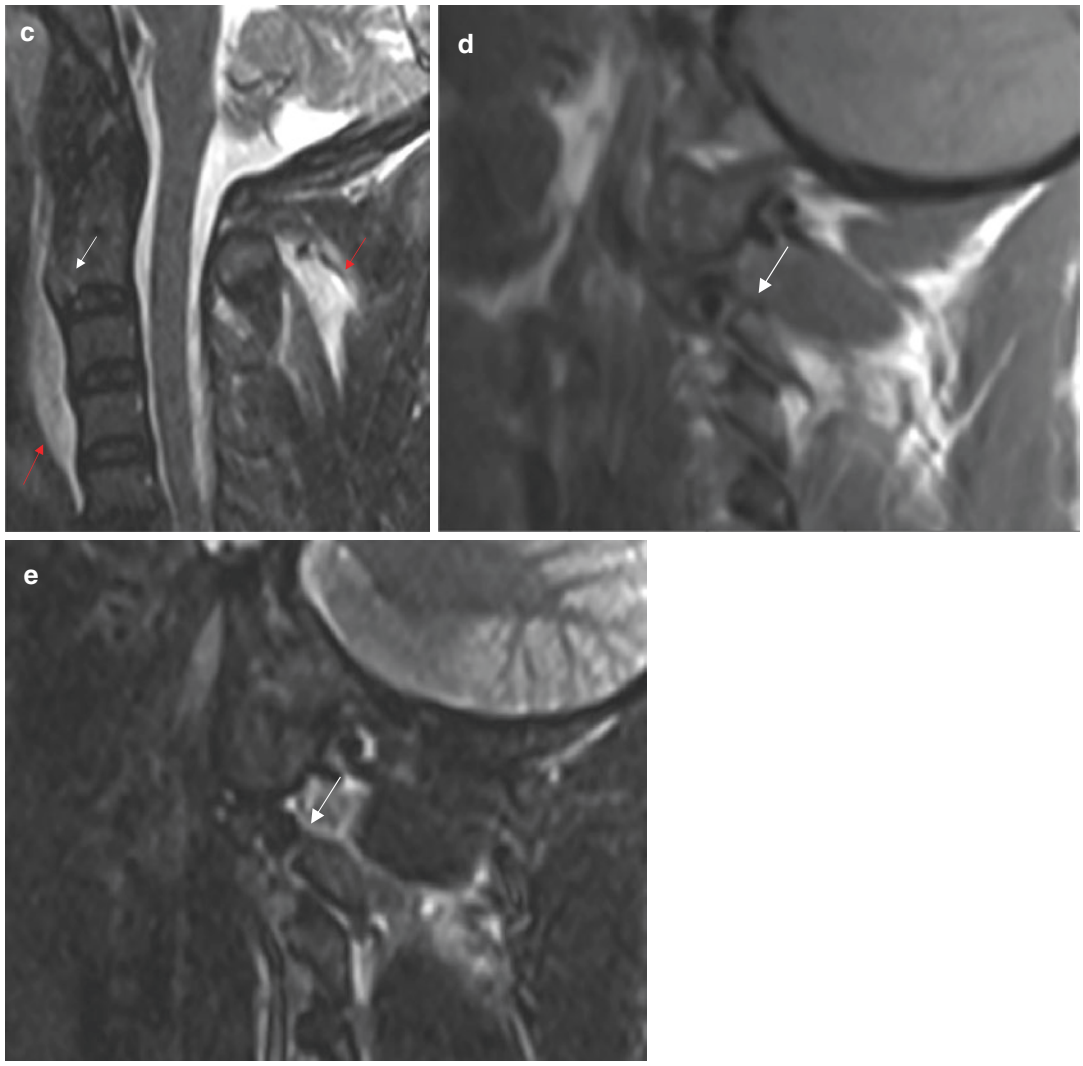

Fig. 3.2 (continued)

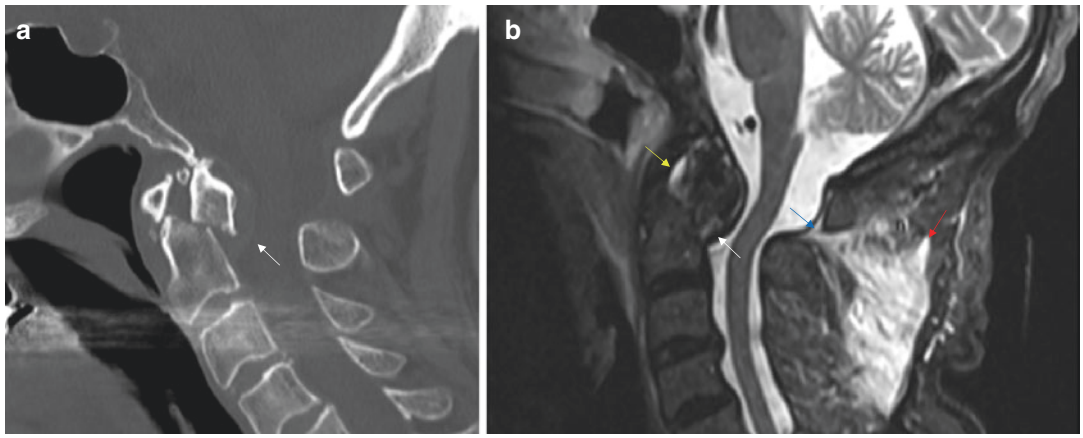

Fig. 3.3 (continued)

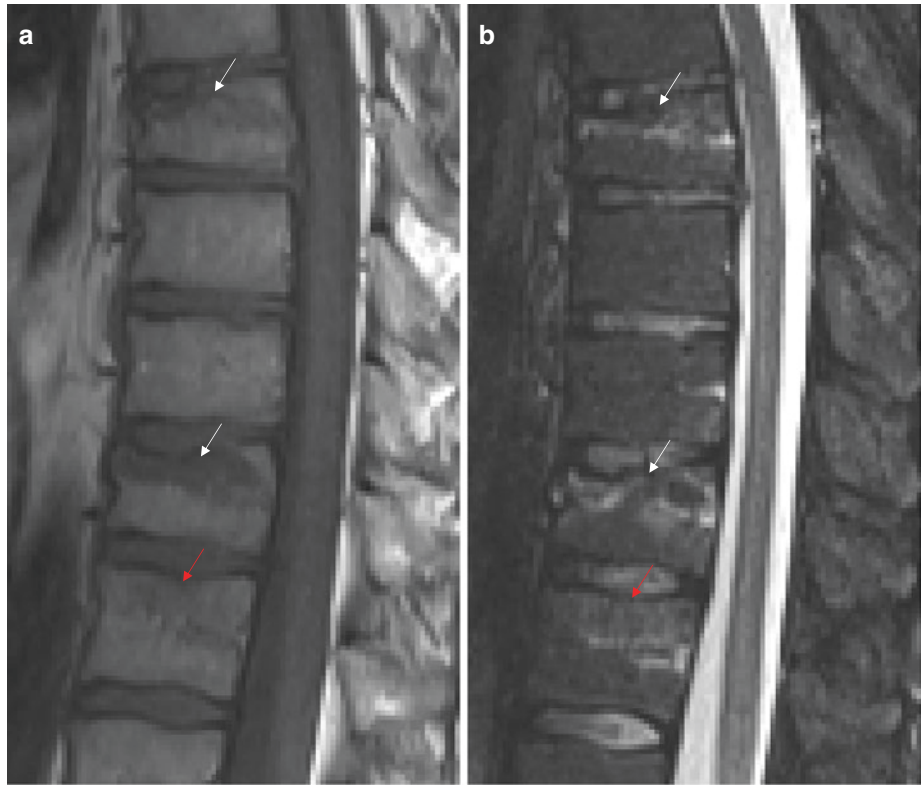

Fig. 3.4 (**a**) Sagittal T1-weighted image demonstrates hypointense bands or lines traversing the T8 and T11 vertebral bodies beneath the superior endplates compatible with wedge compression fractures (white arrows). (**b**) Corresponding sagittal STIR demonstrates linear hyperintensity corresponding to acute fractures (white arrows). Additional faint signal abnormality is demonstrated in the T12 vertebral body without compression deformity in both images (red arrows)

evidenced by edema in the marrow space (Fig. 3.5). MRI is especially important in the evaluation of age-indeterminate compression fractures of the spine. Chronic vertebral compression fractures will show endplate deformity and loss of height, although will not be associated with marrow edema, but, rather, may be associated with fatty signal, appearing bright on both T1- and T2-weighted images (Fig. 3.6) (Box 3.6).

MRI is also useful in differentiating between benign osteoporotic and pathologic compression fracture in the setting of malignancy, more commonly affecting the elderly [65–99] (Box 3.7). In benign fracture, there is typically a linear, fairly well-defined band of altered T1-weighted hypointensity and T2-weighted hyperintensity with adjacent preserved marrow signal, lack of involvement of the posterior elements, and preserved concave posterior vertebral body contours. The "intravertebral fluid sign" has also

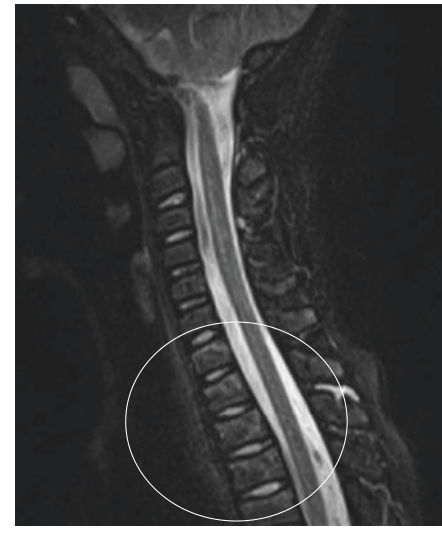

Fig. 3.5 Sagittal STIR in pediatric patient with negative CT demonstrates subtle hyperintensity compatible with edema beneath the superior vertebral endplates of C7 to T4 (circled), compatible with bony contusions or trabecular microfractures

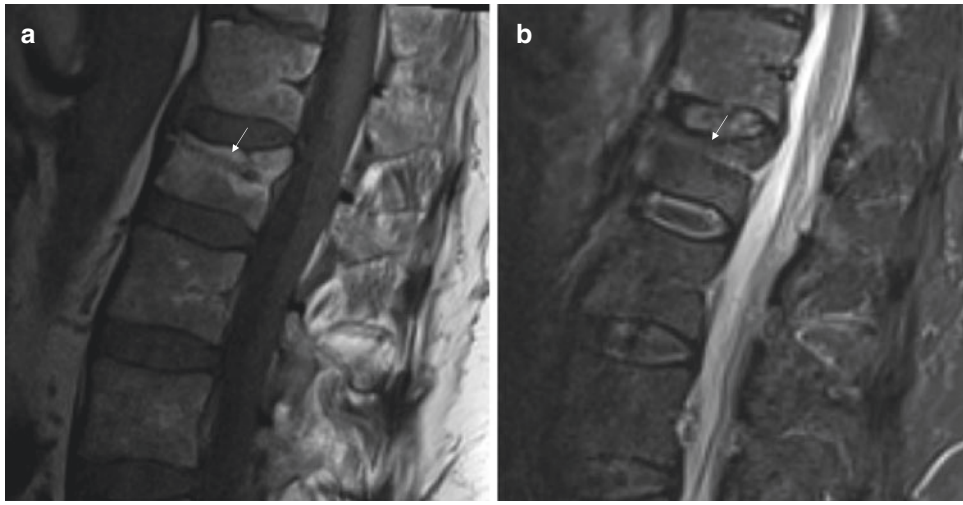

Fig. 3.6 (**a**) Sagittal T1-weighted image demonstrates chronic T11 superior endplate depression with underlying hyperintense bone marrow signal, which suppresses on (b) STIR image, compatible with fatty change (white arrows)

Box 3.6: MRI of Acute Versus Chronic Vertebral Fractures

MRI sequence	Acute fracture	Chronic fracture
T1-weighted	Dark	Bright
T2-weighted	Bright	Bright
STIR	Bright	Dark

STIR short tau inversion recovery

been described in benign acute, subacute, and chronic fractures, appearing as linear T2 hyperintensity due to fluid accumulation within an area of ischemic osteonecrosis [100] (Fig. 3.7). This cleft may at times be filled with gas instead of fluid, appearing hypointense on both T1- and T2-weighted images, yet is more obvious on CT. In malignant fracture, there is more extensive, infiltrative signal abnormality throughout the vertebral body that bulges the posterior cortex and usually extends into the posterior elements. On post-gadolinium T1-weighted images, there is heterogeneous intraosseous enhancement and there may be soft tissue enhancement that extends beyond the cortical margins into the adjacent paravertebral or epidural space (Fig. 3.8). Benign fractures may also enhance, although demonstrate more regular margins (Fig. 3.9). Malignant pathologic fractures are often associated with

Box 3.7: Benign Osteoporotic Versus Malignant Compression Fractures

Imaging modality	Benign compression fractures	Malignant compression fractures
MRI: morphology	Normal posterior element signal, retropulsed bone fragments	Abnormal posterior element signal, epidural or paravertebral soft tissue mass, expanded posterior vertebral contour
MRI: signal and enhancement patterns	Preserved normal marrow signal, regular margins, linear horizontal T1/T2 band, "fluid sign," normal enhancement relative to adjacent vertebrae and at 3 months	Geographic replacement of normal marrow signal, irregular margins, increased enhancement relative to adjacent vertebrae and at 3 months
MRI: diffusion	No restricted diffusion	Increased restricted diffusion
CT	Retropulsed bone, sharp fracture lines, intravertebral vacuum phenomenon	Bone destruction, epidural or focal paravertebral soft tissue mass

Adapted from Mauch et al. [65]

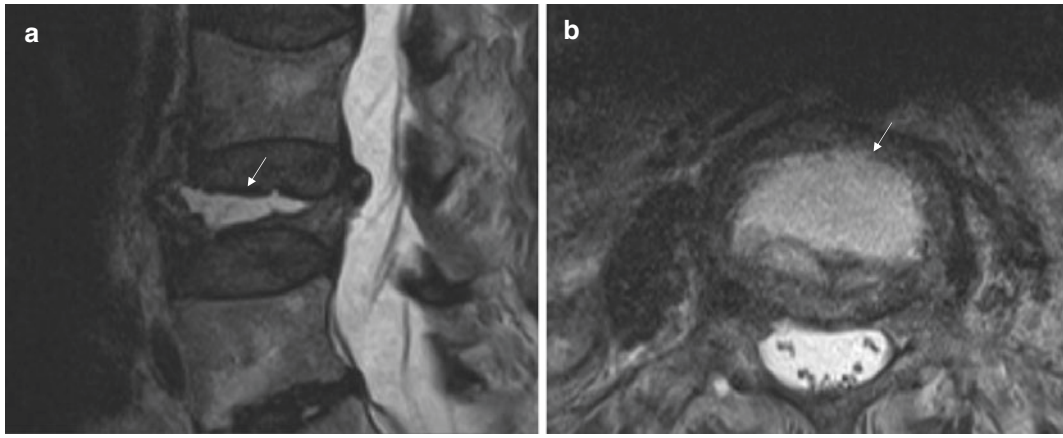

Fig. 3.7 (**a**) Sagittal and (**b**) axial T2-weighted images demonstrate intravertebral cleft or fluid sign at L4, compatible with benign osteoporotic burst fracture (white arrows)

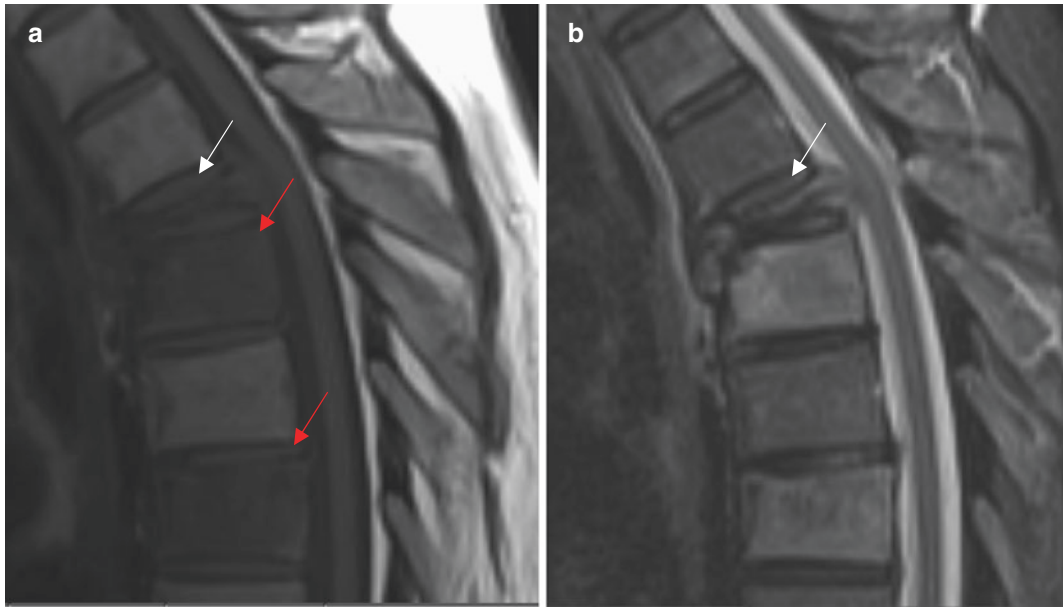

Fig. 3.8 (**a**) Sagittal T1-weighted and (**b**) sagittal STIR images demonstrate pancake compression deformity of T4, which is hypointense on T1-weighted and mildly hyperintense on STIR images (white arrows). There is an outwardly convex posterior vertebral body contour effacing the thecal sac. Note additional areas of marrow replacement at T5 and T7 on the T1-weighted image (red arrows). (**c**) Axial T2-weighted image demonstrates extension of abnormality from the vertebral body into the right pedicle (yellow arrow), including soft tissue in the epidural space effacing the thecal sac (red arrow). (**d**) T1-weighted post-gadolinium image demonstrates enhancing soft tissue compatible with malignant neoplasm in the ventral epidural space, best delineated on (**e**), fat-saturated T1-weighted post-gadolinium image (white arrows), where there is also abnormal enhancement in the dorsal epidural space (yellow arrow). Also note irregular pathologic enhancement in the T5 vertebral body and T2 inferior endplate. (**f**) Axial T1-weighted fat-saturated post-gadolinium image demonstrates irregular osseous enhancement, which extends into the posterior elements, as well as enhancing prevertebral, paravertebral, and epidural soft tissue

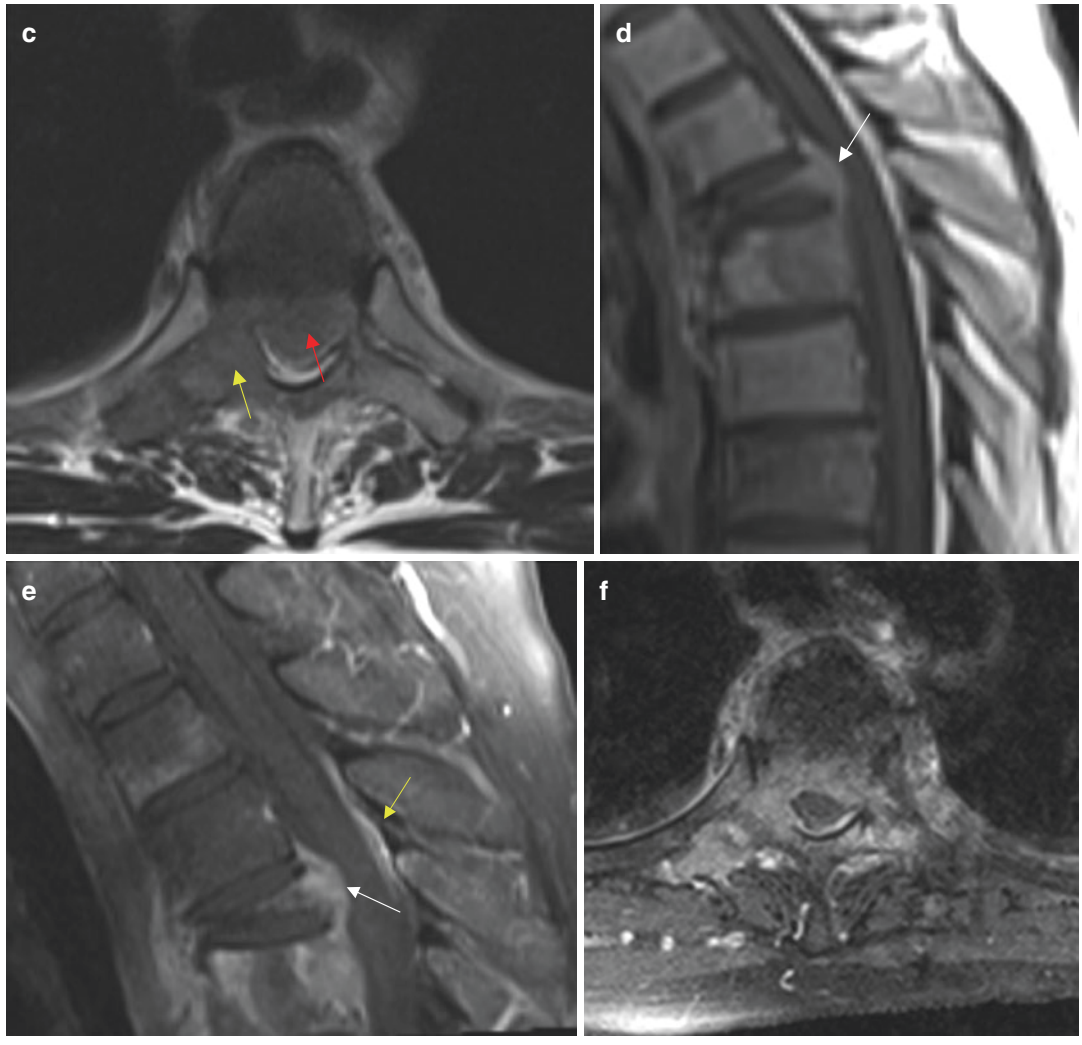

Fig. 3.8 (continued)

abnormalities at additional noncontiguous spine levels, whereas benign fractures usually involve a single or contiguous levels. DWI, as in the brain, has also been utilized in the spine to demonstrate restricted diffusion in malignant pathologic fractures due to high cellularity of tumors. A repeat interval MRI after several weeks can be considered in cases where the distinction is not so obvious to evaluate for improvement or resolution of marrow edema in benign fractures versus persistent or progressive marrow changes in malignant fractures.

An additional source of confusion arises in the distinction between Schmorl's nodes, which are frequently encountered in the thoracolumbar spine, and vertebral compression fractures. Schmorl's nodes represent invagination or herniation of disc material through the vertebral

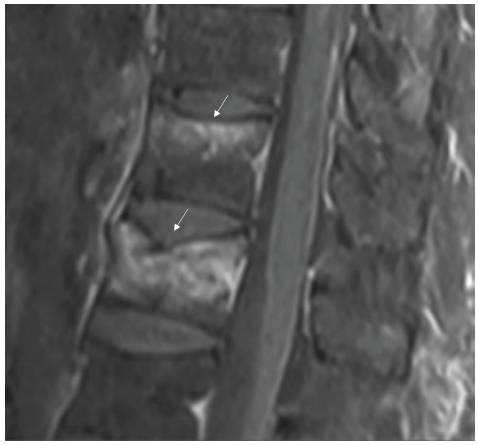

Fig. 3.9 Sagittal fat-saturated post-gadolinium T1-weighted image demonstrates intraosseous enhancement in association with benign T11 and T12 wedge compression fractures (white arrows). The posterior vertebral cortices are smooth, and there is no abnormal enhancement in the prevertebral or epidural space

endplates and are usually asymptomatic. Typically encountered in the setting of weakened cartilaginous endplate and subchondral bone, or trauma, Schmorl's nodes have been associated with Scheuermann's disease [101, 102], metabolic conditions [103], and neoplasm (Fig. 3.10) [104, 105]. On MRI in the sagittal plane, they characteristically appear as focal defects in the vertebral endplate with the same signal characteristic as the intervertebral disc. Larger Schmorl's nodes may be associated with bone marrow edema and enhancement, though this finding is more common is symptomatic patients with back pain than asymptomatic patients (Fig. 3.11) [106, 107].

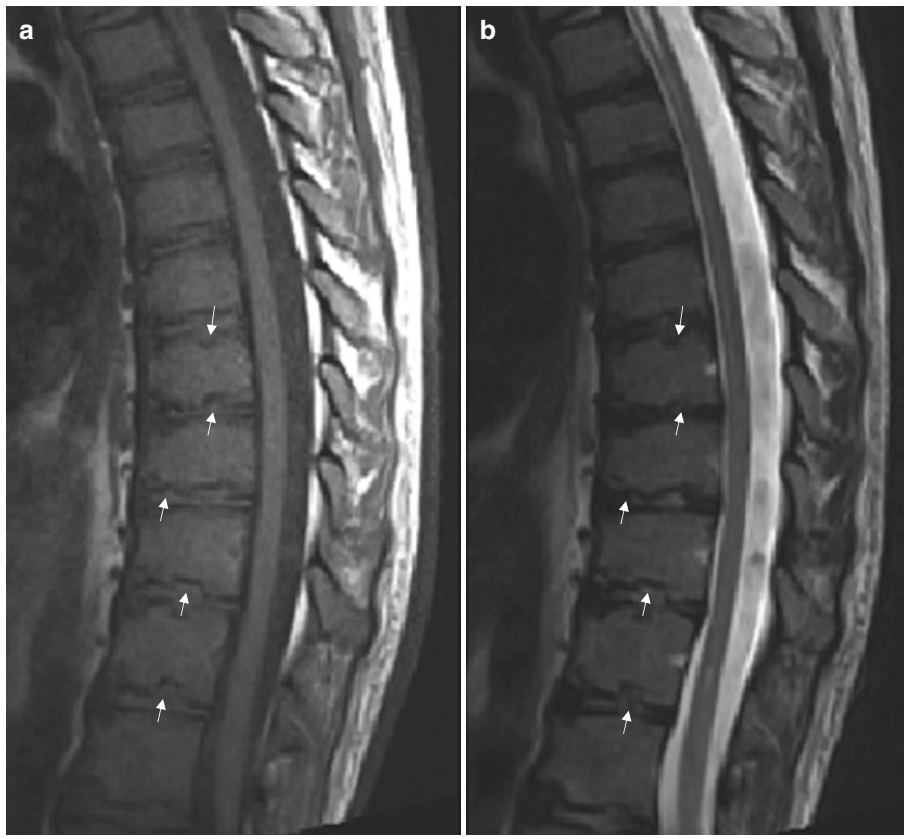

Fig. 3.10 (**a**) Sagittal T1- and (**b**) corresponding T2-weighted images demonstrate multiple small defects in the both the superior and inferior thoracic vertebral endplates in this young patient with back pain, some of which are denoted by white arrows, suggestive of Scheuermann's disease

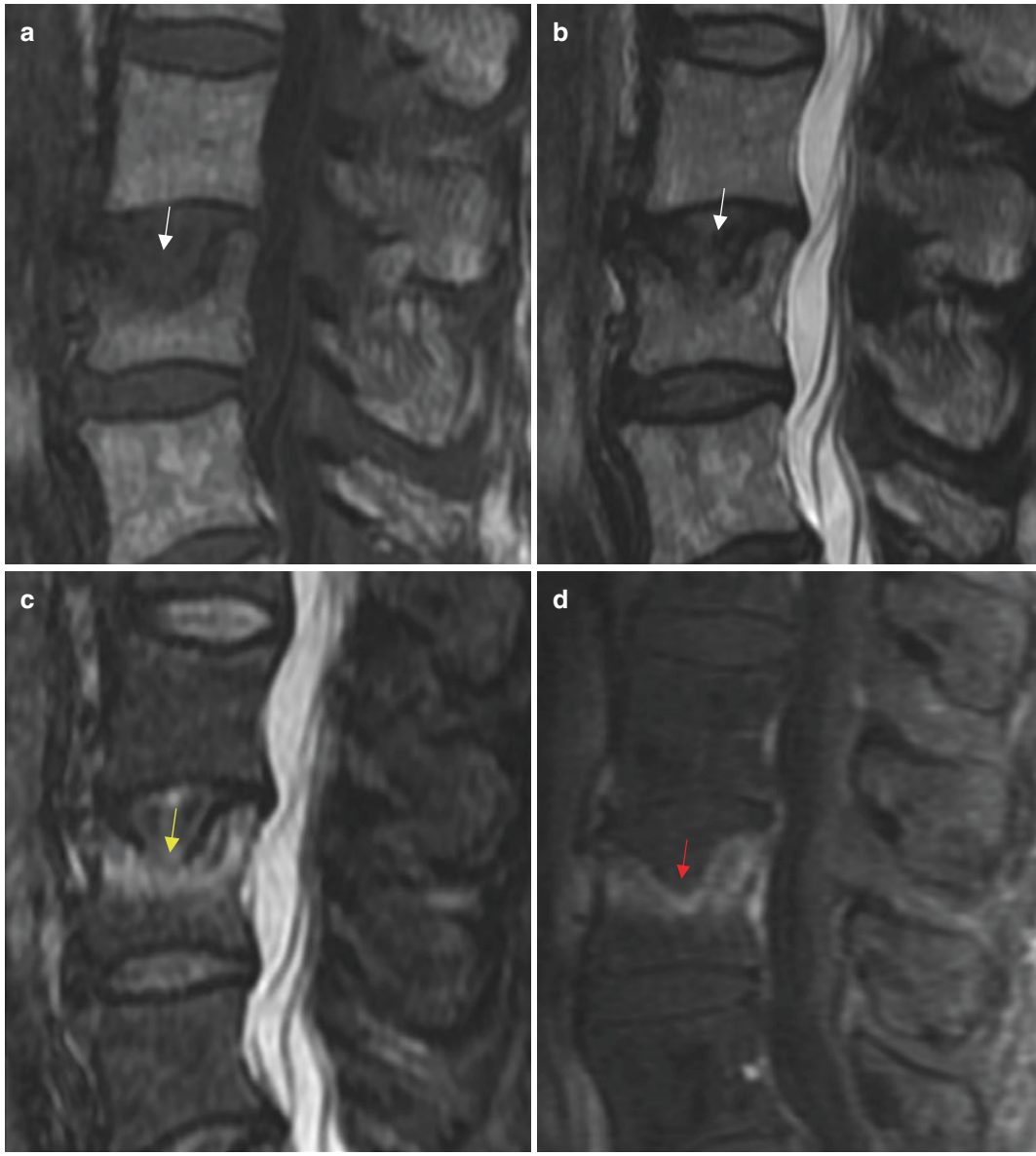

Fig. 3.11 (**a**) Sagittal T1- and (**b**) T2-weighted images demonstrate a large defect in the superior endplate of L3 with fairly similar signal characteristics as the L2-L3 disc, consistent with a Schmorl's node (white arrows). (**c**) Sagittal STIR image and (**d**) corresponding sagittal T1-weighted fat-saturated post-gadolinium image demonstrate edema (yellow arrow) and enhancement (red arrow), respectively, in this patient with low back pain, suggestive of inflammation

MRI of Disc Injury

MRI has replaced conventional and CT myelography in the evaluation of extruded intervertebral disc material, although the high-resolution and isotropic data sets provided by noncontrast CT often depict abnormal soft tissue in the spinal canal. While the presence of disc herniation is not highly correlated with the degree of neurologic deficit, undetected posttraumatic disc herniation can cause new or worsening spinal cord injury with progressive neurologic

impairment after surgical stabilization. Posttraumatic disc herniation is often seen in the cervical and thoracic spine [108–110], in contrast to degenerative disc herniation, which is commonly observed in the lumbar spine. The incidence of posttraumatic disc herniation in the cervical spine has been reported to be up to 54% [111–113].

Normally, the uninjured, hydrated disc appears hypointense relative to bone marrow on T1-weighted images and intermediate in signal on T2-weighted fast spin echo images (Fig. 3.12).

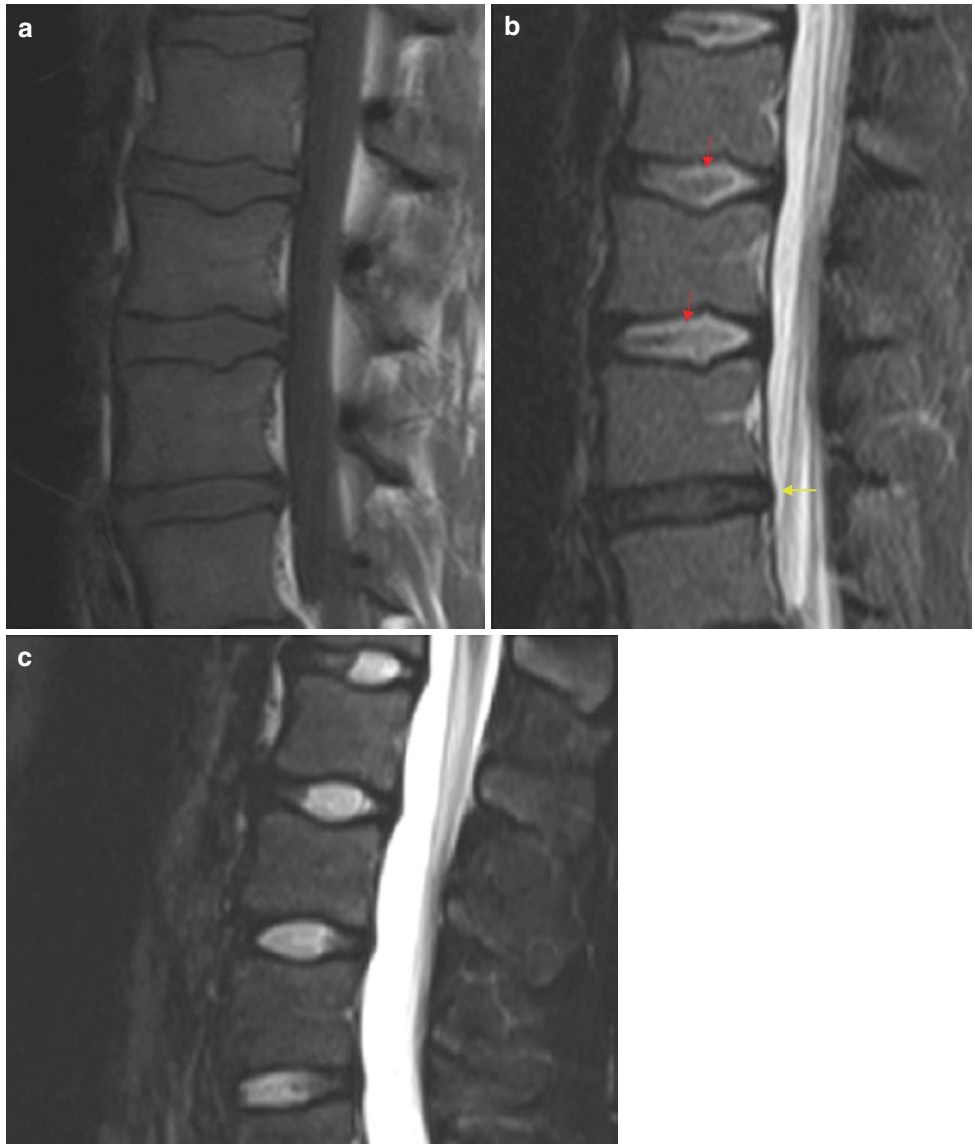

Fig. 3.12 (**a**) Sagittal T1-weighted and (**b**) STIR images in a middle-aged patient demonstrate well-hydrated discs at L2-L3 and L3-L4, although decreased STIR signal at L4-L5, compatible with desiccation (yellow arrow). Note the horizontal band of central low T2/STIR signal at L2-L3 and L3-L4 (red arrows), termed intranuclear cleft, which is a normal physiologic process in aging and represents fibrous transformation of the gelatinous matrix of the nucleus pulposus. (**c**) Sagittal STIR image in an adolescent patient demonstrates absence of discrete internuclear clefts at L2-L3 and L3-L4

The well-hydrated disc is uniform and symmetric in height, and the peripheral fibers of the annulus fibrosus fuse indiscernably with the longitudinal ligaments. Posttraumatic disc pathology can be classified as either intradiscal injury or disc herniation. In intradiscal injury, there is asymmetric widening or narrowing of the disc space on sagittal MRI and focal increased T2-weighted signal within the posterior annulus fibrosus due to tearing of the disc substance. This typically appears as a small, well-demarcated 1–2 mm hyperintense focus on T2-weighted images that can enhance on post-gadolinium T1-weighted images. In fact, the disc overall appears more hyperintense on T2-weighted images than adjacent discs, and this abnormality is contiguous with other damaged soft tissues (Fig. 3.13). Since the adult disc is an avascular structure, these signal changes may be due to hemorrhagic changes occurring at the adjacent vertebral endplates (Fig. 3.14). Moreover, these intradiscal signal abnormalities are easier to identify in degenerated discs that are hypointense on T2-weighted sequences.

In acute posttraumatic disc herniation, the nucleus pulposus protrudes into the peripheral annulus fibrosus and sometimes beyond the vertebral endplate margins into the ventral epidural space (Fig. 3.15). Sagittal MRI shows contiguity between the herniated disc and the parent disc. This may or may not be associated with a vertebral fracture at the same level. On axial images, there is focal distortion of the thecal sac by the disc herniation, corresponding to the abnormality at the same level on sagittal images, and if severe, there may be compression of the neural elements. The degree of canal compromise and neural compression is dependent on the size of the herniated fragment, the width of the spinal canal, and the diameter of the spinal cord. In those with congenitally narrowed spinal canals or pre-existing degenerative disc disease, relatively small disc herniations may produce significant spinal cord compression. This is especially true in the thoracic spine given the already relatively smaller width of the central canal compared to the cervical or lumbar spine. It may be difficult to distin-

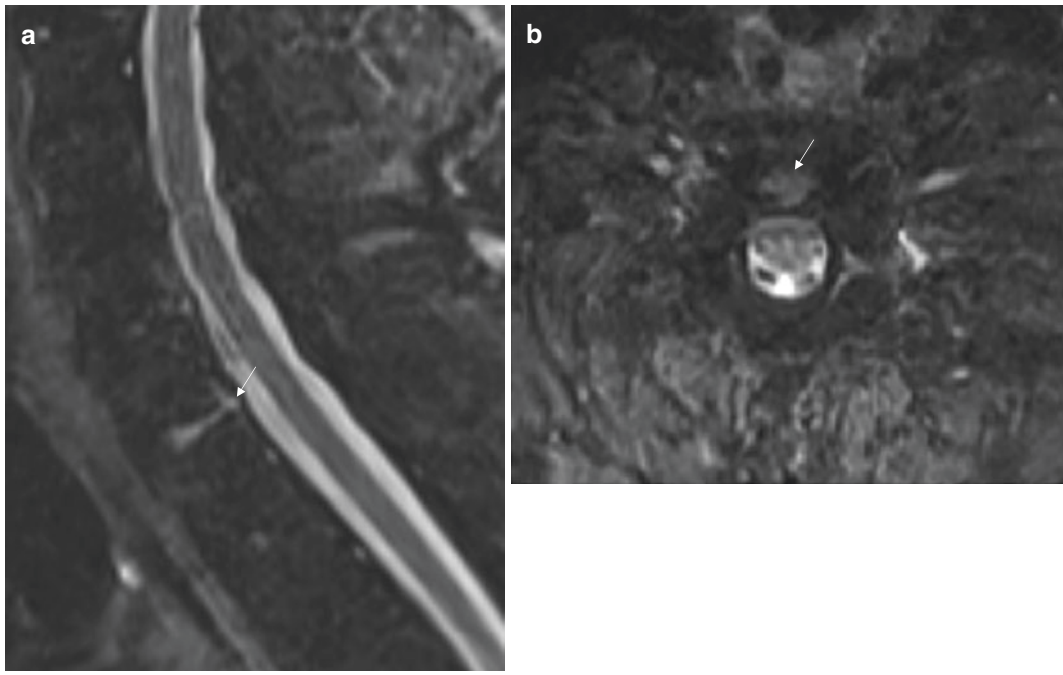

Fig. 3.13 (**a**) Sagittal and (**b**) axial STIR images in a patient post trauma demonstrate T2 hyperintensity in the C7-T1 disc extending into the annulus fibrosis, compatible with intradiscal injury (white arrows)

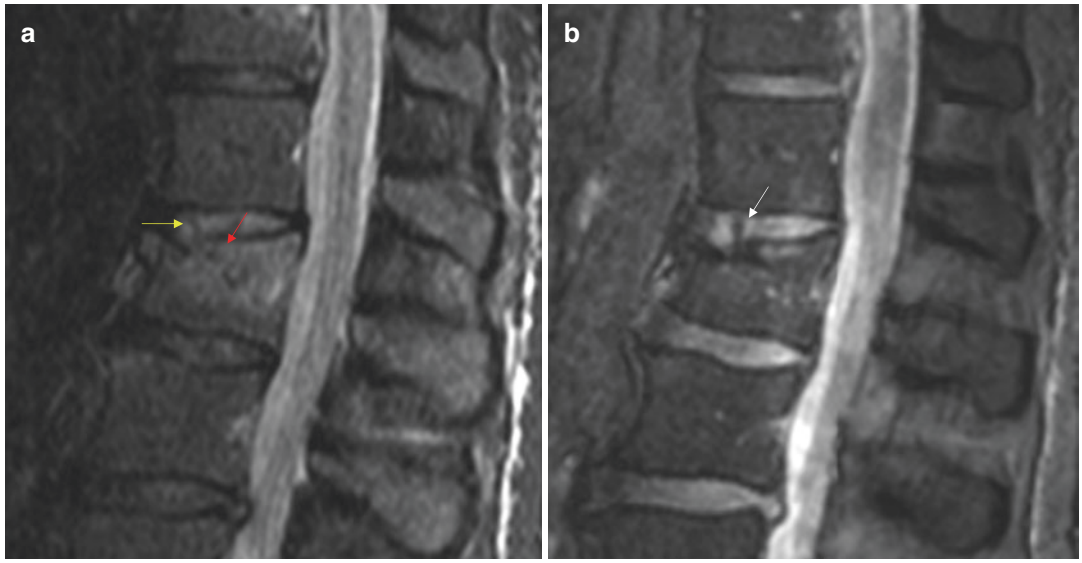

Fig. 3.14 (**a**) Sagittal STIR image demonstrates acute anterior wedge compression fracture of L2 (red arrow) with increased signal in the L1-L2 disc (yellow arrow), concerning for intradiscal injury. (**b**) Sagittal GRE image demonstrates tiny focus of intradiscal hypointensity, concerning for intradiscal hemorrhage (white arrow)

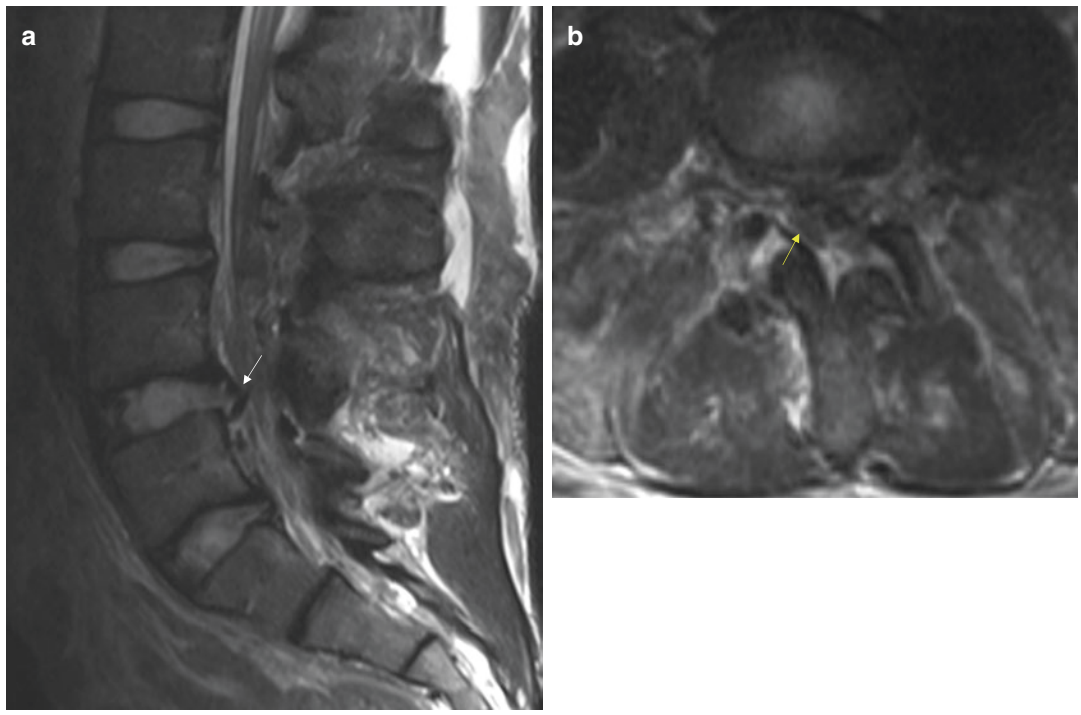

Fig. 3.15 (**a**) Sagittal T2-weighted image demonstrates posttraumatic disc herniation at L4 effacing the thecal sac (white arrow). (**b**) Axial T2-weighted image at the same level demonstrates combination of disc herniation and epidural hemorrhage significantly displacing and compressing the cauda equina, denoted by the yellow arrow

guish acute posttraumatic disc herniation from chronic spondylotic disc herniation, although secondary imaging signs, such as intradiscal signal abnormality at the same level, asymmetric width of the intervertebral disc space, subluxation, and associated soft tissue edema may all help to diagnose acute pathology.

MRI of Ligamentous Injury

MRI is able to directly visualize changes occurring to spinal ligaments as a result of trauma. MRI should be performed as soon as possible in suspected ligamentous injury since sensitivity for edema decreases over time as water is reabsorbed by the soft tissues. Spinal ligaments appear hypointense on all MRI pulse sequences due to their avascular and fibroelastic composition, as well as short T2 relaxation characteristics. Injury that causes abnormal stretching of the spinal ligaments results in intrinsic and extrinsic T2-weighted hyperintensity secondary to increased extracellular fluid and/or hemorrhage. Ligamentous tears can be partial, with varying degrees of intact fibers, or can be complete. Focal discontinuity of the ligament may be seen in severe cases that lead to rupture [110, 114, 115]. It may sometimes be difficult to distinguish cortical bone fragments from ligaments on MRI since both are hypointense on all MRI sequences.

Imaging of the CCJ ligaments is especially challenging, and MRI should be tailored to optimally detect injury in this region. At minimum, a 1.5 Tesla magnet with dedicated head, neck, and spine coil and with slice thickness no greater than 3 mm should be utilized. Axial images should extend to include the entire CCJ. High-resolution imaging is preferred, with requires a longer scan time due to decreased slice thickness, larger matrix size, and higher spatial resolution, although a smaller field of view can be used to decrease overall scan time. High-resolution 3D volumetric acquisitions are especially helpful in this region, with isotropic voxels allowing for reconstruction in any plane and small voxel size resulting in improved spatial resolution. In CCJ injuries, interrogation of the three major stabilizing ligaments, namely, the tectorial membrane, the cruciate ligament, and the alar ligaments, is critical. The cruciate ligament is composed of the horizontal transverse atlantal ligament and vertical components, though only the transverse atlantal ligament is discretely seen on MRI. The transverse atlantal ligament is best visualized in the axial plane, appearing hypointense on T2-weighted and proton density images, although it can become hyperintense with aging. The alar ligaments are best seen in the coronal plane as hypointense bands extending superolaterally from the tip of the dens to the occipital condyles. The tectorial membrane is the continuation of the posterior longitudinal ligament (PLL) as it extends cranially from C1 and is best seen in the sagittal plane on MRI. The anterior longitudinal ligament (ALL) continues along the anterior aspect of the vertebral bodies and terminates at the clivus, and its components at the CCJ include the anterior atlantoaxial ligament and anterior atlanto-occipital membrane. The posterior atlanto-occipital membrane, which is continuous with the posterior atlantoaxial membrane and ligamentum flavum (LF) inferiorly, attaches the posterior arch of the atlas inferiorly to the posterior rim of the foramen magnum superiorly. The apical ligament, which connects the tip of the dens to the basion, plays little, if any, role in CCJ stability (Fig. 3.16). Careful inspection of the CCJ ligaments for increased T2-weighted fluid signal suggesting sprain or partial tear, versus discontinuity compatible with avulsion or complete rupture is critical in the appropriate clinical setting (Fig. 3.17).

In the subaxial cervical (C3-C7) and thoracolumbar spine, the ALL, PLL, LF, and ISPs are well delineated on sagittal MR images (Fig. 3.18). The ALL, a critical component of the anterior column, is a thick strong band extending from the skull base to the sacrum that lies ventral to the anterior cortical surface of the vertebral bodies. Portions of the ALL merge with Sharpey's fibers at the vertebral endplate and outer fibers of the annulus fibrosus. The ALL is often indistinct from the cortex or outer annulus, although is more conspicuous when elevated by fluid, disc, or bone. Hyperextension can rupture the ALL

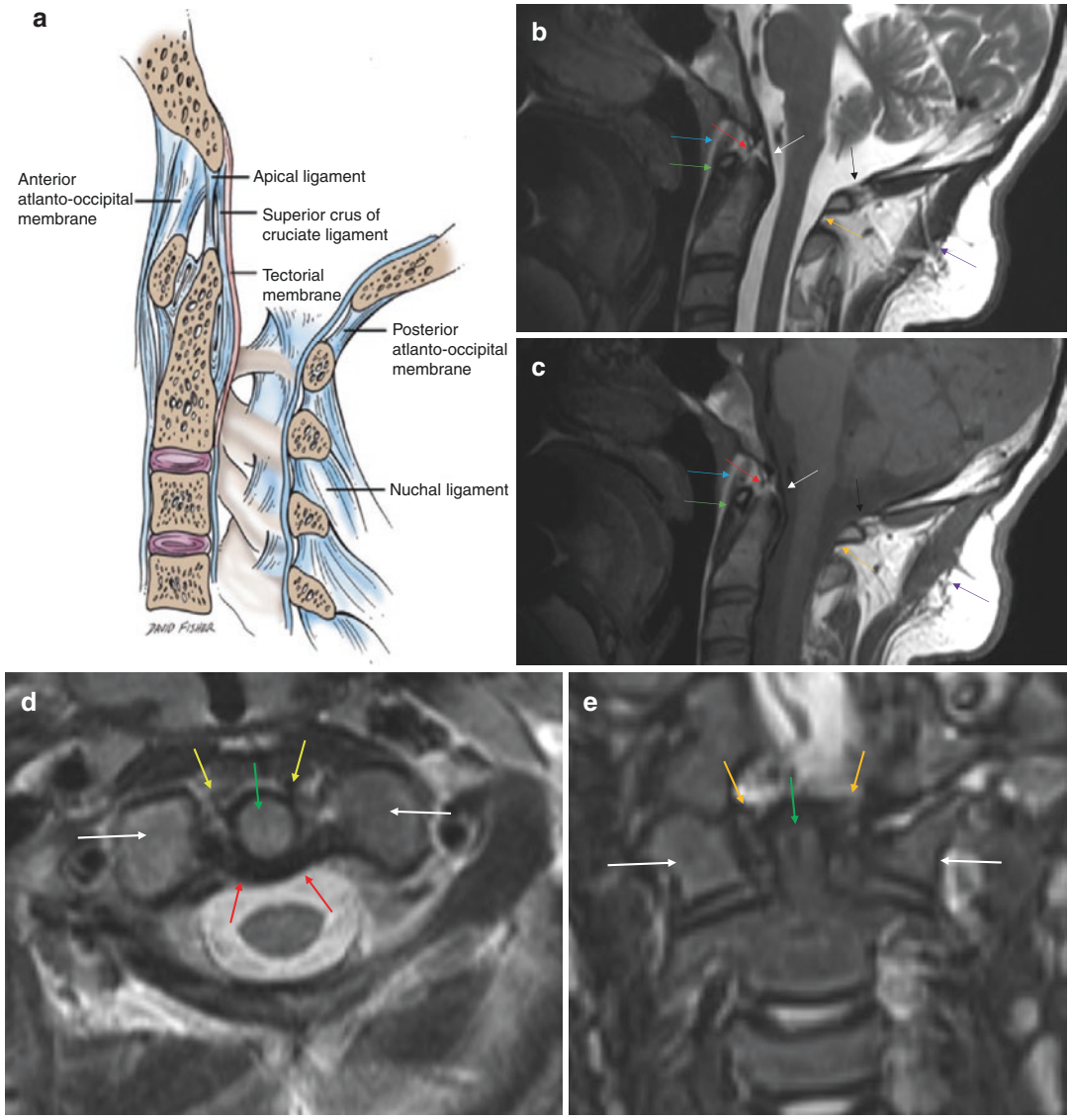

Fig. 3.16 (**a**) Sagittal drawing of the neck and skull base demonstrating the various ligaments of the CCJ. (Reprinted with permission from Tubbs et al. [116].) (**b**) Sagittal T2- and (**c**) sagittal T1-weighted images demonstrate normal appearance of the CCJ ligaments. Apical ligament (red arrows), anterior atlanto-occipital membrane (blue arrows), anterior atlantoaxial membrane (green arrows), posterior atlanto-occipital membrane (black arrows), posterior atlantoaxial membrane (orange arrows), tectorial membrane (white arrows), and nuchal ligament (purple arrows). (**d**) Axial T2-weighted image of the CCJ demonstrates normal transverse ligament (red arrows), anterior atlantodental ligaments (yellow arrows), dens (green arrow), and lateral masses of C1 (white arrows). (**e**) Coronal STIR image in the same patient demonstrates alar ligaments (orange arrows), dens (green arrow), and lateral masses of C1 (white arrows)

and cause avulsion of the anterior vertebral body endplate [109, 118–123] (Fig. 3.19). Sometimes, the only clue to subtle or occult ALL injury may be the accumulation of fluid and/or hemorrhage in the prevertebral space at the level of injury.

The PLL is wider at the level of the intervertebral disc than it is posterior to the vertebral bodies and, therefore, may normally appear discontinuous on MRI. As the principal ligament of the middle column, the PLL is interposed between

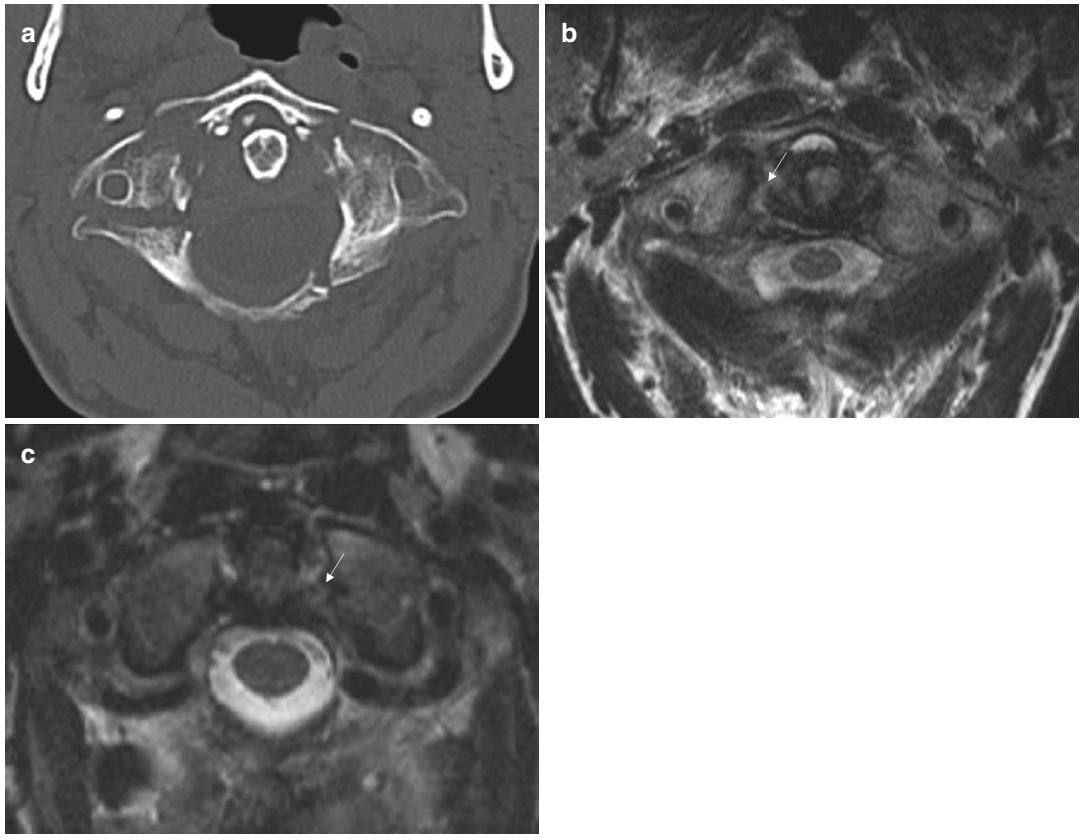

Fig. 3.17 (**a**) Axial CT image demonstrates four part C1 fracture with displaced lateral masses. (**b**) Axial T2-weighted image demonstrates focal full thickness discontinuity at the right C1 attachment of the transverse ligament compatible with avulsion injury (white arrow). (**c**) Axial T2-weighted image in a different patient demonstrates high signal in the left transverse ligament at its attachment, compatible with sprain or partial tear (white arrow)

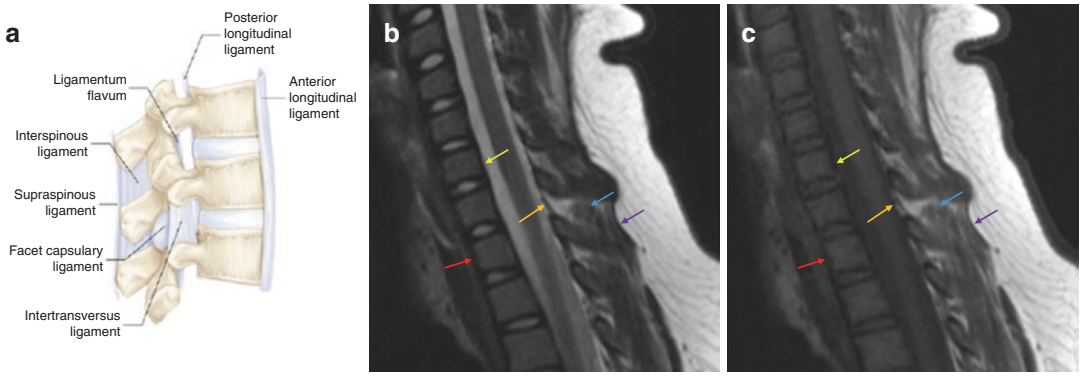

Fig. 3.18 (**a**) Ligaments of the spine. (Reprinted with permission from Arakal et al. [117].) (**b**) Sagittal T2- and (**c**) sagittal T1-weighted images demonstrate normal appearance of the ALL (red arrows), PLL (yellow arrows), LF (orange arrows), ISPs (blue arrows), and supraspinous ligament (purple arrows). ALL, anterior longitudinal ligament; PLL, posterior longitudinal ligament; LF, ligamentum flavum; ISPs, interspinous ligaments

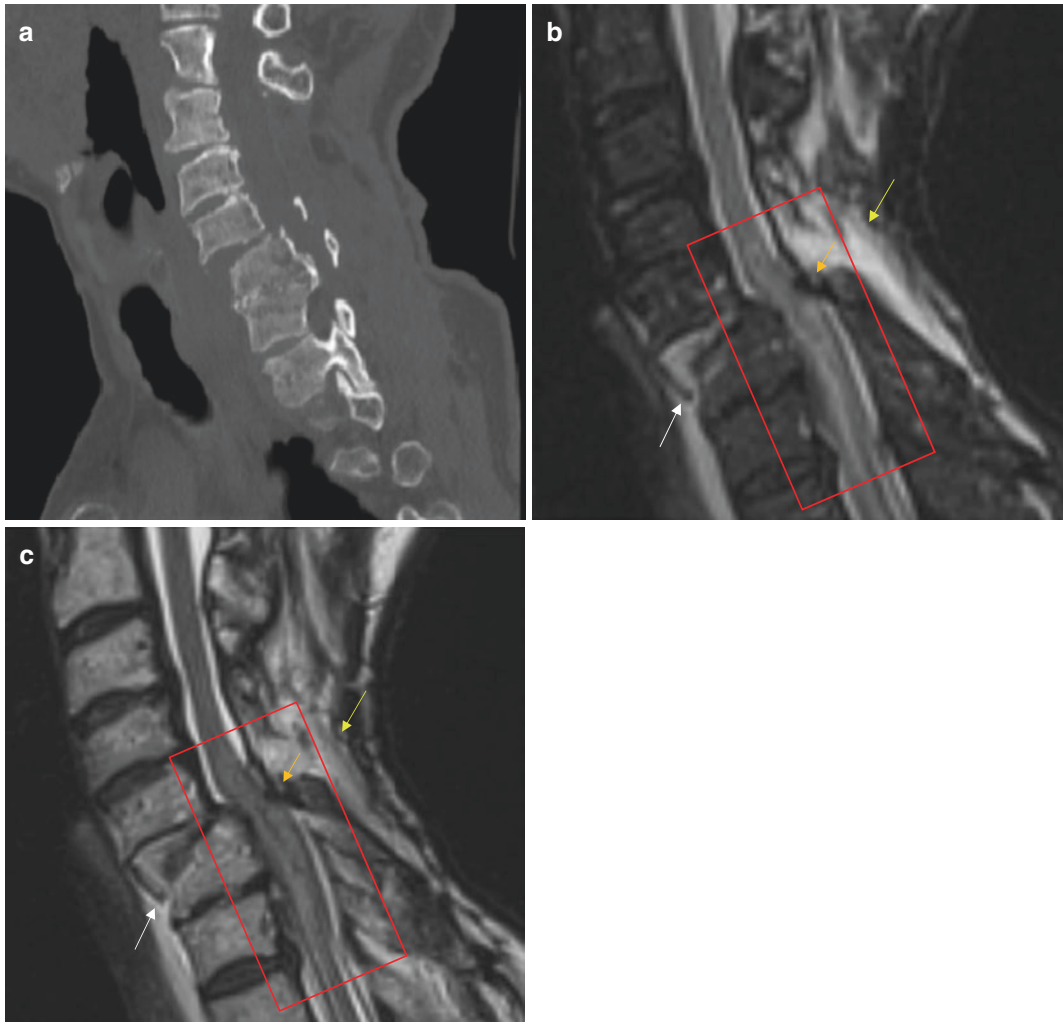

Fig. 3.19 (**a**) Sagittal CT image demonstrates translational injury at C5-C6 with anterior subluxation of C5 on C6 and widening of the anterior disc space. (**b**, **c**) Sagittal STIR and sagittal T2-weighted images demonstrate intradiscal and prevertebral edema with avulsed anterior longitudinal ligament (white arrows). Also note extensive edema compatible with injury of the posterior ligamentous complex (yellow arrows), including buckling of the LF at C5-C6 (orange arrows) and spinal cord contusion (red outlines)

the posterior vertebral body cortex and ventral thecal sac and is nearly impossible to resolve from these structures on sagittal MR images. Hyperextension or hyperflexion can injure the PLL, resulting in intra-ligamentous high signal intensity on fluid-sensitive sequences versus focal discontinuity, which may be associated with disc herniation or epidural fluid collection [124] (Fig. 3.20).

The LF, which bridge adjacent lamina, and ISPs which connect adjacent spinous processes, are the principal ligaments of the posterior column, which oppose hyperflexion and distraction of the posterior elements. Focal discontinuity of the LF is associated with fractures of the posterior elements and can be appreciated on sagittal MR images. In hyperextension injury, much like in degenerative disease, the LF may enlarge and bulge into the posterior spinal canal, distorting the thecal sac. The ISPs are best evaluated on fat-suppressed mid-sagittal T2-weighted images, with injury to them characterized by T2-weighted

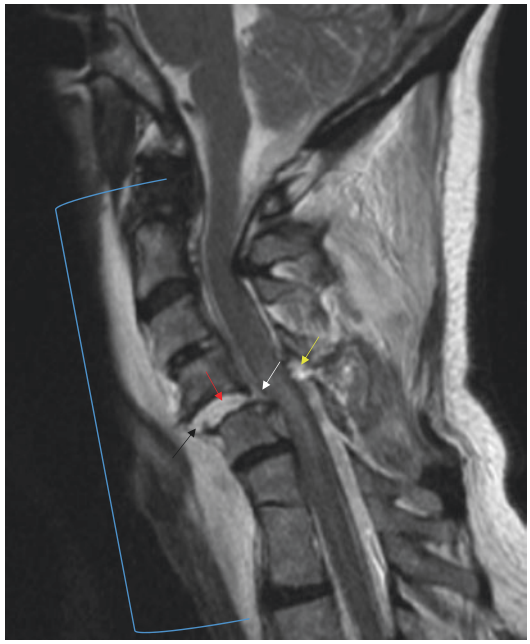

Fig. 3.20 Sagittal T2-weighted image, in addition to demonstrating injury to the ALL (black arrow), demonstrates focal discontinuity of the PLL at C4-C5 compatible with complete rupture (white arrow). Note also discontinuity of the LF (yellow arrow), intradiscal injury (red arrow), and prevertebral hemorrhage (blue bracket)

hyperintensity with or without widening of the space between adjacent spinous processes. The supraspinous ligament, which is continuous with the nuchal ligament above the seventh cervical vertebral body, is a thick hypointense band that connects to the tips of the spinous processes and serves to resist hyperflexion. Partial tears or sprains of these ligaments are more common than complete tears or rupture. Rupture of the supraspinous ligament, which connects the tips of adjacent spinous processes, results in projection of its free edge into the edematous posterior paraspinal soft tissues (Fig. 3.21). The facet joint capsules are more readily visualized in the cervical and lumbar spine where they are larger and the joint plane is oriented in the sagittal direction, as opposed to in the thoracic spine, where they are smaller and oriented in the coronal plane. The facet joint is a complex, dynamic structure that allows for limited compression and distraction of the posterior elements during extension and flexion while resisting rotation and translation. Damage to the facet joint complex manifests as widening of the space between the superior and inferior articular facets on parasagittal MR images, as well as edema within the facet joint, capsule, and perifacetal soft tissues on T2-weighted and STIR images (Fig. 3.22).

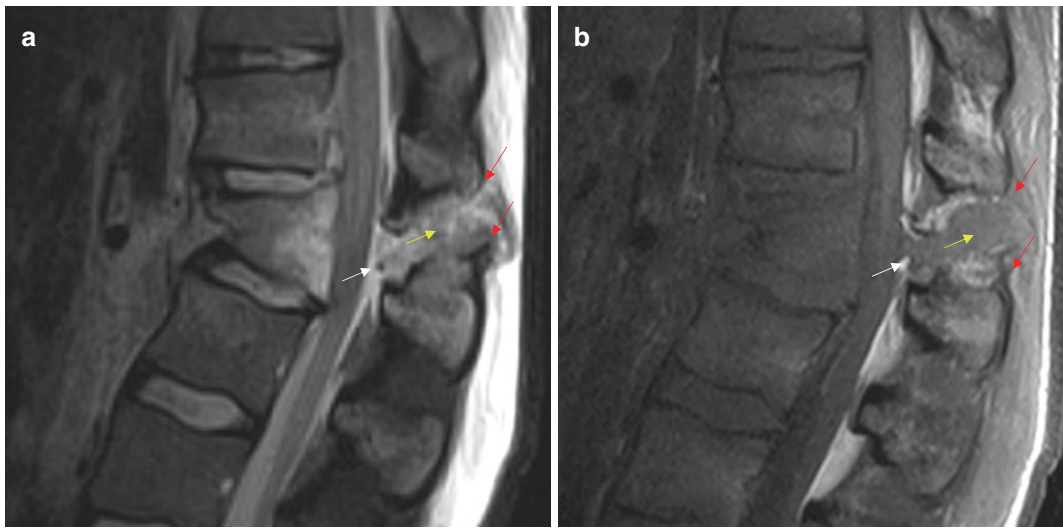

Fig. 3.21 (**a**) Sagittal T2- and (**b**) sagittal T1-weighted images demonstrate ruptured free edges of the supraspinous ligament (red arrows) and interspinous ligaments (yellow arrows) at T12-L1. The LF is also ruptured (white arrows)

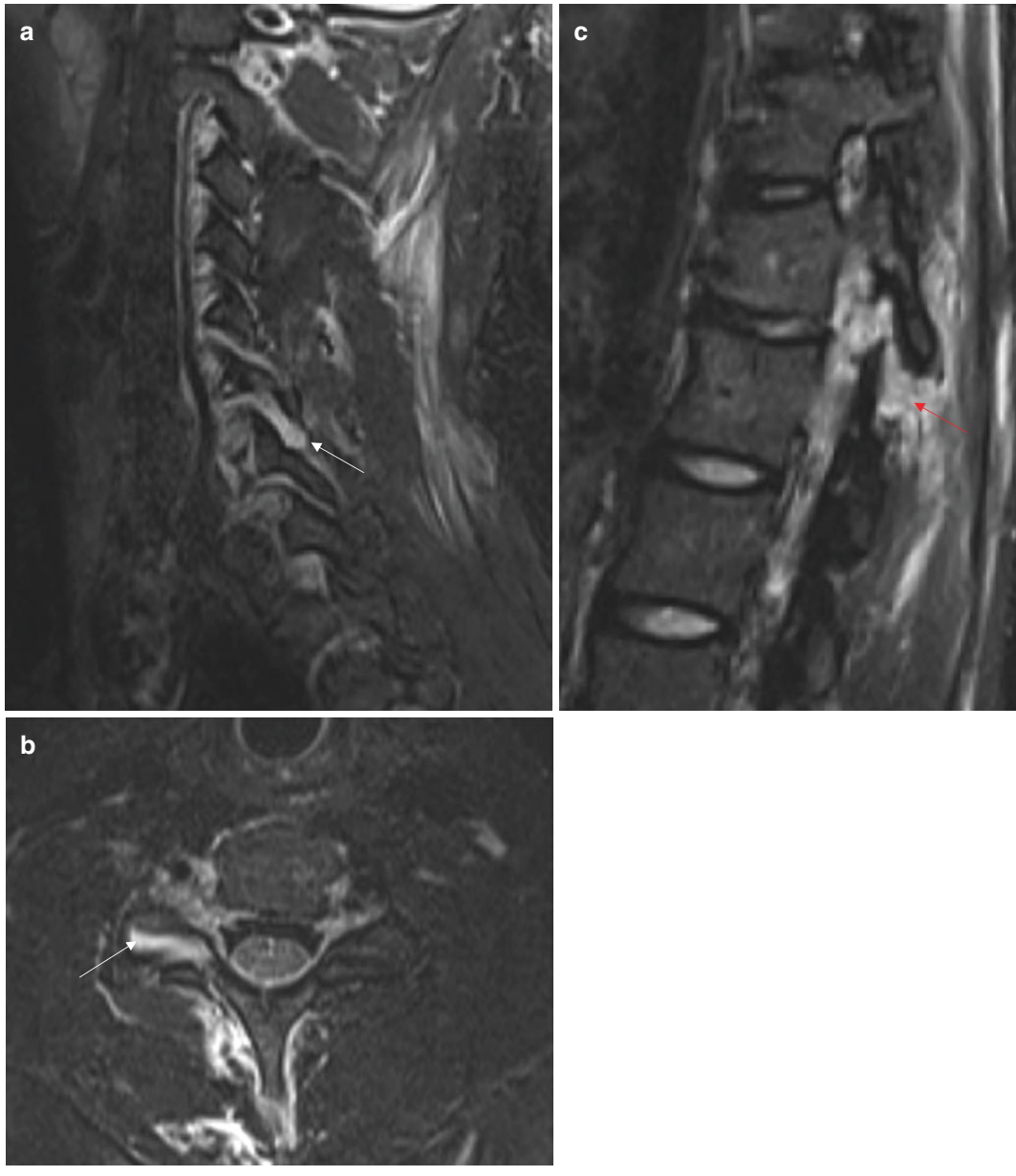

Fig. 3.22 (**a**) Parasagittal and (**b**) axial STIR images demonstrate widening and increased fluid signal in the right C6-C7 facet joint (white arrows) with edema in the surrounding soft tissues, concerning for facet capsular injury without facet subluxation. (**c**) Sagittal STIR image in a different patient reveals distracted facets at T12-L1 and surrounding edema compatible with facet capsular injury (red arrow)

MRI of the spine after trauma will often also demonstrate other soft tissue injuries, such as muscle strain and subcutaneous contusions. Muscle strains will appear as intramuscular hyperintensity on T2-weighted and STIR sequences, with or without muscular enlargement, and, at times, may be associated with more heterogeneous signal if intramuscular hemorrhage is present. It is important to detect these findings as they may be sources of pain after trauma in the absence of osseous or ligamentous injury.

MRI of Spinal Hematomas

The epidural compartment is a fat-containing space situated between the bony and ligamentous components of the spine and the dura mater, extending from the foramen magnum to the sacral hiatus, and also laterally into the neural foramina. This space also contains connective tissue, the internal vertebral venous plexus, small caliber arteries, and the exiting spinal nerve roots. Because of the rich vasculature of the epidural space, epidural hematoma is the most commonly encountered intraspinal hematoma. It is usually idiopathic, though may be seen after trauma as a portion of the epidural venous plexus tears and results in extravasation of blood into the epidural space. Most epidural hematomas are asymptomatic and small; however, they can extend over long portions of the spine without significant compromise of the thecal sac. MRI is the ideal imaging tool for the detection of epidural hematoma, which is only occasionally seen by CT. Most traumatic epidural hematomas occur in the dorsal or dorsolateral aspect of the spinal canal since the LF are more loosely adherent to the dura mater than the PLL, although they typically extend ventrally. They appear as abnormal fluid collections occupying the predominantly fat-containing epidural space, displacing the dura mater, and possibly distorting the thecal sac. Sagittal MRI can delineate the entire craniocaudal extent of the epidural hematoma and may also show an epidural fat cap that surrounds the hematoma (Fig. 3.23). The signal characteristics of epidural hematoma on MRI change over time due to differing magnetic properties of evolving blood products. The stages of blood that have been traditionally described in the brain (hyperacute, acute, early subacute, late subacute, and chronic) can be broadly applied to epidural hematoma, noting, however, that some variation is likely and strict application is not often possible (Box 3.8). In the hyperacute stage, epidural hematoma is difficult to distinguish from CSF, and moreover, GRE images meant to detect blood typically do not show any susceptibility artifact (hypointensity) (Fig. 3.24). Acutely, epidural hematoma is isoin-

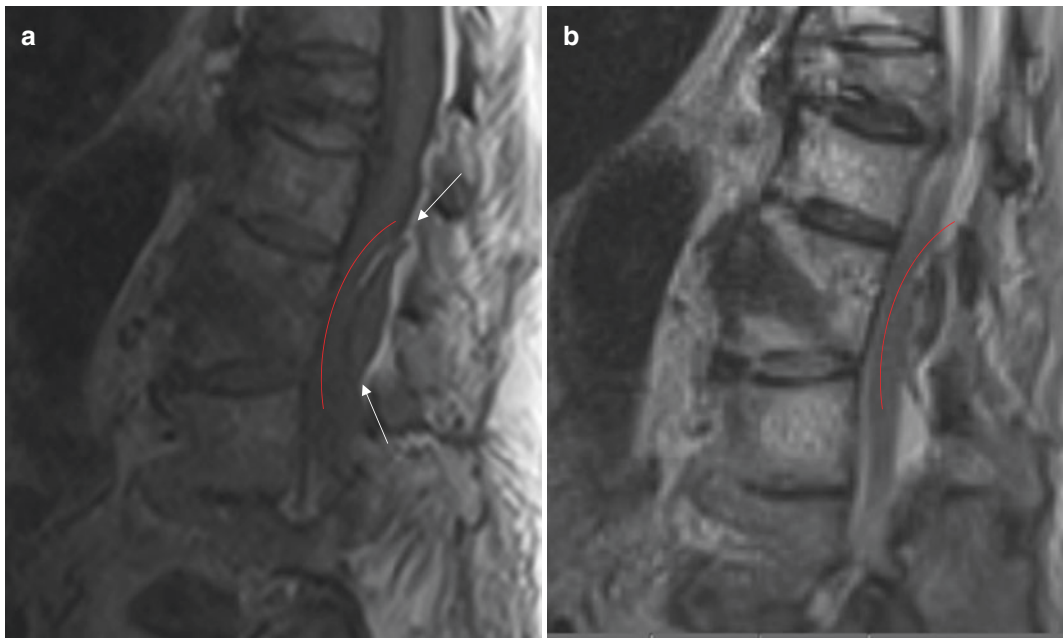

Fig. 3.23 (**a**) Sagittal T1-weighted image in a patient with multiple fractures demonstrates dorsal epidural fluid collection with evidence of bright epidural fat cap (white arrows). (**b**) Sagittal T2-weighted image demonstrates hypointense collection and (**c**) GRE image also reveals hypointensity compatible with hemorrhage

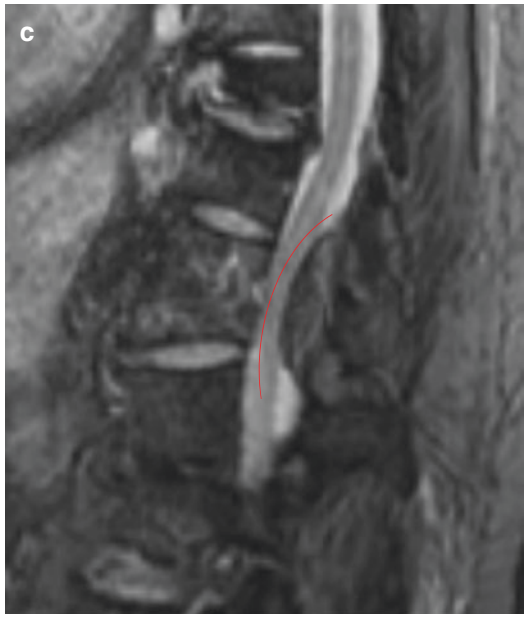

Fig. 3.23 (continued)

Box 3.8: Evolution of Hemorrhage on MRI

Hemorrhage	T1-weighted	T2-weighted
Hyperacute (<12 hours)	Isointense	Bright
Acute (12 hours–2 days)	Isointense	Dark
Early subacute (2–7 days)	Bright	Dark
Late subacute (1 week–2 months)	Bright	Bright
Chronic (>2 months)	Dark	Dark

tense or slightly hyperintense to the spinal cord parenchyma on T1-weighted images and isointense to the CSF on intermediate and T2-weighted images [125]. Subacutely, epidural hematoma appears hyperintense on T1-weighted and hypointense on T2-weighted images. On post-gadolinium MRI, epidural hematoma has been shown to peripherally enhance (Fig. 3.25). Fat-saturated MRI is sometimes needed to differentiate epidural hematoma from epidural lipomatosis, or excess fat in the epidural space, the latter which is typically encountered in the lower thoracic or lower lumbar spine and which may distort the spinal canal (Fig. 3.26). The subdural space is situated between the dura and arachnoid maters and may be separated in the setting of trauma, although spinal subdural hematoma is far less common than epidural hematoma. The dural reflections of the bilateral denticulate ligaments and midline dorsal septum serve to produce a characteristic appearance of larger subdural collections in the spine ("inverted Mercedes-Benz sign"). Since spinal subdural hematoma occurs within the thecal sac, the epidural fat is preserved and there is no displacement of the dura mater. These collections should not contact bone, although this distinction is not always clear anteriorly where the epidural fat is very thin. Unlike epidural hematoma, subdural hematoma does not extend into the neural foramina and has a tapered appearance without evidence of a fat cap (Fig. 3.27).

Spinal subarachnoid hemorrhage is an uncommon cause of neural compression and is typically a result of redistribution of blood products from the intracranial compartment by CSF flow. On MRI, this usually manifests as layering blood in the most dependent aspect of the thecal sac, or rarely, as a nonenhancing intradural, extramedullary mass representing a blood clot. On post-gadolinium MRI, there can be development of arachnoiditis as manifested by clumping and enhancement of the cauda equine nerve roots. GRE images may demonstrate hemosiderin staining as characterized by hypointensity along the dura and pia mater after subarachnoid hemorrhage.

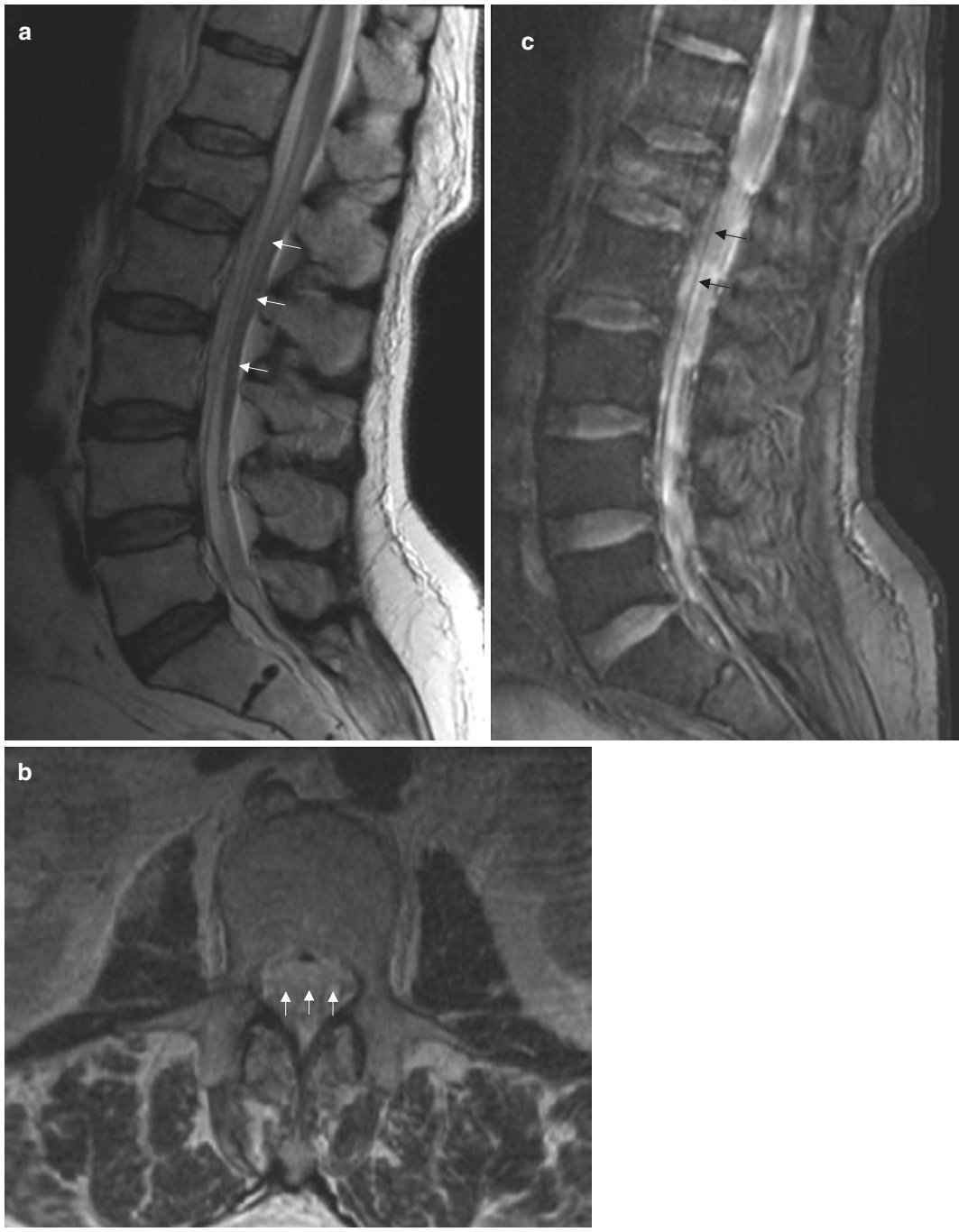

Fig. 3.24 (**a**) Sagittal and (**b**) axial T2-weighted images demonstrate hyperintense ventral epidural fluid collection in the setting of L1 burst fracture (white arrows). (**c**) Sagittal GRE image of the collection is without corresponding magnetic susceptibility artifact, or hypointensity, compatible with hyperacute stage of hemorrhage (black arrows)

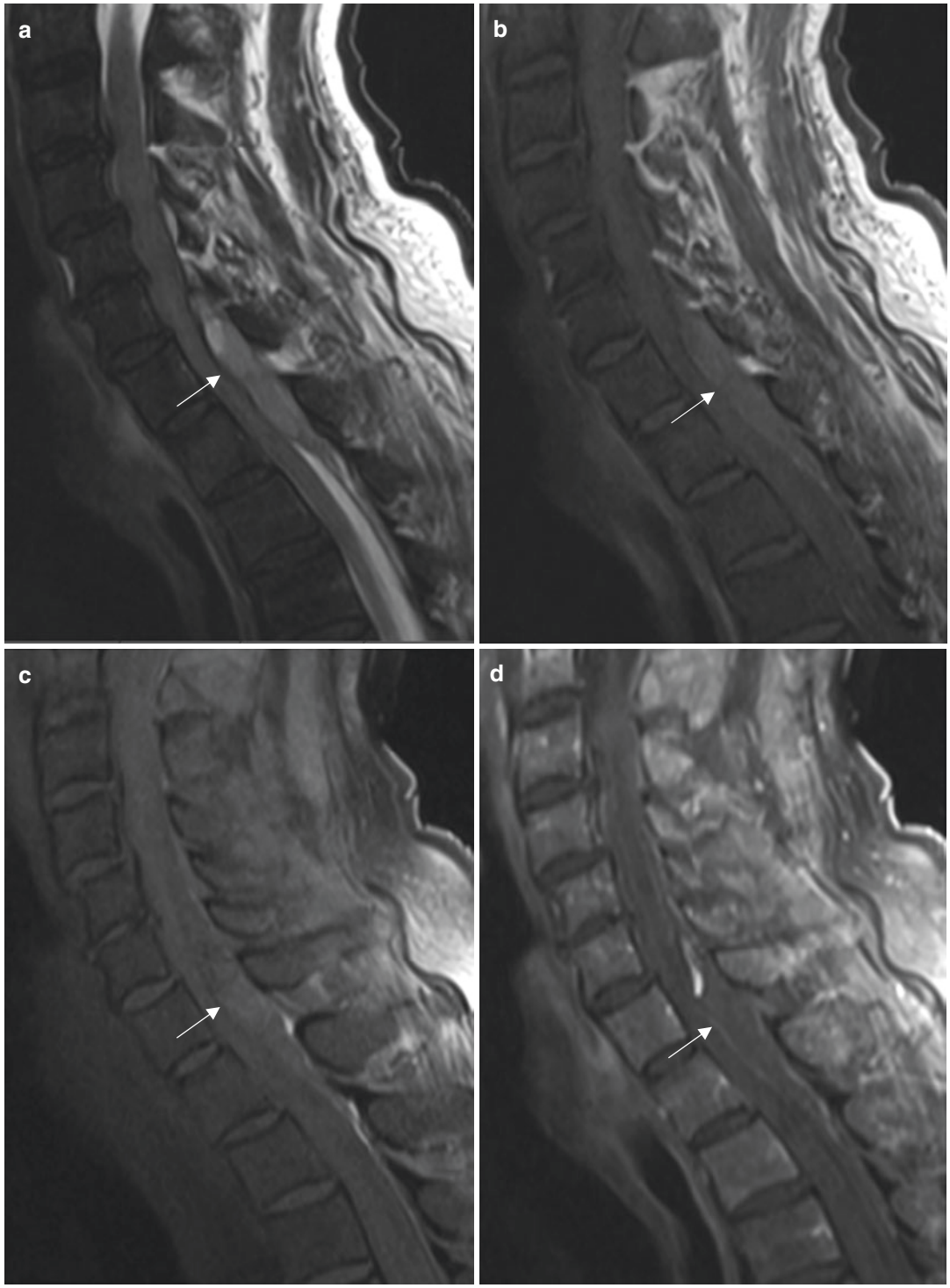

Fig. 3.25 (**a**) Sagittal T2-, (**b**) sagittal T1-, and (**c**) sagittal T2-weighted fat-saturated images of the cervical spine demonstrate an acute dorsal epidural hematoma that is isointense to hypointense to CSF on T2-weighted and mildly hyperintense on T1-weighted images (white arrows). There is associated spinal cord compression. (**d**) Sagittal T1-weighted fat-saturated post-gadolinium image reveals that this hematoma mildly enhances along its periphery (white arrow)

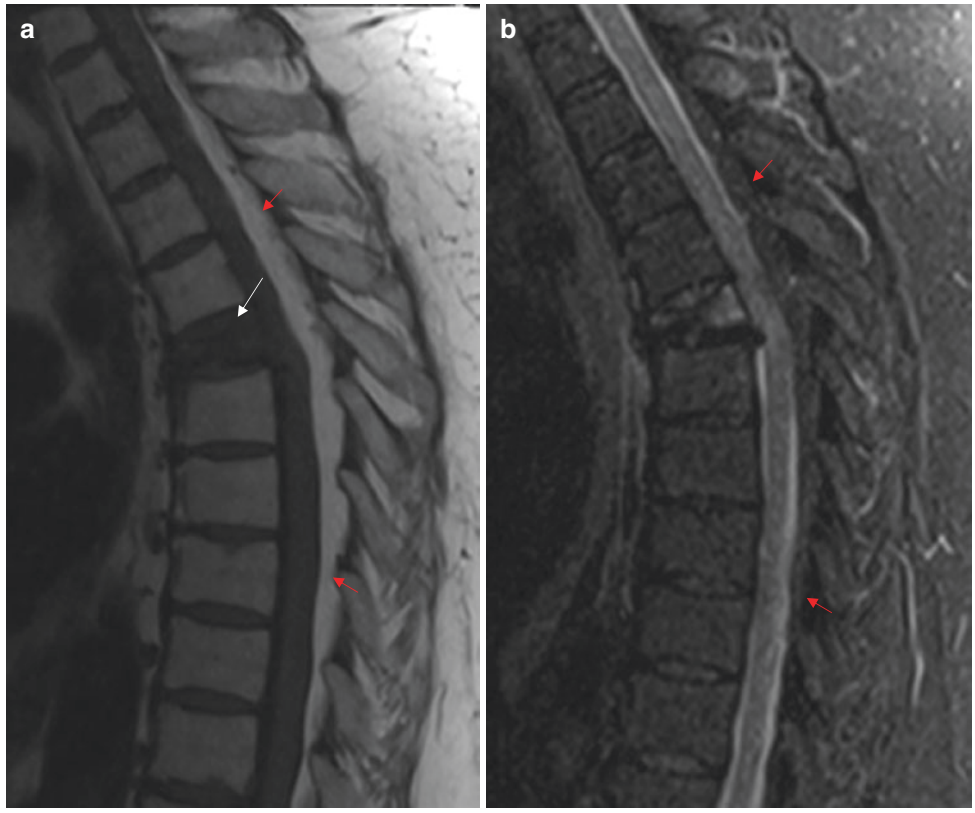

Fig. 3.26 (**a**) Sagittal T1-weighted image of the thoracic spine demonstrates a burst fracture of T5 (white arrow). There is prominent, fairly homogeneous T1 bright signal in the posterior epidural space, which suppresses on (b) STIR image, compatible with epidural lipomatosis (between red arrows). This contributes to severe spinal canal stenosis and cord compression at T5

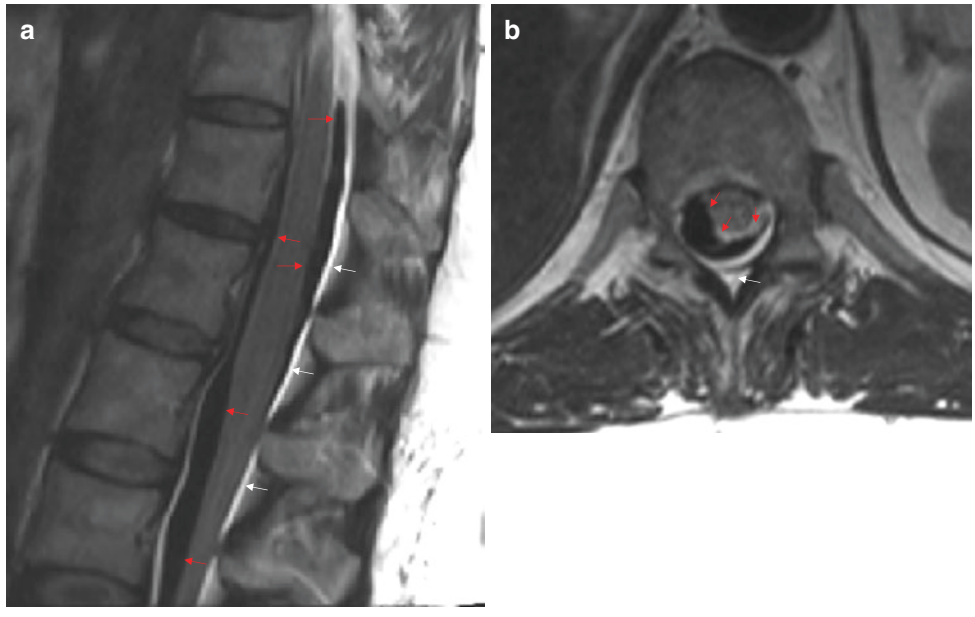

Fig. 3.27 (**a**) Sagittal and (**b**) axial T2-weighted images demonstrate T2 hypointense fluid in the subdural space compatible with subdural hematoma (red arrows). Note that T1 hyperintense fat of the dorsal epidural compartment is preserved (white arrows), although this distinction is less clear anteriorly

MRI of Neck Vascular Injury

Both blunt and penetrating trauma can cause injuries to the spinal vasculature, primarily, dissection or thrombosis of the extracranial carotid and vertebral arteries. The vertebral artery may be subject to an intimal tear by fractures secondary to propagation through the transverse foramen or overstretching by cervical subluxation [126, 127]. This may result in local occlusion of the vessel, which can serve as a nidus for clot formation and subsequent embolization to the brain with resultant stroke, or rather, may dissect and create a false lumen also leading to arterial occlusion. There may also be partial transection of the vessel resulting in the formation of a pseudoaneurysm, or more devastatingly, complete transection resulting in hemorrhage. Traumatic vertebral artery injury is relatively rare, reported in less than 1% of trauma admissions, although its incidence is rising due to increasing awareness and screening, and may be as high as 11% in patients with blunt trauma that meet certain clinical and physical examination criteria [128]. Prompt detection of vertebral injury is vital given its potential to cause primary neurologic impairment and secondary injury, which may be prevented by prophylactic treatments that include, but are not limited to, anticoagulation, embolization, and surgical ligation [129]. The Biffl grading scale, also referred to as the Denver scale, is a widely accepted system that classifies blunt cerebrovascular injury (BCVI), based on its appearance on digital subtraction angiography (DSA) or CT angiography (CTA), into five grades of increasing severity with important prognostic and therapeutic implications (Box 3.9) [130, 131].

Box 3.9: Biffl Grading Schemes for Blunt Cerebrovascular Injury (BCVI)

Injury grade	Description	Stroke rate (%)	Mortality rate (%)
I	Luminal irregularity or dissection with <25% luminal narrowing	3	11
II	Dissection or intramural hematoma with ≥25% luminal narrowing, intraluminal thrombus, or raised intimal flap	11	11
III	Pseudoaneurysm	33	11
IV	Occlusion	44	22
V	Transection with extravasation	100	100

Adapted from Mutze et al. [131] and Shafafy et al. [130]

CTA is the initial diagnostic test of choice for patients with suspected BCVI and has been shown to have a sensitivity of nearly 100% in patients meeting the modified Denver screening criteria, a set of signs/symptoms and risk factors associated with a higher risk of injury [132] (Box 3.10). Although DSA has been long described as the gold standard for diagnosing BCVI, it is invasive, carries a 0.5% risk of stroke, and is less readily available than CTA [133]. Moreover, DSA does not allow visualization of the vessel wall and, therefore, is limited in instances of non-flow-limiting intramural hematoma. MRA has inferior or equivalent specificity for detecting vertebral artery injury when compared with CTA, although recent advances in MRI technology have resulted in excellent imaging quality with the added benefit of being able to concurrently screen for acute ischemic brain infarction [134]. On MRA, dissection appears as irregular and often eccentric narrowing of the vessel that varies from mild stenosis to complete occlusion with thrombosis (Fig. 3.28). Axial GRE images reveal a hypointense clot that replaces normal vessel hyperintensity caused by normal blood flow, while axial T2-weighted images show luminal hyperintensity that replaces the normally hypointense vessel (Fig. 3.29). Subtle intimal injuries are difficult to identify on MRA due to limits in spatial resolution. However, on thin-section, axial T1-weighted images with black-blood techniques, normal blood flow is hypointense, while a subintimal clot associated with dissection will appear as a hyperintense crescent adjacent to the eccentric luminal stenosis (Fig. 3.30). The hema-

Box 3.10: Modified Denver Screening Criteria for BCVI

Modified Denver screening criteria
Symptoms or signs of BCVI
Massive epistaxis
Central or lateral neurologic deficit that is unexplained or incongruent with CT scan
Expanding neck hematoma
Acute or subacute cerebral infarction on CT scan
Transient ischemic attack or stroke after blunt neck trauma
Horner's syndrome (disruption of the sympathetic chain, with ipsilateral ptosis, miosis, and anhidrosis)
Cervical vascular bruit in a patient <50 years old with blunt neck trauma
Midface fracture with cervical hyperextension/rotation/flexion injury
Complex mandible fracture with cervical hyperextension/rotation/flexion injury
Closed head injury with diffuse axonal injury and cervical hyperextension/rotation/flexion injury
Cervical spine fracture with cervical hyperextension/rotation/flexion injury
Displaced midface fracture (Le Fort II or III) from high-energy mechanism
Skull base fracture involving foramen lacerum, sphenoid, mastoid, or petrous bones
Complex mandible fracture from high-energy mechanism
Seatbelt abrasion, hanging bruise, or unexplained contusion or hematoma of neck, resulting in significant cervical swelling or altered mental status
Cervical vertebral fracture extending through the transverse foramen
Cervical vertebral subluxation
Upper cervical vertebral fracture (C1 to C3)

Adapted from Utter et al. [132]

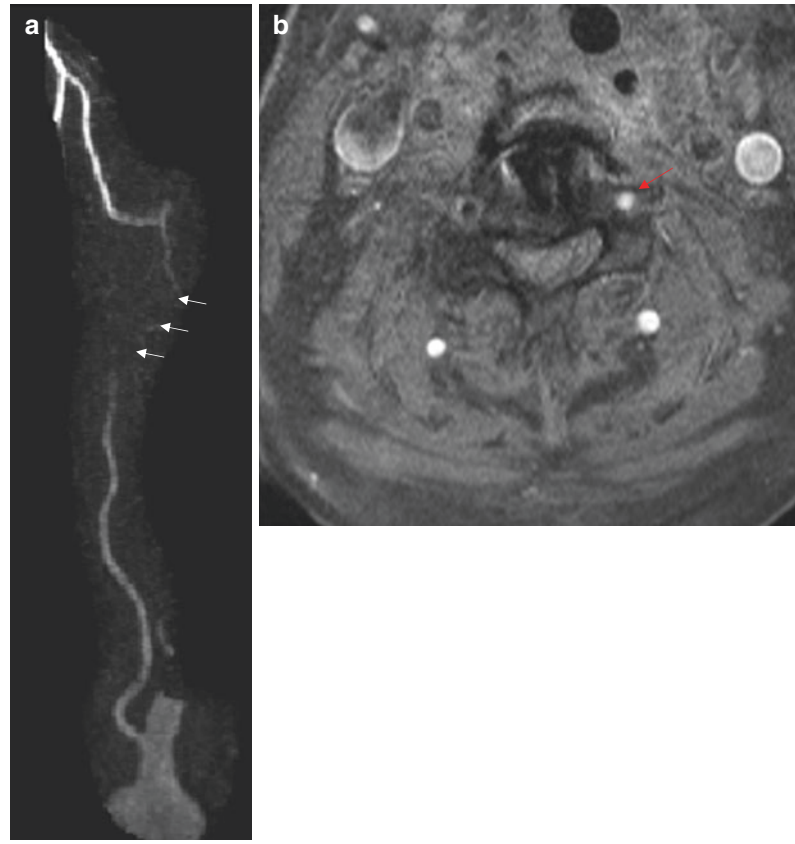

Fig. 3.28 (**a**) 3D maximum intensity projection (MIP) reconstruction of the left vertebral artery from time-of-flight MRA of the neck demonstrates loss of signal in the distal V2 through V3 segments compatible with occlusion (white arrows). (**b**) Axial T1-weighted fat-saturated image at this level demonstrates intraluminal hyperintensity, compatible with occlusive thrombus (red arrow)

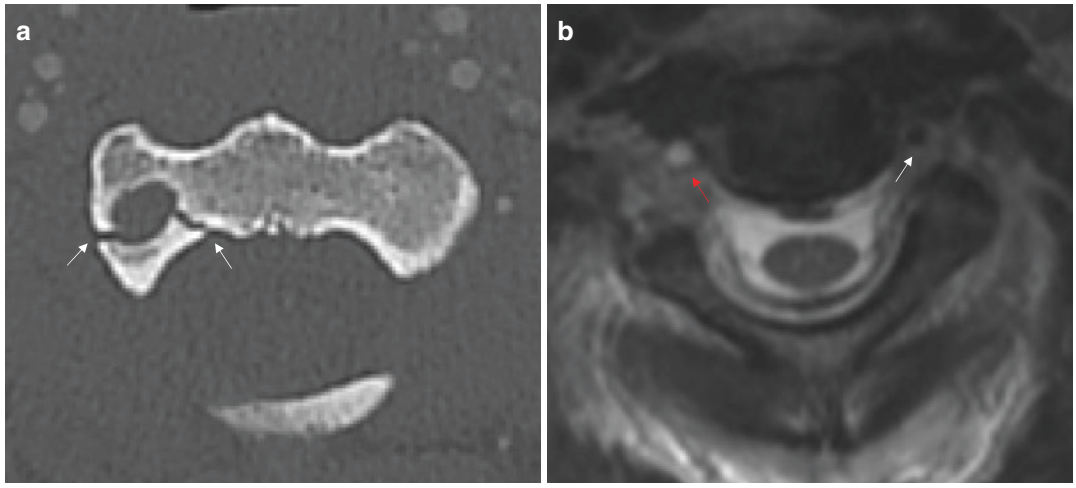

Fig. 3.29 (**a**) Axial CT image demonstrates a fracture involving the right C2 transverse foramen (white arrows). (**b**) Corresponding axial T2-weighted image demonstrates absence of the normal T2 hypointense flow void in the right vertebral artery (red arrow) compared to normal hypointensity in the left vertebral artery (white arrow), compatible with occlusion and/or slow flow, and suggestive of dissection

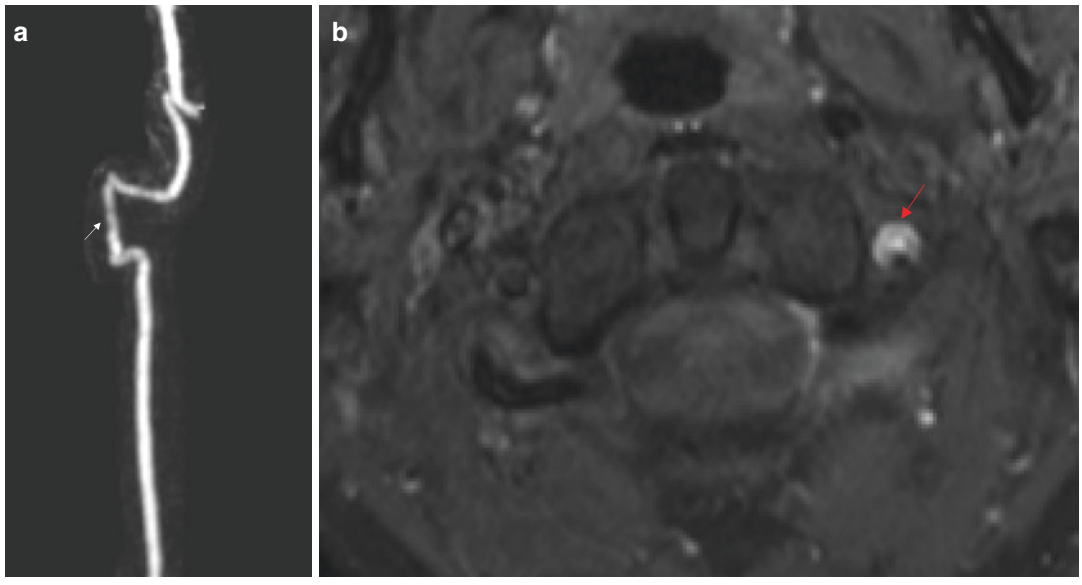

Fig. 3.30 (**a**) 3D MIP reconstruction of the left vertebral artery from MRA neck demonstrates mild intimal irregularity of the V3 segment (white arrow). (**b**) Axial T1-weighted fat-saturated image demonstrates prototypical appearance of crescentic intramural hyperintensity (red arrow), representing subacute subintimal clot in the setting of dissection

toma will evolve according to the paramagnetic effects of hemoglobin breakdown and, as such, will be isointense to surrounding structures in the hyperacute and acute stages due to the presence of oxyhemoglobin and deoxyhemoglobin, respectively, and will be hyperintense on T1-weighted images in the subacute stage due to methemoglobin. Regardless of recent advances in MRI quality, MRI/MRA is not routinely recommended in the acute polytrauma setting for

vascular injury given its decreased availability, contraindications (e.g., metallic foreign bodies, pacemakers), and additional pitfalls, including but not limited to the fact that T1-weighted isointense acute mural hematomas may be missed and T1-weighted hyperintense subacute hematomas may be difficult to differentiate from surrounding hematoma or intraluminal thrombus.

Spine Trauma Classification Systems

Numerous classification systems have been proposed to allow for the standardized description of spinal injuries so as to aid in efficient diagnosis, prognosis, and treatment [135–137]. Older classification systems relied heavily on inferred mechanism of injury and were based exclusively on radiographs and/or CT. In the subaxial cervical spine, the most recognized classification systems included those by Holdsworth [138], Allen-Ferguson [118], Harris [139], and Moore et al. [140] while in the thoracolumbar spine, the most widely used were the Denis three-column system [141] and Arbeitsgemeinschaft Fur Osteosynthesefragen (AO) [142]. Unfortunately, these systems were complex and suffered from high intra- and inter-user variability [42, 143–146]. In 1983, Denis expanded upon previous concepts of biomechanical spine stability by proposing a three-column model: an anterior column, comprised of the anterior half of the vertebral body, the anterior annulus fibrosus, and the ALL; a hypothetical middle column, comprised of the posterior half of the vertebral body and the PLL; and a posterior column, comprised of the posterior bony arch, LF, facets, and ISPs (Fig. 3.31). Mechanical instability, defined as the inability of the spine to maintain normal alignment under normal physiologic loads without development of neurologic deficit or incapacitation deformity, was said to be present whenever more than one column was injured and, as such, required surgical stabilization. The middle column was identified as the key component to spinal stability. Denis' popular three-column classification system was important in defining

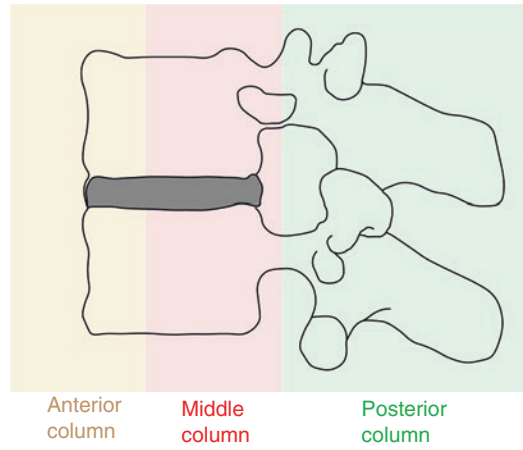

Fig. 3.31 Denis' three-column spine

the "unstable" spine, although did not correlate well with the need for surgery [146]. Additionally, it was acknowledged that stability can be osseous, ligamentous, or neurologic, and that mechanical stability was dependent on both osseous and ligamentous structures of the spine. Although findings on CT, such as translation >2 mm, widened facet joints and interspinous intervals, >50% loss of vertebral body height, disruption of the posterior vertebral body cortex, and >20 degrees of kyphosis, have been associated with ligamentous injury and instability, MRI is the only modality that is able to directly visualize the spinal ligaments. MRI is nearly 100% sensitive and specific in detecting ligamentous injuries of the spine [147]. Unfortunately, MRI also has a high false-positive rate when compared to findings at the time of surgery [54, 57, 148, 149]; moreover, positive MRI findings of ligamentous injury with negative CT rarely warrant surgery [54]. Newer spine injury classification systems have attempted to comprehensively describe injury by taking into account neurologic status and incorporating treatment recommendations. The Spine Trauma Study Group devised a cervical subaxial fracture system (SLIC) and thoracolumbar system (TLICS) in order to guide therapeutic decision-making [150]. These systems, based on classification of injury morphology, integrity of the posterior ligamentous complex (PLC), and neurologic status, are more reliable in guiding treatment decisions, although

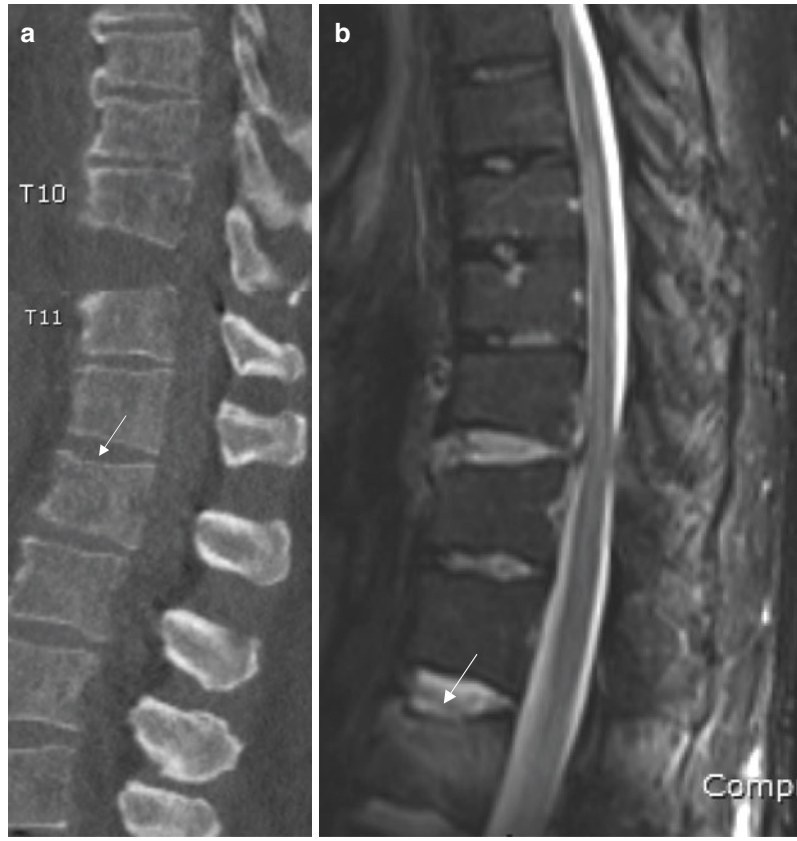

Fig. 3.32 AOSpine Classification, a 53-year-old male, full trauma, intubated. (**a**) Sagittal CT and (**b**) sagittal STIR images demonstrate hyperextension type injury at T10-T11 with ruptured ALL, or anterior band injury, classified as "B3." The posterior tension band appears intact. There is also a wedge compression fracture involving only the superior endplate of L1 (white arrows), classified as "A1." This patient is intubated and unexaminable, and therefore, neurological status is classified as "NX." The totality of this patient's injury is classified as "T10-T11:B3 (L1:A1;NX)"

have been criticized regarding inconsistences in the cataloguing of injury morphology and PLC integrity. In 2008, AOSpine established a Spine Classification group to revise the AO-Magerl classification and devise a comprehensive and user-friendly system, leading to the AOSpine subaxial and AOSpine thoracolumbar systems published in 2013 [151, 152]. These classification systems are based on the evaluation of the following parameters: (1) morphology of the injury; (2) neurological status; (3) clinical modifiers; and (4) facet joint injury (only for C3-C7). Primary injuries are described first by their level and then by their morphology, with secondary injuries and modifiers placed in parentheses (Fig. 3.32). In the subaxial cervical spine, primary injury morphology is broadly classified as either Compression (Type A); Tension Band (Type B), which is subcategorized as posterior (bony only versus bony and capsuloligamentous/ligamentous) and anterior tension band injury; or Translation (Type C), with additional characterization of facet injuries and bilateralism, whenever present (Box 3.11). In the thoracolumbar spine, primary injury morphology is either Compression (Type A); Distraction (Type B), which is further divided into transosseous tension band disruption/chance fracture versus posterior tension band disruption; or Translation (Type C) (Box 3.12). The anterior tension band limits hyperextension and is comprised of the vertebral bodies, intervertebral disc, as well as ALL and PLL, while the posterior tension band refers to the bony posterior elements and capsuloligamentous structures (facet joints, LF, suraspinous ligament, and ISPs). The posterior tension band limits hyperflexion and is the main determinant of mechanical stability in the thoracolumbar spine, while the anterior ligamentous structures play a smaller role. In the subaxial cervical spine, stability is heavily dependent on both the anterior and posterior ligamentous structures.

Box 3.11: AOSpine Classification of Subaxial Injury

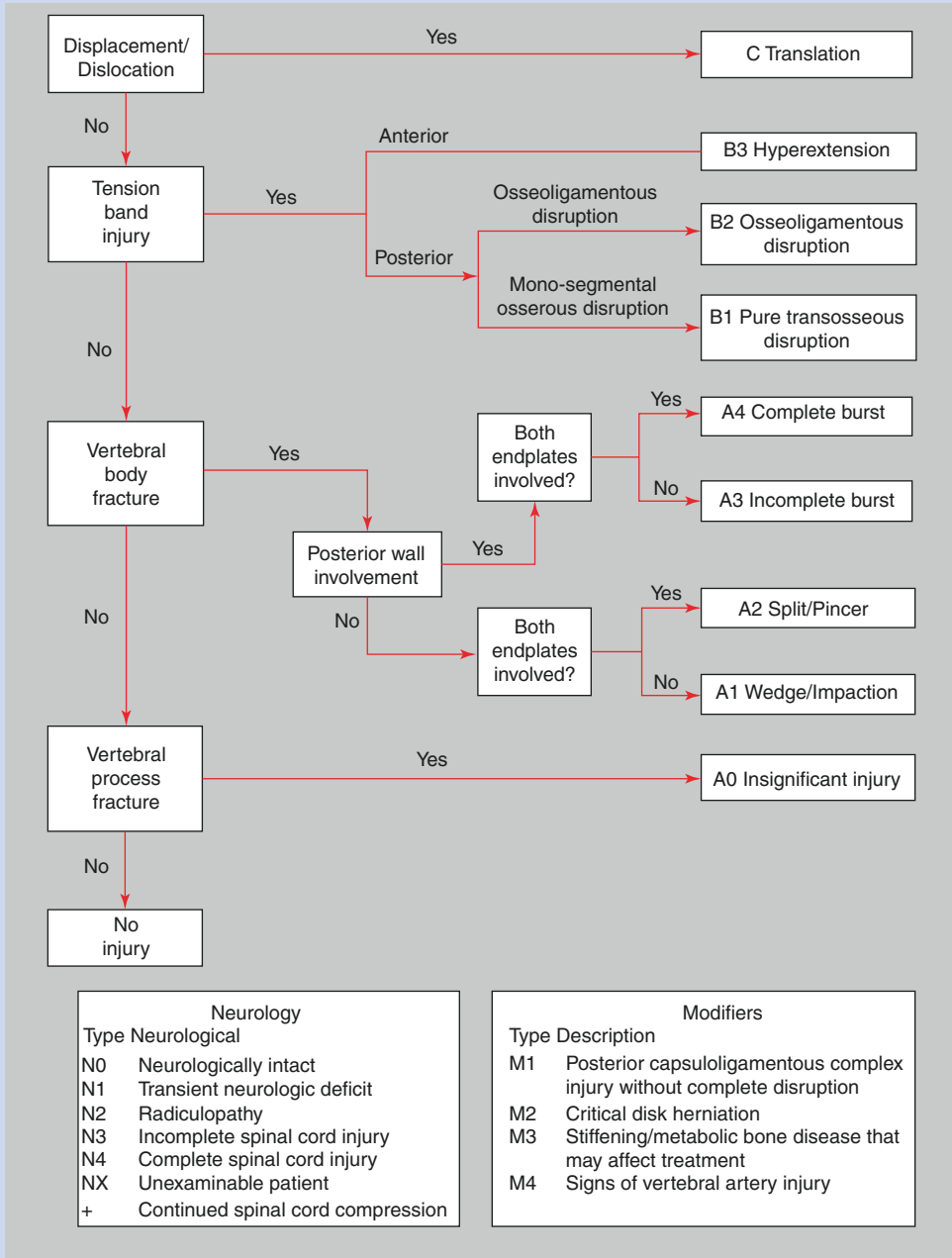

Adapted from AOSpine Classification Systems (https://aospine.aofoundation.org/clinical-library-and-tools/aospine-classification-systems) and Vaccaro et al. [152]

Upper cervical spine injuries are those affecting the skull base, C1 ring, C2 odontoid process, or C2 ring. This spinal segment is anatomically and functionally unique from the subaxial cervical spine, and its stability is heavily dependent on ligamentous structures. Historically, the

Box 3.12: AOSpine Classification of Thoracolumbar Injury

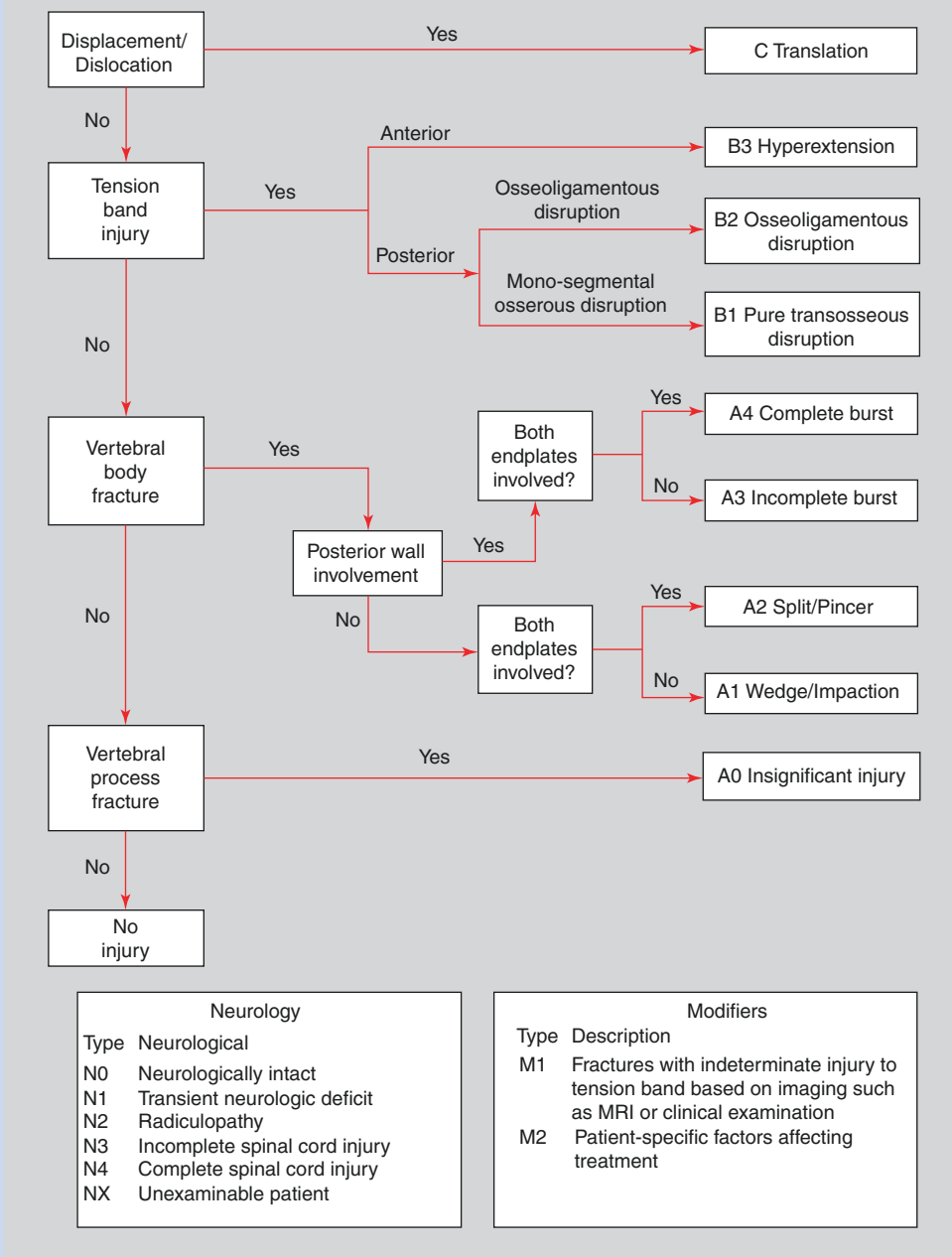

Adapted from AOSpine Classification Systems (https://aospine.aofoundation.org/clinical-library-and-tools/aospine-classification-systems) and Vaccaro et al. [151]

Anderson and Montesano and, later, Tuli et al. classification systems have been used to describe occipital condyle fractures [153, 154]. The Traynelis and Harborview classification schemes have been used for craniocervical dislocation [155, 156]. The integrity of the trans-

verse atlantal ligament has been critical in classifying fractures involving the C1 ring, while fractures of the dens have long been guided by the Anderson and D'Alonzo system [157]. The AOSpine system, as above, has simplified these classifications by dividing the upper cervical spine into three anatomic categories comprised of the bony element and joint complex just caudal to it: "OC," comprised of the occipital condyle and occipitoatlantal junction; "C1," comprised of the C1 ring and C1-C2 joint; and "C2," comprised of C2 and the C2-C3 joint [158]. Within each category, injury is divided into three types of increasing severity: Type A (isolated bony), Type B (tension band or ligamentous injury with or without associated bony injury), and Type C (displacement or translation in any plane). In addition, there are four case-specific modifiers (M1-M4) (Box 3.13) [158].

SCI: Acute

MRI is the only imaging modality that can clearly delineate the internal architecture of the spinal cord and, thus, plays a central role in the characterization of posttraumatic parenchymal abnormalities. Along with clinical scoring using the American Spinal Injury Association Impairment (ASIA) scale, MRI contributes to predicting outcome in the acute setting. Prior studies have shown that MRI features of SCI correlate with posttraumatic neurologic deficit and predict long-term recovery [159–164]. There are three common imaging observations of SCI on MRI: spinal cord hemorrhage, spinal cord edema/contusion, and spinal cord swelling. Each of these MRI features can be further characterized by their location in spinal cord and the amount of cord parenchyma involved. Unfortunately, it is not as easy to differentiate gray matter from white mat-

Box 3.13: AOSpine Classification of Upper Cervical Injury

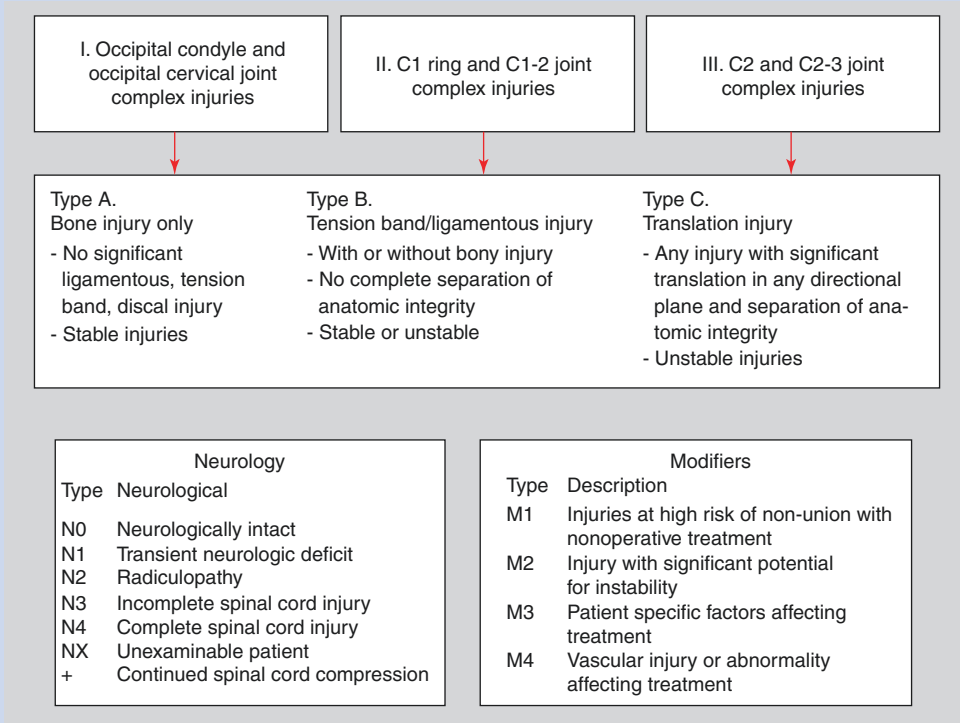

Adapted from AOSpine Classification Systems (https://aospine.aofoundation.org/clinical-library-and-tools/aospine-classification-systems)

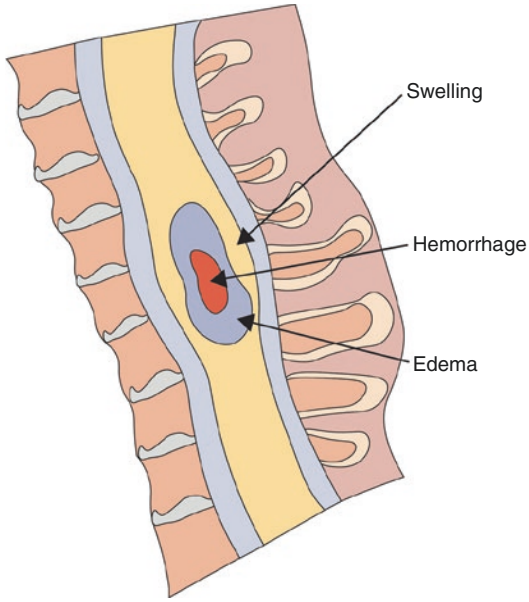

Fig. 3.33 SCI. The typical SCI lesion is spindle-shaped, with a focus of hemorrhage surrounded by a larger zone of edema and swelling of the affected cord segment

ter in the spinal cord as it is in the brain using conventional MRI given that they have very similar T1 and T2 relaxation characteristics. Furthermore, this distinction is even more difficult in the setting of cord parenchymal abnormalities, although best made in cross section using proton density or GRE sequences. On MRI, the typical SCI lesion is spindle-shaped with a hemorrhagic center at the impact zone and surrounding edema (Fig. 3.33). In the most severe yet rarely encountered spinal cord lesion, the cord is transected, seen as complete disruption of the parenchyma with CSF surrounding the severed ends. This is usually encountered in penetrating trauma or severe translational injuries.

Hemorrhage

Posttraumatic spinal cord hemorrhage commonly localizes to the central gray matter at the point of mechanical impact [114, 161, 165–167]. The lesion most often reflects hemorrhagic necrosis, since true hematomyelia is rare. In the acute phase of SCI, hemorrhage appears hypointense on T2-weighted and GRE images, usually with surrounding edema (Fig. 3.34). Intramedullary hemorrhage can be associated with complete or incomplete cord injuries. A large hemorrhage (>4 mm in length on sagittal images) often indicates neurologic injury [168], especially if the lesion is in the cervical spine [165]. Presence of a hemorrhage <4 mm in length is not associated with complete injury and indicates good prognosis [169]. Frank hemorrhage correlates with poor neurologic outcomes [114, 161, 165, 166, 170, 171], and the location of hemorrhage corresponds to the neurologic level of injury [114, 165–167]. Cord compression secondary to bony fragments, disc, or fluid is associated with intramedullary hemorrhage and, thus, is a predictor of poor neurologic recovery and often an indication for early surgical decompression in incomplete injuries [171, 172].

Edema

Spinal cord edema presents as abnormal hyperintense signal within the affected swollen cord segment on T2-weighted images (Fig. 3.35). Edema reflects focal accumulation of intracellular and interstitial fluid in response to injury and involves a variable length of spinal cord above and below the point of mechanical impact. The length of involved spinal cord is proportional to the degree of initial neurologic deficit [112, 165]. Spinal cord edema usually occurs together with spinal cord hemorrhage as small blood vessels near the injured site are damaged (contusion), characterized on MRI by a small central T2-weighted hypointensity demonstrating blooming on GRE images and often, but not always, surrounded by edema (Fig. 3.36). Cord edema alone without hemorrhage confers a more favorable prognosis than cord edema with contusion [161]. In older patients with preexisting cervical spondylosis, a narrowed canal due to osteophytes or buckled LF may result in a central cord syndrome after a relatively mild hyperextension injury.

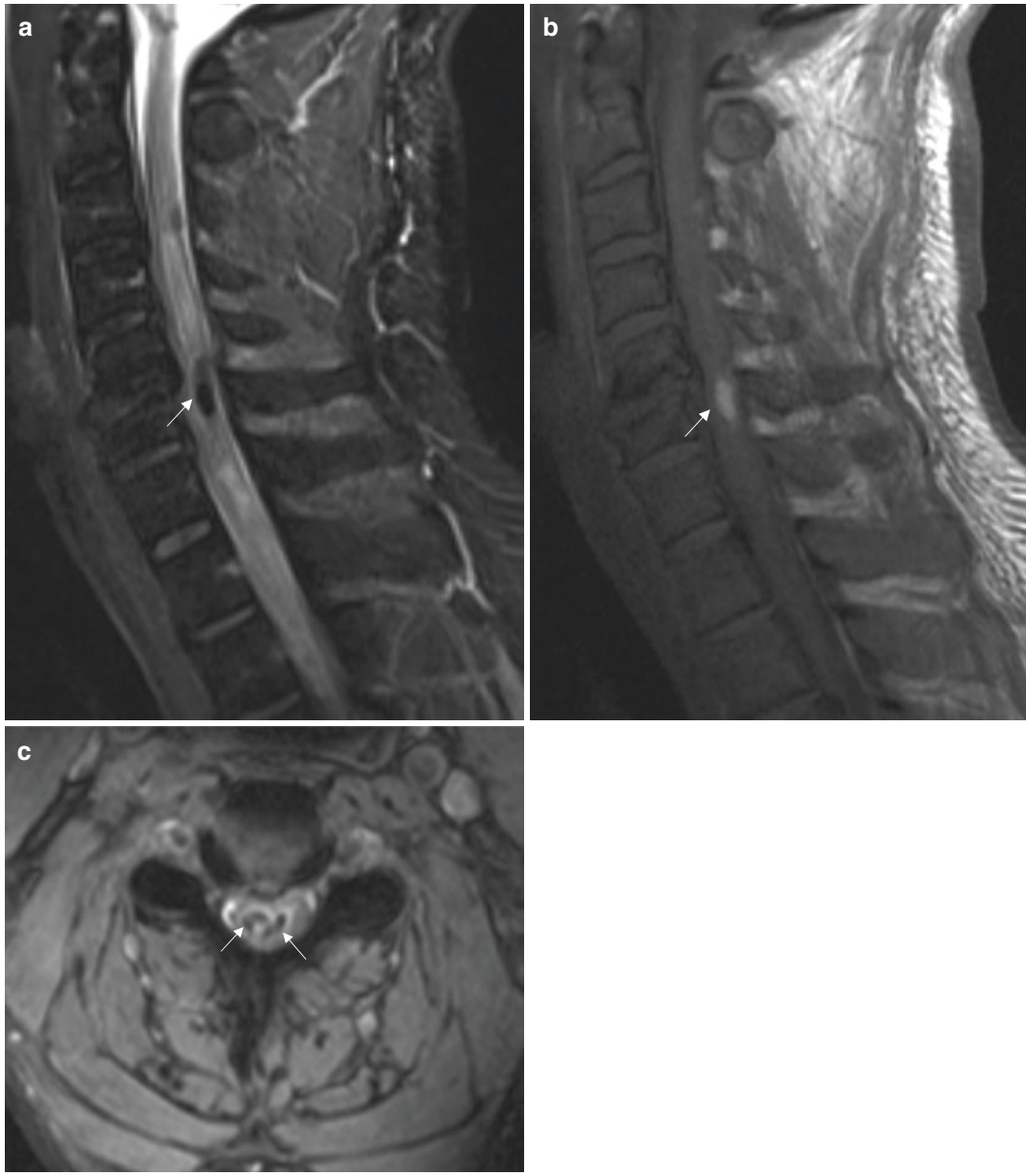

Fig. 3.34 (**a**) Sagittal STIR image demonstrates extensive cord edema and swelling with superimposed hypointense focus at C5-C6, which is hyperintense on (**b**) Sagittal T1-weighted image and hypointense on (**c**) Corresponding GRE image, consistent with intramedullary hemorrhage (white arrows)

Swelling

The normal, uninjured spinal cord is relatively uniform in diameter, except for a slight increase in the lower cervical and lower thoracic regions due to transmission of the brachial and lumbar plexuses, respectively. Spinal cord swelling manifests as a focal increase in caliber centered at the level of injury, best demonstrated on T1-weighted sequences. In spine trauma, the focal enlargement gradually tapers in cranial and caudal directions from the site of injury. Sometimes, the focal enlargement may taper in the cranial direction only. Spinal cord compres-

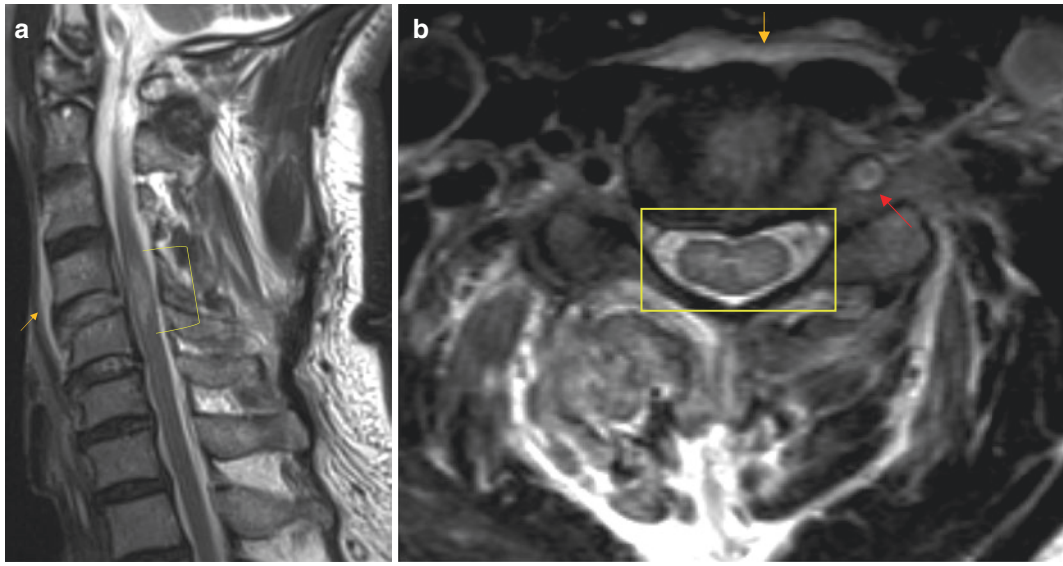

Fig. 3.35 (**a**) Sagittal T2- and (**b**) axial T2-weighted images demonstrate abnormal intramedullary T2 hyperintensity and cord swelling in the setting of injury at C4-C5. Note presence of prevertebral edema (orange arrows) and absence of normal T2 hypointense left vertebral artery flow void (red arrow) compatible with dissection

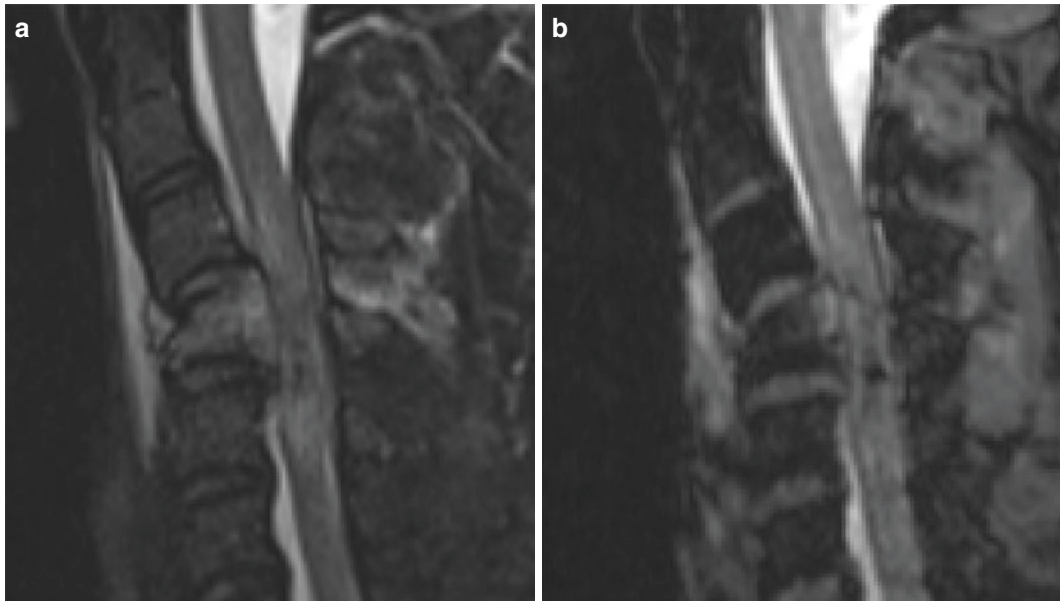

Fig. 3.36 (**a**) Sagittal STIR and (**b**) GRE images demonstrate hemorrhagic cord contusion, characterized by small ill-defined foci of hypointensity surrounded by larger zone of hyperintense edema

sion or spinal canal stenosis can efface the surrounding subarachnoid space and, thus, make swelling difficult to delineate. Spinal cord swelling by itself does not predict the extent of parenchymal injury and is the least descriptive imaging finding in SCI.

SCI: Chronic

In chronic SCI, patients can present with progressive worsening and loss of neurologic function secondary to development of pathological abnormalities in the injured spinal cord. Posttraumatic progressive myelopathy refers to delayed or late deterioration of neurologic dysfunction [173], especially in the setting of spinal cord cysts or myelomalacia, two common posttraumatic spinal cord abnormalities. The pathophysiology underlying the development and growth of spinal cord cysts remains unknown. Since imaging often fails to distinguish between hydromyelia (ependymal lined cavity), syringomyelia (glial lined cavity), and syringohydromyelia (combined or indeterminate cyst), the general term spinal cord cyst is often used to describe the aforementioned cyst types. MRI of spinal cord cysts shows CSF signal intensity on all pulse sequences. Artifacts due to CSF-related flow may be present in larger cysts (Fig. 3.37) [174]. Although cysts often show well-demarcated borders with the surrounding parenchyma, prior hemorrhage, gliosis, or scarring can distort these borders. Spinal cord cysts can be categorized as simple or complex (with varying numbers of septations) and may localize above, below, or at the site of the spine injury (Fig. 3.38). The presence of spinal cord cysts is observed in 9% of patients scanned more than 20 years after the initial injury [175]. Myelomalacia ("soft cord") is characterized by the absence of confluent spinal cord cysts. Unlike spinal cord cysts, myelomalacia presents as an ill-defined area exhibiting noncystic, nonenhancing signal abnormality that is hypointense on

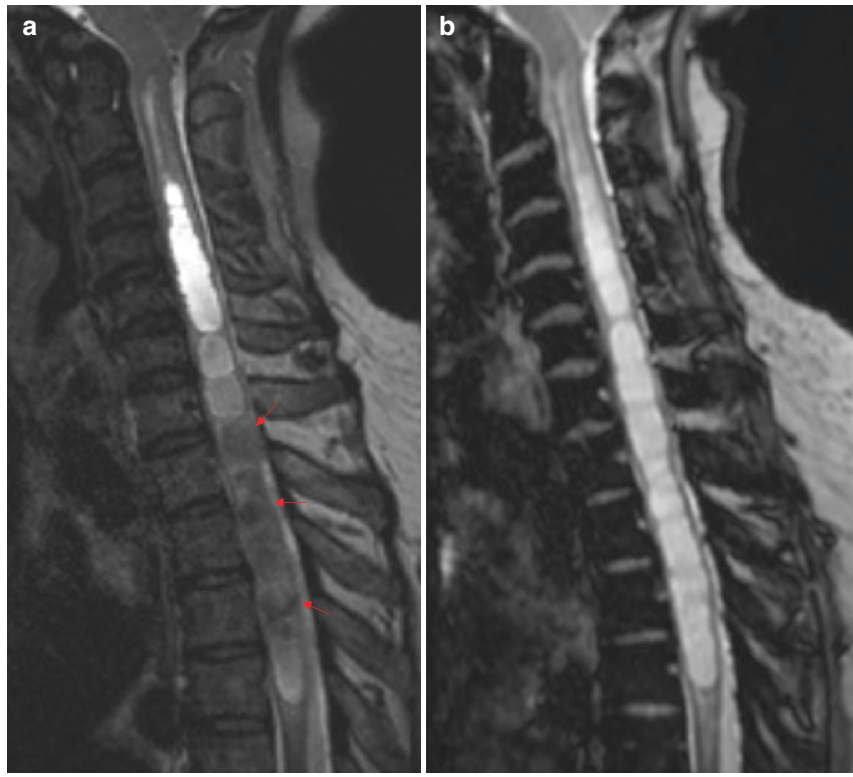

Fig. 3.37 (**a**) Sagittal T2-weighted image demonstrates a long, expansile syrinx in the spinal cord. There is ill-defined T2 hypointensity in the cyst from T1 to T4 (red arrows), raising the possibility of superimposed hemorrhage (hematomyelia). (**b**) Sagittal GRE image demonstrates that these hypointensities disappear, therefore, not compatible with hemorrhage, but rather, CSF-related flow artifact

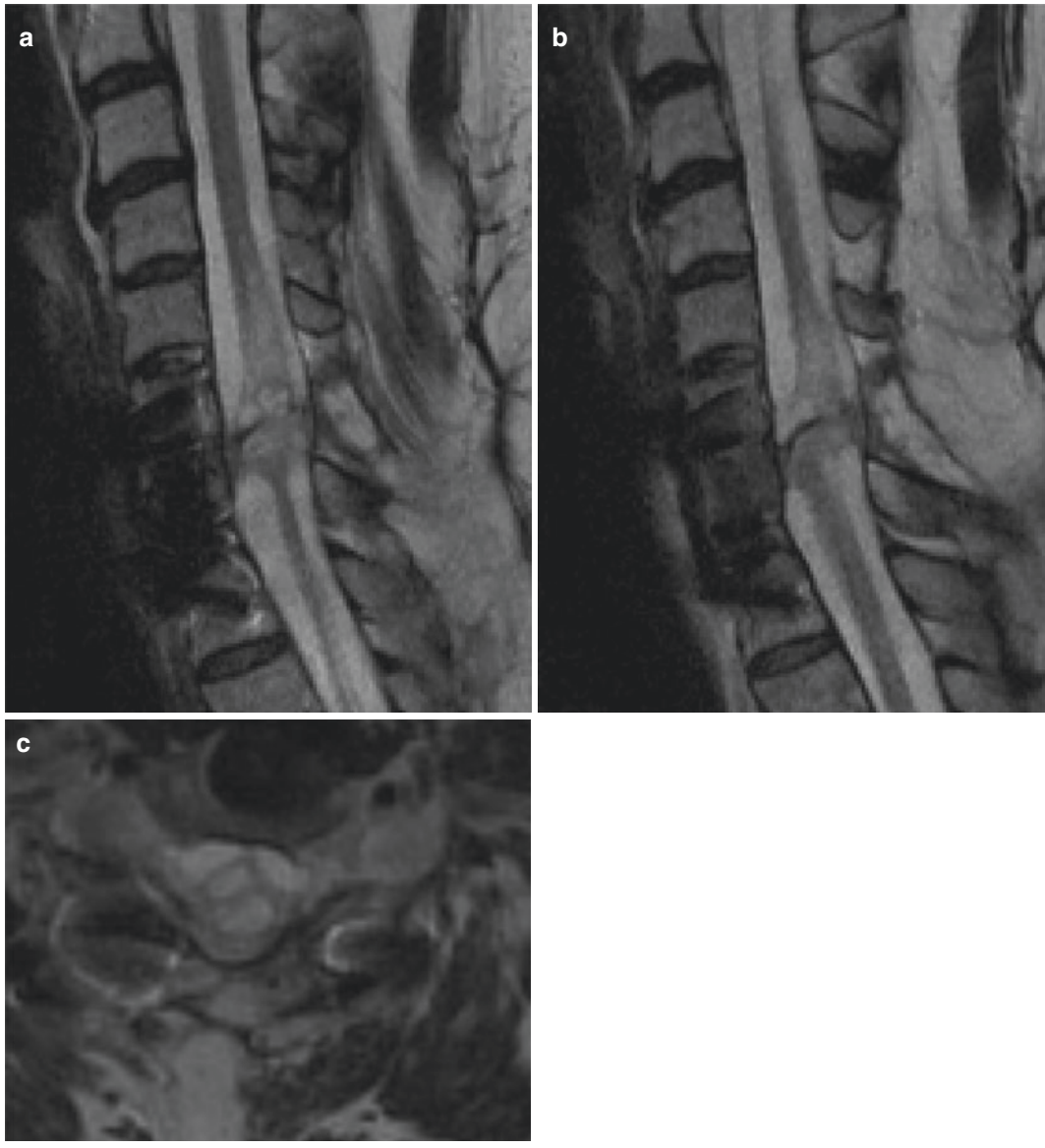

Fig. 3.38 (**a**, **b**) Sagittal T2- and (**c**) axial T2-weighted images demonstrate sequelae of chronic spinal cord transection with multiple loculated, poorly marginated complex cysts and surrounding parenchymal increased T2 signal. The patient has undergone anterior fusion at C6-T1

T1-weighted (but hyperintense compared to CSF) and hyperintense on T2-weighted images with respect to the normal cord [176]. Spinal cord atrophy may be associated with myelomalacia. Axial MRI may demonstrate the characteristic "owl's-eyes" or "snake-eyes" sign in the gray matter (Fig. 3.39). Spinal cord tethering may coexist with myelomalacia, leading to loss of the subarachnoid space and expansion of the parenchyma [176]. Rarely, the cord appears tethered due to a spinal cord herniation secondary to a tear in the anterior dual margin from bony fragments. Myelomalacia is observed in the majority of patients (55%) with chronic SCI [175].

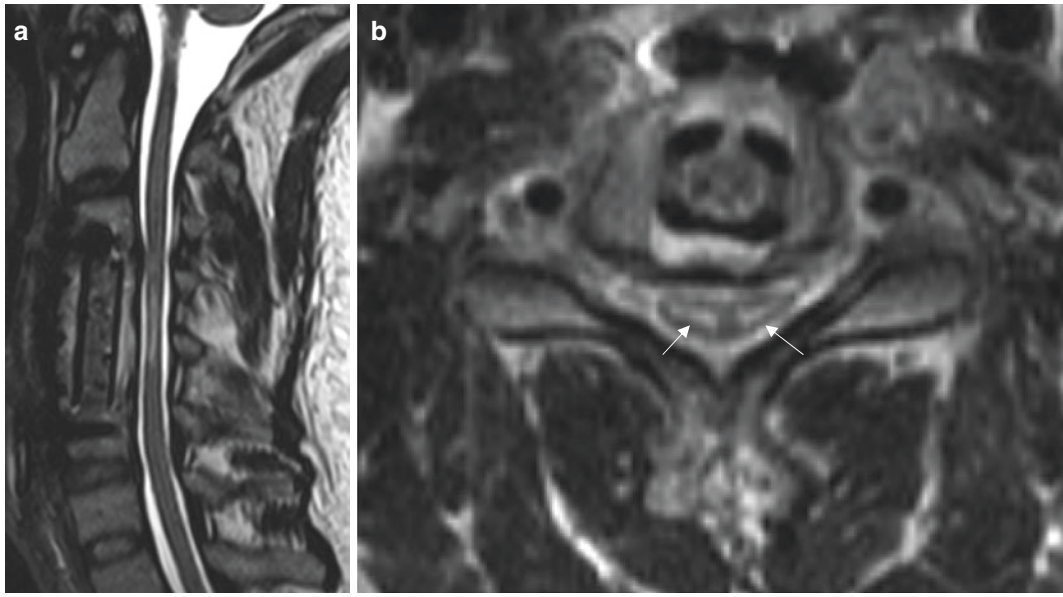

Fig. 3.39 (**a**) Sagittal T2-weighted image in a postoperative patient demonstrates cord thinning and T2 hyperintensity from C3 to C5, compatible with myelomalacia. (**b**) Axial T2-weighted image reveals characteristic "owl's-eye" or "snake-eyes" sign, with hyperintensity localized to the gray matter (white arrows)

SCIWORA and SPAM

Spinal cord injury without radiographic abnormality (SCIWORA) was first described in young children who present with neurologic deficits without imaging abnormalities on plain radiographs, flexion-extension radiographs, and/or CT. Up to 30–40% of children with SCI may exhibit SCIWORA [177], most commonly in the cervical spine. In adults, SCIWORA is believed to arise from hyperextension dislocation or hyperflexion sprain injury in the setting of cervical spondylosis and pre-existing stenosis [109, 120, 178]. The pathogenic mechanism of SCIWORA is compression of the thecal sac between the edge of the dorsally displaced vertebral body and the buckled LF [178]. Recent advances in MRI techniques enable delineation of posttraumatic damage in SCIWORA, which shows intervertebral disc separation, disruption of the ALL and annulus fibrosus, prevertebral hemorrhage, and parenchymal SCI [109, 122]. It is recommended that children who present with neurologic deficits, even if transient, undergo MRI evaluation [177].

Subacute progressive ascending myelopathy (SPAM), first described by Frankel in 1969 [179], is a condition characterized by progression of the initial neurologic level of injury, commonly within days or weeks. Proposed etiologies of this complication include vascular thrombosis, altered CSF flow, apoptosis, and infection [180–184]. MRI shows progression of the edema beyond the initial injury site with a rim of peripheral sparing [178, 181, 185]. Recovery from SPAM is generally good with aggressive therapies, such as administration of steroids and increases in mean arterial pressure, although mortality risk is increased with brainstem involvement. Follow-up MRI shows near normalization of spinal cord changes with myelomalacia and/or atrophy [178].

Nerve Root Injury

In severe trauma, there may be traction injury of the nerve roots resulting in a dural tear through the neural vertebral foramen and extravasation of CSF into the extradural space, entitled a pseudo-

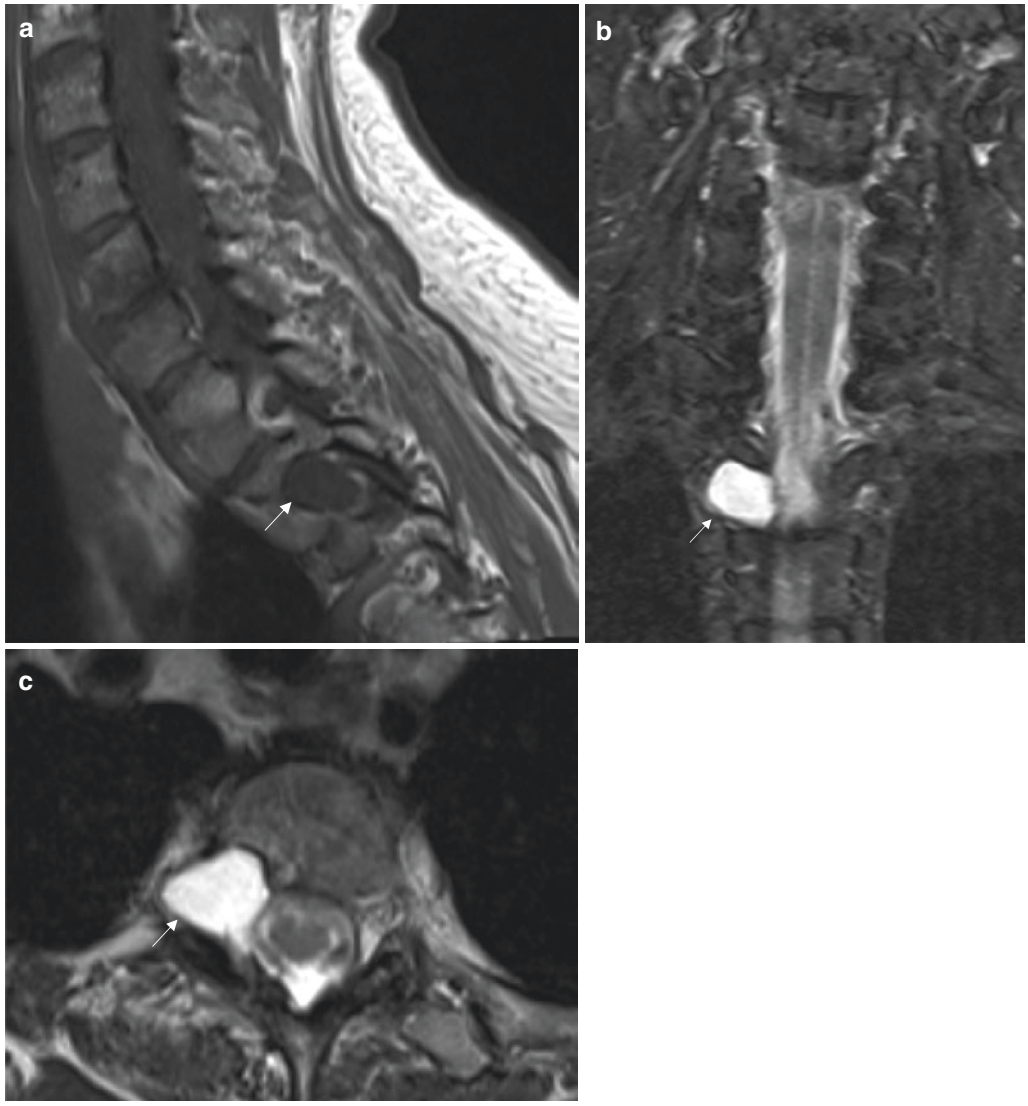

Fig. 3.40 (**a**) Sagittal T1-weighted image demonstrates a dark lesion in the right T2-T3 neural foramen along the nerve root (white arrow). (**b**) Coronal STIR and (**c**) axial T2-weighted images demonstrate that this represents a cyst of CSF signal intensity continuous with the thecal sac (white arrows), compatible with nerve root avulsion and resultant pseudomeningocele

meningocele. On high-resolution, heavily T2-weighted images, this appears as a loculated collection of CSF signal intensity lateral to the spinal cord and extending through the neural foramina continuous with the thecal sac (Fig. 3.40). MRI may also visualize an abnormal caudal orientation of the nerve root. Although pseudomeningocele has been considered a surrogate marker for nerve root avulsion, this has not been reliable across multiple studies [186–190].

Pitfalls of MRI in Spine Trauma

Although MRI is superb in the visualization of the spinal soft tissues, it is prone to artifacts that may be mistaken for pathology. Susceptibility artifact due to metallic hardware, such as with fusion rods or screws, or even dental hardware, will degrade image quality and render some portions of the spine unevaluable due to signal void (Fig. 3.41). This is especially pronounced on GRE sequences, though can be mitigated in several ways, such as by using spin echo sequences, increasing bandwidth, swapping phase- and frequency-encoding directions, and relying on STIR instead of T2-weighted chemical shift fat-saturated images. An additional pitfall in the cervical spine involves T2-weighted or STIR hyperintense blood vessels in the interspinous space, which may be mistaken for edema and ligamentous injury (Fig. 3.42). As mentioned earlier, MRI does not optimally depict marrow edema at C1-C2, and as such, acute fractures here may not be very evident on MRI. In the thoracic spine, dark spots or signal voids due to flow-related artifacts are routinely encountered in the dorsal subarachnoid space, and it is important not to confuse these for spinal hematomas (Fig. 3.43). These are usually demonstrated on T2-weighted spin echo and fast spin echo images and should disappear on corresponding GRE sequences, which is a useful tip to bear in mind should they pose a diagnostic dilemma.

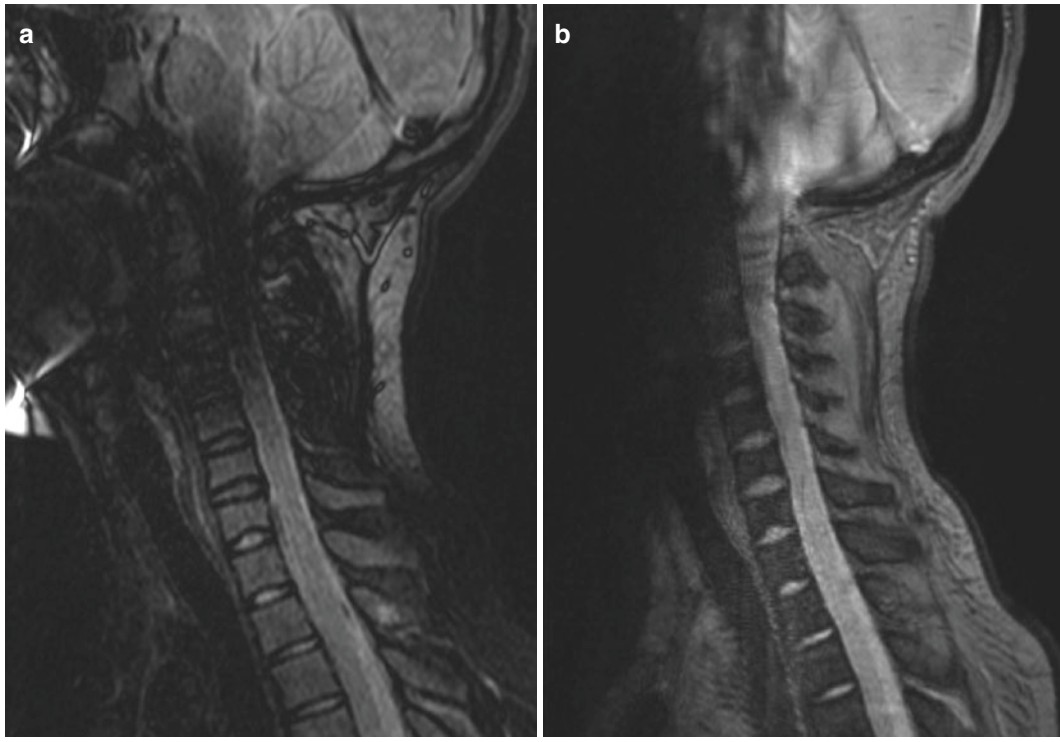

Fig. 3.41 (**a**) Sagittal STIR and (**b**) GRE images in this patient with dental braces demonstrate degradation of image quality in the upper cervical spine. Note that the cervicomedullary junction and upper cervical spinal cord are inevaluable

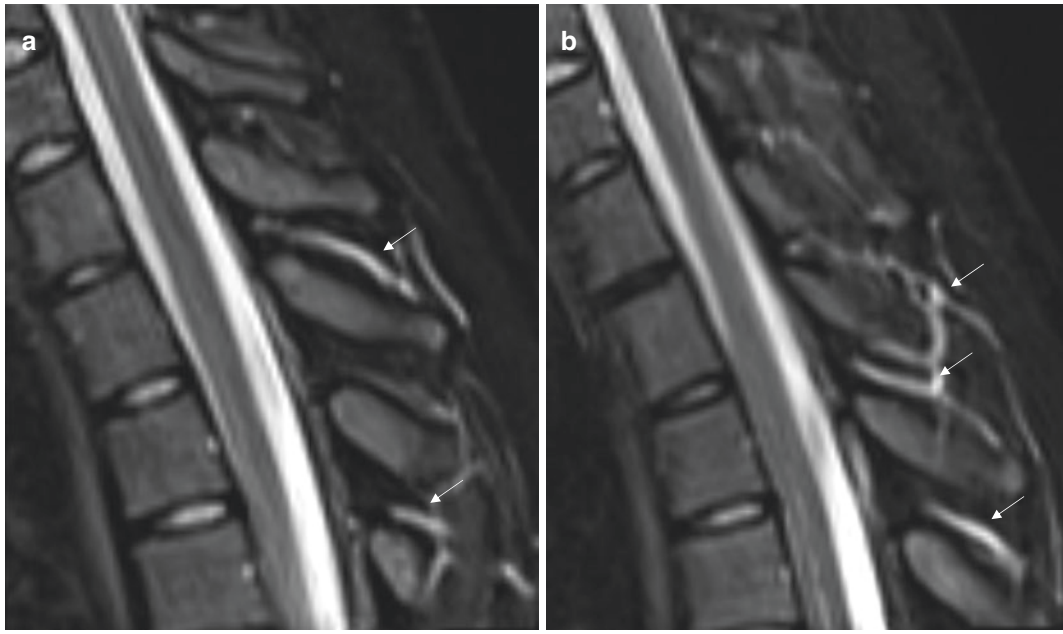

Fig. 3.42 (**a**, **b**) Sagittal STIR images of the cervical spine demonstrate hyperintense blood vessels in the interspinous space (white arrows), not to be confused for edema

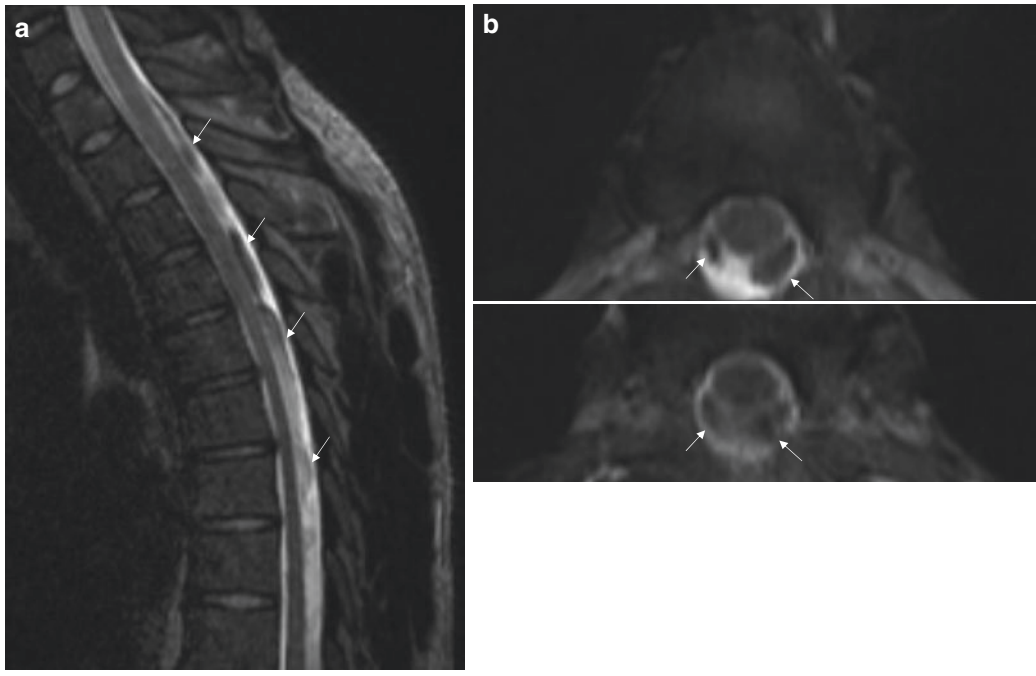

Fig. 3.43 (**a**) Sagittal T2- and (**b**) axial T2-weighted images of the thoracic spine demonstrate artifactual CSF flow voids in the dorsal subarachnoid space (white arrows). It is important not to mistake this for subdural or subarachnoid hemorrhage

Advanced MRI Techniques in SCI

Conventional MRI pulse sequences excel in macroscopic delineation of the spinal cord parenchyma, namely, identification of hemorrhage, edema, and swelling. These conventional sequences are limited in their ability to assess function and alterations in microstructural features of the spinal cord, particularly, axonal integrity. Moreover, prior studies in animal models have shown that MRI techniques may underestimate the degree of injury [191]. Applications of many of the advanced imaging techniques used in the brain, such as magnetization transfer, quantitative T2, q-space/q-ball, high angular resolution diffusion imaging (HARDI), perfusion and arterial spin labeling (ASL), functional MRI (fMRI), and magnetic resonance spectroscopy (MRS), have not been routinely employed in clinical examinations of the spinal cord primarily due to technical barriers related to the small size of the cord, motion from CSF pulsations, carotid/vertebral artery pulsation, and respiratory motion. The higher spatial resolution needed to image the cord lends to long MRI acquisition times and, consequently, more motion artifacts. In addition, utilizing echo planar imaging to reduce scan times, as with many of these advanced techniques in the brain, results in poor image quality in the spine due to magnetic field inhomogeneities at interfaces with bony vertebra. DWI, diffusion tensor imaging (DTI), and fMRI of the spinal cord have shown the most promise in the structural interrogation of the white matter tracts and assessment of post-injury spinal cord function.

DTI

The best studied advanced MRI technique in human SCI, DWI, quantifies random motion of water molecules within a biological tissue. Diffusion of water in specific directions is measured as the apparent diffusion coefficient (ADC). In isotropic tissues, water diffuses at equal rates in all directions, while in anisotropic tissues, water preferentially diffuses toward a particular direction. DTI is an application of DWI in which diffusion coefficients are calculated in six or greater different directions. The most common DTI index of diffusional anisotropy is fractional anisotropy (FA), which ranges from 0 (purely isotropic) to 1 (highly anisotropic). Intact axons of the spinal cord are highly anisotropic (high FA) since water diffusion in white matter tracts is parallel or longitudinal to the long axis of axons [192–194]. Given that diffusion of water molecules in the spinal cord is thought to depend on microstructural elements of the white matter [195], changes in DTI indices, such as FA, directly reflect disruptions to the axon tracts secondary to pathological or injured states. In a rat model of SCI, DWI showed altered ADC values despite normal findings on conventional MRI sequences [196]. DTI studies of human SCI patients have shown significantly decreased FA and ADC values at the site of injury compared to healthy control individuals (Fig. 3.44) [197–200]. Further work has also suggested the applicability of DTI indices as biomarkers for predicting long-term neurological and functional outcomes following SCI [200, 201]. Diffusion tensor tractography, an application of DTI, allows for three-dimensional visualization of disrupted white matter fiber tracts (Fig. 3.45). Although DTI is promising, more prospective studies are needed to characterize the diagnostic and prognostic advantages over conventional MRI methods.

fMRI

Although conventional MRI sequences and DTI are helpful in morphological characterization of the spinal cord, morphology alone does not necessarily reflect changes in spinal cord function following injury. Measurement of neuronal activity in real time may complement anatomical characterization by providing a more direct functional assessment of neural tissue. To that end, fMRI is a blood oxygen level-dependent (BOLD) technique that has commonly been used evaluate neuronal activity, especially in the brain. Neuronal activity is coupled to increased cerebral blood flow to meet greater regional demands for

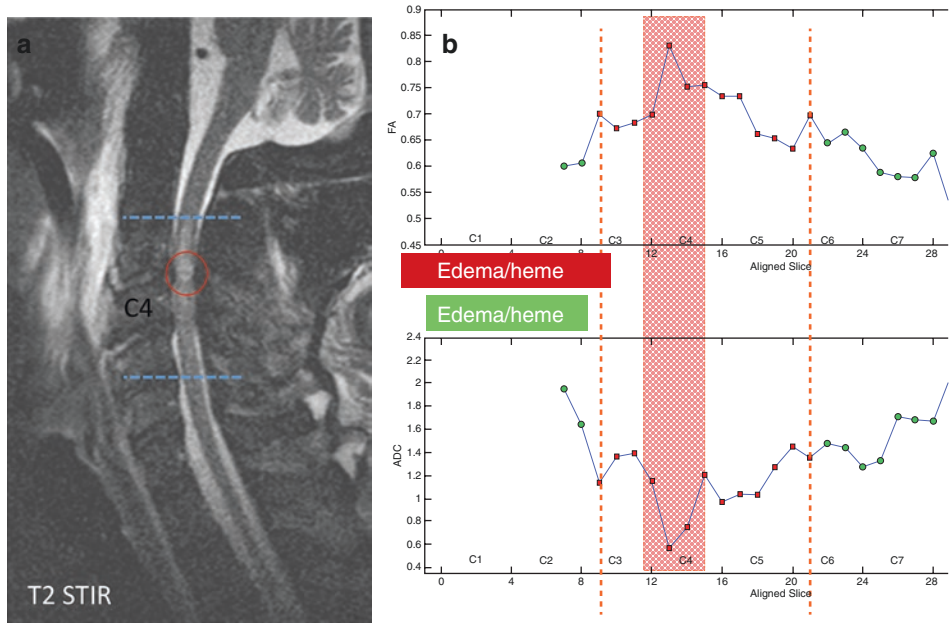

Fig. 3.44 (**a**) Sagittal STIR image in patient with acute spinal cord injury demonstrates parenchymal cord changes characterized by edema and hemorrhage centered at C3-C4. (**b**) The graph on the right demonstrates reduction in ADC at the level of cord injury. The apparent increase in FA is likely due to the acute phase of injury and will decrease with time. (Courtesy of Adam Flanders, MD, Thomas Jefferson University.) STIR, short tau inversion recovery; FA, fractional anisotropy; ADC, apparent diffusion coefficient

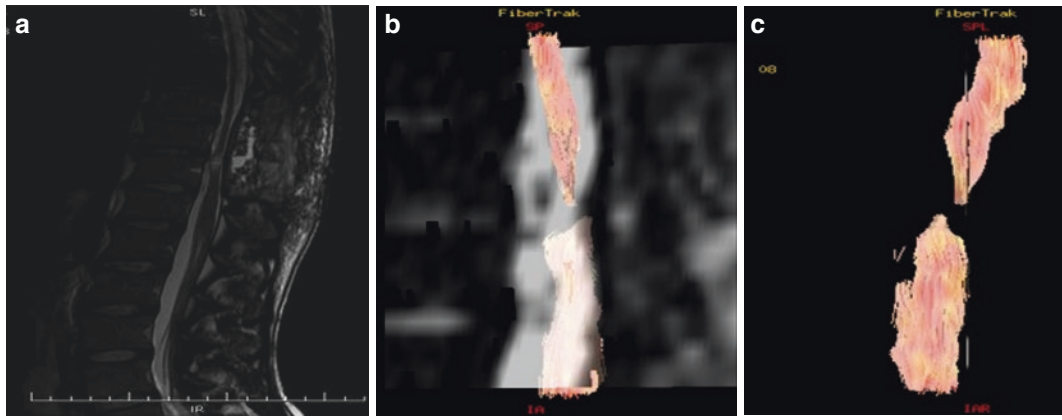

Fig. 3.45 (**a**) Sagittal T2-weighted image demonstrates SCI lesion at T12. (**b**, **c**). DTI tractography images demonstrate disruption of the white matter fibers at the same level. (Reprinted with permission from Sasiadek et al. [202])

oxygenated blood. fMRI measures changes in the magnetic field caused by alterations in oxyhemoglobin and deoxyhemoglobin that accompany greater cerebral blood flow to the active neural tissue, leading to increased BOLD signals in the activated central nervous system region. Brain fMRI studies of SCI patients have shown neural network reorganization of motor cortical representations in unaffected limbs [203–205]. Other studies have also suggested a correlation between the degree of cortical network reorganization and the severity of damage caused by SCI [206, 207]. Such functional reorganization of the brain following SCI may represent endogenous mecha-

nisms to compensate for damaged spinal cord neural circuits. Intriguingly, spinal fMRI of SCI patients has demonstrated residual neural activity in the injured spinal cord in response to thermal stimuli, although the pattern of neural activation has been shown to be different in SCI patients compared to healthy control subjects [208, 209]. Spinal fMRI has also detected neural activity in regions caudal to the site of SCI injury following lower limb movements [210], as well as reorganization of sensory neural networks in patients with incomplete SCI [211]. Altogether, the presence of plastic responses to SCI suggests the potential utility of fMRI in functional assessment of the injured spinal cord that may aid in the selection of therapeutic interventions to promote regenerative reorganization of neural networks.

References

1. Berven SH, Hepler MD, Watkins-Castillo SI. Traumatic spine fractures | BMUS: The Burden of Musculoskeletal Diseases in the United States. 2014. https://www.boneandjointburden.org/2014-report/iiia12/traumatic-spine-fractures. Accessed 30 June 2019.
2. Schleicher P, Pingel A, Kandziora F. Safe management of acute cervical spine injuries. EFORT Open Rev. 2018;3:347–57.
3. Grossman MD, Reilly PM, Gillett T, Gillett D. National survey of the incidence of cervical spine injury and approach to cervical spine clearance in U.S. trauma centers. J Trauma. 1999;47:684–90.
4. Lowery DW, Wald MM, Browne BJ, Tigges S, Hoffman JR, Mower WR, NEXUS Group. Epidemiology of cervical spine injury victims. Ann Emerg Med. 2001;38:12–6.
5. Rhee P, Kuncir EJ, Johnson L, et al. Cervical spine injury is highly dependent on the mechanism of injury following blunt and penetrating assault. J Trauma Inj Infect Crit Care. 2006;61:1166–70.
6. National Spinal Cord Injury Statistical Center, Facts and Figures at a Glance. Birmingham, AL: University of Alabama at Birmingham, 2018 [PDF file]. Retrieved from https://www.nscisc.uab.edu/Public/Facts%20and%20Figures%20-%202018.pdf
7. Papadopoulos MC, Chakraborty A, Waldron G, Bell BA. Lesson of the week: exacerbating cervical spine injury by applying a hard collar. BMJ. 1999;319:171–2.
8. Ben-Galim P, Dreiangel N, Mattox KL, Reitman CA, Kalantar SB, Hipp JA. Extrication collars can result in abnormal separation between vertebrae in the presence of a dissociative injury. J Trauma Inj Infect Crit Care. 2010;69:447–50.
9. Bivins HG, Ford S, Bezmalinovic Z, Price HM, Williams JL. The effect of axial traction during orotracheal intubation of the trauma victim with an unstable cervical spine. Ann Emerg Med. 1988;17:25–9.
10. Podolsky SM, Hoffman JR, Pietrafesa CA. Neurologic complications following immobilization of cervical spine fracture in a patient with ankylosing spondylitis. Ann Emerg Med. 1983;12:578–80.
11. Bauer D, Kowalski R. Effect of spinal immobilization devices on pulmonary function in the healthy, nonsmoking man. Ann Emerg Med. 1988;17:915–8.
12. Aoi Y, Inagawa G, Nakamura K, Sato H, Kariya T, Goto T. Airway Scope versus macintosh laryngoscope in patients with simulated limitation of neck movements. J Trauma Inj Infect Crit Care. 2010;69:838–42.
13. Davies G, Deakin C, Wilson A. The effect of a rigid collar on intracranial pressure. Injury. 1996;27:647–9.
14. Stone MB, Tubridy CM, Curran R. The effect of rigid cervical collars on internal jugular vein dimensions. Acad Emerg Med. 2010;17:100–2.
15. Kolb JC, Summers RL, Galli RL. Cervical collar-induced changes in intracranial pressure. Am J Emerg Med. 1999;17:135–7.
16. Mobbs RJ, Stoodley MA, Fuller J. Effect of cervical hard collar on intracranial pressure after head injury. ANZ J Surg. 2002;72:389–91.
17. Hunt K, Hallworth S, Smith M. The effects of rigid collar placement on intracranial and cerebral perfusion pressures. Anaesthesia. 2001;56:511–3.
18. Houghton DJ, Curley JW. Dysphagia caused by a hard cervical collar. Br J Neurosurg. 1996;10:501–2.
19. Ackland HM, Cooper DJ, Cooper JD, Malham GM, Kossmann T. Factors predicting cervical collar-related decubitus ulceration in major trauma patients. Spine (Phila Pa 1976). 2007;32:423–8.
20. Blaylock B. Solving the problem of pressure ulcers resulting from cervical collars. Ostomy Wound Manage. 1996;42:26–8, 30, 32–33
21. Walker J. Pressure ulcers in cervical spine immobilisation: a retrospective analysis. J Wound Care. 2012;21:323–6.
22. Ham W, Schoonhoven L, Schuurmans MJ, Leenen LPH. Pressure ulcers from spinal immobilization in trauma patients. J Trauma Acute Care Surg. 2014;76:1131–41.
23. Domeier RM, Evans RW, Swor RA, Hancock JB, Fales W, Krohmer J, Frederiksen SM, Shork MA. The reliability of prehospital clinical evaluation for potential spinal injury is not affected by the mechanism of injury. Prehosp Emerg Care. 1999;3:332–7.
24. Brown LH, Gough JE, Simonds WB. Can EMS providers adequately assess trauma patients for cervical spinal injury? Prehosp Emerg Care. 1998;2:33–6.

25. Nypaver M, Treloar D. Neutral cervical spine positioning in children. Ann Emerg Med. 1994;23:208–11.
26. Stiell IG, Clement CM, McKnight RD, et al. The Canadian C-spine rule versus the NEXUS low-risk criteria in patients with trauma. N Engl J Med. 2003;349:2510–8.
27. Hoffman JR, Mower WR, Wolfson AB, Todd KH, Zucker MI. Validity of a set of clinical criteria to rule out injury to the cervical spine in patients with blunt trauma. National Emergency X-Radiography Utilization Study Group. N Engl J Med. 2000;343:94–9.
28. Kreipke DL, Gillespie KR, McCarthy MC, Mail JT, Lappas JC, Broadie TA. Reliability of indications for cervical spine films in trauma patients. J Trauma. 1989;29:1438–9.
29. Como JJ, Diaz JJ, Dunham CM, et al. Practice management guidelines for identification of cervical spine injuries following trauma: update from the eastern Association for the Surgery of Trauma Practice Management Guidelines Committee. J Trauma Inj Infect Crit Care. 2009;67:651–9.
30. Hoffman JR, Wolfson AB, Todd K, Mower WR. Selective cervical spine radiography in blunt trauma: methodology of the National Emergency X-Radiography Utilization Study (NEXUS). Ann Emerg Med. 1998;32:461–9.
31. Stiell IG, Wells GA, Vandemheen KL, et al. The Canadian C-spine rule for radiography in alert and stable trauma patients. JAMA. 2001;286:1841–8.
32. Michaleff ZA, Maher CG, Verhagen AP, Rebbeck T, Lin CW. Accuracy of the Canadian C-spine rule and NEXUS to screen for clinically important cervical spine injury in patients following blunt trauma: a systematic review. CMAJ. 2012;184:E867–76.
33. Morrison J, Jeanmonod R. Imaging in the NEXUS-negative patient: when we break the rule. Am J Emerg Med. 2014;32:67–70.
34. Evans D, Vera L, Jeanmonod D, Pester J, Jeanmonod R. Application of National Emergency X-Ray Utilizations Study low-risk c-spine criteria in high-risk geriatric falls. Am J Emerg Med. 2015;33:1184–7.
35. Tran J, Jeanmonod D, Agresti D, Hamden K, Jeanmonod R. Prospective validation of modified NEXUS cervical spine injury criteria in low-risk elderly fall patients. West J Emerg Med. 2016;17:252–7.
36. Touger M, Gennis P, Nathanson N, Lowery DW, Pollack CV, Hoffman JR, Mower WR. Validity of a decision rule to reduce cervical spine radiography in elderly patients with blunt trauma. Ann Emerg Med. 2002;40:287–93.
37. Viccellio P, Simon H, Pressman BD, Shah MN, Mower WR, Hoffman JR, for the NEXUS Group. A prospective multicenter study of cervical spine injury in children. Pediatrics. 2001;108:e20.
38. Macias CG, Sahouria JJ. The appropriate use of CT: quality improvement and clinical decision-making in pediatric emergency medicine. Pediatr Radiol. 2011;41(Suppl 2):498–504.
39. Slaar A, Fockens MM, Wang J, Maas M, Wilson DJ, Goslings JC, Schep NW, van Rijn RR. Triage tools for detecting cervical spine injury in pediatric trauma patients. Cochrane Database Syst Rev. 2017;12:CD011686.
40. Ehrlich PF, Wee C, Drongowski R, Rana AR. Canadian C-spine rule and the National Emergency X-Radiography Utilization Low-Risk Criteria for C-spine radiography in young trauma patients. J Pediatr Surg. 2009;44:987–91.
41. Leonard JC, Kuppermann N, Olsen C, et al. Factors associated with cervical spine injury in children after blunt trauma. Ann Emerg Med. 2011;58:145–55.
42. Sixta S, Moore FO, Ditillo MF, Fox AD, Garcia AJ, Holena D, Joseph B, Tyrie L, Cotton B. Screening for thoracolumbar spinal injuries in blunt trauma: an Eastern Association for the Surgery of Trauma practice management guideline. J Trauma Acute Care Surg. 2012;73:S326–32.
43. Daffner RH, Hackney DB. ACR appropriateness criteria® on suspected spine trauma. J Am Coll Radiol. 2007;4:762–75.
44. Patel MB, Humble SS, Cullinane DC, et al. Cervical spine collar clearance in the obtunded adult blunt trauma patient. J Trauma Acute Care Surg. 2015;78:430–41.
45. Resnick S, Inaba K, Karamanos E, Pham M, Byerly S, Talving P, Reddy S, Linnebur M, Demetriades D. Clinical relevance of magnetic resonance imaging in cervical spine clearance. JAMA Surg. 2014;149:934.
46. Schuster R, Waxman K, Sanchez B, Becerra S, Chung R, Conner S, Jones T. Magnetic resonance imaging is not needed to clear cervical spines in blunt trauma patients with normal computed tomographic results and no motor deficits. Arch Surg. 2005;140:762.
47. Chew BG, Swartz C, Quigley MR, Altman DT, Daffner RH, Wilberger JE. Cervical spine clearance in the traumatically injured patient: is multidetector CT scanning sufficient alone? J Neurosurg Spine. 2013;19:576–81.
48. Tomycz ND, Chew BG, Chang Y-F, et al. MRI is unnecessary to clear the cervical spine in obtunded/comatose trauma patients: the four-year experience of a level I trauma center. J Trauma Inj Infect Crit Care. 2008;64:1258–63.
49. Sundstrøm T, Asbjørnsen H, Habiba S, Sunde GA, Wester K. Prehospital use of cervical collars in trauma patients: a critical review. J Neurotrauma. 2014;31:531–40.
50. Morris CGT, McCoy E. Cervical immobilisation collars in ICU: friend or foe? Anaesthesia. 2003;58:1051–3.
51. Haut ER, Kalish BT, Efron DT, Haider AH, Stevens KA, Kieninger AN, Cornwell EE, Chang DC. Spine immobilization in penetrating trauma: more harm Than good? J Trauma Inj Infect Crit Care. 2010;68:115–21.

52. Barkana Y, Stein M, Scope A, Maor R, Abramovich Y, Friedman Z, Knoller N. Prehospital stabilization of the cervical spine for penetrating injuries of the neck—is it necessary? Injury. 2000;31:305–9.
53. Stelfox HT, Velmahos GC, Gettings E, Bigatello LM, Schmidt U. Computed tomography for early and safe discontinuation of cervical spine immobilization in obtunded multiply injured patients. J Trauma. 2007;63:630–6.
54. Panczykowski DM, Tomycz ND, Okonkwo DO. Comparative effectiveness of using computed tomography alone to exclude cervical spine injuries in obtunded or intubated patients: meta-analysis of 14,327 patients with blunt trauma. J Neurosurg. 2011;115:541–9.
55. Raza M, Elkhodair S, Zaheer A, Yousaf S. Safe cervical spine clearance in adult obtunded blunt trauma patients on the basis of a normal multidetector CT scan—A meta-analysis and cohort study. Injury. 2013;44:1589–95.
56. Badhiwala JH, Lai CK, Alhazzani W, et al. Cervical spine clearance in obtunded patients after blunt traumatic injury. Ann Intern Med. 2015;162:429.
57. Muchow RD, Resnick DK, Abdel MP, Munoz A, Anderson PA. Magnetic resonance imaging (MRI) in the clearance of the cervical spine in blunt trauma: a meta-analysis. J Trauma. 2008;64:179–89.
58. Schoenfeld AJ, Bono CM, McGuire KJ, Warholic N, Harris MB. Computed tomography alone versus computed tomography and magnetic resonance imaging in the identification of occult injuries to the cervical spine: a meta-analysis. J Trauma Inj Infect Crit Care. 2010;68:109–14.
59. Russin JJ, Attenello FJ, Amar AP, Liu CY, Apuzzo MLJ, Hsieh PC. Computed tomography for clearance of cervical spine injury in the unevaluable patient. World Neurosurg. 2013;80:405–13.
60. James IA, Moukalled M, Yu E, et al. A systematic review of the need for MRI for the clearance of cervical spine injury in obtunded blunt trauma patients after normal cervical spine CT. J Emerg Trauma Shock. 2014;7:251.
61. Malhotra A, Wu X, Kalra VB, Nardini HKG, Liu R, Abbed KM, Forman HP. Utility of MRI for cervical spine clearance after blunt traumatic injury: a meta-analysis. Eur Radiol. 2017;27:1148–60.
62. Selden NR, Quint DJ, Patel N, d'Arcy HS, Papadopoulos SM. Emergency magnetic resonance imaging of cervical spinal cord injuries: clinical correlation and prognosis. Neurosurgery. 1999;44:785–92.
63. Benedetti PF, Fahr LM, Kuhns LR, Hayman LA. MR imaging findings in spinal ligamentous injury. Am J Roentgenol. 2000;175:661–5.
64. Lensing FD, Bisson EF, Wiggins RH, Shah LM. Reliability of the STIR sequence for acute type II odontoid fractures. Am J Neuroradiol. 2014;35:1642–6.
65. Mauch JT, Carr CM, Cloft H, Diehn FE. Review of the imaging features of benign osteoporotic and malignant vertebral compression fractures. AJNR Am J Neuroradiol. 2018;39:1584–92.
66. Kaplan PA, Orton DF, Asleson RJ. Osteoporosis with vertebral compression fractures, retropulsed fragments, and neurologic compromise. Radiology. 1987;165:533–5.
67. An HS, Andreshak TG, Nguyen C, Williams A, Daniels D. Can we distinguish between benign versus malignant compression fractures of the spine by magnetic resonance imaging? Spine (Phila Pa 1976). 1995;20:1776–82.
68. Yamato M, Nishimura G, Kuramochi E, Saiki N, Fujioka M. MR appearance at different ages of osteoporotic compression fractures of the vertebrae. Radiat Med. 1998;16:329–34.
69. Thawait SK, Marcus MA, Morrison WB, Klufas RA, Eng J, Carrino JA. Research synthesis: what is the diagnostic performance of magnetic resonance imaging to discriminate benign from malignant vertebral compression fractures? Systematic review and meta-analysis. Spine (Phila Pa 1976). 2012;37:E736–44.
70. Thawait SK, Kim J, Klufas RA, Morrison WB, Flanders AE, Carrino JA, Ohno-Machado L. Comparison of four prediction models to discriminate benign from malignant vertebral compression fractures according to MRI feature analysis. AJR Am J Roentgenol. 2013;200:493–502.
71. Baur A, Stäbler A, Arbogast S, Duerr HR, Bartl R, Reiser M. Acute osteoporotic and neoplastic vertebral compression fractures: fluid sign at MR imaging. Radiology. 2002;225:730–5.
72. Castillo M, Arbelaez A, Smith JK, Fisher LL. Diffusion-weighted MR imaging offers no advantage over routine noncontrast MR imaging in the detection of vertebral metastases. AJNR Am J Neuroradiol. 2000;21:948–53.
73. Raya JG, Dietrich O, Reiser MF, Baur-Melnyk A. Methods and applications of diffusion imaging of vertebral bone marrow. J Magn Reson Imaging. 2006;24:1207–20.
74. Baur A, Stäbler A, Brüning R, Bartl R, Krödel A, Reiser M, Deimling M. Diffusion-weighted MR imaging of bone marrow: differentiation of benign versus pathologic compression fractures. Radiology. 1998;207:349–56.
75. Zhou XJ, Leeds NE, McKinnon GC, Kumar AJ. Characterization of benign and metastatic vertebral compression fractures with quantitative diffusion MR imaging. AJNR Am J Neuroradiol. 2002;23:165–70.
76. Tang G, Liu Y, Li W, Yao J, Li B, Li P. Optimization of b value in diffusion-weighted MRI for the differential diagnosis of benign and malignant vertebral fractures. Skelet Radiol. 2007;36:1035–41.
77. Abdel-Wanis M, Solyman MTM, Hasan NMA. Sensitivity, specificity and accuracy of magnetic resonance imaging for differentiating vertebral compression fractures caused by malignancy, osteoporosis, and infections. J Orthop Surg. 2011;19:145–50.

78. Baur A, Huber A, Ertl-Wagner B, Dürr R, Zysk S, Arbogast S, Deimling M, Reiser M. Diagnostic value of increased diffusion weighting of a steady-state free precession sequence for differentiating acute benign osteoporotic fractures from pathologic vertebral compression fractures. AJNR Am J Neuroradiol. 2001;22:366–72.
79. Baur-Melnyk A. Malignant versus benign vertebral collapse: are new imaging techniques useful? Cancer Imaging. 2009;9(Spec No A):S49–51.
80. Karchevsky M, Babb JS, Schweitzer ME. Can diffusion-weighted imaging be used to differentiate benign from pathologic fractures? A meta-analysis. Skelet Radiol. 2008;37:791–5.
81. Park S-W, Lee J-H, Ehara S, Park Y-B, Sung SO, Choi J-A, Joo YE. Single shot fast spin echo diffusion-weighted MR imaging of the spine; Is it useful in differentiating malignant metastatic tumor infiltration from benign fracture edema? Clin Imaging. 2004;28:102–8.
82. Biffar A, Baur-Melnyk A, Schmidt GP, Reiser MF, Dietrich O. Quantitative analysis of the diffusion-weighted steady-state free precession signal in vertebral bone marrow lesions. Investig Radiol. 2011. https://doi.org/10.1097/RLI.0b013e31821e637d.
83. Mubarak F, Akhtar W. Acute vertebral compression fracture: differentiation of malignant and benign causes by diffusion weighted magnetic resonance imaging. J Pak Med Assoc. 2011;61:555–8.
84. Wonglaksanapimon S, Chawalparit O, Khumpunnip S, Tritrakarn S-O, Chiewvit P, Charnchaowanish P. Vertebral body compression fracture: discriminating benign from malignant causes by diffusion-weighted MR imaging and apparent diffusion coefficient value. J Med Assoc Thail. 2012;95:81–7.
85. Sung JK, Jee W-H, Jung J-Y, Choi M, Lee S-Y, Kim Y-H, Ha K-Y, Park C-K. Differentiation of acute osteoporotic and malignant compression fractures of the spine: use of additive qualitative and quantitative axial diffusion-weighted MR imaging to conventional MR imaging at 3.0 T. Radiology. 2014;271:488–98.
86. Park HJ, Lee SY, Rho MH, Chung EC, Kim MS, Kwon HJ, Youn IY. Single-shot Echo-planar diffusion-weighted MR imaging at 3T and 1.5T for differentiation of benign vertebral fracture edema and tumor infiltration. Korean J Radiol. 2016;17:590–7.
87. Luo Z, Litao L, Gu S, Luo X, Li D, Yu L, Ma Y. Standard- *b* -value vs low- *b* -value DWI for differentiation of benign and malignant vertebral fractures: a meta-analysis. Br J Radiol. 2016;89:20150384.
88. Cuénod CA, Laredo JD, Chevret S, Hamze B, Naouri JF, Chapaux X, Bondeville JM, Tubiana JM. Acute vertebral collapse due to osteoporosis or malignancy: appearance on unenhanced and gadolinium-enhanced MR images. Radiology. 1996;199:541–9.
89. Dietrich O, Geith T, Reiser MF, Baur-Melnyk A. Diffusion imaging of the vertebral bone marrow. NMR Biomed. 2017;30:e3333.
90. Laredo JD, Lakhdari K, Bellaïche L, Hamze B, Janklewicz P, Tubiana JM. Acute vertebral collapse: CT findings in benign and malignant nontraumatic cases. Radiology. 1995;194:41–8.
91. Kubota T, Yamada K, Ito H, Kizu O, Nishimura T. High-resolution imaging of the spine using multidetector-row computed tomography: differentiation between benign and malignant vertebral compression fractures. J Comput Assist Tomogr. 2005;29:712–9.
92. Tan DYL, Tsou IYY, Chee TSG. Differentiation of malignant vertebral collapse from osteoporotic and other benign causes using magnetic resonance imaging. Ann Acad Med Singap. 2002;31:8–14.
93. Baker LL, Goodman SB, Perkash I, Lane B, Enzmann DR. Benign versus pathologic compression fractures of vertebral bodies: assessment with conventional spin-echo, chemical-shift, and STIR MR imaging. Radiology. 1990;174:495–502.
94. Jung H-S, Jee W-H, McCauley TR, Ha K-Y, Choi K-H. Discrimination of metastatic from acute osteoporotic compression spinal fractures with MR imaging. Radiographics. 2003;23:179–87.
95. Yuh WT, Zachar CK, Barloon TJ, Sato Y, Sickels WJ, Hawes DR. Vertebral compression fractures: distinction between benign and malignant causes with MR imaging. Radiology. 1989;172:215–8.
96. Yuzawa Y, Ebara S, Kamimura M, Tateiwa Y, Kinoshita T, Itoh H, Takahashi J, Karakida O, Sheena Y, Takaoka K. Magnetic resonance and computed tomography-based scoring system for the differential diagnosis of vertebral fractures caused by osteoporosis and malignant tumors. J Orthop Sci. 2005;10:345–52.
97. Moulopoulos LA, Yoshimitsu K, Johnston DA, Leeds NE, Libshitz HI. MR prediction of benign and malignant vertebral compression fractures. J Magn Reson Imaging. 1996;6:667–74.
98. Rupp RE, Ebraheim NA, Coombs RJ. Magnetic resonance imaging differentiation of compression spine fractures or vertebral lesions caused by osteoporosis or tumor. Spine (Phila Pa 1976). 1995;20:2499–503; discussion 2504
99. Shih TT, Huang KM, Li YW. Solitary vertebral collapse: distinction between benign and malignant causes using MR patterns. J Magn Reson Imaging. 1999;9:635–42.
100. Theodorou DJ. The intravertebral vacuum cleft sign. Radiology. 2001;221:787–8.
101. Blumenthal SL, Roach J, Herring JA. Lumbar Scheuermann's. A clinical series and classification. Spine (Phila Pa 1976). 1987;12:929–32.
102. Heithoff KB, Gundry CR, Burton CV, Winter RB. Juvenile discogenic disease. Spine (Phila Pa 1976). 1994;19:335–40.
103. Resnick D, Niwayama G. Intravertebral disk herniations: cartilaginous (Schmorl's) nodes. Radiology. 1978;126:57–65.
104. Daignault CP, Palmer EL, Scott JA, Swan JS, Daniels GH. Papillary thyroid carcinoma metastasis

to the lumbar spine masquerading as a Schmorl's node. Nucl Med Mol Imaging. 2015;49:217–22.
105. Grivé E, Rovira A, Capellades J, Rivas A, Pedraza S. Radiologic findings in two cases of acute Schmörl's nodes. AJNR Am J Neuroradiol. 1999;20:1717–21.
106. Kyere KA, Than KD, Wang AC, Rahman SU, Valdivia–Valdivia JM, La Marca F, Park P. Schmorl's nodes. Eur Spine J. 2012;21:2115–21.
107. Takahashi K, Miyazaki T, Ohnari H, Takino T, Tomita K. Schmorl's nodes and low-back pain. Analysis of magnetic resonance imaging findings in symptomatic and asymptomatic individuals. Eur Spine J. 1995;4:56–9.
108. Pratt ES, Green DA, Spengler DM. Herniated intervertebral discs associated with unstable spinal injuries. Spine (Phila Pa 1976). 1990;15:662–6.
109. Davis SJ, Teresi LM, Bradley WG Jr, Ziemba MA, Bloze AE. Cervical spine hyperextension injuries: MR findings. Radiology. 1991;180:245–51.
110. Kerslake RW, Jaspan T, Worthington BS. Magnetic resonance imaging of spinal trauma. Br J Radiol. 1991;64:386–402.
111. Dai L, Jia L. Central cord injury complicating acute cervical disc herniation in trauma. Spine (Phila Pa 1976). 2000;25:331–5; discussion 336
112. Schaefer DM, Flanders A, Northrup BE, Doan HT, Osterholm JL. Magnetic resonance imaging of acute cervical spine trauma. Correlation with severity of neurologic injury. Spine (Phila Pa 1976). 1989;14:1090–5.
113. Rizzolo SJ, Piazza MR, Cotler JM, Balderston RA, Schaefer D, Flanders A. Intervertebral disc injury complicating cervical spine trauma. Spine (Phila Pa 1976). 1991;16:S187–9.
114. Kulkarni MV, McArdle CB, Kopanicky D, Miner M, Cotler HB, Lee KF, Harris JH. Acute spinal cord injury: MR imaging at 1.5 T. Radiology. 1987;164:837–43.
115. Mirvis SE, Geisler FH, Jelinek JJ, Joslyn JN, Gellad F. Acute cervical spine trauma: evaluation with 1.5-T MR imaging. Radiology. 1988;166:807–16.
116. Tubbs RS, et al. Ligaments of the craniocervical junction. J Neurosurg Spine. 2011;14(6):697–709.
117. Arakal RG, Mani M, Ramachandran R. Applied anatomy of the normal and aging spine. In: Yue JJ, Guyer RD, Johnson JP, Khoo LT, Hochschuler SH, editors. The comprehensive treatment of the aging spine. Philadelphia: WB Saunders; 2011. p. 9–15.
118. Allen BL Jr, Ferguson RL, Lehmann TR, O'Brien RP, Allen BL, Ferguson RL, Lehmann TR, O'Brien RP. A mechanistic classification of closed, indirect fractures and dislocations of the lower cervical spine. Spine (Phila Pa 1976). 1982;7:1–27.
119. Edeiken-Monroe B, Wagner LK, Harris JH Jr. Hyperextension dislocation of the cervical spine. AJR Am J Roentgenol. 1986;146:803–8.
120. Regenbogen VS, Rogers LF, Atlas SW, Kim KS. Cervical spinal cord injuries in patients with cervical spondylosis. AJR Am J Roentgenol. 1986;146:277–84.
121. Harris JH Jr, Edeiken-Monroe BS. The radiology of acute cervical spine trauma. Baltimore: Williams & Wilkins; 1987.
122. Goldberg AL, Rothfus WE, Deeb ZL, Frankel DG, Wilberger JE Jr, Daffner RH. Hyperextension injuries of the cervical spine. Magnetic resonance findings. Skelet Radiol. 1989;18:283–8.
123. Flanders AE, Tartaglino LM, Friedman DP, Aquilone LF. Magnetic resonance imaging in acute spinal injury. Semin Roentgenol. 1992;27:271–98.
124. Shah LM, Ross JS. Imaging of spine trauma. Neurosurgery. 2016;79:626–42.
125. McArdle CB, Crofford MJ, Mirfakhraee M, Amparo EG, Calhoun JS. Surface coil MR of spinal trauma: preliminary experience. Am J Neuroradiol. 1986;7:885–93.
126. Friedman DP, Flanders AE. Unusual dissection of the proximal vertebral artery: description of three cases. Am J Neuroradiol. 1992;13:283–6.
127. Friedman D, Flanders A, Thomas C, Millar W. Vertebral artery injury after acute cervical spine trauma: rate of occurrence as detected by MR angiography and assessment of clinical consequences. AJR Am J Roentgenol. 1995;164:443–7.
128. Simon LV, Mohseni M. Vertebral artery injury. Treasure Island: StatPearls Publishing; 2019.
129. Biffl WL, Moore EE, Offner PJ, Burch JM. Blunt carotid and vertebral arterial injuries. World J Surg. 2001;25:1036–43.
130. Shafafy R, Suresh S, Afolayan JO, Vaccaro AR, Panchmatia JR. Blunt vertebral vascular injury in trauma patients: ATLS® recommendations and review of current evidence. J Spine Surg (Hong Kong). 2017;3:217–25.
131. Mutze S, Rademacher G, Matthes G, Hosten N, Stengel D. Blunt cerebrovascular injury in patients with blunt multiple trauma: diagnostic accuracy of duplex Doppler US and early CT angiography. Radiology. 2005;237:884–92.
132. Utter GH, Hollingworth W, Hallam DK, Jarvik JG, Jurkovich GJ. Sixteen-slice CT angiography in patients with suspected blunt carotid and vertebral artery injuries. J Am Coll Surg. 2006;203:838–48.
133. Heiserman JE, Dean BL, Hodak JA, Flom RA, Bird CR, Drayer BP, Fram EK. Neurologic complications of cerebral angiography. AJNR Am J Neuroradiol. 1994;15:1401–7; discussion 1408-11
134. Hernández-Pérez M, Puig J, Blasco G, Pérez de la Ossa N, Dorado L, Dávalos A, Munuera J. Dynamic magnetic resonance angiography provides collateral circulation and hemodynamic information in acute ischemic stroke. Stroke. 2016;47:531–4.
135. Schnake KJ, Schroeder GD, Vaccaro AR, Oner C. AOSpine classification systems (subaxial, thoracolumbar). J Orthop Trauma. 2017;31:S14–23.
136. Vaccaro AR, Lehman RA, Hurlbert RJ, et al. A new classification of thoracolumbar injuries: the importance of injury morphology, the integrity of the

posterior ligamentous complex, and neurologic status. Spine (Phila Pa 1976). 2005;30:2325–33.
137. Reinhold M, Audigé L, Schnake KJ, Bellabarba C, Dai L-Y, Oner FC. AO spine injury classification system: a revision proposal for the thoracic and lumbar spine. Eur Spine J. 2013;22:2184–201.
138. Holdsworth F. Fractures, dislocations, and fracture-dislocations of the spine. J Bone Joint Surg Am. 1970;52:1534–51.
139. Harris JH, Edeiken-Monroe B, Kopaniky DR. A practical classification of acute cervical spine injuries. Orthop Clin North Am. 1986;17:15–30.
140. Moore TA, Vaccaro AR, Anderson PA. Classification of lower cervical spine injuries. Spine (Phila Pa 1976). 2006;31:S37–43.
141. Denis F. The three column spine and its significance in the classification of acute thoracolumbar spinal injuries. Spine (Phila Pa 1976). 1983;8:817–31.
142. Magerl F, Aebi M. A comprehensive classification of thoracic and lumbar injuries. In: AO ASIF principles in spine surgery. Berli/Heidelberg: Springer; 1998. p. 20–41.
143. Sethi MK, Schoenfeld AJ, Bono CM, Harris MB. The evolution of thoracolumbar injury classification systems. Spine J. 2009;9:780–8.
144. Bono CM, Vaccaro AR, Hurlbert RJ, Arnold P, Oner FC, Harrop J, Anand N. Validating a newly proposed classification system for thoracolumbar spine trauma: looking to the future of the thoracolumbar injury classification and severity score. J Orthop Trauma. 2006;20:567–72.
145. Wood KB, Khanna G, Vaccaro AR, Arnold PM, Harris MB, Mehbod AA. Assessment of two thoracolumbar fracture classification systems as used by multiple surgeons. J Bone Joint Surg Am. 2005;87:1423–9.
146. Mirza SK, Mirza AJ, Chapman JR, Anderson PA. Classifications of thoracic and lumbar fractures: rationale and supporting data. J Am Acad Orthop Surg. 2002;10:364–77.
147. Pizones J, Sánchez-Mariscal F, Zúñiga L, Álvarez P, Izquierdo E. Prospective analysis of magnetic resonance imaging accuracy in diagnosing traumatic injuries of the posterior ligamentous complex of the thoracolumbar spine. Spine (Phila Pa 1976). 2013;38:745–51.
148. Lee JY, Vaccaro AR, Schweitzer KM, et al. Assessment of injury to the thoracolumbar posterior ligamentous complex in the setting of normal-appearing plain radiography. Spine J. 2007;7:422–7.
149. Kirschner J, Seupaul RA. Does computed tomography rule out clinically significant cervical spine injuries in patients with obtunded or intubated blunt trauma? Ann Emerg Med. 2012;60:737–8.
150. Vaccaro AR, Hulbert RJ, Patel AA, et al. The subaxial cervical spine injury classification system. Spine (Phila Pa 1976). 2007;32:2365–74.
151. Vaccaro AR, Oner C, Kepler CK, et al. AOSpine thoracolumbar spine injury classification system. Spine (Phila Pa 1976). 2013;38:2028–37.
152. Vaccaro AR, Koerner JD, Radcliff KE, et al. AOSpine subaxial cervical spine injury classification system. Eur Spine J. 2016;25:2173–84.
153. Anderson PA, Montesano PX. Morphology and treatment of occipital condyle fractures. Spine (Phila Pa 1976). 1988;13:731–6.
154. Tuli S, Tator CH, Fehlings MG, Mackay M. Occipital condyle fractures. Neurosurgery. 1997;41:368–77.
155. Traynelis VC, Marano GD, Dunker RO, Kaufman HH. Traumatic atlanto-occipital dislocation. J Neurosurg. 1986;65:863–70.
156. Bellabarba C, Mirza SK, West GA, Mann FA, Dailey AT, Newell DW, Chapman JR. Diagnosis and treatment of craniocervical dislocation in a series of 17 consecutive survivors during an 8-year period. J Neurosurg Spine. 2006;4:429–40.
157. Anderson LD, D'Alonzo RT. Fractures of the odontoid process of the axis. J Bone Joint Surg Am. 1974;56:1663–74.
158. AOSpine Injury Classification Systems. https://aospine.aofoundation.org/clinical-library-and-tools/aospine-classification-systems. Accessed 28 June 2019.
159. Kulkarni MV, Bondurant FJ, Rose SL, Narayana PA. 1.5 tesla magnetic resonance imaging of acute spinal trauma. Radiographics. 1988;8:1059–82.
160. Schaefer DM, Flanders AE, Osterholm JL, Northrup BE. Prognostic significance of magnetic resonance imaging in the acute phase of cervical spine injury. J Neurosurg. 1992;76:218–23.
161. Marciello MA, Flanders AE, Herbison GJ, Schaefer DM, Friedman DP, Lane JI. Magnetic resonance imaging related to neurologic outcome in cervical spinal cord injury. Arch Phys Med Rehabil. 1993;74:940–6.
162. Hackney DB, Finkelstein SD, Hand CM, Markowitz RS, Black P. Postmortem magnetic resonance imaging of experimental spinal cord injury: magnetic resonance findings versus in vivo functional deficit. Neurosurgery. 1994;35:1104–11.
163. Flanders AE, Spettell CM, Tartaglino LM, Friedman DP, Herbison GJ. Forecasting motor recovery after cervical spinal cord injury: value of MR imaging. Radiology. 1996;201:649–55.
164. Metz GAS, Curt A, Van De Meent H, Klusman I, Schwab ME, Dietz V. Validation of the weight-drop contusion model in rats: a comparative study of human spinal cord injury. J Neurotrauma. 2000;17:1–17.
165. Flanders AE, Schaefer DM, Doan HT, Mishkin MM, Gonzalez CF, Northrup BE. Acute cervical spine trauma: correlation of MR imaging findings with degree of neurologic deficit. Radiology. 1990;177:25–33.
166. Bondurant FJ, Cotler HB, Kulkarni MV, McArdle CB, Harris JH Jr. Acute spinal cord injury. A study using physical examination and magnetic resonance imaging. Spine (Phila Pa 1976). 1990;15:161–8.
167. Sato T, Kokubun S, Rijal KP, Ojima T, Moriai N, Hashimoto M, Hyodo H, Oonuma H. Prognosis of

cervical spinal cord injury in correlation with magnetic resonance imaging. Paraplegia. 1994;32:81–5.
168. Ramon S, Dominguez R, Ramirez L, Paraira M, Olona M, Castello T, Garcia Fernandez L. Clinical and magnetic resonance imaging correlation in acute spinal cord injury. Spinal Cord. 1997;35:664–73.
169. Boldin C, Raith J, Fankhauser F, Haunschmid C, Schwantzer G, Schweighofer F. Predicting neurologic recovery in cervical spinal cord injury with postoperative MR imaging. Spine (Phila Pa 1976). 2006;31:554–9.
170. Cotler HB, Kulkarni MV, Bondurant FJ. Magnetic resonance imaging of acute spinal cord trauma: preliminary report. J Orthop Trauma. 1988;2:1–4.
171. Silberstein M, Tress BM, Hennessy O. Prediction of neurologic outcome in acute spinal cord injury: the role of CT and MR. AJNR Am J Neuroradiol. 1992;13:1597–608.
172. Shah LM, Flanders AE. Update on new imaging techniques for trauma. Neurosurg Clin N Am. 2017;28:1–21.
173. Barnett HJ, Botterell EH, Jousse AT, Wynn-Jones M. Progressive myelopathy as a sequel to traumatic paraplegia. Brain. 1966;89:159–74.
174. Quencer RM, Sheldon JJ, Post MJ, Diaz RD, Montalvo BM, Green BA, Eismont FJ. MRI of the chronically injured cervical spinal cord. AJR Am J Roentgenol. 1986;147:125–32.
175. Wang D, Bodley R, Sett P, Gardner B, Frankel H. A clinical magnetic resonance imaging study of the traumatised spinal cord more than 20 years following injury. Paraplegia. 1996;34:65–81.
176. Falcone S, Quencer RM, Green BA, Patchen SJ, Post MJ. Progressive posttraumatic myelomalacic myelopathy: imaging and clinical features. AJNR Am J Neuroradiol. 1994;15:747–54.
177. Pang D. Spinal cord injury without radiographic abnormality in children, 2 decades later. Neurosurgery. 2004;55:1325–43.
178. Zohrabian VM, Flanders AE. Imaging of trauma of the spine. Handb Clin Neurol. 2016;136:747–67.
179. Frankel HL. Ascending cord lesion in the early stages following spinal injury. Spinal Cord. 1969;7:111.
180. Yablon IG, Ordia J, Mortara R, Reed J, Spatz E. Acute ascending myelopathy of the spine. Spine (Phila Pa 1976). 1989;14:1084–9.
181. Belanger E, Picard C, Lacerte D, Lavallee P, Levi ADO. Subacute posttraumatic ascending myelopathy after spinal cord injury: report of three cases. J Neurosurg Spine. 2000;93:294–9.
182. Visocchi M, Di Rocco F, Meglio M. Subacute clinical onset of postraumatic myelopathy. Acta Neurochir. 2003;145:799–804.
183. Al-Ghatany M, Al-Shraim M, Levi ADO, Midha R. Pathological features including apoptosis in subacute posttraumatic ascending myelopathy: case report and review of the literature. J Neurosurg Spine. 2005;2:619–23.
184. Schmidt BJ. Subacute delayed ascending myelopathy after low spine injury: case report and evidence of a vascular mechanism. Spinal Cord. 2006;44:322.
185. Planner AC, Pretorius PM, Graham A, Meagher TM. Subacute progressive ascending myelopathy following spinal cord injury: MRI appearances and clinical presentation. Spinal Cord. 2008;46:140.
186. Sureka J, Cherian RA, Alexander M, Thomas BP. MRI of brachial plexopathies. Clin Radiol. 2009;64:208–18.
187. Yoshikawa T, Hayashi N, Yamamoto S, Tajiri Y, Yoshioka N, Masumoto T, Mori H, Abe O, Aoki S, Ohtomo K. Brachial plexus injury: clinical manifestations, conventional imaging findings, and the latest imaging techniques. Radiographics. 2006;26:S133–43.
188. Aralasmak A, Karaali K, Cevikol C, Uysal H, Senol U. MR imaging findings in brachial plexopathy with thoracic outlet syndrome. Am J Neuroradiol. 2010;31:410–7.
189. van Es HW, Bollen TL, van Heesewijk HPM. MRI of the brachial plexus: a pictorial review. Eur J Radiol. 2010;74:391–402.
190. Doi K, Otsuka K, Okamoto Y, Fujii H, Hattori Y, Baliarsing AS. Cervical nerve root avulsion in brachial plexus injuries: magnetic resonance imaging classification and comparison with myelography and computerized tomography myelography. J Neurosurg. 2002;96:277–84.
191. Falconer JC, Narayana PA, Bhattacharjee MB, Liu SJ. Quantitative MRI of spinal cord injury in a rat model. Magn Reson Med. 1994;32:484–91.
192. Doran M, Bydder GM. Magnetic resonance: perfusion and diffusion imaging. Neuroradiology. 1990;32:392–8.
193. Hajnal JV, Doran M, Hall AS, Collins AG, Oatridge A, Pennock JM, Young IR, Bydder GM. MR imaging of anisotropically restricted diffusion of water in the nervous system: technical, anatomic, and pathologic considerations. J Comput Assist Tomogr. 1991;15:1–18.
194. Barkovich AJ. Concepts of myelin and myelination in neuroradiology. AJNR Am J Neuroradiol. 2000;21:1099–109.
195. Beaulieu C. The basis of anisotropic water diffusion in the nervous system – a technical review. NMR Biomed. 2002;15:435–55.
196. Ford JC, Hackney DB, Alsop DC, Jara H, Joseph PM, Hand CM, Black P. MRI characterization of diffusion coefficients in a rat spinal cord injury model. Magn Reson Med. 1994;31:488–94.
197. Facon D, Ozanne A, Fillard P, Lepeintre JF, Tournoux-Facon C, Ducreux D. MR diffusion tensor imaging and fiber tracking in spinal cord compression. AJNR Am J Neuroradiol. 2005;26:1587–94.
198. Shanmuganathan K, Gullapalli RP, Zhuo J, Mirvis SE. Diffusion tensor MR imaging in cervical spine trauma. AJNR Am J Neuroradiol. 2008;29:655–9.
199. Cheran S, Shanmuganathan K, Zhuo J, Mirvis SE, Aarabi B, Alexander MT, Gullapalli RP. Correlation of MR diffusion tensor imaging parameters with

ASIA motor scores in hemorrhagic and nonhemorrhagic acute spinal cord injury. J Neurotrauma. 2011;28:1881–92.
200. Poplawski MM, Alizadeh M, Oleson CV, Fisher J, Marino RJ, Gorniak RJ, Leiby BE, Flanders AE. Application of diffusion tensor imaging in forecasting neurological injury and recovery after human cervical spinal cord injury. J Neurotrauma. 2019;36(21):3051–61. https://doi.org/10.1089/neu.2018.6092.
201. Shanmuganathan K, Zhuo J, Chen HH, Aarabi B, Adams J, Miller C, Menakar J, Gullapalli RP, Mirvis SE. Diffusion tensor imaging parameter obtained during acute blunt cervical spinal cord injury in predicting long-term outcome. J Neurotrauma. 2017;34:2964–71.
202. Sasiadek MJ, Szewczyk P, Bladowska J. Application of diffusion tensor imaging (DTI) in pathological changes of the spinal cord. Med Sci Monit. 2012;18(6):RA73–9.
203. Foltys H, Kemeny S, Krings T, Boroojerdi B, Sparing R, Thron A, Topper R. The representation of the plegic hand in the motor cortex: a combined fMRI and TMS study. Neuroreport. 2000;11:147–50.
204. Mikulis DJ, Jurkiewicz MT, McIlroy WE, Staines WR, Rickards L, Kalsi-Ryan S, Crawley AP, Fehlings MG, Verrier MC. Adaptation in the motor cortex following cervical spinal cord injury. Neurology. 2002;58:794–801.
205. Turner JA, Lee JS, Schandler SL, Cohen MJ. An fMRI investigation of hand representation in paraplegic humans. Neurorehabil Neural Repair. 2003;17:37–47.
206. Freund P, Weiskopf N, Ward NS, Hutton C, Gall A, Ciccarelli O, Craggs M, Friston K, Thompson AJ. Disability, atrophy and cortical reorganization following spinal cord injury. Brain. 2011;134:1610–22.
207. Lundell H, Christensen MS, Barthelemy D, Willerslev-Olsen M, Biering-Sorensen F, Nielsen JB. Cerebral activation is correlated to regional atrophy of the spinal cord and functional motor disability in spinal cord injured individuals. NeuroImage. 2011;54:1254–61.
208. Stroman PW, Tomanek B, Krause V, Frankenstein UN, Malisza KL. Mapping of neuronal function in the healthy and injured human spinal cord with spinal fMRI. NeuroImage. 2002;17:1854–60.
209. Stroman PW, Kornelsen J, Bergman A, Krause V, Ethans K, Malisza KL, Tomanek B. Noninvasive assessment of the injured human spinal cord by means of functional magnetic resonance imaging. Spinal Cord. 2004;42:59–66.
210. Kornelsen J, Stroman PW. Detection of the neuronal activity occurring caudal to the site of spinal cord injury that is elicited during lower limb movement tasks. Spinal Cord. 2007;45:485–90.
211. Cadotte DW, Bosma R, Mikulis D, Nugaeva N, Smith K, Pokrupa R, Islam O, Stroman PW, Fehlings MG. Plasticity of the injured human spinal cord: insights revealed by spinal cord functional MRI. PLoS One. 2012;7:e45560.

MRI in Degenerative Disease of the Spine

4

Alessandra J. Sax

Introduction

Although the spine is prone to a diverse range of pathology, degenerative changes are the most prevalent and the most common indication for spinal MR imaging [1, 2]. Degenerative changes occur within the intervertebral disk which desiccates and becomes more prone to fissuring and bulging. This disk degeneration shifts the biomechanical stress to other joints, such as the synovial facet joints, which can become narrowed with reactive edema, develop osteophytes, and hypertrophy, and causes buckling of the ligamentum flavum. Such changes can cause clinically relevant symptoms themselves, or they may contact the nearby spinal cord or nerves, which may or may not be an additional potential source of the patient's symptoms [3]. Correlation between the clinical exam and imaging findings is imperative to determine both the location and the cause of the patient's pain in order for the appropriate treatment to be initiated [4–6].

A. J. Sax (✉)
Department of Radiology, Thomas Jefferson University Hospital, Philadelphia, PA, USA
e-mail: alessandra.sax@jefferson.edu

Cervical Spine

The cervical spine is the most mobile of the spinal segments, allowing for not only flexion and extension but also lateral bending and rotation to a greater degree than the other spinal segments. This motion is most robust in the lower cervical spine, particularly from C4–C7, where we also see the most degenerative disease, particularly at the facet joints, but also within the intervertebral disks [7]. Additionally, the cervical spine has some unique anatomy including uncovertebral joints, which are also prone to degenerative changes, as well as transverse foramina.

When first evaluating images of the spine, it is important to gain a general gestalt as to the degree of pathology. This is usually done in the sagittal plane, looking at the alignment, bone marrow signal abnormalities, and severity of the degenerative disease. From there, assessment is done level by level in the axial plane, with reference to the sagittal plane for both troubleshooting and completeness.

The Disk-Osteophyte Complex (DOC) or Bulge

As described previously, a normal intervertebral disk is composed of a central nucleus pulposus and peripheral annulus fibrosus. Because the nucleus pulposus is composed of mainly water, it appears as low signal on T1-weighted images and

W. B. Morrison et al. (eds.), *MRI of the Spine*, https://doi.org/10.1007/978-3-030-43627-8_4

high signal on T2-weighted images. This is in contrast to the annulus fibrosus which appears as low signal on both T1- and T2-weighted images. Normally, the disk does not extend beyond the margins of the vertebral bodies (Fig. 4.1). However, with normal aging and degeneration, the nucleus pulposus can progressively lose hydration and flatten, resulting in loss of disk height and the normal hyperintense signal on T2-weighted images, with extension beyond the margins of the adjacent vertebral bodies [8].

Because of the increased mobility in the cervical spine, disk-osteophyte complexes (DOCs) can develop as a result of increased biomechanical stress as the disk degenerates. DOCs are more common in the cervical spine (whereas simple disk bulges predominate in the lumbar spine). The DOC can be identified as a hypointense (dark) line which bulges beyond the expected margin of a normal vertebral body (Fig. 4.2). This hypointense line represents bony cortex, whereas disk material (without the osteophyte

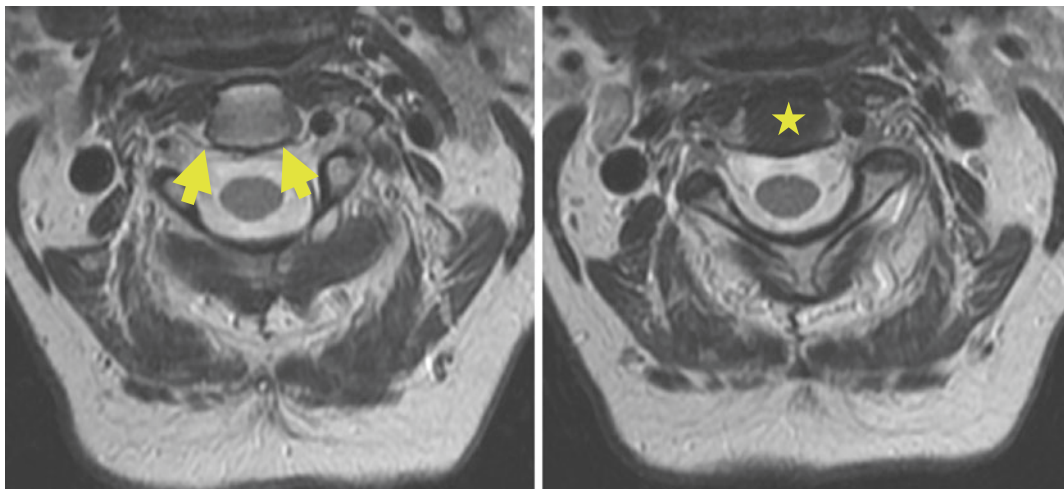

Fig. 4.1 Axial T2-weighted imaging of the cervical spine demonstrates a normal disk (yellow star) which does not extend beyond the margins of the vertebral body (arrows)

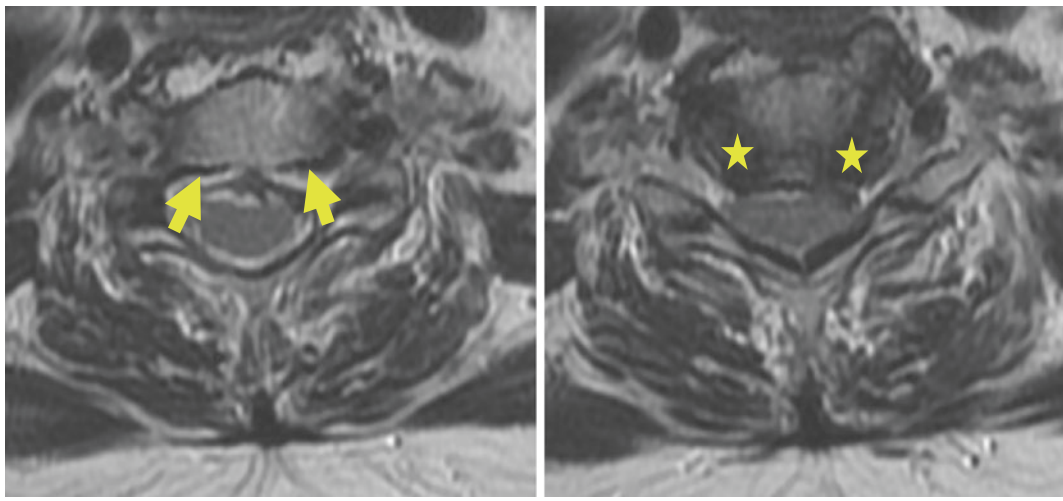

Fig. 4.2 Axial T2-weighted images of the cervical spine demonstrating a diffuse disk bulge (stars) which overhangs the margins of the vertebral body (arrows)

portion) is slightly less hypointense, and fatty marrow is hyperintense (bright). When a bulge is described as diffuse, there is circumferential bulging beyond the margins of the adjacent vertebral bodies (greater than 180°). When the bulge is not circumferential but still involves a large proportion of the disk (90–180°), it is referred to as a broad bulge (Fig. 4.3).

In some instances, the disk bulge may be even more focal (involving less than 25% of the disk circumference or less than 90°) and described instead as a herniation, which can be further broken down into protrusions or extrusions. Protrusions are a direct continuation of the disk and have a wide base whose lateral dimension at its junction with the disk is larger than its anterior-posterior dimension (Fig. 4.4). Extrusions on the other hand usually have a narrow base whose lateral dimension is smaller than its anterior-posterior dimension and can be somewhat

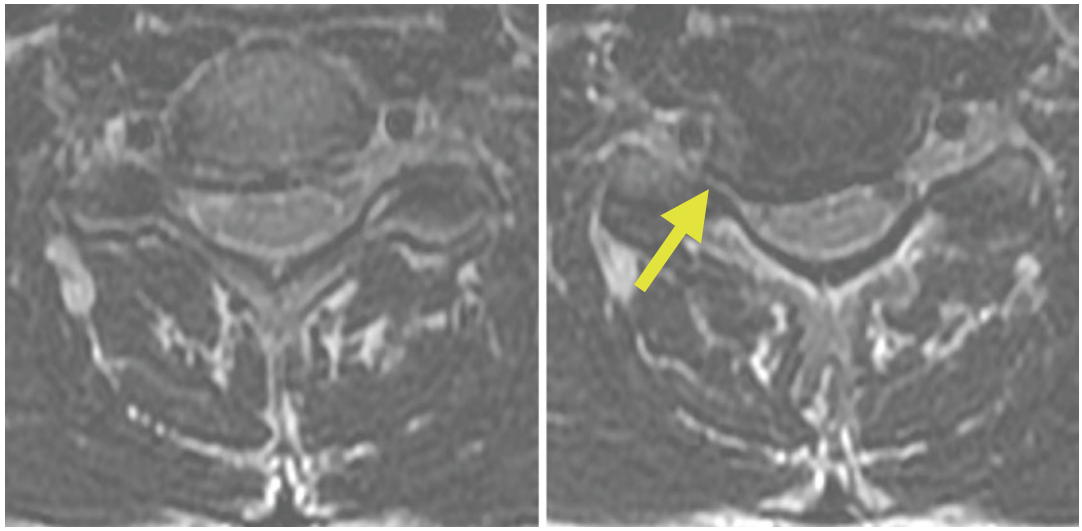

Fig. 4.3 Axial T2-weighted images of the cervical spine demonstrating a right paracentral disk bulge (arrow)

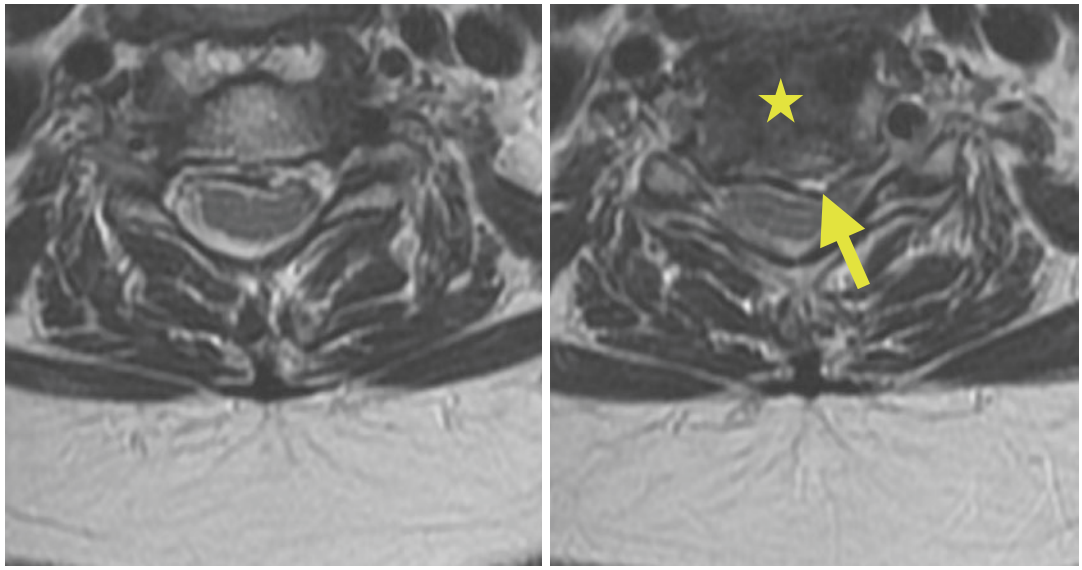

Fig. 4.4 Axial T2-weighted images of the cervical spine demonstrating a diffuse disk bulge (star) with a superimposed left paracentral disk protrusion and annular fissure (arrow)

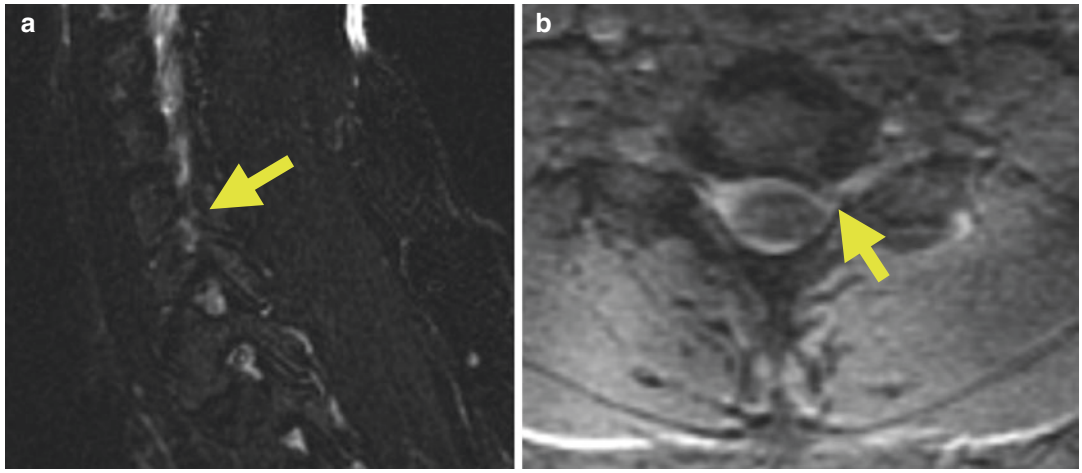

Fig. 4.5 Sagittal (**a**) and axial (**b**) T2-weighted imaging of the cervical spine demonstrating a left neural foraminal disk extrusion (arrows)

displaced or migrated from the disk (Fig. 4.5). In either case, the location of the protrusion or extrusion should always be described. Clinically relevant descriptors (as they relate to the cord and nerve roots, potentially causing clinical symptoms) include central, paracentral, subarticular, and foraminal. In other instances, a portion of the disk may become detached and can also migrate. This is referred to as a disk sequestration. Because sequestered disk may demonstrate more hyperintensity on T2-weighted images and exhibit contrast enhancement, it is important not to misidentify this disk fragment as a mass. In the case of extrusions and sequestrations, the direction of migration should also always be described, such as inferior and superior migration.

The (usual) precursor to the abovementioned disk bulges/herniations is called the annular fissure, which is a separation of the annular fibers from their attachment to the vertebral body. This can be identified as a hyperintense (bright) signal on T2-weighted imaging (Fig. 4.4) which runs along the annulus fibrosus [9].

In addition to the abovementioned disk changes, the adjacent vertebral bodies can also undergo degeneration. This can be seen as abnormal bone marrow signal paralleling the endplates and designated as Modic type 1, 2, or 3 changes. Modic type 1 changes are inflammatory in etiology and are thus seen as hyperintense signal on T2-weighted imaging, with normal or low signal on T1-weighted imaging. Modic type 2 changes are characterized by fatty marrow conversion and thus appear hyperintense on both T1- and T2-weighted images. Lastly, Modic type 3 changes are defined by sclerosis and appear as low signal intensity of T1- and T2-weighted images [10, 11] (Fig. 4.6).

The Facet Joints

The facet joints can be another source of degenerative changes within the vertebral body. A normal facet joint should have a thin, smooth bony cortex which is distinct from the more central, fattier marrow cavity. Degeneration of the facet joints, on the other hand, manifests as cartilage fibrillation, subchondral sclerosis, and osteophytosis, the latter two of which appear as hypointense signal on T1- and T2-weighted images. This hypertrophied facet with irregular joint spaces can encroach on both the joint space itself and the neural foramina. These changes can be described as mild, moderate, and severe (Fig. 4.7). Although no formal grading system exists for these designations, gen-

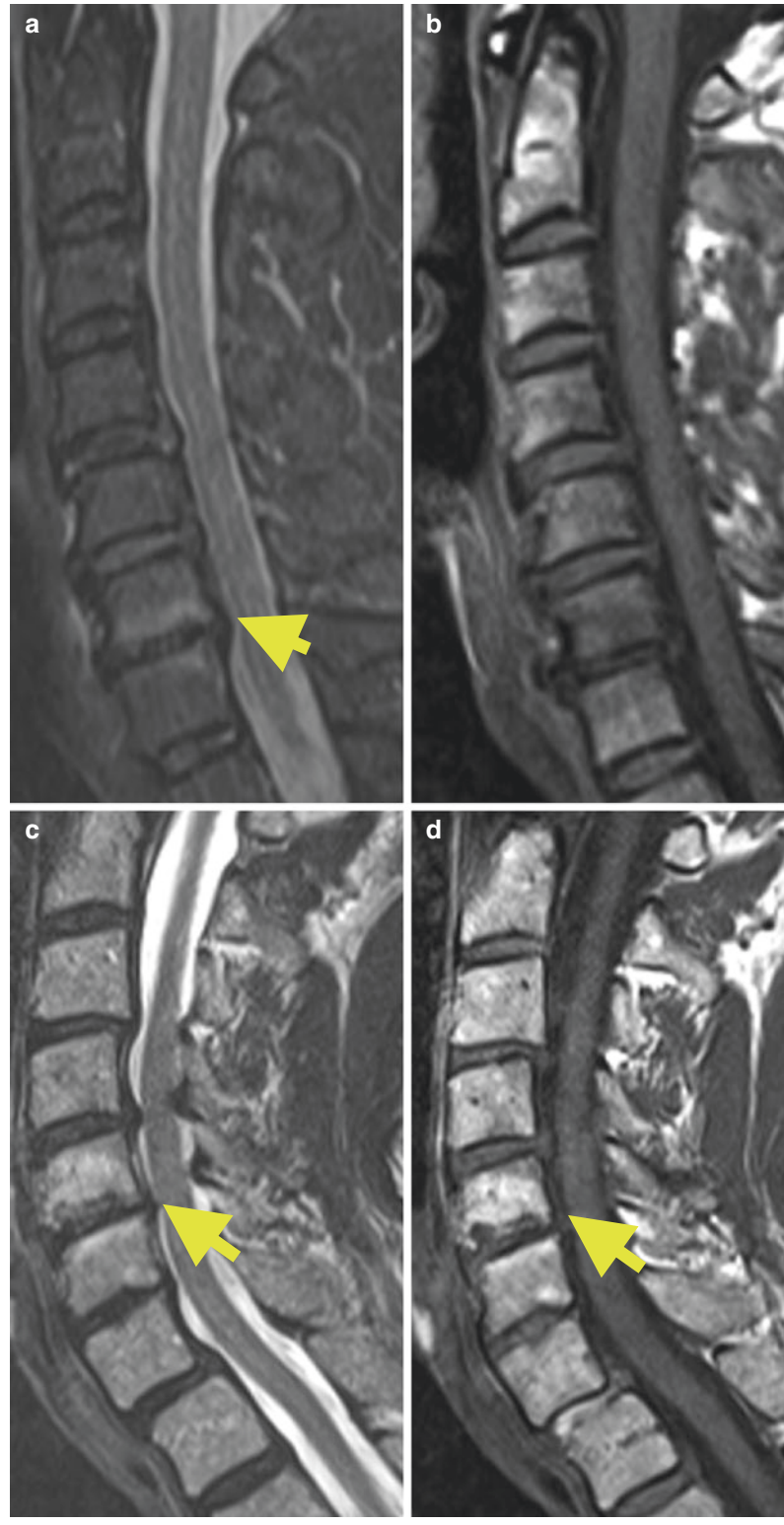

Fig. 4.6 Sagittal images of the cervical spine demonstrating Modic changes. Modic type 1 changes are seen in (**a**) where there is T2 signal hyperintensity at the superior and inferior endplates of C6–C7 (arrow), without a corresponding signal on the T1-weighted image (**b**). Sagittal T2-weighted (**c**) and T1-weighted (**d**) images demonstrate signal hyperintensity at the endplates of C5–C6 compatible with Modic type 2 changes (arrows). Sagittal T2-weighted (**e**) and T1-weighted (**f**) images demonstrate sclerosis and signal hypointensity at the superior endplate of C5 compatible with Modic type 3 changes (arrows)

Fig. 4.6 (continued)

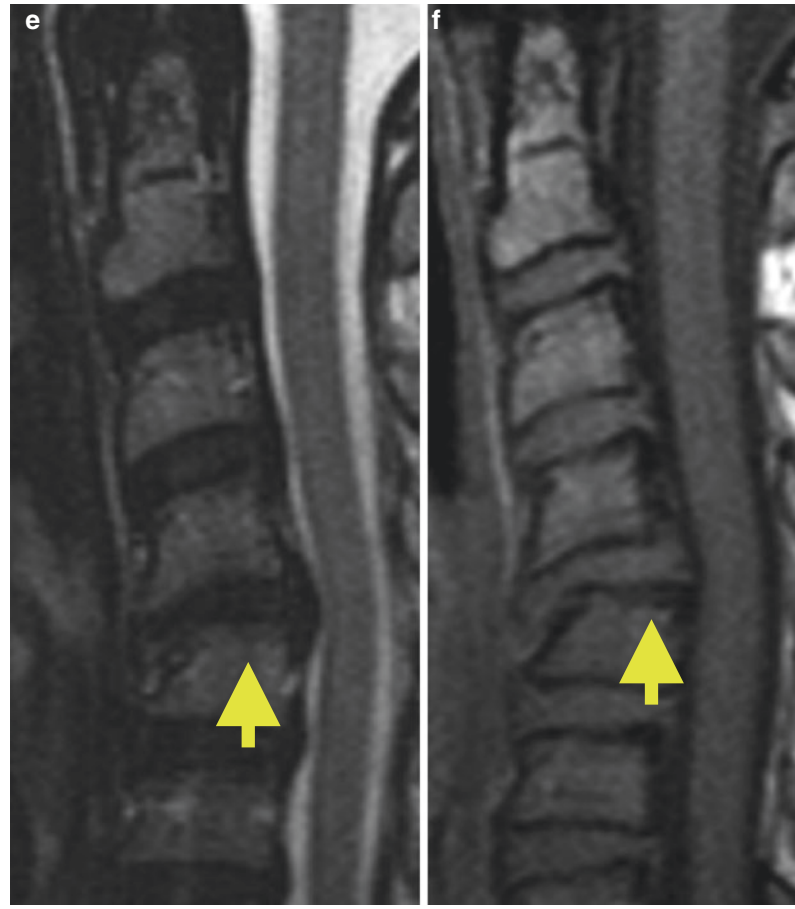

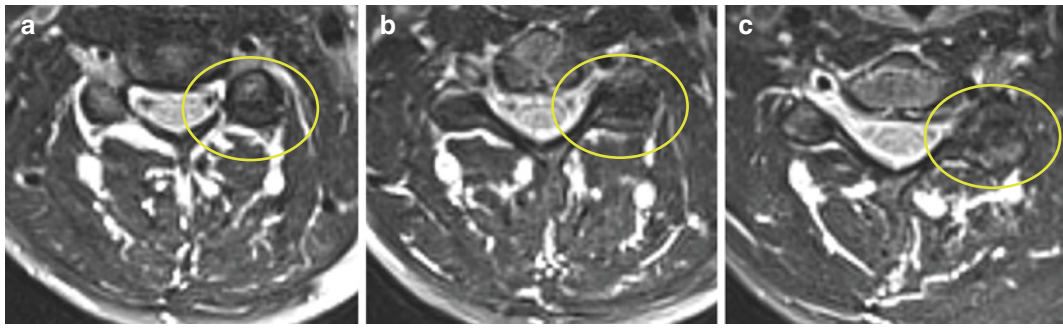

Fig. 4.7 Axial T2-weighed imaging of the cervical spine demonstrating mild (**a**), moderate (**b**), and severe (**c**) left facet hypertrophy (ovals)

erally, mild facet hypertrophy is defined by small osteophytes and subchondral sclerosis, moderate by the addition of irregularity of the joints and larger osteophytes, and severe by even larger osteophytes and more pronounced subchondral sclerosis [12–15].

Ligaments

The ligaments of the spine are made of mostly collagen, normally appearing as hypointense bands on both T1- and T2-weighted imaging. An additional change that can occur when the disk loses its

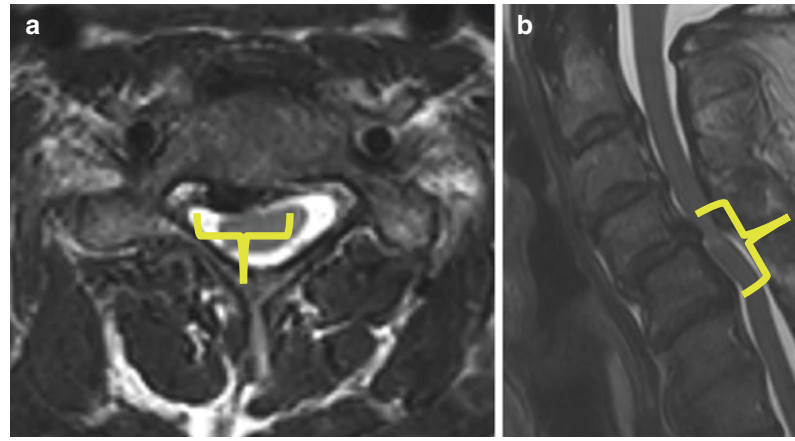

Fig. 4.8 Axial (**a**) and sagittal (**b**) T2-weighted imaging of the cervical spine demonstrates ossification of the posterior longitudinal ligament (OPLL) as evidenced by a hypointense line running along the posterior aspect of the vertebral bodies (brackets)

normal height and structure is ligamentum flavum infolding. This loss of disk height, as well as narrowing of the synovial joint spaces, results in buckling of the ligamentum flavum, manifesting as increased dark signal between the lamina of the vertebral bodies. This can further encroach on the neural foramina or central spinal canal.

Additional changes can occur within the posterior longitudinal ligament, which runs along the posterior aspect of the vertebral bodies attaching to both the vertebral bodies and disks. When this ligament becomes calcified, it is referred to as ossification of the posterior longitudinal ligament (OPLL). This manifests as hypointensity of both T1- and T2 weighted imaging and may also contribute to central canal narrowing (Fig. 4.8). It also predisposes patients to cord injury from minor trauma, which can be particularly devastating as OPLL is most common in the cervical spine.

The Uncovertebral Joints

As mentioned previously, uncovertebral joints are unique to the cervical spine, and they can also undergo hypertrophy. Normally, uncovertebral joints are indistinct, "cat ear"-like articulations of the uncinate process and adjacent vertebral body (Fig. 4.8a). However, when they undergo hypertrophy, they become bulky and irregular and protrude posteriorly. These changes can also be described as mild, moderate, and severe depending on their size and degree of impingement, although no distinct criteria for these designations exist (Fig. 4.9).

Central Canal Narrowing

All of the abovementioned degenerative changes can have cumulative effects, narrowing the central spinal canal and encroaching on the neural foramina and lateral recesses. Normally, the spinal canal maintains a smooth oval shape on axial images. When it becomes flattened or triangular in shape, this is indicative of stenosis. Just like with degenerative changes, the degree of central canal stenosis can be quantified as mild, moderate, or severe, without any universally agreed-upon criteria for such quantifications (Fig. 4.10). However, generally speaking, in mild central canal stenosis, the canal is less than 10 mm in the AP dimension, and/or there is a small amount of effacement surrounding the cord. In moderate central canal stenosis, the cord is usually less than 7 mm in the AP dimension with effacement of the spaces around the cord and also with slight cord deformity. However, when the degree of stenosis results in abnormal cord signal (T2 signal hyperintensity), or myelomalacia (thinning of the

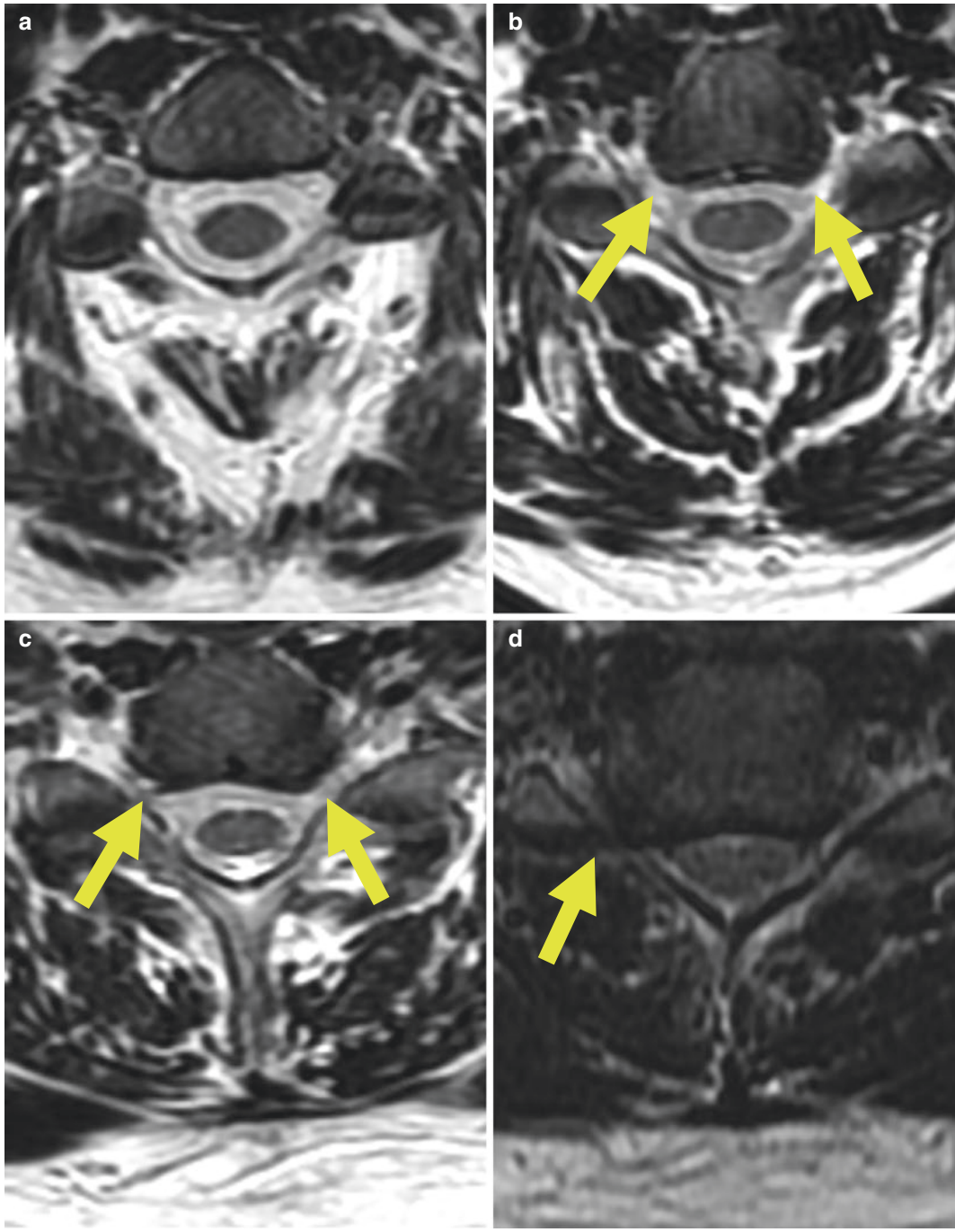

Fig. 4.9 Axial T2-weighted imaging of the cervical spine first demonstrating normal uncovertebral joints (**a**) which are imperceptible. Mild uncovertebral joint hypertrophy (**b**) is slightly bulky (arrows), while moderate hypertrophy (**c**) begins to protrude and is more irregular (arrows), and severe left-sided hypertrophy (**d**) is even more bulky and ill-defined (arrow)

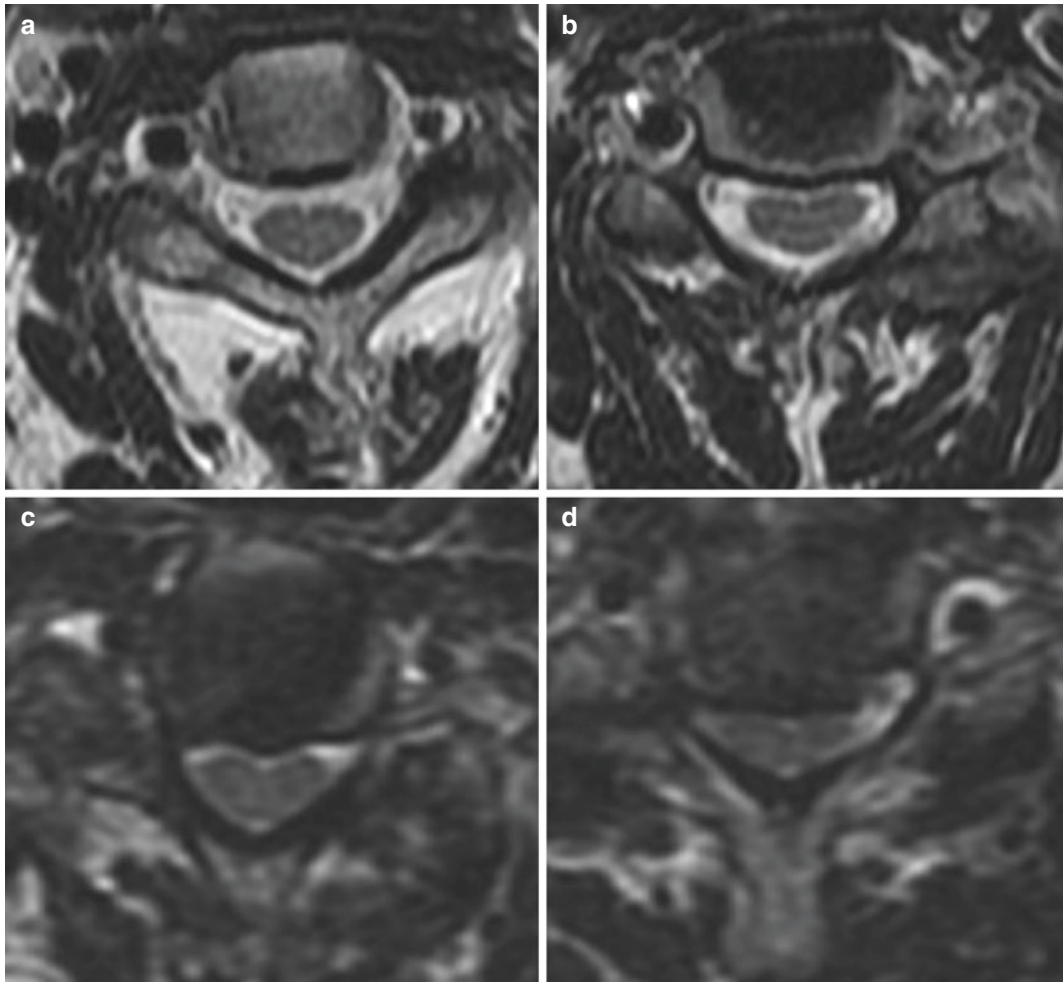

Fig. 4.10 Axial (**a**–**d**) T2-weighted images of the cervical spine. In contrast to the normal central canal (**a**), in mild central canal stenosis (**b**), there is mild effacement of the surrounding CSF space, which may or may not be bilateral. In moderate central canal stenosis (**c**), there is usually an associated deformity of the thecal sac or spinal cord. In severe central canal stenosis (**d**), there is marked effacement, deformity, and abnormal signal representing edema within the cord. Over time, the cord becomes ischemic and atrophies resulting in myelomalacia or thinning of the cord

cord), this is usually the result of cord ischemia in the setting of severe central canal stenosis. Another criterion for severe central canal stenosis is an AP dimension of less than 5 mm.

Neural Foraminal Narrowing

The neural foramina are the spaces between the facet joints and posterior lateral aspect of the vertebral bodies. Within the neural foramen are exiting nerve roots and dorsal root ganglia. Normally, the neural foramina appear as smooth keyhole-like shapes on sagittal images with the nerve bundles running obliquely through them. This space can be effaced by degenerative disk disease and osteophytosis, affecting those exiting nerve roots in both the superior and inferior portions of the foramen. The degree of narrowing can

also be quantified as mild, moderate, and severe. In mild neural foraminal narrowing, there is slight encroachment. In moderate narrowing, there is much more obvious encroachment, but with preservation of the fat within the neural foramen. In severe narrowing, there is complete obliteration of the fat within the neural foramen (Fig. 4.11).

The lateral recess is located on the medial aspect of the pedicles, adjacent to the nerve roots before they exit through the neural foramina. This area is more vulnerable to facet hypertrophy and ligamentum flavum infolding. Stenosis here is usually manifest as displacement or compression of those traversing nerve roots and/or by loss of the normal shape of the recess.

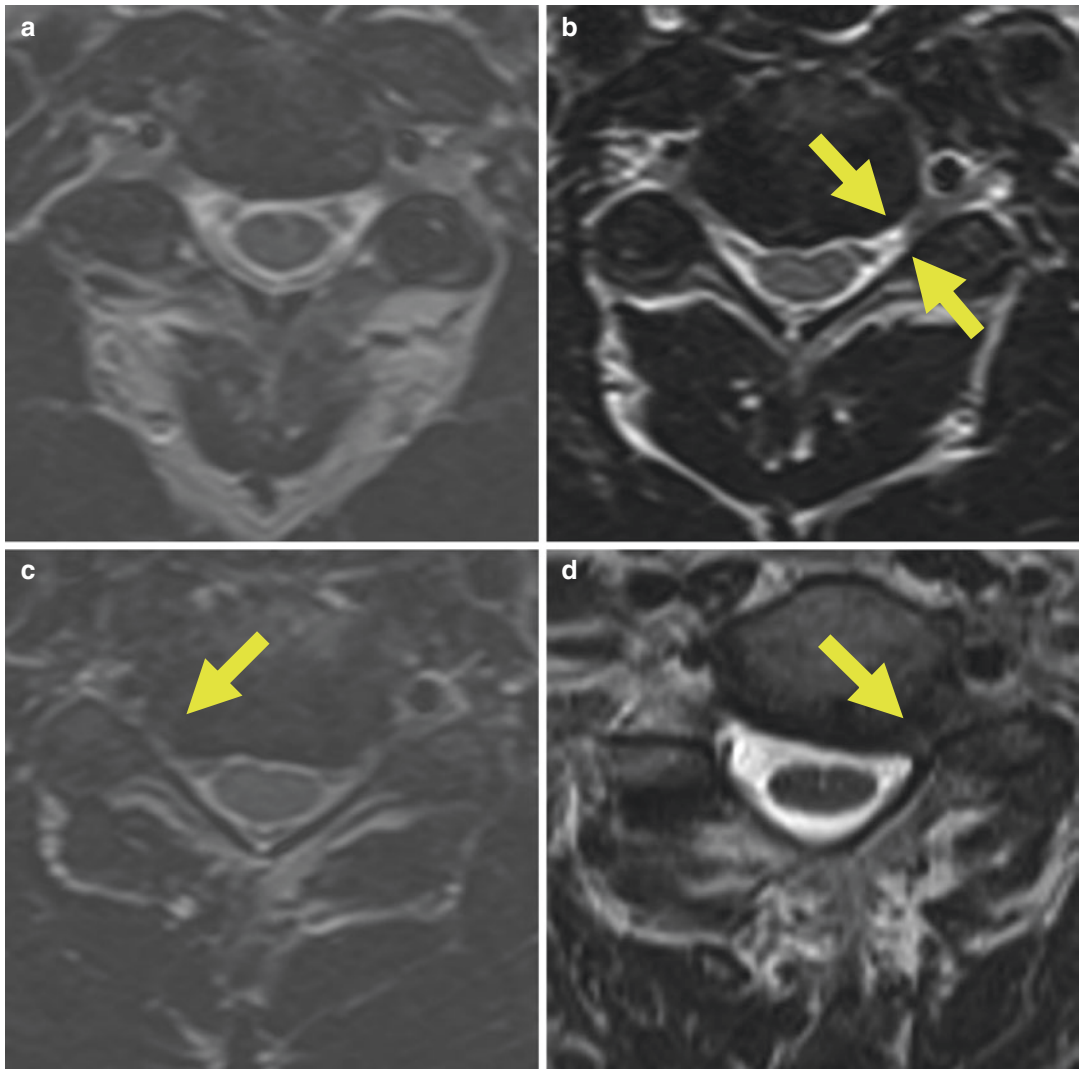

Fig. 4.11 Axial T2-weighted images of the cervical spine. The normal neural foramina (**a**) are smooth with clean fat surrounding the exiting nerves. In mild stenosis (**b**), there is slight encroachment on this space (arrow). In moderate stenosis (**c**), the encroachment results in contact of the exiting nerve roots (arrow). In severe stenosis (**d**), there is obliteration of the fat in the neural foramen (arrow)

Thoracic Spine

Unlike in the cervical spine, there is much more limited motion in the thoracic spine. As a result, there is a lower risk of degenerative disease. When degenerative disease does occur, it is usually secondary to disk bulges (Figs. 4.12, 4.13, and 4.14), as osteophytes and DOCs are less common. Additionally, there is no unique anatomy of the thoracic spine. As such, the pathology

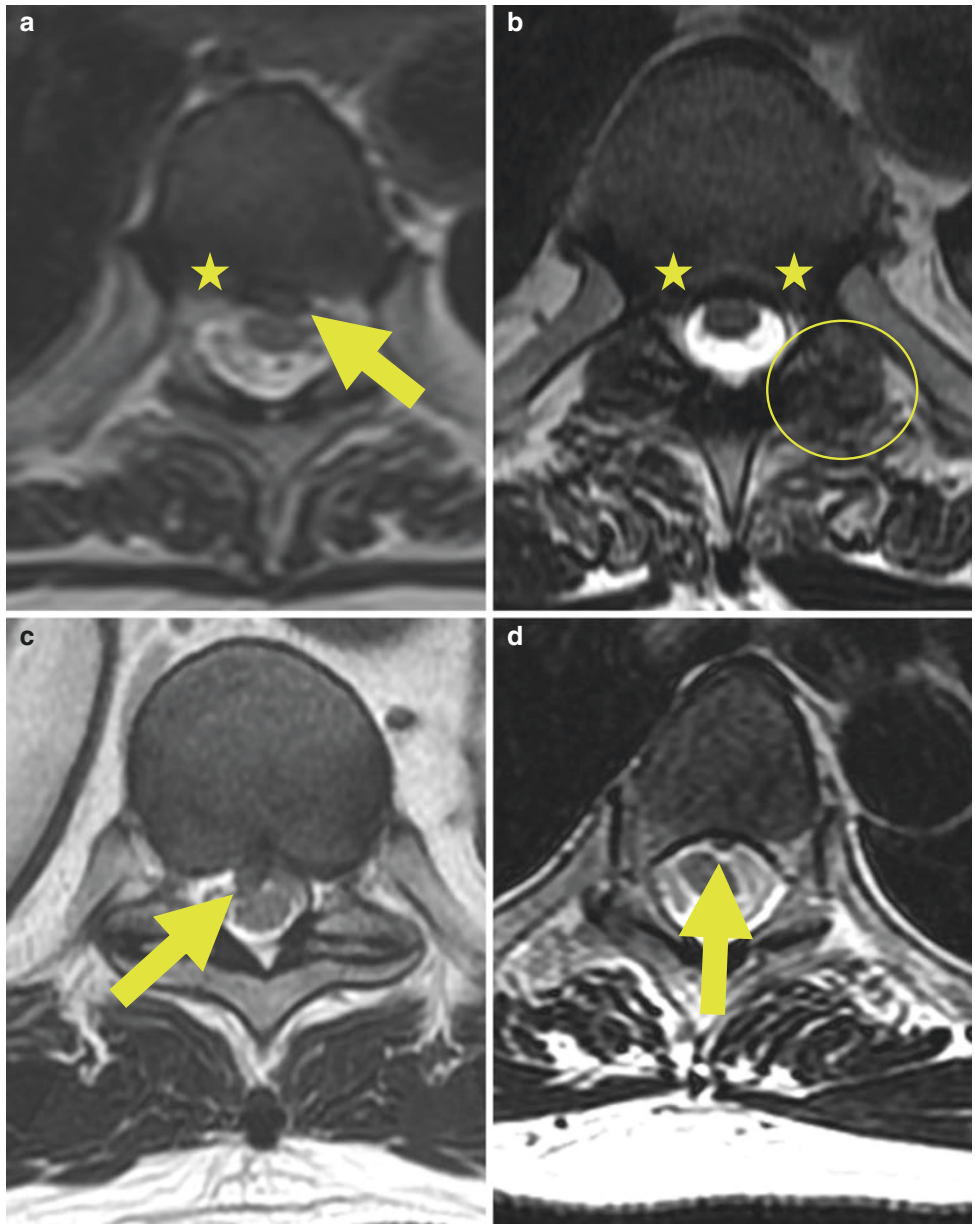

Fig. 4.12 Axial T2-weighted imaging of the thoracic spine. In (**a**), there is a disk herniation (star) with a superimposed left central disk extrusion (arrow) which causes mild central canal narrowing. In (**b**), there is a diffuse disk bulge (stars) and bilateral facet hypertrophy (oval) causing moderate bilateral neuroforaminal narrowing. In (**c**), there is a right central disk extrusion (arrow) whose base in the lateral dimension is narrower than its AP dimension, while in (**d**), there is a central disk protrusion (arrow) whose base is wider than its AP dimension

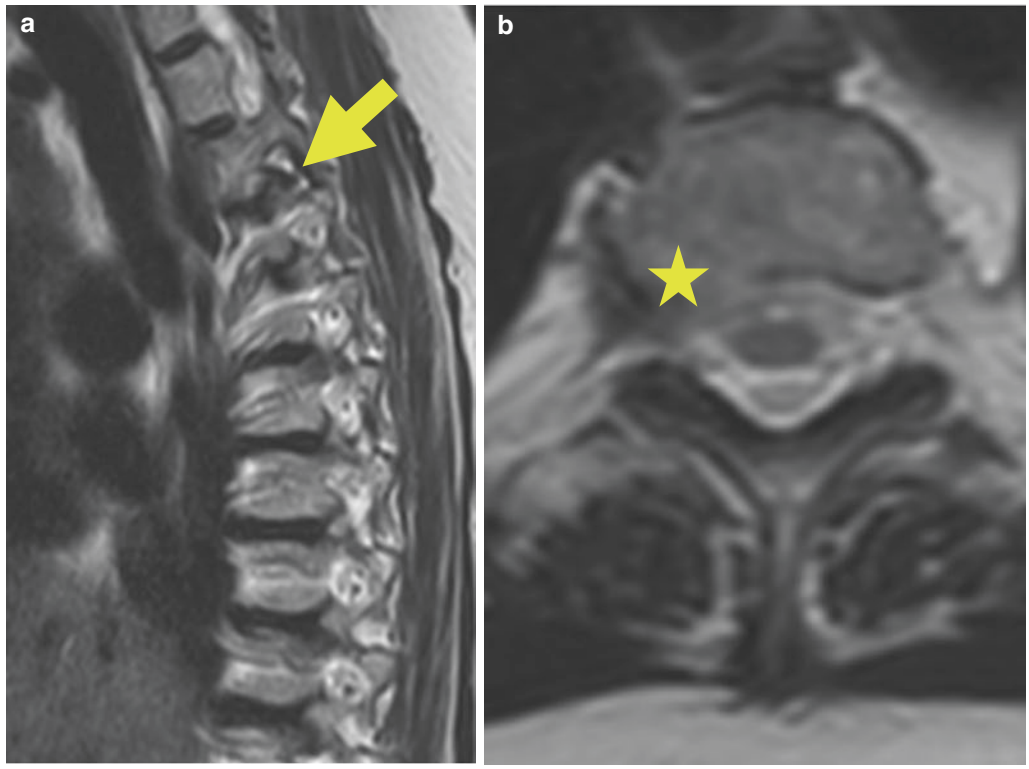

Fig. 4.13 Sagittal (**a**) and axial (**b**) T2-weighted imaging of the thoracic spine demonstrates a right foraminal disk protrusion (star) causing moderate right neural foraminal stenosis

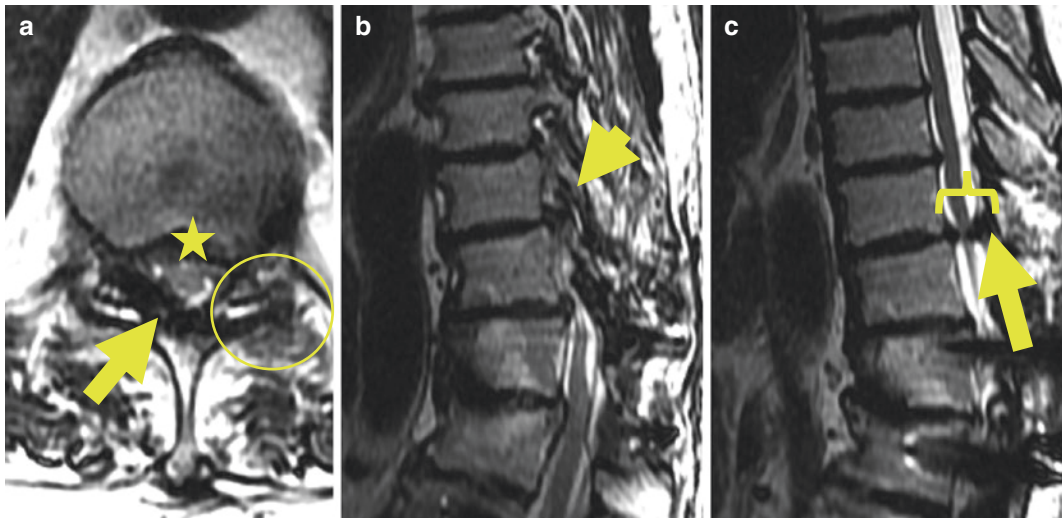

Fig. 4.14 Axial (**a**) and sagittal (**b**, **c**) imaging of the thoracic spine demonstrating a disk bulge (star), ligamentum flavum infolding (arrows), and facet hypertrophy (ovals) which causes severe central canal (bracket) and neural foraminal narrowing (arrowhead)

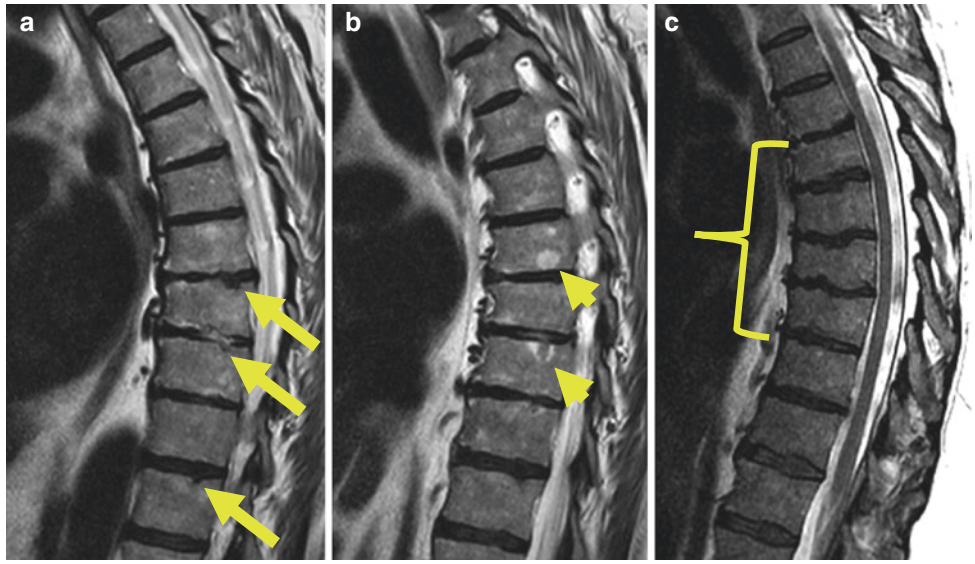

Fig. 4.15 Sagittal T2-weighted imaging of the thoracic spine. In (**a**), multiple Schmorl's nodes are noted (arrows), while in (**b**), the Schmorl's nodes are associated with edema as evidenced by the hyperintense signal (arrowheads). In (**c**), the Schmorl's nodes (arrows) are associated with endplate irregularity and wedging of several contiguous vertebral bodies (bracket) compatible with Scheuermann's disease

at this spinal level originates predominantly from the disks and facet joints and is quantified in a similar manner to the cervical and lumbar spine.

Schmorl's Nodes

Instead of projecting into the spinal canal, disk material can also project into the adjacent vertebral body (Fig. 4.15a), usually when the bone has been weakened by osteoporosis, metabolic disease, and congenital or infiltrative tumor. In this case, they are referred to as Schmorl's nodes and are seen as "defects" in the vertebral body whose signal resembles that of the disk material. Sometimes there is an inflammatory response around the intraosseous disk herniation which causes vascularization and edema (hypointense on T1-weighted imaging and hyperintense on T2-weighted imaging) and can be painful (Fig. 4.15b). These can also occur in the setting of trauma when it is also associated with edema and pain. Over time this edema evolves into sclerotic (hypointensity on both T1- and T2-weighted imaging), in a similar fashion to how Modic changes progress. Occasionally, Schmorl's nodes are also associated with endplate irregularity and loss of disk height, resulting in a focal kyphosis. In this case, it is referred to as Scheuermann's disease (Fig. 4.15c).

Lumbar Spine

The lumbar spine is also mobile, although less mobile than the cervical spine. However, the lumbar spine is more weight bearing than the other spinal segments, and as a result, it is more prone to degenerative changes. Additionally, there is also some unique anatomy in the lumbar spine such as the conus and the cauda equina, as well as unique pathology such as spondylolysis.

Spondylolysis

Spondylolysis is a stress fracture in the pars interarticularis that usually occurs at L5 and much less commonly at other higher spinal levels. It is seen most commonly in young athletes and, when there is edema from stress response in the pedicles, can be a considerable source of pain. This defect itself is actually quite difficult to identify on MRI but is

best visualized on the sagittal T1-weighted images as a low signal focus with/without reactive, Modic type changes (Fig. 4.16). Additionally, spondylolysis can also result in widening (defined as an AP diameter 25% greater than the AP diameter at L1) of the spinal canal as the posterior elements are free to move slightly even more posterior. However, in some instances, spondylolysis actually results in spondylolisthesis where the L5 vertebral body moves anterior relative to S1, actually narrowing the spinal canal. The degree of spondylolisthesis is graded by dividing the inferior vertebral body's AP dimension into four quadrants and determining where the posterior border of the more superior vertebral body lies in respect to those quadrants. In grade I spondylolisthesis, this slippage is less than 25% of the inferior vertebral body's AP dimension; in grade II, it ranges from 26 to 50 %; in grade III, it ranges from 51 to 75%; in grade IV, it ranges from 76 to 100%; and in grade V, it is >100%. Additionally, this excess movement across the defect can cause the formation of a pseudarthrosis and reactive buildup of excess cartilage, bone, and fibrous material, further increasing the degree of spinal stenosis.

The DOC or Bulge

Just like in the cervical spine, the lumbar spine is prone to disk bulges and annular fissures. Bulges are usually broad based and involve more than 25% of the disk circumference. When a bulge is more focal with a wide neck, again, it is referred to as a protrusion. Disk protrusions can be either central, paracentral, foraminal, or far lateral. Depending on the location, the disk protrusion can contact either the traversing nerve roots in the lateral recess or the exiting nerve roots in the neural foramina (Figs. 4.17 and 4.18). When the neck is narrow, this is

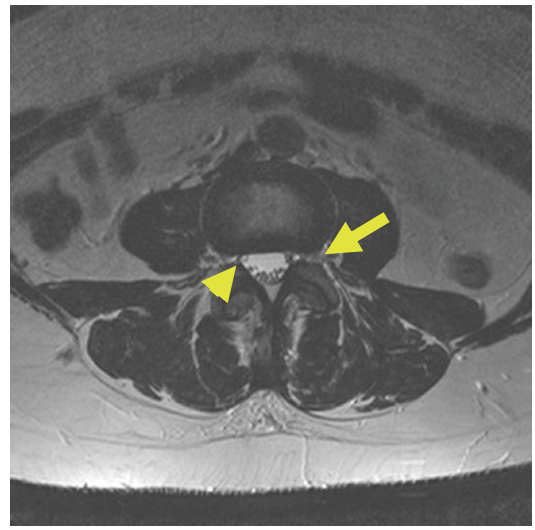

Fig. 4.17 Axial T2-weighted image of the lumbar spine demonstrating the exiting nerve roots in the neural foramen (arrow) and the traversing nerve roots in the lateral recess (arrowhead)

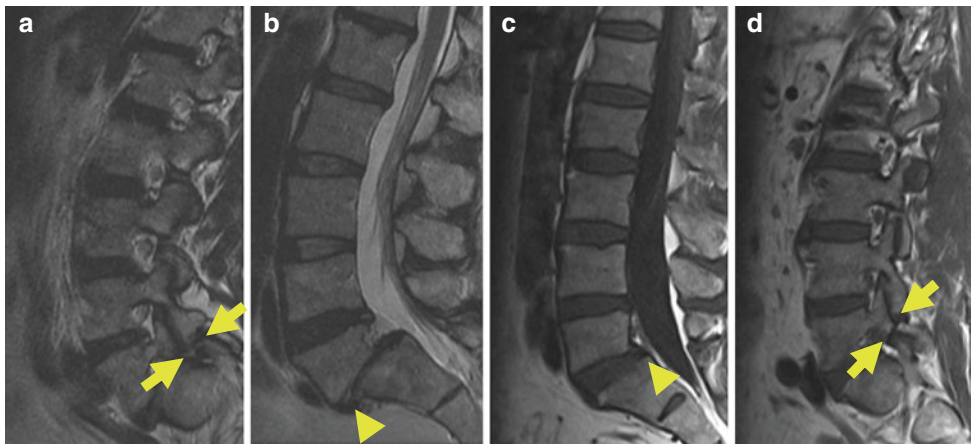

Fig. 4.16 Sagittal T1-weighted (**a**, **b**) images of the lumbar spine demonstrating a pars defect at L5 (arrows), which causes grade II anterolisthesis of L5 on S1 (arrowhead). Sagittal T1-weighted images in (**c**, **d**) demonstrate another example of a pars defect at L5 (arrows) and grade I anterolisthesis of L5 on S1 (arrowhead)

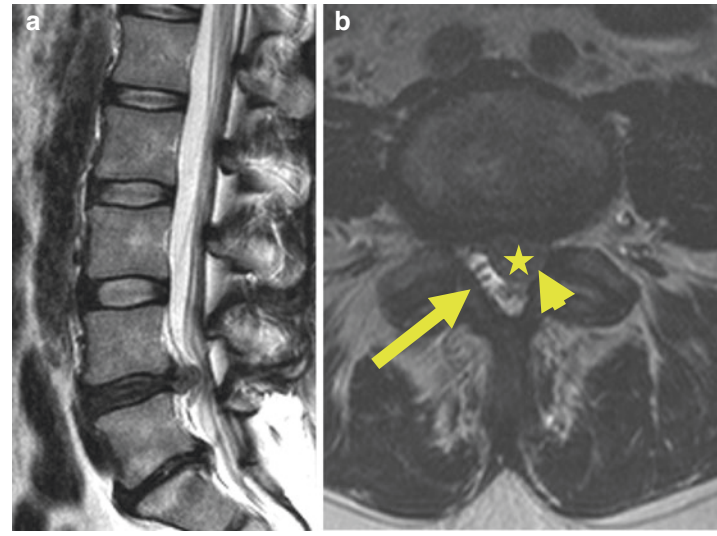

Fig. 4.18 Sagittal (**a**) and axial (**b**) T2-weighted images of the lumbar spine demonstrate a diffuse disk bulge with a superimposed left paracentral disk protrusion (star) into the lateral recess (arrowhead) and effacing the thecal sac (arrow)

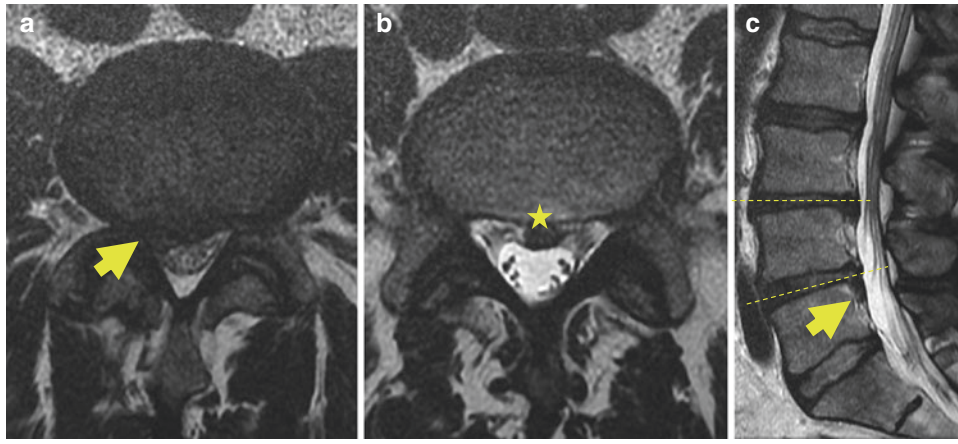

Fig. 4.19 Axial T2-weighted images at levels (**a**) and (**b**) as designated in the sagittal T2-weighted image (**c**). In (**a**), there is a diffuse disk bulge with a superimposed right disk extrusion which contacts the traversing nerve roots in the lateral recess at L3–L4 (arrow). In (**b**, **c**), there is a central disk extrusion (star) at L4–L5, with interior migration (arrow)

referred to as an extrusion. Just like in the cervical spine, disk extrusions have the ability to migrate superiorly, inferiorly, or laterally into the lateral recess or neural foramen (Fig. 4.19). If a piece of disk detaches, this is called a sequestered disk, which, just like with a disk extrusion, can also migrate [16] (Fig. 4.20).

The Facet Joints

The facet joints are also prone to degeneration. Just like in the cervical spine, a normal facet joint is thin and smooth without any osseous overgrowth. With mild hypertrophy, the facets appear bulkier, while with moderate hypertrophy, the bony overgrowth starts to appear more irregular and may cause impingement. In either case, the joint itself may undergo reactive stress as evidenced by an effusion. In severe hypertrophy, the osseous overgrowth causes more obvious deformities and is almost always associated with impingement [14, 17, 18] (Fig. 4.21).

Within the lumbar spine, the facet joints are more prone to develop synovial cysts, which are usually well-defined lesions adjacent to the facet

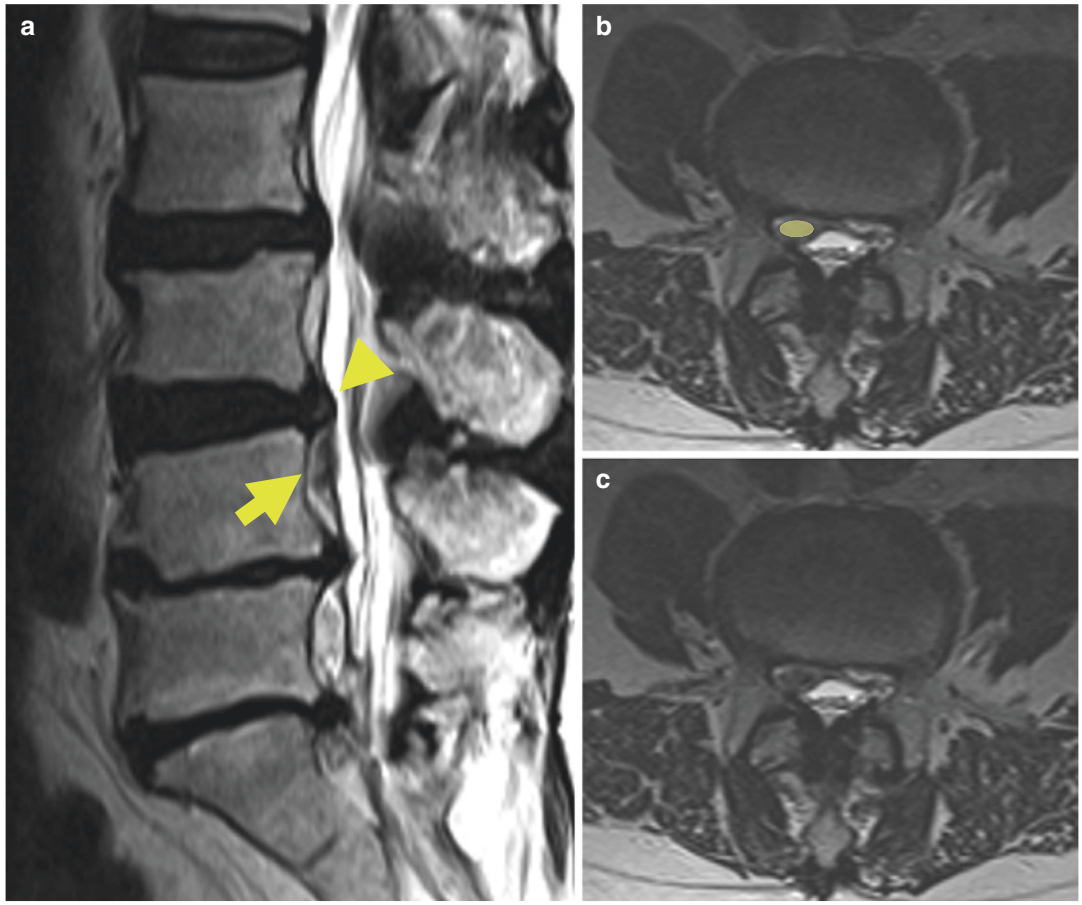

Fig. 4.20 Sagittal T2-weighted (**a**) image of the lumbar spine demonstrates a diffuse disk bulge with a right subarticular disk herniation (arrowhead) and superimposed sequestration with inferior migration (arrow). Axial T2-weighted (**b**, **c**) images of the lumbar spine at L3–L4 demonstrate the inferiorly migrated disk sequestration (oval)

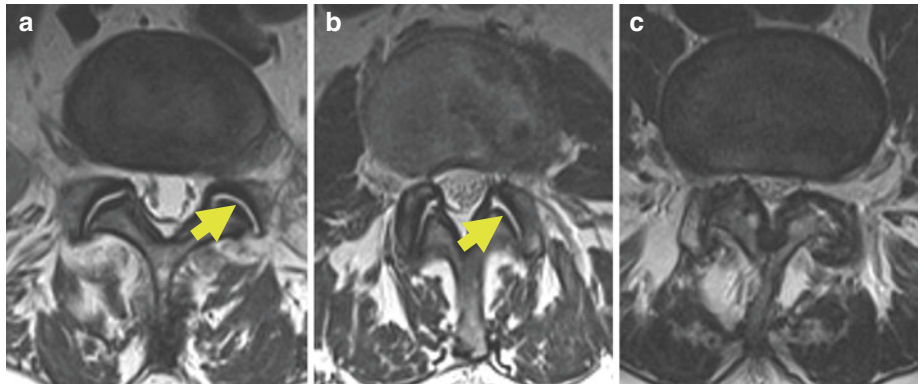

Fig. 4.21 Axial T2-weighted imaging of the lumbar spine. In (**a**), there is mild facet hypertrophy, while in (**b**), there is increased hypertrophy and impingement compatible with moderate facet hypertrophy. In (**c**), the facet joints are even more enlarged and irregular with increased impingement compatible with severe facet hypertrophy. Note the fluid within the facet joints in (**a**) and (**b**) (arrows)

joint. Because their internal contents vary (fluid, blood, proteinaceous debris), their signal characteristics also vary. Synovial cysts can also vary in location. They can be intracanalicular where they have the potential to impinge on the neural foramen, lateral recess, or central canal. Or they can be extracanalicular where they are much less likely to cause clinical symptoms (Fig. 4.22).

Just like in the cervical spine, with degenerative disk disease and facet arthropathy comes ligamentum flavum infolding. Normally, the ligamentum flavum is a smooth, hypointense structure between the facet joints posteriorly. When the disk height narrows, this ligament buckles and protrudes into the canal, potentially obliterating the epidural fat (Fig. 4.23).

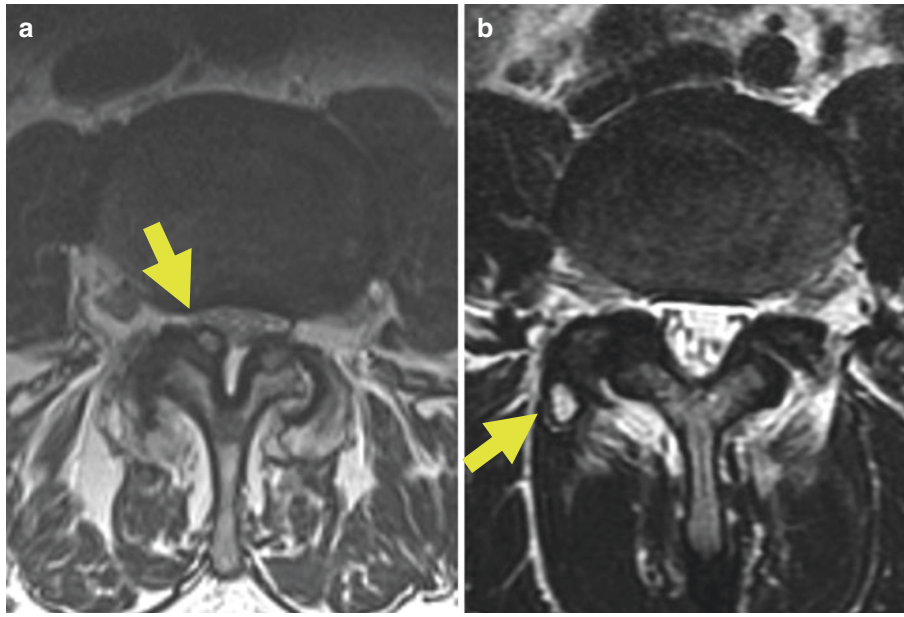

Fig. 4.22 Axial T2-weighted imaging of the lumbar spine demonstrates an intracanalicular synovial cyst (arrow) in (**a**) and an extracanalicular synovial cyst (arrow) in (**b**)

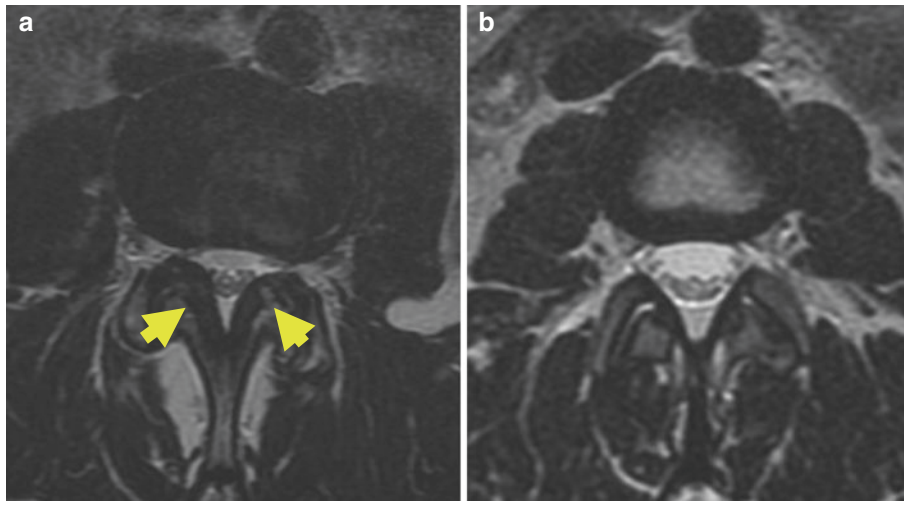

Fig. 4.23 Axial T2-weighted images of the lumbar spine demonstrating ligamentum flavum infolding (arrows in **a**), compared to a normal ligamentum flavum (**b**)

Central Canal and Neural Foraminal Narrowing

The abovementioned changes in the lumbar spine can cause narrowing of both the central canal and neural foramen. Normally, the central canal is oval shaped with the cord or nerve roots floating freely within the CSF. With mild central canal narrowing, the canal appears more triangular in shape, but the cord or nerve roots are still floating freely within the CSF. With moderate narrowing, there is further flattening of the central canal and clumping of the nerve roots as the CSF space begins to get effaced. In severe narrowing, there is complete obliteration of the CSF space and more pronounced nerve root clumping (Fig. 4.24).

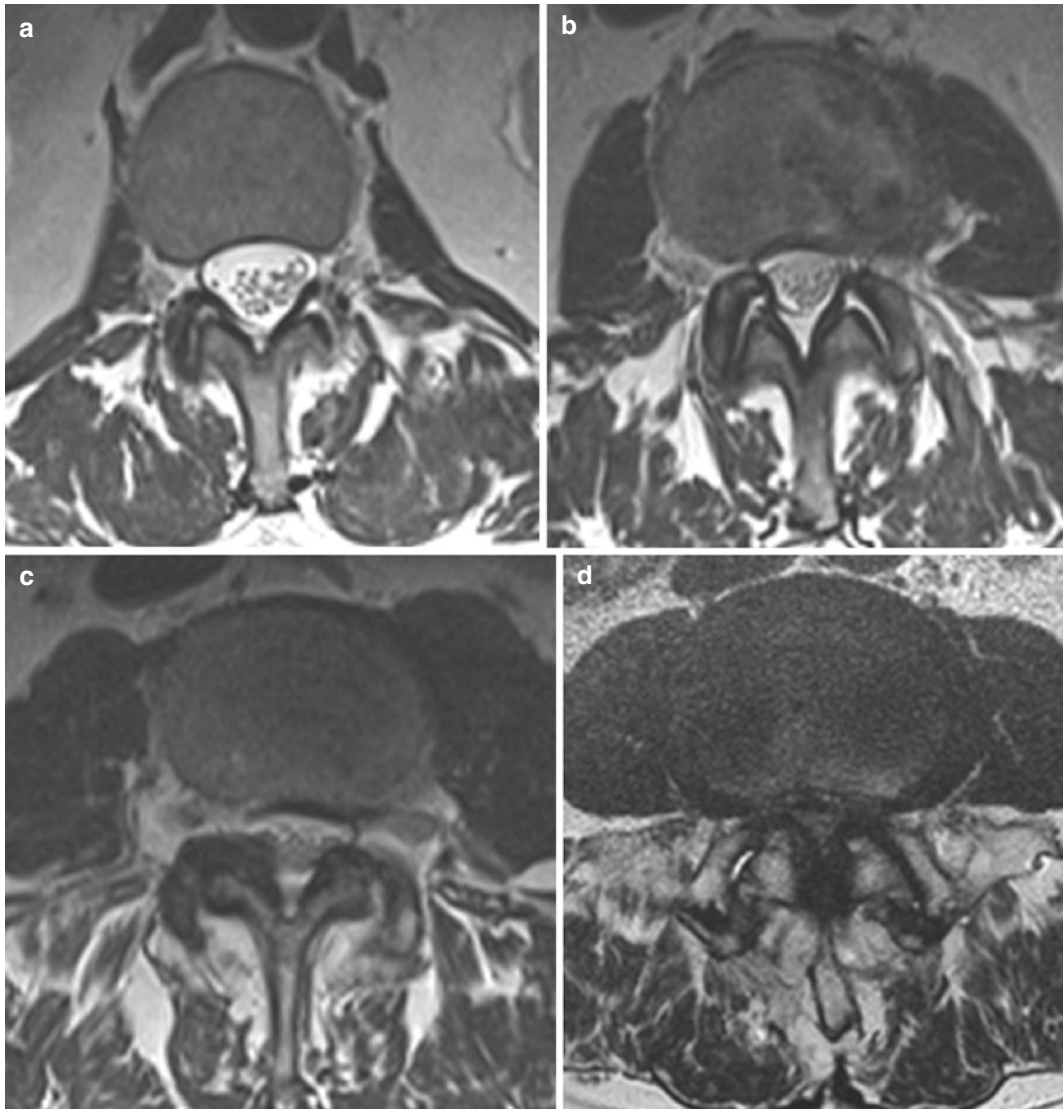

Fig. 4.24 Axial T2-weighted imaging of the lumbar spine comparing a normal central canal (**a**) with varying degrees of stenosis. In (**b**), there is mild stenosis but the nerve roots are floating freely in the CSF. In moderate stenosis (**c**), there is increased narrowing with clumping of the nerve roots and flattening of the thecal sac. In severe stenosis (**d**), there is complete obliteration of the CSF space with tight clumping of the nerve roots

Within the lumbar spine, the neural foramina are smooth, elongated keyhole-like shapes on sagittal images with the nerve bundles running obliquely through them. When there is mild encroachment, there is slight narrowing of this space, but with preservation of the fat surrounding the nerve bundles. In moderate narrowing, there is almost complete loss of the fat signal by the degenerative changes that encroach upon the exiting nerve roots. In severe narrowing, there is complete obliteration of the neural foramen (Fig. 4.25).

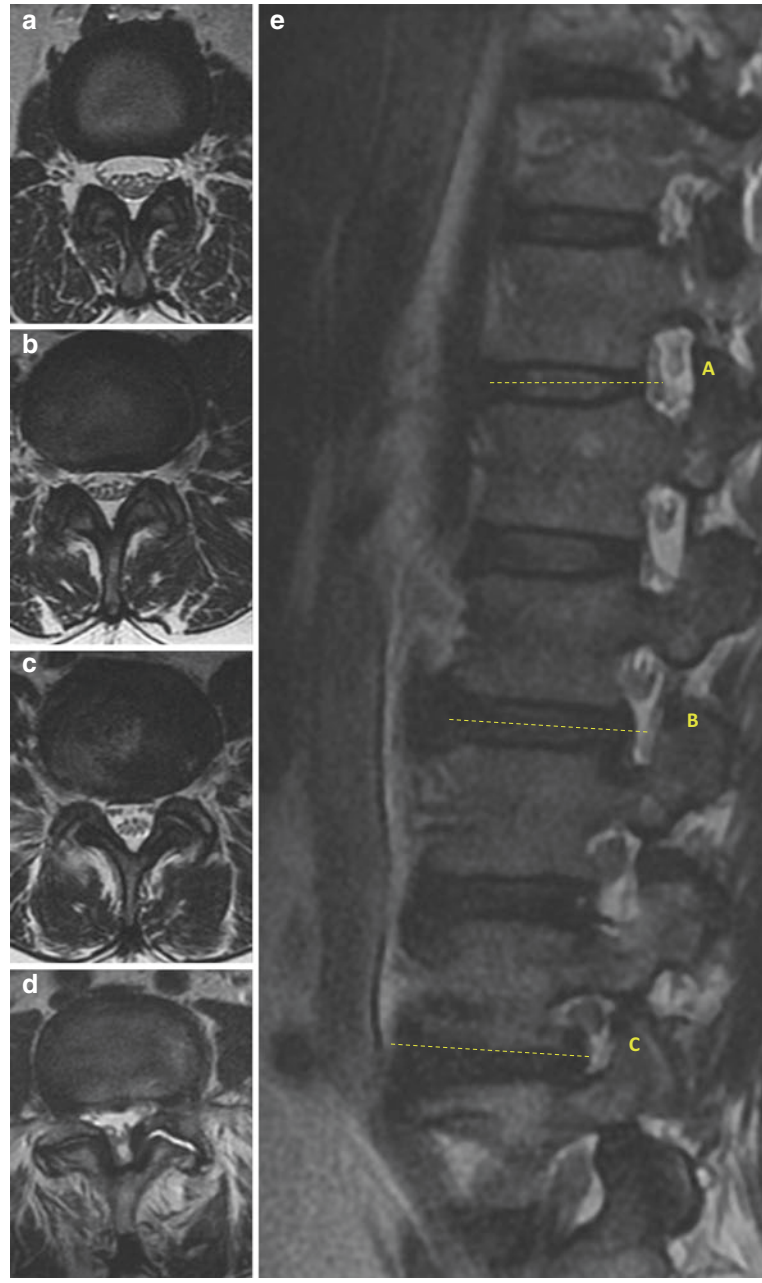

Fig. 4.25 Axial and sagittal T2-weighted images of the lumbar spine. Note the normal neural foramen in (**a**) with an elongated keyhole shape on the sagittal images and scout line in (**e**). With mild stenosis (**b**), there is slight narrowing with near-complete preservation of the surrounding fat. In moderate stenosis (**c**), the degree of narrowing is increased, and there is contact with the nerve roots. In severe stenosis (**d**), there is obliteration of the neural foraminal fat

References

1. Manelfe C. Imaging of degenerative processes of the spine. Curr Opin Radiol. 1992;4(1):63–70.
2. Izzo R, Popolizio T, D'Aprile P, Muto M. Spinal pain. Eur J Radiol. 2015;84(5):746–56. https://doi.org/10.1016/j.ejrad.2015.01.018.
3. Kelly JC, Groarke PJ, Butler JS, Poynton AR, O'Byrne JM. The natural history and clinical syndromes of degenerative cervical spondylosis. Adv Orthop. 2012;2012:393642. https://doi.org/10.1155/2012/393642.
4. Brinjikji W, Diehn FE, Jarvik JG, et al. MRI findings of disc degeneration are more prevalent in adults with low Back pain than in asymptomatic controls: a systematic review and meta-analysis. AJNR Am J Neuroradiol. 2015;36(12):2394–9. https://doi.org/10.3174/ajnr.A4498.
5. Petersen T, Laslett M, Juhl C. Clinical classification in low back pain: best-evidence diagnostic rules based on systematic reviews. BMC Musculoskelet Disord. 2017;18(1):188. https://doi.org/10.1186/s12891-017-1549-6.
6. Maus T. Imaging the back pain patient. Phys Med Rehabil Clin N Am. 2010;21(4):725–66.
7. Ferrara LA. The biomechanics of cervical spondylosis. Adv Orthop. 2012;2012:493605. https://doi.org/10.1155/2012/493605.
8. Pfirrmann CW, Metzdorf A, Zanetti M, Hodler J, Boos N. Magnetic resonance classification of lumbar intervertebral disc degeneration. Spine (Phila Pa 1976). 2001;26(17):1873–8.
9. Fardon DF, Williams AL, Dohring EJ, Murtagh FR, Gabriel Rothman SL, Sze GK. Lumbar disc nomenclature: version 2.0: recommendations of the combined task forces of the North American Spine Society, the American Society of Spine Radiology and the American Society of Neuroradiology. Spine J. 2014;14(11):2525–45. https://doi.org/10.1016/j.spinee.2014.04.022.
10. Tsuji T, Fujiwara H, Nishiwaki Y, et al. Modic changes in the cervical spine: prospective 20-year follow-up study in asymptomatic subjects. J Orthop Sci. 2019; https://doi.org/10.1016/j.jos.2018.12.015.
11. Modic MT, Steinberg PM, Ross JS, Masaryk TJ, Carter JR. Degenerative disk disease: assessment of changes in vertebral body marrow with MR imaging. Radiology. 1988;166(1 Pt 1):193–9. https://doi.org/10.1148/radiology.166.1.3336678.
12. Kettler A, Wilke H-J. Review of existing grading systems for cervical or lumbar disc and facet joint degeneration. Eur Spine J. 2006;15(6):705–18. https://doi.org/10.1007/s00586-005-0954-y.
13. Rydman E, Bankler S, Ponzer S, Jarnbert-Pettersson H. Quantifying cervical spondylosis: reliability testing of a coherent CT-based scoring system. BMC Med Imaging. 2019;19(1):45. https://doi.org/10.1186/s12880-019-0342-4.
14. Gellhorn AC, Katz JN, Suri P. Osteoarthritis of the spine: the facet joints. Nat Rev Rheumatol. 2013;9(4):216–24.
15. Kalichman L, Li L, Kim DH, et al. Facet joint osteoarthritis and low back pain in the community-based population. Spine (Phila Pa 1976). 2008;33(23):2560–5.
16. Kushchayev SV, Glushko T, Jarraya M, et al. ABCs of the degenerative spine. Insights Imaging. 2018;9(2):253–74.
17. Walraevens J, Liu B, Meersschaert J, et al. Qualitative and quantitative assessment of degeneration of cervical intervertebral discs and facet joints. Eur Spine J. 2009;18(3):358–69. https://doi.org/10.1007/s00586-008-0820-9.
18. Fardon DF, Milette PC. Nomenclature and classification of lumbar disc pathology. Recommendations of the Combined task Forces of the North American Spine Society, American Society of Spine Radiology, and American Society of Neuroradiology. Spine (Phila Pa 1976). 2001;26(5):E93–E113. https://doi.org/10.1097/00007632-200103010-00006.

MRI in Spine Infection

5

M. K. Jesse and Corey K. Ho

Introduction

Spine infection is a rare and often misdiagnosed condition with critical implications for patient care. Over the last 30 years, spine infection has steadily increased not only due to the rising epidemic of intravenous drug use and immune disorders but also from the inevitable side effects of advancements in modern medicine. Patients with debilitating chronic disease and severe immune compromise are experiencing longer life expectancy leading to a greater number of patients at high risk for infection. Surgical and procedural instrumentation procedures in the spine are steadily increasing, offering life-altering benefits to many patients but also elevating the number of high-risk patients [1]. Prompt identification and characterization of spine infection is essential to optimize patient outcomes. Navigation of infectious and non-infectious diseases in the spine poses not only a clinical dilemma because of the substantial overlap in the clinical symptomatology and laboratory findings but also poses a substantial diagnostic dilemma because of the confusing overlap in the imaging features. It is critical for all providers to understand the nuances and subtleties in imaging features of infectious disease processes to ensure accurate diagnosis and treatment, especially in this high-risk patient population.

M. K. Jesse (✉) · C. K. Ho
University of Colorado Anschutz Campus, Aurora, CO, USA
e-mail: mary.jesse@ucdenver.edu; Corey.k.ho@ucdenver.edu

Pyogenic Spondylodiscitis (Bacterial Spondylodiscitis)

Pathophysiology

Pyogenic spondylodiscitis is defined as the infection of a vertebral body and intervertebral disc with or without involvement of the adjacent epidural space and paraspinal soft tissues. It is unfortunately common, affecting 2 per 100,000 each year with a propensity to affect intravenous drug users, diabetics, immune-compromised patients, and patients with recent surgery or intervention [2, 3]. Men are two to three times more often affected for reasons that are not entirely understood [4]. Early diagnosis of pyogenic spondylodiscitis is critical as the mortality reaches 17% according to some studies and even higher when associated with advanced comorbidities [4–6].

Staphylococcus aureus is overwhelmingly the most common causative agent, seen in 40–70% of cases and typically transmitted to the spine via the bloodstream (hematogenous spread) [7, 8]. Hematogenous spread of infection occurs when organisms from the blood are deposited in the small arterioles of the endplates in adults and in the disc itself in very young children [9]. The deposition of bacteria at the endplates of adults

W. B. Morrison et al. (eds.), *MRI of the Spine*, https://doi.org/10.1007/978-3-030-43627-8_5

rapidly progresses to intradiscal infection due to the virulent proteolytic enzymes produced by common organisms like *S. aureus*.

Batson described an alternative mode of pathogen transit to the spine that occurs by way of retrograde venous flow from the genitourinary and gastroenteric tract introducing the less common *Enterococcus* and *Escherichia* genus to the spine. *Pseudomonas* and *Streptococcus* species have been shown to seed to the spine in patients with a history of intravenous drug use and diabetes, respectively.

Acquiring blood cultures in suspected cases of spondylodiscitis is critically important as culture positivity is present in 50–70% of spondylodiscitis cases. The organism isolated from the blood is identical to that isolated from bone/disc biopsy 70–80% of the time [4]. Positive blood cultures arguably can negate the need for bone biopsy in straightforward cases.

Imaging in Pyogenic Spondylodiscitis

Various imaging modalities including radiographs, computed tomography (CT), magnetic resonance imaging (MRI), and nuclear medicine bone scan may be utilized in the evaluation of spine infection. Each of these imaging modalities offers unique benefits and limitations that should be considered prior to utilization. Many modalities may be used in tandem to increase specificity and sensitivity.

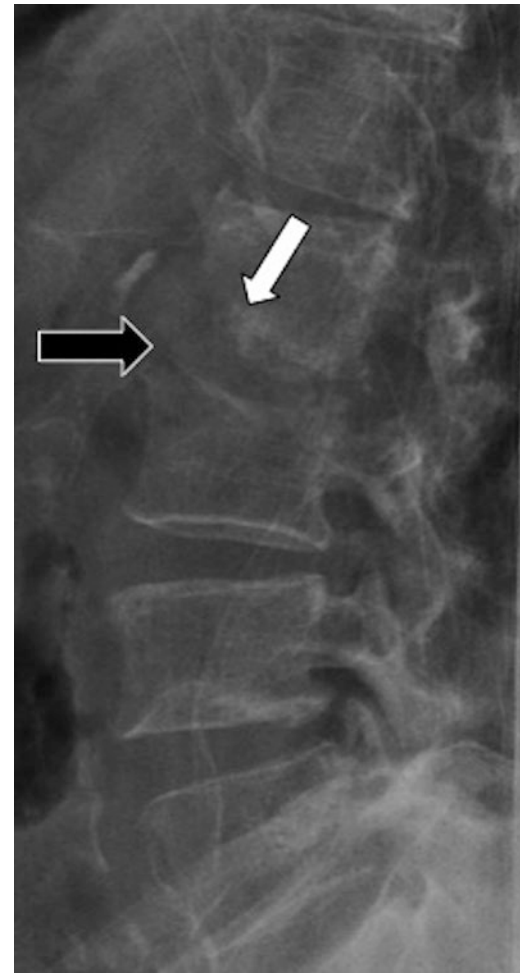

Fig. 5.1 Lateral radiograph of the lumbar spine demonstrates early disc height loss at L2–L3 (black arrow) in combination with ill-defined endplate erosions (white arrow), findings in keeping with discitis

Radiographs

Radiographs of the spine in the setting of spondylodiscitis are a reasonable first step in assessment. Providing fast and inexpensive evaluation is an attractive benefit of radiographs. However, radiographs may be prohibitively insensitive in the first 2 weeks after inoculation [10]. A normal radiograph in a patient with suspected osteomyelitis should not be considered an indication of disease absence. The temporal evolution of radiographic changes in spondylodiscitis begins at about 7 days after infection onset where one may note only a subtle loss of intervertebral disc height. Over the next 1–2 weeks, this disc height loss will evolve to the more specific and sensitive finding of endplate irregularity and erosion typically occurring along the anterior margin [11] (Fig. 5.1).

Computed Tomography

Computed tomography (CT) can be useful as an adjunct to radiographs. The imaging features are similar and include focal osteopenia, disc height loss, cortical irregularity, and endplate erosions.

However, CT may illustrate these subtle findings earlier in the disease process due to the increased detail provided.

Keep in mind that sub-endplate cysts in the setting of degenerative disease may mimic the endplate erosions of infection. In spite of this, these findings can be differentiated through an understanding of the pathophysiology. Sub-endplate degenerative cysts, like virtually all degenerative disease processes in the skeleton, will demonstrate a well-defined sclerotic rim of bone production indicating a chronic process. By contrast, sub-endplate erosions in infection occur rapidly and aggressively with a preponderance of osteoclastic activity. Because of this, the margin of the erosion will be ill-defined and non-sclerotic, indicative of an acute process (Fig. 5.2).

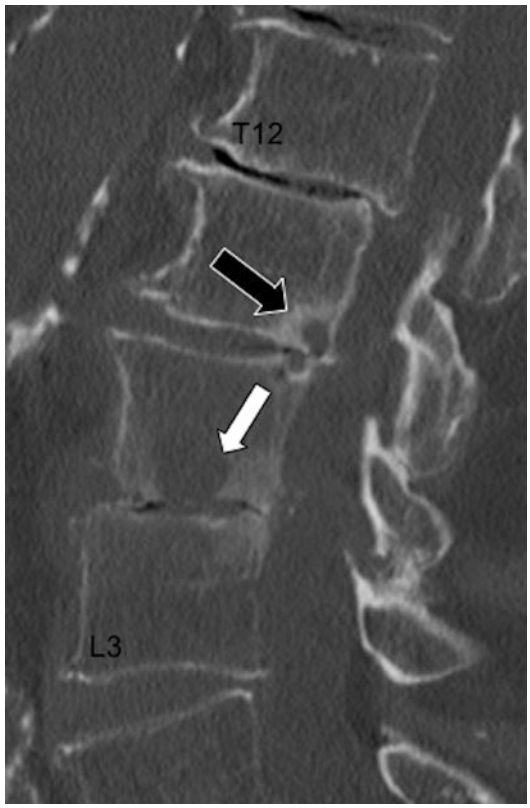

Fig. 5.2 Sagittal CT image of the lumbar spine demonstrates disc height loss at L2–L3 with focal acute erosion at the L2 endplate (white arrow). A non-infectious degenerative sub-endplate cyst at the posterior L1 vertebra can be differentiated from the infectious erosion by the clearly defined sclerotic rim (black arrow)

Paraspinal phlegmon and soft tissue inflammation is reflected on CT as fat stranding adjacent to the spine with loss of the intramuscular and perimuscular fat planes. The addition of contrast aids in detection of phlegmonous enhancement and epidural/paraspinal abscess formation. CT is limited in the evaluation of the postoperative patient with indwelling spinal fusion due to the potential for beam-hardening artifact and image degradation.

Nuclear Medicine

Nuclear medicine technetium-99-labeled methylene diphosphonate (^{99m}Tc-MDP) bone scan, or more generally termed bone scintigraphy, may be used to identify spondylodiscitis with increased sensitivity over CT and radiograph in the early phases of disease. Through the adsorption of radiotracer at the surface of hydroxyapatite crystals of bone matrix, bone scintigraphy identifies areas of high osteoblastic activity and bone remodeling with a high level of sensitivity (Fig. 5.3). ^{99m}Tc-MDP bone scan can detect areas of osteomyelitis as early as 48 h after the onset of infection with a sensitivity of 70–100% [12]. In addition, ^{99m}Tc-MDP bone scan may also help overcome the limitations of spine hardware in a postoperative patient. Bone scan, as opposed to CT and MRI, is not susceptible to metal artifact and therefore may be a reasonable choice for the evaluation of spondylodiscitis in a postoperative patient. The limitation of bone scintigraphy lies in the poor specificity and high false-positive rates. Any disease process resulting in a relative increase in osteoblast activity and hyperemia will result in a focal radiotracer uptake making it difficult to differentiate between infection and other degenerative, traumatic, or malignant disease processes.

^{67}Gallium SPECT imaging may be added to routine bone scintigraphy in an attempt to increase the specificity of the exam in the setting of infection. Used primarily in the spine, ^{67}Gallium citrate isolates potential infection by binding to neutrophil membranes and siderophore chelates produced by bacterium. The routine use

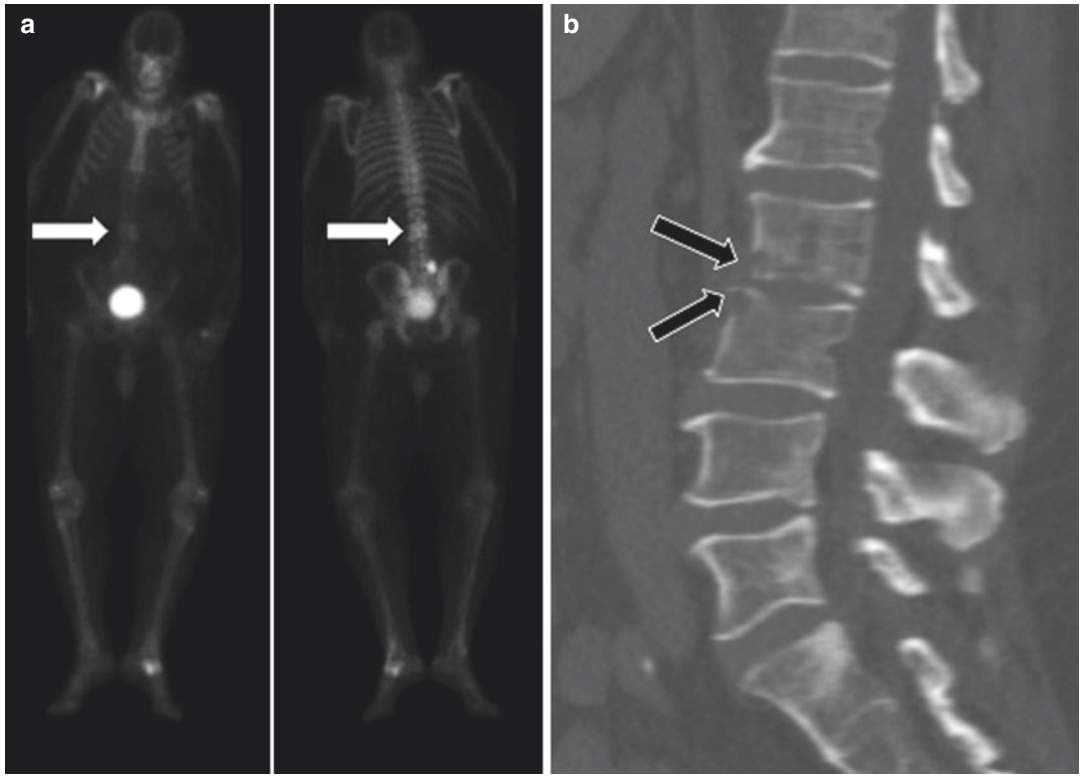

Fig. 5.3 A 46-year-old male with L2–L3 pyogenic spondylodiscitis. ^{99m}Tc-MDP whole-body bone scan (**a**) demonstrates increased radiotracer activity within the L2 and L3 vertebra (white arrows) in keeping with spondylodiscitis. Sagittal CT image (**b**) demonstrates acute endplate erosions and relative osteopenia (black arrows), confirming the diagnosis of L2–L3 infectious spondylodiscitis

of ^{67}Gallium SPECT is limited, however, due to the high effective dose, long half-life, and poor spatial resolution of the scan [13]. It should also be considered that the target organ for ^{67}Gallium citrate is the large bowel, which can obscure areas of interest depending on the location of the bowel.

^{18}F-FDG PET has an extremely high sensitivity for detecting spondylodiscitis and can arguably exclude the diagnosis of spondylodiscitis with a negative scan. Current literature has suggested a superiority of PET/CT over MRI both in specificity and sensitivity [14]. As the availability of this modality becomes more widespread, we may see PET replacing MRI as the modality of choice especially in patients with indwelling hardware and other MRI limitations.

Magnetic Resonance Imaging

Magnetic resonance imaging (MRI) is the current modality of choice for the evaluation of spondylodiscitis due to its high sensitivity (96%), high specificity (94%), and ability to provide detailed assessment of the paraspinal soft tissues and epidural space [15, 16]. Standard MR imaging protocols should include fluid-sensitive sequences such as T2-weighted spin echo or short tau inversion recovery (STIR) in axial and sagittal planes for the detection of fluid and edema. Fat saturation is often used in fluid-sensitive sequences to increase the sensitivity for detecting edema against a background of marrow and soft tissue fat [15]. The addition of T1-weighted fat-sensitive sequences in sagittal and/or axial planes is important to eval-

uate anatomic structures and detect replacement of marrow and soft tissue fat in the vertebra and neural foramen. Although these sequences may be sufficient for the diagnosis of spondylodiscitis, whenever possible, post-gadolinium contrast images should be included to improve detection of small epidural and paraspinal abscesses. A sample MRI protocol is illustrated in Table 5.1.

Pyogenic infection in the vertebral body results in an exudative proliferation within the bone that imbibes and replaces the normal intraosseous fatty marrow. This intraosseous exudate appears as increased fluid (T2 signal) in two consecutive vertebrae with concomitant confluent hypointense T1 signal in the marrow space (Fig. 5.3). Hyperintense T2 signal and confluent hypointense T1 signal are the quintessential imaging features of osteomyelitis anywhere in the skeleton but must be used with caution in the spine due to the propensity to misdiagnose infection in otherwise benign conditions. Degenerative disc disease, for example, may also result in similar endplate signal characteristics known as Modic change [17, 18]. Evaluating the transverse and craniocaudal extent of the signal abnormality within the vertebra may help to increase diagnostic specificity. In a study by Malgorzata, corresponding signal abnormality on T1- and T2-weighted sequences involved 50% or more of the vertebral body in 89% of spondylodiscitis cases studied. In degenerative disease, the hyperintense T2 and hypointense T1 signal abnormalities are rarely seen involving more than half of the vertebra and more typically affect the bone immediately adjacent to the affected endplate (Fig. 5.4).

Gadolinium enhancement of the vertebra may be seen on post-contrast imaging and is expected to match the pattern of T2 signal. Contrast

Table 5.1 Sample magnetic resonance imaging (MRI) protocol for spine infection

Fluid-sensitive sequences	Fat-sensitive sequence	Post-contrast sequences
Sagittal T2-weighted with/without fat saturation	Sagittal T1-weighted without fat saturation	Sagittal T1-weighted with fat saturation
STIR with fat saturation		Axial T1-weighted with fat saturation
Axial T2-weighted without fat saturation		

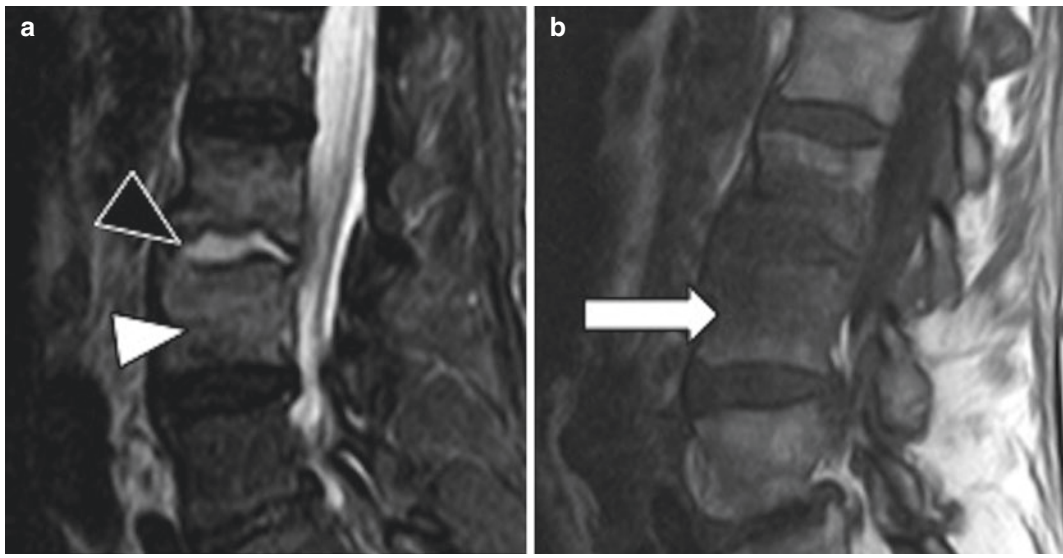

Fig. 5.4 A 56-year-old male with L2–L3 pyogenic spondylodiscitis. Sagittal STIR fat-saturated MR image (**a**) demonstrates diffuse hyperintense signal >50% of the vertebral body height (white arrowhead) and uniform increased signal within the affected intervertebral disc (black arrowhead). Sagittal non-fat-saturated T1 image (**b**) demonstrates confluent hypointense T1 signal occupying >50% of the vertebral height (white arrow)

enhancement of the edematous vertebra alone does not assist in narrowing the differential diagnosis, as essentially all bone marrow edema will enhance similarly regardless of the origin of the edema. Post-contrast images do however assist in the identification of paraspinal inflammation as well as psoas and epidural abscess, the most specific findings in the diagnosis of spondylodiscitis [19]. Abscesses, whether outside or within the canal, demonstrate internal hyperintense T2 signal with peripheral contrast enhancement (Fig. 5.5).

Signal intensity within the intervertebral disc is like that of the bone. T2-weighted images demonstrate hyperintense T2 intradiscal signal intensity usually accompanied by uniform hypointense T1 signal and enhancement on post-contrast images. Disc enhancement patterns include homogeneous disc enhancement, patchy heterogeneous areas of disc enhancement, or non-enhancement in advanced disease [20].

Some authors have described effacement of the central fibrous band of the intervertebral nucleus pulposus, the intranuclear cleft, as a sign of disc infection although this finding is often absent in early stages of disease [21] (Fig. 5.6).

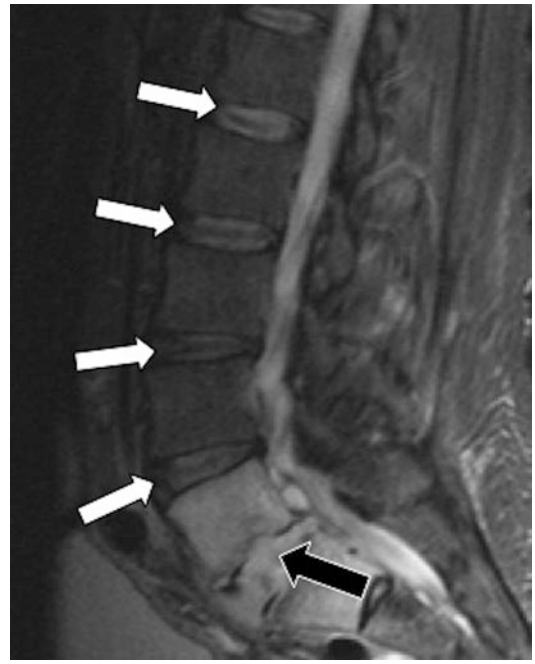

Fig. 5.6 A 44-year-old male with pyogenic spondylodiscitis involving L5–S1. Sagittal STIR fat-saturated MR image demonstrates normal fibrous intranuclear clefts (white arrows) within the uninvolved intervertebral discs. The intranuclear cleft at L5–S1 is effaced (black arrow)

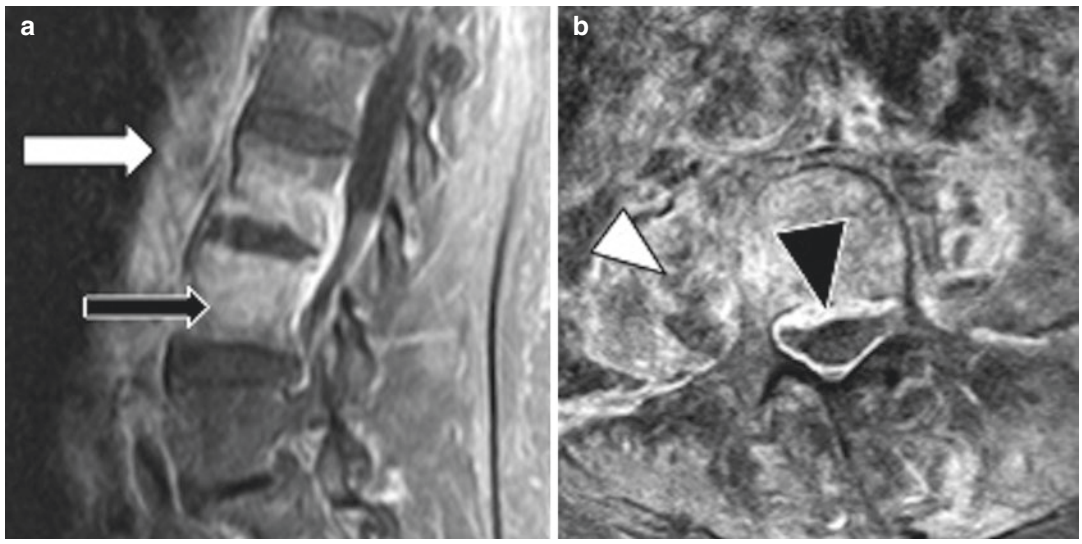

Fig. 5.5 A 56-year-old male with L2–L3 pyogenic spondylodiscitis. Sagittal T1 fat-saturated post-contrast image (**a**) demonstrates diffuse vertebral body enhancement (black arrow) and paraspinal soft tissue edema/phlegmon (white arrow). Axial T1 fat-saturated post-contrast image (**b**) demonstrates a peripherally enhancing right paraspinal abscess (white arrowhead) and epidural thickening with enhancement (black arrowhead)

Temporal Changes of Pyogenic Spondylodiscitis

When classic imaging features of pyogenic spondylodiscitis are present, there is usually very little diagnostic uncertainty. However, diagnostic problems arise during early- and late-stage disease, where imaging features may be subtle or confusing with overlapping findings. Understanding the expected temporal changes of spondylodiscitis is critical in determining the appropriate diagnosis and treatment plan.

Not surprisingly, spondylodiscitis can be quite subtle in the early stages and may mimic other conditions like degenerative disc disease, acute Schmorl's nodes, malignancy, or trauma. In hematogenous spread of pyogenic spondylodiscitis, the earliest MRI findings of inoculation include hazy hyperintense T2 signal at the anterior or posterior endplates in a single vertebra or at two consecutive vertebral body endplates [21, 22]. This signal abnormality reflects the initial end arteriole bacterial deposition prior to the enzymatic endplate breakdown. Other subtle findings include faint paraspinal soft tissue edema and focal epidural enhancement. These early findings are uniformly non-specific, and infection can only be suggested and not confirmed with a single MRI evaluation. In individuals with high risk history or concerning clinical picture, a repeat MRI in 8 days is recommended to exclude infection in the setting of subtle MRI changes. Any interval progression in the imaging features over this 8-day period should be considered highly suspicious for an infectious etiology [23].

The other period of diagnostic uncertainty lies in the later stages of disease after the initiation of antibiotic therapy. Misunderstandings as to the expected temporal evolution of MRI findings in the post-treatment phase are dangerous and may result in unnecessary surgery [24]. Recent evidence suggests that many MR imaging features of spondylodiscitis worsen in the post-treatment period despite the initiation of appropriate antibiotic therapy and clinical improvement [25–27]. Bone marrow edema, enhancement of the vertebral body and disc, endplate erosions, and loss of intervertebral disc height may be expected to worsen for up to 4–6 months following appropriate and effective antibiotic therapy. The most reliable feature of appropriate therapy is the improvement or resolution of soft tissue and/or epidural abscess which tends to occur in the earlier stages of therapy. Worsening of an abscess following treatment would therefore be the most reliable indicator of treatment failure [25, 26] (Fig. 5.7)

Tuberculous Spondylodiscitis

Pathophysiology

Tuberculous (mycobacterial) spondylodiscitis (TS) is a rare but serious condition that is unfortunately common in underdeveloped countries but has been steadily rising in incidence in all countries around the world [28]. Tuberculosis of the spine accounts for only 1% of cases of tuberculosis but makes up 25–60% of the skeletal involvement of the disease [29]. The clinical presentation of TS is more insidious and mild, often without back pain and fever or the profound elevations in inflammatory markers or leukocytosis seen with pyogenic spondylodiscitis. Because of this insidious course, patients suffering from TS may not present until in very late stages of disease, sometimes 12 months or more after initial inoculation, often after substantial destruction has occurred [30, 31].

Differentiating TS from pyogenic spondylodiscitis is of critical importance as to not delay appropriate therapy but can be difficult as there is overlap in the imaging features. Unlike pyogenic spondylodiscitis, TS is most often transmitted to the spine via Batson's venous plexus rather than through the end arterioles. Venous transmission of bacteria results in primary inoculation at the anterior-inferior endplates of the cancellous vertebral body. It is suggested that tuberculous spondylodiscitis may also differ from pyogenic spondylodiscitis in that it favors the thoracic spine. The largest cohort demonstrates a thoracic predominance with 56% of cases presenting from T1–T12 and only around 20% presenting in the lumbar spine [32, 33]. This thoracic predilection,

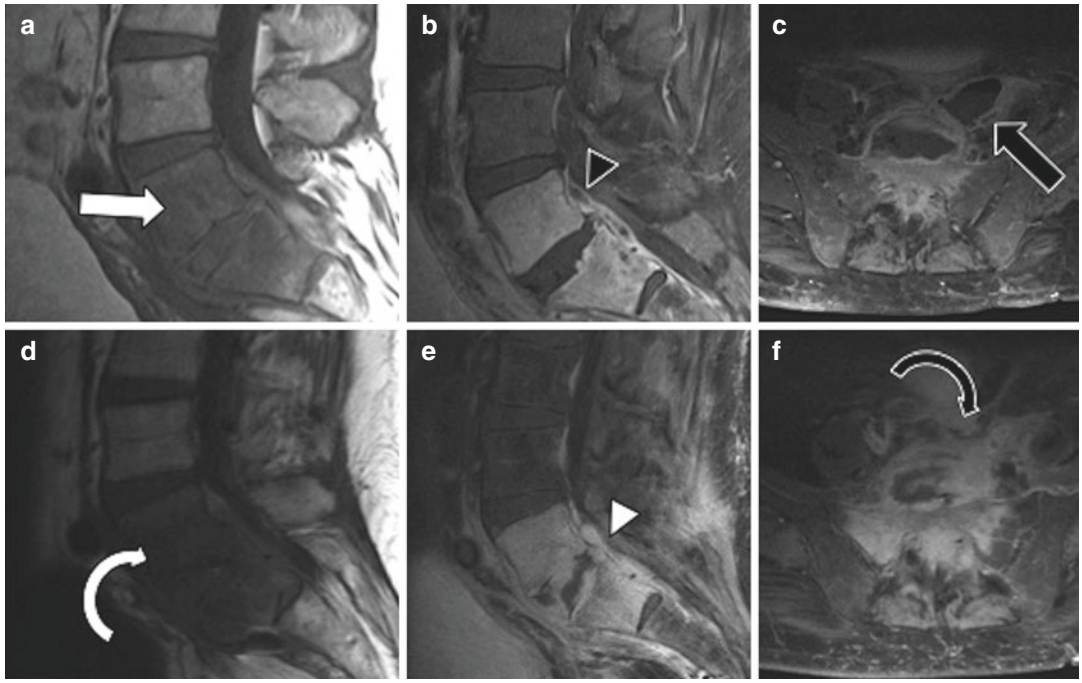

Fig. 5.7 A 54-year-old male with *S. aureus* spondylodiscitis of L5–S1. Pre-treatment sagittal T1 (**a**), sagittal T1 fat-saturated post-contrast (**b**), and axial T1 fat-saturated post-contrast (**c**) images of the spine demonstrate confluent hypointense T1 signal (white arrow) and vertebral body enhancement with small epidural abscess (black arrowhead) and large paraspinal abscess (black arrow). Repeat sagittal T1 (**d**), sagittal T1 fat-saturated post-contrast (**e**), and axial T1 fat-saturated post-contrast (**f**) images at *5 weeks* following appropriate antibiotic therapy and clinical improvement demonstrate worsening hypointense T1 signal (white arrowhead) and worsening enhancement and endplate destruction (white curved arrow). There is complete resolution of the small epidural abscess (white arrowhead) and paraspinal abscess (black curved arrow)

however, has been debated with several reports demonstrating equal involvement of the thoracic and lumbar spine in mycobacterial cases [34].

Imaging in Tuberculous Spondylodiscitis

One of the key imaging features differentiating tuberculous spondylodiscitis from pyogenic spondylodiscitis is a product of the inability of mycobacterium to produce the proteolytic enzymes which are common in pyogenic forms of the disease. The absence of proteolytic enzymes prevents the mycobacterial species from traversing dense fibrous structures around the spine such as the fibrous annulus of the intervertebral disc and the paraspinal ligaments [35]. Rather than entering and destroying the disc, mycobacterium spreads in the spine via a sub-ligamentous course typically under the anterior longitudinal ligament to the adjacent vertebral level, sparing the intervertebral discs until very late stages of disease. The absence of disc destruction and the sub-ligamentous transmission allows for multiple consecutive levels (three or more) of the spine to be involved simultaneously [32, 33]. This is contrary to pyogenic disease which typically involves no more than two consecutive spinal levels with significant disc destruction early in the disease process.

Radiographs

Radiographs serve as an acceptable initial screening tool in the evaluation of tuberculous spondylodiscitis but can be insensitive in early disease.

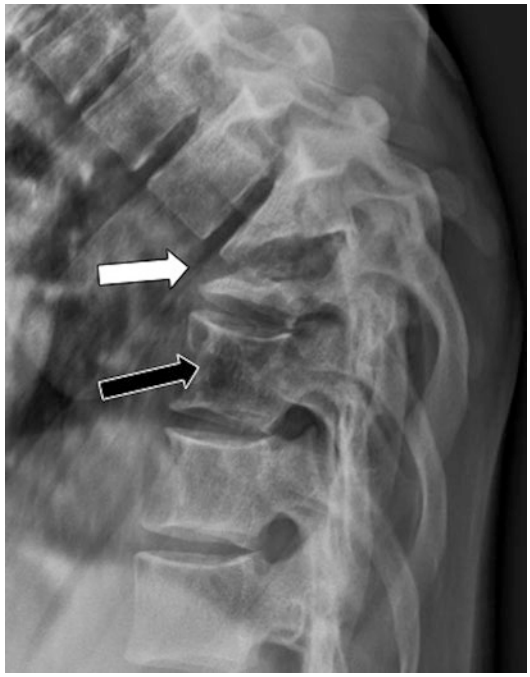

Fig. 5.8 A 37-year-old female with *Mycobacterium tuberculosis* infection of the spine. Lateral radiograph demonstrates multilevel vertebral body collapse (white arrow) with severe Gibbus kyphotic deformity. Subtle findings of relative vertebral body osteopenia can be appreciated at the adjacent levels (black arrow)

The earliest findings of TS include relative osteopenia of the vertebra, an extremely difficult finding to appreciate when disease is localizing to the upper or mid thoracic spine due to the overlapping soft tissue and bone. In later stages of disease, more classic radiographic features of multilevel vertebral body involvement and Gibbus deformity can be appreciated. Gibbus deformity is a term reserved for advanced cases of TS and is used to describe the severe kyphotic angulation produced by multilevel vertebral body collapse (Fig. 5.8).

Magnetic Resonance Imaging

MRI in tuberculous spondylodiscitis is a valuable tool in diagnosis. Imaging features differentiating this disease process from pyogenic spondylodiscitis are largely related to the unique subligamentous spread of infection discussed above. Often on MRI, hyperintense T2 signal can be

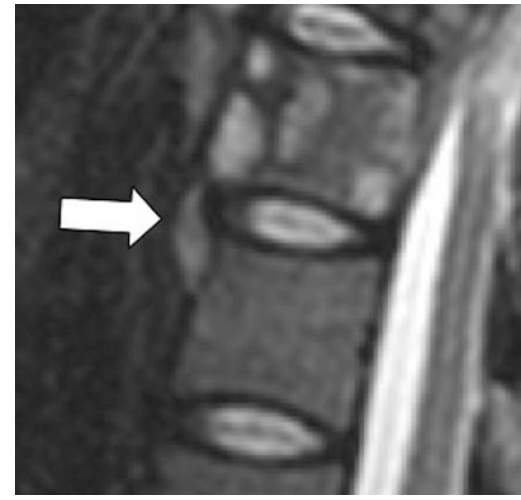

Fig. 5.9 A 37-year-old female with tuberculous spondylodiscitis. Sagittal STIR fat-saturated image demonstrates hyperintense T2 signal within the mid-thoracic vertebral body. Hyperintense T2 signal can be seen undermining the anterior longitudinal ligament in keeping with subligamentous spread (white arrow)

seen tracking beneath the anterior longitudinal ligament to the adjacent vertebral body, sparing the intervertebral discs and confirming this unique behavior (Fig. 5.9). Inoculation of multiple consecutive levels (three or more) is also suggestive of a mycobacterial organism over pyogenic disease. Imaging features within the vertebra are similar to that of pyogenic spondylodiscitis with hyperintense T2 signal, enhancement, and confluent hypointense T1 signal occupying the majority of the vertebral marrow space [32, 33].

Intervertebral abscess appearing as a variable size hyperintense T2 marrow lesion with peripheral enhancement is a feature suggestive of TS and should be considered suspicious for atypical infection [32, 33] (Fig. 5.10) The MRI appearance of paraspinal abscesses may also help to differentiate these two disease processes. Specifically, the post-contrast pattern of rim enhancement has been shown to correlate with the underlying etiology. Paraspinal abscesses in tuberculous infection demonstrate a thin peripheral rim enhancement that is homogeneous across the entire abscess wall. This in distinction to pyogenic abscesses which typically demonstrate a thick and irregular enhancement along the wall [32].

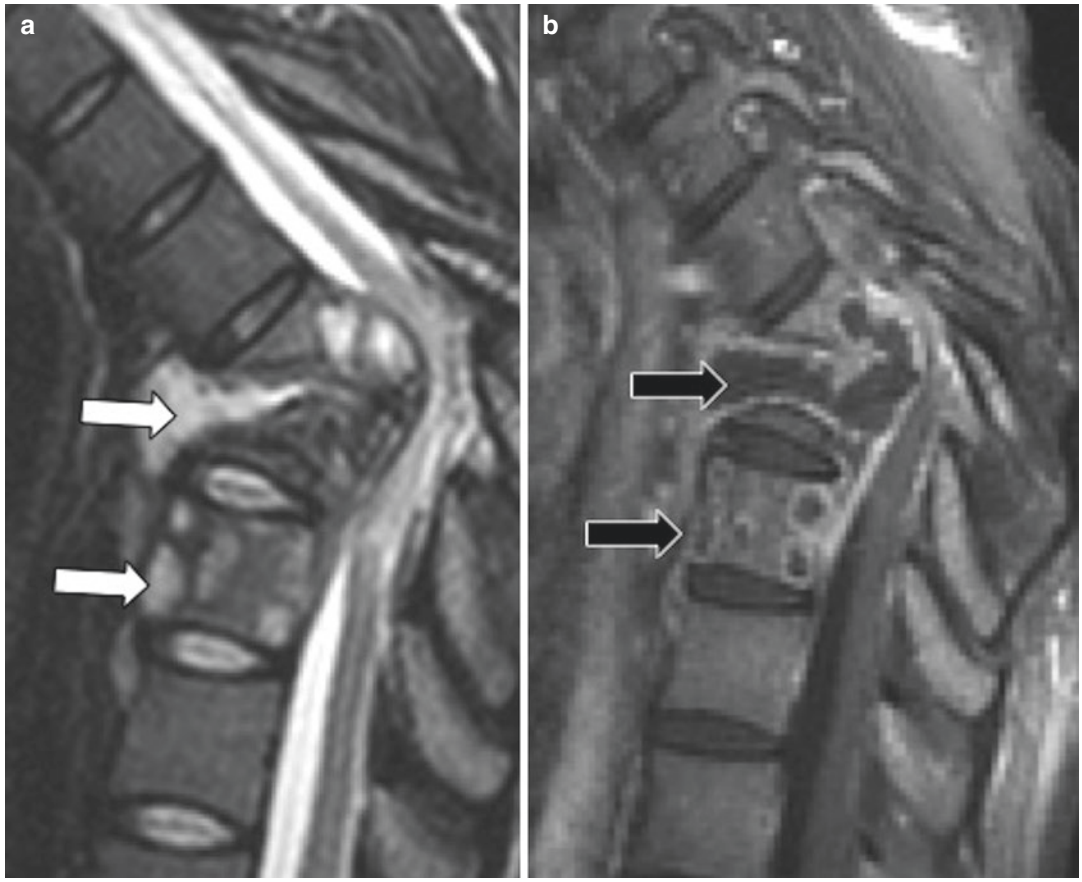

Fig. 5.10 A 37-year-old female with tuberculous spondylodiscitis. Sagittal STIR fat-saturated image (**a**) and sagittal T1 fat-saturated post-contrast image (**b**) demonstrate hyperintense T2 foci within the mid-thoracic vertebra (white arrow) with thin peripheral enhancement in keeping with intraosseous abscesses (black arrow)

Fungal Spondylodiscitis

Pathophysiology

Similar to tuberculous spondylodiscitis, fungal spondylodiscitis tends to present with an indolent course in contrast to pyogenic spondylodiscitis. Patients with immune compromise, diabetics, and postoperative patients are at a higher risk of developing the disease and often present with vague symptoms of back pain without fever or profound leukocytosis. The most common fungi isolated in spondylodiscitis fall in the *Candida*, *Aspergillus*, and *Mucor* genus. Yet there are regional predilections that introduce other more exotic species. Histoplasmosis infection, for example, is seen in higher number in the Midwest states (Indiana, Arkansas). Blastomycosis is more common in Mississippi and Wisconsin with coccidioidomycosis seen in the Western United States (Arizona, California) [36]. Although the immune-compromised patient is most commonly affected, reports of aggressive fungal infection have been described in otherwise healthy immune-competent patients, and the consideration of fungal etiologies can be considered in all patient populations.

Imaging in Fungal Spondylodiscitis

Radiographs

Fungal infection in the spine is the great mimicker of spinal infections with imaging similar to pyogenic infection, tuberculous infection, or even, in some instances, malignancy. Radiographic appearance in fungal disease is therefore quite broad and non-specific. Again, because of the absence of proteolytic enzymes, a sub-ligamentous, disc sparing pattern mimicking that of tuberculous spondylodiscitis is the most common presentation. Radiographs may demonstrate the classic vertebral collapse and Gibbus deformity seen also in TS.

Magnetic Resonance Imaging

MRI is the gold standard imaging for the detection of the often subtle imaging findings in fungal disease. T1 and T2 signal abnormalities are similar to that of other infections but may be even more faint due to the relatively mild inflammatory response initiated by the fungal elements [37]. Various fungal organisms result in different presentations on imaging. For example, *Candida* species, the most common fungal organism isolated in spondylodiscitis, typically involves the lumbar spine and mimics that of pyogenic infection primarily with disc involvement and endplate erosions [37, 38] (Fig. 5.11). Disc destruction is seen in about 50% of *Candida* cases but is thought to be a common feature in many fungal infections. *Aspergillus* and *Blastomyces* infections have a propensity to involve multiple and sometimes non-contiguous vertebral levels, resulting in enhancement of the ligamentous structures themselves in addition to sub-ligamentous spread [39, 40] (Fig. 5.12).

Suspicion for fungal infection should increase if MRI shows spondylitis in two adjacent vertebral bodies with small paraspinal abscess. These abscesses in fungal infection can be differentiated from the typical and atypical bacterial abscesses in the degree of internal complexity and intermediate T2-weighted signal in contrast to the hyperintensity expected in pyogenic or tuberculosis infection. Clear disc destruction with a notable absence of T2 signal within the intervertebral disc involvement may also suggest fungal rather than pyogenic spondylitis [41]. This absence of T2 signal in the disc is thought to be related to paramagnetic and ferromagnetic elements within the fungi themselves, which alter the relaxation times and thus signal intensity of T2-weighted imaging [42].

A rare but interesting manifestation of fungal disease is that of multifocal marrow lesions that may easily be mistaken for metastatic disease [43] (Fig. 5.13).

Brucella Spondylodiscitis

Pathophysiology

Spine infection is caused by a wide array of organisms including the *Brucella* species. Brucellosis is a zoonotic infection caused by Gram-negative bacilli from the *Brucella* genus. *Brucella* is transmitted to human through contact with unpasteurized, contaminated milk products [44, 45].

In endemic areas, spondylodiscitis is caused by the *Brucella* organism in an impressive 35–48% of cases [46, 47]. Even in non-endemic areas like the United States, this organism should be considered in the differential of spine infection. *Brucella* spondylodiscitis is worthy of independent discussion because of the unique features of the disease as well as the clinical implications this has on treatment. The most appropriate and effective treatment of *Brucella* spondylodiscitis is still unknown, and management of these patients can be difficult [46]. Clinical improvement can lag behind treatment initiation by up to 12 weeks, and a high rate of treated patients ultimately fail therapy (25%) [46–49].

Brucella most commonly affects male patients over 50 years of age and classically patients residing in rural areas with occupational risk factors. Despite this, as the disease process and our understanding of the illness evolves, the classic patient population becomes more broad, now often seen in women from urban areas without risk factors for the disease [46, 48].

The most affected spinal segment is lumbar (50–80%) followed by the thoracic and cervical spine. Involvement of one spinal level (two

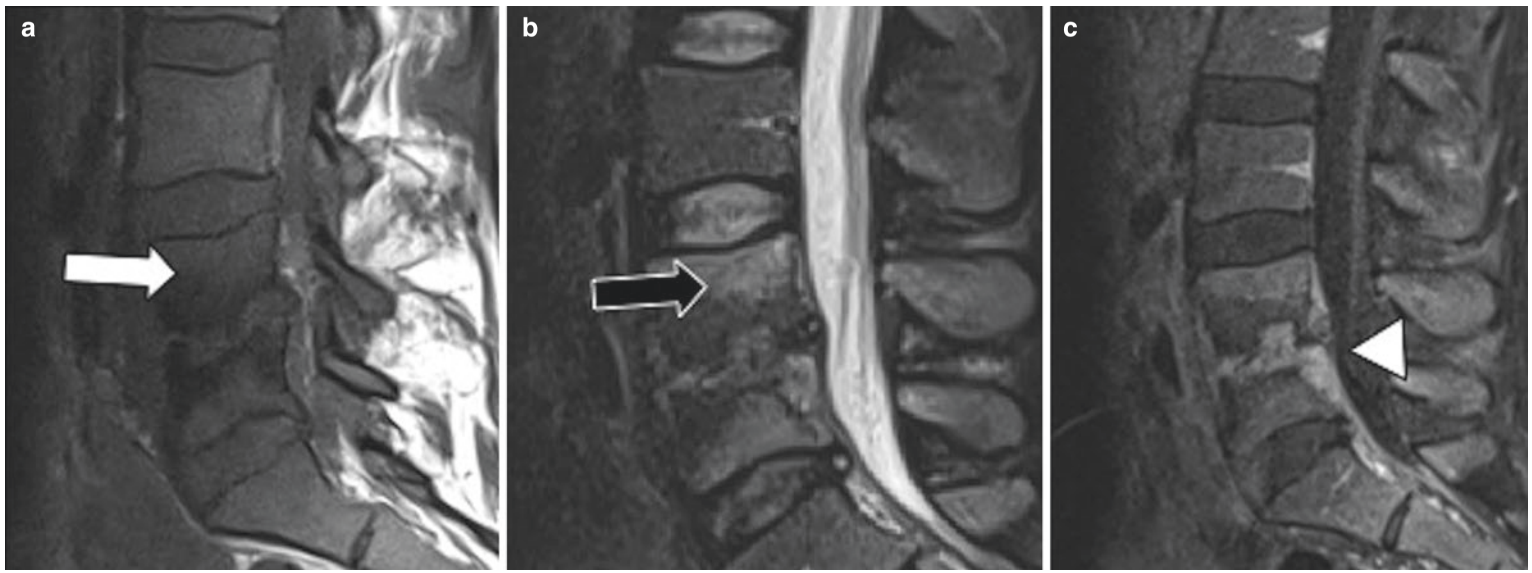

Fig. 5.11 A 67-year-old male with *Candida* spondylodiscitis. Sagittal T1 (**a**), STIR fat-saturated (**b**), and T1 fat-saturated post-contrast (**c**) images demonstrate findings similar to pyogenic spondylodiscitis with disc height loss, confluent hypointense T1 signal (white arrow), and hyperintense T2 signal (black arrow) with disc and epidural enhancement (white arrowhead)

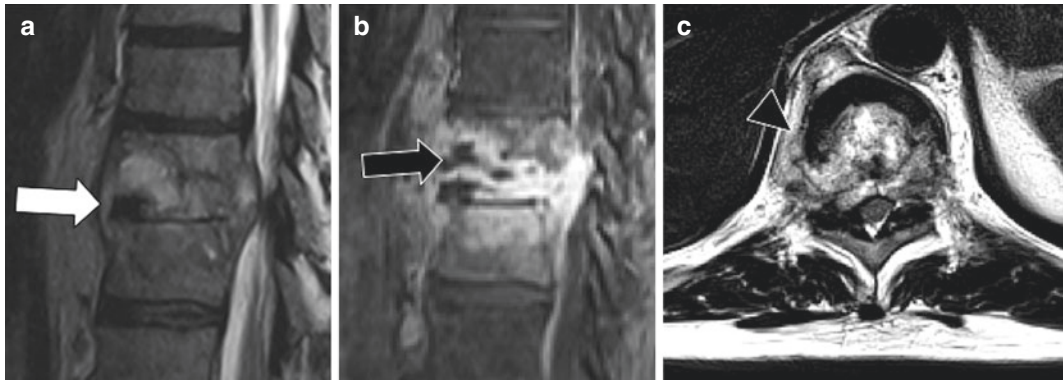

Fig. 5.12 A 49-year-old male with *Aspergillus* spondylodiscitis. Sagittal T2 (**a**), T1 fat-saturated post-contrast (**b**), and axial T2 (**c**) images of the spine demonstrate T9 and T10 vertebral edema with enhancement and subligamentous hyperintense T2 signal (white arrow) as well as peripheral rim-enhancing intravertebral abscess (black arrow). Imaging mimics tuberculous spondylodiscitis but with features more in keeping with fungal disease including disc height loss and a complex T2 paraspinal abscess (black arrowhead)

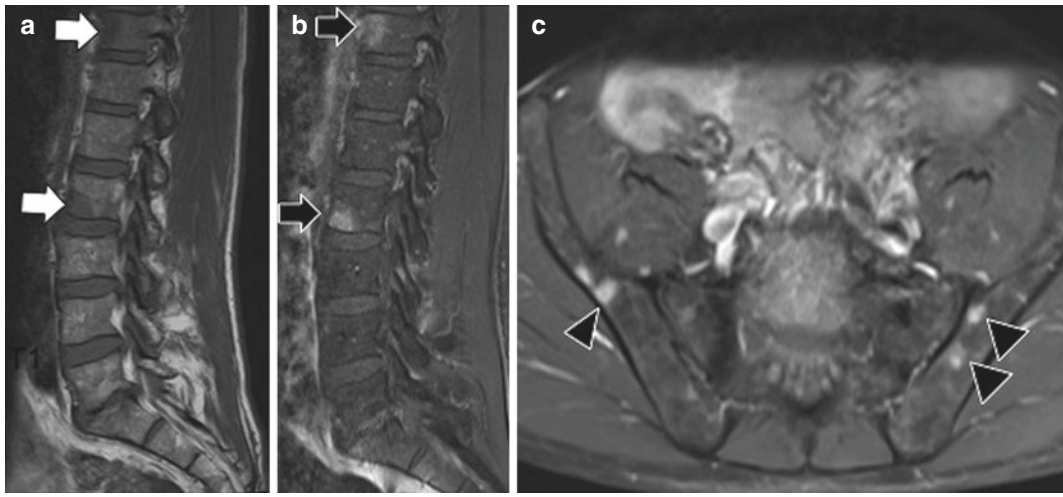

Fig. 5.13 A 63-year-old with disseminated coccidiomycosis. Sagittal T1 (**a**), sagittal T1 fat-saturated post-contrast (**b**), and axial T1 fat-saturated post-contrast (**c**) images demonstrate multifocal hypointense T1, enhancing lesions throughout the spine and pelvis, mimicking metastatic disease. Lesions were biopsied and shown to be disseminated coccidiomycosis

consecutive vertebrae) is the most common presentation. However, multifocal consecutive and non-consecutive involvement has been described. Both epidural and paraspinal abscesses have been seen in the setting of *Brucella* spine infection [46, 48, 49].

Imaging of *Brucella* Spondylodiscitis

Differentiating *Brucella* spondylodiscitis from other infectious spondylodiscitis can be exceedingly difficult due to the overlap in imaging findings. The most common MRI features of *Brucella* spondylodiscitis include osseous hypointense T1 signal, hyperintense T2 signal, diffuse enhancement, disc height loss with endplate destruction, and presence or absence of epidural or paraspinal abscesses. Characteristic MRI features of *Brucella* spondylodiscitis have been described and include the preservation of vertebral architecture despite extensive marrow involvement, profound increased signal in the intervertebral disc, and facet joint involvement

[48, 50]. Unfortunately none of these features are pathognomonic for the disease, and clinical history and risk factors may arguably be the most important features for the assumption of the diagnosis.

Infectious Spondylodiscitis Versus Degeneration

Degenerative disc disease and neuropathic (Charcot) spine often present with similar MRI signal changes to infectious spondylodiscitis creating intricacy in differentiating these entities. Further compounding the muddied imaging picture is the propensity of bacterial pathogens to preferentially seed degenerative discs over normal discs. Ingrowth of vascularized granulation tissue occurs with intervertebral disc desiccation owing to increased blood flow resulting in higher risk of bacterial seeding. While a few of the defining imaging features of infectious and degenerative discitis have been discussed, there are other defining features of these conditions that should be considered when attempting to narrow the differential diagnosis in patients with back pain.

Neuropathic (Charcot) spine is a condition whereby the vertebral facets and intervertebral discs become denervated owing to a rapid and often profound degeneration of the spine with subsequent inflammatory imaging features and pain. Because of the degree of bony destruction, endplate irregularities, and inflammation, differentiating this condition from the aggressive infectious spondylodiscitis is difficult. On CT and radiography, features suggestive of neuropathic spine include involvement of the vertebral facet joints, osseous debris around the vertebra, spondylolisthesis, and intradiscal vacuum phenomenon [51] (Fig. 5.14).

The finding of intradiscal vacuum phenomenon is a common finding, which deserves additional consideration. In this condition, gas bubbles, usually nitrogen, are removed from solution through a negative pressure mechanism and accumulate within the intervertebral discs [52]. The notion that vacuum phenomenon excludes the possibility of infectious discitis is widely debated in the literature. Many reports suggest that intradiscal vacuum phenomenon is an indication of benign conditions (i.e., neuropathic spine, osteonecrosis, and vertebral compression fracture), occurring as a result of negative pressure across the disc space [51, 53, 54]. In spine infection, the influx of inflammatory cells into the discs, vertebra, and adjacent soft tissues creates a positive pressure environment that is not conducive to the formation of the vacuum effect. Although case reports of intradiscal gas in the setting of infection exist, the incidence of this finding is exceedingly rare [55, 56]. In a report examining 307 patients with known disc infection, intradiscal gas was identified in only 1 patient (0.003%) [53]. Despite the low incidence of infectious related intradiscal gas, some degree of caution should be applied when interpreting this finding especially when the distribution and the morphology of the gas are heterogeneous, nonlinear, or otherwise atypical in appearance.

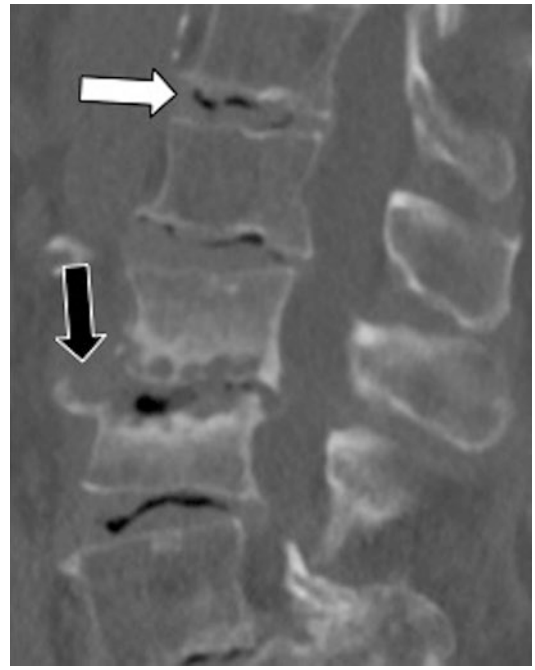

Fig. 5.14 Sagittal CT image of the lumbar spine in a patient with neuropathic/Charcot spine demonstrates multilevel intradiscal vacuum phenomenon (white arrow) and bony debris (black arrow)

Several advanced MR imaging techniques proposed in the literature have shown promise in differentiating degenerative and infectious discitis. Diffusion-weighted imaging (DWI), for example, is an established technique in brain imaging that has recently been adapted to the spine as a means to differentiate Modic endplate edema from infection. Authors suggest that degenerative Modic edema restricts in a linear sub-endplate morphology creating a "claw sign" on DWI. Infection, by contrast, restricts more diffusely through the vertebra [57].

Berry et al. in 2009 described an advanced MR imaging technique that uses iron oxide injection to aid in the determination of endplate edema. In this technique, supra-paramagnetic iron oxide particles are injected intravenously and phagocytized by macrophages, ultimately resulting in an iron oxide accumulation along the endplates of infected vertebra. The supra-paramagnetic properties of iron oxide result in a post-injection T2 signal dropout along the infected endplates, a finding absent in the setting of degenerative Modic edema [58].

Sacroiliac Joint Septic Arthritis

Pathophysiology

Disorders of the sacroiliac joint include degenerative, traumatic, inflammatory, and infectious etiologies. Inflammatory sacroiliitis is seen with some frequency in both seronegative and seropositive arthropathies and is almost always bilateral and symmetric, a key imaging feature of this disease process. Unilateral inflammatory sacroiliitis, however, has been described in both, posing a challenge when differentiating inflammatory from septic arthritis [59].

Infectious sacroiliitis is a relatively uncommon condition making up only 1–4% of all cases of sacroiliac arthritis [60]. Most cases are caused by hematogenous spread of bacteria, but direct inoculation from adjacent infection, deep sacral ulceration, or instrumentation has also been described [61]. The typical presentation of septic sacroiliitis includes low back pain, sciatica, fevers, and elevated inflammatory markers. These are relatively non-specific findings often overlapping the clinical presentations of other diseases such as acute spondyloarthropathy, lumbar degenerative disease, diverticulitis, or appendicitis. Evaluation with MRI or CT has been shown to be useful in the diagnosis of septic arthritis but requires a sophisticated understanding of the imaging subtleties as to not confuse the imaging with that of unilateral inflammatory sacroiliitis [61, 62].

Imaging

Radiographic findings of septic sacroiliitis are often subtle and include periarticular osteopenia and erosions. Differentiating infection from inflammatory sacroiliitis on radiography is largely dependent on the unilateral nature of the sacroiliac joint involvement. When considering the possibility of unilateral inflammatory disease, for example, psoriasis or unilateral ankylosing spondylitis, radiographs can be non-specific.

MRI is arguably the most sensitive imaging modality for the differentiation of inflammatory and infectious sacroiliitis. Kang et al. found that the most accurate independent variable identified in these patients is the presence of periarticular edema and iliopsoas muscle swelling [63]. Fluid signal tracking along the muscle belly and intermuscular fat planes of the pelvic side wall on fluid-sensitive MRI sequences corresponded to a high accuracy and specificity for the diagnosis of septic arthritis in other studies as well [62–64] (Fig. 5.15)

The pattern of bone marrow edema may also be helpful in determining the origin of the inflammation. A well-established feature of seronegative spondyloarthropathy is the iliac predominant bone marrow edema pattern that occurs early in the disease process. The iliac predominance is thought to be related to the differences in the makeup of sacral and iliac cartilage with the iliac fibrocartilage layer serving as an enthesis that is prone to inflammation in conditions like ankylosing spondylitis [63, 65]. In the setting of infection, both the sacral hyaline cartilage and

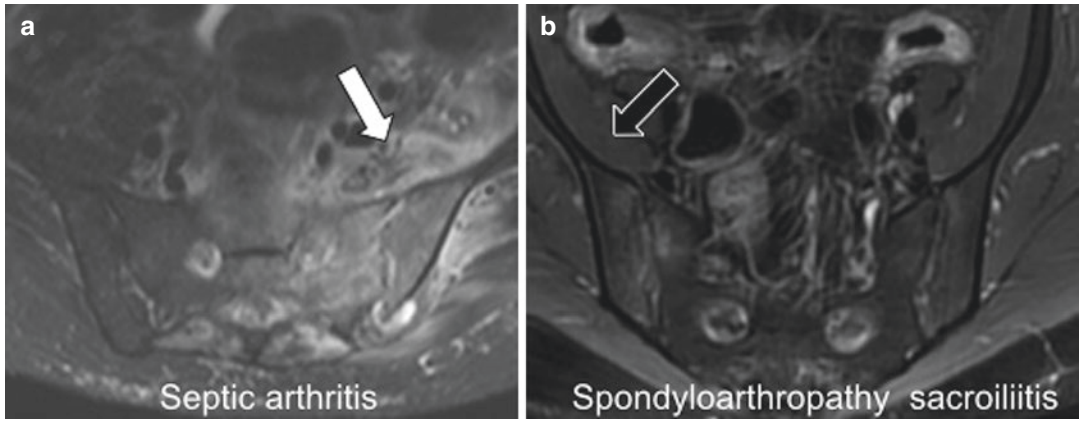

Fig. 5.15 Axial T2 fat-saturated images in a patient with septic arthritis (**a**) demonstrate profound hyperintense T2 signal within and around the iliopsoas muscle and pelvic side wall (white arrow). T2 fat-saturated images in a patient with ankylosing spondylitis and inflammatory sacroiliitis (**b**) demonstrate bone marrow edema with a notable absence of periarticular pelvic side wall edema (black arrow)

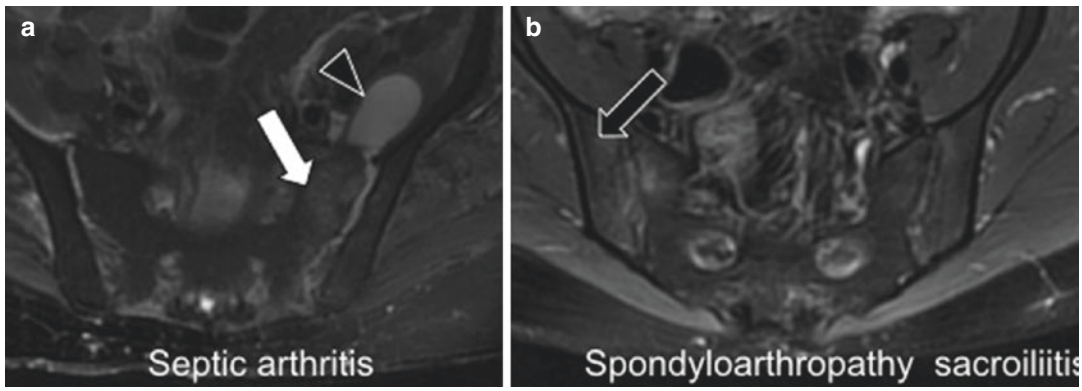

Fig. 5.16 Axial T2 fat-saturated images in a patient with septic arthritis (**a**) demonstrate sacral predominant bone marrow manifesting as hyperintense T2 signal (white arrow). The presence of a large pericapsular hyperintense T2 fluid collection (black arrowhead) favors the diagnosis of septic arthritis. T2 fat-saturated images in a patient with ankylosing spondylitis and inflammatory sacroiliitis (**b**) demonstrate the classic iliac predominant bone marrow edema (black arrow)

the iliac fibrocartilage are equally susceptible to inflammation. This manifests in a unique sacral predominant or equal sacral and iliac bone marrow edema pattern in septic arthritis [65] (Fig. 5.16).

Extracapsular fluid collections are seen exclusively in septic arthritis and when present should be considered highly suspicious for infection. Other features favoring septic arthritis include large subchondral erosions and thick capsulitis with absence of joint enhancement [62, 63]. The imaging findings in septic versus inflammatory sacroiliitis are illustrated in Table 5.2.

Table 5.2 MR imaging features of septic versus inflammatory sacroiliitis [63]

MR imaging feature	Septic sacroiliitis	Inflammatory sacroiliitis
Bone marrow edema	Sacral predominant, equal sacral and iliac edema	Iliac predominant edema
Periarticular soft tissue edema	Severe, often extending into the iliopsoas muscle and pelvic side wall	Mild or non-existent
Capsulitis	Severe	Mild
Periarticular fluid collection	Present	Absent
Subchondral erosions	Large (>1 cm), irregular	Small, uniform

Epidural Abscess

Pathophysiology

Epidural abscess refers to an infectious fluid collection contained between the dura of the thecal sac and the periosteum of the adjacent bone. The incidence of epidural abscess is about 2–3 per 100,000 hospital admissions and is seen most frequently in the fifth to seventh decades of life [66]. Risk factors for the formation of epidural abscesses include diabetes, intravenous drug abuse, immune compromise, and recent intervention. While hematogenous seeding of the epidural space does occur, epidural abscess most commonly forms as a direct extension of infection from adjacent osteomyelitis/discitis [67].

Failure of medical treatment is unfortunately common, especially in the setting of diabetes and bacteremia. Prompt identification of epidural abscess and initiation of therapy, either medical or surgical, is imperative to treatment success [68]. Epidural abscesses, when hematogenously spread, usually occur at the dorsal epidural space and have a propensity to affect multiple levels of the spine resulting in "skip lesions" along the neural axis. For this reason, whole spine imaging is recommended in patients with known or suspected hematogenously spread epidural infection [68, 69].

Imaging

MRI is the modality of choice for the evaluation of epidural abscess, offering superior spatial resolution and sensitivity [70]. Although non-contrast MRI has reasonable sensitivity in the detection of epidural disease, the addition of post-contrast images increases sensitivity and specificity over non-contrast images alone and should be preferentially performed in all cases of suspected epidural abscess [71].

There are two main imaging appearances of epidural abscess, differing in signal characteristics and enhancement based on the age of the lesion. The first imaging pattern is seen in the early phlegmonous stages of infection. In this phase, the epidural abscess is made up of predominantly thick enhancing granulation tissue that appears as a confluent but often heterogeneous hyperintense T2 signal epidural mass with diffuse internal enhancement (Fig. 5.17). As the epidural abscess matures, the central areas of granulation become necrotic and fluid-like, appearing as homogeneous hyperintense T2 signal with thick peripheral enhancement [67, 72] (Fig. 5.18).

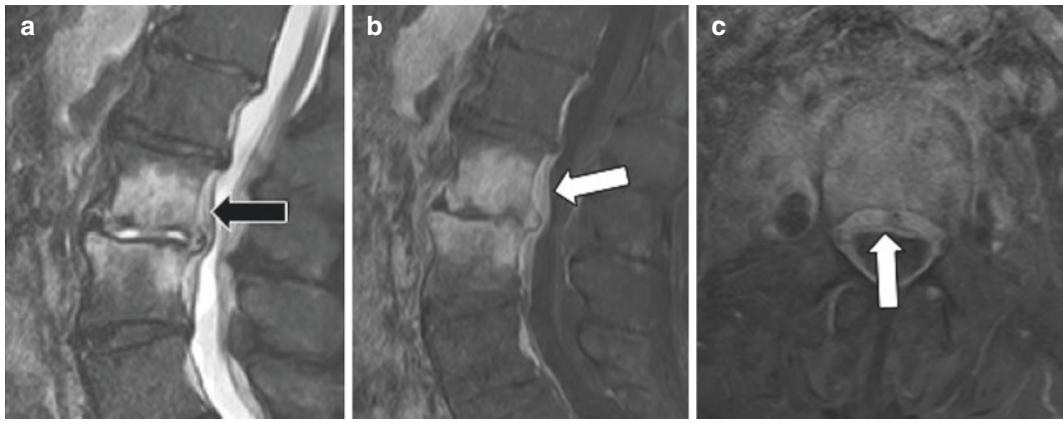

Fig. 5.17 A 67-year-old male with L2–L3 spondylodiscitis and early epidural abscess. Sagittal STIR fat-saturated (**a**), sagittal T1 fat-saturated post-contrast (**b**), and axial T1 fat-saturated post-contrast images (**c**) demonstrate focal thickening of the ventral epidural space posterior to the L2–L3 disc. There is heterogeneous T2 signal (black arrow) and internal enhancement (white arrows)

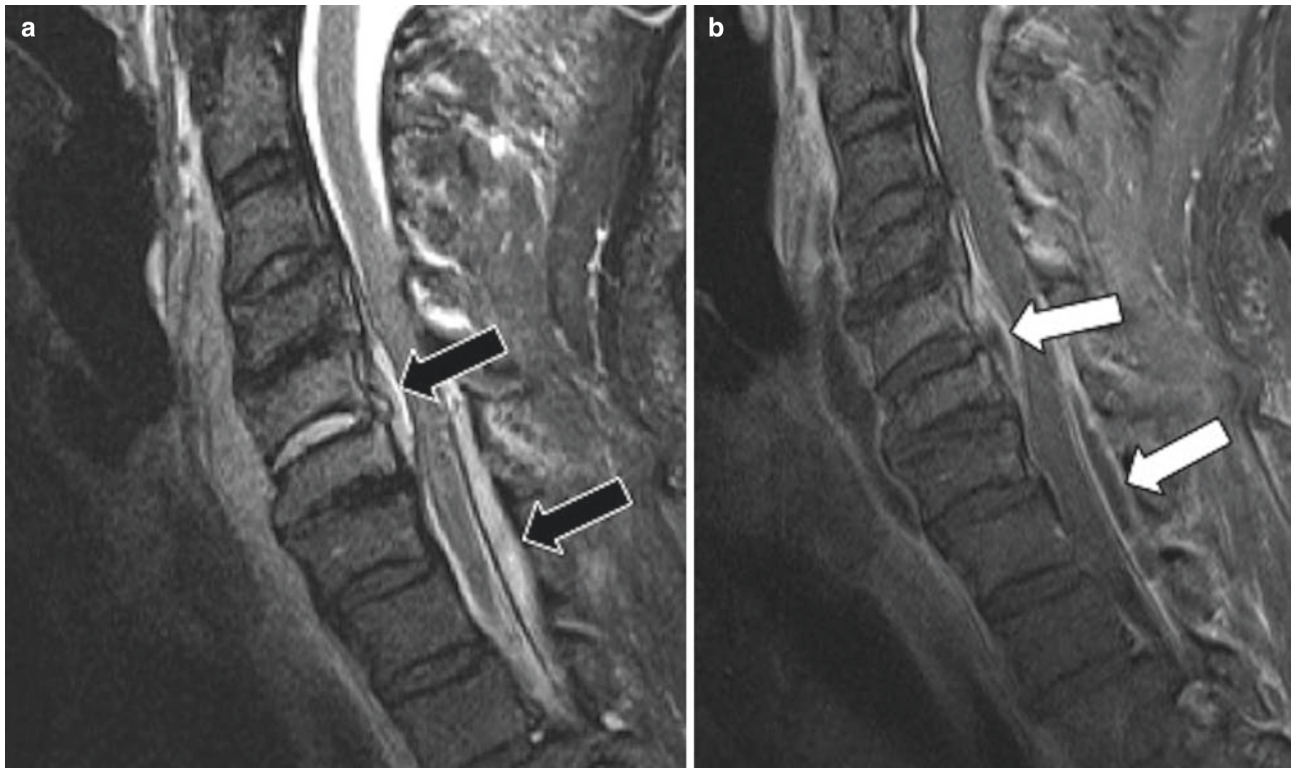

Fig. 5.18 A 50-year-old male IV drug abuser with neck pain. Sagittal STIR fat-saturated (**a**) and T1 fat-saturated post-contrast images (**b**) demonstrate C5–C6 spondylodiscitis with an adjacent ventral epidural abscess as well as a secondary dorsal abscess "skip lesion." The abscesses are mature demonstrating hyperintense T2 signal (black arrows) with peripheral enhancement (white arrows) indicative of central necrotic avascular material

Conclusion

Spine infection is unfortunately a common occurrence, especially in susceptible patient populations. While the imaging findings in spine infection are not always subtle, differentiating findings of infection from other disease processes can be extremely difficult. A sophisticated understanding of the unique imaging features in both infectious and non-infectious disease processes is critical to the accurate diagnosis and prompt treatment of this high-risk patient population.

References

1. Berhouma M, Krolak-Salmon P, editors. Brain and spine surgery in the elderly. Cham: Springer; 2017. p. 305–27.
2. Cramer J, Haase N, Behre I, Ostermann PAW. Spondylitis und Spondylodiszitis. Trauma und Berufskrankheit. 2003;5:336–41.
3. Stoffel M, Hecker J, Ringel F, Meyer B, Stüer C. A staged treatment algorithm for spinal infections. J Neurol Surg Part A. 2013;74:087–95.
4. Nolla JM, Ariza J, Gómez-Vaquero C, Fiter J, Bermejo J, Valverde J, Escofet DR, Gudiol F. Spontaneous pyogenic vertebral osteomyelitis in nondrug users. Semin Arthritis Rheum. 2002;31:271–8.
5. Mchenry MC, Easley KA, Locker GA. Vertebral osteomyelitis: long-term outcome for 253 patients from 7 cleveland-area hospitals. Clin Infect Dis. 2002;34:1342–50.
6. Karadimas EJ, Bunger C, Lindblad BE, Hansen ES, Høy K, Helmig P, Kannerup AS, Niedermann B. Spondylodiscitis. A retrospective study of 163 patients. Acta Orthop. 2008;79:650–9.
7. Waldvogel FA, Medoff G, Swartz MN. Osteomyelitis: a review of clinical features, therapeutic considerations and unusual aspects. N Engl J Med. 1970;282:198–206.
8. Gouliouris T, Aliyu SH, Brown NM. Spondylodiscitis: update on diagnosis and management – authors responses. J Antimicrob Chemother. 2011;66:1200–2.
9. Ratcliffe JF. Anatomic basis for the pathogenesis and radiologic features of vertebral osteomyelitis and its differentiation from childhood discitis. Acta Radiologica Diagnosis. 1985;26:137–43.
10. Maiuri F, Laconetta G, Gallicchio B, Manto A, Briganti F. Spondylodiscitis~. Spine. 1997;22:1741–6.
11. Cheung WY, Luk KDK. Pyogenic spondylitis. Int Orthop. 2011;36:397–404.
12. Pineda C, Vargas A, Rodríguez AV. Imaging of osteomyelitis: current concepts. Infect Dis Clin N Am. 2006;20:789–825.
13. Hadjipavlou AG, Cesani-Vazquez F, Villaneuva-Meyer J. The effectiveness of gallium citrate Ga 67 radionuclide imaging in vertebral osteomyelitis revisited. Am J Orthop. 1998;27:179–83.
14. Smids C, Kouijzer IJE, Vos FJ, Sprong T, Hosman AJF, Rooy JWJD, Aarntzen EHJG, Geus-Oei L-FD, Oyen WJG, Bleeker-Rovers CP. A comparison of the diagnostic value of MRI and 18F-FDG-PET/CT in suspected spondylodiscitis. Infection. 2016;45:41–9.
15. Leone A, Dell'Atti C, Magarelli N, Colelli P, Balanika A, Casale R, Bonomo L. Imaging of spondylodiscitis. Eur Rev Med Pharmacol Sci. 2012;16(Suppl 2):8–19.
16. Modic MT, Feiglin DH, Piraino DW, Boumphrey F, Weinstein MA, Duchesneau PM, Rehm S. Vertebral osteomyelitis: assessment using MR. Radiology. 1985;157:157–66.
17. Modic MT, Steinberg PM, Ross JS, Masaryk TJ, Carter JR. Degenerative disk disease: assessment of changes in vertebral body marrow with MR imaging. Radiology. 1988;166:193–9.
18. Luoma K, Vehmas T, Grönblad M, Kerttula L, Kääpä E. Relationship of Modic type 1 change with disc degeneration: a prospective MRI study. Skelet Radiol. 2008;38:237–44.
19. Ledermann HP, Schweitzer ME, Morrison WB, Carrino JA. MR imaging findings in spinal infections: rules or myths? Radiology. 2003;228:506–14.
20. Varma R, Lander P, Assaf A. Imaging of pyogenic infectious spondylodiskitis. Radiol Clin N Am. 2001;39:203–13.
21. Yeom JA, Lee IS, Suh HB, Song YS, Song JW. Magnetic resonance imaging findings of early spondylodiscitis: interpretive challenges and atypical findings. Korean J Radiol. 2016;17:565.
22. Desanto J, Ross JS. Spine infection/inflammation. Radiol Clin N Am. 2011;49:105–27.
23. Dunbar J, Sandoe J, Rao A, Crimmins D, Baig W, Rankine J. The MRI appearances of early vertebral osteomyelitis and discitis. Clin Radiol. 2010;65:974–81.
24. Carragee EJ. The clinical use of magnetic resonance imaging in pyogenic vertebral osteomyelitis. Spine. 1997;22:780–5.
25. Zarrouk V, Feydy A, Salles F, Dufour V, Guigui P, Redondo A, Fantin B. Imaging does not predict the clinical outcome of bacterial vertebral osteomyelitis. Rheumatology. 2006;46:292–5.
26. Gillams AR, Chaddha B, Carter AP. MR appearances of the temporal evolution and resolution of infectious spondylitis. Am J Roentgenol. 1996;166:903–7.
27. Kowalski TJ, Berbari EF, Huddleston PM, Steckelberg JM, Osmon DR. Do follow-up imaging examinations provide useful prognostic information in patients with spine infection? Clin Infect Dis. 2006;43:172–9.
28. Watson JM. Tuberculosis in Britain today. BMJ. 1993;306:221–2.
29. Tsiodras S, Falagas ME. Clinical assessment and medical treatment of spine infections. Clin Orthop Relat Res. 2006;443:38–50.

30. Koo K-H, Lee H-J, Chang B-S, Yeom J-S, Park K-W, Lee C-K. Differential diagnosis between tuberculous spondylitis and pyogenic spondylitis. J Korean Soc Spine Surg. 2009;16:112.
31. Lee KY. Comparison of pyogenic spondylitis and tuberculous spondylitis. Asian Spine J. 2014;8:216.
32. Jung N-Y, Jee W-H, Ha K-Y, Park C-K, Byun J-Y. Discrimination of tuberculous spondylitis from pyogenic spondylitis on MRI. Am J Roentgenol. 2004;182:1405–10.
33. Chang M-C, Wu HTH, Lee C-H, Liu C-L, Chen T-H. Tuberculous spondylitis and pyogenic spondylitis. Spine. 2006;31:782–8.
34. Alothman A, Memish ZA, Awada A, Mahmood SA, Sadoon SA, Rahman MM, Khan MY. Tuberculous spondylitis. Spine. 2001;26:E565. https://doi.org/10.1097/00007632-200112150-00020.
35. Shanley DJ. Tuberculosis of the spine: imaging features. Am J Roentgenol. 1995;164:659–64.
36. Baddley J. Geographic distribution of endemic fungal infections among older persons, United States. Emerg Infect Dis. 2011;17:1664–9.
37. Frazier DD, Campbell DR, Garvey TA, Wiesel S, Bohlman HH, Eismont FJ. Fungal infections of the spine. J Bone Joint Surg Am Vol. 2001;83:560–5.
38. Kim CW, Perry A, Currier B, Yaszemski M, Garfin SR. Fungal infections of the spine. Clin Orthop Relat Res. 2006;444:92–9.
39. Dotis J, Roilides E. Osteomyelitis due to Aspergillus species in chronic granulomatous disease: an update of the literature. Mycoses. 2011;54:e686. https://doi.org/10.1111/j.1439-0507.2010.02001.x.
40. Horn D, Sae-Tia S, Neofytos D. Aspergillus osteomyelitis: review of 12 cases identified by the prospective antifungal therapy Alliance registry. Diagn Microbiol Infect Dis. 2009;63:384–7.
41. Lee S-W, Lee SH, Chung HW, Kim MJ, Seo MJ, Shin MJ. Candida spondylitis: comparison of MRI findings with bacterial and tuberculous causes. Am J Roentgenol. 2013;201:872–7.
42. Williams RL, Fukui MB, Meltzer CC, Swarnkar A, Johnson DW, Welch W. Fungal spinal osteomyelitis in the immunocompromised patient: MR findings in three cases. AJNR Am J Neuroradiol. 1999;20:381–5.
43. Mcconnell MF, Shi A, Lasco TM, Yoon L. Disseminated coccidioidomycosis with multifocal musculoskeletal disease involvement. Radiol Case Rep. 2017;12:141–5.
44. Tekkök IH, Berker M, Özcan OE, Özgen T, Akalin E. Brucellosis of the spine. Neurosurgery. 1993;33:838–44.
45. Gotuzzo E, Seas C, Guerra JG, Carrillo C, Bocanegra TS, Calvo A, Castaneda O, Alarcon GS. Brucellar arthritis: a study of 39 Peruvian families. Ann Rheum Dis. 1987;46:506–9.
46. Colmenero JD, Jimenez-Mejias ME, Sanchez-Lora FJ, Reguera JM, Palomino-Nicas J, Martos F, Heras JGDL, Pachon J. Pyogenic, tuberculous, and brucellar vertebral osteomyelitis: a descriptive and comparative study of 219 cases. Ann Rheum Dis. 1997;56:709–15.
47. Sakkas LI, Davas EM, Kapsalaki E, Boulbou M, Makaritsis K, Alexiou I, Tsikrikas T, Stathakis N. Hematogenous spinal infection in Central Greece. Spine. 2009;34:E513. https://doi.org/10.1097/brs.0b013e3181a9897e.
48. Kaptan F, Gulduren HM, Sarsilmaz A, Sucu HK, Ural S, Vardar I, Coskun NA. Brucellar spondylodiscitis: comparison of patients with and without abscesses. Rheumatol Int. 2012;33:985–92.
49. Solera J, Lozano E, Martinez-Alfaro E, Espinosa A, Castillejos ML, Abad L. Brucellar spondylitis: review of 35 cases and literature survey. Clin Infect Dis. 1999;29:1440–9.
50. Özaksoy D, Yücesoy K, Yücesoy M, Kovanlıkaya I, Yüce A, Naderi S. Brucellar spondylitis: MRI findings. Eur Spine J. 2001;10:529–33.
51. Wagner SC, Schweitzer ME, Morrison WB, Przybylski GJ, Parker L. Can imaging findings help differentiate spinal neuropathic arthropathy from disk space infection? Initial experience. Radiology. 2000;214:693–9.
52. Resnick D, Niwayama G, Guerra J, Vint V, Usselman J. Spinal vacuum phenomena: anatomical study and review. Radiology. 1981;139:341–8.
53. Feng S-W, Chang M-C, Wu H-T, Yu J-K, Wang S-T, Liu C-L. Are intravertebral vacuum phenomena benign lesions? Eur Spine J. 2011;20:1341–8.
54. Libicher M, Appelt A, Berger I, Baier M, Meeder P-J, Grafe I, Dafonseca K, Nöldge G, Kasperk C. The intravertebral vacuum phenomenon as specific sign of osteonecrosis in vertebral compression fractures: results from a radiological and histological study. Eur Radiol. 2007;17:2248–52.
55. Pate D, Katz A. Clostridia discitis: a case report. Arthritis Rheum. 1979;22:1039–40.
56. Bielecki D, Sartoris D, Resnick D, Lom KV, Fierer J, Haghighi P. Intraosseous and intradiscal gas in association with spinal infection: report of three cases. Am J Roentgenol. 1986;147:83–6.
57. Patel KB, Poplawski MM, Pawha PS, Naidich TP, Tanenbaum LN. Diffusion-weighted MRI "claw sign" improves differentiation of infectious from degenerative Modic type 1 signal changes of the spine. Am J Neuroradiol. 2014;35:1647–52.
58. Bierry G, Jehl F, Holl N, Sibilia J, Froelich S, Froehlig P, Dietemann J-L, Kremer S. Cellular magnetic resonance imaging for the differentiation of infectious and degenerative vertebral disorders: preliminary results. J Magn Reson Imaging. 2009;30:901–6.
59. Canella C, Schau B, Ribeiro E, Sbaffi B, Marchiori E. MRI in seronegative spondyloarthritis: imaging features and differential diagnosis in the spine and sacroiliac joints. Am J Roentgenol. 2013;200:149–57.
60. Forrester D, Kilcoyne R. Osteomyelitis and septic arthritis. Musculoskelet Dis. 2005:138–42.
61. Resnick D, Kransdorf MJ. Osteomyelitis, septic arthritis, and soft tissue infection: axial skeleton. Bone Joint Imaging. 2005:743–52.
62. Klein MA, Winalski CS, Wax MR, Piwnica-Worms DR. MR imaging of septic sacroiliitis. J Comput Assist Tomogr. 1991;15:126–32.

63. Kang Y, Hong SH, Kim JY, Yoo HJ, Choi J-Y, Yi M, Kang HS. Unilateral sacroiliitis: differential diagnosis between infectious sacroiliitis and spondyloarthritis based on MRI findings. Am J Roentgenol. 2015;205:1048–55.
64. Sandrasegaran K, Saifuddin A, Coral A, Butt WP. Magnetic resonance imaging of septic sacroiliitis. Skelet Radiol. 1994;23:289–92.
65. Prabhu S, Irodi A, Prakash D. Seronegative spondyloarthropathy-related sacroiliitis: CT, MRI features and differentials. Indian J Radiol Imaging. 2014;24:271.
66. Reihsaus E, Waldbaur H, Seeling W. Spinal epidural abscess: a meta-analysis of 915 patients. Neurosurg Rev. 2000;23:175–204.
67. Darouiche RO. Spinal epidural abscess. N Engl J Med. 2006;355:2012–20.
68. Patel AR, Alton TB, Bransford RJ, Lee MJ, Bellabarba CB, Chapman JR. Spinal epidural abscesses: risk factors, medical versus surgical management, a retrospective review of 128 cases. Spine J. 2014;14:326–30.
69. Ju KL, Kim SD, Melikian R, Bono CM, Harris MB. Predicting patients with concurrent noncontiguous spinal epidural abscess lesions. Spine J. 2015;15:95–101.
70. Laur O, Mandell JC, Titelbaum DS, Cho C, Smith SE, Khurana B. Acute nontraumatic back pain: infections and mimics. Radiographics. 2019;39(1):287–8.
71. Dillon WP, Norman D, Newton TH, Bolla K, Mark A. Intradural spinal cord lesions: Gd-DTPA-enhanced MR imaging. Radiology. 1989;170:229–37.
72. Numaguchi Y, Rigamonti D, Rothman MI, Sato S, Mihara F, Sadato N. Spinal epidural abscess: evaluation with gadolinium-enhanced MR imaging. Radiographics. 1993;13:545–59.

6 MRI in Non-infectious Inflammation and Arthropathies

Sachin Dheer

Rheumatoid Arthritis (RA)

RA is a chronically progressive, autoimmune, inflammatory arthropathy, more common in women, affecting the synovial joints, and has characteristic findings in the spine. Although screening for RA and evaluation of spinal instability are performed with radiographs, these have limited sensitivity for detecting RA, particularly in the early stages of disease. CT evaluation is most often used for preoperative planning and in the setting of trauma. MRI allows comprehensive evaluation of inflammatory lesions, including erosions and pannus formation, the spinal cord, nerve roots, and associated impingement. Additionally, findings on contrast-enhanced MRI correlate with disease activity and response to therapy; and MRI is far more sensitive than both radiographs and CT in demonstrating the full extent of disease (Figs. 6.1 and 6.2) [1, 2].

Involvement typically occurs in the cervical (40–86% of patients) and upper thoracic (up to 30% of patients) portions of the spine. At the level of the dens, there is characteristic erosion with pannus formation which can compromise the posterior transverse ligament, resulting in instability and potentially significant upper cervical cord impingement (Fig. 6.3) [3–5].

S. Dheer (✉)
Department of Radiology, Thomas Jefferson University Hospital, Jefferson Health, Philadelphia, PA, USA

In the lower cervical and upper thoracic portions of the spine, referred to as sub-axial disease, advanced RA sometimes results in characteristic, progressive "stepwise" anterolisthesis, which is the result of inflammatory changes of the apophyseal and uncovertebral joints (Fig. 6.3) [6].

On MRI, intense synovial enhancement and bone marrow edema (low T1, increased T2 signal) are noted. Often, characteristic marginal erosions are present as well. Pannus formation demonstrates variable MRI signal, intermediate to low on T1-weighted sequences and low, intermediate, or high on T2-weighted sequences, reflecting variability and the relative amounts of fibrosis, cellularity, and vascularization present within the pannus (Figs. 6.1, 6.2, and 6.3) [3, 6].

Given the radiographic limitations in measuring the extent of instability, particularly vertical (aka cranial settling) in the setting of significant osseous erosion, both CT and MR are routinely used in measuring the degree of instability and monitoring progression. Compared to CT, MRI has the added benefit of evaluating the cord and other anatomic sites of inflammation [3, 5].

Additional, non-specific findings of RA include erosion of the spinous processes, accompanied by soft tissue inflammatory changes and pannus formation in the region of the interspinous ligament, and non-infectious spondylodiscitis [3]. Later stages of inactive or "burned-out" disease can result in fibrosis, soft tissue (ligamentous and tendinous) ossification, sclerotic erosions of the vertebrae, and vertebral

W. B. Morrison et al. (eds.), *MRI of the Spine*, https://doi.org/10.1007/978-3-030-43627-8_6

ankylosis [3], though this is less common with current, more targeted, and successful treatment regimens.

Seronegative Spondyloarthropathies (SpAs)

Ankylosing Spondylitis (AS)

The most common of the SpAs, AS is associated with the HLA-B27 genotype (present in >80% of AS patients) and is often the most disabling as well. AS typically presents in early adulthood and demonstrates a chronic, progressive course. Involvement of the sacroiliac joints, which is usually symmetric, is part of the diagnostic criteria, and, as with other inflammatory arthritides, MRI is far more sensitive than both radiographs and CT in detecting early, and the full extent of, disease [6–8]. Contrast-enhanced MRI findings correlate with disease activity and response to therapy [1, 2]. Sacroiliitis results in periarticular marrow edema (low T1, increased T2 and STIR

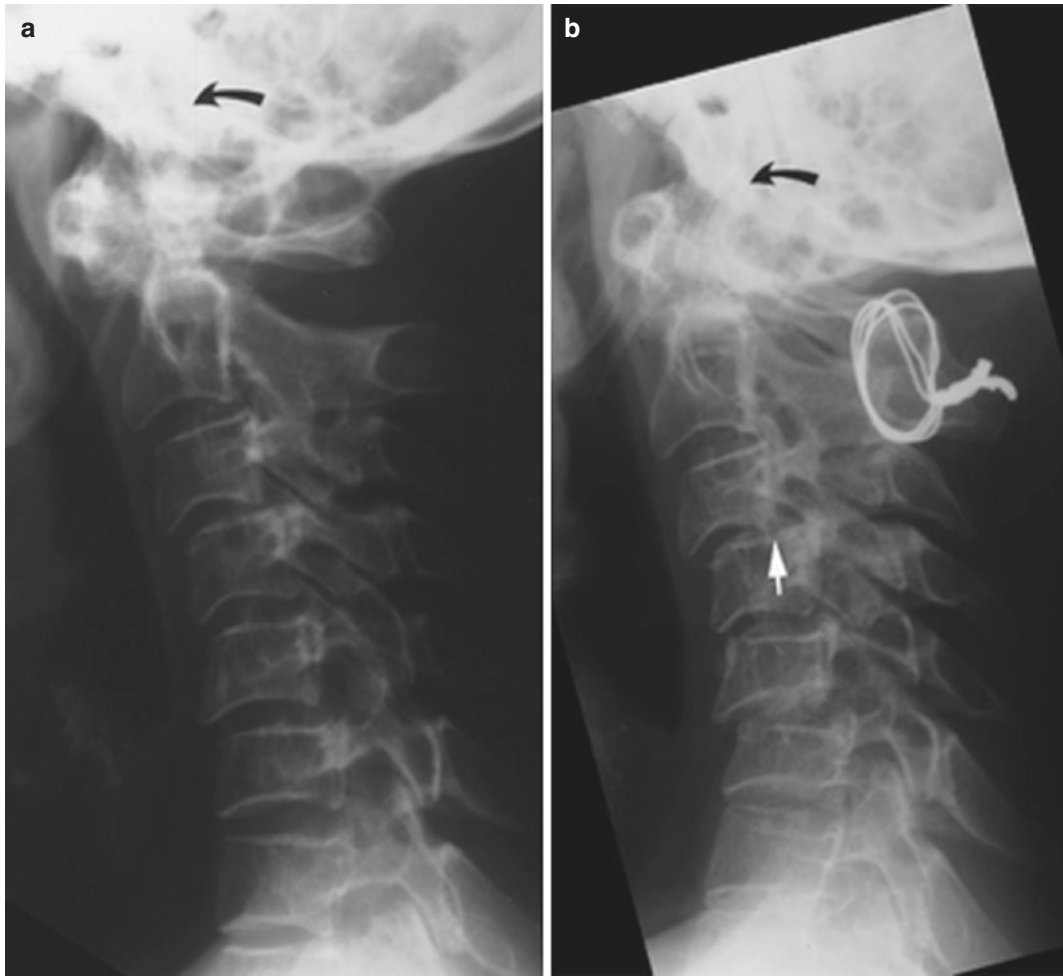

Fig. 6.1 (**a** and **b**) Radiographs, (**c**) CT, and (**d**–**h**) MRI of a 64-year-old woman with RA of the cervical spine. The initial radiograph (**a**) demonstrates characteristic "stepwise" anterolisthesis indicative of instability. Following posterior stabilization at C1–C2, there is progressive listhesis at C3–C4. Coronal image of C1, the dens, and C3 (**c**) reveals radiographically occult, characteristic erosions. Sagittal STIR (**d**), T1-weighted (**e**), and post-contrast (**f**–**h**) images demonstrate pronounced, inflammatory (active) pannus surrounding the dens, which is not apparent on radiographs and CT. Note the absence of mass effect on the cord, cranial settling, and cervical canal stenosis [6]

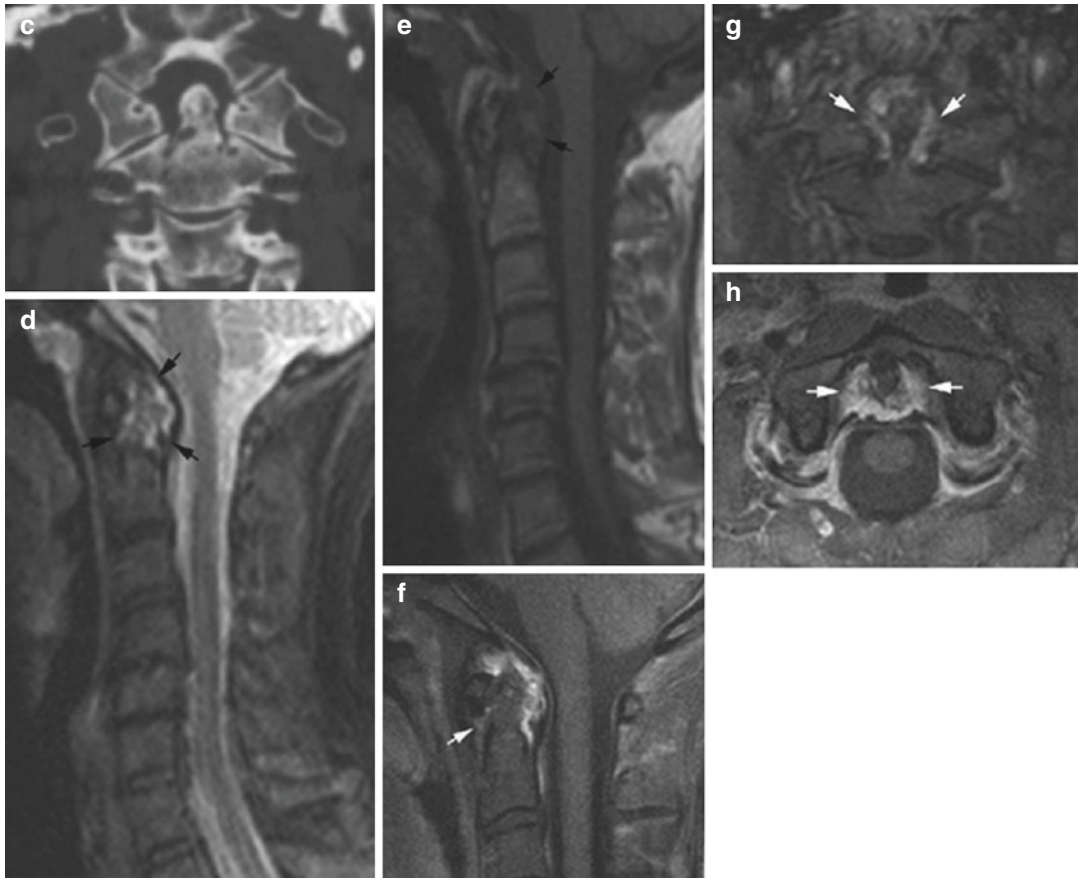

Fig. 6.1 (continued)

signal), erosions, and intense gadolinium enhancement (Fig. 6.4).

In addition to bilateral sacroiliitis, characteristic findings include an inflammatory enthesopathy of the vertebral body margins, at the insertion of the annulus fibrosus, termed *Romanus lesions*, which are of low signal on T1-weighted images and demonstrate increased signal on T2-weighted and STIR images (Fig. 6.5). "Squaring" of the vertebral bodies occurs, and syndesmophytes (thin ossification of the annulus fibrosis, uniformly low signal on MRI) develop, followed by sclerosis ("shiny corners," also uniformly low on T1- and T2-weighted images). As the disease progresses, fusion of the apophyseal and sacroiliac joints and ossification across the interspinous ligament occur, resulting in the characteristic "bamboo spine" (Fig. 6.6).

Notably, the thin, ossified syndesmophytes are often difficult to differentiate from the normal anterior and posterior longitudinal ligaments on MRI (Fig. 6.6). Also seen in chronic disease, chronic, fatty (increased T1 and T2 signal, low signal on fat-saturated and STIR sequences) changes develop at sites of prior inflammation, including the sacroiliac joint and the vertebral body entheses (Fig. 6.7).

Erosive changes within the intervertebral spaces (*Andersson lesions*) are the result of a non-infectious spondylodiscitis and more often detected on MRI than with radiographs [6–8]. These present in up to 60% of patients with AS and approximately 33% of patients with other forms of SpA [8]. Andersson lesions typically result in vertebral endplate and disc space edema (low T1, increased T2 and STIR signal)

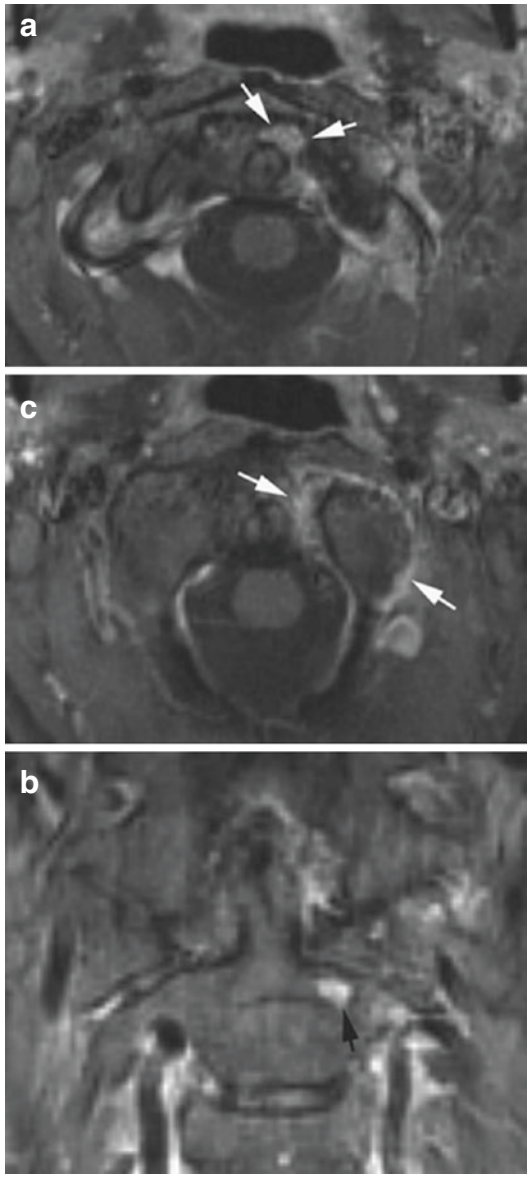

Fig. 6.2 A 42-year-old woman with RA and neck pain. Radiographs (not shown) were normal; post-contrast axial (**a** and **b**) and coronal (**c**) T1-weighted, fat-saturated images on the dens demonstrate enhancing pannus (white arrows) and subchondral enhancement (black arrow), both without erosions, indicating early, or pre-erosive, disease, expected to be occult on both radiographs and CT [6]

and ultimately result in erosion of the endplates themselves. Additional sites of inflammation and erosion include the costovertebral joints (at the posterior margins of the vertebrae) and facet joints (Figs. 6.8 and 6.9).

Chronic biomechanical complications include the development of osteoporosis, associated with compression fractures; pseudoarthrosis formation at an individual disc level due to excessive mechanical load/torsion in the setting of an otherwise ankylosed spine; and potentially life-threatening spinal fractures, which are often associated with minor trauma (Fig. 6.10).

Particularly in the setting of trauma, MRI has a valuable role in not only detecting radiographically occult fractures but also any significant soft tissue complications including epidural or paraspinal hematoma, cord hemorrhage, and additional, concomitant injuries such as ligamentous and muscular sprain/strain. It is important to note that the only MRI manifestation of trans-discal fracture, usually the result of a hyperextension mechanism, can be the accumulation of fluid in the disc space (increased T2 signal), sometimes with subtle increased disc space anteriorly.

Psoriatic Arthritis (PsA)

Also an autoimmune inflammatory arthropathy, PsA affects anywhere from 7% to 36% of patients with psoriasis and typically pre-dates the dermatologic manifestations by as many as 10 years. Approximately 50% of patients with extremity (hand, foot) manifestations of PsA will develop spine involvement (axial PsA) [2, 9]. The syndesmophytes in these patients are typically more voluminous than seen in cases of AS, extending laterally in addition to vertically between the margins of the vertebral bodies (Fig. 6.11). In addition, involvement of the sacroiliac joints is more often asymmetric.

Similar to RA, involvement of the cervical spine, specifically the anterior C1–C2 articulation, is most common. However, characteristic PsA changes include new bone formation, as opposed to erosion, in the region of the dens. While CT is the most sensitive modality in detecting bone formation, MRI demonstrates the precursor inflammatory changes (Fig. 6.12). Spinal involvement is most common in the cervical followed by lumbar regions; thoracic and costovertebral involvement is less common [7, 9].

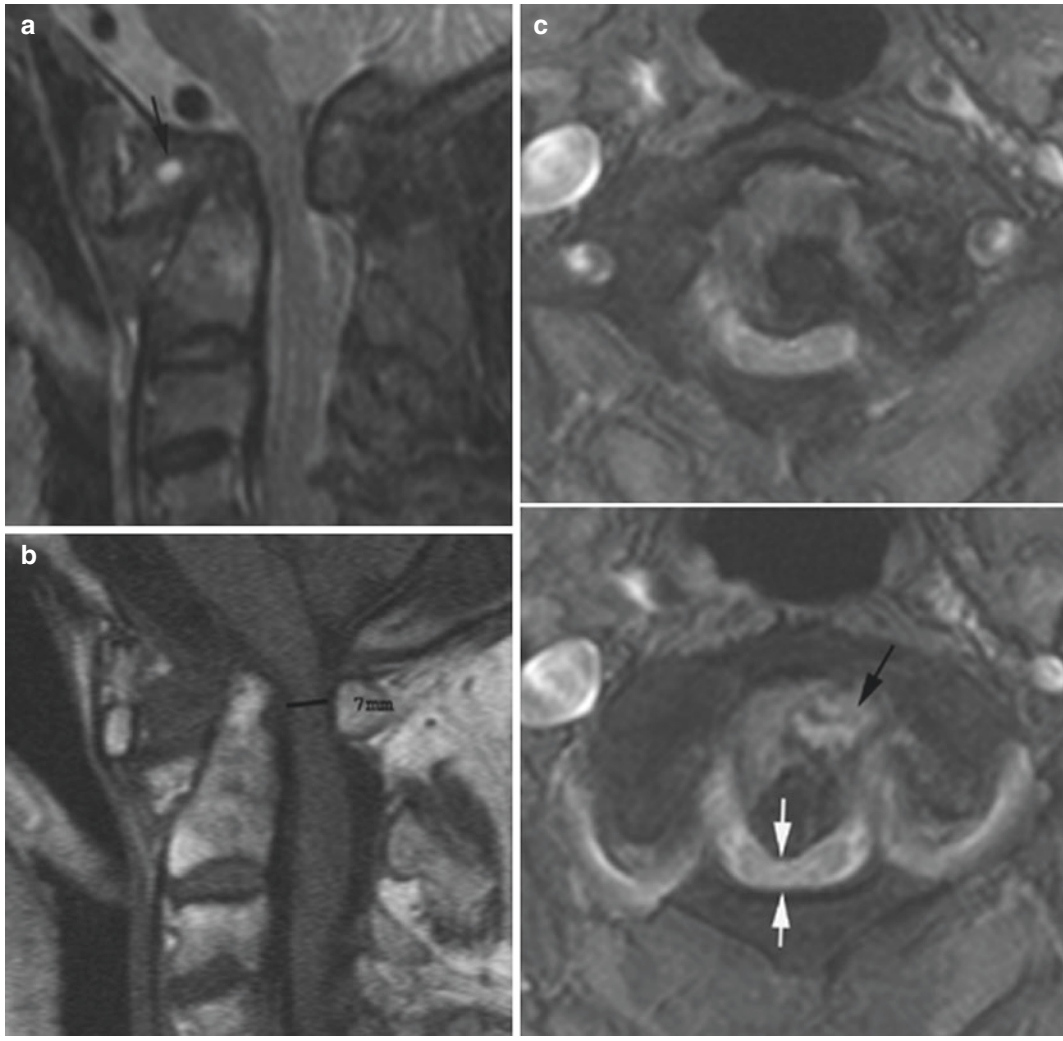

Fig. 6.3 A 69-year-old woman with RA and myelopathy. Sagittal STIR (**a**), T1-weighted (**b**), and axial T2-weighted, fat-saturated images of the dens (**c**) demonstrate erosion of the dens (image **a**, black arrow) with protrusion of the tip of the dens into the foramen magnum, resulting in stenosis of the canal and impingement of the upper cervical cord (image **b**). Note the heterogeneous appearance of the pannus (axial images **c**, black arrows), indicating both fibrotic and active inflammatory tissue. Also note the abnormally increased space between the anterior arch of C1 and the dens due to pannus [6]

Reactive Arthritis (ReA)

ReA develops as an immune reaction to gastrointestinal or genitourinary infections, typically *Chlamydia*, *Campylobacter*, *Salmonella*, *Shigella*, and *Yersinia*. It is often self-limiting, resulting in the acute inflammatory changes of enthesitis (low T1, increased T2 and STIR signal) at the vertebral body margins. A minority of individuals, typically those with HLA-B27, can develop a chronic, reactive arthritis. These individuals are classified as "AS elicited by infection." The imaging, including MRI, findings are indistinguishable from the other SpAs, though sacroiliitis and non-infectious spondylodiscitis are seen more often than in PsA and vertebral/sacroiliac ankylosis is uncommon [2, 7].

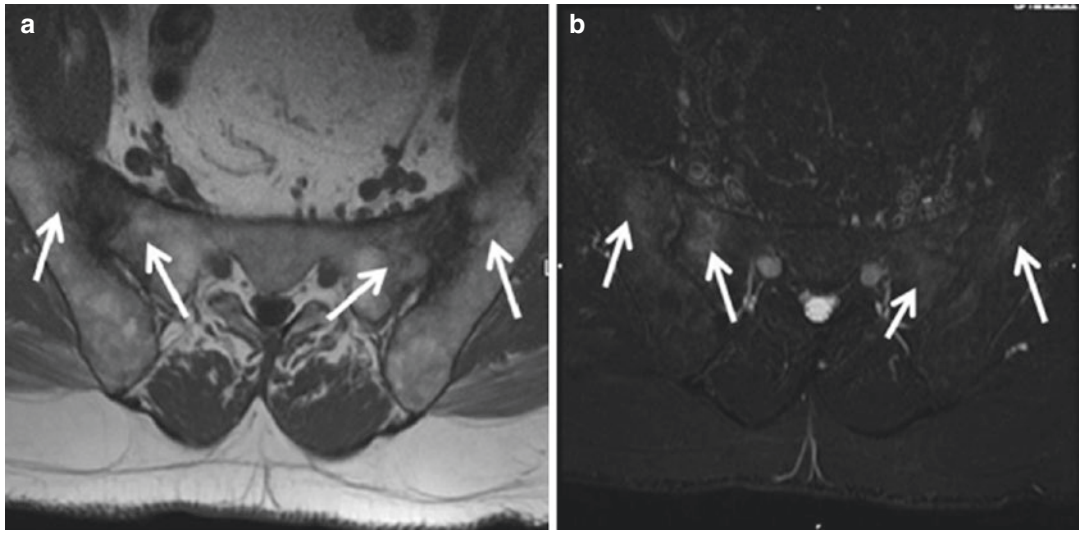

Fig. 6.4 A 58-year-old with AS. Axial (**a**) T1-weighted and (**b**) T2-weighted, fat-saturated MRI demonstrate symmetric, subarticular, bone marrow edema-like signal (dark on T1, bright on T2) due to active sacroiliitis. (With permission from [8])

Enteropathic Arthritis (EnA)

EA can affect up to 20% of patients with inflammatory bowel disorders. Diffuse osteoporosis is noted, in the setting of AS-like changes such as symmetric sacroiliitis and enthesitis, followed by chronic, osseous fusion of both the vertebrae and sacroiliac joints. On imaging, these changes are indistinguishable from typical AS. However, EnA either affects the extremities *or* the axial skeleton, including the sacroiliac joints and spine; but concomitant distribution is extremely rare [2, 7].

Additionally, predominant involvement of the interspinous ligaments and spinous processes in the axial skeleton has been described as a distinguishing feature of EnA (Fig. 6.13) [6, 7]. Interestingly, while the appendicular arthropathy parallels the course of the bowel involvement, the severity and progression of the spondylitis and sacroiliitis are completely independent of the intestinal disease [2].

Synovitis-Acne-Pustulosis-Hyperostosis-Osteitis (SAPHO) Syndrome

First described as a distinct syndrome in 1987, SAPHO is now considered by most authors as a spectrum entity, among a group of 50+ osteoarticular conditions with associated skin disorders, the most well-known of which are chronic recurrent multifocal osteomyelitis (CRMO) and SAPHO. Although the pathogenesis of SAPHO is unknown, proposed etiologies include infection with an agent of low virulence and an autoimmune mechanism, similar to the SpAs. The latter theory is supported by the fact that between 13 and 30% of patients with SAPHO are HLA-B27 positive and the syndrome manifestations are similar to those present in AS and PsA [10].

The unifying, and central, component of these conditions is an aseptic inflammatory osteitis which is often associated with dermatologic manifestations. Classic anatomic sites of involvement depend upon the age of the patient: adults typically manifest changes in the anterior chest wall (classically the sternoclavicular joints, seen in 65–90% of patients), intervertebral discs (non-infectious spondylodiscitis), sacroiliac joints, and, to a lesser extent, appendicular joints, while children manifest changes of the anterior chest wall (classically the clavicle) and symmetrical lesions of the long bones. The osteoarticular manifestations include synovitis, hyperostosis, and osteitis, the latter of which manifests as a chronic inflammatory reaction involving both the bony cortex and medullary cavity [11].

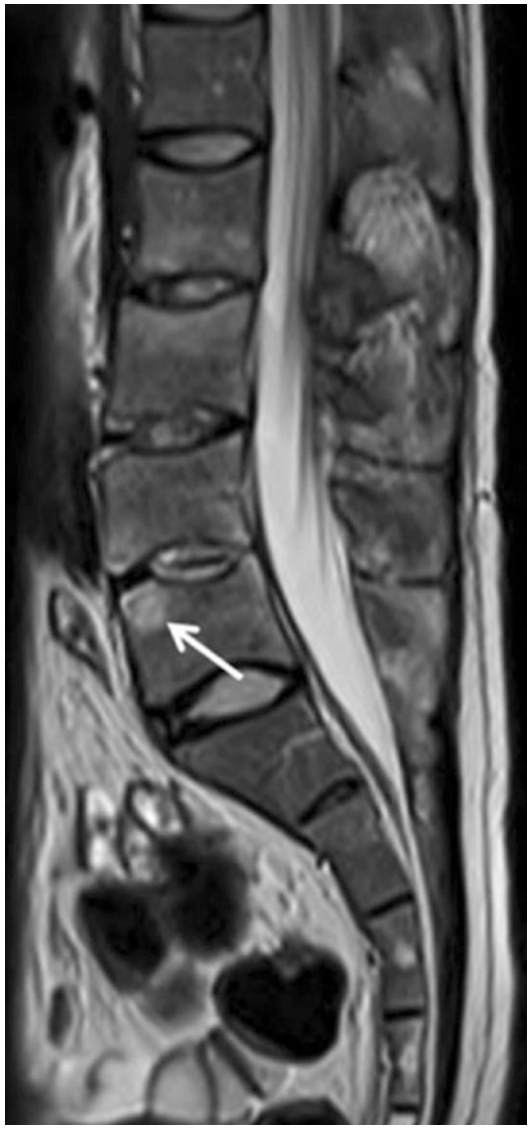

Fig. 6.5 Romanus lesion demonstrating characteristic bone marrow edema-like signal within the L5 vertebral body on a sagittal T2-weighted MRI sequence. (With permission from [8])

Radiographs and CT are used to demonstrate bony cortical thickening, narrowing of the medullary cavity, sclerosis, and osteolysis. MRI demonstrates intense, regional bone marrow edema, including enthesitis, pronounced periosteal soft tissue edema, and, when gadolinium contrast is administered, avid enhancement. Bony detail is less appreciable on MRI, though loss of the diffuse low signal at the outer margins of the bone indicates osteolysis [10].

Spine involvement is typically segmental, occurring most often in the thoracic portion, and is present in approximately 33% of adults. Initial stages of disease demonstrate a non-infectious, and non-specific, spondylodiscitis (Fig. 6.14) and enthesitis, best appreciated with MRI (bone marrow edema at the vertebral body corners and endplates, disc space edema), which demonstrate decreased T1 and increased T2 signal and associated enhancement. CT and radiographs often demonstrate vertebral endplate irregularity, erosions, and, later, sclerosis (Fig. 6.15). It is common to see complete obliteration of the disc spaces. In chronic cases, vertebral ankylosis across the disc spaces and facet joints has been described. Paravertebral ossification is typically unilateral and resembles that seen in PsA. Sacroiliac involvement is present in approximately 13–52% of cases and is usually asymmetric. Additionally, sclerotic changes predominating on the iliac side are said to be a distinguishing feature of SAPHO (Fig. 6.16) [10].

In pediatric patients, spinal involvement is less common and often limited to a single disc level, manifesting as a non-infectious spondylodiscitis (Fig. 6.17), with associated enthesitis, including vertebral body corner and endplate bone marrow edema (decreased T1, increased T2 signal, enhancement with intravenous contrast), erosion, and sclerosis [10].

Diffuse Idiopathic Skeletal Hyperostosis (DISH)

Also referred to as Forestier disease, DISH is an idiopathic condition, with an estimated prevalence of 4–7% in the adult population. It is characterized by the development of relatively florid, "flowing" *ossifications* between the anterolateral margins of at least four continuous vertebral bodies [11]. Involvement of the T4–T11 levels is most common (Fig. 6.18), though cervical and lumbar involvement is well described. Additional

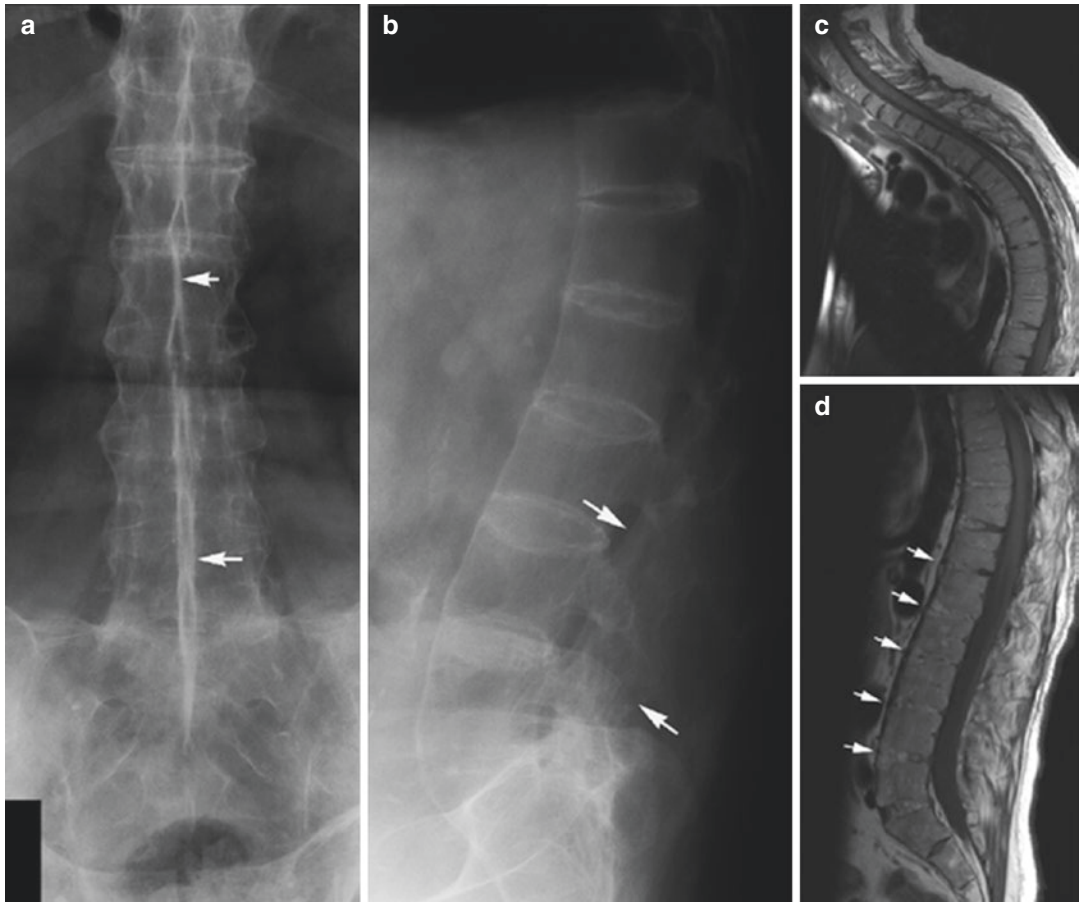

Fig. 6.6 A 55-year-old man with advanced AS. (**a**) AP and (**b**) lateral radiographs of the lumbar spine demonstrate the characteristic squared vertebral bodies, syndesmophytes, and fusion of the facet joints (arrows), resulting in a "bamboo spine." Corresponding sagittal, T1-weighted MRI (**c** and **d**) also reveals the same appearance; note the uniformly low-signal syndesmophytes (arrows) which are difficult to differentiate from the appearance of normal anterior and posterior longitudinal ligaments on MRI [6]

features include ossification of the anterior and posterior longitudinal ligaments (OALL and OPLL, respectively, most often in the cervical spine), paraspinal connective tissue, ligamentum flavum (most often in the lumbar spine), and annulus fibrosus of the intervertebral discs. Bridging ossifications of the sacroiliac joints are often present (Fig. 6.19) [12].

In this regard, DISH can have a similar appearance to PsA and ReA. However, in contrast to the SpAs, ankylosis of the facet, sacroiliac, and costovertebral joints is not a feature of DISH. Additionally, also in contrast to the SpAs and crystal deposition diseases, there is relatively preserved intervertebral disc spaces and the absence of spondylodiscitis, calcium deposition, and erosive/inflammatory disease. Finally, osteoporosis is not a feature of DISH [12].

DISH characteristically results in mild pain and stiffness but can also be associated with radicular and myelopathic signs and symptoms, depending on the extent and location of the disease. Radiographs and CT are usually adequate in delineating the presence and extent of spinal involvement; MRI is utilized in evaluating potential neural impingement [11].

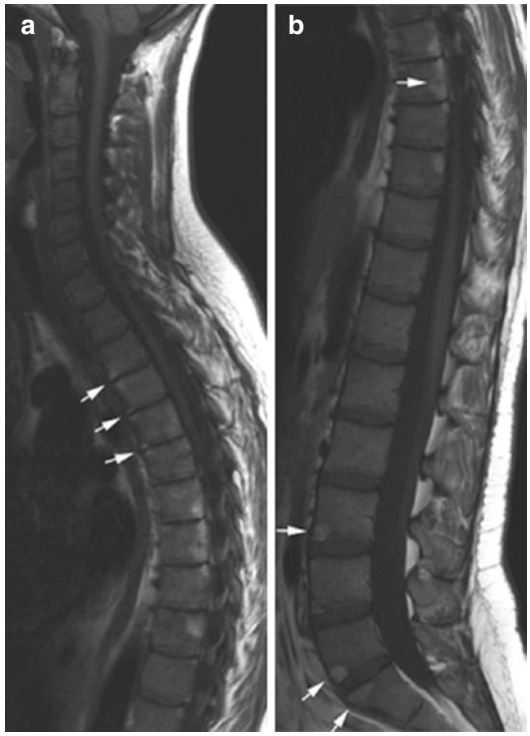

Fig. 6.7 Chronic (post-inflammatory) AS. Sagittal, T1-weighted images of the (**a**) cervicothoracic and (**b**) lumbar spine demonstrate fatty marrow changes at the vertebral entheses (arrows) [6]

Similar to the SpAs, acute spinal fractures can have significant consequences in the setting of DISH. Fractures typically occur through the mid-vertebral bodies, at the vertebral attachments of the flowing ossifications, and either above or below fused vertebral segments (Fig. 6.20). As with evaluation of trauma in other conditions, MRI is routinely utilized for soft tissue involvement (ligamentous disruption, epidural or paraspinal hematoma, cord or nerve root injury; Fig. 6.21), while CT excels at characterizing the osseous extent of injury. Similar to the SpAs, pseudoarthrosis formation can be a complication of vertebral fracture. Also similar to the SpAs, fracture through the disc itself can sometimes be extremely subtle, with the accumulation of edema/fluid (increased T2 signal) and relatively minor, if any, distraction [12].

Crystal Deposition

Gout

A disorder of purine metabolism, with a genetic predisposition, gout can result in the deposition of uric acid, in the form of monosodium urate crystals, in any of the soft tissues of the body, typically joints and tendons. The urate crystals cause an acute, inflammatory reaction; while ongoing deposition results in the formation of nodular, inflammatory pseudo-masses, known as tophi, and soft tissue destruction including the bone and cartilage. As a rule of thumb, tophaceous deposition, and therefore gout arthropathy, develops in individuals with long-standing (10+ years) hyperuricemia [8, 13].

Spinal and sacroiliac involvement is less common than the more typical distribution of the hands and feet, but is well documented [13, 14]. Within the spine, lumbar involvement is most common. Tophaceous deposition can occur in the epidural space, the intervertebral discs themselves (non-infectious spondylodiscitis), and the facet joints, resulting in erosions at each of these locations and the formation of subchondral cysts (Fig. 6.22). The tophi themselves can result in spinal cord and nerve root compression. The presence of neurologic symptoms, including myelopathy or radiculopathy, warrants MRI evaluation. Contrast administration is helpful in delineating smaller tophaceous depositions and inflammatory changes [8, 13].

As with other forms of sacroiliitis and inflammatory spondylotic changes, there are osseous erosion, periarticular and articular marrow edema (low T2, increased T2 and STIR signal), and intense enhancement with intravenous contrast. The tophi themselves aid considerably in determining gout as the etiology of the inflammatory changes and demonstrate variable MRI signal (usually intermediate to low T1 and low, intermediate, or high T2 signal), depending upon the relative abundance of fibrosis, inflammatory cellularity, and vascularization within a given tophaceous deposition. As such, tophi can demonstrate either peripheral, heterogeneous, or intense,

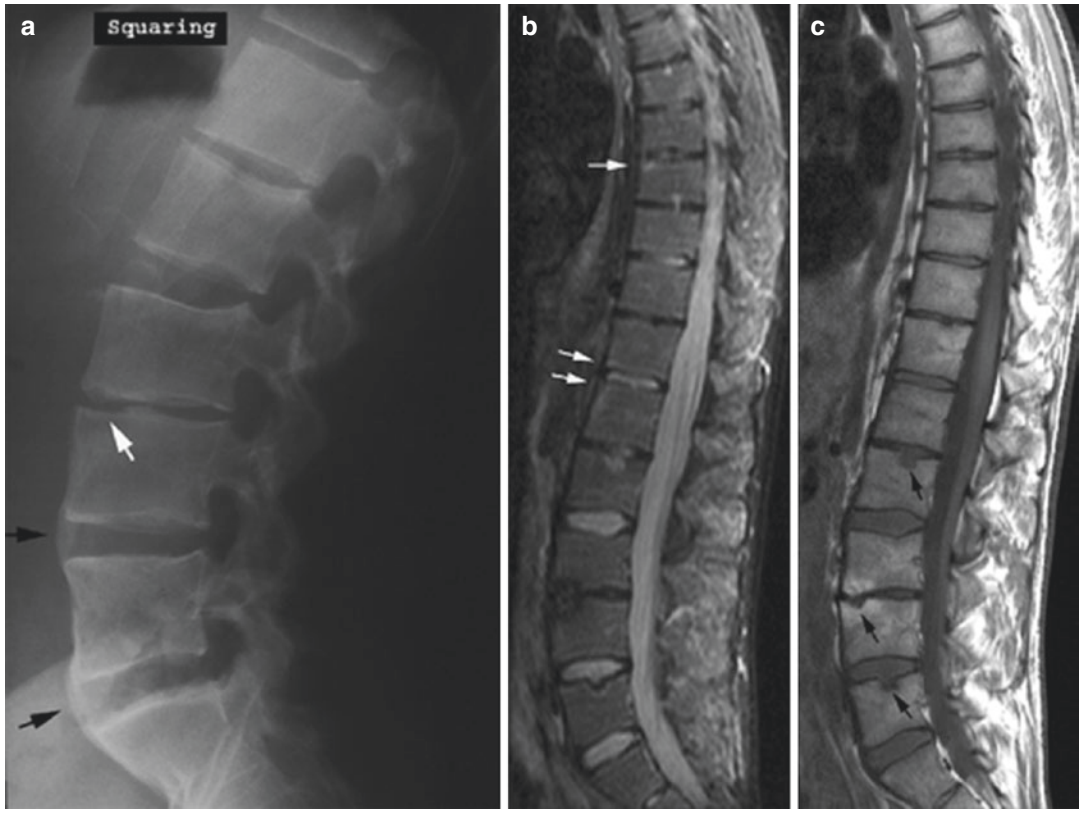

Fig. 6.8 Lateral radiograph (**a**) of the lumbar spine in a 29-year-old with AS reveals not only syndesmophytes (black arrows) but Andersson lesions at L3–L4 (endplate erosions, white arrow). Corresponding sagittal (**b**) STIR and (**c**) post-contrast, T1-weighted, fat-saturated images demonstrate corresponding edema and enhancement at L3–L4 (black arrow) [6]

homogeneous enhancement. Differential considerations include amyloid deposition [8, 13].

Calcium Pyrophosphate Deposition Disease (CPPD)

CPPD is a metabolic disorder, slightly more common in females, and with an age-proportionate prevalence, in which calcium pyrophosphate dihydrate crystals are deposited in the articular and periarticular soft tissues. This can be asymptomatic (referred to as chondrocalcinosis) or associated with episodic painful, inflammatory episodes (referred to as pseudo-gout). The resulting chondral calcification most often affects the hyaline and fibrocartilage of the non-weightbearing (shoulder, elbow, wrist, patellofemoral and metacarpal-phalangeal) joints in a fairly symmetric fashion and has a characteristic, linear or sheet-like, appearance [13].

Involvement of the spine is less common than the extremities and is also less often symptomatic. When present, CPPD results in a non-specific non-infectious spondylodiscitis (Fig. 6.23) and can also involve the facet and apophyseal joints. Cervical involvement has been described as more common than thoracic and lumbar. A rather specific manifestation of CPPD arthropathy in the C1–C2 region has been termed the "crowned dens syndrome," in which there is erosion of the dens in the presence of calcified, or partially calcified, inflammatory soft tissue, either with a characteristic linear or punctate pattern, which can be associated with pain and/or instability (Fig. 6.24) [13].

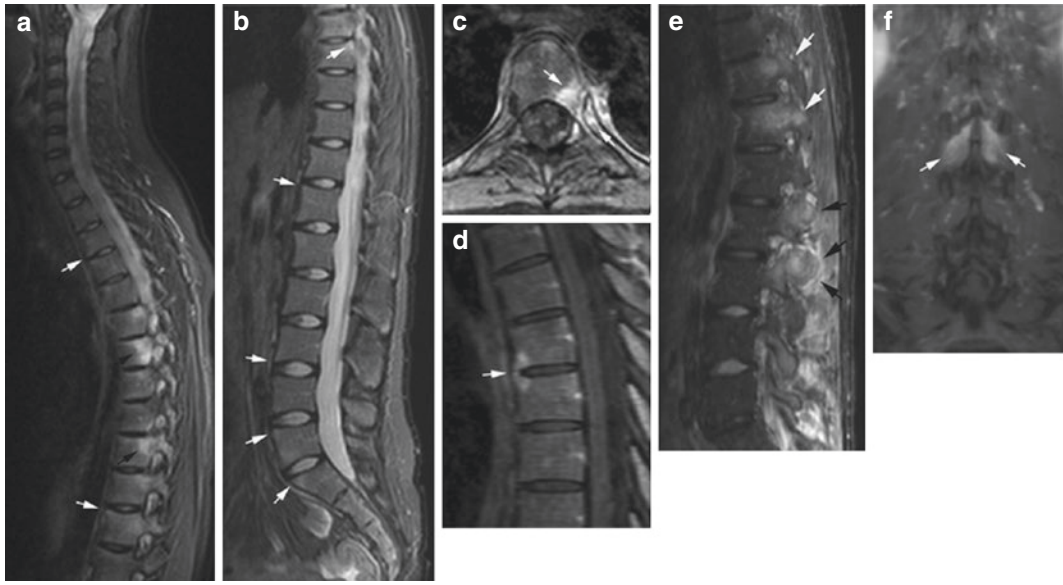

Fig. 6.9 MRI of the cervical, thoracic, and lumbar spine performed 3 years prior to radiographically apparent AS. Sagittal STIR (**a** and **b**) images show areas of bone marrow edema within the anterior vertebral bodies (white arrows) consistent with Romanus lesions. More posteriorly (black arrows) correspond to costovertebral inflammation, which are well-delineated on an axial, STIR image (white arrow, **c**). Following intravenous gadolinium contrast administration, T1-weighted, fat-saturated images (**d** and **e**) show there are anterior, subenthesial enhancement (white arrow in (**d**)) and pronounced enhancement of the facet joints (white arrows in (**e**)) and interspinous ligament (black arrows in (**e**) and white arrows in (**f**)) [6]

Typically, the calcification associated with CPPD is not visible with routine MRI of the spine. Certain sequences, such as gradient echo, can result in a *"blooming" or susceptibility artifact* which accentuates the calcification as areas of pronounced and uniformly low signal on T1- and T2-weighted sequences. However, calcifications associated with CPPD have also been described as demonstrating intermediate and even increased signal on T1-weighted sequences [13]. Following gadolinium contrast administration, enhancement of the inflammatory changes in the periarticular and articular soft tissues and adjacent bone is routinely observed [8, 13].

Given the non-specific nature of the findings, correlation with radiographs and CT, which demonstrate the characteristic chondral calcification and less common findings such as ligamentous and tendon calcification, is helpful. Specifically with regard to CPPD-related spondylodiscitis, a potential mimic is intervertebral disc vacuum phenomenon (a manifestation of age-related spondylosis), which also demonstrates uniformly low signal on T1- and T2-weighted MRI sequences. Unfortunately, both intervertebral disc gas (in the setting of vacuum phenomenon) and CPPD-related calcification result in susceptibility (or "blooming") artifact on gradient echo sequences. In these cases, correlation with radiographs and CT is needed [14].

Calcium Hydroxyapatite Deposition Disease (Ca-HADD)

Ca-HADD is an idiopathic condition, also with a prevalence that increases with age, in which calcium hydroxyapatite is deposited within or, in close proximity to, the joints of the body, often alongside or within tendons and bursae. Potential etiologies include chronic, repetitive microtrauma or necrotic connective tissue

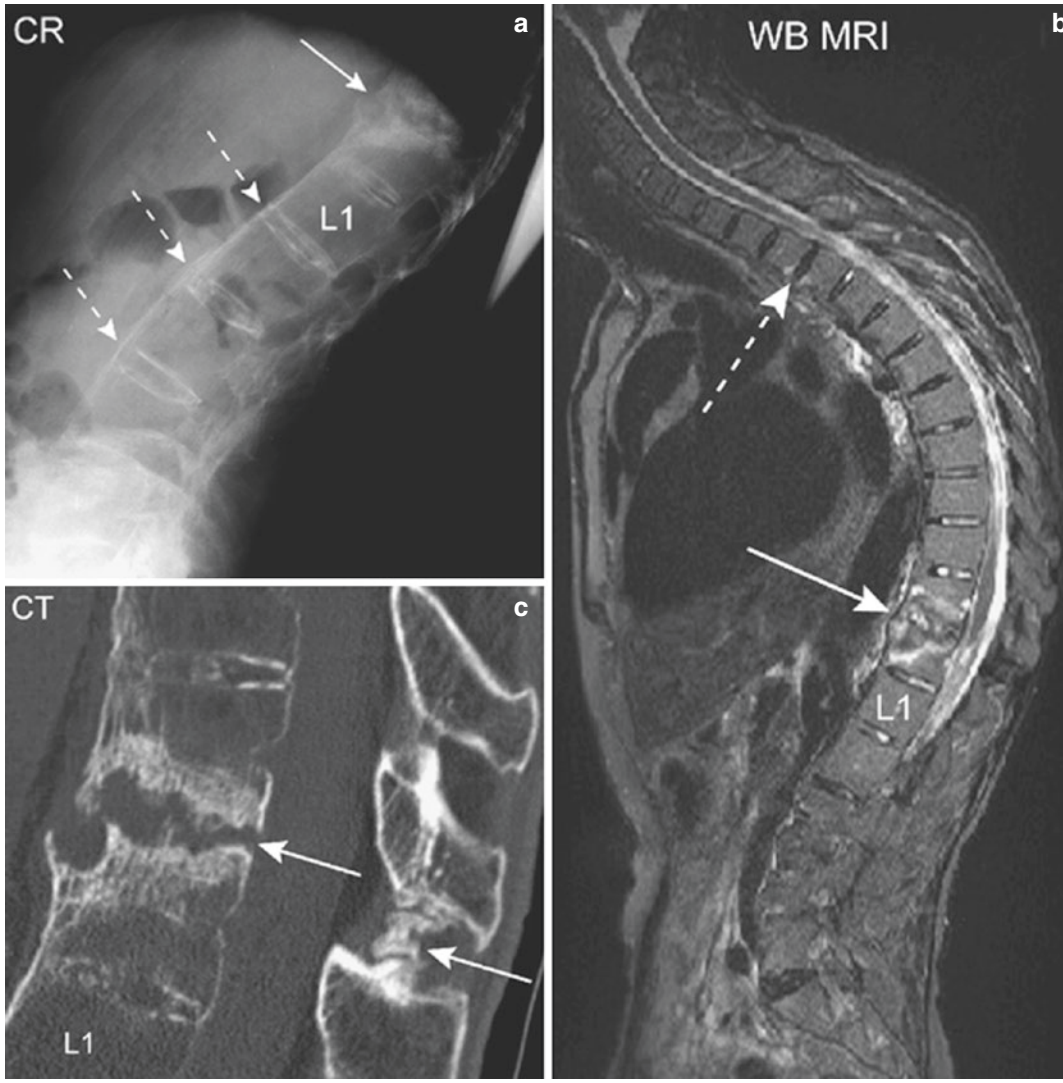

Fig. 6.10 A 57-year-old man, with no recollection of prior trauma and with an approximately 32-year history of AS, being evaluated for TNF α-inhibitor therapy. (**a**) Lateral radiograph shows the characteristic syndesmophytes (dashed arrows) and pseudoarthrosis formation at T11–T12 (solid arrow). Corresponding sagittal STIR (**b**) reveals a Romanus lesion (dashed arrow) and bone marrow and disc space edema along with bony erosion associated with the pseudoarthrosis (solid arrow). A follow-up CT (**c**) more precisely delineates the bony erosion, sclerosis, and chronic periosteal reaction, characteristic of pseudoarthrosis (white arrows), as a result of remote prior trans-spinal fracture through the syndesmophytes, disc, and posterior elements. (With permission from [2])

changes. Although the characteristic *amorphous, "cloud-like," or "toothpaste," calcification* can be deposited anywhere in the body, the shoulders, hips, elbows, and knees are most common. Therefore, the appearance of the calcification is distinct from CPPD (see above). Spinal involvement has also been described, including the intervertebral discs (non-infectious spondylodiscitis; Fig. 6.25), epidural space, and interspinous region. A characteristic location of involvement is within, or adjacent to, the cervical prevertebral soft tissues and longus colli muscle, typically at the C2 level (Fig. 6.26) [8, 13].

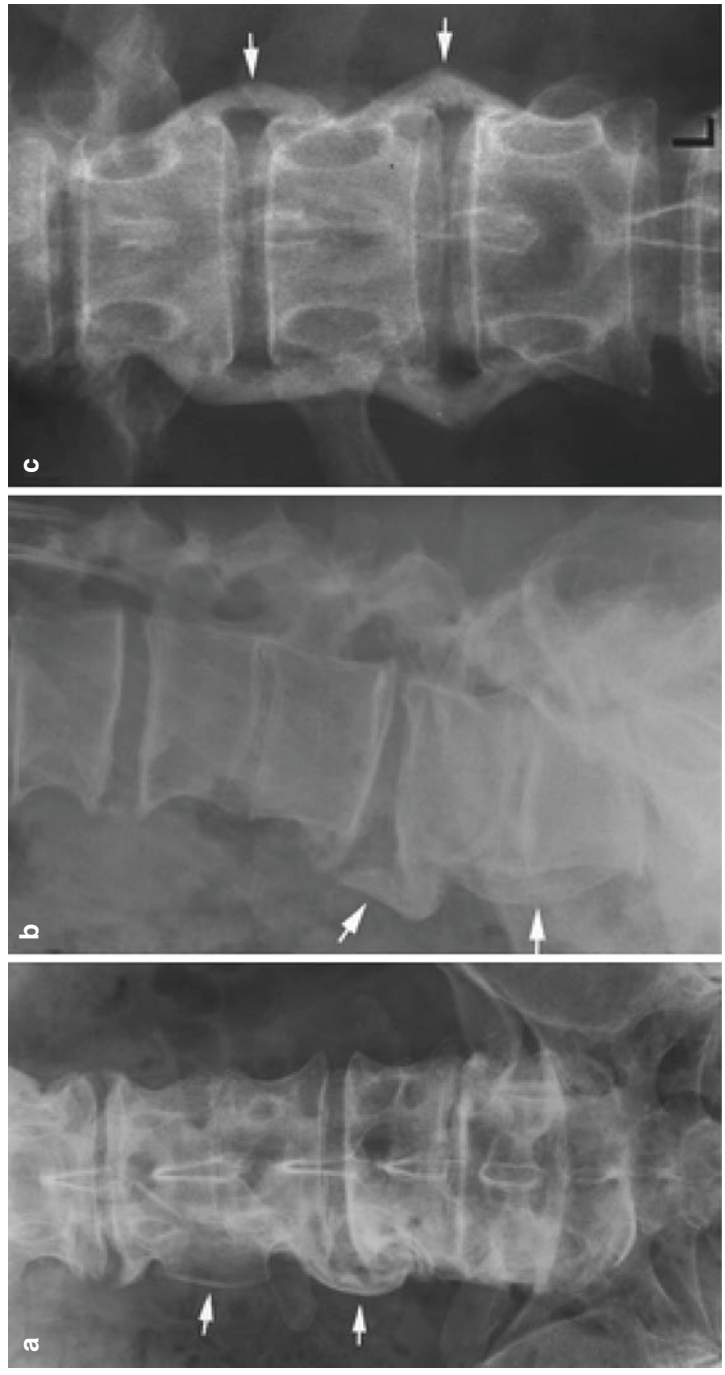

Fig. 6.11 A 48-year-old man with PsA; (**a** and **c**) and (**b**) lateral radiographs of the lumbar spine notable for characteristic syndesmophytes (arrows) which are more voluminous and laterally projecting than those of AS [6]

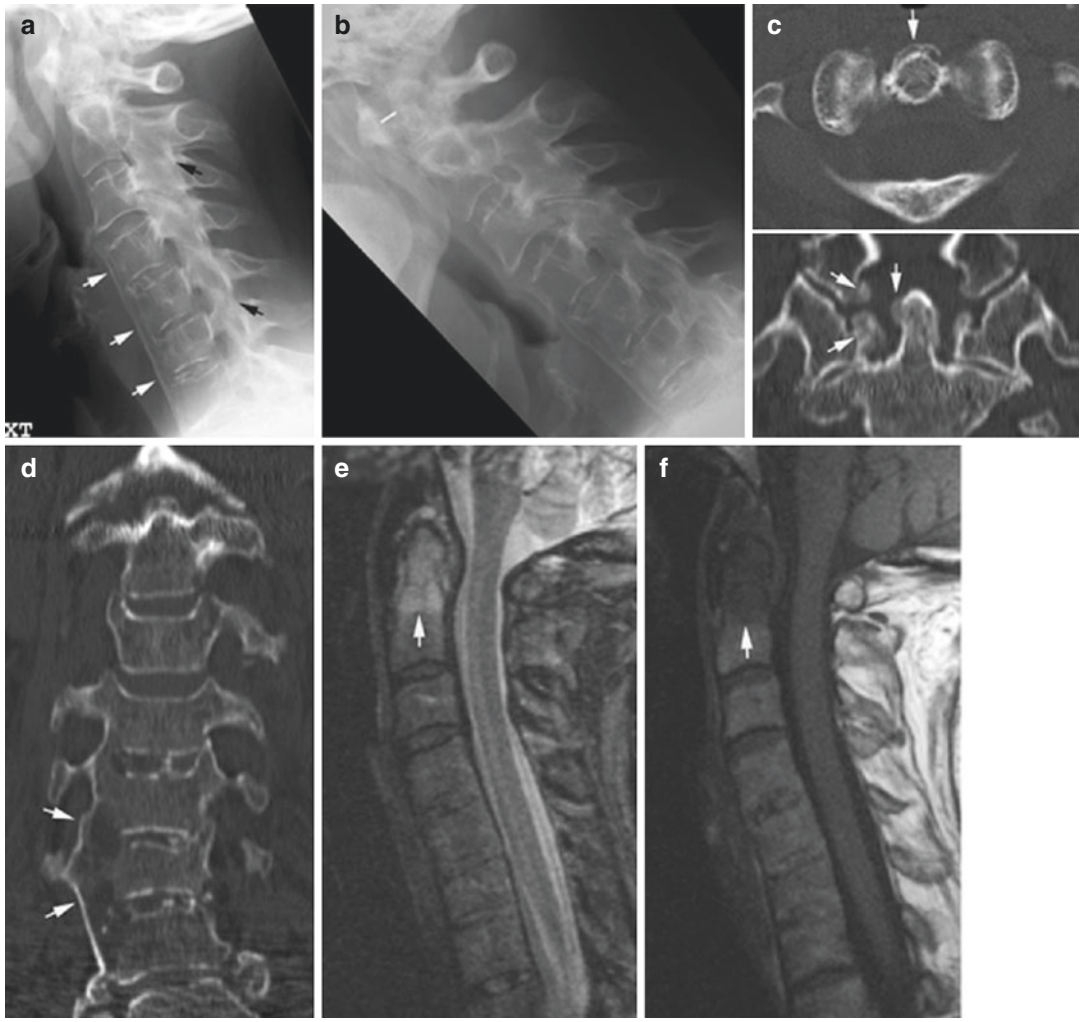

Fig. 6.12 Lateral cervical radiographs obtained in neutral position (**a**) and with flexion (**b**) in a 61-year-old woman with PsA demonstrate thick, anterior syndesmophytes (white arrows), fusion of the facet joints (black arrows), and abnormal increase in the distance between the anterior arch of C1 and the dens with flexion (4 mm, white line in **b**), indicating instability. Corresponding axial (**c**) and coronal (**d**) CT images demonstrate new bone formation, voluminous syndesmophytes (white arrows), and the absence of erosion, typical of PsA. Sagittal STIR (**e**) and T1-weighted (**f**) cervical MRI reveals corresponding marrow and adjacent soft tissue edema due to inflammatory changes (white arrow). Note the prominent anterior syndesmophytes are not readily apparent [6]

The Ca-HA itself can result in an intense, painful inflammatory reaction, particularly if it migrates from within a confined tissue, such as a tendon, into an adjacent tissue, bursa, or joint space. In fact, the inflammatory reaction can be so intense, so as to mimic soft tissue infection [8, 14].

On MRI, the calcification is uniformly low in signal intensity on T1- and T2-weighted sequences. Any associated soft tissue inflammatory changes will demonstrate the characteristic avid enhancement and T2-weighted signal, sometimes with associated bursitis, joint effusion, and adjacent bone marrow edema. Sometimes, corre-

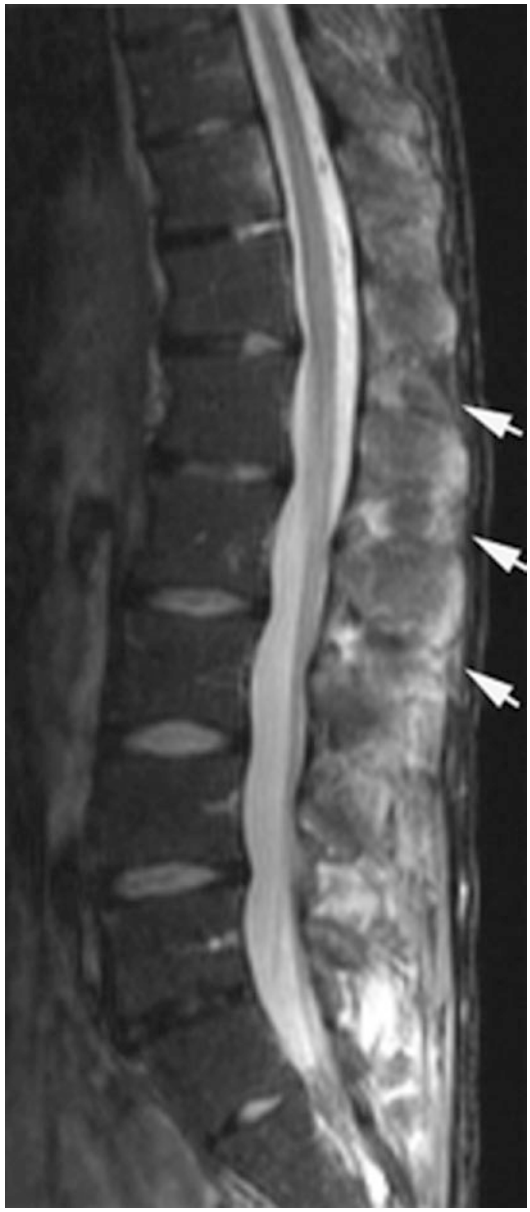

Fig. 6.13 A 27-year-old man with ulcerative colitis and diffuse back pain. Sagittal STIR of the thoracolumbar spine demonstrates pronounced subenthesial and ligamentous edema involving the spinous processes and interspinous ligament (white arrows). There is relatively minimal activity involving the posterior vertebral bodies [6]

lation with radiographs and CT is extremely helpful in delineating the underlying presence and appearance of the calcification. As the CaHA itself is slowly resorbed, the inflammatory changes and symptoms also subside [8, 13, 14].

Differentiating Infectious Spondylodiscitis and Modic Lesions from Spondyloarthropathies and Crystal Deposition

Differentiating the non-infectious spondylodiscitis and pseudoarthroses associated with the SpAs and crystal deposition arthropathies from infectious spondylodiscitis often requires correlation with patient history, laboratory results, and comparison/follow-up imaging.

Infectious spondylodiscitis more often demonstrates circumferential (anterior, posterior, bilateral) inflammatory changes, paraspinal and/or epidural collections, and single-level involvement. Andersson lesions (SpA-associated spondylodiscitis) and spondylodiscitis secondary to crystal deposition, by contrast, are often multifocal and without the florid soft tissue inflammatory changes associated with infection (Fig. 6.27). Additionally, characteristic arthropathy of the extremities is sometimes present, which aids in diagnosis [7].

Modic lesions are uniformly associated with other degenerative changes of the intervertebral discs, such as desiccation, vacuum phenomenon, and loss of height, while Andersson lesions are often present with other findings of SpA [7] (Fig. 6.27).

In the case of inflammatory spondyloarthropathy related to crystal deposition, additional characteristic changes are often helpful. Gout arthropathy demonstrates tophi, which are typically intermediate to low on T1-weighted sequences and demonstrate low, intermediate, or high T2 signal with either peripheral, heterogeneous, or confluent enhancement following intravenous gadolinium contrast [8]. Isolated or initial spinal involvement with gout is extremely rare, and radiographic evaluation of the extremities and correlation with serum uric acid levels is often performed [7].

Calcium pyrophosphate deposition cannot be directly visualized with MRI, and correlation with radiographs or CT, demonstrating characteristic hyaline and fibrocartilage calcification in a linear pattern, is helpful. Furthermore, CPPD arthropathy is extremely common in the smaller

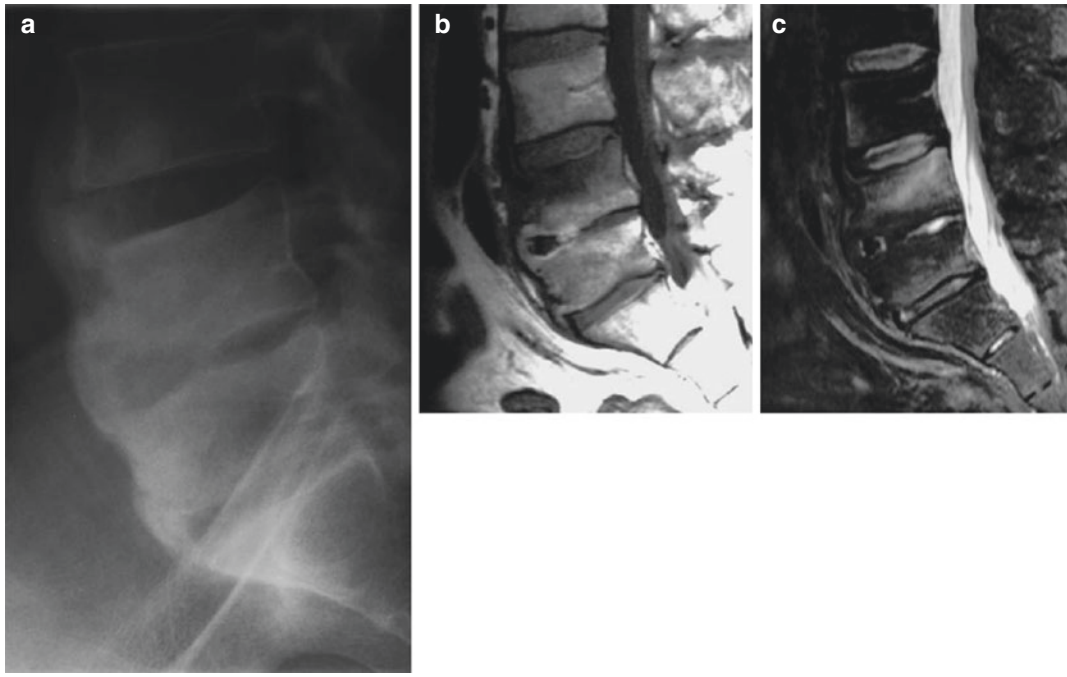

Fig. 6.14 Lateral radiograph of the lower lumbar spine (**a**) and corresponding sagittal T1-weighted (**b**) and STIR (**c**) MRI demonstrate non-specific prominent anterior syndesmophytes and a spondylodiscitis at L4–L5 in this patient with a history of SAPHO and low back pain. (With permission from [10])

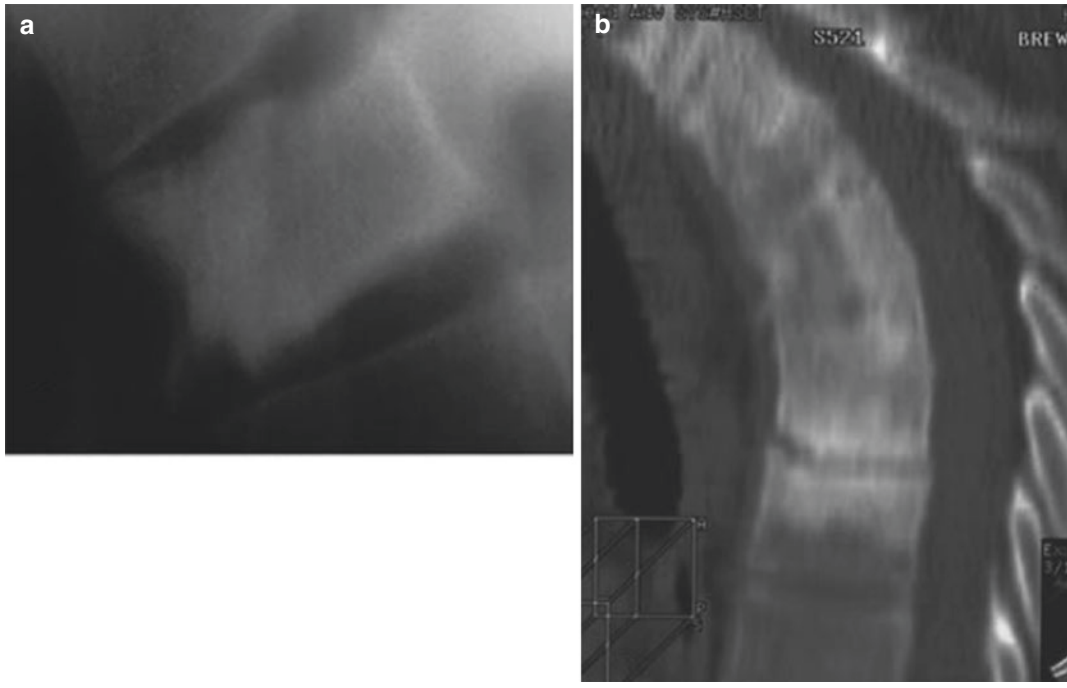

Fig. 6.15 An 18-year-old male with SAPHO; sagittal tomogram (**a**) demonstrates T4 vertebral body sclerosis. A follow-up sagittal, reformatted CT of the thoracic spine (**b**) performed 17 years later demonstrates resolved T4 vertebral body sclerosis, now with 4 level ankylosis with spondylodiscitis/pseudoarthrosis at T6–T7. (With permission from [10])

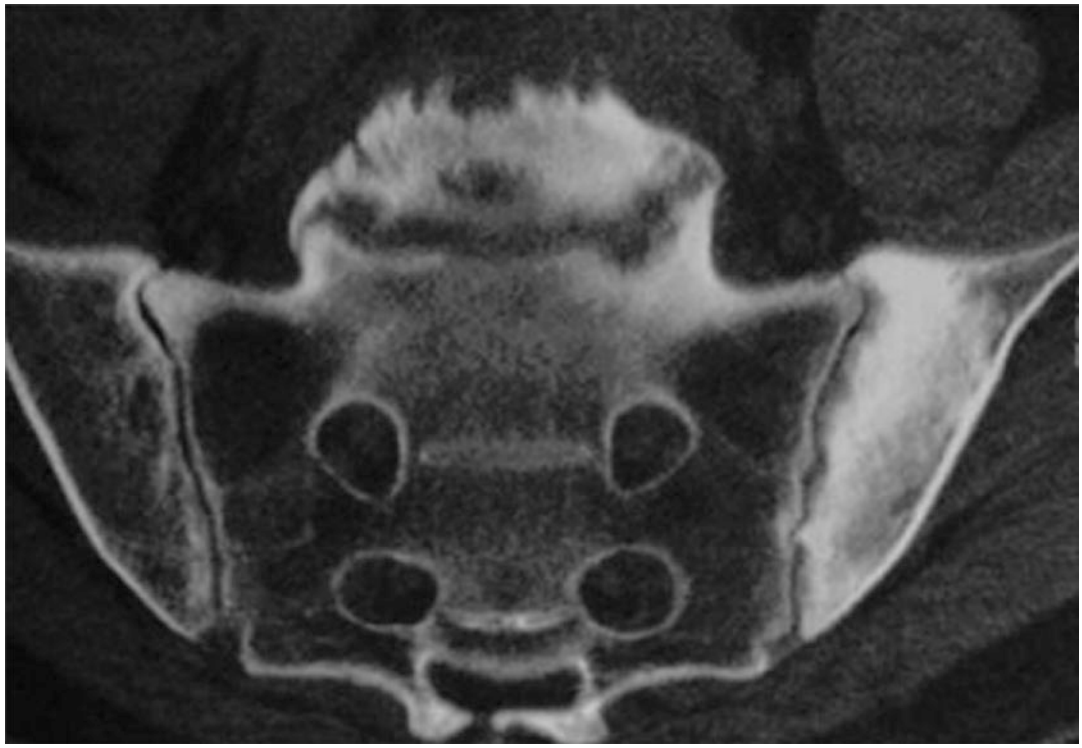

Fig. 6.16 Axial CT of the sacrum demonstrates unilateral sacroiliitis with iliac-sided sclerosis in a patient with SAPHO. (With permission from [10])

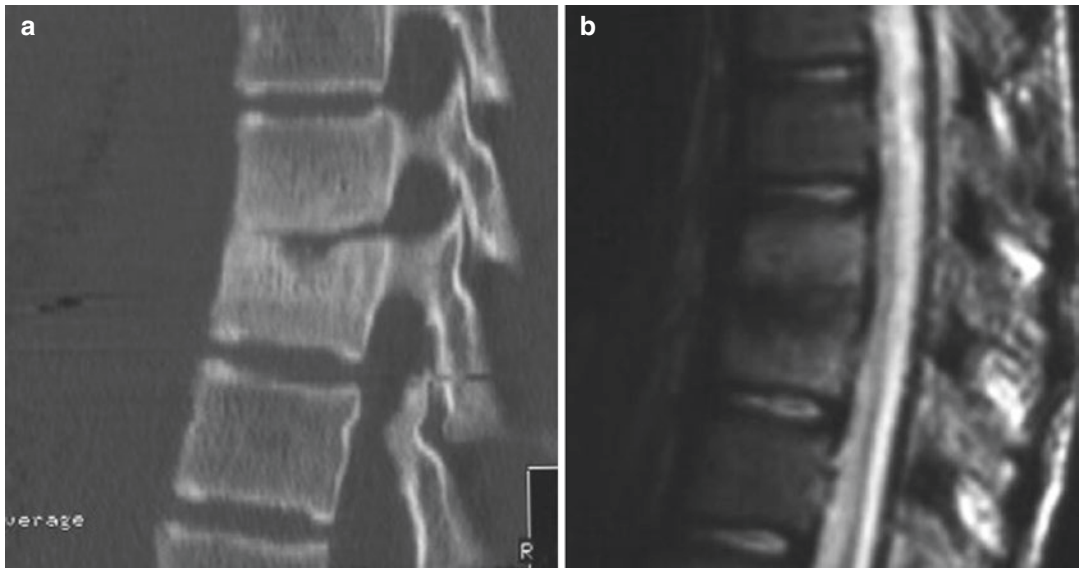

Fig. 6.17 (**a**) Sagittal, reformatted CT of the thoracic spine demonstrates single-level, subtle endplate irregularity, consistent with non-infectious spondylodiscitis. Corresponding sagittal, T2-weighted MRI (**b**) cannot delineate the erosion as clearly but has the advantage of revealing pronounced edema, indicative of inflammation. (With permission from [10])

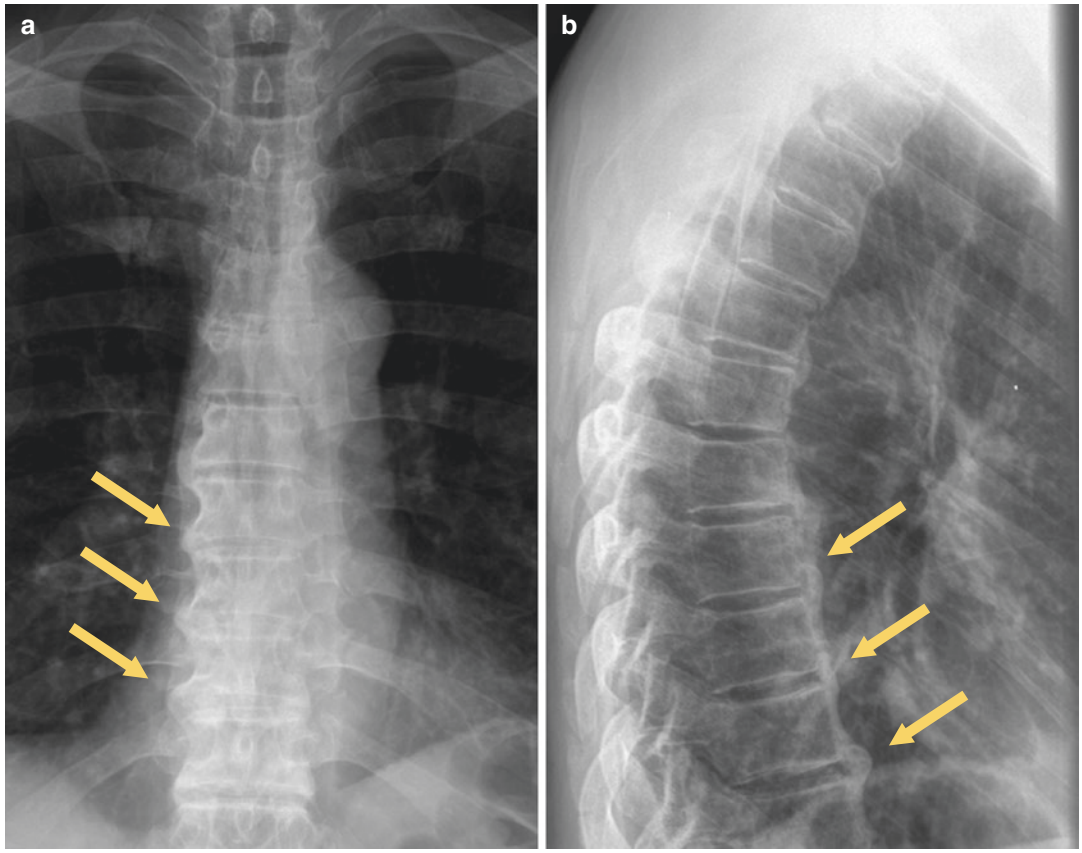

Fig. 6.18 AP (**a**) and lateral (**b**) radiographs of the thoracic spine demonstrate the characteristic anterolateral "flowing ossifications" (arrows) representing DISH

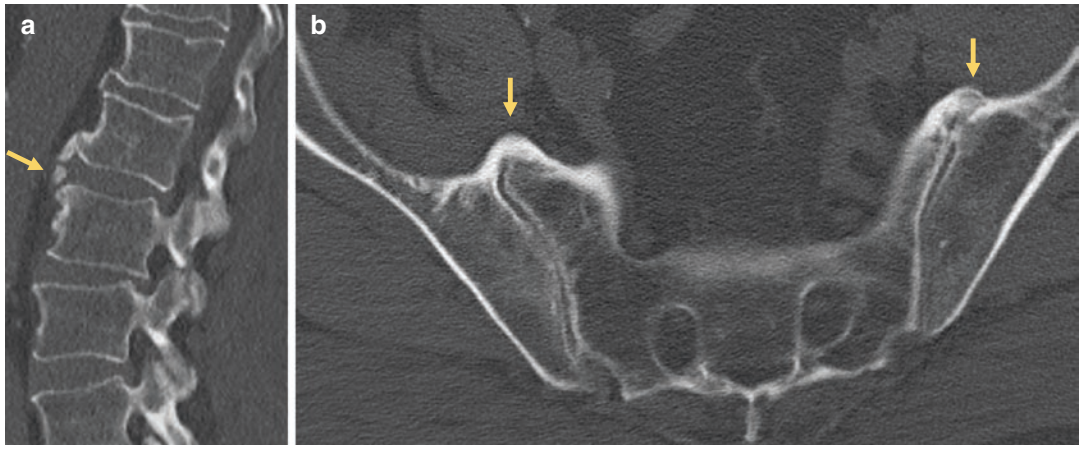

Fig. 6.19 Sagittal (**a**) and axial (**b**) CT images of a 73-year-old with DISH demonstrate the characteristic hyperostotic changes of the anterior cervical disc space and sacroiliac joints (arrows)

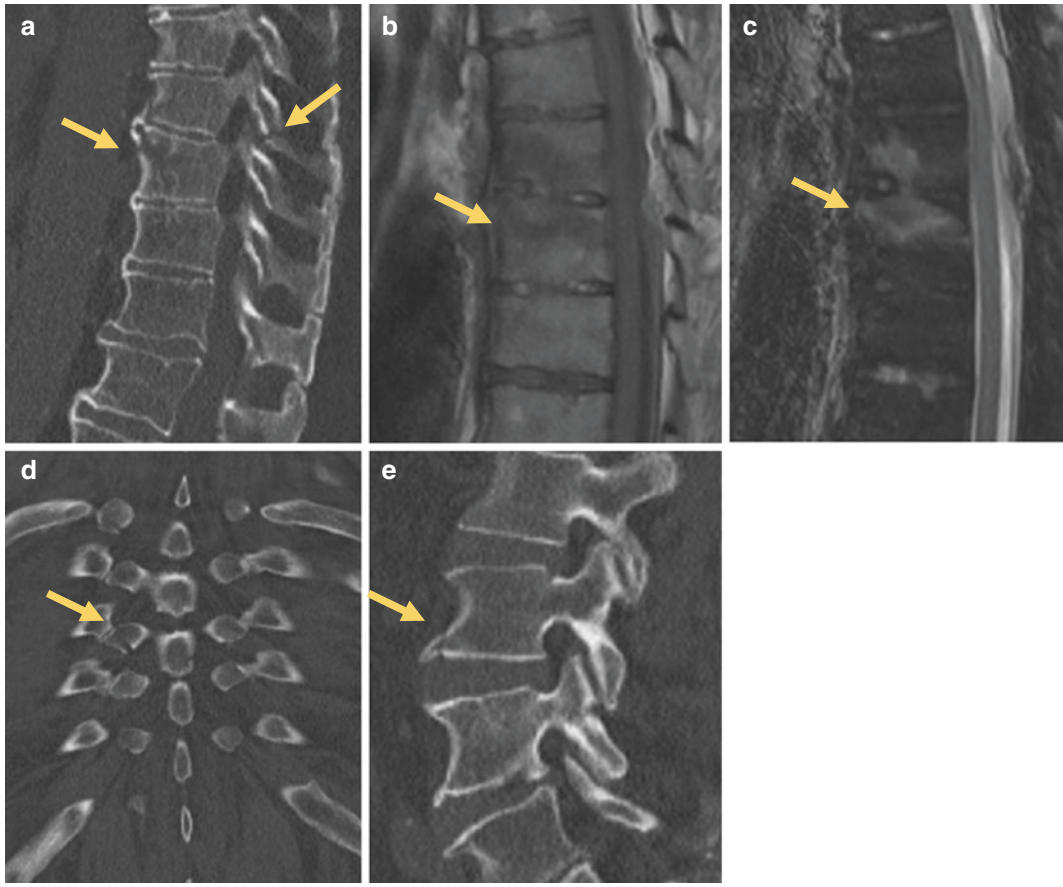

Fig. 6.20 A 52-year-old man with DISH following trauma. Sagittal CT (**a**), T1-weighted (**b**), and T2-weighted, fat-saturated MR (**c**) images demonstrate a transverse fracture through the T9 vertebral body with extension into the posterior elements of T8 (arrows) and a small amount of anterior distraction. The MRI has the added benefit of revealing a small amount of epidural hemorrhage and evaluating the spinal cord. Additional coronal CT image (**d**) further demonstrates the involvement of the posterior elements, and sagittal CT image of the lumbar spine (**e**) demonstrates an additional compression fracture of the anterior, inferior L3 vertebral body endplate

joints of the upper extremity, which is readily diagnosed with radiographs [8].

Calcium hydroxyapatite has a characteristic amorphous, uniformly low signal on MRI sequences, often with intense surrounding inflammatory changes, including enhancement. Smaller foci of hydroxyapatite deposition are not visible with MRI, and radiographic or CT correlation is helpful. HADD can be isolated to the spine, and therefore evaluation of the appendicular skeleton is not necessarily indicated [8].

Pigmented Villonodular Synovitis (PVNS)

PVNS is an uncommon, benign, but potentially locally aggressive, idiopathic neoplasia in which villous and/or nodular (mass-like) overgrowth of the synovium occurs, typically within the large joints and bursae, particularly the knee and hip. An extra-articular variant, known as giant cell tumor of the tendon sheath, is more common in the hands and feet. Spinal involvement can occur,

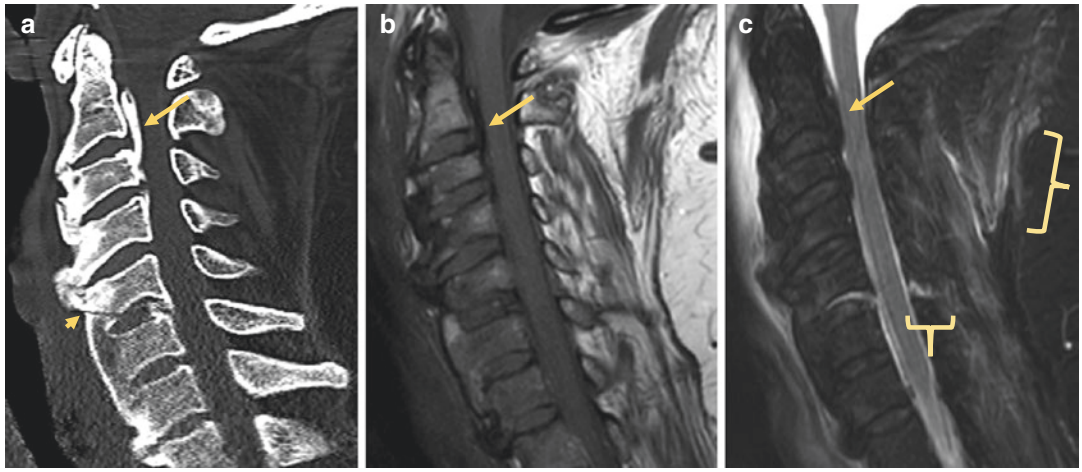

Fig. 6.21 A 53-year-old man with DISH, following fall off a ladder. Sagittal CT (**a**) demonstrates characteristic flowing hyperostosis anteriorly with a fracture of the C5 vertebral body anteriorly (arrow head) and segmental ossification of the posterior longitudinal ligament (yellow arrow). Corresponding sagittal T1- (**b**) and fat-saturated, T2-weighted (**c**) MRI demonstrates edema in the interspinous ligament at C5–C6 and posteriorly (brackets), consistent with musculotendinous sprain/strain. Note that ossification of the posterior longitudinal ligament at C6–C7 is more difficult to appreciate on MRI (yellow arrows)

favoring the cervical region, but is less common. More than 90% of spinal PVNS involves the posterior elements, particularly the facet joints (Fig. 6.28), paraspinal soft tissues, foramina, pedicles, and lamina, while spinous process involvement is exceedingly uncommon [15–17].

CT most often demonstrates a well-defined lytic lesion of the bone, due to an intermediate density soft tissue mass; calcification is not a feature of PVNS, and the presence of calcification indicates an alternative etiology (see next paragraph). MRI further characterizes the soft tissues; PVNS most often demonstrates intermediate T1 and intermediate to low T2 signal, with heterogeneity within the lesion itself. Sometimes, gradient echo sequences will demonstrate "blooming" or susceptibility artifact due to *hemosiderin deposition* within the mass. With newer, fast spin echo, and intermediate density MR imaging techniques, this is less often noted. Heterogeneous enhancement is common with larger lesions (>2 cm); smaller lesions often enhance homogeneously [18–20].

Differential considerations in the spine include osteoblastoma, aneurysmal bone cyst, giant cell tumor of the bone, and synovial cyst of the facet joint. Each of these lesions has unique imaging features; in most cases, biopsy is required [19, 20].

Synovial Osteochondromatosis (SOC)

SOC is a relatively uncommon, benign, but potentially recurrent, mono-articular, neoplastic process resulting in the formation of islands of chondrocytes within a proliferative synovial lining. Most often, it occurs in the large appendicular joints, such as the shoulder, knee, and hip, and presents in patients in their third through fifth decades. As the chondrocytes get extruded into the joint space, they form osteocartilaginous articular bodies, resulting in the characteristic appearance of numerous, similarly sized articular bodies, modest synovial proliferation, and, in some cases, pressure erosions and remodeling of the intra-articular portions of the bone [21, 22].

Spinal involvement has been reported in a handful of cases; approximately half of the cases occur in the cervical region, and most (approximately 96%) involve the facet joints,

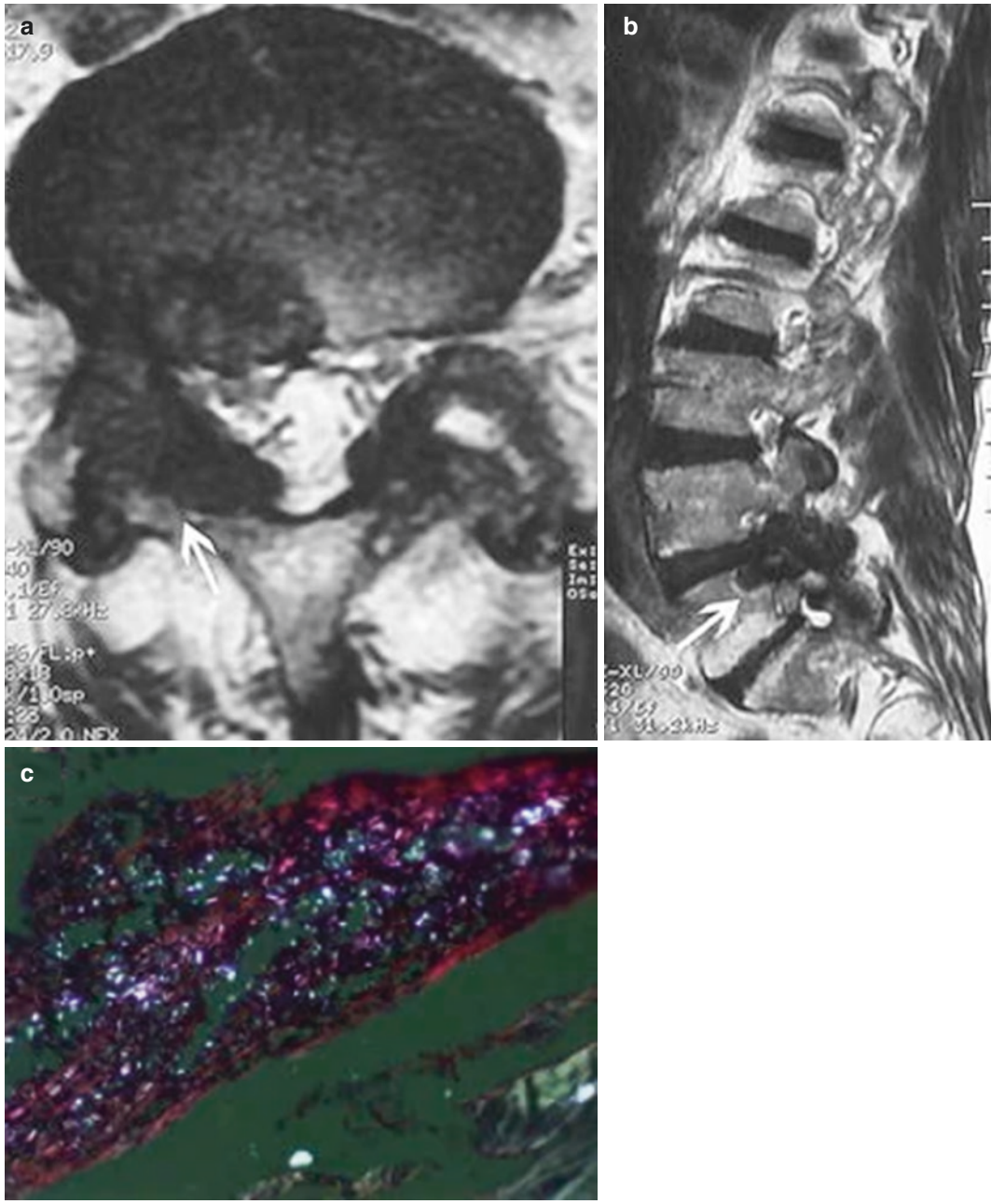

Fig. 6.22 Axial (**a**) and sagittal (**b**) T2-weighted MRI of a 77-year-old female with right lower extremity radiculopathy and long-standing gout arthropathy of the hands and feet. Amorphous, diffuse low-signal material associated with the right L4–L5 facet joint, posterior disc space, and adjacent vertebral body (white arrows) is consistent with tophus deposition. Corresponding axial CT (**c**) demonstrates sclerotic erosions and bony remodeling due to chronic, progressive tophus deposition (white arrow). (With permission from Springer: Hasturk AE, Basmaci M, Vural C (2012) Spinal Gout Tophus: a very rare cause of radiculopathy. European Spine Journal, supplement 4: pages 400–403)

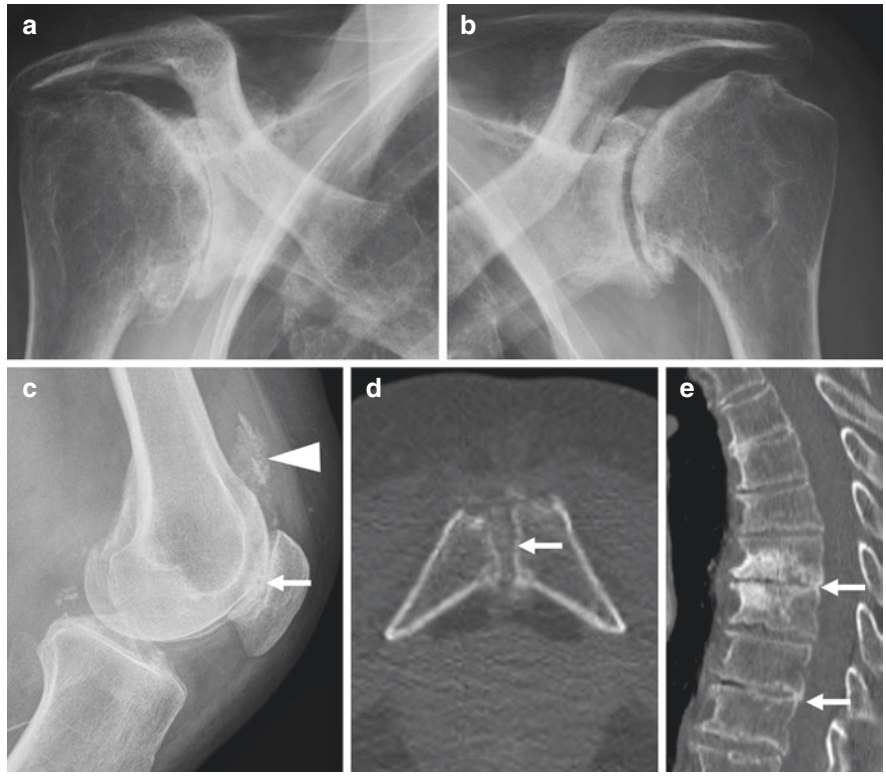

Fig. 6.23 A 79-year-old woman with known CPPD arthropathy, including the bilateral shoulders (**a** and **b**) and patello-femoral articulation (arrow, **c**) of the knee. Typical calcium pyrophosphate deposition, with a linear, sheet-like appearance in the suprapatellar recess (arrowhead, **c**) and visible at the pubic symphysis (arrow, **d**) with axial CT. Sagittal CT (**e**), performed for unrelated reasons, reveals a non-specific spondylodiscitis with associated erosion and sclerosis (white arrows). (With permission from Elsevier)

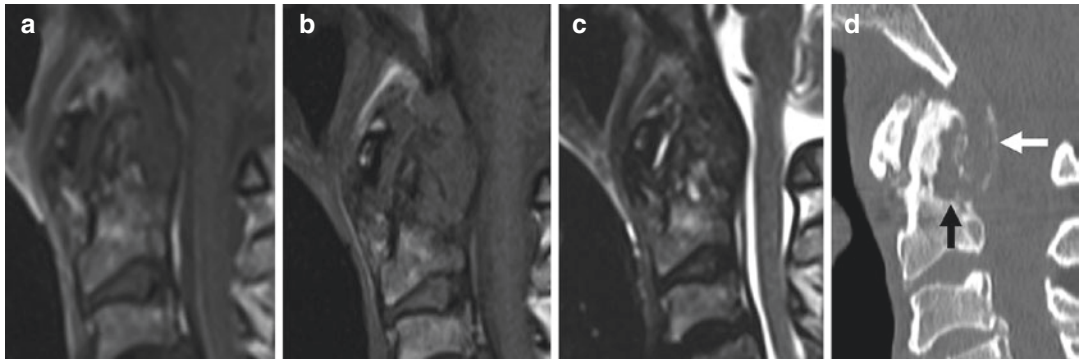

Fig. 6.24 A 62-year-old with CPPD and chronic neck pain. Sagittal T1-weighted, pre- (**a**) and post-contrast (**b**), and T2-weighted (**c**) images demonstrate pronounced erosion/destruction of the C1–C2 articulation and dens with diffuse, low-signal material and very little enhancement. Corresponding CT (**d**) demonstrates erosion of the dens (black arrow) and foci of calcifications (white arrow) suggestive of CPPD involvement. (With permission from Elsevier)

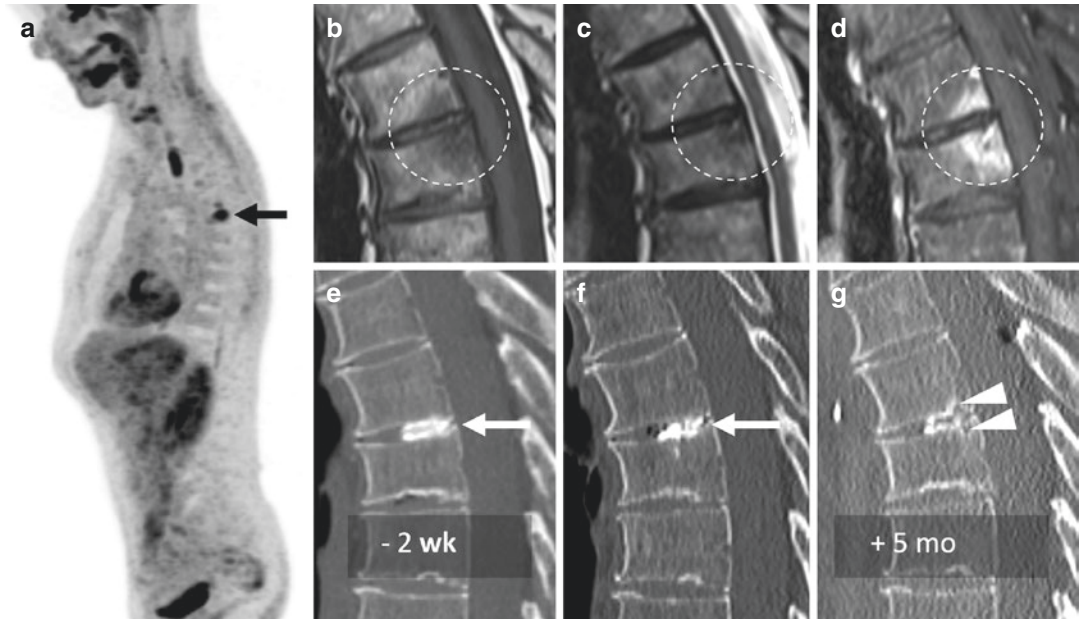

Fig. 6.25 A 56-year-old man undergoing PET scan (**a**) for staging of esophageal carcinoma, which demonstrates increased activity in the thoracic spine (black arrow), suspected to be metastatic disease. Corresponding T1-weighted (**b**), T2-weighted (**c**), and T1-weighted, post-contrast (**d**) sagittal MRI demonstrates changes indicative of an inflammatory enthesitis, as opposed to a mass. Corresponding sagittal CT images, obtained over a course of 5 months (**e**–**g**), demonstrates amorphous disc space calcification, which evolves to more organized, and partially resorbed, calcification, typical of Ca-HADD. (With permission from Elsevier)

demonstrating some degree of erosive change. Notably, almost half (44%) of the described cases lack discernable calcification, and a minority of cases (28%) demonstrated the classic appearance of discrete, round calcifications. In the absence of calcification, SOC presents as a non-specific mass centered about, or adjacent to, one of the facet joints. Intra-canalicular lesions are typically associated with signs and symptoms of neural compression [22, 23].

Smaller lesions, and those without extensive calcification, may be obscured on routine spine radiographs; CT is often used to delineate the extent of spine involvement and accurately detect calcification, which can be absent or quite faint. On MRI, SOC demonstrates a heterogeneous or homogeneous appearance, depending on the presence and degree of calcification. In the absence of significant calcification, SOC is intermediate to low signal on T1-weighted sequences and low, intermediate, or increased signal on T2-weighted images. In the presence of significant calcification, MRI signal becomes uniformly low, with associated susceptibility artifact on gradient echo sequences. Most often, approximately 83% of the time, SOC demonstrates avid, peripheral enhancement (either thin or nodular); more confluent enhancement is noted in cases where SOC resembles a non-specific, synovial mass in the absence of discrete bodies or calcification (Fig. 6.29) [21–23].

Due to the variable appearance and low rates of prevalence in the spine, SOC can be difficult to distinguish from synovial cysts of the facet joints. Synovial cysts are always associated with osteoarthritic changes of the facet joints and, even when complex, demonstrate peripheral enhancement. Calcification is not a typical feature of synovial cysts [18].

Secondary SOC refers to the development of SOC-like changes (calcified articular bodies) in the setting of primary osteoarthritis or remote prior articular trauma. In the spine, SOC has been described in the setting of chronic isthmic

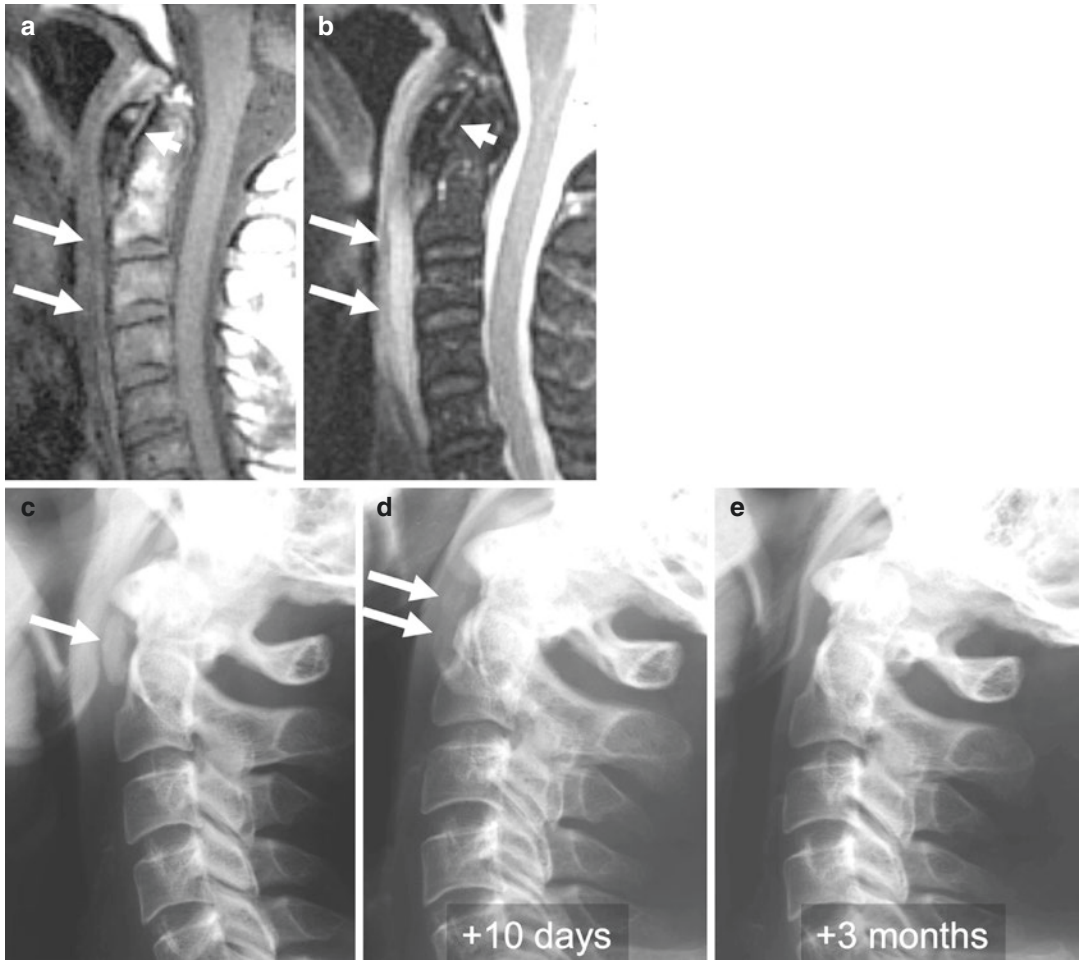

Fig. 6.26 A 60-year-old with painful swallowing. Sagittal T1-weighted (**a**) and STIR (**b**) MRI depicts abnormal thickening and inflammatory changes (white arrows) of the prevertebral soft tissues, specifically the longus colli muscles. Also note the presence of a C1–C2 arthropathy (short arrow). Sequential lateral radiographs (**c**–**e**) performed over 3 months demonstrate characteristic Ca-HA deposition, undergoing progressive regression

Fig. 6.27 A 41-year-old with spondyloarthritis: (**a**) sagittal T1-weighted, (**b**) T2-weighted, and (**c**) STIR MRI of the lumbar spine demonstrates bone marrow edema involving the vertebral endplates, surrounding the T12–L1 disc, compatible with non-infectious spondyloarthropathy (Andersson lesions, yellow arrows). A 27-year-old with spondyloarthritis: (**d**) sagittal T1-weighted, (**e**) T2-weighted, and (**f**) STIR MRI of the thoracic spine demonstrates Romanus lesions (yellow arrows) spanning T7–T12, consistent with SpA. Note the absence of degenerative changes in the disc itself, which effectively excludes Modic type I changes. Also note the absence of more florid inflammatory changes of the disc and surrounding soft tissues, which makes infection less likely. In contrast, a 71-year-old with back pain: sagittal T1-weighted (**g**), T2-weighted (**h**), and STIR (**i**) MRI of the lumbar spine demonstrates endplate edema (yellow arrows) and osteophytes (white arrows) with associated disc desiccation and loss of height (arrowhead), all consistent with Modic I degenerative changes. Finally, a 26-year-old with back pain: axial (**g**) and sagittal T1-weighted, fat-saturated MRI both before (**h**) and following intravenous gadolinium contrast administration (**i**) demonstrates pronounced vertebral and surrounding, paraspinal (white arrows), and posterior (yellow arrows) soft tissue enhancement along with endplate erosion (asterisk). These findings are all consistent with an infectious spondylodiscitis

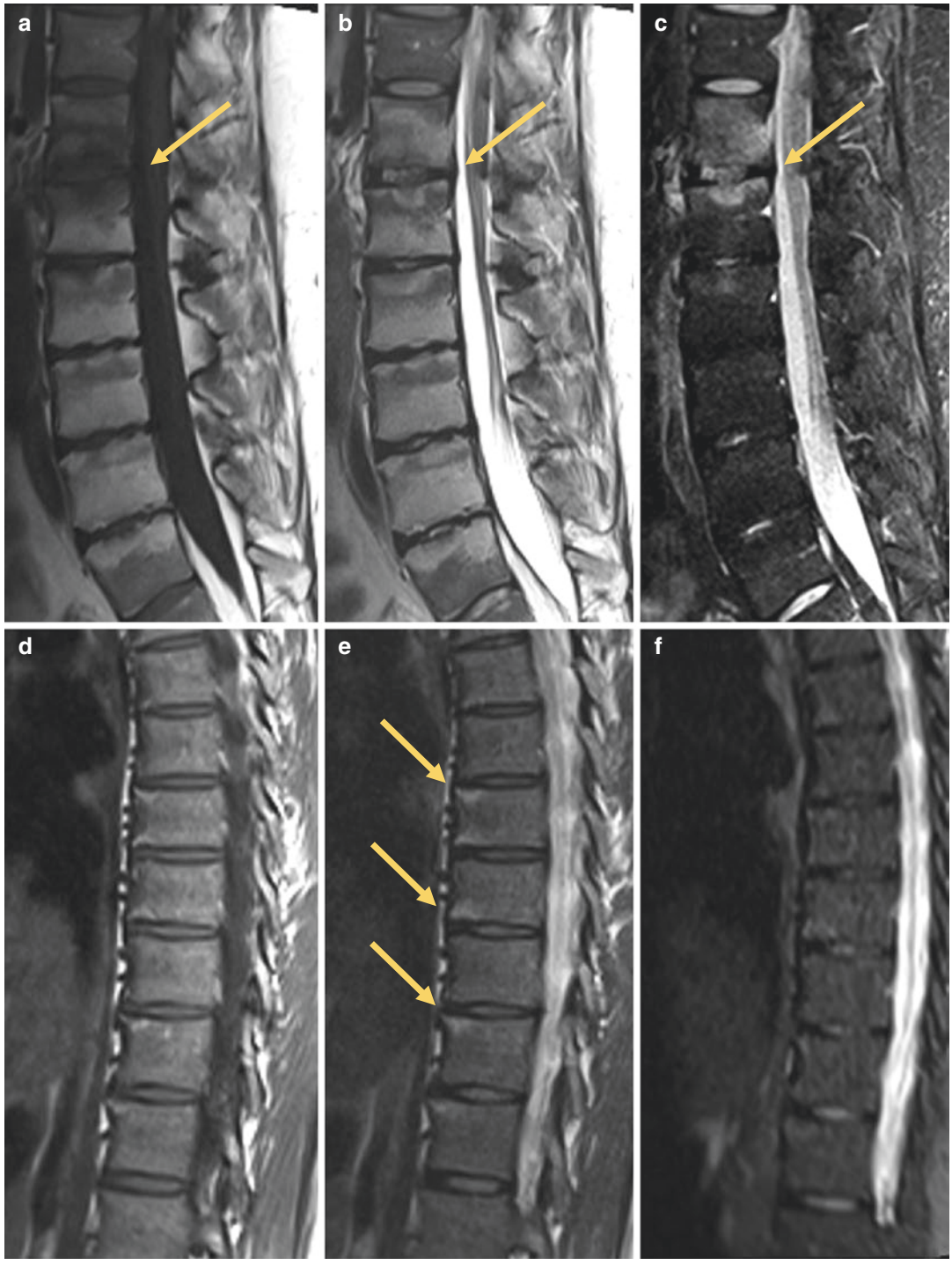
a
b
c
d
e
f

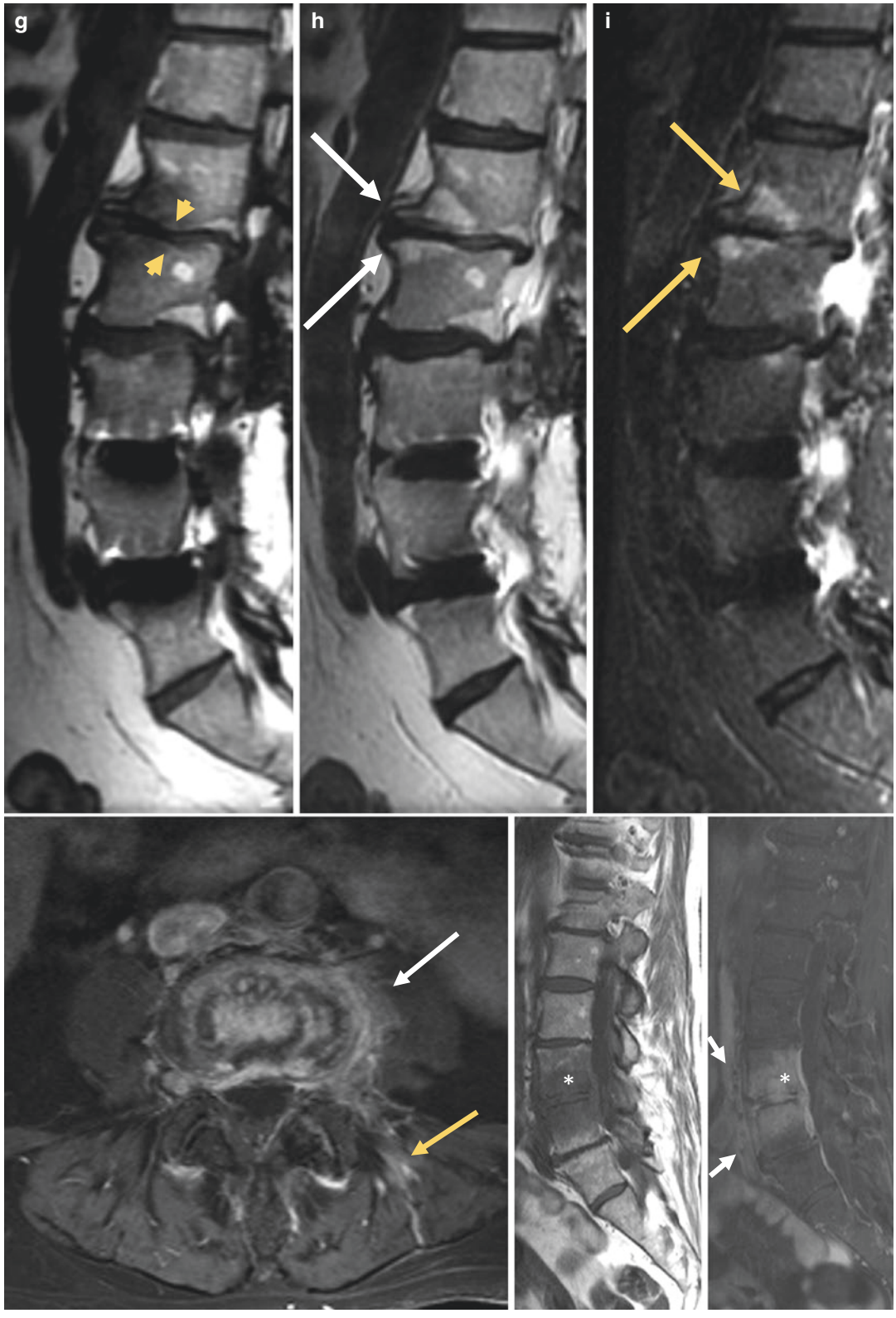

Fig. 6.27 (continued)

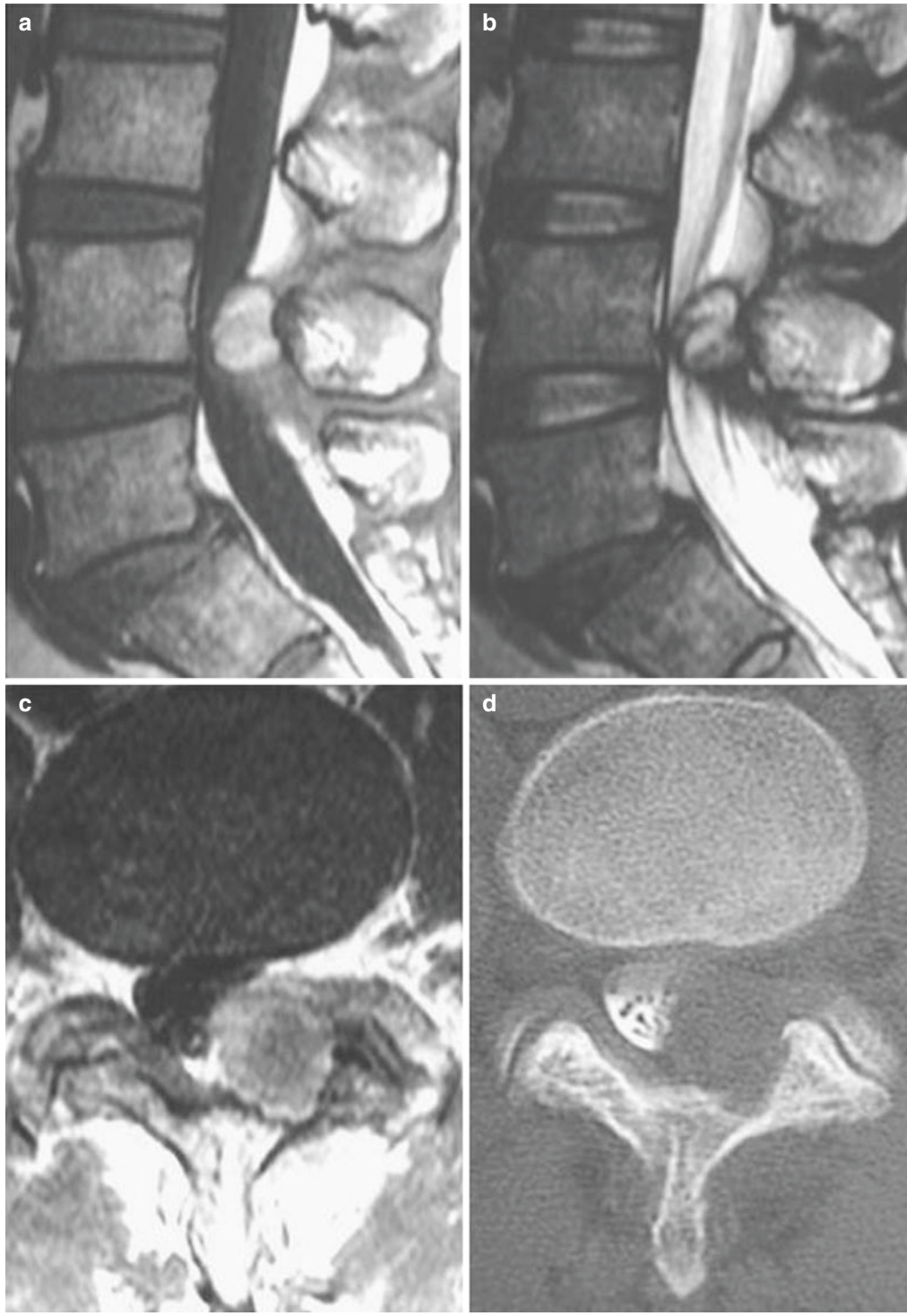

Fig. 6.28 A 43-year-old man with 2 years of low back pain: sagittal T1-weighted (**a**), T2-weighted (**b**), and axial, T1-weighted, fat-saturated, post-contrast (b) MRI demonstrate an extradural mass originating from the left facet joint. The most likely lesion in this location would be a synovial cyst. However, the lesion demonstrates confluent enhancement following intravenous gadolinium contrast (**c**), which would not be expected with a synovial cyst. Corresponding CT myelogram (**d**) demonstrates no intrathecal communication and chronic, pressure erosion of the lamina, indicative of a slow-growing process. Surgical specimen was consistent with PVNS. (With permission from [20])

spondylolysis (aka pars fractures). These osteocartilaginous bodies are typically more variable in size and are also associated with osteoarthritic facet joint changes [23].

Other, less common neoplastic lesions of the facet joints include osteoblastoma and other chondroid lesions, such as chondrosarcoma. These are typically larger at presentation and have their own, unique imaging features; but biopsy is often required for definitive diagnosis. Malignant degeneration of SOC to synovial chondrosarcoma has rarely been reported and is estimated to be up to 6%. Soft tissue masses, such as nerve sheath tumors and meningiomas, can also overlap in their appearance with non-calcified SOC; however, these lesions are much more commonly encountered in the spine and are not associated with facet joint erosive changes or calcified bodies [21–23].

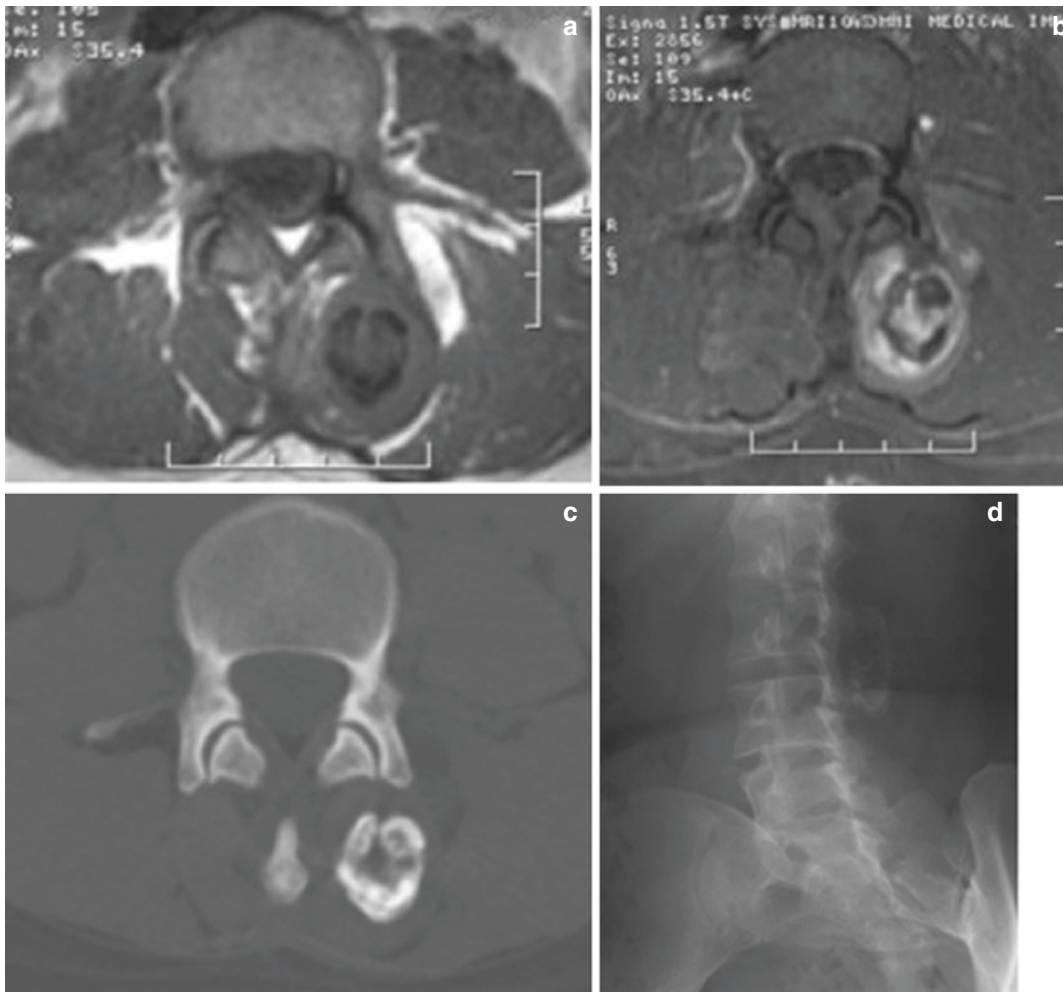

Fig. 6.29 Three different patients with SOC of the spine. In the first patient, axial T1-weighted (**a**), contrast-enhanced, T1-weighted, fat-saturated (**b**) MRI, axial CT (**c**), and oblique radiograph of the lumbar spine (**d**) demonstrate a single, large calcification posterior to the left L3–L4 facet joint, without changes of facet joint arthropathy. Another patient with SOC demonstrates multiple calcifications of varying sizes, best appreciated on CT (**e**) centered about a right lumbar facet joint. A third patient with SOC demonstrates a homogeneously enhancing cervical epidural soft tissue mass without low-signal foci to suggest calcification on sequential axial, T1-weighted, fat-saturated, post-contrast MR images (**f** and **g**). (With permission from [21])

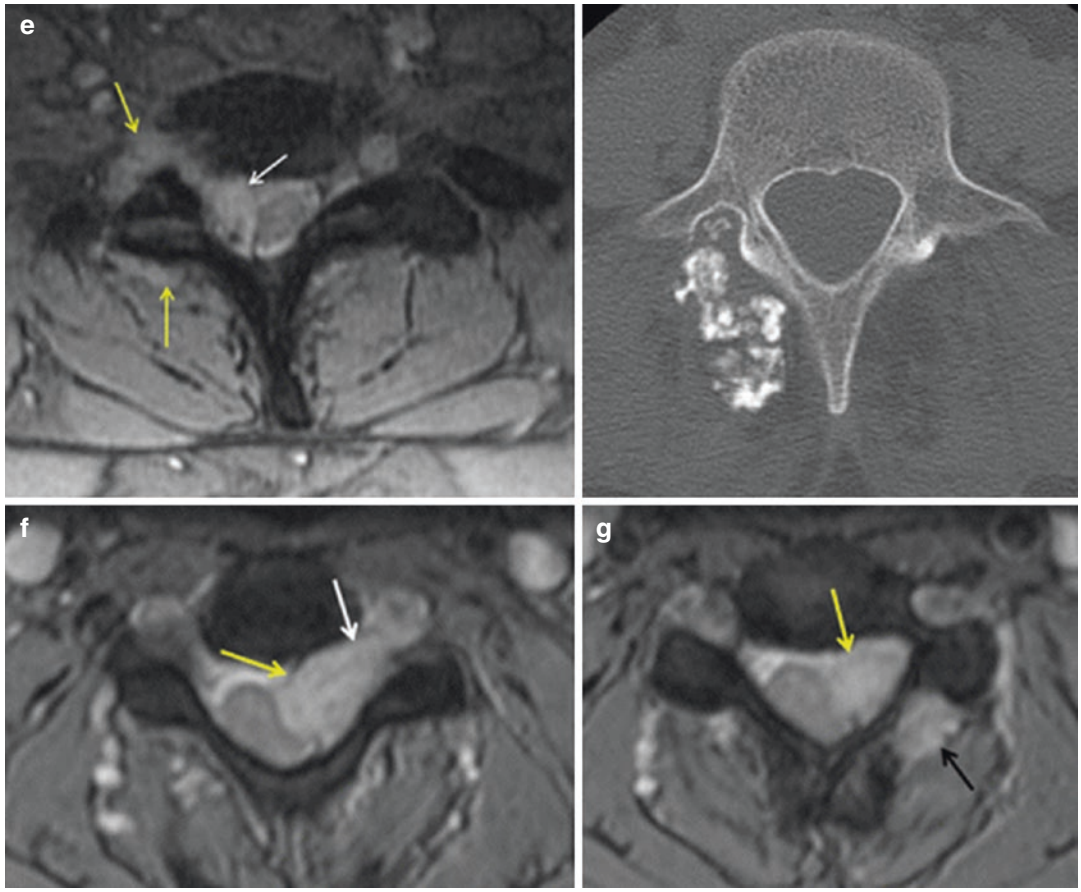

Fig. 6.29 (continued)

Acknowledgment Figures 6.18, 6.19, 6.20, 6.21, and 6.27 are courtesy of Dr. Alessandra J. Sax. The author acknowledges and thanks Dr. Alessandra J. Sax for assistance in preparing and providing the images.

References

1. Bierry G, Dietemann JL. Imaging evaluation of inflammation in the musculoskeletal system: current concepts and perspectives. Skelet Radiol. 2013;42:1347–59.
2. Weber U, et al. The impact of MRI on the clinical management of inflammatory arthritides. Skelet Radiol. 2011;40:1153–73.
3. Bouchaud-Chabot A, Liote F. Cervical spine involvement in rheumatoid arthritis. Joint Bone Spine. 2002;69:141–54.
4. Gillick JL, Wainwright J, Das K. Rheumatoid arthritis and the cervical spine: a review on the role of surgery. Int J Rheumatol. 2015;2015:1–12.
5. Redlund-Johnell I, Larsson EM. Subluxation of the upper thoracic spine in rheumatoid arthritis. Skelet Radiol. 1993;22:105–8.
6. Jurik AG. Imaging the spine in arthritis – a pictorial review. Insights Imaging. 2011;2:177–91.
7. Canella C, Schau B, Ribeiro E, et al. MRI in seronegative spondyloarthritis: imaging features and differential diagnosis in the spine and sacroiliac joints. Am J Roentgenol. 2013;200:149–57.
8. Soldatos T, et al. Cross-sectional imaging of adult crystal and inflammatory arthropathies. Skelet Radiol. 2016;45:1173–91.
9. Lee EY, Sundel RP, Kim S, et al. MRI findings of juvenile psoriatic arthritis. Skelet Radiol. 2008;37:987–96.
10. Earwaker JWS, Cotton A. SAPHO: syndrome of concept? Imaging findings. Skelet Radiol. 2003;32:311–27.
11. Mader R, Verlaan JJ, Eshed I, et al. Diffuse idiopathic skeletal hyperostosis (DISH): where we are now and where to go next. RMD Open. 2017;3:e000472.
12. Taljanovic MS, Hunter TB, Wisneski RJ, et al. Imaging characteristics of diffuse idiopathic

skeletal hyperostosis with an emphasis on acute spinal fractures: review. Am J Roentgenol. 2009; 193:S10–9.
13. Omumi P, Zufferey P, Malghem J, et al. Imaging in Gout and other crystal-related arthropathies. Rheum Dis Clin N Am. 2016;42:621–44.
14. Lam HY, Cheung KY, Law SW, et al. Crystal arthropathy of the lumbar spine: a report of 4 cases. J Orthop Surg. 2007;15:94–101.
15. Koontz NA, Quigley EP, Witt BL, et al. Pigmented villonodular synovitis of the cervical spine: case report and review of the literature. BJR Case Rep. 2016;2:20150264.
16. Parmar HA, Sitoh YY, Tan KK, et al. MRI imaging features of pigmented villonodular synovitis of the cervical spine. Am J Neuroradiol. 2004;25:146–9.
17. Celiktas M, Asik MO, Gezercan Y, et al. Pigmented villonodular synovitis of the thoracic vertebra presenting with progressive spastic paraparesis. Case Rep Orthop. 2013;2013:1–4.
18. Musluman AM, Causoglu H, Yilmaz A, et al. Pigmented villonodular synovitis of a lumbar intervertebral facet joint. Spine J. 2008;9:e6–9.
19. Woon S, Lee MH, Eoh W, et al. Pigmented villonodular synovitis on lumbar spine: a case report and literature review. J Korean Neurosurg. 2014;56:272–7.
20. Oe K, et al. Pigmented villonodular synovitis originating from the lumbar facet joint: a case report. Eur Spine. 2007;16(Suppl 3):S301–5.
21. Littrell LA, Inward CY, Sim FH, et al. Imaging features of synovial chondromatosis of the spine: a review of 28 cases. Skelet Radiol. 2016;45:63–71.
22. Moody P, Bui MM, Vrionis F, et al. Synovial chondromatosis of the spine: case report and review of the literature. Ann Clin Lab Sci. 2010;40:71–3.
23. Takeshima Y, Hanakita J, Takahashi T, et al. Multiple osseous loose bodies associated with lumbar isthmic spondylolisthesis. World Neurosurg. 2016;95:623e1–4.

MRI in Metabolic Disease

7

Ricardo Hernandez, Philip K. Wong,
Monica Umpierrez, and Felix M. Gonzalez

Introduction

The pathophysiology behind metabolic spine disease relies on the dynamic nature of bone tissue, which is constantly changing and adapting in response to load variations in the body. Osteoblasts and osteoclasts constitutively and simultaneously mediate the series of anabolic and catabolic reactions required to maintain mechanical stability. When this fragile balance of biochemical processes is disturbed, the architecture of the spine can be compromised in such a way as to translate into mechanical dysfunction. In this chapter, we will delve into some of the most common metabolic diseases of the spine encountered by orthopedic surgeons: osteoporosis and Paget's. We will briefly review the pathophysiology of each disease, the American College of Radiology (ACR) Appropriateness Criteria, and how magnetic resonance imaging (MRI) can be used to guide our diagnosis and treatment.

R. Hernandez
Philadelphia College of Osteopathic Medicine, Suwanee, GA, USA
e-mail: ricardohe@pcom.edu

P. K. Wong · M. Umpierrez
Department of Radiology and Imaging Sciences, Emory University Hospital, Atlanta, GA, USA
e-mail: philip.kin-wai.wong@emory.edu; monica.umpierrez@emory.edu

F. M. Gonzalez (✉)
Department of Radiology and Imaging Sciences, Emory University Hospital, Atlanta, GA, USA

Emory University Orthopaedics & Spine Center, Atlanta, GA, USA
e-mail: Felix.m.gonzalez@emory.edu

Osteoporosis

Introduction

Osteoporosis is defined as a skeletal disorder characterized by reduction in bone mass due to depletion of calcium and bone protein predisposing a person to an increased risk of fracture [1].

Pathophysiology

This loss of bone strength seen in osteoporosis is due to a quantitative deficiency, rather than a qualitative one. Osteoporotic bone can be likened to a bridge constructed with an insufficient amount of steel beams. As you can imagine, even though the engineers may have utilized the best material for the job, a dearth of even the choicest materials will limit the load-bearing capabilities of the bridge, eventually leading to mechanical failure. Likewise, the scarcity of trabeculae in osteoporotic bone compromises the load-bearing capacity of bone, increasing its susceptibility to fracture. Vertebral compression fractures are the most common type of insufficiency fractures due to osteoporosis [2].

W. B. Morrison et al. (eds.), *MRI of the Spine*, https://doi.org/10.1007/978-3-030-43627-8_7

This is thought to be due to the axial skeleton being primarily composed of cancellous bone, which is more metabolically active than cortical bone [3].

ACR Appropriateness Criteria for Osteoporosis

The ability of MRI to detect even the slightest changes in water content makes it an invaluable tool for imaging soft tissue pathology and edema. The American College of Radiology (ACR) has published appropriateness criteria for the imaging of osteoporosis, and a summary table of indications for MRI can be seen in Table 7.1. Among these indications, MRI of the lumbar spine without contrast received the highest rating in the evaluation of possible vertebral fractures based on symptomatology in patients with suspected osteoporosis or those who have had more than 3 months of corticosteroids, after initial radiographs were negative [4].

The Role of MRI in Vertebral Augmentation

The utility of MRI extends beyond its diagnostic capabilities. After vertebral compression fractures have been confirmed, MRI findings can serve as a surgeon's guide to preoperative planning and intraoperative care [5]. At the time of this publication, the preferred surgical management of painful osteoporotic vertebral compression fractures is vertebral augmentation. Vertebral augmentation is a blanket term that includes all percutaneous techniques used to achieve internal vertebral body stabilization through the process of bone cement injection [6]. The most commonly used vertebral augmentation techniques are vertebroplasty and kyphoplasty. Both techniques involve injection of polymethylmethacrylate bone cement into a vertebral body to limit bone collapse by providing vertebral body support, thereby preventing further vertebral body height collapse and reducing pain [7, 8]. Vertebroplasty involves the percutaneous injection of bone cement into the cancellous bone of a vertebral body with the objective of alleviating the pain and preventing further vertebral collapse. On the other hand, kyphoplasty employs an inflatable balloon to create a cavity for the cement with the likelihood of restoring the vertebral body loss reestablishing a better spinal alignment. Vertebroplasty and kyphoplasty are effective treatment options for the reduction of pain associated with vertebral body compression fractures. Although both procedures have been associated with favorable outcomes, kyphoplasty has been shown to reduce the incidence of cement leakage compared to that of percutaneous vertebroplasty [9]. MRI, in particular, the short tau inversion recovery (STIR) sequence, is the preoperative imaging study of choice in evaluating candidates for vertebral augmentation. These modalities permit the visualization of vertebral marrow edema usually seen in the setting

Table 7.1 ACR appropriateness criteria for osteoporosis MRI

Variant	Modality	Rating	RRL
Suspected fracture (non-screening) of a vertebral body based on acute or subacute symptomatology in a patient with suspected osteoporosis or a patient treated with corticosteroids (>3 months); first examination	MRI spine area of interest without IV contrast	2	O
	MRI spine area of interest without IV contrast	1	O
Suspected fracture (non-screening) of a vertebral body based on acute or subacute symptomatology in a patient with suspected osteoporosis or a patient treated with corticosteroids (>3 months); initial radiograph is negative	MRI lumbar spine without IV contrast	9	O
	MRI lumbar spine without and with IV contrast	1	O
Patients on long-term treatment (3–5 years) of bisphosphonates with thigh or groin pain; first examination	MRI thigh without IV contrast bilateral	1	O
	MRI thigh without and with IV contrast bilateral	1	O
Patients on long-term treatment (3–5 years) of bisphosphonates with thigh or groin pain and negative radiographs	MRI thigh without IV contrast bilateral	9	O
	MRI thigh without and with IV contrast bilateral	1	O

ACR American College of Radiology, *MRI* magnetic resonance imaging, *RRL* relative radiation level, *IV* intravenous

of recent fractures or microfractures as outlined in Table 7.2.

The chronicity of vertebral fractures is often difficult to fully evaluate and extrapolate from radiographs alone. Fluid-sensitive magnetic resonance (MR) modalities (i.e., STIR and T2-fat suppressed [FS]-MRI) can be exquisitely sensitive in detecting bone marrow edema, a finding closely associated with acute fractures [14–16]. Post-traumatic edema can persist for up to a year after the inciting event [17] and therefore correlation with clinical exam is paramount in assessing injury chronicity. Fluid-sensitive MR modalities have also allowed an increase in the diagnosis of vertebral clefts, a complication of vertebral compression fractures that can lead to further collapse of vertebral bodies [10, 11]. Clefts are found in up to one-third of vertebral compression fractures and may be a representation of malunion leading to a symptomatic pseudarthrosis (fracture non-union; Fig. 7.1) [18, 19]. These air-filled clefts may fill with fluid and manifest on MRI as a fluid-intensity surrounded by a hypointense rim on STIR images [20]. Identification of these signs on MR is significant in that patients with clefts have been shown to be more prone to re-collapse after balloon kyphoplasty and may require a longer postoperative rehabilitative course [21].

Table 7.2 Advantages of preoperative MRI in vertebral augmentation

Differentiating acute versus chronic fractures
Identifying fracture clefts [10, 11]
Identifying additional fractures
Identifying subtle fractures
Differentiating osteoporotic fractures from neoplastic processes [12, 13]
Assessing posterior ligament complex stability

Lastly, differentiating malignant vertebral fractures from osteoporotic fractures is facilitated by MRI. The spine is the third most common site for metastatic disease following the lung and the liver. This is especially critical in the elderly population, as both osteoporosis and vertebral metastasis are much more common than in the

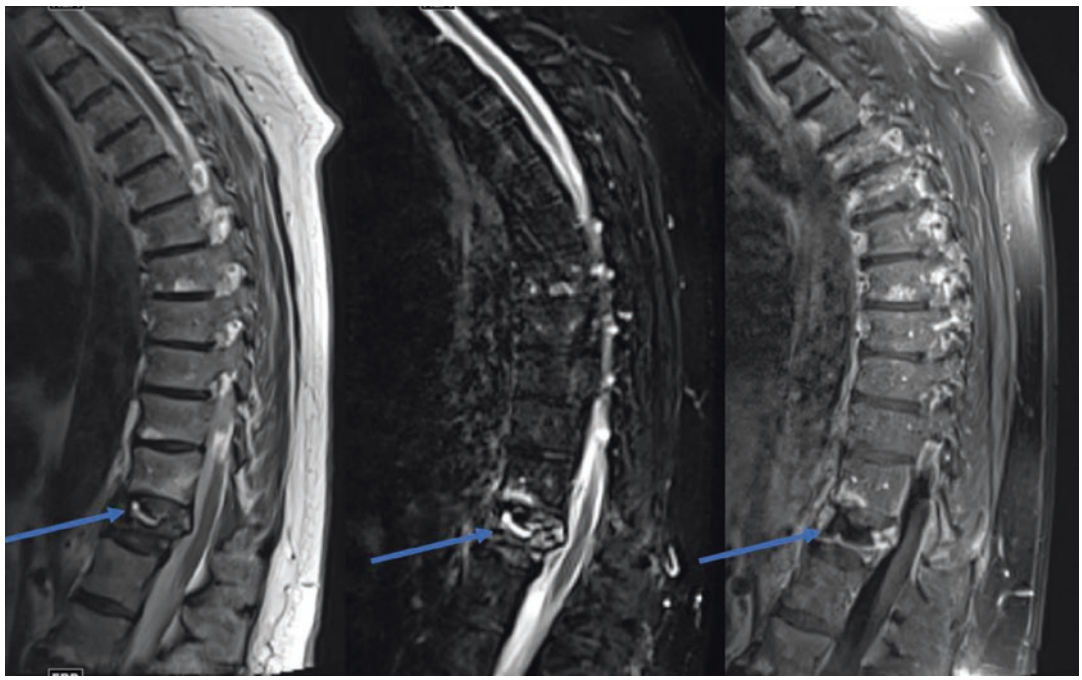

Fig. 7.1 Sagittal T2, short tau inversion recovery (STIR), and T1-fat suppressed (FS) post-gadolinium magnetic resonance (MR) images showing corresponding fluid signal (arrows) within a collapsed T12 vertebral body indicative of pseudoarthrosis and osteonecrosis

general population. Unlike computed tomography (CT), which detects osseous abnormalities including cortical and medullary destruction, MRI can detect early bone marrow deposits (Fig. 7.2). Convex posterior borders of the vertebral bodies, pedicle involvement, or any evidence of malignant masses or paraspinal metastasis are all red flags that should point the physician to investigate malignant etiologies [22]. MR imaging also permits characterization of the levels of involvement and any associated cord or neural element compression. The combination of unenhanced T1-weighted-spin-echo- and STIR-sequences has shown to be the most useful for detection of bone marrow abnormalities and is able to discriminate benign from suspicious/malignant bone marrow changes [3]. The areas of abnormal marrow signal intensity can serve as a guide for targeted image-guided biopsy. In contrast, retropulsed vertebral bone fragments, multiple benign fractures, and the aforementioned fluid-filled "cleft sign" are all suggestive of fractures due to osteoporosis [15, 22–24].

Paget's Disease

Introduction

Paget's disease of the bone, originally coined osteitis deformans, is a metabolic bone disease characterized by pathologic bone remodeling [25]. It is the second most common metabolic disease affecting the spine. For the same reasons discussed in the osteoporosis section, Paget's disease also has a propensity to affect the axial skeleton. The spine therefore is a common site of involvement, second only to the pelvis. The etiology of this disease is not well understood, but there have been many hypotheses put forward in the literature [25, 26].

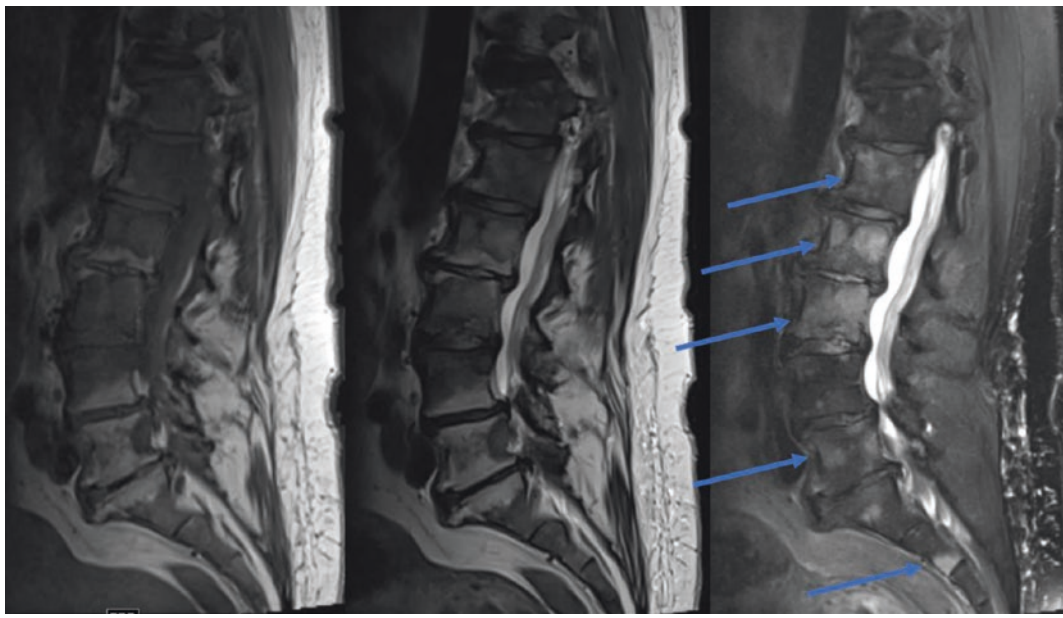

Fig. 7.2 Sagittal T1, T2, and T2-FS showing extensive metastatic disease throughout the lumbar spine and sacrum. Please note on the T1 image the darker marrow replacing vertebral areas relatively sparing the L5 level. On the T2-FS image, the metastatic disease appears brighter or hyperintense (arrows)

Pathophysiology

Unlike the dearth of bone seen in osteoporosis, the pathology of Paget's is not due to lack of quantity, but rather lack of quality. In Paget's, the overactivation of osteoblasts and osteoclast results in an unbalanced end-product that is susceptible to fracture. The progression of this disease has been described in three distinct stages, each of which has characteristic imaging findings, which will be discussed later on in this chapter. The stages are described according to the predominant cell type at work. The disease begins with an osteoclastic predominant stage, progresses to a mixed phase where both osteoclasts and osteoblasts are active, and finalizes with an overactivation of osteoblasts forming the aforementioned disorganization of bone [26].

The Role of MRI in Paget's Disease

MRI is often used in Paget's as an adjuvant imaging modality in patients with new-onset signs and symptoms, as MR offers the added benefit of bone marrow visualization. Radiologic findings of pagetic bone manifest themselves according to the stage of the disease. However, the stages of the disease are often not discrete or independent of each other, making it difficult to isolate changes related to specific stages. A plethora of different findings have therefore been reported in the literature and have been summarized in Table 7.3.

During the osteolytic phase of the disease, it is exceptionally rare to find changes in the spine. During the lytic phase, other modalities such as CT or conventional radiographs may be more useful in evaluating sclerotic changes in the vertebra. Subtle anteroposterior expansive changes in the vertebral body as well as cortical thickening have been noted [27]. The normal bone marrow in MR may be useful in differentiating lytic pagetic bone from a malignant lytic process, where the bone marrow is infiltrated rather than preserved [28].

In the spine, the earliest changes appreciated radiologically are often found in the mixed phase [29]. There may be high signal bone intensity on T2, low signal intensity on T1 with gadolinium enhancement on T1 fat saturation sequences, corresponding to hypervascularity of the marrow. Finally, in the osteoblastic phase, both T1 and T2 show low-intensity signal corresponding to fibrosis and marrow sclerosis.

Although most patients with Paget's are asymptomatic, many complications have been reported. Complications include but are not limited to: back pain, spinal stenosis, neural dysfunction, compression fractures, facet joint arthropathy, spondylolysis, spondylolisthesis, intervertebral disc involvement, or neoplastic transformation [29–31].

Table 7.3 Magnetic resonance (MR) findings in different stages of Paget's disease

Disease phase	MR finding
Osteolytic	Normal or minimally involved bone marrow, minimal anteroposterior vertebral expansion, and cortical thickening [26–28]
Mixed	High signal bone marrow intensity on T2; low signal intensity with contrast enhancement on T1 [26–28]
Osteoblastic	Low signal intensity on both T1 and T2; vertebral shape abnormalities [26–28]

Renal Osteodystrophy/CKD-MBD

Introduction

Chronic Kidney Disease Mineral and Bone Disorder (CKD-MBD) is a term introduced in 2006 to describe the pathological consequences of chronic kidney disease on bone. It is yet another example of how systemic metabolic derangements manifest pathologically in bone. The more historical term, "renal osteodystrophy," has been recommended to be used only in reference to specific histopathological findings of bony abnormalities in the setting of CKD-MDB [32, 33]. This section will touch briefly on the pathophysiology of the disease and outline the MRI findings consistent with CKD-MBD affecting the spine.

Pathophysiology

The kidneys play a pivotal role in calcium, phosphorous, and vitamin D homeostasis. Specifically, the kidneys are the site responsible for the final hydroxylation step of the storage form of vitamin D (25-hydroxycholecalciferol) to its active form, 1,25-dihydroxycholecalciferol (calcitriol). In the setting of chronic renal failure, low calcitriol levels lead to a decrease in both calcium and phosphorous (through a series of complicated feedback loops beyond the scope of this chapter), increasing levels of parathyroid hormone. This secondary hyperparathyroidism is the primary driving force behind the bony derangement seen in CKD-MBD [33]. This compromised bone is at increased risk of fracture, and this risk is inversely proportional to kidney function as measured by the glomerular filtration rate (GFR) [34].

MRI

As stated previously, the term "renal osteodystrophy" refers to the pathologic bone biopsy findings on bone quantitative histomorphometry, the gold-standard for the diagnosis of renal osteodystrophy [35]. Bone biopsy, however, has many limitations due to its invasiveness, cost, and expertise required to perform. MRI provides clinicians a non-invasive, non-ionizing approach to evaluating morphological changes in bony microarchitecture, soft tissue changes, and treatment response in patients with chronic kidney disease [36].

The Rugger Jersey Spine

The classic spinal manifestation of renal osteodystrophy is the "Rugger Jersey Spine," a term derived from the characteristic pattern of alternating light and dark horizontal lines on rugby uniforms [37]. Although this finding is classically described on simple radiographs, the osteosclerotic pattern on vertebral end plates can also be visualized on MRI (Fig. 7.3).

Amyloidosis

Patients on maintenance hemodialysis (HD) are at increased risk for the development of amyloidosis [38]. Amyloidosis is the extracellular deposition of insoluble protein fibrils, namely, ß-2 microglobulin (B2M). Patients who are on long-term HD have a markedly reduced GFR, and therefore cannot adequately filter out these said proteins. This leads to the accumulation and

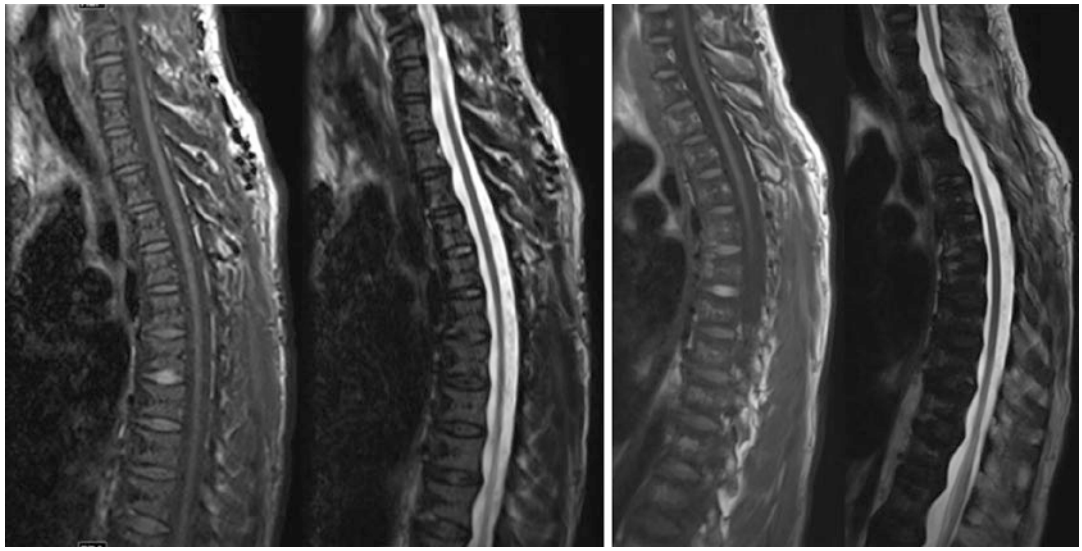

Fig. 7.3 Sagittal T1 and T2-FS showing progressing of osseous changes in the cervico-thoracic spine over a course of 4 years on a patient with renal osteodystrophy (aka Rugger Jersey Spine). Note marked loss of T1 and T2 in the endplates of all vertebrae producing alternating "hoops" as seen in older style rugby tops

deposition of B2M on multiple musculoskeletal tissues, including the spine (Fig. 7.4).

Spinal amyloidosis can manifest itself as synovial thickening, pathological bone fractures, neurovascular compromise, or neural compression secondary to deposits stenosing the spinal canal (Fig. 7.4; see if you can find a figure showing this). A low-density signal on both T1- and T2-weighted spine MR in a patient with CKD should raise suspicion for HD-induced amyloidosis [39, 40]. This is an important distinction as the differential diagnosis for spinal osteolytic

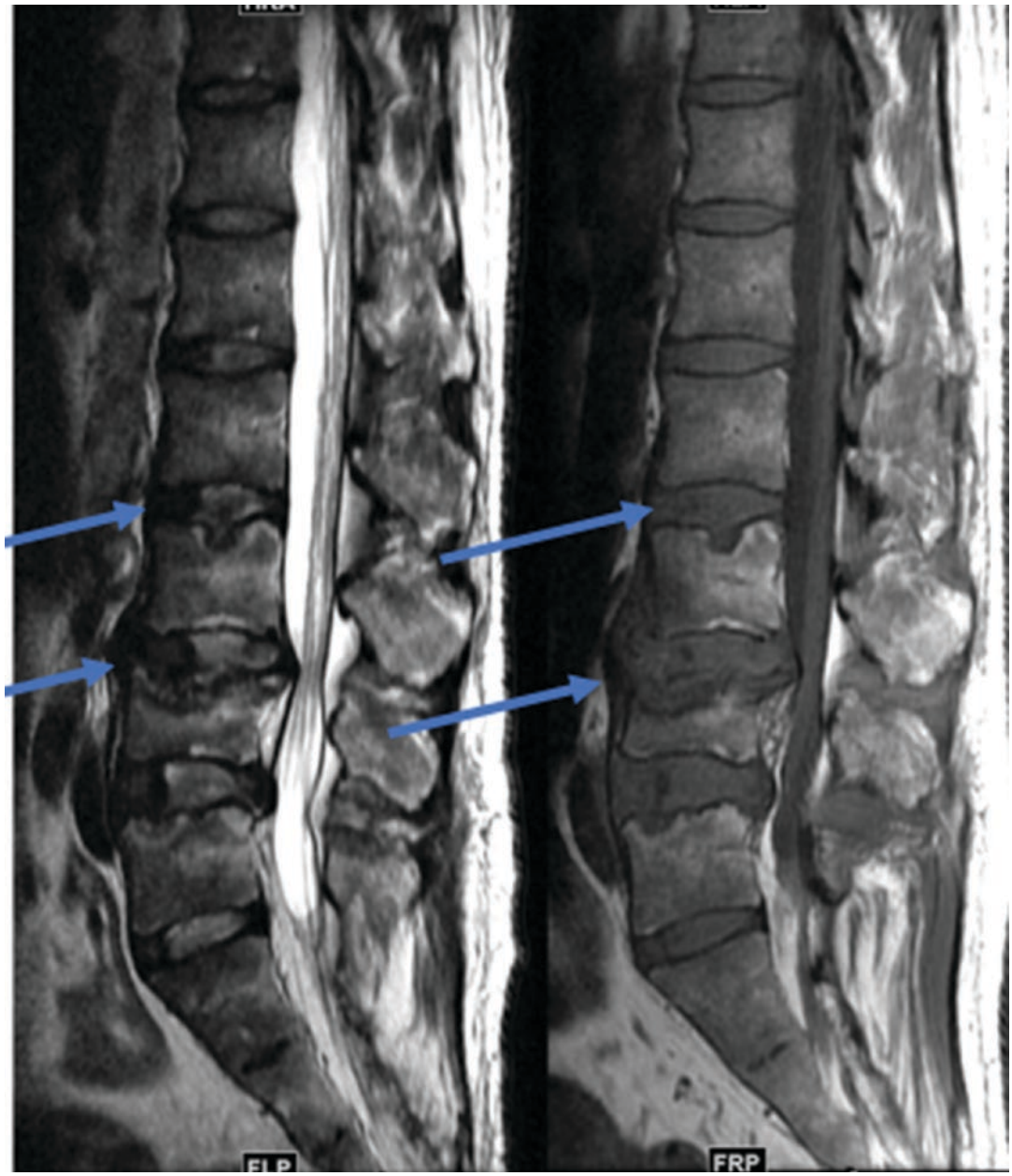

Fig. 7.4 Sagittal T2 and T1 showing progressing dark areas of amyloid deposition (arrows). Dialysis-related spondyloarthropathy is most likely related to amyloid deposition in the disc and ligamentum flavum. On plain films and CT, destruction of the end plates and severe disc space narrowing can mimic infectious discitis

lesions is quite extensive, and many of these (e.g., infectious spondylodiskitis, synovial chondromatosis) have increased signal intensity on T2-weighted images [41].

Brown Tumors

Osteoclastomas, or brown tumors, are yet another manifestation of renal osteodystrophy. These lesions are consequences of hyperparathyroidism in general but are more prevalent in cases of secondary hyperparathyroidism [42]. Although exceedingly rare in the spine, tumor infiltration can lead to spinal stenosis and neurological compromise. Brown tumors are T1-iso or hypointense, but can vary in intensity on T2-weighted images due to their tendency to form cystic lesions that can subsequently hemorrhage (Fig. 7.5) [43].

High-Resolution Magnetic Resonance Imaging

Recent studies have shown the utility of high-resolution MRI (HR-MRI) in measuring various musculoskeletal parameters in patients with CKD. Findings on HR-MRI in patients with CKD include the discrimination of fractures, decreased cortical thickness, trabecular disruption, and a decrease in stiffness and failure strength [44]. Although these studies are predominantly focused on the peripheral skeleton, they serve as pilots for future studies to evaluate the utility of these imaging modalities in metabolic diseases of the axial skeleton.

A summary of the MRI findings consistent with renal osteodystrophy have been summarized for your convenience in Table 7.4.

Table 7.4 Magnetic resonance (MR) findings in complications of renal osteodystrophy

Complication	MR findings
Rugger Jersey spine	Alternating pattern of hyper- and hypointensities secondary to sclerotic changes in vertebral end plates
Amyloidosis and destructive spondyloarthropathy	Polyarticular hypointense lytic lesions on both T1 and T2
Brown tumor	Iso- or hypointense lesions on T1 with varying intensity on T2-weighted images

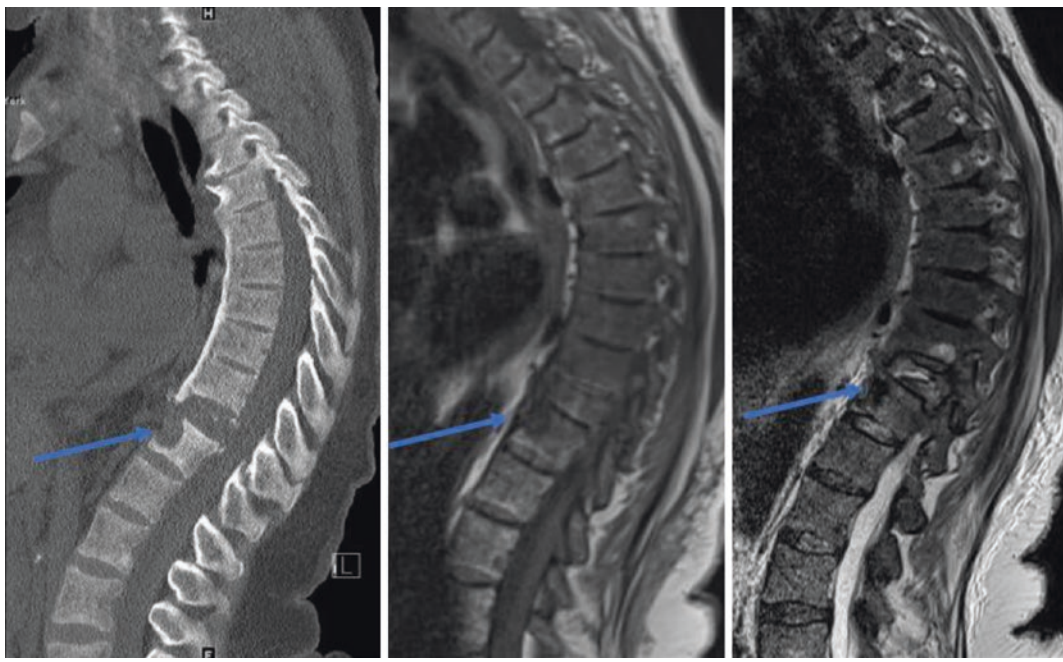

Fig. 7.5 Sagittal CT, T1-, and T2-weighted images demonstrating a brown tumor (arrows) involving the anterior aspect of the T12 vertebral body with significant collapse and osteonecrosis of the level above on this patient with findings of renal osteodystrophy

References

1. NIH Consensus Development Panel on Osteoporosis Prevention, Diagnosis, and Therapy. Osteoporosis prevention, diagnosis, and therapy. JAMA. 2001;285:785–95.
2. Copper C, Atkinson EJ, O'Fallon WM, Melton LJ III. Incidence of clinically diagnosed vertebral fractures: a population based study in Rochester, Minnesota, 1985–1989. J Bone Miner Res. 1992;7:221–7.
3. Pope T, Bloem H, Beltran J, et al., editors. Musculoskeletal imaging. 2nd ed. Philadelphia: Elsevier/Saunders; 2015.
4. American College of Radiology. ACR Appropriateness Criteria: Osteoporosis and Bone Mineral Density. Available at: https://acsearch.acr.org/docs/69358/Narrative/. Accessed 18 Feb 2019.
5. American College of Radiology. ACR Appropriateness Criteria: Management of Vertebral compression fractures.
6. American College of Radiology. ACR–ASNR–ASSR–SIR–SNIS Practice Parameter for the Performance of Vertebral Augmentation. Available at: https://www.acr.org/-/media/ACR/Files/Practice-Parameters/VerebralAug.pdf.
7. Cloft HJ, Jensen ME. Kyphoplasty: an assessment of a new technology. Am J Neuroradiol. 2007;28:200–3.
8. Garfin SR, Yuan HA, Reiley MA. New technologies in spine: kyphoplasty and vertebroplasty for the treatment of painful osteoporotic compression fractures. Spine. 2001;26:1511–5.
9. Jung JY, Lee MH, Ahn JM. Leakage of polymethylmethacrylate in percutaneous vertebroplasty: comparison of osteoporotic vertebral compression fractures with and without an intravertebral vacuum cleft. J Comput Assist Tomogr. 2006;30:501–6.
10. Wang G, Yang H, Chen K. Osteoporotic vertebral compression fractures with an intravertebral cleft treated by percutaneous balloon kyphoplasty. J Bone Joint Surg Br Vol. 2010;92:1553–7.
11. Stäbler A, Schneider P, Link TM, et al. Intra-vertebral vacuum phenomenon following fractures: CT study on frequency and etiology. J Comput Assist Tomogr. 1999;23:976–80.
12. Pozzi G, Garcia Parra C, Stradiotti P, Tien TV, Luzzati A, Serbi A. Diffusion weighted MR imaging in differentiation between osteoporotic and neoplastic vertebral fractures. Eur Spine J. 2012;21(Suppl 1):S123–7.
13. Jung HS, Jee WH, McCauley TR, Ha KY, Choi KH. Discrimination of metastatic from acute osteoporotic compression spinal fractures with MR imaging. Radiographics. 2003;23:179–87.
14. Green RA, Saifuddin A. Whole spine MRI in the assessment of acute vertebral body trauma. Skelet Radiol. 2004;33:129–35.
15. Lenchik L, Rogers LF, Delmas PD, Genant HK. Diagnosis of osteoporotic vertebral fractures: importance of recognition and description by radiologists. AJR. 2004;183:949–58.
16. Uppin AA, Hirsch JA, Centenera LV, et al. Occurrence of new vertebral body fractures after percutaneous vertebroplasty in patients with osteoporosis. Radiology. 2003;226(1):119–24.
17. Jhanna AJ, editor. MRI for orthopaedic surgeons. New York: Thieme; 2010.
18. Berquist TH, editor. MRI of the musculoskeletal system. 6th ed. Philadelphia: Lippincott Williams & Wilkins; 2013.
19. Rajasekaran S, Kanna RM, Schnake KJ, et al. Osteoporotic thoracolumbar fractures: how are they different?: classification and treatment algorithm. J Orthop Trauma. 2017;31:S49.
20. Libicher M, Appelt A, Berger I, et al. The intravertebral vacuum phenomenon as specific sign of osteonecrosis in vertebral compression fractures: results from a radiological and histological study. Eur Radiol. 2007;17:2248–52.
21. Lin Z, Liu T, Yin P, et al. The therapeutic effects of percutaneous kyphoplasty on osteoporotic vertebral compression fractures with or without intravertebral cleft. Int Orthop. 2019;43(2):359–65.
22. Cicala D, Briganti F, Casale L, et al. Atraumatic vertebral compression fractures: differential diagnosis between benign osteoporotic and malignant fractures by MRI. Musculoskelet Surg. 2013;97(Suppl 2):S169–79.
23. Kaplan PA, Orton DF, Asleson RJ. Osteoporosis with vertebral compression fractures, retropulsed fragments, and neurologic compromise. Radiology. 1987;165:533–5.
24. Krestan C, Hojreh A. Imaging of insufficiency fractures. Eur J Radiol. 2009;71:398.
25. Paget J. On a form of chronic inflammation of bones (osteitis deformans). MedChirTrans. 1877;60:37–64.
26. Valenzuela EN, Pietschmann P. Epidemiology and pathology of Paget's disease of bone – a review. Wien Med Wochenschr. 2017;167
27. Winn N, Lalam R, Cassar-Pullicino V. Imaging of Paget's disease of bone. Wien Med Wochenschr. 2018 Feb;167:9–17.
28. Dohan A, Parlier-Cuau C, Kaci R, Touraine S, Bousson V, Laredo JD. Vertebral involvement in Paget's disease: morphological classification of CT and MR appearances. Joint Bone Spine. 2014;82(1):18–24.
29. Morales H. MR imaging findings of Paget's disease of the spine. Clin Neuroradiol. 2015;25:225–32.
30. Dell'Atti C, Cassar-Pullicino VN, Lalam RK, Tins BJ, Tyrrell P. The spine in Paget's disease. Skelet Radiol. 2007;36:609–26.
31. Boutin RD, Spitz DJ, Newman JS, Lenchik L, Steinbach LS. Complications in Paget disease at MR imaging. Radiology. 1998;209(3):641–51.
32. Moe S, Drüeke T, Cunningham J, Goodman W, Martin K, Eknoyan G, et al. Definition, evaluation, and classification of renal osteodystrophy: a position statement from Kidney Disease: Improving Global Outcomes (KDIGO). Kidney Int. 2006;69(11):1945–53.

33. Cunningham J, Locatelli F, Rodriguez M. Secondary hyperparathyroidism: pathogenesis, disease progression, and therapeutic options. Clin J Am Soc Nephrol. 2011;6:913–21.
34. Naylor KL, McArthur E, Leslie WD, Fraser LA, Jamal SA, Cadarette SM, et al. The three-year incidence of fracture in chronic kidney disease. Kidney Int. 2014;86:810–8.
35. Barreto FC, Costa CRVD, Reis LMD, Custodio MR. Bone biopsy in nephrology practice. J Bras Nefrol. 2018;40(4):366–74.
36. Sharma AK, Toussaint ND, Elder GJ, et al. Magnetic resonance imaging based assessment of bone microstructure as a noninvasive alternative to histomorphometry in patients with chronic kidney disease. Bone. 2018;114:14–21.
37. Guler I, Koplay M, Nayman A, Kivrak AS, Tolu I. The rugger jersey spine sign. Spine J. 2015;15(8):1903.
38. Sargent MA, Fleming SJ, Cattopadhyay C, Ackrill P, Sambrook P. Bone cysts and haemodialysis-related amyloidosis. Clin Radiol. 1989;40:277–81.
39. Jevtic V. Imaging of renal osteodystrophy. Eur J Radiol. 2003;46(2):85–95.
40. Sigaux J, Abdelkefi I, Bardin T, Laredo JD, Ea HK, UreñaTorres P, Cohen-Solal M. Tendon thickening in dialysis-related joint arthritis is due to amyloid deposits at the surface of the tendon. Joint Bone Spine. 2019;86(2):233–8.
41. Cobby MJ, Adler RS, Swartz R, et al. Dialysis-related amyloid arthropathy findings in four patients. AJR Am J Roentgenol. 1991;157(5):1023–7.
42. Knowles NG, Smith DL, Outwater RK. MRI diagnosis of brown tumor based on magnetic susceptibility. J Magn Reson Imaging. 2008;28(3):759–61.
43. Colucci PG, Schweitzer AD, Saab J, Lavi E, Chazen JL. Imaging findings of spinal brown tumors: a rare but important cause of pathologic fracture and spinal cord compression. Clin Imaging. 2016;40(5):865–9.
44. Sharma K, Masterson R, Holt S, Toissaint N. Emerging role of high-resolution imaging in the detection of renal osteodystrophy. Nephrology. 2016;21:801–11.

MRI in Neoplastic Bone Disease and Differential Considerations

8

John V. Dennison, Alexander Leyva, Andrew T. Cibulas, Kurt F. Scherer, Jack A. Porrino, Sean C. Dodson, Richard D. Beegle, and Laura W. Bancroft

Introduction

Attempting to differentiate between benign and malignant lesions of the osseous spine can be a daunting task for even the most seasoned radiologist. In addition to recognizing specific magnetic resonance imaging (MRI) features of osseous spinal tumors, radiologists can narrow the differential diagnosis by factoring in patient demographics and tumor location along the longitudinal extent of the spine as well as within a vertebra. Furthermore, familiarity with the current World Health Organization's (WHO) tumor designations and the incidence of specific tumors based upon patient age is important for the interpreting radiologist. This chapter will cover unique and sometimes overlapping MRI features of a variety of benign and malignant osseous spinal tumors, and the utility of other imaging modalities in suggesting a specific diagnosis. Ultimately, pathologic evaluation and genetic testing may be required to make an accurate diagnosis and tailor patient treatment.

J. V. Dennison (✉) · A. Leyva · A. T. Cibulas
AdventHealth GME Radiology, Orlando, FL, USA
e-mail: John.Dennison.MD@AdventHealth.com; Alexander.Leyva.MD@AdventHealth.com; Andrew.Cibulas.MD@AdventHealth.com

K. F. Scherer · L. W. Bancroft
University of Central Florida School of Medicine, Orlando, FL, USA

Florida State University School of Medicine, AdventHealth, Orlando, FL, USA
e-mail: Kurt.Scherer.MD@AdventHealth.com

J. A. Porrino
Yale School of Medicine – New Haven Hospital, New Haven, CT, USA
e-mail: Jack.Porrino@yale.edu

S. C. Dodson · R. D. Beegle
Department of Diagnostic Radiology, AdventHealth, Orlando, FL, USA
e-mail: Sean.Dodson.MD@AdventHealth.com; Richard.Beegle.MD@AdventHealth.com

Benign Lesions of the Osseous Spine

Hemangioma

Background

Hemangioma of bone (also known as venous malformation) is the most commonly encountered benign entity in the adult spine and is almost always found incidentally on imaging. Although the current World Health Organization classification maintains the term hemangioma, it is a misnomer since these lesions contain thin-walled vascular channels and areas of intervening bone and adipose tissue [1, 2]. Atypical hemangioma often lacks fat, which alters the MRI appearance and makes the diagnosis more challenging. Lesions are most often confined to the vertebral body, but may rarely demonstrate extraosseous extension into the paravertebral soft tissues and epidural space.

W. B. Morrison et al. (eds.), *MRI of the Spine*, https://doi.org/10.1007/978-3-030-43627-8_8

Imaging

- Common incidental lesion in the adult vertebral bodies
- Classic hemangiomas are rounded T1- and T2-hyperintense foci with "corduroy" and "polka-dot" patterns of prominent trabecula
- Atypical hemangiomas may be nonspecific

MRI features of hemangioma reflect the bony trabeculations surrounded by thin-walled vascular channels and adipose tissue. Classic hemangioma demonstrates T1- and T2-hyperintense foci within a vertebral body caused by its predominant fatty content and T2 hyperintensity because of its inherent vascularity (Fig. 8.1). Hemangiomas rarely extend into the posterior elements. Prominent vertical trabecula in vertebral lesions may render a "corduroy" appearance on coronal and sagittal imaging and a stippled or "polka-dot" pattern when viewed in cross-section on axial

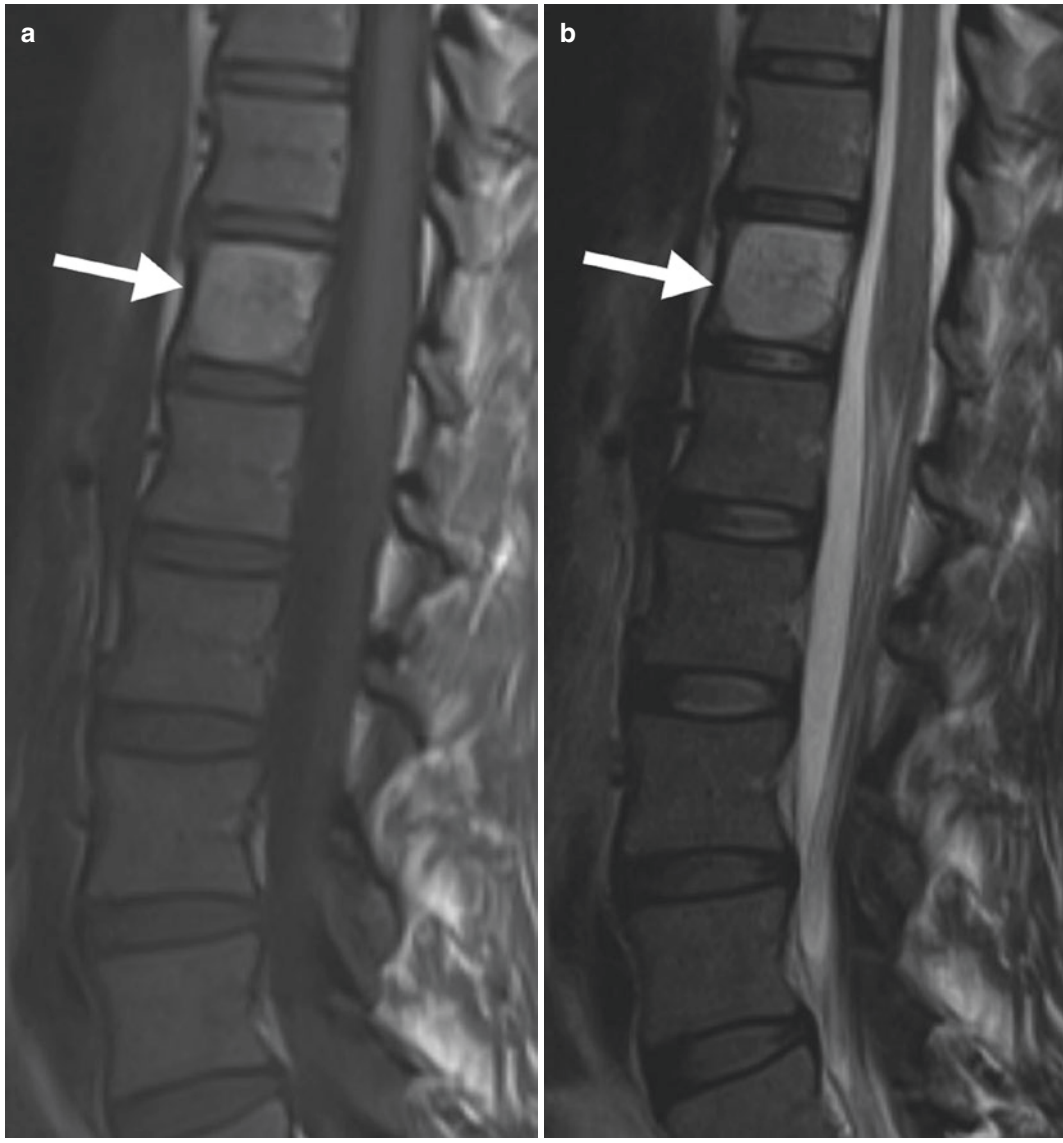

Fig. 8.1 A 47-year-old woman with imaging features of classic hemangioma in the lumbar spine. Sagittal T1 (**a**) and T2 (**b**) images of the thoracic spine show a rounded T1 and T2 hyperintense focus with subtle internal trabeculae in the T12 vertebral body, reflecting the bony trabeculations surrounded by thin-walled vascular channels and adipose tissue

MRI and computed tomography (CT) imaging [1, 3]. Of note, atypical venous malformations may lack fat and be T1 isointense or hypointense (Fig. 8.2), making it difficult to differentiate them from more concerning spinal lesions. Contrast administration is not helpful because of the wide range of vascularity and magnetic resonance (MR) enhancement. Hemangioma may rarely be complicated by pathologic fracture, pain, cord compression, and neurologic symptoms [1, 4].

Differential Considerations

Intraosseous lipoma is a potential diagnostic consideration on MRI since both lipoma and classic hemangioma contain fat and would be hyperintense on T1-weighted images. However, lipoma suppresses on fat-suppressed fluid-sensitive (i.e., T2, STIR—short tau inversion recovery) sequences and the surrounding bone is often sclerotic [5]. Furthermore, intraosseous lipoma is very rare and only a small percentage involve the spine [5]. Myeloid elements within a radiated field can be compromised, producing regional, non-anatomic fatty marrow signal; this is rarely a diagnostic dilemma. Atypical hemangiomas can be nonspecific on MRI due to lack of fat, and can be difficult to differentiate from metastases, myeloma, and, occasionally, infection.

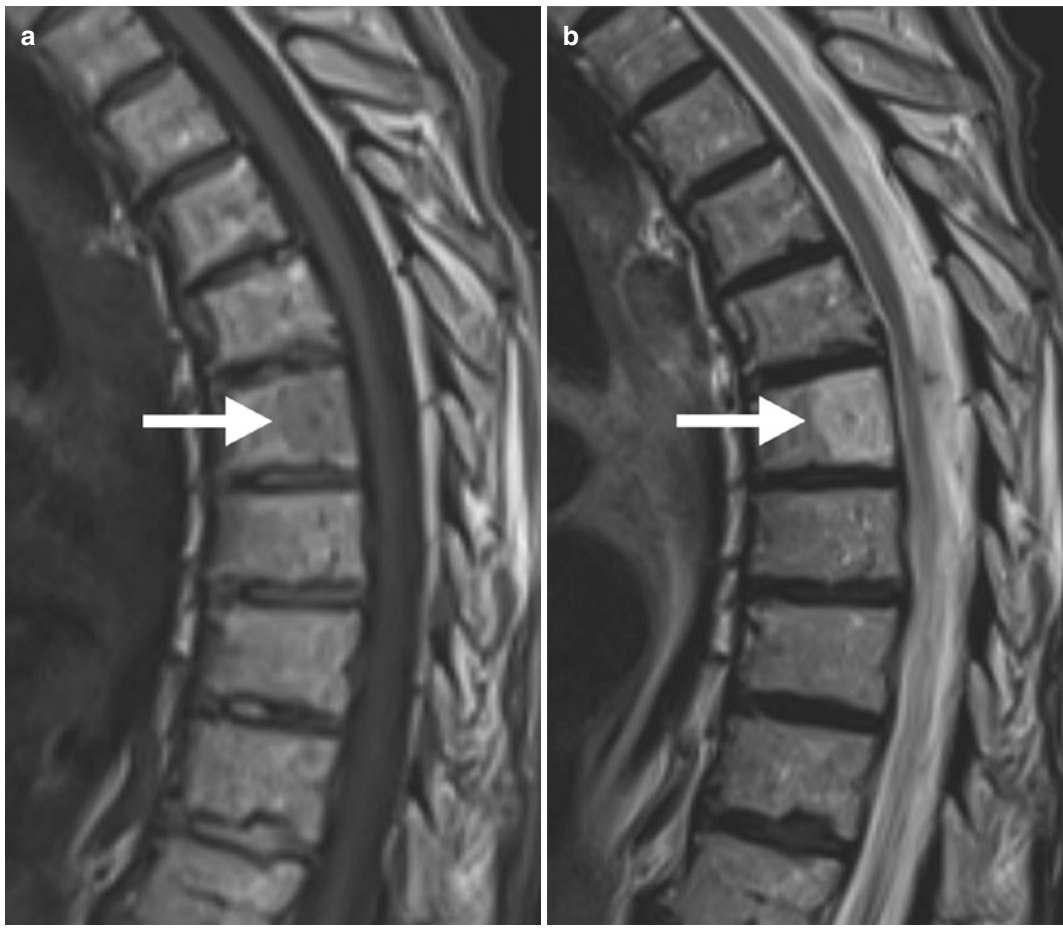

Fig. 8.2 An 87-year-old woman with presumed atypical hemangioma in the thoracic spine. Sagittal T1 (**a**) and T2 (**b**) images of the thoracic spine demonstrate a mildly T1 hypointense and T2 hyperintense lesion in the T8 vertebral body (*arrows*). This lesion remained stable for many years

Aneurysmal Bone Cyst

Background Information

As the name implies, aneurysmal bone cyst (ABC) is a cystic lesion that results in osseous expansile remodeling. ABC occurs most commonly in patients in the first two decades of life, and has an equal sex predilection [6, 7]. ABCs may be isolated (primary) or originate within a preexisting lesion (secondary), and are characterized by multiseptated fluid-fluid levels within cysts of varying sizes. The fluid components are composed of dependent blood and nondependent simple fluid. The septations seen between the cysts are either fibrous or osseous. Classically, these lesions originate near the base of the pedicle and extend into the vertebral body [8].

Imaging Findings

- Fluid-fluid levels and expansile remodeling of bone
- MRI of secondary ABCs reflect the complex and/or solid composition of the underlying lesion

MRI of ABC typically shows an expansile mass with fluid-fluid levels within multiple small cysts (Fig. 8.3). Internal signal is variable secondary to the blood products. Secondary ABCs may develop within a variety of both benign and malignant lesions such as giant cell tumor (GCT), osteosarcoma, chondroblastoma, and metastases [8]. In these cases, MRI signal will reflect the variable solid composition of these lesions. Postcontrast imaging may demonstrate enhancement of the internal septations. CT imaging of ABCs parallels MRI findings, and often delineates bony remodeling and thin bony septations to better advantage.

Differential Considerations

Imaging differential considerations for ABC in the appendicular skeleton would include telangiectatic osteosarcoma because of the various fluid-fluid levels. However, telangiectatic osteosarcoma is exceedingly rare in the spine and there were no cases reported in the spine among over 10,000 bone tumor cases in the Mayo Clinic series [7].

Giant Cell Tumor

Background Information

Giant cell tumor (GCT) is a benign, but locally aggressive, neoplasm composed of osteoclast-like giant cells that tend to present in early adulthood

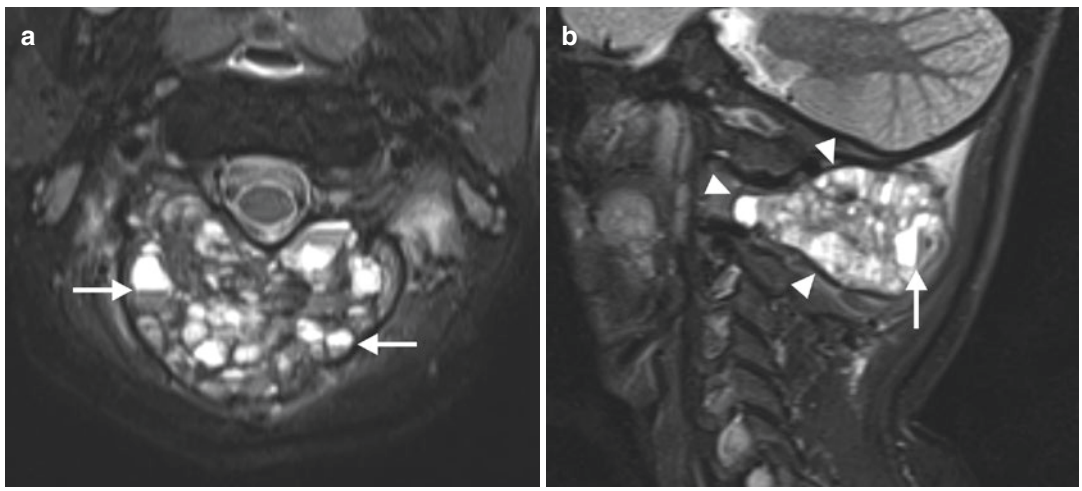

Fig. 8.3 An 8-year-old girl with aneurysmal bone cyst involving the C2 posterior elements. Axial fat-suppressed T2 (**a**) and sagittal STIR (**b**) images of the cervical spine show a heterogenous expansile mass involving the C2 posterior elements, with multiple well-defined cystic spaces containing fluid-fluid levels (*arrows*). The thinned, remodeled hypointense cortices (*arrowheads*) are intact

[9, 10]. Lesions are rare in the spine. When they occur, they most commonly involve the sacral body, followed by the lumbar, thoracic, and cervical vertebrae [9]; posterior elements are less commonly involved. Although benign, giant cell tumors can exhibit aggressive imaging features. In addition, lesions can rarely develop after radiation therapy or within Pagetoid bone, and can have associated secondary ABC formation [11, 12].

Imaging Findings

- Most common in sacral vertebral body
- Nonspecific MRI features, but can be hypointense on multiple sequences due to hemosiderin deposition from prior hemorrhage
- May have aggressive imaging features despite being histologically benign

Imaging findings for giant cell tumor are often highly variable, and aggressive features include wide zone of transition, cortical thinning, expansile remodeling, bone destruction, and associated soft tissue mass [11]. The lesions are typically T1 hypo- to isointense and T2 iso- to hyperintense on MRI (Fig. 8.4), but can be more hypointense due to hemosiderin deposition from prior tumoral hemorrhage. Fluid-fluid levels should raise suspicion for development of a secondary aneurysmal bone cyst. Tumoral enhancement is heterogenous, if contrast is administered.

CT is useful to exclude mineralized tumor matrix, and typically shows a lytic lesion with a non-sclerotic margin and narrow zone of transition. Cortical destruction and paravertebral or parasacral extension are common.

Differential Considerations

Unlike appendicular giant cell tumors that have characteristic eccentric location within the metaphysis and epiphyseal extension, spinal ABCs are not as specific on imaging. Aggressive features of spinal GCT (i.e., cortical destruction and extraosseous soft tissue extension) raise the possibility of metastases and myeloma, and biopsy is often required for definitive diagnosis.

Osteochondroma

Background Information

Osteochondroma is a benign, exophytic, or broad-based osseous lesion that has cortical and medullary continuity with the stalk and parent bone [13–15]. Lesions most often present in the first three decades of life, and rarely occur in the spine [13]. They are usually solitary, asymptomatic, and incidentally found on imaging. However, osteochondromas may present due to palpable findings or symptoms related to local trauma. When multiple, one should consider the heritable diagnosis of Multiple Osteochondromas (also known as hereditary multiple exostoses) [16].

Imaging Findings

- Exophytic bony mass with cortical and medullary continuity with the parent bone
- Cartilage cap thicker than 1.5–2 cm is suspicious for malignant transformation

Spinal osteochondroma is most commonly an exophytic bony mass with cortical and medullary continuity with the parent vertebra. MRI signal of an osteochondroma should mirror that of the parent bone on both T1- and T2-weighted imaging. The cartilaginous cap covering the most protruding portion of the tumor should not measure more than 1.5–2 cm in thickness, otherwise it should be considered suspicious for chondrosarcoma [17, 18]. The cartilaginous cap is measured from the outermost layer of cortex to the outermost layer of cartilage along the long axis of the lesion, not the width. Of note, the cartilaginous cap will demonstrate T1 hypointense and T2 hyperintense signal with corresponding contrast enhancement (Fig. 8.5).

Differential Considerations

Chondrosarcoma is the primary differential consideration when a painful osteochondroma develops a thick cartilage carp, an associated lytic destructive osseous mass, or chondroid calcifications within a soft tissue mass [18]. A prominent degenerative osteophyte could potentially be confused for an osteochondroma; however,

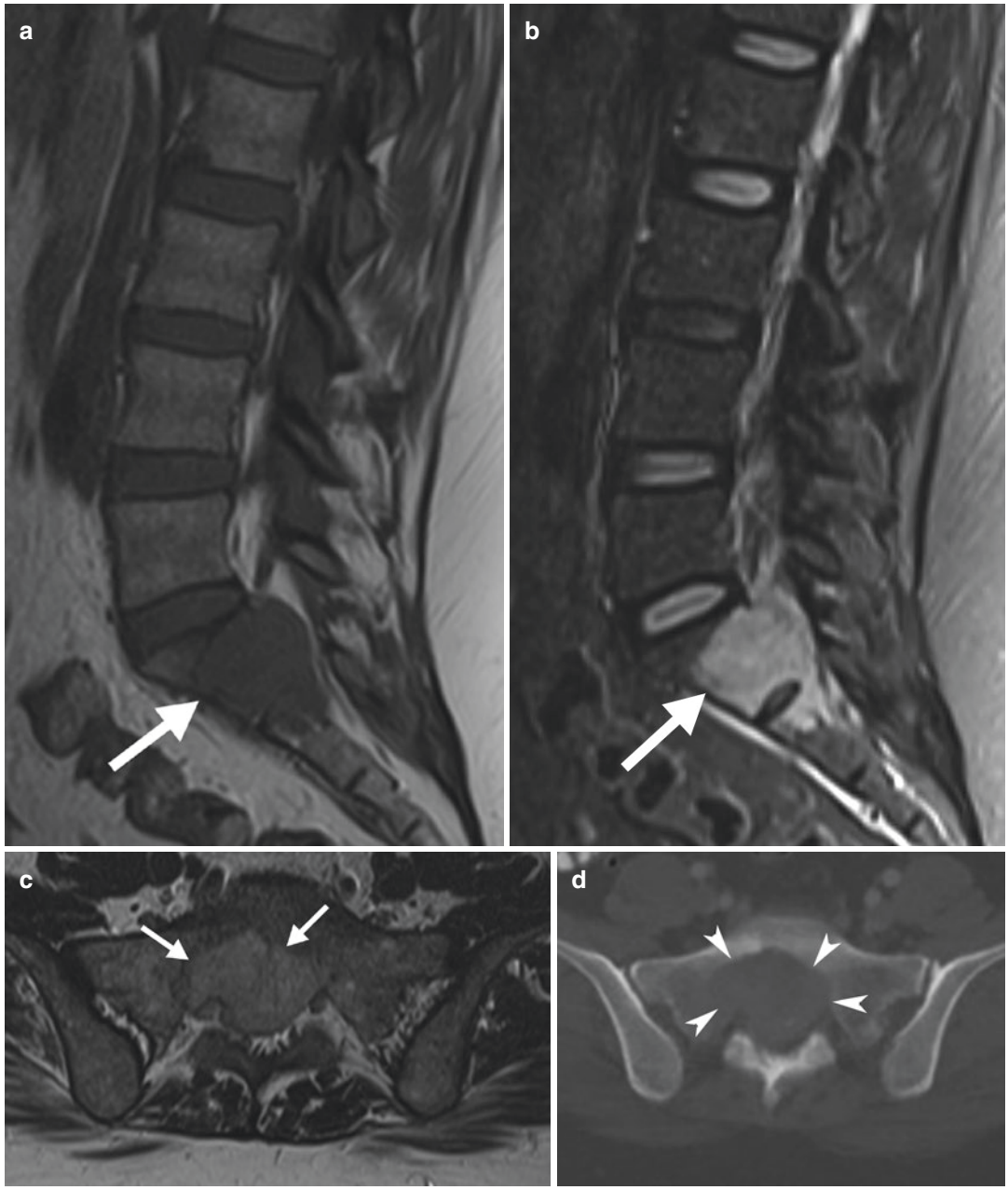

Fig. 8.4 A 49-year-old woman with sacral giant cell tumor. Sagittal T1 (**a**), STIR (**b**), and axial T2-weighted (**c**) images of the lumbosacral spine demonstrate a marrow-replacing lesion (*arrows*) within the S1 and S2 sacral bodies, resulting in expansile remodeling of the posterior cortices and tumoral extension into the epidural space. (**d**) Note the corresponding non-mineralized, hypodense lesion on CT with non-sclerotic, narrow zone of transition (*arrowheads*)

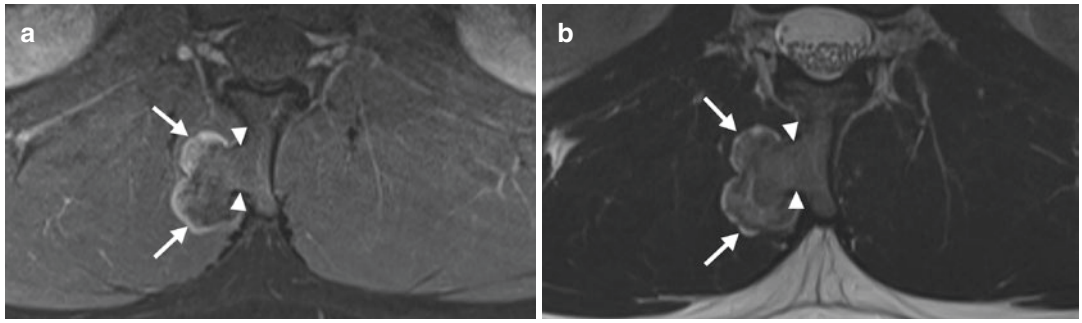

Fig. 8.5 A 16-year-old boy with L1 spinous process osteochondroma. Axial T1 fat-suppressed postcontrast image (**a**) and T2 (**b**) of the lumbar spine show a lobulated, right-sided exophytic L1 spinous process mass with cortical and medullary continuity (*arrowheads*) with the parent bone. Note the overlying thin, lobulated cartilaginous cap (*arrows*)

osteophytes would neither have a cartilaginous cap nor have medullary continuity with the adjacent spine.

Osteoid Osteoma/Osteoblastoma

Background

Osteoid osteoma and osteoblastoma are histologically very similar entities and, therefore, will be discussed together [19–22]. These lesions are differentiated by their size, with osteoid osteoma measuring less than 1.5 cm and osteoblastoma measuring greater than 1.5 cm [19, 20]. Both lesions are bone-forming tumors and are characterized by a small, lucent central nidus, and osteoid osteoma often has a surrounding sclerotic rim. In addition to producing osteoid, both lesions also produce prostaglandins that cause a large amount of edema/inflammation of the adjacent bone and soft tissue, accounting for the association with scoliosis and the classic night pain that can be relieved with nonsteroidal anti-inflammatory drug (NSAID) therapy.

Osteoblastoma of the spine can present with numbness, tingling, paraparesis, and paraplegia due to osseous expansion and/or extraosseous soft tissue extension with mass effect upon the spinal canal or nerve roots. Malignant transformation is rare, but more commonly associated with osteoblastoma [21].

Imaging Findings

- Both classically have a targetoid appearance on MRI and CT, with a central radiolucent nidus (with or without central calcifications)
- Osteoid osteoma is smaller than 1.5 cm, and commonly has a surrounding rim of sclerosis and marrow edema
- Osteoblastoma is larger than 1.5 cm, can lack a sclerotic margin, and can be locally aggressive and confused with malignancy

Osteoid osteoma is smaller than 1.5 cm and osteoblastoma is larger than 1.5 cm. Signal characteristics of both lesions are variable and dependent upon the degree of nidus, surrounding sclerosis, and degree of associated reactive edema [23, 24]. Both osteoid osteoma and osteoblastoma are highly vascular and, therefore, will demonstrate avid contrast enhancement on MRI (Figs. 8.6 and 8.7). CT is often used in conjunction with MRI for better appreciation of the nidus. The nidus is characteristically lucent with a rim of reactive sclerosis involving the adjacent medullary cavity, overlying cortex, and periosteum.

Osteoblastoma can have a different imaging appearance than osteoid osteoma. Osteoblastoma can have a narrow, intermediate, or wide zone of transition; only a minority will demonstrate mineralization; over 50% will have a sclerotic margin; and some lesions will have associated

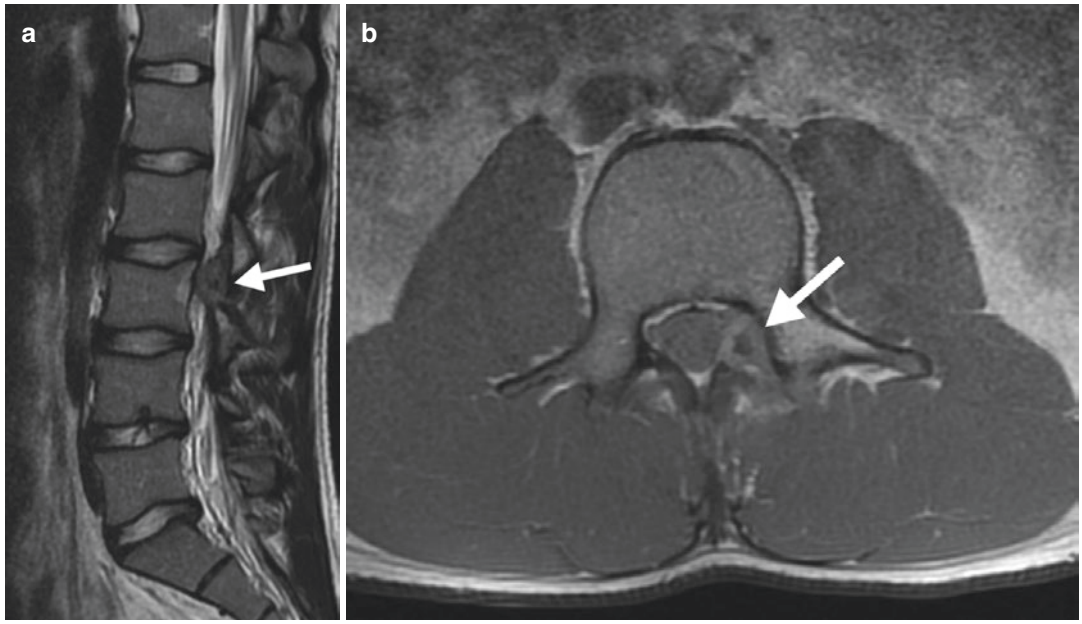

Fig. 8.6 A 16-year-old boy with an osteoid osteoma involving the left L3 vertebra. Sagittal T2 (**a**) and axial-enhanced T1 (**b**) images show an enhancing osteoid osteoma (*arrows*) with a central hypointense nidus that expands the left L3 pedicle and results in mass effect upon the thecal sac

periosteal new bone formation [22]. Furthermore, 40% of osteoblastomas will involve the spinal column and sacrum, and 55% of those lesions will involve the posterior elements [22, 25].

Differential Considerations

Differential considerations for osteoid osteoma and osteoblastoma include subacute osteomyelitis with Brodie abscess, since both can have a similar clinical and imaging appearance. Sequestra (isolated necrotic, infected bone fragments) are often more irregular than the organized, central calcifications within osteoid osteoma and osteoblastoma.

Differential diagnosis for osteoblastoma includes giant cell tumor and osteosarcoma, because all lesions may have an aggressive imaging appearance and extraosseous soft tissue extension. Both osteoblastoma and osteosarcoma may or may not produce mineralized tumor matrix, and giant cell tumor does not produce matrix. Therefore, biopsy is often required for definitive diagnosis.

Bone Island

Background Information

Bone islands are very common in the adult spine, and are also referred to as enostoses or osteomas by the World Health Organization classification [26, 27]. Pathologically, bone islands are hamartomas that can be either congenital or developmental. They are commonly situated near the endosteum of the bone and are the result of incomplete resorption of bone during endochondral ossification. Bone islands are nearly always incidental and asymptomatic.

Imaging Findings

- Non-enhancing signal void on MRI, often with spiculated margins
- Dense, sclerotic lesion that blends with the surrounding trabecula on CT (computed tomography) and radiographs

MRI findings of bone islands are fairly straightforward, characterized by non-enhancing signal

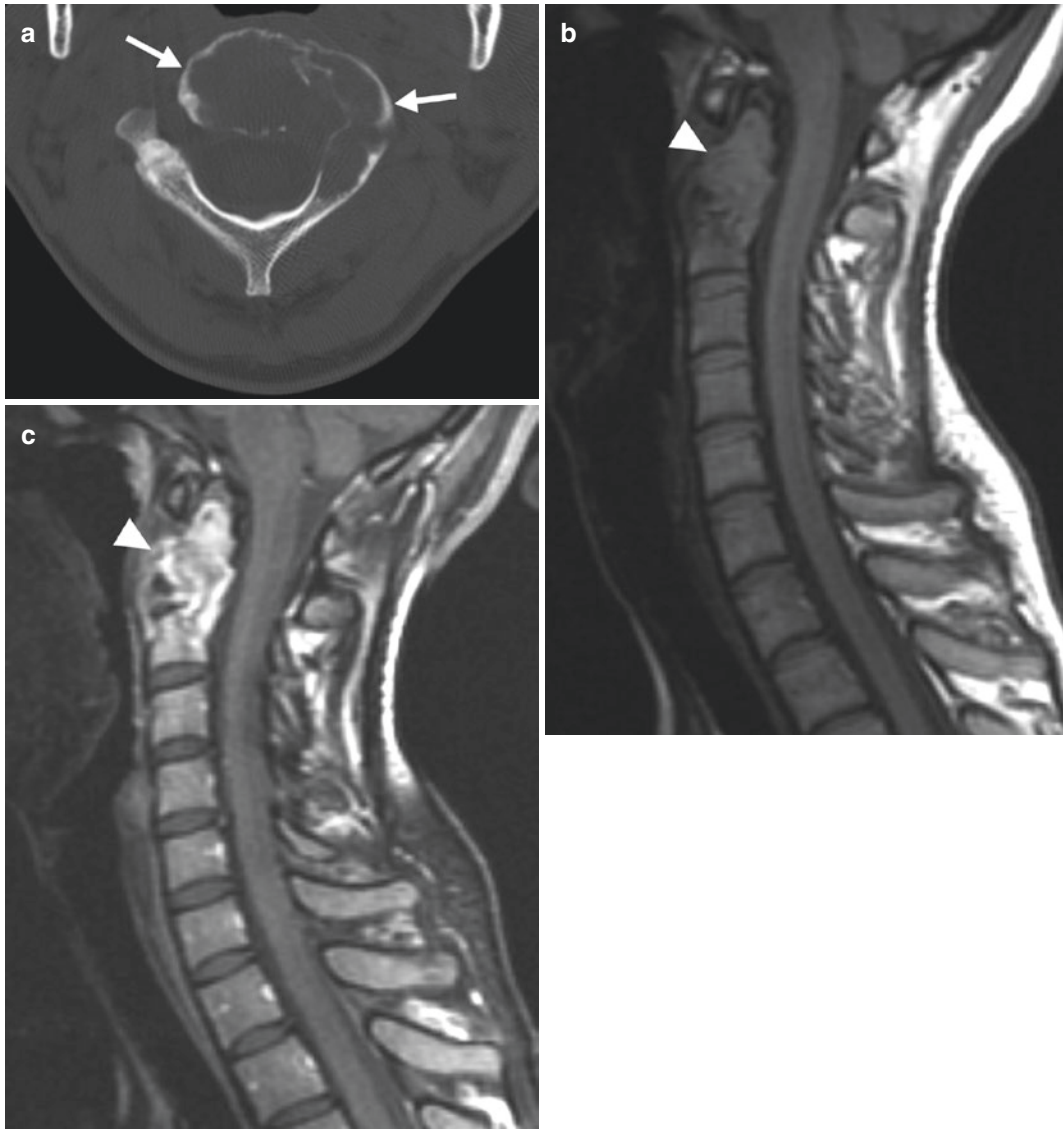

Fig. 8.7 A 31-year-old woman with an osteoblastoma of the C2 vertebral body, left pedicle, and lamina. (**a**) Axial CT demonstrates a lucent, non-mineralized lesion (*arrows*) with expansile remodeling and focal effacement of the cortices. Sagittal T1 (**b**) and T1-enhanced (**c**) midline images show the vertebral body component of the expansile, markedly enhancing lesion (*arrowheads*)

voids on MRI, often with spiculated margins (Fig. 8.8) [28]. CT often has more characteristic findings, with a non-enhancing densely sclerotic focus that blends with the surrounding trabecula, rendering a spiculated margin.

Differential Considerations

The most common consideration for bone islands is sclerotic metastases. However, metastatic lesions are often not as hypointense on T1-weighted images, as bone islands are often iso- to hyperintense on T2-weighted imaging and enhance with contrast administration. CT can delineate the spiculated margins due to merging (not destroying) the adjacent trabecula. CT density measurements can be quite useful for differentiation of bone islands from untreated metastases, as bone islands are denser

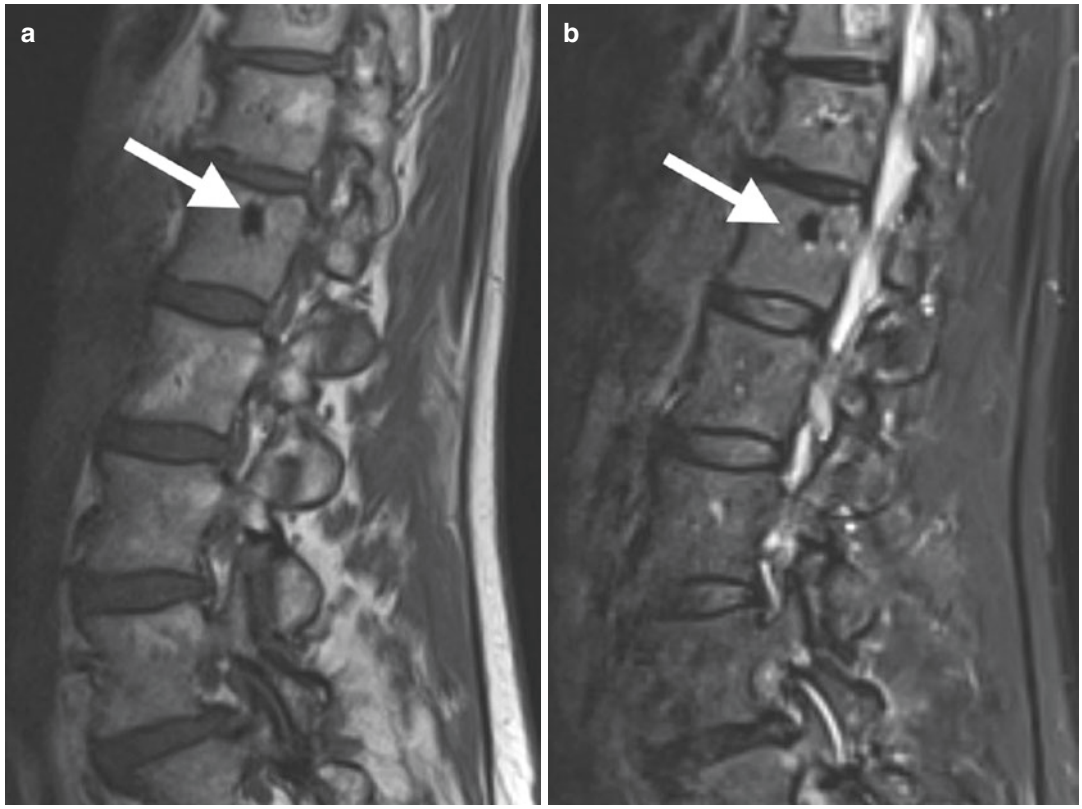

Fig. 8.8 A 69-year-old woman with L1 bone island. Sagittal T1 (**a**) and STIR (**b**) images of the lumbar spine demonstrate a small spiculated signal void (*arrows*) in the L1 vertebral body, consistent with bone island

and have a mean attenuation of greater than 885 Hounsfield Units (HU) [29].

Malignant Lesions of the Osseous Spine

Metastases

Background

Metastatic lesions to the spine are far more common than primary bone malignancies [30, 31]. Metastases tend to target red marrow as they spread hematogenously, with the most common site of involvement being the axial skeleton. Although specific malignant etiologies of metastatic lesions are most commonly lytic (i.e., lung, renal, thyroid) or osteoblastic (i.e., breast, prostate), lesions can be variable.

Imaging Findings

- Multiple, rounded, marrow-replacing lesions

The MRI appearance of metastatic disease of the spine is often variable and dependent upon the primary tumor. Metastases are marrow-replacing lesions that are often rounded or diffuse, and may involve the pedicles. Lesions are typically T1 hypointense secondary to replacement of normal T1 hyperintense marrow fat (Fig. 8.9) and tend to be hyperintense on fluid-sensitive sequences, although the appearance can range from hypo- to hyperintense. Renal and thyroid metastases may be expansile and demonstrate prominent vessels due to their increased vascularity. Lesions will most often show some degree of enhancement, regardless of the cell type, and show restricted diffusion on diffusion-weighted imaging.

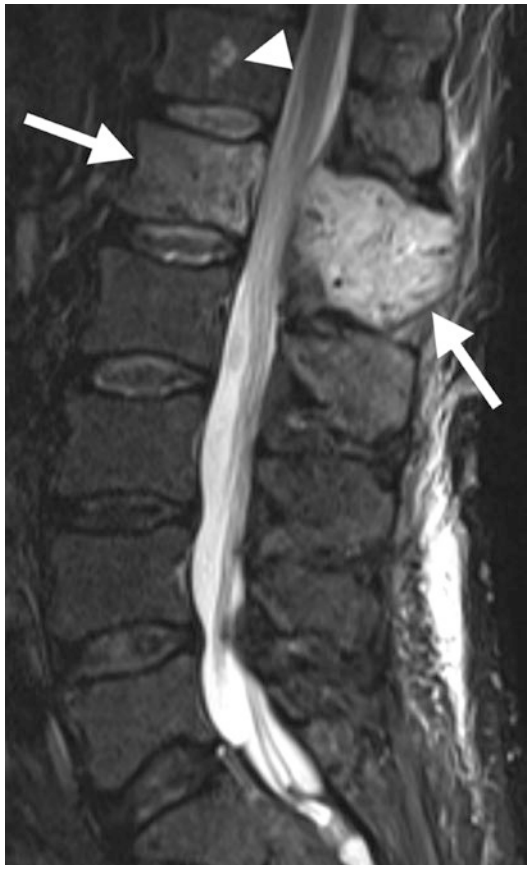

Fig. 8.9 A 72-year-old man with metastatic renal cell carcinoma. Sagittal STIR image of the lumbar spine demonstrates a marrow-replacing lesion in the L1 vertebral body and expanded spinous process (*arrows*), resulting in central canal stenosis. Note the additional small metastatic lesion in the T12 vertebral body (*arrowhead*)

Differential Considerations

The differential considerations of multiple marrow-replacing spinal lesions include myeloma, lymphoma, sarcoid, Langerhans cell histiocytosis, and chronic recurrent multifocal osteomyelitis. Since imaging features among these entities may be overlapping, correlation with patient history, laboratory values, chest CT (in the case of sarcoid), and, oftentimes, biopsy is required.

Myeloma

Background

Plasma cell myeloma (more commonly known as myeloma or multiple myeloma) is the most common primary bone malignancy, resulting in uncontrolled proliferation of plasma B-cells [32, 33]. Plasmacytoma is a single myelomatous lesion that will, in most cases, progress to myeloma [33, 34]. Myeloma is characterized by monoclonal gammopathy, bone pain, hypercalcemia, osteolytic lesions, and disorders due to amyloid deposition. Myeloma most commonly presents in the sixth and seventh decades, has no gender predilection, and has a higher incidence in African Americans [32].

Imaging Findings

- T1 hypointense and T2 hyperintense marrow-replacing lesions, may be expansile, and with avid contrast enhancement
- Positron-emission tomography (PET)/CT is also widely used for monitoring disease progression and is the preferred modality for assessing response to therapy

MRI is excellent in evaluating the extent of disease at the time of diagnosis, during and post treatment [35–38]. On MRI, myeloma demonstrates marrow-replacing lesions that are hypo- to isointense on T1-weighted images and hyperintense on fluid-sensitive sequences (Fig. 8.10). Extraosseous tumor extension can cause neurologic deficits, and tumor extending into the epidural space can cause spinal canal stenosis. Myeloma avidly enhances with intravenous contrast, although treated and inactive lesions may not enhance as strongly.

Myelomatous lesions are typically radiolucent lesions with narrow zones of transition on radiographs, CT, or PET/CT, but lesions can also be sclerotic or mixed in patients with POEMS—polyneuropathy, organomegaly, endocrinopathy, monoclonal gammopathy and skin changes—syndrome [38]. Pathologic fractures are common with myeloma, and CT can better assess cortical thinning that may predispose to pathologic fracture.

Differential Considerations

The differential for myeloma includes other lytic malignancies such as metastases and lymphoma, and patient history should be sought to help exclude these diagnoses. The diagnosis of

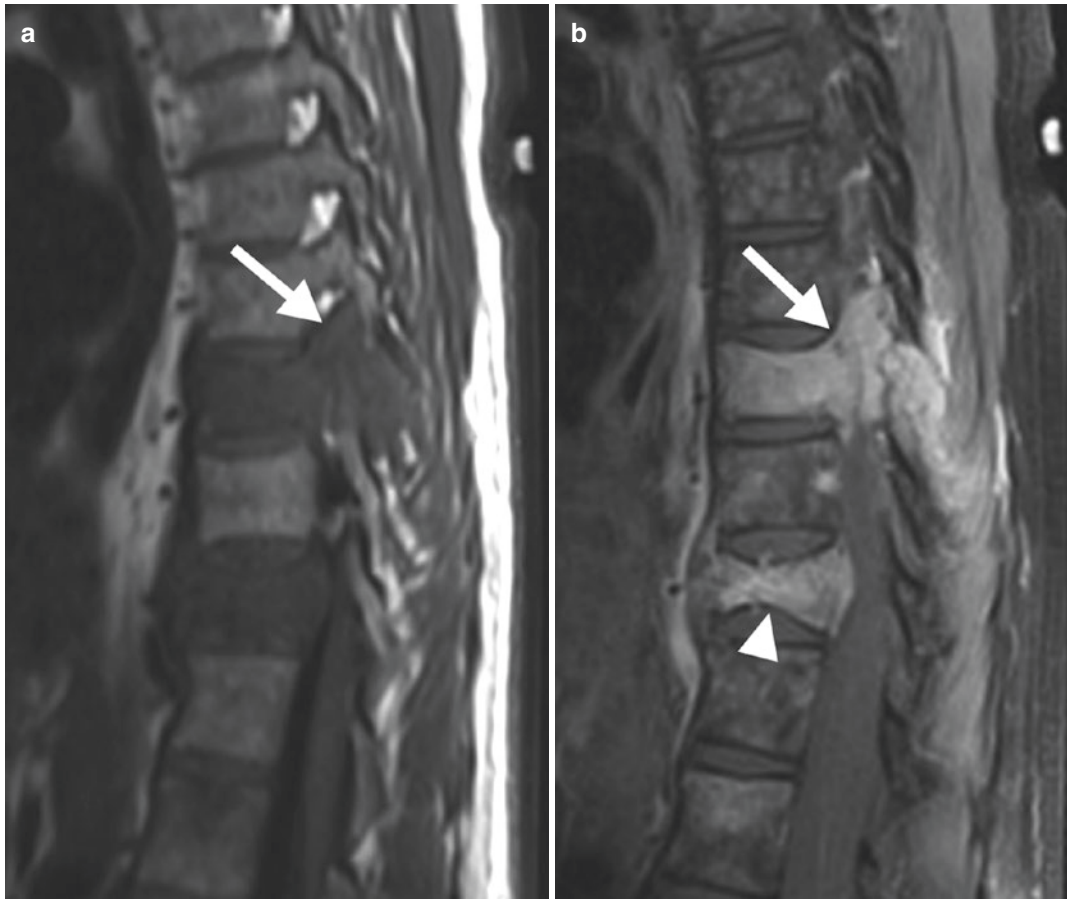

Fig. 8.10 A 58-year-old man with myeloma and pathologic fractures. Sagittal T1 (**a**) and contrast-enhanced fat-saturated T1 (**b**) images of the thoracic spine demonstrate a marrow-replacing lesion diffusely involving the T9 vertebra, with expansile remodeling of the posterior elements (*arrow*) and mild vertebral body pathologic compression fracture. Notice the similar lesion in the T11 vertebral body (*arrowhead*) with moderate pathologic compression fracture resulting in bulging of the posterior cortex and multiple small additional lesions

myeloma is made in the clinical setting of symptomatic and progressive disease using a combination of serum IgG and IgA levels, urine immunoglobulin levels, lytic bone lesions, and bone marrow biopsy [32].

Leukemia

Background

Acute and chronic leukemia subtypes include acute myeloid leukemia (AML), acute lymphocytic leukemia (ALL), and chronic lymphocytic leukemia (CLL), among others. AML accounts for 70% of all acute leukemia, and the vast majority of cases occurs in adults [39].

Imaging Findings

- Diffuse homogeneous or heterogeneous marrow infiltration

MRI of leukemic patients may demonstrate a diffusely homogeneous or heterogeneous marrow infiltrative pattern (Fig. 8.11) that could be potentially overlooked if unaware of the normal T1 fatty signal in patients older than 1 year of age. T2-weighted imaging may be slightly increased in signal intensity, and lesions typically enhance.

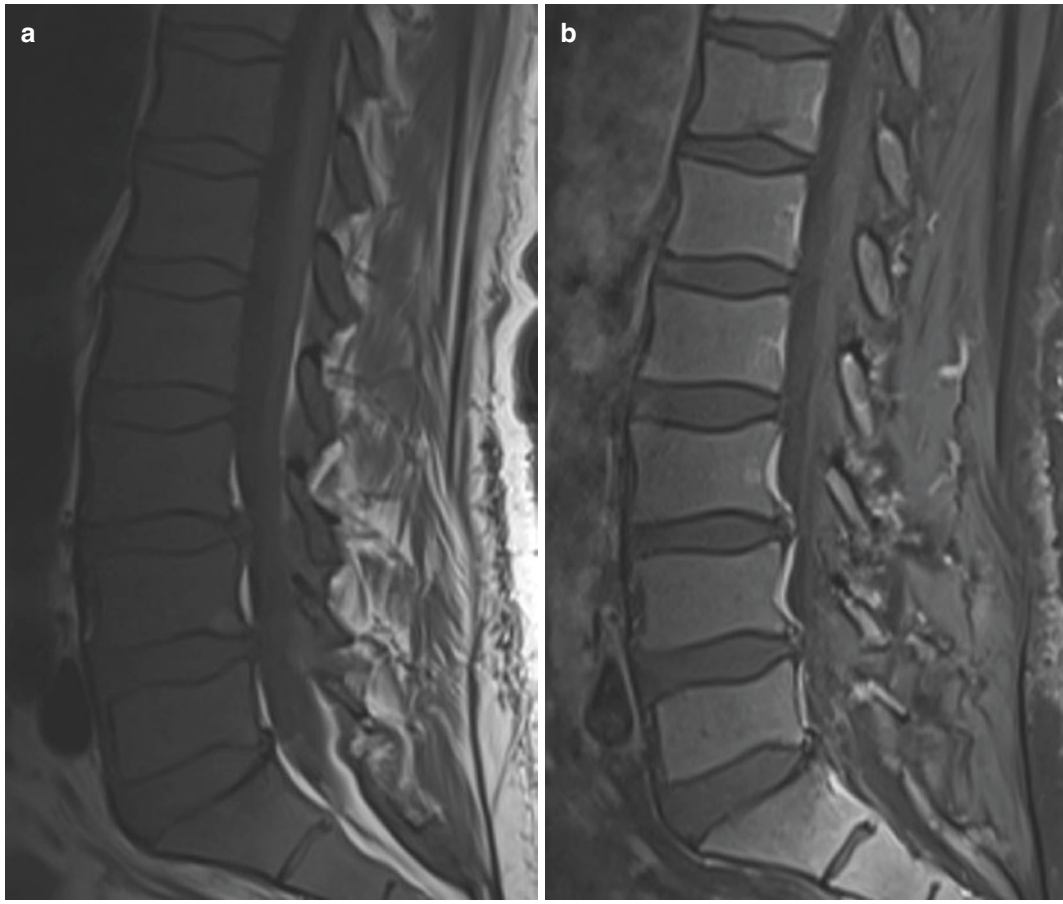

Fig. 8.11 A 76-year-old man with marrow replacement secondary to chronic myelogenous leukemia. (**a**) Sagittal T1 image of the lumbar spine demonstrates diffuse hypointense marrow that is nearly isointense to the intervertebral discs. (**b**) Fat-suppressed post-contrast T1 image shows diffuse marrow enhancement

Radiographs and CT may show osteopenia, cortical thinning, loss of trabeculae, and/or focal lytic lesions.

Differential Considerations

Diffuse leukemic marrow infiltration may be difficult to distinguish from other diffuse marrow processes such as diffuse lymphomatous, metastatic, or myelomatous disease and red marrow reconversion due to a variety of reasons [40]. However, laboratory evaluation of the peripheral blood should assist in making a definitive diagnosis. In- and out-of-phase gradient echo MRI should also demonstrate signal drop out with non-malignant causes of marrow abnormalities, such as red marrow reconversion.

Chordoma

Background

Chordoma is a rare malignancy that develops from the remnants of the primitive notochord [41, 42]. Chordoma is unique because it is a midline tumor that occurs at the ends of the spinal column—most commonly the sacrococcygeal and spheno-occipital regions and clivus [41, 42]. Chordomas are slowly growing, locally aggressive tumors that can exist for months to years before becoming symptomatic [43]. Tumors occur more commonly in men, most often in the fifth–seventh decades [41]. Complications from an enlarging, malignant, exophytic mass include compression of the spinal cord, brainstem, or cranial nerves [42].

Imaging Findings

- Midline destructive mass that most frequently involves the sacrum/coccyx and is associated with a presacral mass

Imaging almost always demonstrates a midline bony destructive mass involving two or more vertebrae with a disproportionately large soft tissue mass [42, 43]. Chordomas tend to be very heterogeneous tumors, reflecting a variety of components—mucus, hemorrhage, cartilage, and necrosis. Therefore, MRI can vary quite a bit, although lesions are largely hypo- to isointense to skeletal muscle on T1-weighted imaging (Fig. 8.12) and hyperintense on T2-weighted images. Contrast enhancement is common and usually very heterogeneous. Development of mineralization tumor matrix is rare, but tiny foci of destroyed bone may be evident on CT [42].

Differential Considerations

Multiple benign and other malignant tumors can involve the sacrum, but the epicenter is rarely the midline. Chondrosarcoma can present as a somewhat similar bony destructive T2 hyperintense mass on MRI; however, chondrosarcoma is distinctive when mineralized chondroid matrix (i.e., "rings and arcs") is present. Although sacrococcygeal teratoma might be considered due to a similar mass emanating from the sacrum, patient age and MRI features would not be consistent with a diagnosis of chordoma. Sacrococcygeal teratoma is a congenital germ cell tumor that usually presents in a different age range (i.e., prenatal or perinatal period) and contains macroscopic fat (unlike chordoma) that is identifiable on MRI.

Chondrosarcoma

Background

Chondrosarcoma is a malignant tumor occurring in middle-aged adults with a predilection for men [44, 45]. This tumor is characterized by production of chondroid matrix and, when involving the spine, occurs most frequently in the posterior elements [45, 46]. Chondrosarcoma may be primary or arise secondarily within an osteochondroma or enchondroma. As with other malignant tumors, there may be extraosseous extension into the paravertebral or epidural space [47].

Imaging Findings

- Destructive mass with mineralized chondroid matrix, better appreciated on CT

Chondrosarcoma is often a lobulated mass that is hypointense on T1-weighted images and

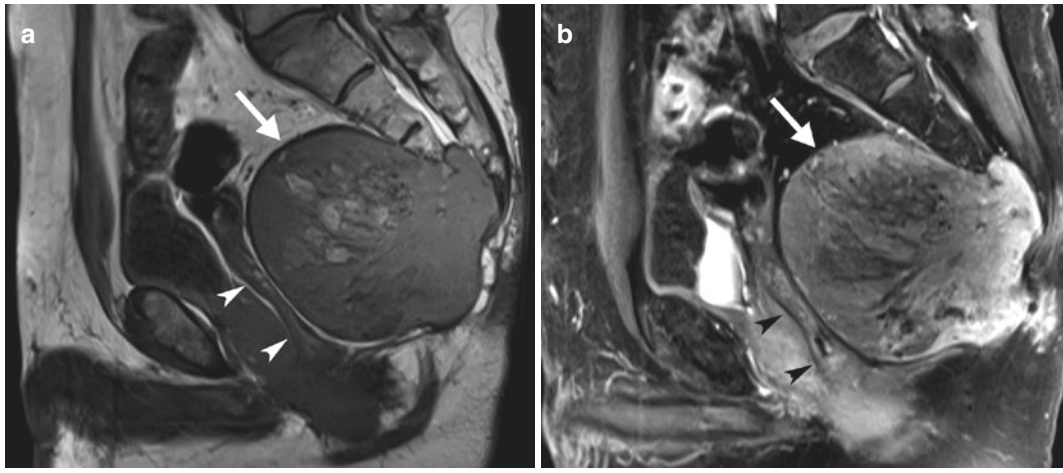

Fig. 8.12 A 66-year-old man with sacral chordoma. Sagittal T1 (**a**) and T1-enhanced (**b**) images through the sacrum demonstrate a large, enhancing, heterogenous, well-circumscribed presacral mass (*arrows*) extending from the midline of the S3–5 vertebra and superior coccyx. The multifocal T1-hyperintensity is due to hemorrhagic and mucinous components. Notice the anterior displacement and compression of the rectum (*arrowheads*)

hyperintense on T2-weighted images (Fig. 8.13), except if dedifferentiated tumor component is present [48]. Classic mineralized "rings and arcs" chondroid tumor matrix will be evident as scattered hypointense T1 and T2 signal foci on MRI (Fig. 8.13). Chondrosarcoma typically exhibits only peripheral enhancement, since the cartilaginous component does not enhance [48]. If septations are present, they will also enhance.

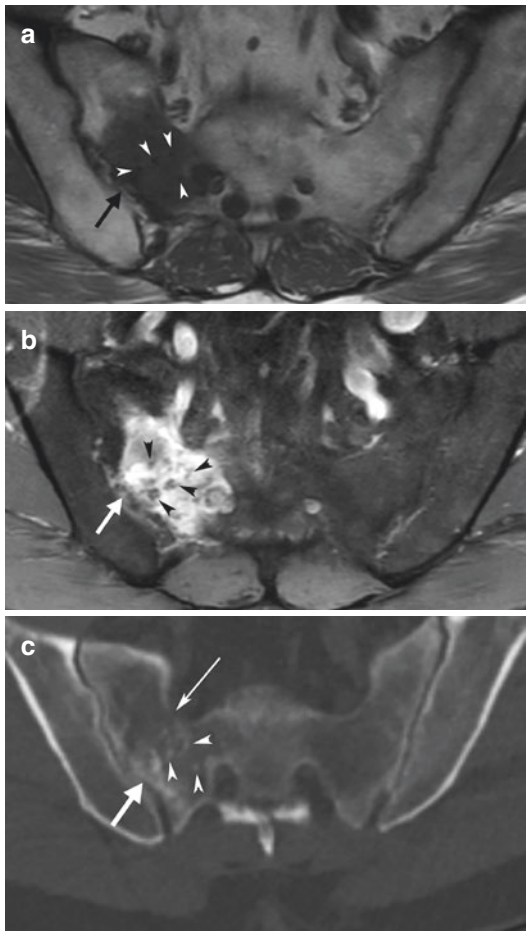

Fig. 8.13 A 60-year-old man with sacral chondrosarcoma. Axial T1 (**a**) and T2 (**b**) images of the sacrum demonstrate a heterogeneous marrow-replacing lesion (*arrows*) in the right S1 sacral ala, with multiple punctate hypointense foci (*arrowheads*). (**c**) Corresponding unenhanced CT confirms mineralized chondroid matrix (*arrowheads*) within the mass (*large arrow*) and focal anterior cortical destruction associated with the mass (*thin arrow*)

Differential Considerations

Other chondroid-producing lesions such as enchondroma are sometimes a differential dilemma. Enchondroma, however, is exceedingly rare in the spine; the vast majority of lesions occurs in the hands, feet, and metadiaphyses of long bones. Other imaging features that favor chondrosarcoma over enchondroma are deep endosteal scalloping (more than two-thirds of the cortical thickness), cortical destruction, periosteal reaction, and extraosseous soft tissue mass that may or may not contain chondroid matrix. Other malignant lesions such as metastasis and osteosarcoma may also be considered, although mineralized osteoid matrix in osteosarcoma has a cloud-like pattern, not "rings and arcs."

Ewing Sarcoma

Background

Ewing sarcoma is a small, round cell sarcoma predominantly seen in the pediatric and young adult population with a male predominance. Ewing sarcoma is included in the same family of tumors as Askin tumor and peripheral primitive neuroectodermal tumors (PNET) [49–51]. Ewing sarcoma has a genetic mutation in the vast majority of cases that involves a translocation of the EWSR1 gene on chromosome 22 and the FLI1 gene on chromosome 11 [49, 52]. When Ewing sarcoma occurs in the spine, it is most commonly located in the sacrococcygeal region followed by the lumbar spine [50]. These tumors are quite locally aggressive, and can cause a large degree of osteolysis of adjacent bones and extraosseous soft tissue extension into the spinal canal, leading to neurologic symptoms. Unique initial presenting features of Ewing sarcoma include fever, leukocytosis, and elevated erythrocyte sedimentation rate (ESR) [51].

Imaging Findings

- MRI demonstrates a marrow-replacing bone lesion, cortical destruction, and associated soft tissue mass (T1 isointense and T2 iso- to hyperintense)

MRI demonstrates a marrow-replacing bone lesion, cortical destruction, and associated soft tissue mass in 96% of cases [52]. MRI best demonstrates the full intraosseous and extraosseous extent of the tumor. On T1-weighted imaging, the mass is isointense and on T2 the mass is iso- to hyperintense (Fig. 8.14). Larger masses tend to exhibit central necrosis, which will be hyperintense on T2-weighted images. There is enhancement, but it is very heterogeneous. Corresponding radiographs most commonly show moth-eaten or permeative osseous destruction with wide zone of transition, lamellated or spiculated (sunburst or hair-on-end) periosteal reaction, and areas of sclerosis [52]. Vertebra plana is unusual in Ewing [52].

Differential Consideration

Because of the clinical presentation with fever, leukocytosis, and elevated ESR in patients with Ewing's sarcoma, osteomyelitis of the spine would be a differential consideration. Osteomyelitis most often originates from hematogenous seeding of the vertebral endplate, with subsequent involvement of the intervertebral disc and adjacent vertebral body endplate. Ewing sarcoma rarely affects the intervertebral disc and, thus, could be a distinguishing feature. Metastatic neuroblastoma could have a similar imaging appearance, but occurs earlier in childhood.

Osteosarcoma

Background

Osteosarcoma is a very aggressive osseous tumor that produces osteoid matrix and occasionally presents in the spine. It is comprised of several subtypes, can be a primary tumor, or can rarely occur secondarily in previously radiated or Pagetoid bone [53, 54]. Osteosarcoma has a bimodal distribution in children between 10 and

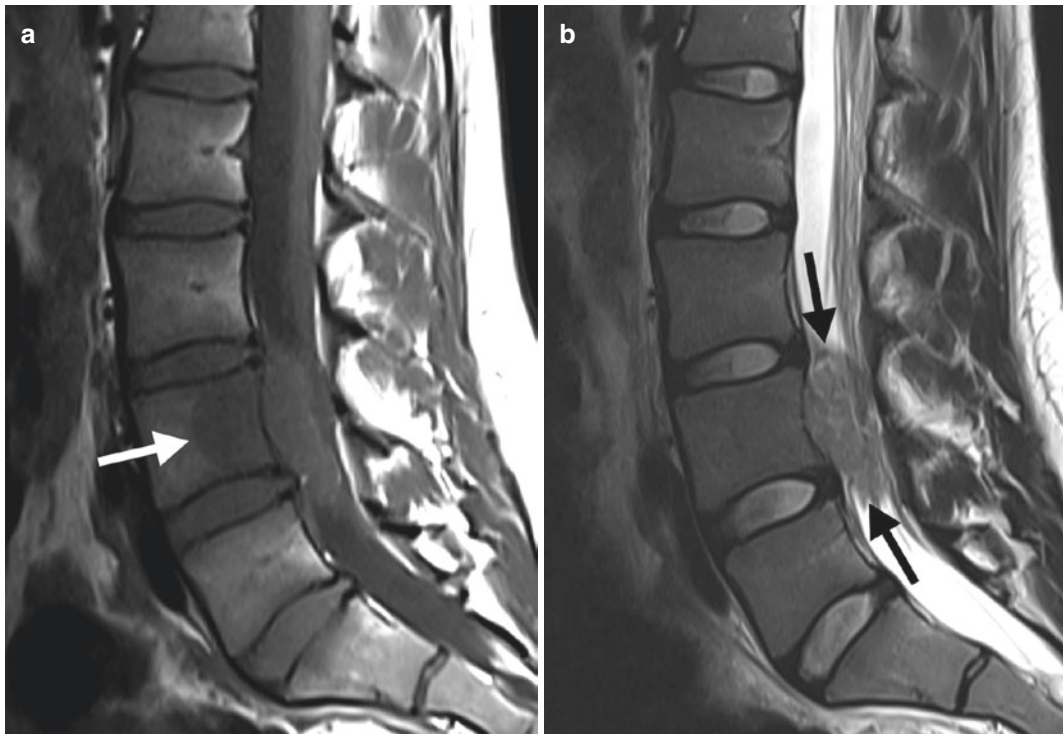

Fig. 8.14 A 20-year-old woman with Ewing sarcoma of the lumbar spine. Sagittal T1 (**a**) and T2 (**b**) images demonstrate an L4 body T1-hypointense marrow-replacing lesion (*white arrow*), which is nearly occult on T2-weighted imaging. Extraosseous tumor extends posteriorly into the spinal canal (*black arrows*), and encases and compresses the cauda equina

14 years of age and older adults, although spinal lesions tend to occur more commonly in older adults [53, 54]. Genetic markers for diagnosing osteosarcoma are well established [53]. Given its aggressive nature, osteosarcoma often invades the adjacent spinal canal, soft tissues, and neighboring vertebral bodies [55, 56].

Imaging Findings

- Highly aggressive, nonspecific destructive osseous lesion on MRI
- Presence of osteoid matrix on CT can suggest the diagnosis

Osteosarcoma involving the spine most commonly involves the sacrum, followed by the lumbar spine [54]. Radiographs and/or CT can suggest the diagnosis of osteosarcoma when "cloud-like" osteoid tumoral matrix is present within an ill-defined or permeative lytic lesion; however, mineralized matrix is not always present. Overall, the findings of osteosarcoma are variable on MRI. MRI demonstrates an aggressive lesion with destruction of local bone (Fig. 8.15) and is valuable in assessing osteosarcoma's soft tissue component and involvement of the adjacent structures. Osteoid matrix will be variable signal on T1-weighted images and heterogeneously T2 hyperintense, but areas of dense mineralization will be hypointense on both T1- and T2-weighted images [56].

Differential Consideration

Ewing sarcoma of the spine can have a very similar appearance to osteosarcoma; however, Ewing primarily affects children and adolescents.

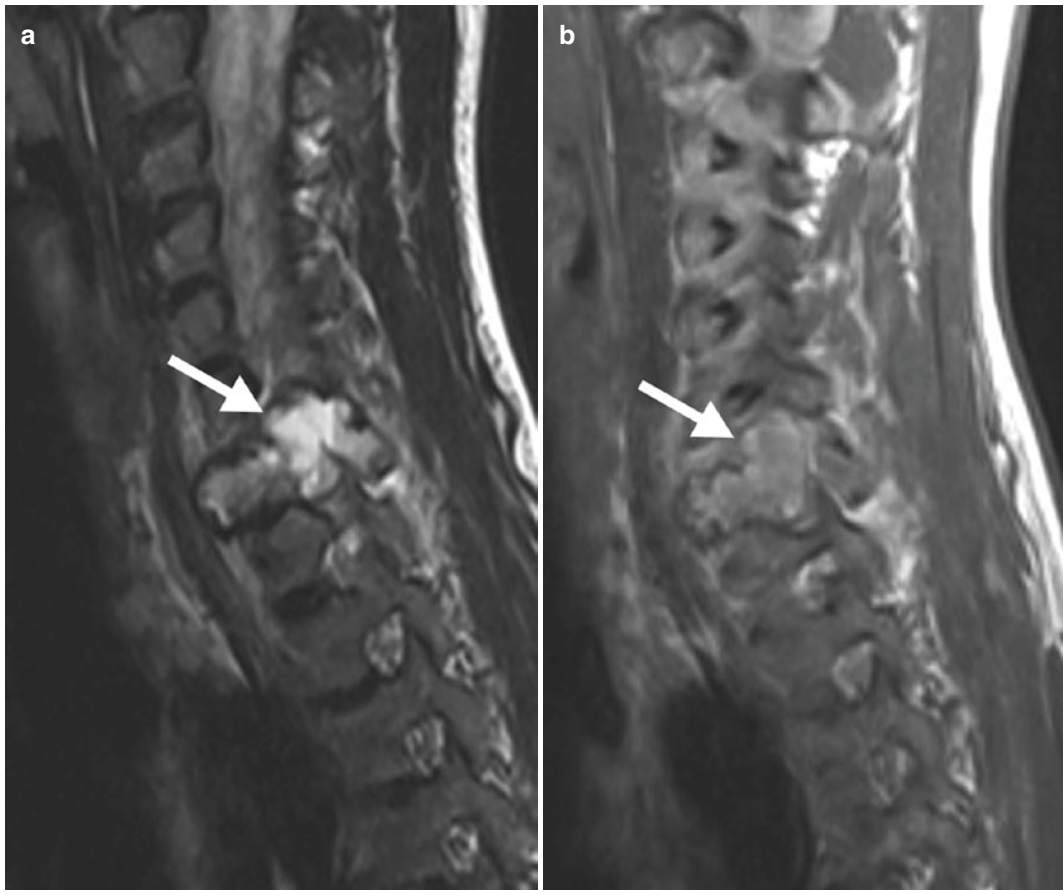

Fig. 8.15 A 13-year-old boy with osteosarcoma of C7. Sagittal T2 (**a**) and T1-enhanced (**b**) images of the cervical spine demonstrate a nonspecific destructive, lobulated and expansile, enhancing lesion in the C7 vertebra (*arrows*) with fluid-fluid levels and effacement of the C7-T1 neural foraminal fat

Chondrosarcoma is also an aggressive, destructive spinal lesion, but the presence of "rings and arcs" chondroid matrix would distinguish it from osteosarcoma. Giant cell tumor with secondary aneurysmal bone cyst formation has many overlapping features with the telangiectatic subtype of osteosarcoma; however, telangiectatic osteosarcoma is exceedingly rare in the spine.

References

1. Hameed M, Wold LE. Hemangioma. In: Fletcher DM, et al., editors. WHO classification of tumours of soft tissue and bone. 4th ed. Lyon: IARC; 2013. p. 332.
2. Unni KK, Inwards CY. Benign vascular tumors. In: Unni KK, Inwards CY, editors. Dahlin's bone tumors. 6th ed. Philadelphia: Lippincott; 2010. p. 262–71.
3. Flemming DJ, Murphey MD, Carmichael BB, et al. Primary tumors of the spine. Semin Musculoskelet Radiol. 2000;4:299–320.
4. Alexander J, Meir A, Vrodos N, et al. Vertebral hemangioma: an important differential in the evaluation of locally aggressive spinal lesions. Spine. 2010;35:E917–20.
5. Rosenberg AE, Bridge JA. Lipoma. In: Fletcher DM, et al., editors. WHO classification of tumours of soft tissue and bone. 4th ed. Lyon: IARC; 2013. p. 341.
6. Nielsen GP, Fletcher JA, Oliviera AM. Aneurysmal bone cyst. In: Fletcher DM, et al., editors. WHO classification of tumours of soft tissue and bone. 4th ed. Lyon: IARC; 2013. p. 348–9.
7. Unni KK, Inwards CY. Conditions that commonly simulate primary neoplasms of bone. In: Unni KK, Inwards CY, editors. Dahlin's bone tumors. 6th ed. Philadelphia: Lippincott; 2010. p. 305–80.
8. Mankin HJ, Hornicek FJ, Ortiz-Cruz E, et al. Aneurysmal bone cyst: a review of 150 patients. J Clin Oncol. 2005;23(27):6756–62.
9. Athanasou NA, Bensai M, Forsyth R, et al. Giant cell tumour of bone. In: Fletcher DM, et al., editors. WHO classification of tumours of soft tissue and bone. 4th ed. Lyon: IARC; 2013. p. 321.
10. Unni KK, Inwards CY. Giant cell tumor (osteoclastoma). In: Unni KK, Inwards CY, editors. Dahlin's bone tumors. 6th ed. Philadelphia: Lippincott; 2010. p. 225–42.
11. Chakarun CJ, Forrester DM, Gottsegen CJ, et al. Giant cell tumor of bone: review, mimics, and new developments in treatment. Radiographics. 2013;33:197–211.
12. Raskin KA, Schwab JH, Mankin HJ, et al. Giant cell tumor of bone. J Am Acad Orthop Surg. 2013;21(2):118–26.
13. JVMG B, Heymann D, Wuyts W. Osteochondroma. In: Fletcher DM, et al., editors. WHO classification of tumours of soft tissue and bone. 4th ed. Lyon: IARC; 2013. p. 250–1.
14. Unni KK, Inwards CY. Osteochondroma (osteocartilaginous exostosis). In: Unni KK, Inwards CY, editors. Dahlin's bone tumors. 6th ed. Philadelphia: Lippincott; 2010. p. 9–20.
15. Murphey MD, Choi JJ, Kransdorf MJ, et al. Imaging of osteochondroma: variants and complications with radiologic-pathologic correlation. Radiographics. 2000;20(5):1407–34.
16. Bernard SA, Murphey MD, Flemming DJ, et al. Improved differentiation of benign osteochondromas from secondary chondrosarcomas with standardized measurement of cartilage cap at CT and MR imaging. Radiology. 2010;255:857–65.
17. Pierz KA, Stieber JR, Kusumi K, et al. Hereditary multiple exostoses: one center's experience and review of etiology. Clin Orthop Relat Res. 2002;401:49–59.
18. Ruivo C, Hopper MA. Spinal chondrosarcoma arising from a solitary lumbar osteochondroma. JBR-BTR. 2014;97(1):21–4.
19. Horvai A, Klein M. Osteoid osteoma. In: Fletcher DM, et al., editors. WHO classification of tumours of soft tissue and bone. 4th ed. Lyon: IARC; 2013. p. 227–8.
20. Unni KK, Inwards CY. Osteoid osteoma. In: Unni KK, Inwards CY, editors. Dahlin's bone tumors. 6th ed. Philadelphia: Lippincott; 2010. p. 102–10.
21. deAndrea CE, Bridge JA, Schiller A. Osteoblastoma. In: Fletcher DM, et al., editors. WHO classification of tumours of soft tissue and bone. 4th ed. Lyon: IARC; 2013. p. 279–80.
22. Unni KK, Inwards CY. Osteoblastoma (giant osteoid osteoma). In: Unni KK, Inwards CY, editors. Dahlin's bone tumors. 6th ed. Philadelphia: Lippincott; 2010. p. 112–21.
23. Chai JW, Hong SH, Choi JY, et al. Radiologic diagnosis of osteoid osteoma: from simple to challenging findings. Radiographics. 2010;30:737–49.
24. Davies M, Cassar-Pullicino VN, McCall IW, et al. The diagnostic accuracy of MR imaging in osteoid osteoma. Skelet Radiol. 2002;31(10):559–69.
25. Lucas DR, Unni KK, McLeod RA, et al. Osteoblastoma: clinicopathologic study of 306 cases. Hum Pathol. 1994;25:117–34.
26. Baumhoer D, Bras J. Osteoma. In: Fletcher DM, et al., editors. WHO classification of tumours of soft tissue and bone. 4th ed. Lyon: IARC; 2013. p. 276.
27. Unni KK, Inwards CY. Conditions that commonly simulate primary neoplasms of bones. In: Unni KK, Inwards CY, editors. Dahlin's bone tumors. 6th ed. Philadelphia: Lippincott; 2010. p. 305–80.
28. Ihde LL, Forrester DM, Gottsegen CJ, et al. Sclerosing bone dysplasias: review and differentiation from other causes of osteosclerosis. Radiographics. 2011;31(7):1865–82.
29. Ulano A, Bredella MA, Burke P, et al. Distinguishing untreated osteoblastic metastases from enostoses using CT attenuation measurements. AJR Am J Roentgenol. 2016;207(2):362–8.
30. Unni KK, Inwards CY. Conditions that commonly simulate primary neoplasms of bones. In: Unni KK,

Inwards CY, editors. Dahlin's bone tumors. 6th ed. Philadelphia: Lippincott; 2010. p. 305–80.
31. Kaloostian PE, Yurter A, Zadnik PL, et al. Current paradigms for metastatic spinal disease: an evidence-based review. Ann Surg Oncol. 2014;21(1):248–62.
32. Lorsbach R, Kluin PM. Plasma cell myeloma. In: Fletcher DM, et al., editors. WHO classification of tumours of soft tissue and bone. 4th ed. Lyon: IARC; 2013. p. 312–4.
33. Unni KK, Inwards CY. Myeloma. In: Unni KK, Inwards CY, editors. Dahlin's bone tumors. 6th ed. Philadelphia: Lippincott; 2010. p. 191–200.
34. Lorsbach R, Kluin PM. Solitary plasmacytoma of bone. In: Fletcher DM, et al., editors. WHO classification of tumours of soft tissue and bone. 4th ed. Lyon: IARC; 2013. p. 315.
35. Dimopoulos MA, Hillengass J, Usmani S, et al. Role of magnetic resonance imaging in the management of patients with multiple myeloma: a consensus statement. J Clin Oncol. 2015;33(6):657–64.
36. Ferraro R, Agarwal A, Martin-Macintosh EL, et al. MR imaging and PET/CT in diagnosis and management of multiple myeloma. Radiographics. 2015;35:438–54.
37. Mulligan ME, Badros AZ. PET/CT and MR imaging in myeloma. Skelet Radiol. 2007;36:5–16.
38. Hanrahan CJ, Cr C, Crim JR. Current concepts in the evaluation of multiple myeloma with MR imaging and FDG PET/CT. Radiographics. 2010;30(1):127–42.
39. Brunning RD, Matutes E, Harris NL, et al. Acute myeloid leukemia. In: Jaffe ES, et al., editors. Pathology and genetics: tumours of haematopoietic and lymphoid tissues. Lyon: IARC; 2001. p. 77–80.
40. Unni KK, Inwards CY. Malignant lymphoma of bone. In: Unni KK, Inwards CY, editors. Dahlin's bone tumors. 6th ed. Philadelphia: Lippincott; 2010. p. 201–10.
41. Flanagan AM, Yamaguchi T. Chordoma. In: Fletcher DM, et al., editors. WHO classification of tumours of soft tissue and bone. 4th ed. Lyon: IARC; 2013. p. 328–9.
42. Unni KK, Inwards CY. Chordoma. In: Unni KK, Inwards CY, editors. Dahlin's bone tumors. 6th ed. Philadelphia: Lippincott; 2010. p. 248–60.
43. Sciubba DM, Chi JH, Rhines LD, et al. Chordoma of the spinal column. Neurosurg Clin N Am. 2008;19(1):5–15.
44. Hogendoorn PCW, Bovee JVMG, Nielsen GP. Chondrosarcoma (grades I-III), including primary and secondary variants and periosteal chondrosarcoma. In: Fletcher DM, et al., editors. WHO classification of tumours of soft tissue and bone. 4th ed. Lyon: IARC; 2013. p. 264–8.
45. Unni KK, Inwards CY. Chondrosarcoma (primary, secondary, dedifferentiated, and clear cell). In: Unni KK, Inwards CY, editors. Dahlin's bone tumors. 6th ed. Philadelphia: Lippincott; 2010. p. 60–91.
46. Giuffrida AY, Burgueno J, Gutierrez JC, et al. Chondrosarcoma in the United States (1973 to 2003): an analysis of 2890 cases from the SEER database. J Bone Joint Surg Am. 2009;91(5):1063–72.
47. McLoughlin GS, Sciubba DM, Wolinsky JP. Chondroma/chondrosarcoma of the spine. Neurosurg Clin N Am. 2008;19(1):57–63.
48. Murphey MD, Walker EA, Wilson AJ, et al. From the archives of the AFIP: imaging of primary chondrosarcoma: radiologic-pathologic correlation. Radiographics. 2003;23:1245–78.
49. deAlava E, Lesnick SL, Sorensen PH. Ewing sarcoma. In: Fletcher DM, et al., editors. WHO classification of tumours of soft tissue and bone. 4th ed. Lyon: IARC; 2013. p. 306–9.
50. Unni KK, Inwards CY. Ewing tumor. In: Unni KK, Inwards CY, editors. Dahlin's bone tumors. 6th ed. Philadelphia: Lippincott; 2010. p. 211–24.
51. Balamuth NJ, Womer RB. Ewing's sarcoma. Lancet Oncol. 2010;11(2):184–92.
52. Murphey MD, Senchak LT, Mambalam PK, et al. From the radiologic pathology archives: Ewing sarcoma family of tumors: radiologic-pathologic correlation. Radiographics. 2013;33:803–31.
53. Rosenberg AE, Cleton-Jansen AM, de Pinieux G, et al. Conventional osteosarcoma. In: Fletcher DM, et al., editors. WHO classification of tumours of soft tissue and bone. 4th ed. Lyon: IARC; 2013. p. 282–8.
54. Unni KK, Inwards CY. Conditions that commonly simulate primary neoplasms of bones. In: Unni KK, Inwards CY, editors. Dahlin's bone tumors. 6th ed. Philadelphia: Lippincott; 2010. p. 122–54.
55. Ropper AE, Cahill KS, Hanna JW, et al. Primary vertebral tumors: a review of epidemiologic, histological and imaging findings, Part II: Locally aggressive and malignant tumors. Neurosurgery. 2012;70:211–9.
56. Orguc S, Arkun R. Primary tumors of the spine. Semin Musculoskelet Radiol. 2014;18:280–99.

MRI in Dural Lesions

9

Mougnyan Cox

Anatomy of the Dura

The spinal dura is a continuation of the intracranial dura [1]. It contains three layers: the dura mater, arachnoid mater, and pia. The dura and arachnoid mater in the spine are closely adherent, and together, form the outer layer of the thecal sac. A potential space, the subdural space, exists between the dura and arachnoid mater. This space is usually not visible on normal cross-sectional images of the spine but can become apparent when distended with blood, fluid, pus, or occasionally iodinated contrast from a suboptimally placed spinal needle during the performance of a myelogram. The subarachnoid space is subjacent to the arachnoid mater and contains cerebrospinal fluid (CSF) that bathes the spinal cord and nerves. This is the target of lumbar punctures and myelograms. The pia mater is intimately connected to the surface of the spinal cord and nerves. The thecal sac extends from the foramen magnum to the level of S2. Below S2, the filum terminale extends caudally from the end of the thecal sac to the sacrum. The space within the bony spinal canal that is superficial to or outside the thecal sac is called the epidural space. This space contains mostly fat, nerves, and blood vessels. The nerves within this space are usually the target of epidural spinal injections and can be accessed via a transforaminal or interlaminar approach.

Pathology of the Dura

Magnetic resonance imaging (MRI) is the imaging modality of choice to evaluate the anatomy and pathology of the dura and its adjacent spaces. In cases where MRI is contraindicated, computed tomographic (CT) myelogram can be performed to assess the dura and adjacent spaces. Pathology of the dura is most efficiently analyzed by a compartment-based approach. The location of the lesion or mass is an important clue to the identity of the lesion. Localizing a lesion to epidural space, dura, intradural extramedullary space, or within the substance of the cord is straightforward in most instances, but can be challenging when the lesion is large, trans-spatial, or when the spinal anatomy has been distorted by prior surgery. Some important clues can help localize a lesion to a particular space. Epidural

M. Cox (✉)
Hospital of the University of Pennsylvania,
Philadelphia, PA, USA
e-mail: mougnyan.cox@pennmedicine.upenn.edu

W. B. Morrison et al. (eds.), *MRI of the Spine*, https://doi.org/10.1007/978-3-030-43627-8_9

lesions are superficial to the hypointense layer of the thecal sac and will displace the dura inwards. Subdural lesions are located within the layers of the thecal sac and do not distort the outer margin of the thecal sac. However, the subdural collection or mass distends the thecal sac inwards, and there is usually a thinner layer of the dura that displaces/compresses nerves and CSF inwards. Intradural extramedullary lesions are located within the thecal sac, cause mass effect on the cord or cauda equina when large, and widen the CSF space between the cord and the lesion [2].

Epidural Lesions

Epidural tumors usually (but not always) represent extra-osseous extension of bony metastases into the epidural space. Almost any metastasis can have epidural extension. Common examples include lymphoma and primary cancers originating from the lung, prostate, breast, and kidneys (Figs. 9.1 and 9.2). Benign but aggressive-appearing lesions such as atypical hemangiomas may also have a prominent epidural component and cause cord compression (Fig. 9.3).

Epidural abscesses in the spine usually present with back pain. The patient may be febrile and have an elevated white blood cell count, but these clinical markers are not reliable enough to exclude the diagnosis. The erythrocyte sedimentation rate and C-reactive protein are usually elevated. MRI is the best imaging modality to exclude an epidural abscess and will show a heterogeneous collection in the epidural space, usually with peripheral enhancement (Fig. 9.4). Associated discitis-osteomyelitis or septic facet arthritis is usually also present, and lends further support to the diagnosis of an epidural abscess [3].

Epidural hematomas also appear as a heterogeneous collection in the epidural space, with mass effect on and inward displacement of the thecal sac/dura (Fig. 9.5). Epidural hematomas can be trauma-related in the setting of spinal fractures, but spontaneous hematomas also occur, particularly in patients on anticoagulation or with coagulopathies. Spontaneous epidural hematomas tend to occur in the dorsal epidural space, which is less tightly packed. On MRI, the hematoma usually appears heterogeneous or even hypointense on T2, and may be isointense to hyperintense on T1 (with increasing amounts of methemoglobin).

Large disc herniations can also protrude into the epidural space and cause substantial mass effect on the thecal sac and cord/cauda equina (Fig. 9.6). Discs are probably the most common epidural mass. The diagnosis is usually straightforward when the herniated disc remains attached to the parent disc. Herniated discs that lose their attachment to the parent disc and migrate away from the disc level can be challenging to diagnose and may simulate other masses. These sequestered migrated discs are also an important cause of failed back surgery, especially if unrecognized on preoperative imaging.

Subdural Lesions

Subdural lesions usually represent fluid or blood and are typically iatrogenic/related to recent procedures. Less commonly, pus or tumor can be present in the subdural space (Fig. 9.7). Subdural lesions do not distort the outer layer of the thecal sac, but cause inward displacement of the inner thecal sac layer with mass effect on the cord and nerves (Fig. 9.8). The collections are limited by thin ligaments that attach the cord to the inner layer of the thecal sac, causing a triangular or "Mercedes benz" shape on MRI [4]. Surgical evacuation of subdural lesions requires incision of the dura, and the subdural location of the lesion should be communicated to the surgeon preoperative for surgical planning.

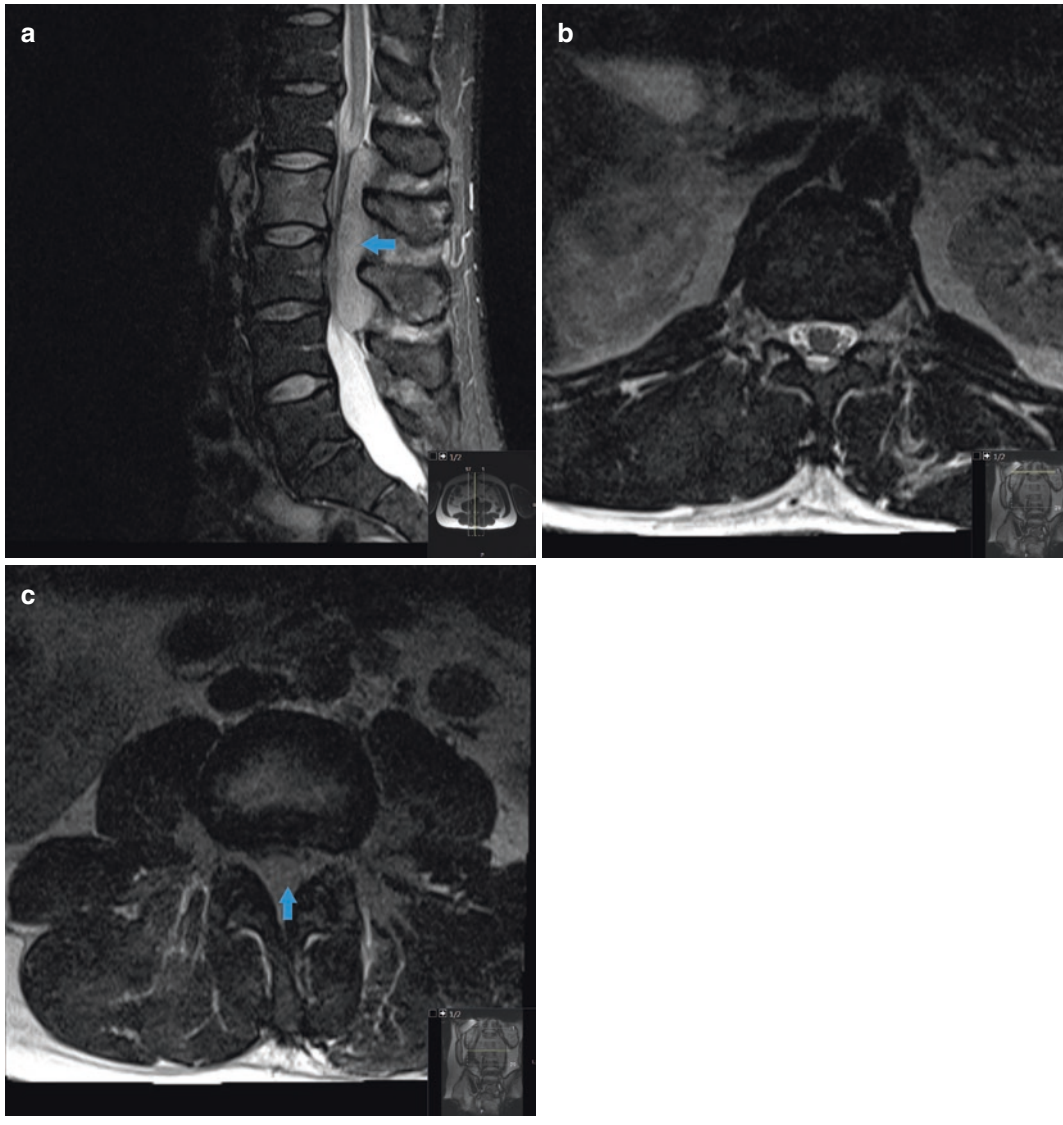

Fig. 9.1 Lymphoma. Figure 9.1**a** is a sagittal fat-saturated T2-weighted MR image showing a large primarily dorsal epidural soft tissue mass causing marked spinal canal stenosis and compression of the cauda equina (arrow). Figure 9.1**b** is an axial T2-weighted MR image taken above the level of compression, showing normal appearance of the distal conus medullaris and thecal sac. Figure 9.1**c** is an axial T2-weighted MR image at the level of compression, showing marked spinal canal stenosis and compression of the thecal sac and cauda equina by the large epidural mass (arrow). There is also near-complete marrow replacement of the L2 vertebral body by tumor, as well as additional osseous metastases

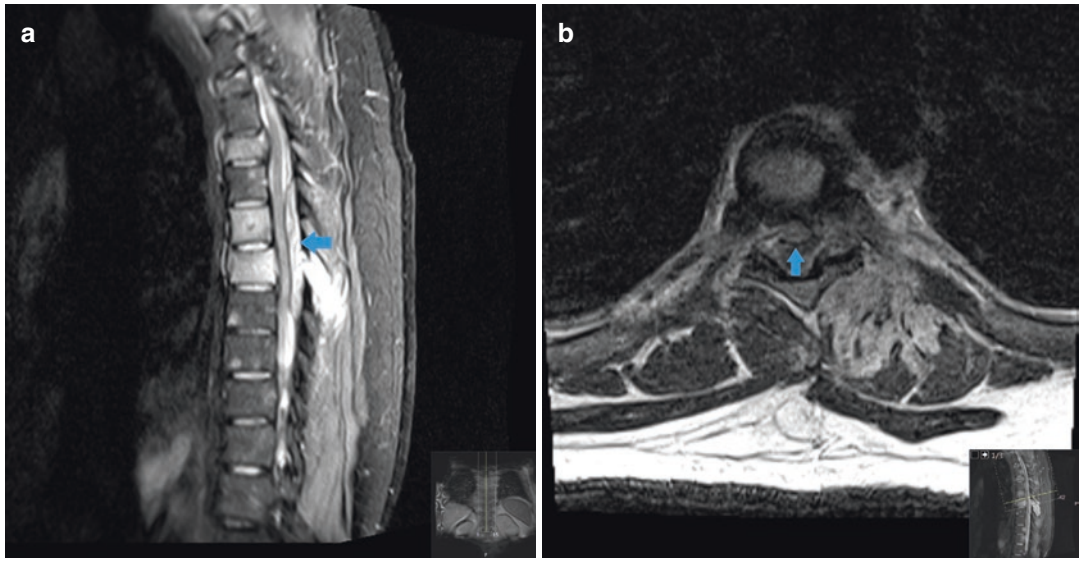

Fig. 9.2 Dysplastic small round cell tumor Figure 9.2**a** is a sagittal fat-saturated postcontrast T1-weighted MR image showing a dorsal epidural tumor in the mid-thoracic spine, causing mass effect on the thoracic cord (arrow). There are also osseous metastases. Figure 9.2**b** is an axial T2-weighted MR image showing mass effect on the thecal sac by the dorsal epidural tumor. This image also nicely depicts the inwardly displaced T2 hypointense dural layer (arrow)

Intradural Extramedullary Lesions

Intradural extramedullary lesions refers to lesions that are within the subarachnoid space of the thecal sac but outside the substance of the spinal cord. Common lesions in this space include meningiomas, nerve sheath tumors, metastases, and rarely, discs that have migrated into the intradural space. Imaging features of some of the more common intradural extramedullary lesions are discussed later.

Nerve Sheath Tumors

Nerve sheath tumors are among the most common intradural extramedullary masses of the spine. They are usually schwannomas or neurofibromas, with malignant peripheral nerve sheath tumors making up a small minority of these lesions. The difference between schwannomas and neurofibromas is a histologic one; both lesions can appear similar on imaging. Typically, these lesions present as a fusiform mass along the course of the nerve on imaging, iso- to hypodense to muscle on CT, T1 hypointense and T2 hyperintense on MRI, with enhancement. The lesions may be heterogeneous on imaging, depending on the amount of myxoid tissue, hemorrhage, or calcification. Schwannomas commonly involve the dorsal sensory nerve root, and may be dumbbell-shaped in appearance when they extend from the spinal canal into the neuroforamen (Fig. 9.9). Malignant peripheral nerve sheath tumors may appear similar to their benign counterparts but should be suspected when osseous destruction (rather than bony remodeling), rapid growth, and metastases are present (Fig. 9.10).

Meningioma

Meningiomas in the spine are probably the most common intradural extramedullary masses in the spine along with nerve sheath tumors, and appear similar to meningiomas in the intracranial compartment on imaging. These lesions most commonly occur in the thoracic spine, and are more

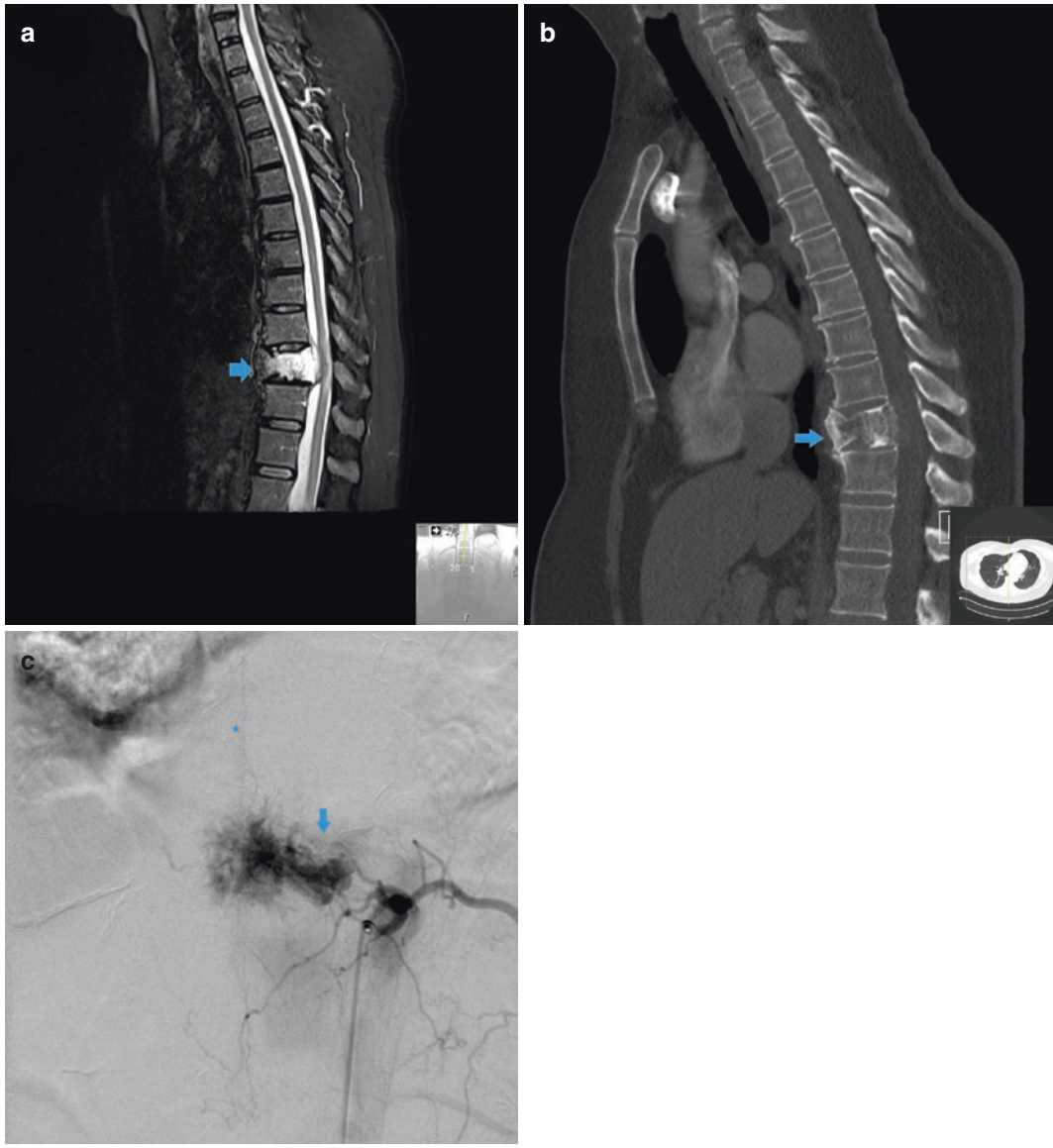

Fig. 9.3 Atypical hemangioma Figure 9.3**a** is a sagittal fat-saturated T2-weighted MR image showing an expansile T2-weighted lesion of the T10 vertebral body, causing marked displacement of the thecal sac and mass effect on the cord (arrow). There is associated cord signal abnormality at that level. Figure 9.3**b** is an unenhanced CT of the thorax showing abnormal medullary architecture of the T10 vertebral body (arrow). Given the marked T2 hyperintensity of the vertebral body on MRI, an atypical/aggressive hemangioma was favored. Figure 9.3**c** is a frontal projection of a preoperative conventional spinal angiogram in the peak arterial phase, showing marked vascularity of the T10 vertebral body compatible with a hemangioma (arrow). The anterior spinal artery (star) was supplied by the same radiculomedullary pedicle at this level, so embolization of this feeder was not performed. Histopathologic examination confirmed the findings of an atypical hemangioma

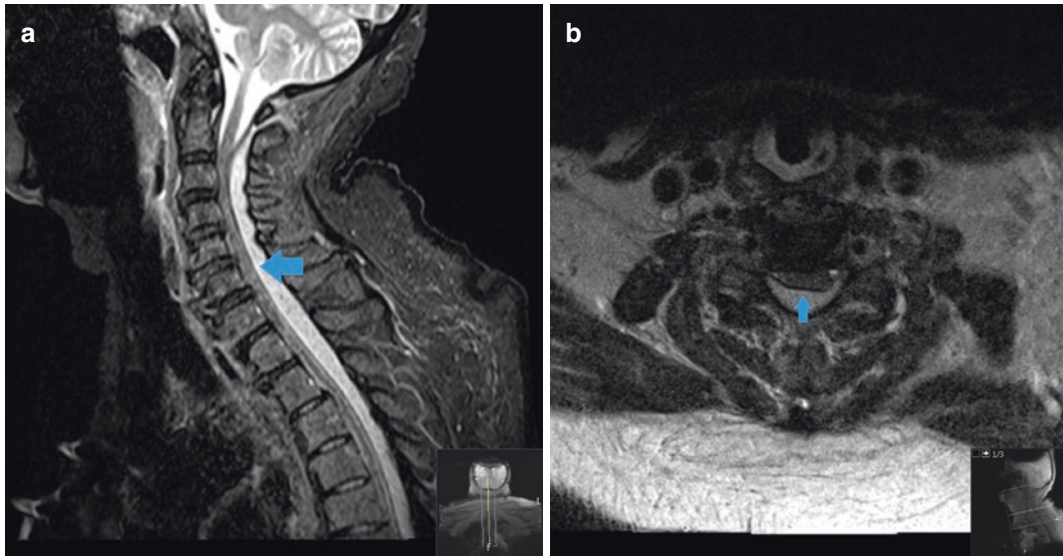

Fig. 9.4 Epidural abscess Figure 9.4**a** is a sagittal fat-saturated T2-weighted MR image showing a large dorsal epidural collection causing mass effect on the cervical cord (arrow). In Fig. 9.4**b**, an axial T2-weighted MR image, the inwardly displaced hypointense layer of the dura/thecal sac is well depicted. A large epidural abscess was evacuated at surgery

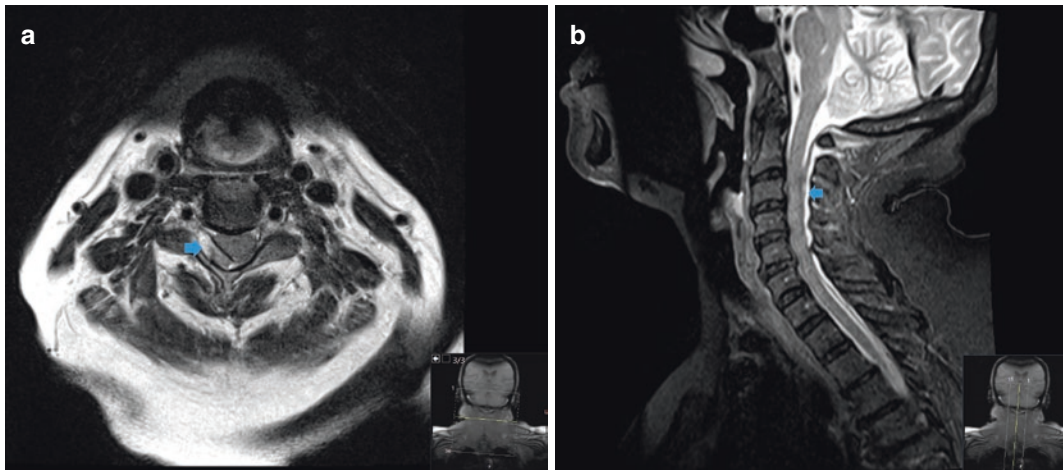

Fig. 9.5 Epidural hematoma Figure 9.5**a** is an axial T2-weighted MR image through the cervical spine, showing a heterogeneous dorsal epidural hematoma at the right dorsolateral aspect of the spinal canal causing mass effect on the thecal sac (arrow). Figure 9.5**b** is a sagittal Short tau inversion recovery (STIR) MR image showing the full extent of the dorsal epidural hematoma causing mass effect on the cervical cord (arrow)

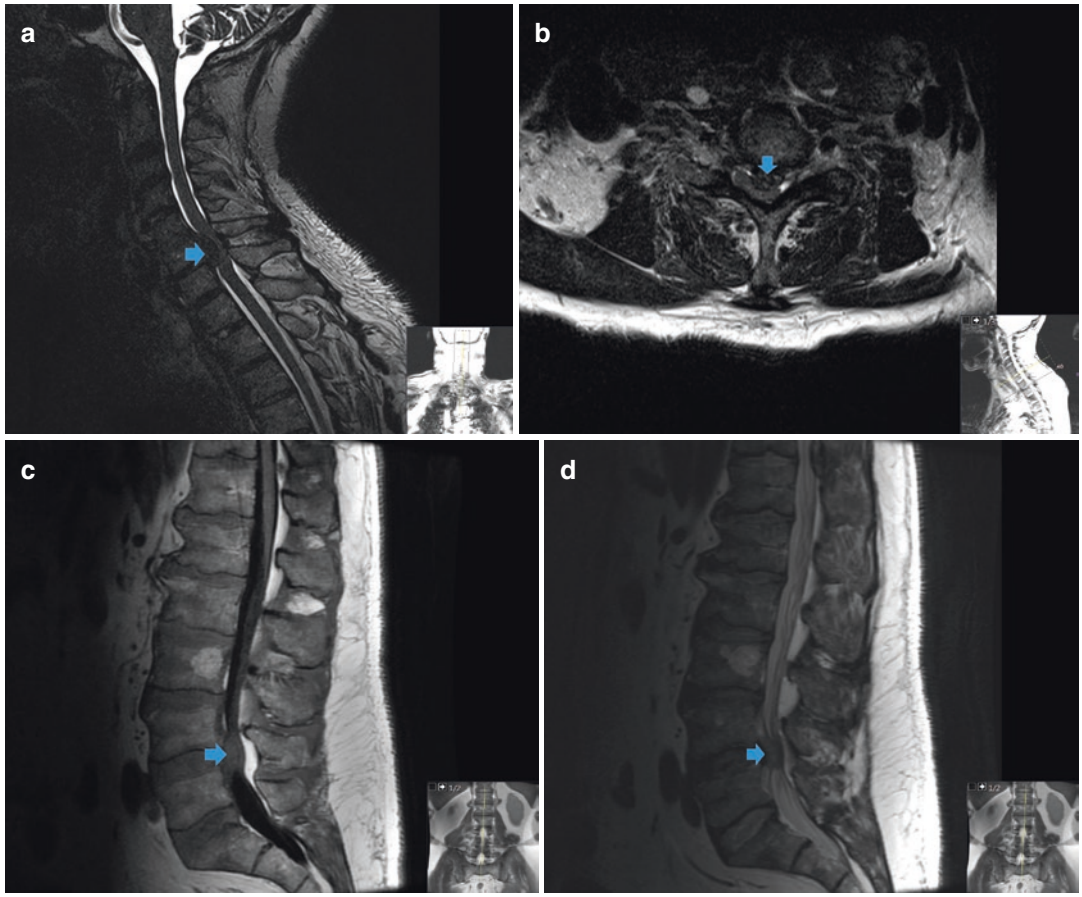

Fig. 9.6 Disc extrusion Figure 9.6**a** is a sagittal heavily T2-weighted MR image of the cervical spine showing a large disc extrusion at C6–C7 causing marked spinal canal stenosis and compression of the cervical cord (arrow). Figure 9.6**b** is an axial T2-weighted MR image showing the disc extrusion causing mass effect on the cord (arrow). Figure 9.6**c** is a sagittal T1-weighted MR image in a different patient showing a large disc extrusion at L4–L5 causing narrowing of the spinal canal and mass effect on the cauda equina (arrow). Figure 9.6**d** is a sagittal T2-weighted MR image of the lumbar spine in the same patient, showing mass effect on the cauda equina by the disc extrusion (arrow)

common in females. On imaging, meningiomas are usually homogeneously enhancing round or plaque-like masses with a broad attachment site to the dura (Fig. 9.11). Calcification may be present, and resection of densely calcified lesions poses an increased risk of postoperative deficits.

Metastases

Drop metastases from intracranial malignancies are fairly common with certain tumors, particularly ependymomas and World Health Organization (WHO) grade IV gliomas. Other causes of intradural extramedullary metastases include systemic malignancies like lung cancer, breast cancer, leukemia, and lymphoma. On images, these lesions have a variety of appearances. There may be small nodular masses along the surface of the cord and cauda equina, with a tumor deposit at the bottom of the thecal sac. Other cases may show diffuse thickening and enhancement of the cauda equina nerve roots.

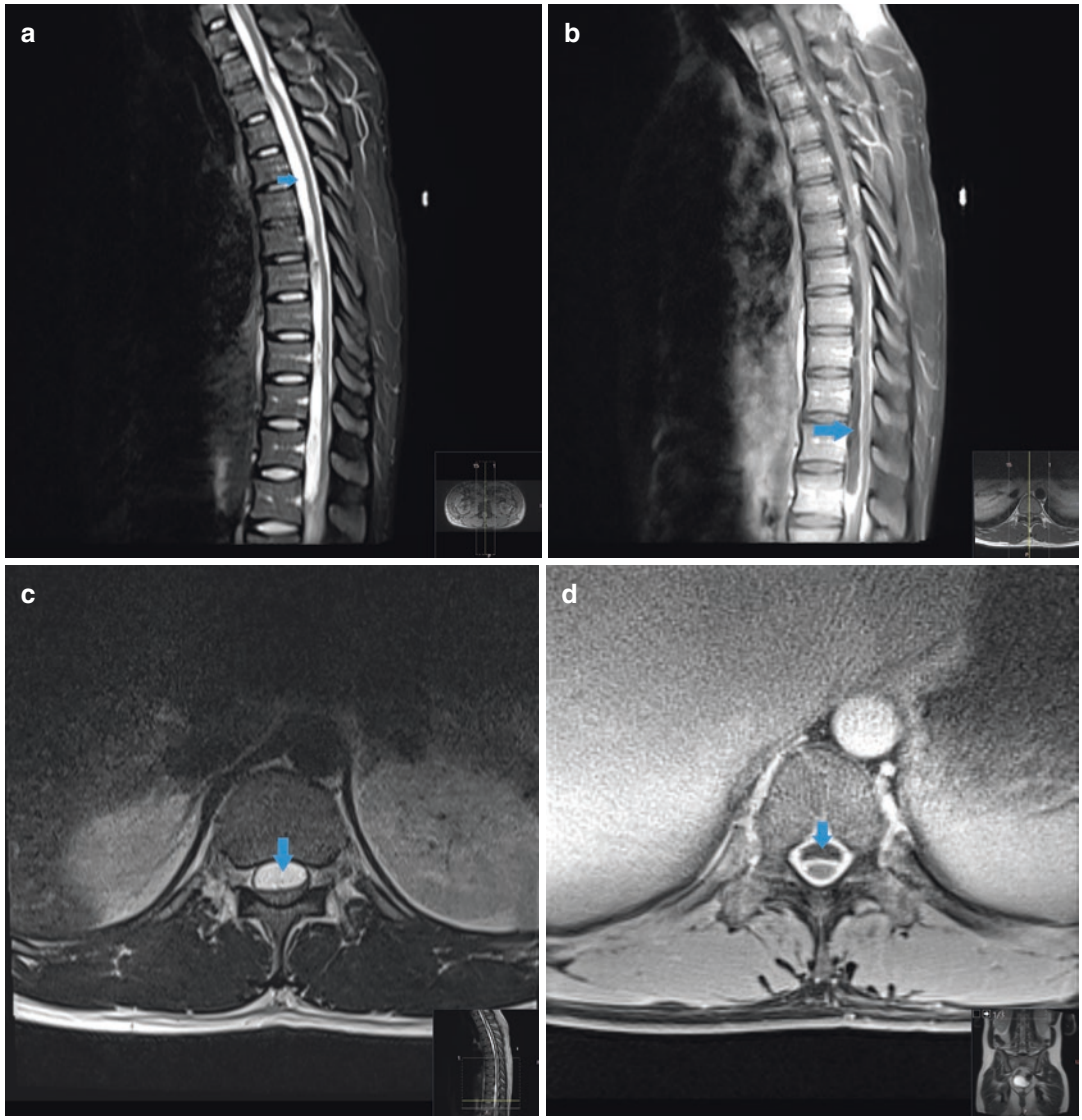

Fig. 9.7 Subdural abscess Figure 9.7**a** is a sagittal STIR MR image showing a large subdural collection in the ventral thoracic spine causing mild mass effect on the thoracic cord (arrow). Unlike the prior case of an epidural abscess, no inward displacement of the dura is present in this case of subdural pathology. Figure 9.7**b** is a sagittal fat-saturated postcontrast T1-weighted MR image of the thoracic spine showing the loculated peripherally enhancing collection in the ventral subdural space (arrow). Findings are confirmed on the axial T2 MR image (Fig. 9.7**c**) and axial postcontrast T1-weighted image (Fig. 9.7**d**) of the thoracic spine. A subdural abscess was evacuated at surgery upon incision of the thecal sac (durotomy)

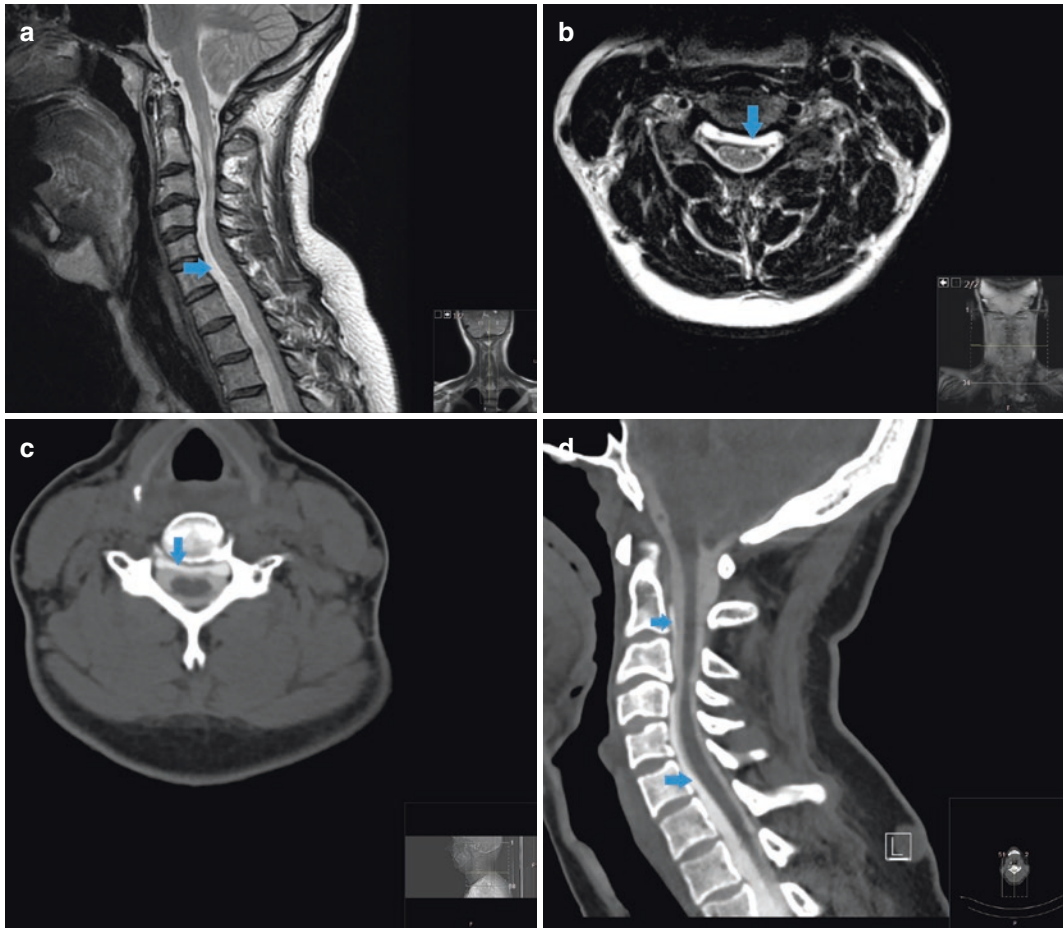

Fig. 9.8 Subdural collection Figure 9.8**a** is a sagittal T2-weighted MR image of the cervical spine showing a large ventral CSF-density collection causing mild mass effect on the cervical cord. At first glance, it appears as if the collection may be epidural. Figure 9.8**b** is an axial T2-weighted MR image showing the collection. However, the outer border/wall of the thecal sac is preserved, without inward displacement. Axial (Figure 9.8**c**) and sagittal images from a CT myelogram better depict the nature of the collection, and confirm that its location is likely subdural (arrows in Fig. 9.8**d**). The collection was caused by a CSF leak from a dural defect in the high cervical spine. The distinction between spinal epidural and subdural collections can be difficult at times

Myxopapillary Ependymoma

Myxopapillary ependymomas are a special subtype of ependymoma that arise from the ependymal cells of the conus medullaris and filum terminale. A large heterogeneous mass of the conus medullaris and/or filum terminale is typical, with associated enhancement (Fig. 9.12). These lesions are an important cause of unexplained superficial siderosis, due to their tendency for repeated hemorrhage into the subarachnoid space.

Paragangliomas

Paragangliomas are neuroendocrine tumors derived from neural crest cells dispersed throughout the body. In the spine, these tumors are most commonly located in the region of the filum terminale (Fig. 9.13). Together with myxopapillary ependymomas, paragangliomas make up the majority of primary tumors located in the cauda equina/filum terminale region. Paragangliomas are highly vascular tumors, with avid enhancement and peritumoral blood vessels/flow voids

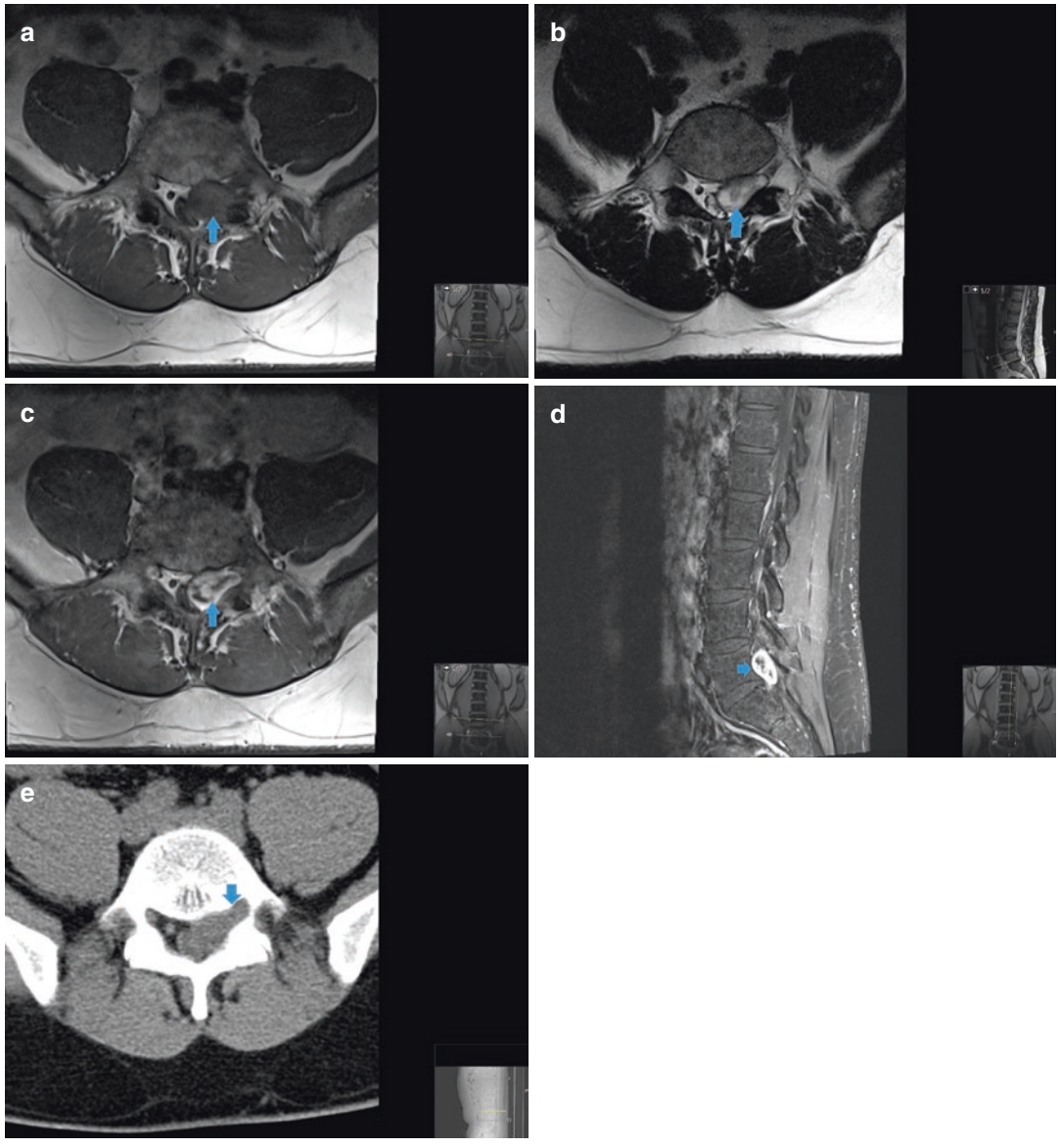

Fig. 9.9 Schwannoma. Figure 9.9**a** is an axial T1-weighted MR image showing an intradural extramedullary mass centered in the left lower lumbar thecal sac, extending through the left L4–L5 neural foramen (arrow). The lesion has a mild dumb-bell-shaped appearance, is mildly hyperintense on the T2-weighted MR image (Fig. 9.9**b**), and shows heterogeneous enhancement on the axial and sagittal postcontrast T1-weighted MR images (Figs. 9.9**c** and **d**). On the noncontrast CT image (Fig. 9.9**e**), there is mild expansion of the ipsilateral left neural foramen through which the lesion extends (arrow)

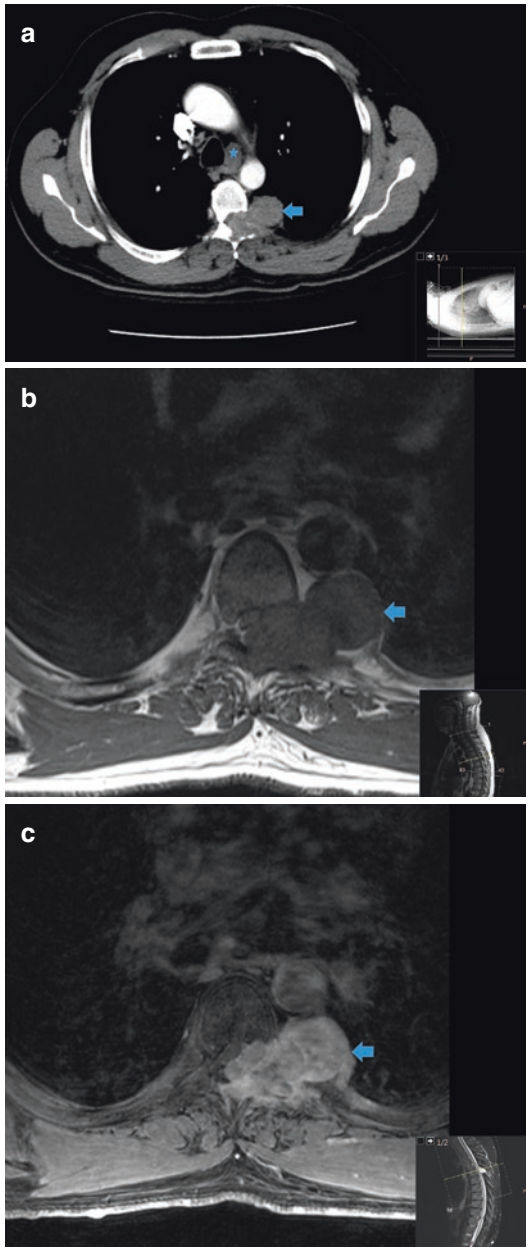

Fig. 9.10 Malignant peripheral nerve sheath tumor. Figure 9.10**a** is a contrast-enhanced CT of the chest, showing a solid intradural extramedullary mass in the thoracic spine (arrow), eroding the adjacent bony spine, and extending through the left neural foramen into the adjacent pleural space. There is also pathologic mediastinal lymph node (star). Figures 9.10**b** and **c** are unenhanced T1 and postcontrast T1-weighted MR images, respectively, showing the solid enhancing mass in the thoracic spine (arrows). The mass was excised, and the pathology was consistent with a malignant peripheral nerve sheath tumor

on MR. There may be a T2 hypointense hemosiderin cap at the ends of the tumor, reflecting its vascular nature and propensity for bleeding.

Cystic Intradural Extramedullary Lesions

Intradural extramedullary cystic lesions are fairly common in any busy spine practice. Many of the lesions are CSF-density or similar to CSF density, and present with only subtle mass effect on and displacement of the cord and widening of the CSF space adjacent to the cord. Probably one of the most common intradural extramedullary cyst is an arachnoid cyst. This lesion follows CSF signal on all MRI sequences, similar to arachnoid cysts in the intracranial compartment. Epidermoid cysts can be similar to CSF density on MRI, but usually show restricted diffusion within the lesion. Teratomas are congenital lesions in the spine that usually contain areas of fat signal, with some areas of soft tissue density. Foci of calcification may be present within the lesion, most easily appreciated on CT scans.

Intramedullary Lesions

Intramedullary lesions arise within the substance of the cord and are easy to distinguish from the extramedullary lesions in the majority of cases. These lesions cause edema or edema-like signal within the cord, with or without enhancement. Some degree of cord expansion is usually present, which is an important clue that the lesion is intramedullary (Fig. 9.14). Common intramedullary lesions include primary tumors like ependymomas and astrocytomas, metastases from systemic malignancies, transverse myelitis, and venous congestion or hemorrhage from vascular pathologies.

Other

Other pathologic conditions of the dura do not fit neatly into any classification, but are important for the orthopedic surgeon to be aware of. Some

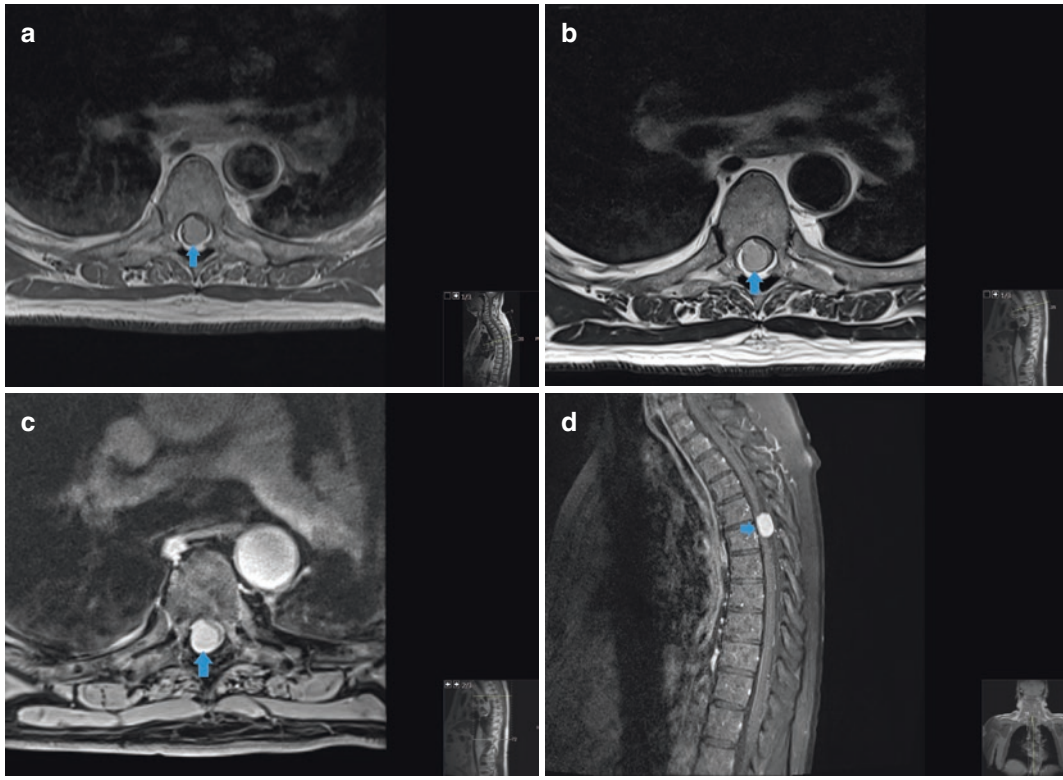

Fig. 9.11 Meningioma. Figure 9.11**a** is an axial T1-weighted MR image showing a round isointense intradural extramedullary mass in the thoracic spine causing marked cord displacement and cord compression (arrow). The mass appears isointense on the T2-weighted MR image (Fig. 9.11**b**) and enhances avidly on the postcontrast axial and sagittal T1-weighted images (Figs. 9.11**c** and **d**). The mass was resected, and pathology showed a meningioma

of these entities present with nonspecific symptoms, and the imaging may offer the first clue to uncover this condition on cross-sectional image of the spine. Some uncommon but important pathologic conditions of the dura are discussed below.

Spinal CSF Leak

Spinal CSF leaks may occur spontaneously or after a recent procedure like a lumbar puncture or spinal surgery. Patients present with postural headaches that are most severe with standing or walking and improve when the patient is recumbent or supine. The clinical picture is straightforward after a recent procedure, but can be more confusing when the leak occurs spontaneously. Characteristically there may be findings of CSF hypotension on cranial MRI which include sagging of the base of the brain, downward displacement of the brainstem, and the presence of bifrontal hygromas. The site of the leak is usually not visible even with conventional myelography. An important clue on routine spinal MRs is subtle pooling of CSF adjacent to a root pouch cyst or a intradural collection of CSF. Rarely is the CSF collection large unless it is preceded by surgery. A large extradural CSF collection in the spine may be seen with fast CSF leaks (Fig. 9.15); the site of these fast leaks may only be evident on dynamic CT myelography. Other potential findings include prominence of the spinal epidural veins, large lobulated perineural cysts, and fluid at the C1–C2 interspinous space. CSF leaks are initially treated with epidural blood patch, and most leaks respond well to this intervention. Persistent, large, or recurrent leaks may require surgery.

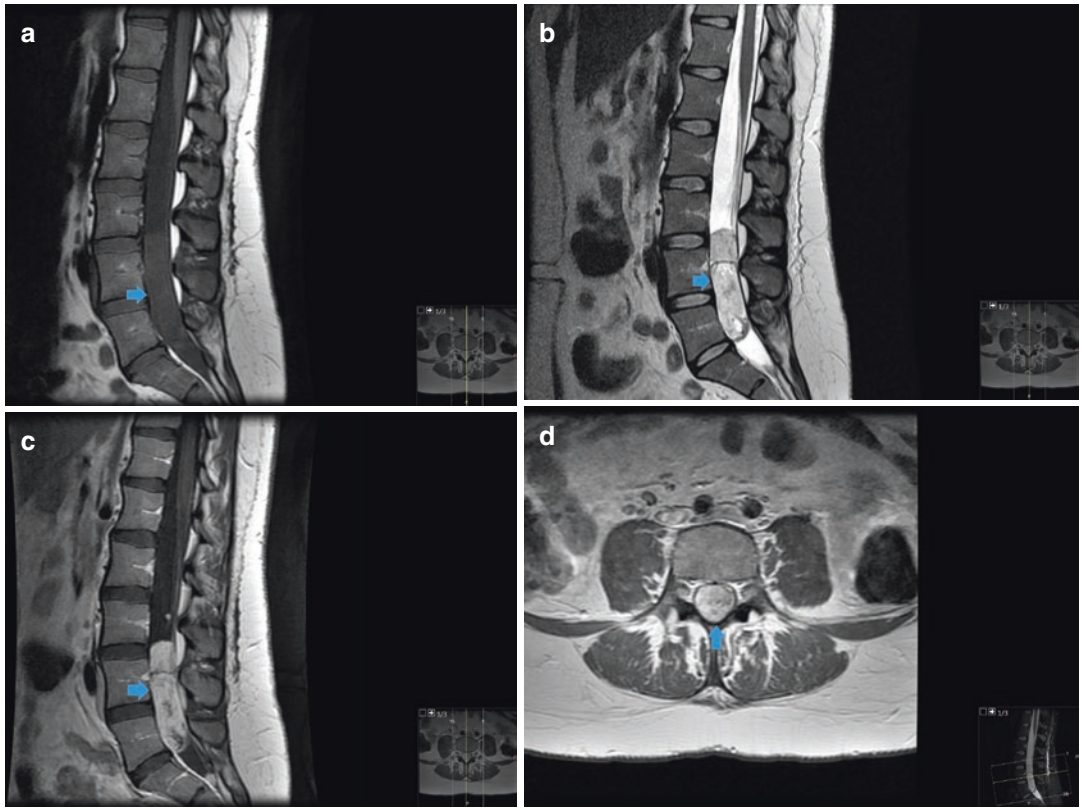

Fig. 9.12 Myxopapillary ependymoma. Figure 9.12**a** is a sagittal T1-weighted MR image showing a large sausage-shaped isointense intradural extramedullary mass filling the thecal sac in the region of the cauda equina (arrow). The mass is heterogeneous and mildly hyperintense on the T2-weighted MR image (Fig. 9.12**b**), and shows avid heterogeneous enhancement on the postcontrast sagittal T1-weighted image (Fig. 9.12**c**). On the axial postcontrast T1-weighted image, the enhancing mass entirely fills the cross-sectional thecal sac below the conus medullaris (arrow, Fig. 9.12**d**)

Cord Herniation

Cord herniation is an uncommon and likely underdiagnosed cause of myelopathy. In this condition, a defect in the dura allows a portion of the spinal cord to herniate through the thecal sac and cause neurologic deficits via cord tethering. Patients may present with a Brown–Sequard syndrome or subtle myelopathy or pain [5]. The mid thoracic spine is the most common location for cord herniation, likely due to the natural thoracic kyphosis at this level and the proximity of the thoracic cord to the ventral bony spinal canal. MRI is the initial imaging modality of choice for this condition and usually shows focal kinking of the cord at the site of herniation, with widening of the CSF space dorsal to the cord at that level. A small amount of soft tissue may be seen ventrally outside the dura at the site of kinging, representing the herniated portion of the cord. These herniations usually occur at the level of the disc, and some authors postulate that calcified discs and osteophytes may play a role in weakening the dura and increasing the risk for cord herniation. An important differential diagnosis for cord herniation is a dorsal arachnoid cyst or other cystic lesion causing mass effect on the cord, and CT myelogram can be used for problem solving if needed.

Dorsal Arachnoid Web

An important clinical entity that can mimic a cord herniation is a dorsal arachnoid web. Like

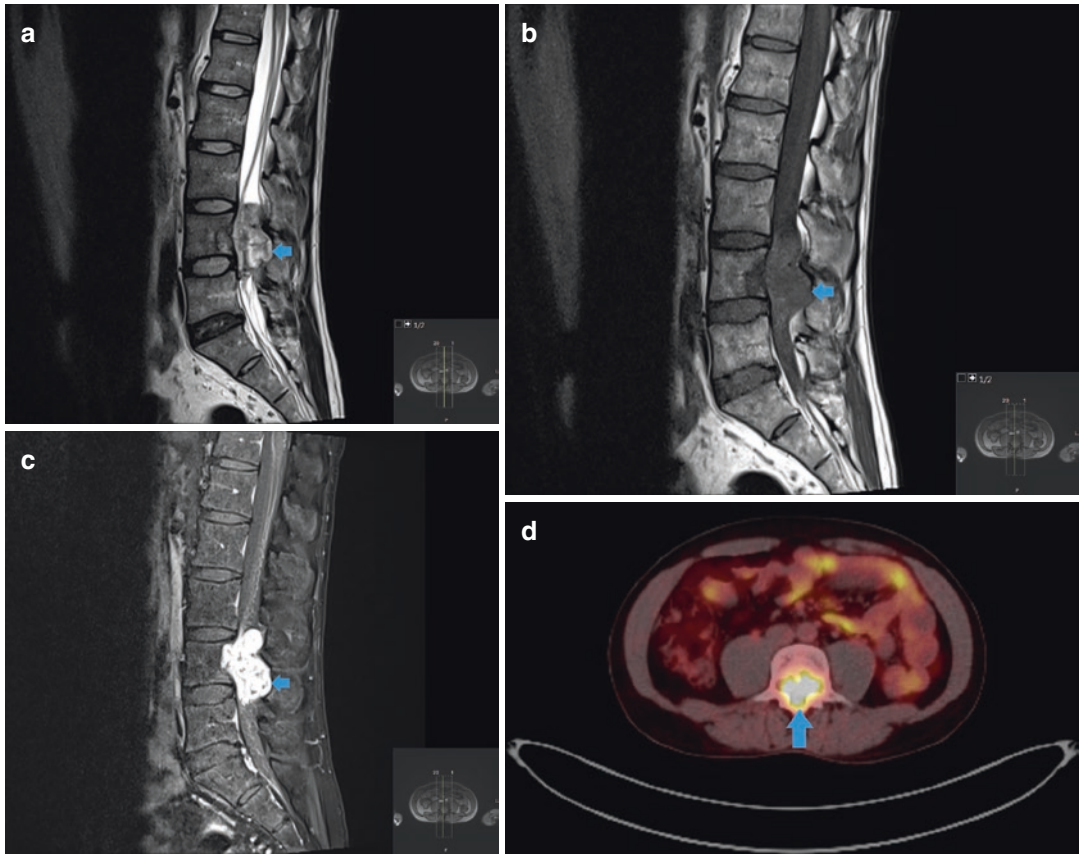

Fig. 9.13 Paraganglioma. Figure 9.13**a** is a sagittal T2-weighted MR image showing a heterogeneous intradural extramedullary mass arising below the conus medullaris, and causing mass effect on the cauda equina, expansion of the spinal canal, and smooth bony remodeling of the adjacent vertebral bodies (arrow). Figures 9.13**b** and **c** and sagittal unenhanced T1 and postcontrast T1-weighted MR images, respectively, showing avid enhancement of the mass (arrows). Figure 9.13**d** is a Positron emission tomography (PET) CT showing avid somatostatin receptor uptake. The mass was resected, and the pathology was consistent with a paraganglioma

cord herniation, dorsal arachnoid webs are most common in the mid to upper thoracic spine. In this condition, an intradural extramedullary web in the dorsal subarachnoid space causes mass effect on the cord and results in myelopathy. The web itself is usually not visible on MRI or CT myelography but is very obvious on intraoperative ultrasound. The web(s) diverts flow of CSF around the spinal cord at this level creating turbulence and the adhesions cause the abrupt distortion of the spinal cord giving a characteristic appearance of the cord referred to as the "scalpel sign" related to its compressive effects on the cord [6] (Fig. 9.16). Treatment is surgical and requires a durotomy and excision of the web to release the cord.

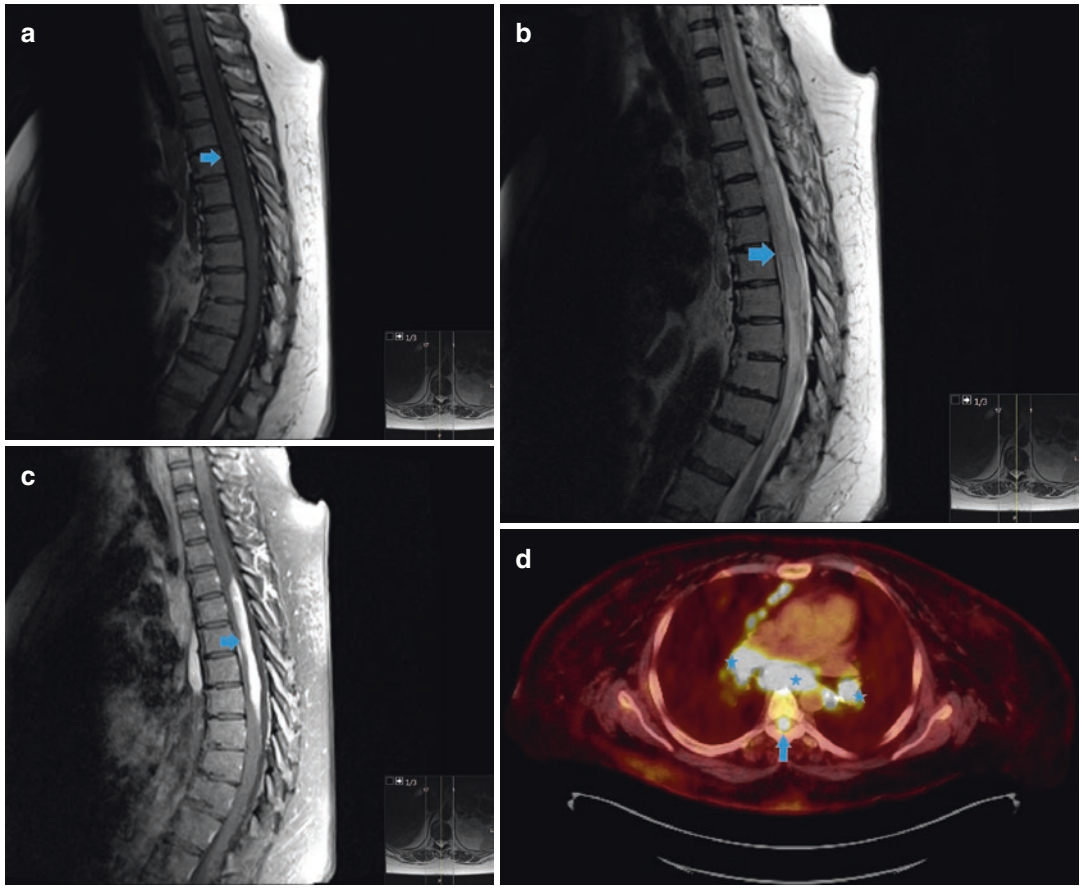

Fig. 9.14 Intramedullary sarcoidosis. Figure 9.14**a** is a sagittal T1-weighted MR image showing mild expansion of the thoracic cord, with mild low T1 signal change within the cord (arrow). On the sagittal T2-weighted image (Fig. 9.14**b**), there is long-segment diffuse edema-like signal within the mildly expanded cord (arrow). The postcontrast sagittal image shows avid enhancement within the dorsal two-thirds of the cord (arrow, Fig. 9.14**c**). A PET CT (Fig. 9.14**d**) shows avid uptake within the cord lesion (arrow), and avid uptake within multiple enlarged intrathoracic lymph nodes (stars). Further workup revealed sarcoidosis

Arachnoiditis

Arachnoiditis refers to chronic inflammation of the cauda equina nerve roots, usually from prior surgery, hemorrhage, infection, or inflammation. The nerve roots of the cauda equina are usually thickened and clumped, with or without associated enhancement. The nerve roots may be clumped together in the center of the thecal sac, producing a "pseudo-cord" appearance, or they also be displaced and adherent to the outer layer of the thecal sac, producing a "pseudo empty thecal sac" sign.

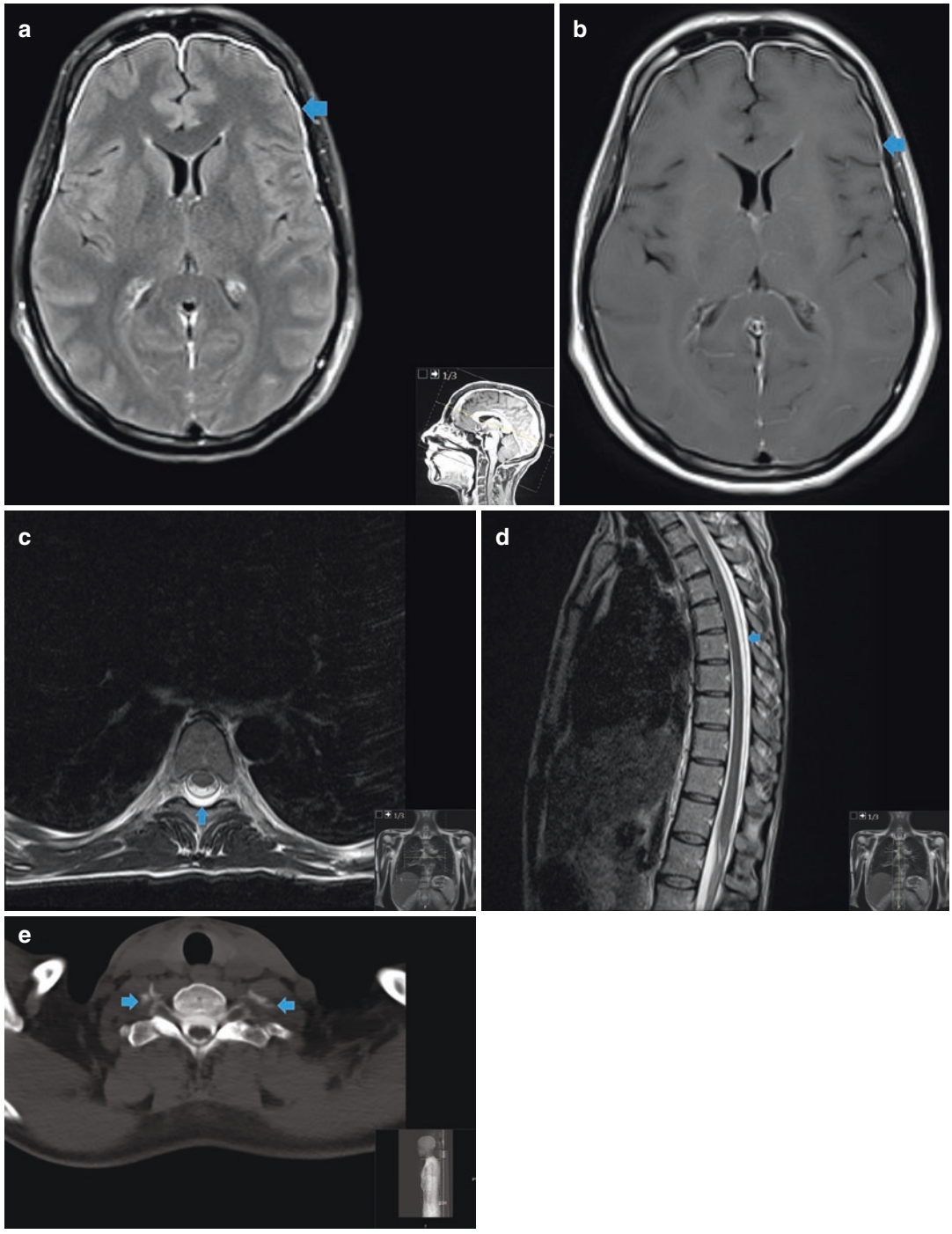

Fig. 9.15 CSF leak. Figures 9.15**a** and **b** are axial FLAIR and postcontrast MR images of the brain, respectively, showing thin diffuse subdural collections and diffuse dural thickening and enhancement (arrows), in keeping with spontaneous intracranial hypotension. Figures 9.15**c** and **d** are axial and sagittal T2-weighted MR images of the thoracic spine, respectively, showing an extradural CSF collection in the dorsal spinal canal (arrows). Figure 9.15**e** is an axial CT myelogram showing bilateral CSF leaks at the bilateral C7–T1 neural foramina, with contrast/CSF leaking into the upper cervical musculature (arrows)

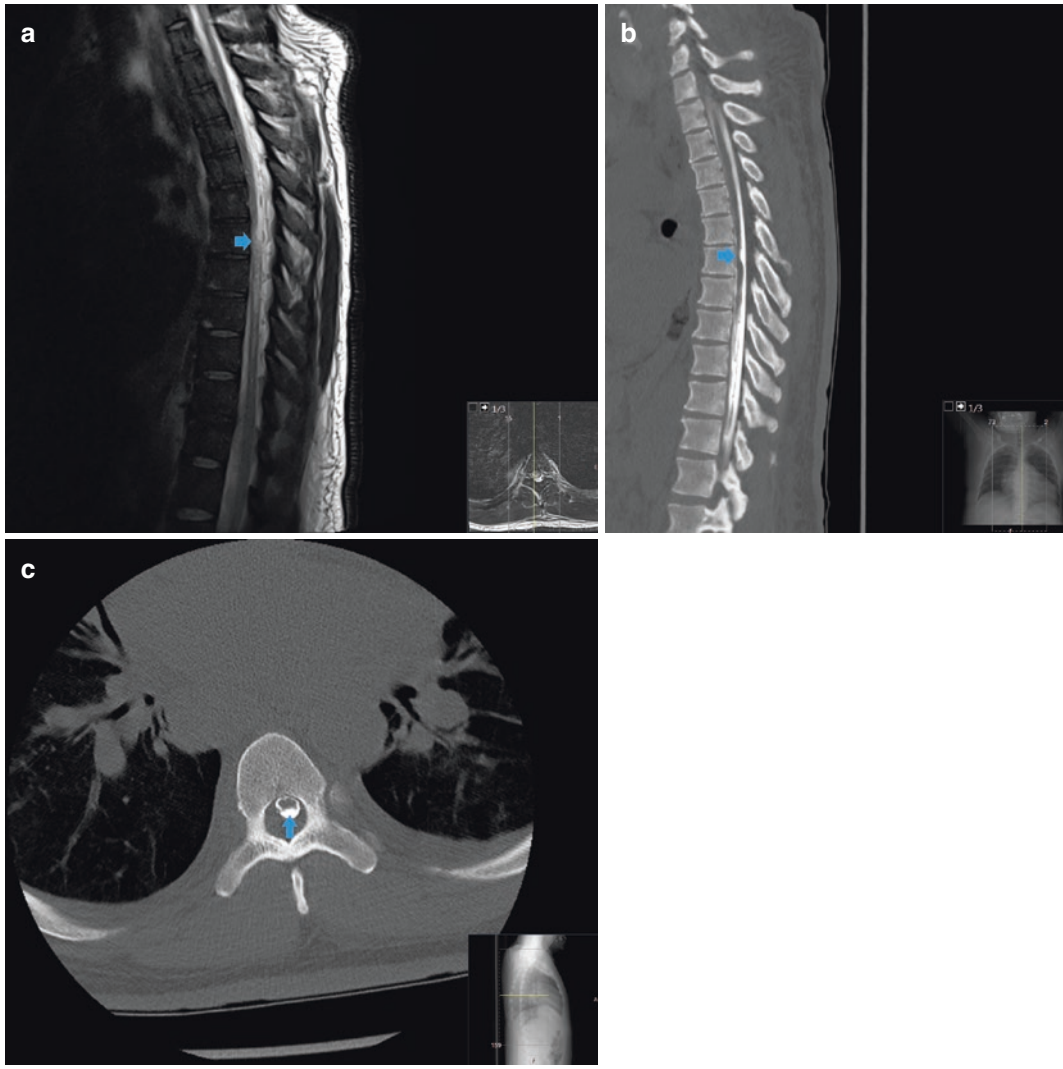

Fig. 9.16 Dorsal arachnoid web. Figure 9.16**a** is a sagittal T2-weighted MR image done for progressive bilateral lower extremity weakness over several months, which showed focal indentation of the dorsal thoracic cord, with abnormal cord signal below the level of indentation (arrow). A CT myelogram performed for further evaluation showed the focal indentation of the dorsal cord to better advantage (arrows, Figs. 9.16**b** and **c**). the ventral CSF space at the level of thoracic indentation was preserved, arguing against thoracic cord herniation as a cause for the contour abnormality and signal change. A dorsal arachnoid web was confirmed at surgery

References

1. Jindal G, Pukenas B. Normal spinal anatomy on magnetic resonance imaging. Magn Reson Imaging Clinics. 2011;19(3):475–88.
2. Koeller KK, Shih RY. Intradural extramedullary spinal neoplasms: radiologic-pathologic correlation. Radiographics. 2019;39(2):468–90.
3. Cox M, Curtis B, Patel M, Babatunde V, Flanders AE. Utility of sagittal MR imaging of the whole spine in cases of known or suspected single-level spinal infection: overkill or good clinical practice? Clin Imaging. 2018;51:98–103.
4. Pierce JL, Donahue JH, Nacey NC, Quirk CR, Perry MT, Faulconer N, Falkowski GA, Maldonado MD, Shaeffer CA, Shen FH. Spinal hematomas: what a radiologist needs to know. Radiographics. 2018;38(5):1516–35.
5. Parmar H, Park P, Brahma B, Gandhi D. Imaging of idiopathic spinal cord herniation. Radiographics. 2008;28(2):511–8.
6. Reardon MA, Raghavan P, Carpenter-Bailey K, Mukherjee S, Smith JS, Matsumoto JA, Yen CP, Shaffrey ME, Lee RR, Shaffrey CI, Wintermark M. Dorsal thoracic arachnoid web and the "scalpel sign": a distinct clinical-radiologic entity. Am J Neuroradiol. 2013;34(5):1104–10.

MRI in Cord Lesions

10

Kofi-Buaku Atsina

Traumatic

Acute traumatic cord injury is a devastating illness which can be associated with significant long-term morbidity and expense [1]. The pattern of injury to the spinal cord following blunt trauma as well as associated soft tissue and ligamentous injury is best evaluated with MRI [2]. Injury to the spinal cord can be categorized into primary and secondary damage as follows. Primary injury results from mechanical forces that may include compression, shearing, laceration, and acute distraction [1, 3]. This primary injury is thought to be the determinant of injury severity [1]. Following primary injury, a series of inflammatory processes occur which invariably serve to expand the initial zone of injury. This represents secondary injury and also impacts neurological outcome if not addressed [1, 3]. The spectrum of acute cord injury can range from concussion, cord edema, cord contusion, cord hematoma, and transection [4].

Patients with cord concussions have symptoms but with no abnormal imaging findings on conventional T1 and T2 weighted sequences [4]. Such acute spinal cord injury patients have the most favorable outcome. In cases of more severe injury, traumatic spinal cord lesions are characterized by intramedullary cord edema, which is represented as hyperintense signal on T2 weighted/STIR imaging, which may extend beyond the zone of injury. In the early post-injury period, cord edema increases significantly, peaking at about 48–72 hours for mild injury and up to 96 hours for severe injury (Fig. 10.1a) [5]. Not uncommonly, there is associated cord expansion [4].

Hemorrhagic cord contusion reflects more severe injury and is depicted on imaging as a central intramedullary focus or foci of hypointense signal less than 4 mm in size, surrounded by a thin area of hyperintense signal on T2/GRE imaging, whereby the hypointense signal is attributable to deoxyhemoglobin [2, 4–9]. By contrast, in cord hematomas, the central intramedullary focus of low signal is greater than 4 mm on T2/GRE imaging. The extent of cord hemorrhage and degree of cord edema have been associated with poor prognosis for neurological outcome [4, 6] after injury, which is clinically assessed by the American Spinal Injury Association (ASIA) Impairment scale. The ASIA Impairment scale is the best known predictor of outcome in the acute setting [4]. Complete/incomplete cord transection represents the most severe form of injury whereby the fibers of the spinal cord are disrupted, with evidence of T2 hyperintense signal intervening between the severed fibers [4, 8] (Fig. 10.1d–f).

In the subacute phase of spinal cord injury (2–6 weeks), the edema progressively fades. In rare cases, the edema may continue to progress

K.-B. Atsina (✉)
Department of Radiology, Thomas Jefferson University Hospital, Philadelphia, PA, USA

W. B. Morrison et al. (eds.), *MRI of the Spine*, https://doi.org/10.1007/978-3-030-43627-8_10

and extend rostrally by greater than four segments above the original injury, before it subsides. The hyperintense signal characteristically remains central with sparing of the cord periphery. This phenomenon has been termed subacute ascending progressive myelopathy and correlates with worsening neurological symptoms [4, 10].

Chronic changes of post-traumatic spinal cord injury include myelomalacia, cord atrophy, and cord tethering (Fig. 10.1b), as well as cyst and syrinx formation (Fig. 10.1c) [11, 12].

Neoplastic

Intramedullary spinal cord neoplasms account for 4–10% of all CNS tumors and 2–4% of CNS glial tumors. Spinal cord neoplasms constitute 20% in adults and 35% in children of all intraspinal tumors. Majority (90–95%) of spinal cord neoplasms are glial tumors with ependymomas and astrocytomas, which make up 70%. The most common adult spinal cord neoplasm is ependymoma, while astrocytoma is the most common in children. Hemangioblastomas are the third most common cord neoplasm. Other less common intramedullary tumors include ganglioglioma, paraganglioma, metastasis, lymphoma, embryonal tumors with multilayered rosettes (formerly primitive neuroectodermal tumor or PNET), and subependymoma. The hallmark features on imaging for intramedullary tumors is cord expansion and enhancement. Not uncommonly, there is formation of cysts at the polar ends of the tumor, which do not enhance and are generally thought to represent reactive dilation of the central canal (syringomyelia) and are termed non-tumoral cysts. Tumoral cysts can also be

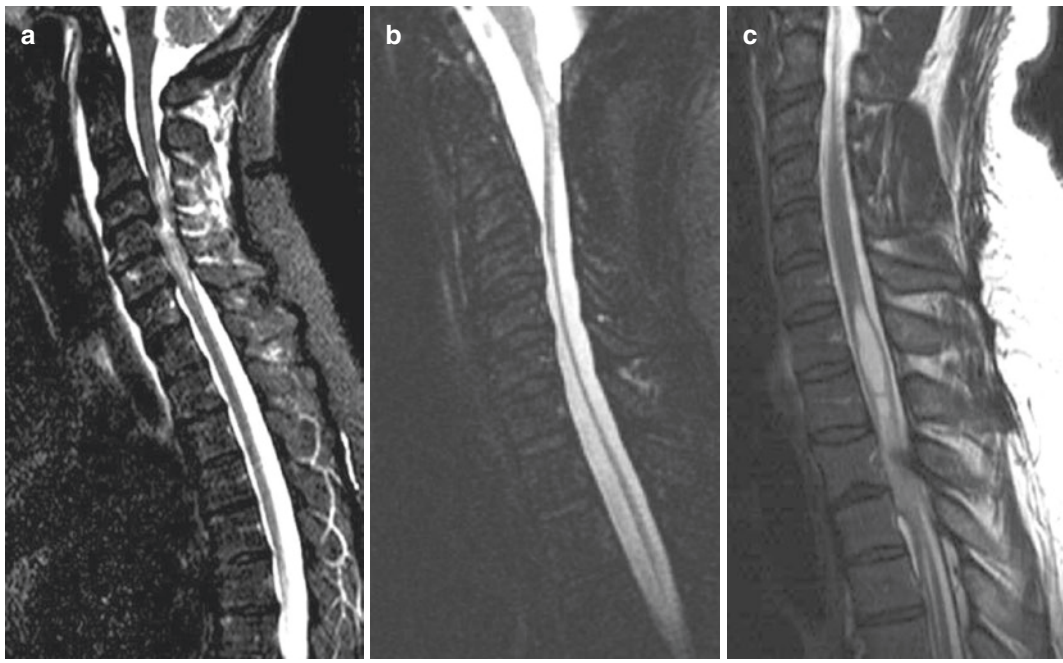

Fig. 10.1 (**a**) Sagittal T2W image demonstrates edema and expansion of the cervical cord. There is edema in the posterior cervical soft tissues following a recent fall. Findings are consistent with acute cervical cord injury. (**b**) Sagittal T2W image demonstrates thinning of the cord several months after traumatic injury, consistent with cord atrophy. (**c**) Sagittal T2W image demonstrates post-traumatic syrinx and ventral cord herniation. (**d**) Axial T2W and (**e**) sagittal T2W images demonstrate complete cervical cord transection with intervening T2 hyperintense signal between the severed cord segments, associated hematoma, and edema in the left posterior soft tissues secondary to stab injury. (**f**) Sagittal T2W image demonstrates near-complete cord transection secondary to fracture-dislocation through C6-C7 disc resulting from a fall

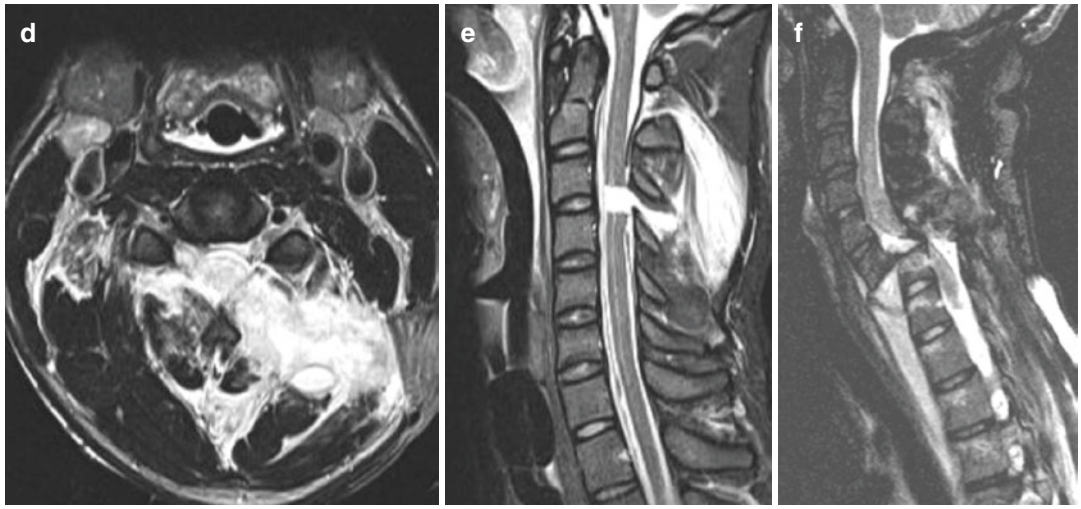

Fig. 10.1 (continued)

present, but typically are located within the tumor itself and frequently demonstrate rim enhancement [13].

- *Ependymomas* are the most common adult, and second most common pediatric spinal intramedullary neoplasm arising from the ependymal lining of the central canal. Typically, there is a long antecedent history prior to diagnosis. Ependymomas more commonly affect young people with mean age of about 40 years, with slight male predominance. They can present sporadically, but are also associated with Neurofibromatosis type II [14]. Back pain and sensory symptoms are common presentations. The most common location is in the cervical cord followed by the upper thoracic cord, and less commonly the distal cord or conus medullaris [13, 15]. Several histological variants of ependymoma exist with the conventional WHO grade II subtypes (papillary, clear cell, tanycytic, RELA fusion positive) being the most common. Two WHO grade I (low-grade) variants exist - myxopapillary ependymoma and subependymoma - which have distinct histological and imaging features. On imaging, the conventional WHO grade II ependymomas typically have a well-defined central expansile appearance. They are typically isointense or hypointense and rarely slightly hyperintense on T1 (Fig. 10.2a). On T2, they are hyperintense relative to the spinal cord and demonstrate surrounding edema. Not uncommonly, these tumors will demonstrate a cap sign, which is depicted as very hypointense signal on T2 at the poles of the tumor indicating hemosiderin from chronic hemorrhage. On post-contrast imaging, they demonstrate avid homogenous enhancement (Fig. 10.1b) [13, 15]. Nontumoral cysts are not uncommon (Fig. 10.2a. b). Leptomeningeal spread is more common with higher grade tumors [14, 15].
  - *Myxopapillary ependymomas* are found most commonly in the intradural extramedullary space involving the filum terminale, and account for about 13% of ependymomas, but make up 80% of all ependymomas occurring in the conus medullaris or filum terminale [15, 16]. Not uncommonly, they are extradural and extraspinal in location [13]. On imaging, they appear as lobular, soft, sausage-shaped masses, which are often encapsulated, span 2–4 vertebral levels and can cause posterior vertebral scalloping [13, 15]. They are usually T1 isointense or hypointense (Fig. 10.2d) although they can have T1 hyperintense components due to production of

mucin and hemorrhage. They are T2 hyperintense (Fig. 10.2c) and commonly have susceptibility signal from chronic hemorrhage. They also demonstrate avid contrast enhancement [13, 15, 17, 18] (Fig. 10.2e).

– *Subependymomas* are a rare variant of ependymomas that most commonly occur in the fourth and lateral ventricles. On rare occasions, they may present in the spinal cord with imaging findings that overlap with the conventional WHO grade II ependymoma. In the spine, they are usually intramedullary, and rarely extramedullary in location. They are well circumscribed

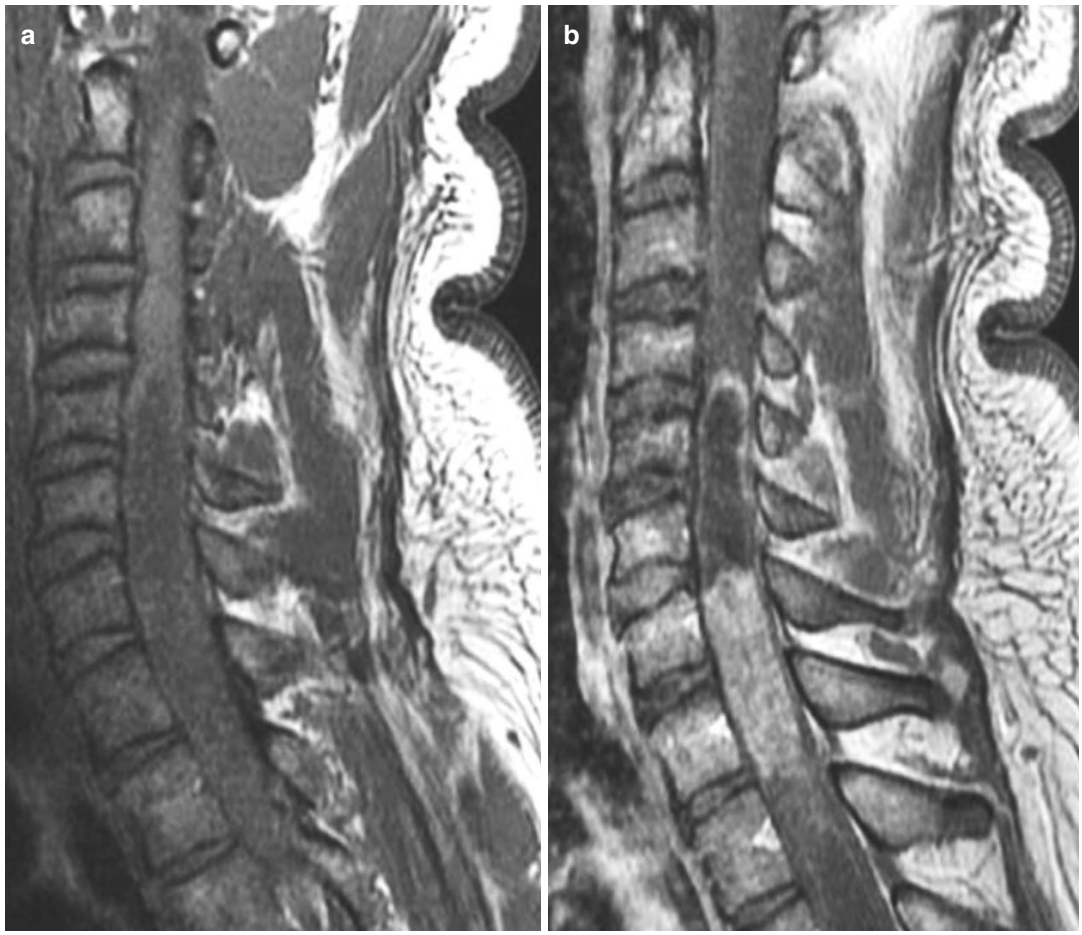

Fig. 10.2 (**a**) Non-contrast sagittal T1W and (**b**) contrast-enhanced sagittal T1W images of intramedullary ependymoma with associated syrinx. (**c**) Sagittal T2W, (**d**) non-contrast sagittal T1W, and (**e**) contrast-enhanced sagittal T1W images of myxopapillary ependymoma involving the conus medullaris and cauda equina. (**f**) Sagittal T2W and (**g**) contrast-enhanced sagittal T1W images of intramedullary astrocytoma with associated syrinx. (**h**) Sagittal T2W and (**i**) contrast-enhanced sagittal T1W images of intramedullary ganglioglioma in the upper to mid thoracic cord. (**j**) Axial T2W and (**k**) contrast-enhanced axial T1W images demonstrate cervical cord hemangioblastoma; (**l**) sagittal T2W image demonstrates a hemangioblastoma in the conus medullaris, with apical cap sign from hemosiderin staining. (**m**) Sagittal T2W, (**n**) non-contrast sagittal T1W, and (**o**) contrast-enhanced fat saturated sagittal T1W images of paraganglioma involving the cauda equina. (**p**) Sagittal T2W, (**q**) non-contrast sagittal T1W, and (**r**) contrast-enhanced sagittal T1W images an expansile mass involving a lumbar vertebral body and intramedullary involvement of the conus medullaris in a patient with spinal lymphoma. (**s**) Sagittal T2W, (**t**) non-contrast sagittal T1W, and (**u**) contrast-enhanced sagittal T1W images show an intensely enhancing mass in the conus medullaris in a patient with breast cancer, consistent with intramedullary metastasis

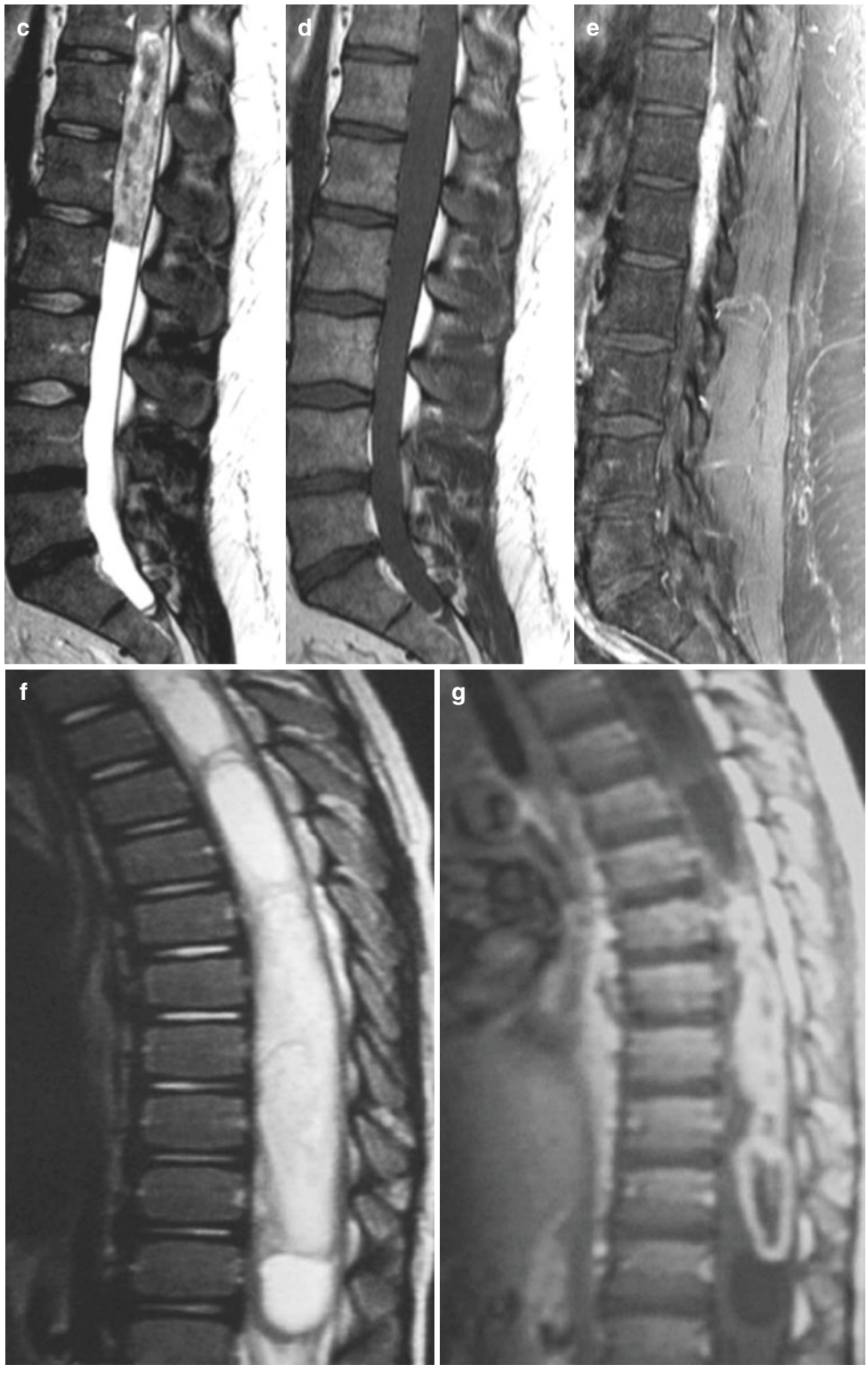

Fig. 10.2 (continued)

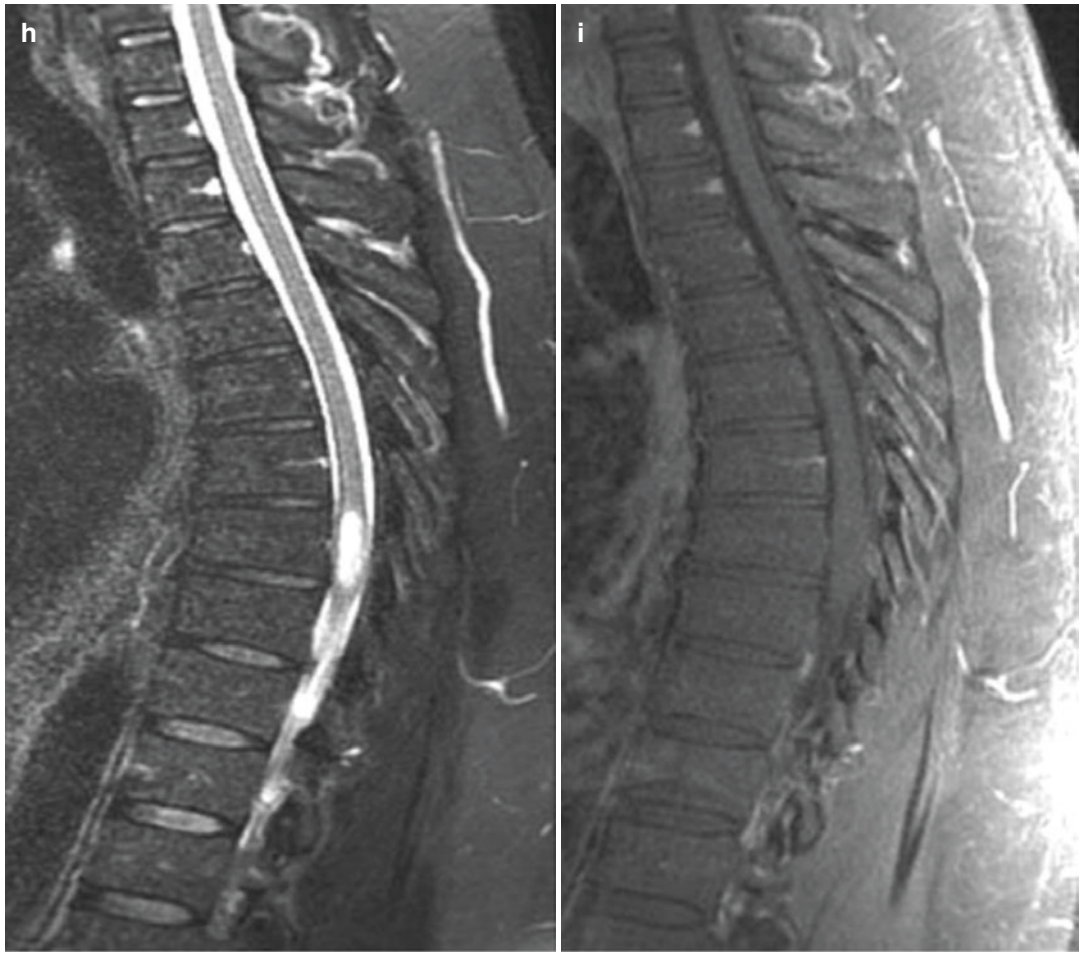

Fig. 10.2 (continued)

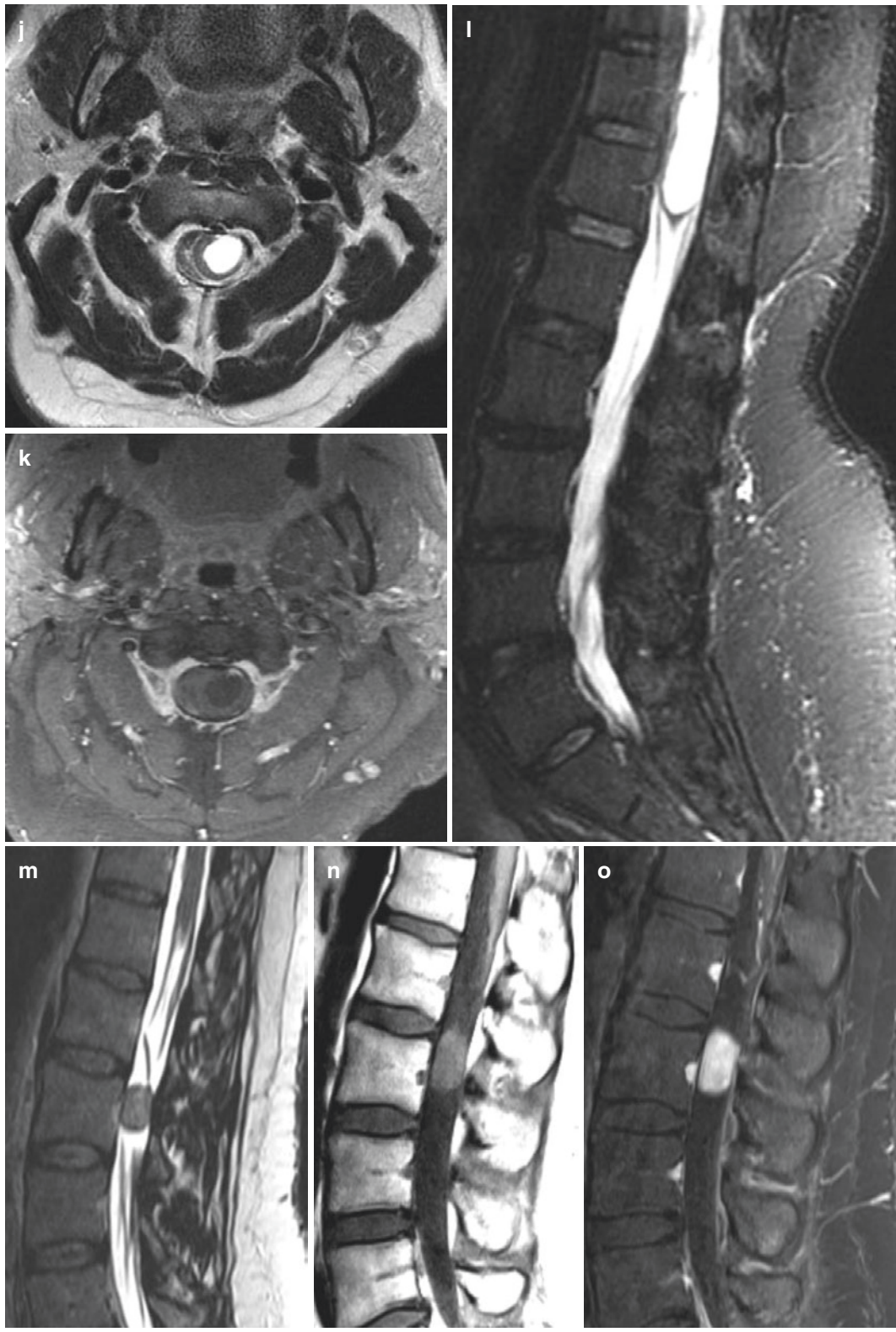

Fig. 10.2 (continued)

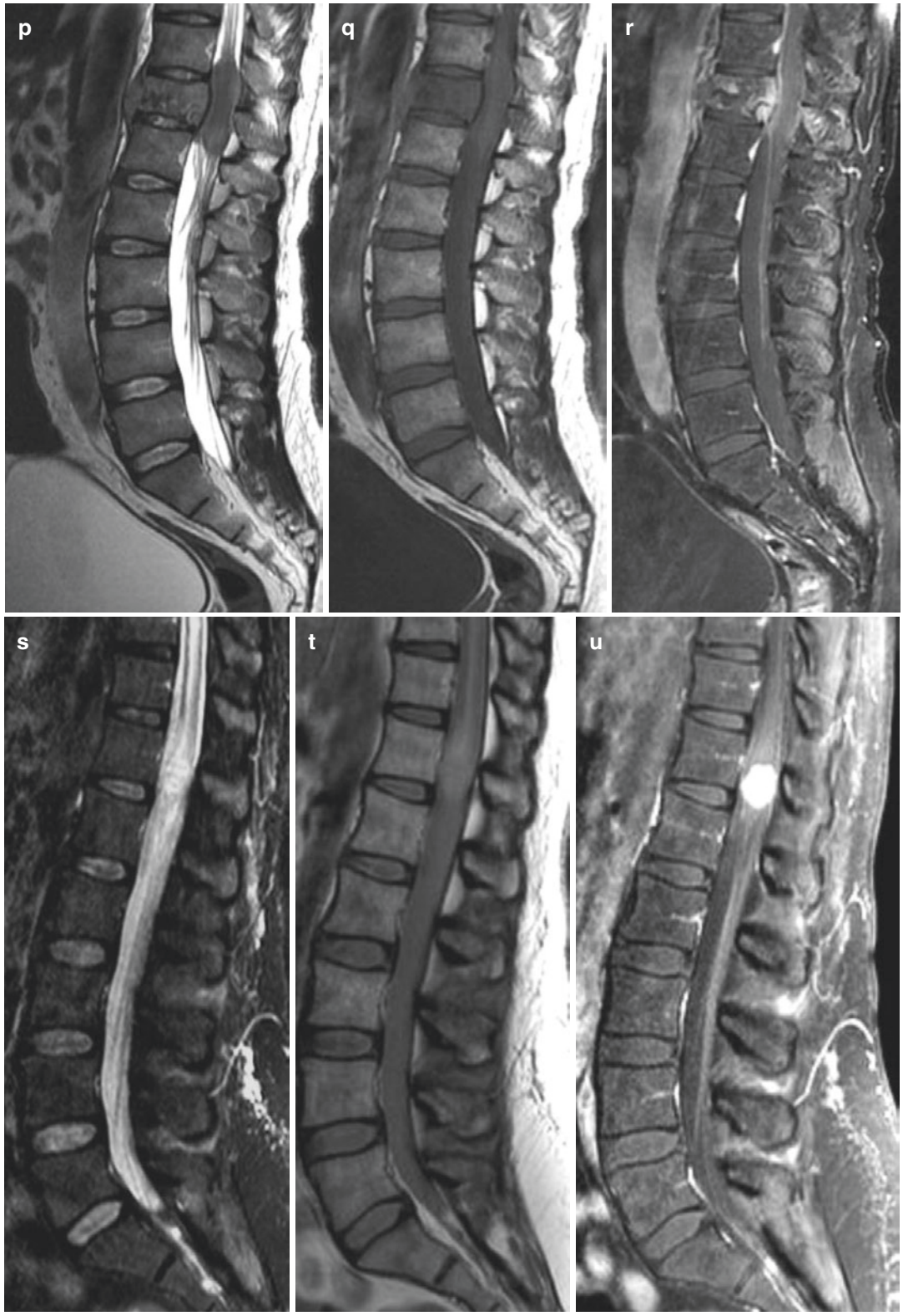

Fig. 10.2 (continued)

nonvascular, eccentrically located, nodular masses that cause fusiform expansion, and are typically seen in the cervical and cervicothoracic regions. Like conventional WHO grade II ependymomas, they are typically T1 hypointense and T2 hyperintense, but demonstrate mild to moderate enhancement [13, 19–21].

- *Astrocytomas* are the second most common spinal intramedullary tumors affecting adults; however in children, they are the most common [13, 14]. They can present sporadically, but are associated with Neurofibromatosis type I [14]. Like ependymomas, they have a slight male predilection. The most common histologic subtype is pilocytic astrocytoma (WHO grade I) and fibrillary astrocytoma (WHO grade II), although other more aggressive subtypes (anaplastic WHO grade III, and glioblastoma WHO grade IV) can occur, but are far less common. Generally, they are more infiltrative than ependymomas and tend to have a worse prognosis. An exception to this is pilocytic astrocytoma, which tends to displace rather than infiltrate. In children, common presentations are pain that wakes them up at night, abdominal pain, motor symptoms, and scoliosis. In adults, back pain, and sensory and motor symptoms are common presentations [13, 14]. On imaging, the classic appearance of cord astrocytoma is an expansile T1 hypo- to isointense, T2 hyperintense mass with surrounding edema [13–15, 22, 23] (Fig. 10.2f). They typically demonstrate some ill-defined patchy irregular enhancement, although non-enhancement is seen in 20–30% of cases (Fig. 10.2g). Tumoral and peritumoral cysts are common [14, 22]. Unlike ependymomas, they are typically eccentric and hemorrhage is uncommon. When there is holocord involvement, the tumor involves a portion of the cord and polar cysts involve the rest [14]. True holocord involvement whereby the tumor involves the entire cord is rare [14, 15]. Holocord involvement is associated with scoliosis and canal widening which can be seen on imaging. Leptomeningeal spread is fairly common in more aggressive subtypes [13, 14].
- *Gangliogliomas* are relatively rare primary tumors of the spinal cord, although they are more common in pediatric population accounting for 15% of intramedullary neoplasms [14]. They are typically slow-growing tumors, but can vary in grading from low grade to anaplastic subtypes. They are made of a combination of neoplastic ganglia cells and glial elements [14, 24]. They have no gender predilection and commonly involve the cervical and thoracic levels. Signal characteristics can be variable on T1 (hypointense, hyperintense, isointense, or mixed), but are usually hyperintense of T2 (Fig. 10.2h). They are long, eccentric masses that commonly have tumoral cysts, syrinx, absence of edema, and occasionally calcifications. Enhancement is typically patchy in appearance or may involve the pial surface, but no enhancement has also been described [13, 14, 24, 25] (Fig. 10.2i). Osseous changes including scoliosis and remodeling are commonly seen when compared to other tumors [13, 14].
- *Hemangioblastoma* are slow growing non-glial neoplasm that are typically benign. They can occur sporadically, but are associated with Von Hippel Lindau (VHL) syndrome in 1/3–1/2 of cases [14]. The presence of multiple tumors is highly suggestive of VHL syndrome. They most commonly occur in the thoracic spine, followed by the cervical spine. Majority of lesions are intramedullary (75%), but they can also occur within the intradural extramedullary space where they may be attached to the dorsal cord pia or even in the extradural space along the nerve roots. Hemangioblastomas are highly vascular masses that demonstrate a dense blush on angiographic imaging with dilated arterial feeders and tortuous prominent draining veins. On MRI, they are well defined nodular masses with isointense or hypointense signal on T1, hyperintense signal on T2 with flow voids, and avid enhancement. Adjacent cysts formation, and apical cap due to hemosiderin deposits are common findings [13, 14, 26] (Fig. 10.2j, l). Syrinx may also be present and tend to be relatively larger when com-

pared to the size of the tumor [26]. The appearance of a well-defined homogenously enhancing appearance helps to distinguish them from vascular malformations [13, 14] (Fig. 10.2k).

- *Paragangliomas* are benign WHO grade I tumors of neuroendocrine origin arising in the paraganglia that are associated with the peripheral nervous system. They most commonly occur in the adrenal gland (pheochromocytomas), carotid body (carotid body tumor), jugular foramen (glomus jugulare), middle ear cavity (glomus tympanicum), and along the vagal nerve (glomus vagale) [13, 27, 28]. On rare occasions, they can occur in the spine, where they are called spinal paragangliomas. Spinal paraganglioma have a slight male predilection and mean age of presentation is in the mid-40s. Common presenting symptoms include back pain, and radiculopathy; however, other symptoms such as neurogenic claudication and bowel/bladder disturbance can also occur. In the spine, paragangliomas are intradural extramedullary lesions that are most commonly associated with the filum terminale or cauda equina [13, 15]. On imaging, these tumors are well delineated oval masses that are T1 isointense/hypointense, mildly T2 hyperintense, and can demonstrate avid homogenous or heterogeneous enhancement [13, 15, 27, 28] (Fig. 10.2m–o). Frequently, these masses will have flow voids and tortuous peritumoral veins extending from one end of the mass, so called tadpole sign [28]. As they are highly vascular tumors, superficial siderosis along the spinal cord and nerve roots and even within the brain can be seen due to chronic repetitive hemorrhage within the subpial space [13, 27]. When they get large, they can cause posterior vertebral body scalloping [29].
- *Spinal lymphoma* is an extremely rare tumor that comprises 1% of primary CNS lymphoma [13, 15, 30]. It tends to occur in the middle-aged and elderly in immunocompetent hosts, but younger adults in the immunocompromised host [15]. It is a slight male predominance with an average age in the mid-50s [30]. Risk factors include immunodeficiency and EBV infection. The most common presenting symptoms are backpain, progressive weakness from myelopathy, and sensory disturbance from radiculopathy [13, 15]. The cervical cord is the most common site of spinal involvement, followed by the thoracolumbar spine. On CT, these tumors are hyperdense with homogenous contrast enhancement. On MRI, these tumors are isointense on T1, and hyperintense on T2 [13], although hypointense lesions can occasionally be seen [31] (Fig. 10.2p, q). This is in contrast to intracranial lesions, which are generally hypointense on T2 [13]. They typically demonstrate homogeneous enhancement [13, 15] (Fig. 10.2r) after contrast administration and restricted diffusion on DWI related to their hypercellularity [15]. Multifocal involvement is not uncommon. They are hypermetabolic on PET imaging [15, 31].
- *Intramedullary spinal metastases* are relatively rare with a prevalence of 2.1% on autopsy studies. They commonly occur in the cervical cord, followed by the thoracic cord and lumbar region. The presence of spinal metastases confers poor prognosis. Metastases most commonly originate from primary lung malignancy, followed by breast, melanoma, and renal cell carcinoma. Metastases from intracranial tumors such as medulloblastoma and glioblastoma are common [13, 32]. On occasion, a primary lesion may not be found; however, this should not dissuade from considering intraspinal cord metastases [32]. Extension to the spinal cord can be through hematogenous spread, and direct extension from the leptomeninges [13, 14]. On imaging, lesions are isointense on T1, with intense homogenous enhancement on postcontrast imaging (Figs. 10.2t, u). On T2, long segment hyperintense signal reflecting edema or infiltration usually spans up to three or more segments. The extent of T2 signal is usually disproportionate when compared to the size of the lesion itself (Fig. 10.2s). Cystic changes and hemorrhage are typically uncommon [13, 32].

- Spinal embryonal tumors with multilayered rosettes, primitive neuroectodermal tumors (PNET) are rare tumors and are usually secondary to drop metastasis from intracranial PNET lesions [13, 14]. Involvement of the spine can however be in the intramedullary, intradural extramedullary, or extradural spaces [13]. Unlike intracranial tumors spinal tumors are more common in adults than children. Primary spinal lesions have the ability to metastasize intracranially and outside the CNS [13, 33]. The imaging features are non-specific. On MRI, tumors are hypo- to isointense on T1, iso- to hyperintense on T2 [33] and will show diffuse heterogeneous enhancement. As these tumors frequently spreads through the CSF, leptomeningeal enhancement is a common finding [13].

Infectious

Most infections of the spine typically involve the musculoskeletal components including paraspinal and epidural abscess, osteomyelitis, osteodiscitis, and septic arthropathy. Spinal cord infections are quite rare; however, they can be associated with significant morbidity and mortality if not diagnosed and treated early [34]. MRI is the gold standard imaging modality for evaluating patients with a clinical suspicion for infection, and the use of intravenous contrast increases sensitivity. Intramedullary infections have a variable appearance on imaging with considerable overlap with non-infectious etiologies. Regardless, Talbott et al. proposed a classification scheme for spinal cord infections as follows: Extramedullary (lesions of the spinal meninges, intervening extra-axial spaces, spinal nerve roots), Centromedullary (centrally located T2 lesions), Eccentric tract-specific myelitis (eccentrically located lesions, but primarily, peripheral posterior and lateral white matter tracts), Frontal horns, and Irregular (eccentric, nodular, or tumefactive lesions without predilection for specific regional subsites within the cord) [34].

Within the extramedullary category, infection isolated to the meningeal spaces is rare. Typically, extradural involvement including spondylodiscitis, septic facet arthropathy, epidural phlegmon or abscess, paraspinal, and retroperitoneal infections are often also present. Infections included in this category are described as follows. Pyogenic meningitis (Fig. 10.3a, b) presents with spondylitis, paraspinal infection, epidural phlegmon, or abscess [34–40]. Tuberculous meningitis presents with spondylodiscitis, LETM (involving three or more vertebral segments), lumbosacral nerve root enhancement and thickening, and rarely intramedullary tuberculomas [34, 41–43]. Neurocysticercosis typically presents with arachnoiditis, intradural extramedullary cysts, CE hyperenhancement, and clumping [34, 44, 45]. Coccidioidomycosis can present with nodular leptomeningeal enhancement with nerve root clumping & thickening, and non-enhancing transverse myelitis leading to syrinx [34, 46–50]. CMV infection has normal findings in 50% of cases, but can be associated with lumbosacral radiculitis/arachnoiditis, CE thickening and enhancement, and GBS [34, 51–54]. Zika virus presents with CE thickening and enhancement and GBS [34, 55–57]. HSV-1/HSV-2 radiculitis presents with nerve-root thickening and hyperenhancement [34, 44, 52].

Imaging features that characterize the centromedullary category include central, relatively symmetric elliptical intramedullary T2 hyperintense signal, which can extend to involve the entire cross-sectional diameter of the cord, and can have variable craniocaudal length and cord expansion. Infections that are present in this category include viral infections such as EBV (associated with LETM with cord expansion with or without enhancement, T2 hyperintensity and swelling of the nerve roots, and rarely associated with GBS) [34, 44, 51], and Hepatitis C virus (associated with LETM and cord expansion, no enhancement, and at times may be normal) [34, 58, 59]. Bacterial infections such as Lyme disease (Borrelia Burgdorferi) (which is associated with variable expansile centromedullary T2 hyperintensity, with patchy spinal cord

enhancement and prominent nerve-root enhancement, but can be normal at times) can also have centromedullary appearance [34, 44, 60]. Finally, parainfectious transverse myelitis, which includes a broad category of disorders related to autoimmune myelitis following an infection, during the convalescent stage, most commonly has a centromedullary imaging appearance [34, 61–65].

Imaging features in the eccentric tract-specific category demonstrate a characteristic peripheral tract-specific cord involvement. Non-infectious etiologies such as MS, vitamin B12 and copper deficiencies, and some paraneoplastic syndromes may demonstrate similar appearance and should be considered in the differential diagnosis. Infectious etiologies include HTLV-1 (which can be normal, but when abnormal is associated with T2 hyperintense signal frequently involving the lateral columns, and diffuse cord atrophy) [34, 35, 51]; HIV (associated with diffuse spinal cord atrophy with T2 hyperintense signal involving the dorsal and lateral columns, no enhancement and rarely LETM); VZV (associated with T2 hyperintense signal in segmental dorsal horns and columns, nerve root and DRG thickening & enhancement, and rarely LETM) [51, 66–69]; neurosyphilis (Treponema pallidum) (which can be normal, but is associated with LETM involving the dorsal columns with or without enhancement, otherwise known as Tabes dorsalis) (Fig. 10.3c–f); and PML (JC virus) (associated T2 hyperintense signal in the dorsal columns especially fasciculus gracilis) [34, 44, 61].

Within the frontal horns category, lesions characteristically involve the ventral gray matter structures presenting with acute flaccid

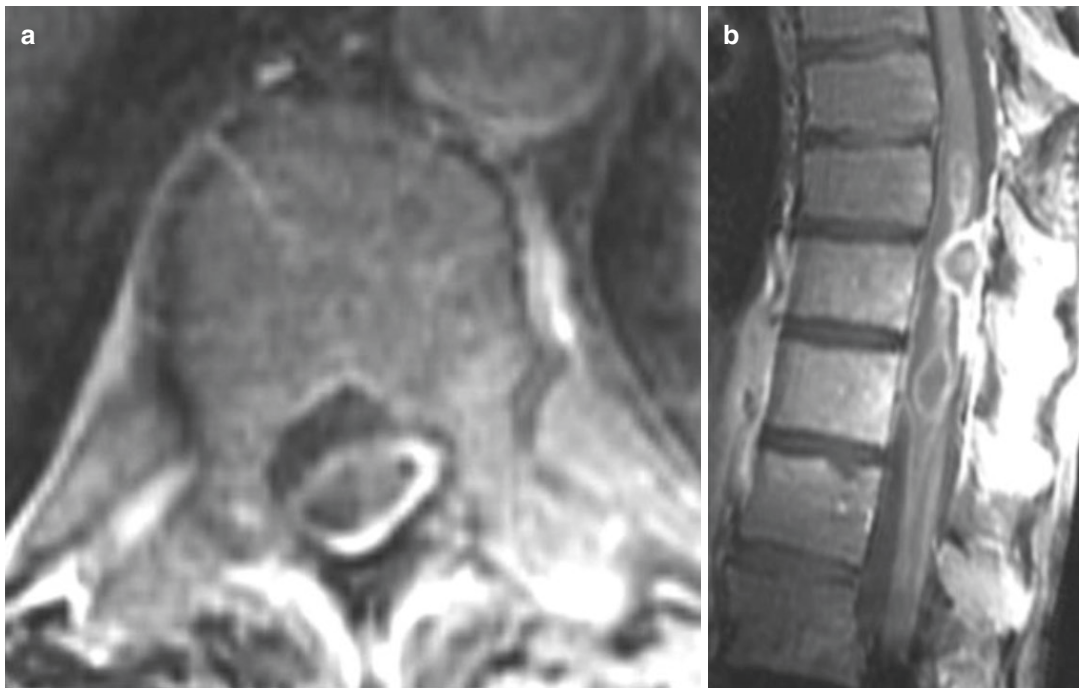

Fig. 10.3 Contrast-enhanced (**a**) axial and (**b**) sagittal T1W images demonstrate multiloculated rim enhancement collections in the intramedullary and extramedullary spaces representing spinal abscesses. (**c**) Axial T2W and (**d**) contrast-enhanced axial image of the cervical cord show hyperintense signal in the dorsal columns and associated enhancement respectively in keeping with eccentric-tract specific cord involvement in a patient with neurosyphilis. LETM pattern is demonstrated in (**e**) sagittal T2W and (**f**) contrast enhanced sagittal T1W images. (**g**) Axial T2W and (**h**) sagittal T2W images of the cervical cord show hyperintense signal in the right frontal horn with LETM pattern

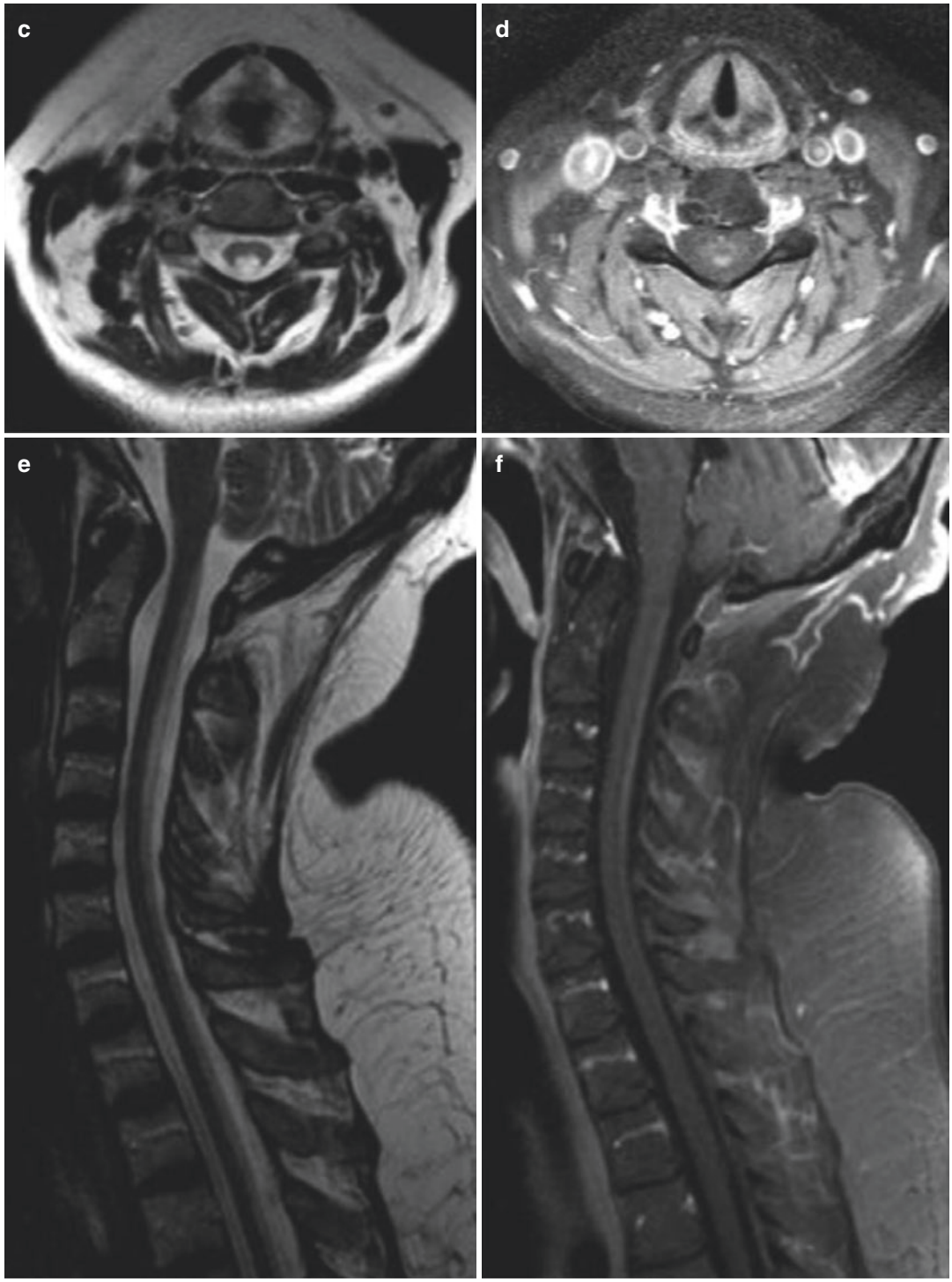

Fig. 10.3 (continued)

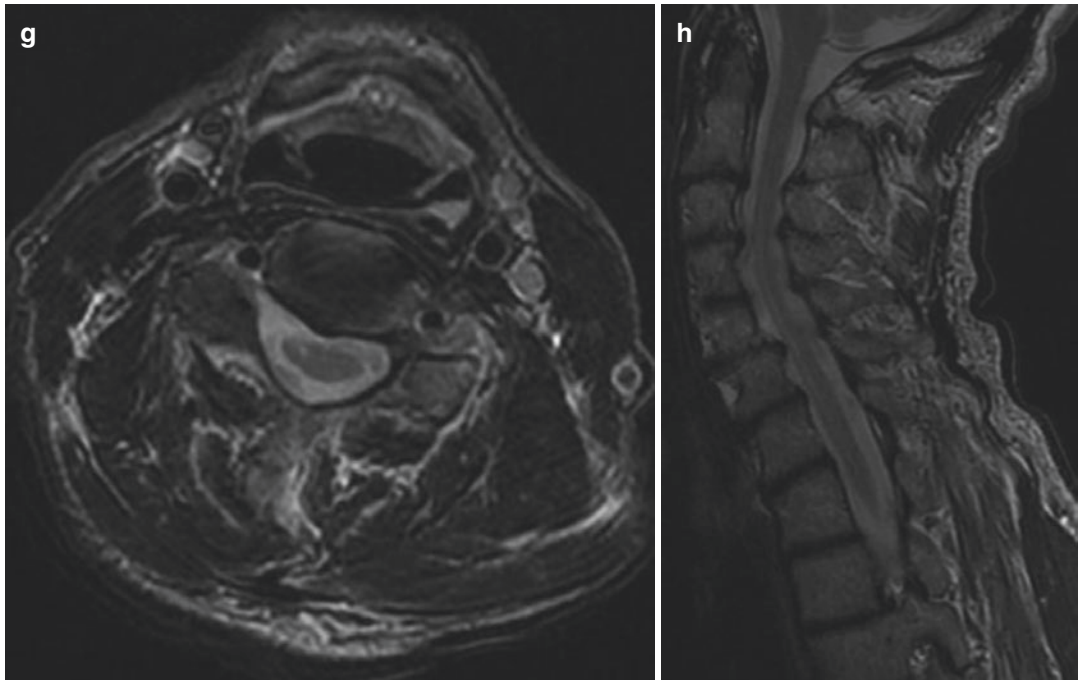

Fig. 10.3 (continued)

myelitis due to its effect on the motor neurons present. The most well-known infection with this presentation and imaging features is Poliomyelitis, with unilateral or bilateral T2 hyperintense signal centered in the frontal horns [34, 70, 71] (Fig. 10.3g, h). Enterovirus-71 or D68, may have a similar appearance, but is also associated with ventral nerve rootlet thickening, and hyperenhancement, and less commonly LETM with centromedullary pattern [51, 70–73]. West Nile virus may have a similar appearance, but may also be normal [74, 75].

Finally, the irregular pattern is characterized by abnormal signal that does not restrict to a particular subsite of the spinal cord, and involves both gray and white matter. Two characteristic infections with this pattern are pyogenic abscess most commonly caused by *Staphylococcus aureus* and *Streptococcus* species (central T1 hypointensity with corresponding T2/DWI hyperintensity, with T2 hypointense margins and rim enhancement) (Fig. 10.3a, b) [34, 35, 76, 77], and schistosomiasis (patchy, mass-like multinodular lesions with T2 hyperintense signal, heterogeneous enhancement, most commonly from T11 to L1 levels, and associated CE thickening and hyperenhancement) [45, 78].

Abbreviations

LETM - Longitudinal Extensive Transverse Myelitis, CE - Cauda Equina, DRG – Dorsal Root Ganglion, GBS - Guillian Barre Syndrome, PML – Progressive Multifocal Leukodystrophy, EBV - Ebstein Barr Virus, JC virus - John Cunningham Virus, VZV – Varicella Zoster Virus, HTLV- Human T-cell Lymphocytic Virus, HIV – Human Immunodeficiency Virus

Demyelinating and Inflammatory

Multiple sclerosis (*MS*) is a demyelinating disease that presents with lesions in the brain and spinal cord, which affects approximately two million people worldwide, and has a predilection for females (F:M = 3:1) [79]. MRI is particularly helpful in evaluation of the central nervous system (CNS) to document lesions disseminated in space and time, which form a component of the diagnostic criteria. Commonly,

MS lesions in the spine are associated with lesions in the brain; however, in minority of patients, the lesions may be present exclusively in the spinal cord [68, 80]. Cord lesions have been shown to correlate more with disability and less with disease duration [80, 81].

MS lesions in the spinal cord are characteristically peripherally located where pial veins are adjacent to the white matter, with the most common location in the dorsal and lateral aspect of the cord. While lesions in the brain are almost exclusively seen in the white matter, within the spinal cord, MS lesions, not infrequently, violate the gray-white matter boundaries. These lesions rarely extend beyond two vertebral levels; however, majority of the lesions span one vertebral body or less, and most commonly involve the cervical cord. Additionally, they occupy less than half of the cross-sectional area of the cord [81–83]. On T2 and FLAIR MRI sequences, MS lesions are characterized by hyperintense signal (Fig. 10.4a, b). Cord expansion and enhancement indicate active inflammation due to increased blood-brain barrier permeability (Fig. 10.4c, d). The most common pattern of enhancement is an incomplete or open ring [82, 83]. In cases of long-term disease, the cord may demonstrate atrophic changes [68, 80].

- *Acute disseminated encephalomyelitis (ADEM)* is a demyelinating disease of the central nervous system (CNS), which is monophasic in its course, and has a predilection for early childhood demographic. It typically occurs following an infection or vaccination and has a polyfocal presentation [84, 85]. Brain MRI is essential in evaluation for ADEM where abnormalities consistent with demyelination during the acute (3 months) phase are considered part of the new diagnostic criteria [85]. Brain lesions are usually multiple, bilateral, and asymmetric. They poorly defined lesions, and usually larger than MS plaques. They can involve the subcortical, central, and cortical gray-white matter junction, thalami, basal ganglia, cerebellum, and brainstem [85, 86] (Fig. 10.4e).

  Up to one-third of ADEM patients will also have spinal cord lesions [85]. Isolated spinal cord involvement is extremely rare [87]. Cord lesions are large and confluent usually spanning more than two segments on initial presentation and frequently spanning three or more segments [85, 86, 88, 89]. On MRI, the lesions are T2 hyperintense, and may be associated with mild cord expansion [85, 87] (Fig. 10.4f, g). Enhancement can be variable, and can be seen in approximately 30% of patients [84, 85, 87] (Fig. 10.4h). Follow-up imaging upon treatment will usually demonstrate complete or partial resolution of brain and cord lesions. Since ADEM is a monophasic disease, there are no new lesions on serial imaging [85].
- *Neuromyelitis Optica Spectrum Disorder (NMOSD)* is a relapsing-remitting autoimmune inflammatory demyelinating disease of the CNS. The presence of antibodies against the aquaporin-4 immunoglobin G (AQP4-IgG) has been implicated in the pathogenesis; however, there are AQP4-IgG seronegative patients that still meet clinical and imaging criteria for diagnosis. The presence of AQP4-IgG has however been associated with relapse [88–90]. AQP4-IgG has also been discovered in patients with non-organ specific autoimmune conditions such as Sjogren's disease and systemic lupus erythematosus (SLE) [90, 91]. Although historically described to involve the optic nerves and spinal cord, lesions in the mid-brain, brainstem, and cerebral hemispheres (where there is a high concentration of AQP4 water channel), have been described [89–91]. MRI of the CNS is vital in the diagnosis and evaluation.

  Within the spinal cord, LETM is the most common imaging appearance [88, 90]. Lesions typically involve the cervical or thoracic spine. The central gray matter along the central canal of the spinal cord has the highest expression of AQP4 antigen, and are the areas of involvement [90]. Thus, lesions generally are either centrally located or both centrally and peripherally located and can and involve more than 50% of the cord cross-sectional area [88, 90]. Lesions are characteristically highly T2 hyperintense (bright spotty lesion) when compared to CSF with

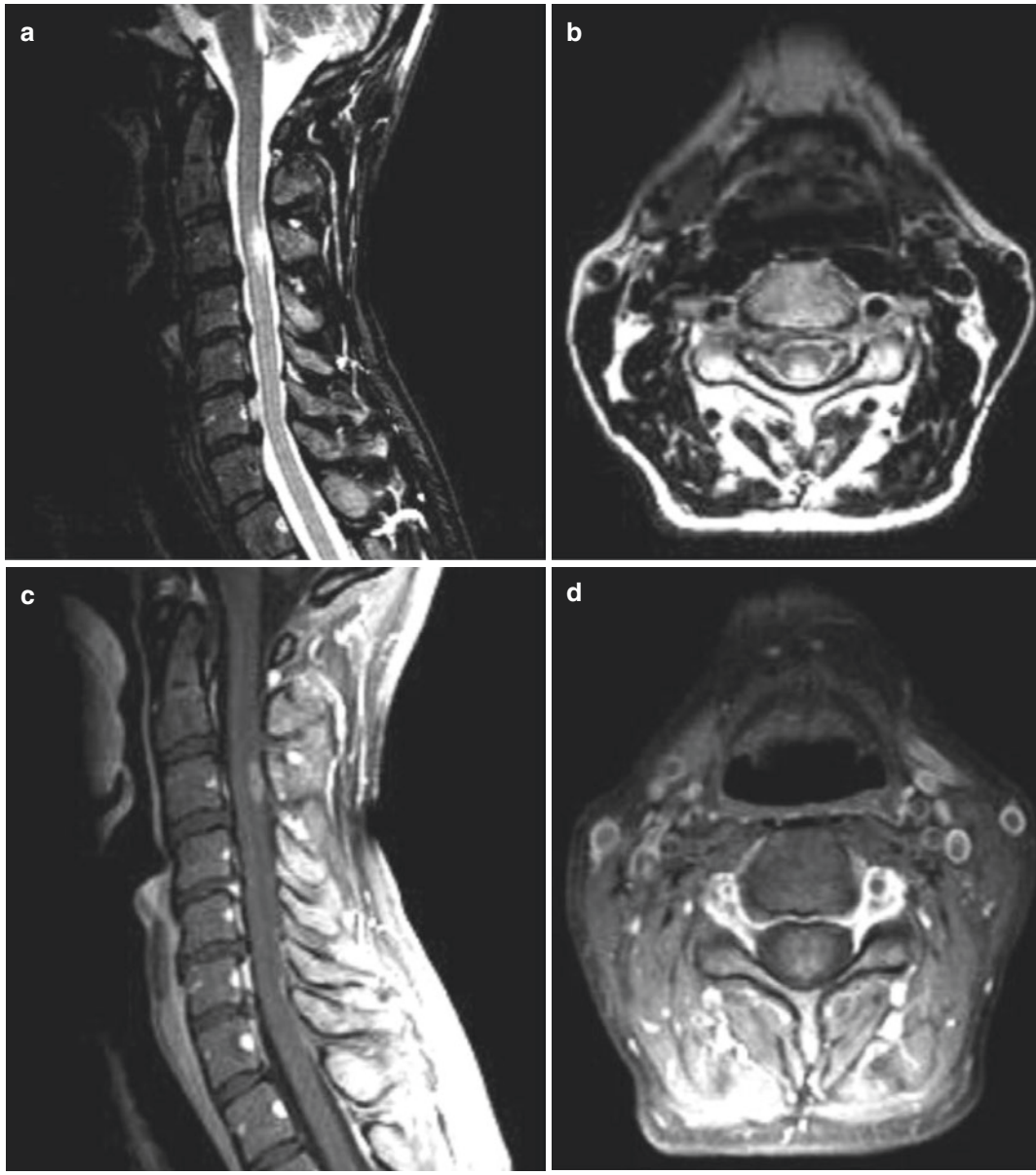

Fig. 10.4 (**a**) Sagittal T2W and (**b**) axial T2W images demonstrate short segment T2 hyperintense signal abnormality in the dorsal columns of the cervical cord in a patient with multiple sclerosis. The presence of enhancement in (**c**) contrast-enhanced sagittal T1W and (**d**) contrast-enhanced axial T1W images indicates active inflammation. Patient with acute disseminated encephalomyelitis (ADEM) demonstrates abnormal hyperintense signal on (**e**) axial FLAIR image of the brain, as well as (**f**) axial T2W, (**g**) sagittal T2W, and (**h**) contrast-enhanced sagittal T1W images of the thoracic cord. There is mild expansion of the thoracic cord. (**i**) Sagittal T2W and (**j**) sagittal contrast-enhanced T1W images demonstrate longitudinal extensive T2 hyperintense signal abnormality with patchy enhancement in the cervical cord in a patient with neuromyelitis optica. This patient also had right optic nerve enhancement indicative of optic neuritis (not shown). (**k**) Sagittal T2W and (**l**) contrast-enhanced sagittal T1W images of the thoracic cord demonstrate hyperintense signal abnormality with associated intramedullary and dural enhancement in a patient with neurosarcoidosis

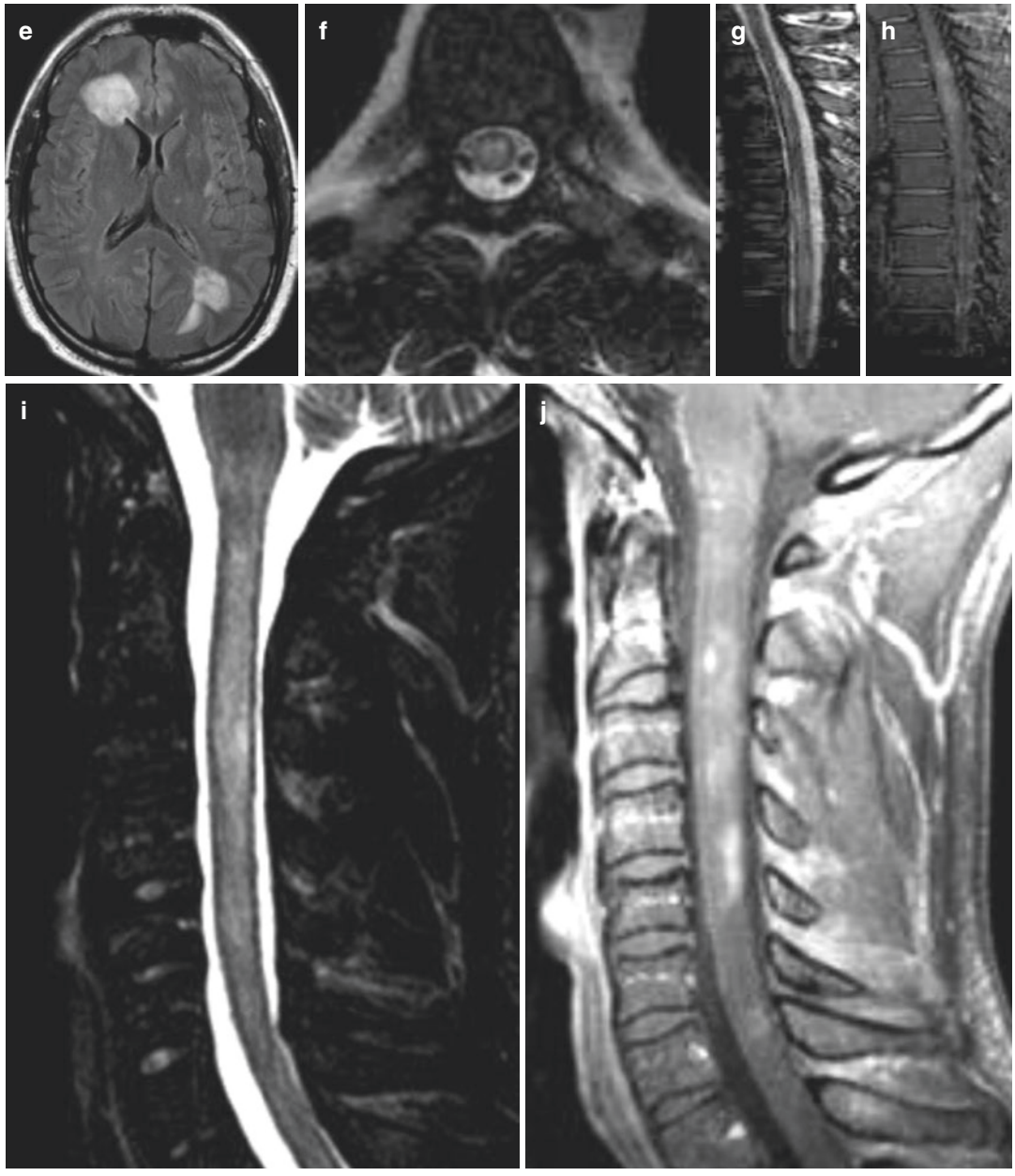

Fig. 10.4 (continued)

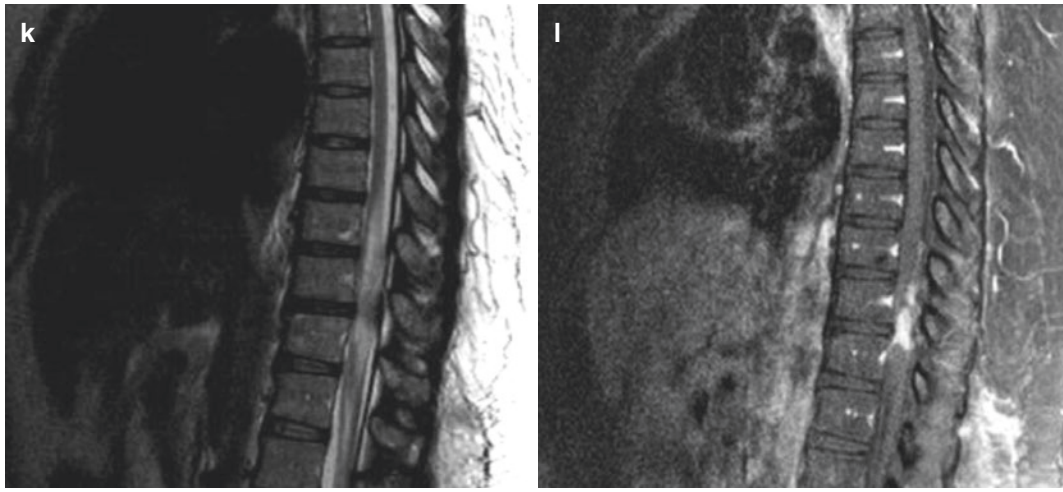

Fig. 10.4 (continued)

corresponding T1 hypointense signal (Fig. 10.4i), which can be helpful in distinguishing it from other demyelinating or ischemic lesions, which may not be as T2 hyperintense [92]. In the acute phase, there may be cord swelling. On post-contrast images, the most commonly described pattern is a ring enhancement pattern, giving it a lenticular appearance on sagittal images, although irregular enhancement pattern has also been described (Fig. 10.4j). In a smaller proportion of patients, cord lesions are short segment (involving less than three vertebral segments), but still involve the central gray matter and more than 50% of the cross-sectional area of the cord [90].

- *Sarcoidosis* is an idiopathic multisystem granulomatous disease that affects all parts of the body, but especially the lungs and pulmonary lymph nodes. It affects people of all races, but is most prevalent amongst African Americans and North European Caucasians [93]. When the CNS is involved, it is termed neurosarcoidosis. The most typical presentation in the CNS is basal meningitis and cranial neuropathy. On cranial imaging, this is depicted by thickening and enhancement of the leptomeninges at the cranial base as well as cranial nerve enhancement [93, 94]. When the spinal cord is involved, it presents clinically with weakness and other nonspecific signs of myelopathy. Typically, the presence of other systemic manifestations of disease is a clue to the diagnosis. On rare occasions, spinal cord symptoms may be the initial presentation making the diagnosis difficult [95, 96].

  Imaging findings within the spine are varied including intramedullary, intradural extramedullary, extradural, vertebral, and disc space lesions at the cervical and thoracic levels [94, 96]. Cord lesions can be varied, but commonly have an LETM appearance demonstrating T2 hyperintense signal (Fig. 10.4k). Leptomeningeal enhancement (Fig. 10.4l) may or may not be present [89, 91, 94, 97]. There may be increased signal on ADC maps [96]. In a retrospective study of 16 patients with intramedullary spinal sarcoidosis, Junger et al. proposed imaging stages and histopathological correlates as follows: Phase 1: linear leptomeningeal enhancement related to early inflammation; Phase 2: faint parenchymal enhancement and diffuse swelling related to centripetal spread of leptomeningeal disease through Virchow Robin spaces; Phase 3: resolution of cord swelling with associated focal or multiple enhancement; and Phase 4: Normal or atrophic spinal cord with no enhancement related to resolution of the

inflammatory process [94, 98]. In their study, phases 2 and 3 were the most common imaging appearance. Rarely, cord lesions may be associated with calcifications, and syrinx or cyst formation [94, 99].

- *Behcet's disease (BD)* is a multisystem small vessel vasculitis that presents with the classical triad of oral ulcerations, genital ulcerations, and uveitis. However, frequently there are other manifestations of the disease involving the skin and mucosa, joints, cardiovascular, pulmonary, and neurological systems. It has a predilection for young men of the Mediterranean and Middle Eastern descent. When there is neurological involvement of BD, it is termed neuro-Behcet's disease (NBD) [100, 101], which affects about 5–30% of patients with systemic BD [101].

  The most common neurological involvement can be divided into two subtypes: a) a parenchymal subtype which typically is a vasculitis that involves the brainstem, and diencephalon region, and b) nonparenchymal subtype which typically presents as cerebral sinovenous thrombosis [100, 101]. Spinal involvement is rare; however, when present, it confers poorer prognosis. Spinal NMD most commonly manifests as LETM [89, 91, 101] and frequently involves the posterolateral cord [100].

Ischemic

Spinal cord ischemia/infarction is a relatively rare cause of acute myelopathy with generally poor prognosis. Ischemia in the cord can be caused by arterial or venous etiologies. Common arterial etiologies include severe atherosclerotic disease, embolus, and aortic dissection. Cardiac surgery, vasculitis, compression of a radicular artery by a disc, and degenerative disease associated with minor trauma are less common causes. Common venous etiologies include arteriovenous malformations or fistulas, coagulopathy, epidural venous thrombosis from infection, spinal cord neoplasm, myelopathy from chronic cervical stenosis, and sepsis [68, 102, 103].

Clinical presentation depends on the location and extent of the infarction. Diagnostic imaging findings are varied but may have considerable overlap with other pathologies such as Neuromyelitis Optica [92]. MRI is the most useful imaging modality in the evaluation of ischemia and infarction. Similar to the brain, acute cord infarction will present as restricted diffusion on diffusion weighted imaging (Fig. 10.5a, b). On T2 or STIR sequences, there is abnormal hyperintense signal depicting edema (Fig 10.5c) which may span multiple levels giving the appearance of LETM, or may be limited to a single level (Fig. 10.5d). There may be associated cord swelling. In the acute setting, there may be no enhancement due to occlusion. In the subacute phase, the blood brain barrier breaks down and enhancement can be seen [68]. Abnormal signal may persist in the subacute setting, but begins to fade over time. In chronic phases, focal cord atrophy may be seen [102].

The spinal cord is supplied by a centrally located anterior spinal artery, two posterolateral spinal arteries, and the artery of Adamkiewicz. The anterior spinal artery arises from two descending branches originating from the fourth segment of the vertebral arteries and supplies the anterior two-thirds of the cross-section of the cord. Additional arteries, including the artery of Adamkiewicz, the ascending cervical, inferior thyroid, intercostal, lumbar, iliolumbar, and lateral sacral arteries supply branches to the anterior spinal artery as it descends. The posterior spinal arteries arise from the posterior inferior cerebellar arteries and supply the posterior one-third of the cord including the dorsal columns, posterior roots, and dorsal horns [102–104].

Clinical manifestations and patterns of imaging are variable depending on the affected artery. Anterior spinal artery syndrome is the most common presentation whereby patients present with bilateral loss of motor function and pain/temperature sensation. In less severe cases, the ischemia may be limited to the level of the anterior horns. Correspondingly, signal abnormality may be limited to the anterior horns and surrounding white matter, bilaterally or unilaterally, involving one or multiple levels depending on severity. The classic

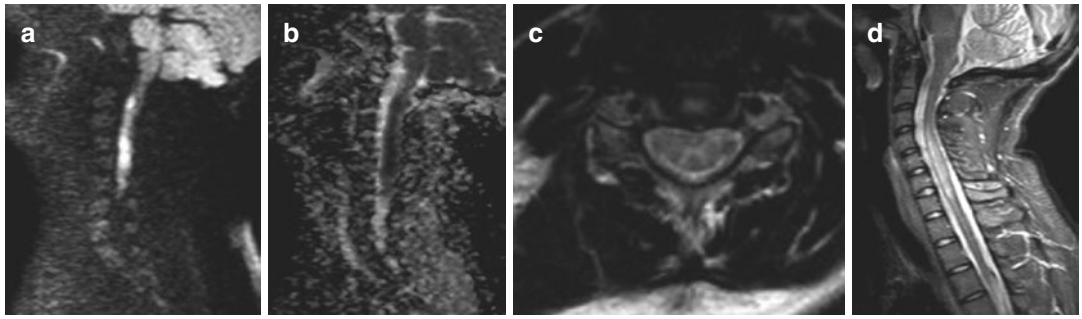

Fig. 10.5 (**a**) Sagittal DWI and (**b**) sagittal ADC images demonstrate restricted diffusion in the cervical cord with corresponding T2 hyperintense signal seen on (**c**) axial T2W and (**d**) sagittal T2W images consistent with cord infarction. In **c**, there is signal abnormality involving the anterior and posterior horns

owl's eyes pattern depicted by hyperintense signal limited to the anterior horns of the central gray matter occurs; however, this sign is nonspecific [103, 105]. Mawad et al. previously described four patterns of imaging as follows: type 1: abnormal signal limited to the anterior horns of the central gray matter; type 2: abnormal signal limited to the anterior and posterior horns of the central gray matter (Fig. 10.5c); type 3: abnormal signal limited to the anterior and posterior horns of the central gray matter and surrounding white matter; and type 4: diffuse intramedullary hyperintensity with or without peripheral sparing [106].

When watershed infarctions occur secondary to hypotension, the areas that are typically affected are mid-thoracic region and conus medullaris. These infarcts result from ischemia in the arterial border zone between the terminal branches of the anterior and posterior spinal arteries. The predominant imaging finding in this setting is central signal abnormality affecting the gray matter with some associated central or ring-like enhancement. There is typically sparing of the periphery. Thus, imaging findings can be difficult to distinguish from anterior spinal cord syndrome [68].

Posterior spinal artery syndrome results in loss of proprioception, touch, and vibratory sensation at the level of the injury. This may be unilateral or bilateral in presentation, with or without some mild transient weakness. Correspondingly, signal abnormality may be limited to the posterior horns and columns unilaterally or bilaterally [102, 103, 107] and enhancement may be limited to one-half of the cord [68]. Other less typical presentations can occur such as sulcocommissural syndrome, which presents clinically as a Brown-Sequard syndrome; conus medullaris infarction, which presents as a cauda equina syndrome; central cord infarction, which presents as a central cord syndrome; and transverse medullary syndrome [102].

Venous ischemia is characterized by intramedullary edema and subsequent hemorrhage [68]. The imaging findings in venous ischemia will be more extensively covered in the vascular section.

Vascular

Spinal vascular lesions are relatively uncommon causes of cord pathology that can present with acute or progressive myelopathy, pain, and radiculopathy due to hemorrhage, venous congestion or hypertension, venous infarction, and cord compression. Vascular lesions in the spine can be divided into vascular neoplasms, aneurysms, and arteriovenous lesions [108]. Refer to the tumor section for a brief discussion of vascular neoplasms. Isolated spinal aneurysms (not associated with arteriovenous malformations) are extremely rare, and can results from either blood flow or dissection [108]. Presentation is usually related to subarachnoid hemorrhage and sudden onset of back pain. Spetzler et al. described two patients with spinal aneurysms that were treated

successfully with surgery [108]. Arteriovenous fistulas (AVF) form the largest subdivision of non-neoplastic vascular lesions in the spinal cord, which also comprise cavernous malformation and arteriovenous malformation (AVM).

Cavernous malformations are small low-flow lesions that are supplied by thin-wall sinusoidal vessels lined by a single layer of epithelium, and lack of intervening nervous tissue. Within the central nervous system, the incidence is reported to be 0.5%, with 10% being familial [109]; they are more commonly found in the brain parenchyma than spinal cord [110]. On imaging, they are found most commonly in the thoracic spine [111], typically have a rim of low signal on T2 representing hemosiderin due to prior hemorrhage [112], have heterogeneous signal on T1 and T2 due to blood products of varying ages (Fig. 10.6a, b), and bloom on gradient recalled echo sequence. Unless there has been acute hemorrhage, they demonstrate minimal edema and cord expansion. There may be minimal enhancement of post-contrast imaging (Fig. 10.6c). These lesions are angiographically occult [113].

Arteriovenous lesions historically have had numerous classification systems. However, the most common classification was by Anson and Spetzler, who subdivided lesions into four categories as follows. Type I: a dural arteriovenous fistula (AVF) located between a dural branch of

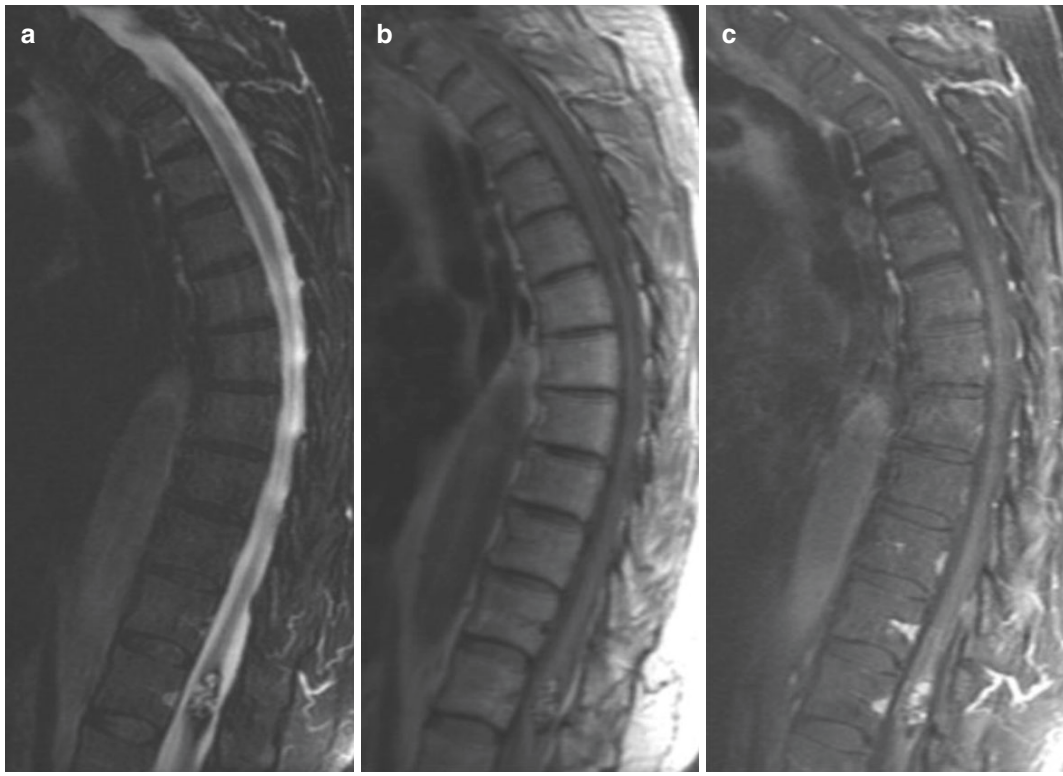

Fig. 10.6 (**a**) Sagittal T2W (**b**) non-contrast sagittal T1W, and (**c**) contrast-enhanced sagittal T1W images demonstrate hyperintense and hypointense signals indicative of varying stages of blood products within a cavernous malformation in the lower thoracic cord. (**d**) Sagittal T2W and (**e**) contrast-enhanced sagittal T1W images demonstrate numerous flow voids and serpiginous tiny vessels along the dorsal aspect of the cervical cord. In another patient, (**f**) sagittal T2W image demonstrates long segment T2 hyperintense signal in the thoracic cord in keeping with venous hypertension. There are numerous flow voids along the dorsal surface of the cord. Findings likely represent a type 1 dural arteriovenous fistula. (**g**) Contrast-enhanced sagittal T1W and (**h**) sagittal T2W images demonstrate a tangle of vessels in the cervical cord with intramedullary nidus compatible with type 2 arteriovenous malformation. (**i**) Frontal projection of right vertebral artery injection in a cerebral angiogram demonstrates arterial feeders from the right vertebral artery

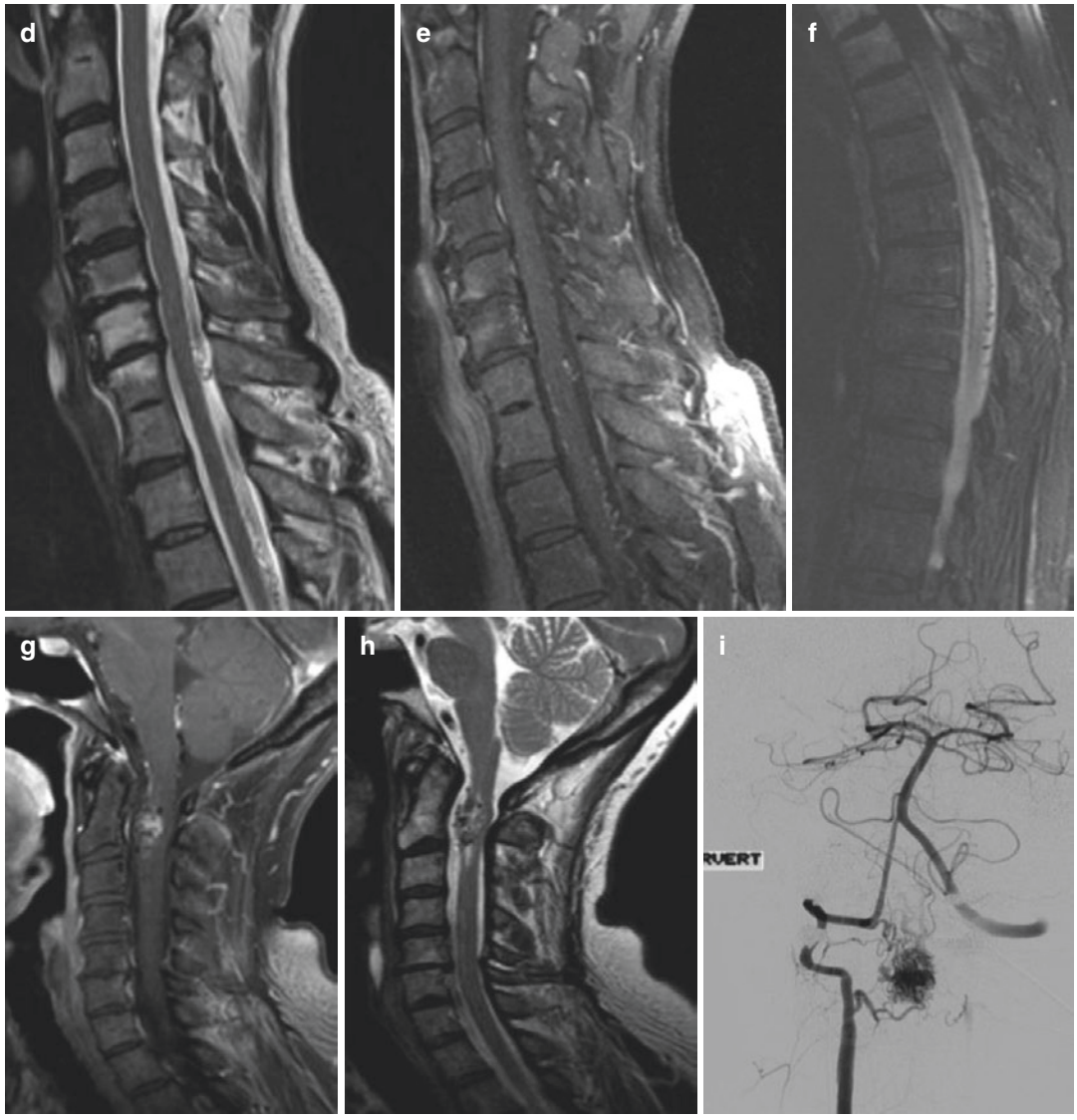

Fig. 10.6 (continued)

the spinal ramus of the radicular artery and an intradural medullary vein – this is the most common type (Fig. 10.6d–f); type II: an intramedullary glomus malformation with a compact nidus within the substance of the spinal cord (Fig. 10.6g–i); type III: an extensive arteriovenous malformation (AVM) often extending into the vertebral body and paraspinal tissues; type IV: an intradural perimedullary AVF, which can be subdivided into type IV-A, IV-B, and IV-C depending on lesion size [114]. However, more recently, Spetzler et al. proposed a modified classification with inclusion of a new category called the conus medullaris AVM [108].

On MRI, dural AVFs (type I) demonstrate diffuse edema usually in the lower thoracic cord (Fig. 10.6f) and conus medullaris, which does not necessarily correlate with the location of the lesion. There is frequently T2 hypointense signal along the periphery of the cord due to pial capillaries containing deoxyhemoglobin secondary to venous congestion, which can cause progressive

neurological deterioration, the so called Foix Alajouanine Syndrome. Additionally, there are prominent serpiginous flow voids which span multiple segments (Fig. 10.6d). Patchy enhancement can be seen in the cord due to capillary leak or chronic infarction. Digital subtraction angiography is the gold standard method of evaluation and confirming the diagnosis, and also provides an option for treatment (Fig. 10.6i) [115–117].

Congenital

A comprehensive discussion of congenital spinal cord lesions and associated extramedullary manifestations far exceed the purposes of this chapter. Briefly, congenital spinal cord lesions can be divided into Open (OSD) and closed spinal dysraphisms (CSD). In OSD, neural and meningeal elements are exposed to air. OSD can have underlying causes such as cord ischemia, arachnoid cysts, scar tethering, and epidermoid or dermoid lesions. The most common OSD is myelomeningocele (Fig. 10.7a, b) where there is a defect in the closure of the primary neural tube resulting in exposure of the neural placode [118, 119]. Myelomeningocele has 100% association with Chiari II malformation. In myelomeningocele, the neural placode protrudes through the skin defect. Conversely in myelocele, which is relatively rare, the placode is flush with the skin surface. Meningoceles are CSF-filled sacs lined by dural and arachnoid, but unlike myelomeningoceles, they do not contain neural elements [119] (Fig. 10.7c, d). When a meningomyelocele or myelocele is associated with split cord malformation, with failure of neurulation of one hemicord, it is termed hemimeningomyelocele or hemimyelocele [119, 120].

In CSD, the neural and meningeal elements are covered by skin. Lipomyelomeningocele and lipomyelocele make up 16% of CSD [121]. They usually protrude posteriorly as a back mass in the lumbosacral region which is either lipomatous or hamartomatous [122]. Posterior meningocele, which is a CSF-filled meningeal sac through a posterior spina bifida, makes up 2.5% of CSD [121]. Other CSDs include terminal myelocysto-

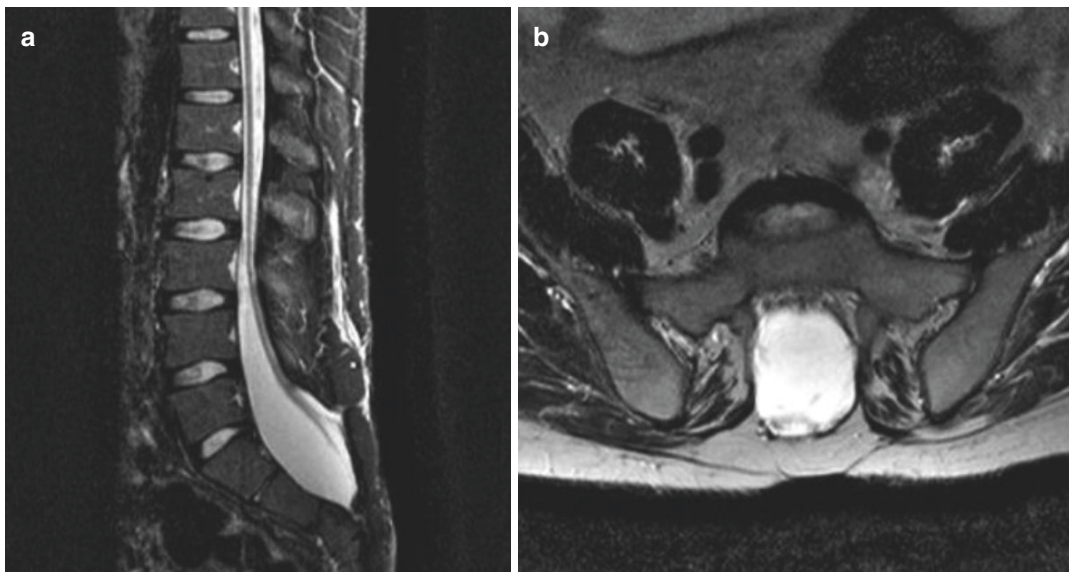

Fig. 10.7 (**a**) Sagittal T2W with fat saturation and (**b**) axial T2W images of myelomeningocele. Note that neural elements are contained in the CSF-filled sac. (**c**) Sagittal T2W with fat saturation and (**d**) axial T2W images of meningocele. Note that there are no neural elements in the CSF-filled sac. (**e**) Sagittal T1W and (**f**) axial T1W images of intraspinal lipoma with intramedullary component in the cervical cord. (**g**) Sagittal T1W and (**h**) sagittal T2W images of a filum terminale lipoma with tethered cord. (**i**) Axial T2W images of type II split cord malformation with individual dural covering and intervening septum

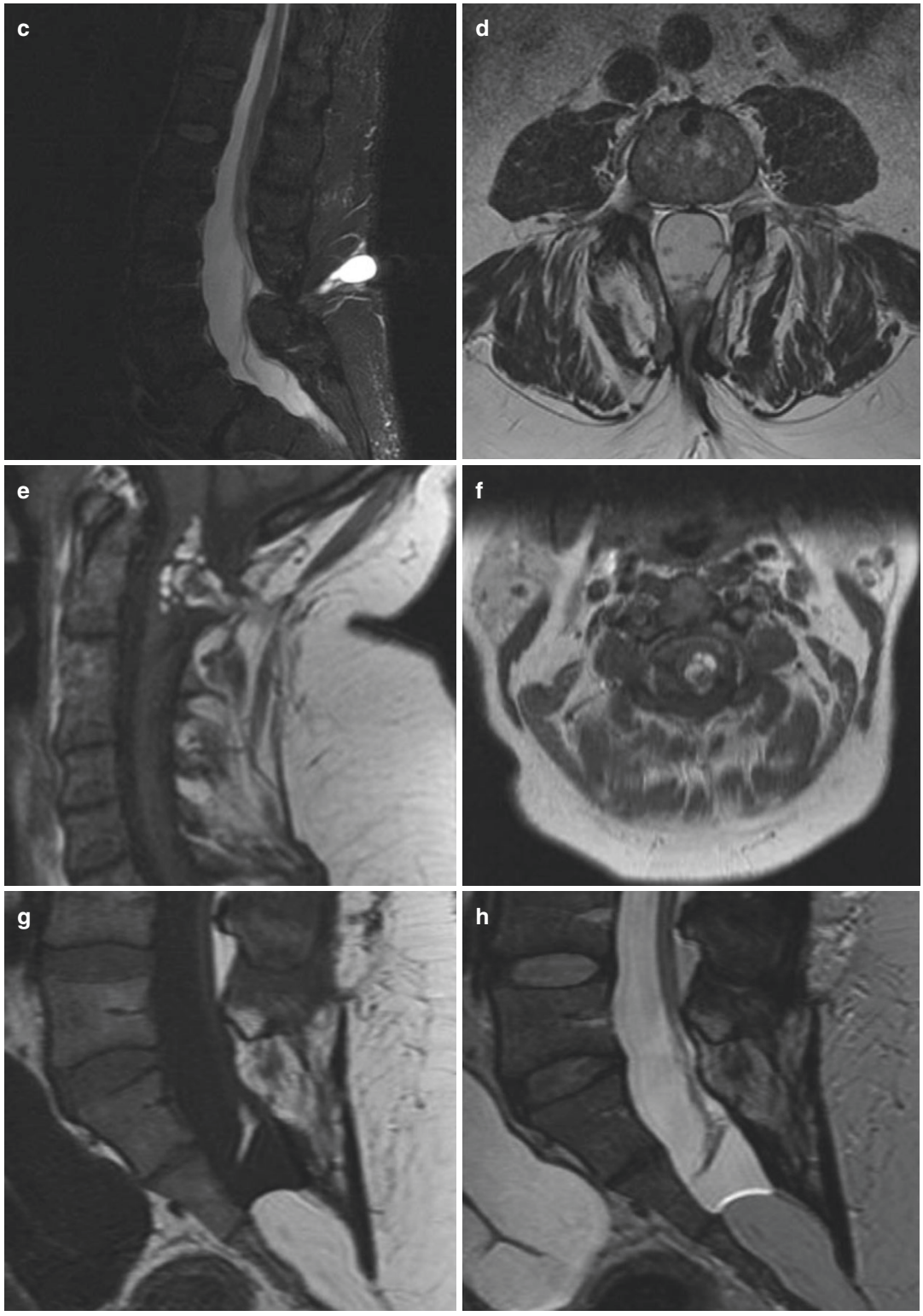

Fig. 10.7 (continued)

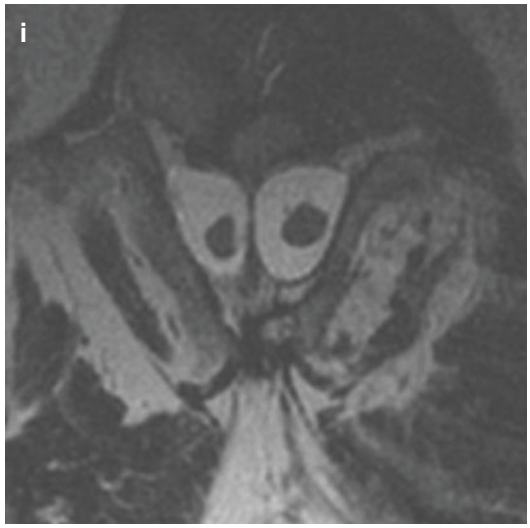

Fig. 10.7 (continued)

cele, cervical myelocystocele, filar lipoma (Fig. 10.7e, d), tight filum terminale, persistent terminal ventricle, dermal sinus tract, and abnormally elongated cord [118, 119].

Complex dysraphic states such as split cord malformations result due to persistent connection between the amniotic cavity and yolk sac resulting in failure of integration of both notochords. Split chord malformations (Fig. 10.7i) make up 3.5% of CSD. Split cord malformation (formerly known as Diastetomyelia) represents a rare complex dysraphic state characterized by longitudinal splitting of the spinal cord into two. The two hemicords may or may not be symmetric [123], and the length of separation may be variable [119]. Each hemicord has a central canal, as well as dorsal and ventral nerve roots [123]. They are classified into two types. In type 1, each hemicord has its own dura, and they are separated by an osseous or cartilaginous septum. In type 2, the hemicords have a single dural covering, and there is no intervening fibrous septum [119].

Other complex dysraphic states include caudal regression syndrome (CRS) which makes up 16% of CSD; segmental spinal dysgenesis, which is less common; and dorsal enteric fistula, which is rare [118]. CRS can be categorized into two forms: type I, which is the more severe form, and type II, which is less severe. In type I, the spine ends at S2 or above, and there is high-lying spinal cord with abrupt termination, which has the appearance of a club or wedge. In type II, the spine ends at or below S3, and the conus appears stretched to a tight filum [118].

Finally, congenital intraspinal tumors can have extradural, subdural, or intramedullary location. Dermoid tumors are the most common and occur primarily in the lumbosacral spine. Epidermoid tumors on the other hand most commonly occur in the thoracic spine. Other tumors include sacrococcygeal teratomas which involve all three germ cell layers, intraspinal lipomas (Fig. 10.7e–h), and neuroenteric cysts, which represent displaced endodermal tissue commonly occurring in the lower cervical/upper thoracic spine [118].

MRI is the modality of choice in evaluation of the afore-mentioned congenital lesions. CT can be helpful for demonstrating vertebral anomalies. In the neonate, the first imaging study is usually performed with ultrasound.

Genetic and Metabolic

Metabolic and genetic causes of spinal cord lesions have considerable overlap on MR imaging. For ease of understanding, Marelli et al., categorized metabolic and genetic causes of spinal cord lesions based on imaging characteristics as follows: a) Selective white matter hyperintensity (WMH) of the dorsal with/without involvement of the lateral columns, b) hyperintensity not involving a selective spinal tract, c) presence of gadolinium enhancement, and d) medullary atrophy without signal alterations [124].

Selective T2 hyperintense signal involving the white matter of the dorsal columns and, in some cases, the lateral columns have been shown in several conditions such as acquired vitamin B12 (Fig. 10.8a, b), copper and folate deficiencies, nitrous oxide toxicity, (primarily cervical and thoracic involvement without intracranial involvement), vitamin E deficiency (primarily cervical involvement without intracranial involvement), intrathecal methotrexate (cervical or thoracic involvement with possible extensive

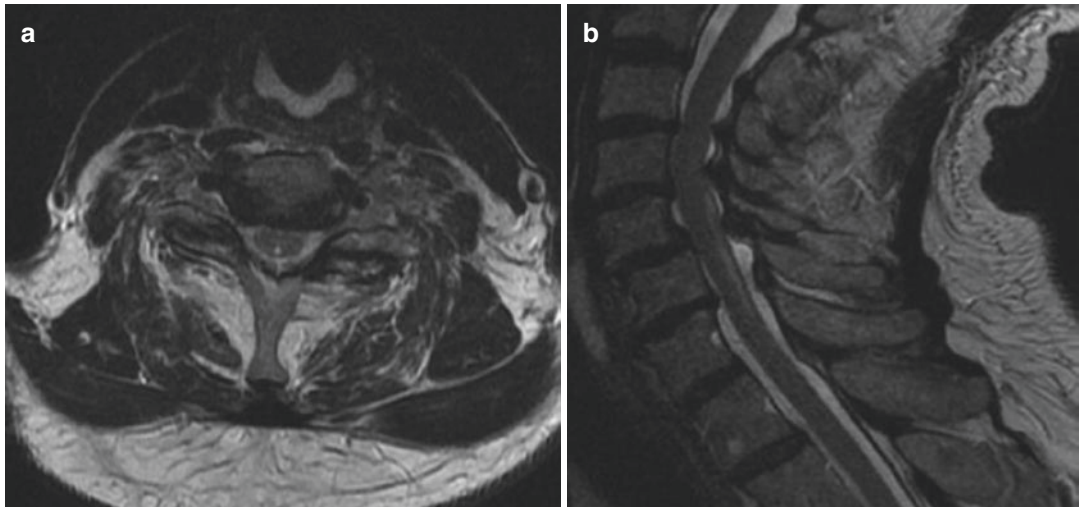

Fig. 10.8 (**a**) Axial T2W and (**b**) sagittal T2W images demonstrate hyperintense signal in the posterior columns in a patient with subacute combined degeneration

cerebral leukopathy), and genetic diseases with hyperhomocysteinemia (cervical involvement with or without cerebral atrophy and abnormal periventricular white matter signal) [124]. In conditions such as hypomyelination with brainstem and spinal involvement and leg spasticity (HBSL), leukoencephalopathy with brainstem, spinal cord involvement, and lactate elevation (LSBL), adult-onset autosomal dominant leukodystrophy (ADLD), and spinal cerebrotendinous-xanthomatosis (CTX), intramedullary T2 signal abnormality is typically longitudinally extensive, frequently with intracranial abnormalities [125–131].

Abnormal T2 signal hyperintensity not involving a selective spinal tract can be seen in conditions such as biotinidase deficiency, Alexander disease, and mitochondrial disease (OPA1-LHON), where there is frequent optic and intracranial involvement [124, 132–135]. Biotinidase deficiency has been noted to mimic neuromyelitis optica with visual symptoms [133, 136, 137]. In Alexander disease, the imaging features are primarily at the bulbomedullary junction with extension inferiorly to involve the cervical spine. Biotinidase deficiency and Alexander disease can also present with selective T2 hyperintense signal alterations involving the dorsal and lateral columns [124].

The presence of gadolinium enhancement is seen in Alexander disease, biotinidase deficiency, genetic and acquired hyperhomocysteinemia, nitrous oxide exposure, and intrathecal methotrexate [124, 136, 138].

Finally, medullary atrophy without medullary signal alterations is the characteristic spinal imaging appearance of adrenomyeloneuropathy (ALD) (generalized atrophy), APBD (focal or generalized atrophy), Friedreich's ataxia (cervical atrophy), amylotrophic lateral sclerosis (ALS) (generalized atrophy), and genetic hereditary spastic paraplegia (HSP) [124, 139, 140]. Alexander disease can also present with focal atrophy of the medulla oblongata and cervical spine; thoracic spine involvement is rare [141–143].

MRI is the most useful imaging modality in the evaluation of the CNS in the aforementioned genetic and metabolic conditions.

References

1. Ahuja CS, Nori S, Tetreault L, et al. Traumatic spinal cord injury – repair and regeneration. Neurosurgery. 2017;80:S9–22.
2. Martínez-Pérez R, Paredes I, Cepeda S, et al. Spinal cord injury after blunt cervical spine trauma: correlation of soft-tissue damage and extension of lesion. Am J Neuroradiol. 2014;35:1029–34.

3. Tator CH. Update on the pathophysiology and pathology of acute spinal cord injury. Brain Pathol. 1995;5:407–13.
4. Chandra J, Sheerin F, Lopez De Heredia L, et al. MRI in acute and subacute post-traumatic spinal cord injury: pictorial review. Spinal Cord. 2012;50:2–7.
5. Leypold BG, Flanders AE, Burns AS. The early evolution of spinal cord lesions on MR imaging following traumatic spinal cord injury. Am J Neuroradiol. 2008;29:1012–6.
6. Miyanji F, Furlan JC, Aarabi B, et al. Acute cervical traumatic spinal cord injury: MR imaging findings correlated with neurologic outcome-prospective study with 100 consecutive patients 1. Radiology. 2007;243:820–7.
7. Kumar Y, Hayashi D. Role of magnetic resonance imaging in acute spinal trauma: a pictorial review. BMC Musculoskelet Disord. 2016;17(310):2–11.
8. Kulkarni MV, McArdle CB, Kopanicky D, et al. Acute spinal cord injury: MR imaging at 1.5 T. Radiology. 1987;164:837–43.
9. Talekar K, Poplawski M, Hegde R, et al. Imaging of spinal cord injury: acute cervical spinal cord injury, cervical Spondylotic myelopathy, and cord herniation. Semin Ultrasound CT MRI. 2016;37:431–47.
10. Planner AC, Pretorius PM, Graham A, et al. Subacute progressive ascending myelopathy following spinal cord injury: MRI appearances and clinical presentation. Spinal Cord. 2008;46:140–4.
11. Potter K, Saifuddin A. MRI of chronic spinal cord injury. Br J Radiol. 2003;76:347–52.
12. Robert H, Quencer M, Sheldon JJ, et al. MRI of the chronically injured cervical spinal cord. Am J Roentgenol. 1986;147:125–32.
13. Koeller K, Rosenblum R, Morrison A. Neoplasms of the spinal cord and filum terminale: radiologic-pathologic correlation. Radiographics. 2000;20:1721–49.
14. Smith AB, Soderlund KA, Rushing EJ, et al. Radiologic-pathologic correlation of pediatric and adolescent spinal neoplasms: part 1, intramedullary spinal neoplasms. Am J Roentgenol. 2012;198:34–43.
15. Mechtler LL, Nandigam K. Spinal cord tumors. New views and future directions. Neurol Clin. 2013;31:241–68.
16. Celano E, Salehani A, Malcolm JG, et al. Spinal cord ependymoma: a review of the literature and case series of ten patients. J Neuro-Oncol. 2016;128:377–86.
17. Shors SM, Jones TA, Jhaveri MD, et al. Myxopapillary ependymoma of the sacrum. Radiographics. 2006;26:S111–6.
18. Wippold FJ, Smirniotopoulos JG, Moran CJ, et al. MR imaging of myxopapillary ependymoma: findings and value to determine extent of tumor and its relation to Intraspinal structures. Am J Roentgenol. 1995;165:1263–7.
19. Cure LM, Hancock CR, Barrocas AM, et al. Interesting case of subependymoma of the spinal cord. Spine J. 2014;14:e9–12.
20. Jallo GI, Zagzag D, Epstein F. Intramedullary subependymoma of the spinal cord. Neurosurgery. 1996;38:251–7.
21. Hoeffel C, Boukobza M, Polivka M, et al. MR manifestations of subependymomas. AJNR Am J Neuroradiol. 1995;16:2121–9.
22. Seo H, Kim J-H, Lee D, et al. Nonenhancing intramedullary astrocytomas and other MR imaging features: a retrospective study and systematic review. Am J Neuroradiol. 2009;31:498–503.
23. Tobin MK, Geraghty JR, Engelhard HH, et al. Intramedullary spinal cord tumors: a review of current and future treatment strategies. Neurosurg Focus. 2015;39:E14.
24. Patel U, Pinto RS, Miller DC, et al. MR of spinal cord ganglioglioma. Am J Neuroradiol. 1998;19:879–87.
25. Oppenheimer DC, Johnson MD, Judkins AR. Ganglioglioma of the spinal cord. J Clin Imaging Sci. 2015;5:53.
26. Chu B-C, Terae S, Hida K, et al. MR findings in spinal hemangioblastoma: correlation with symptoms and with angiographic and surgical findings. AJNR Am J Neuroradiol. 2001;22:206–17.
27. Dillard-Cannon E, Atsina K-B, Ghobrial G, et al. Lumbar paraganglioma. J Clin Neurosci. 2016;30:149–51.
28. Yi X, Zhang Y, Zhou C, et al. Lumbosacral intraspinal paraganglioma: clinicopathologic and computed tomography/magnetic resonance imaging features of 13 cases. World Neurosurg. 2018;113:e586–97.
29. Chou S-C, Chen T-F, Kuo M-F, et al. Posterior vertebral scalloping of the lumbar spine due to a large cauda equina paraganglioma. Spine J. 2016;16:e327–8.
30. Yang W, Garzon-Muvdi T, Braileanu M, et al. Primary intramedullary spinal cord lymphoma: a population-based study. Neuro-Oncology. 2017;19:414–21.
31. Flanagan EP, O'Neill BP, Porter AB, et al. Primary intramedullary spinal cord lymphoma. Neurology. 2011;77:784–91.
32. Rykken J, Diehn F, Hunt C, et al. Intramedullary spinal cord metastases: MRI and relevant clinical features from a 13-year institutional case series. Am J Neuroradiol. 2013;34:2043–9.
33. Ellis JA, Rothrock RJ, Moise G, et al. Primitive neuroectodermal tumors of the spine: a comprehensive review with illustrative clinical cases. Neurosurg Focus. 2010;30:E1.
34. Talbott JF, Narvid J, Chazen JL, et al. An imaging-based approach to spinal cord infection. Semin Ultrasound CT MRI. 2016;37:411–30.
35. DeSanto J, Ross JS. Spine infection/inflammation. Radiol Clin N Am. 2011;49:105–27.
36. Danner RL, Hartman BJ. Update on spinal epidural abscess: 35 cases and review of the literature. Rev Infect Dis. 1987;9:265–74.
37. Wang VY, Chou D, Chin C. Spine and spinal cord emergencies: vascular and infectious causes. Neuroimaging Clin N Am. 2010;20:639–50.

38. Chen W-C, Wang J-L, Wang J-T, et al. Spinal epidural abscess due to Staphylococcus aureus: clinical manifestations and outcomes. J Microbiol Immunol Infect. 2008;41:215–21.
39. Curry WT, Hoh BL, Amin-Hanjani S, et al. Spinal epidural abscess: clinical presentation, management, and outcome. Surg Neurol. 2005;63:364–71.
40. Eastwood JD, Vollmer RT, Provenzale JM. Diffusion-weighted imaging in a patient with vertebral and epidural abscesses. AJNR Am J Neuroradiol. 2002;23:496–8.
41. Erdem H, Elaldi N, Batirel A, et al. Comparison of brucellar and tuberculous spondylodiscitis patients: results of the multicenter "Backbone-1 Study.". Spine J. 2015;15:2509–17.
42. Hristea A, Constantinescu RVM, Exergian F, et al. Paraplegia due to non-osseous spinal tuberculosis: report of three cases and review of the literature. Int J Infect Dis. 2008;12:425–9.
43. Bernaerts OA, Vanhoenacker FM, Parizel PM, et al. Tuberculosis of the central nervous system: overview of neuroradiological findings. Eur Radiol. 2003;13:1876–90.
44. Richie MB, Pruitt AA. Spinal cord infections. Neurol Clin. 2013;31:19–53.
45. Faria do Amaral LL, Nunes RH, da Rocha AJ. Parasitic and rare spinal infections. Neuroimaging Clin N Am. 2015;25:259–79.
46. McGahan JP, Graves DS, Palmer PE. Coccidioidal spondylitis: usual and unusual radiographic manifestations. Radiology. 1980;136:5–9.
47. Erly WK, Bellon RJ, Seeger JF, et al. MR Imaging of Acute Coccidioidal Meningitis. Am J Neuroradiol. 1999;13:1241–5.
48. Lammering JC, Iv M, Gupta N, et al. Imaging spectrum of CNS coccidioidomycosis: prevalence and significance of concurrent brain and spinal disease. Am J Roentgenol. 2013;200:1334–46.
49. Tan LA, Kasliwal MK, Nag S, et al. Rapidly progressive quadriparesis heralding disseminated coccidioidomycosis in an immunocompetent patient. J Clin Neurosci. 2014;21:1049–51.
50. Wrobel CJ, Meyer S, Johnson RH, et al. MR findings in acute and chronic coccidioidomycosis meningitis. AJNR Am J Neuroradiol. 1992;13:1241–5.
51. Yokota H, Yamada K. Viral infection of the spinal cord and roots. Neuroimaging Clin N Am. 2015;25:247–58.
52. Pinto A, Santos E, Correa DF, et al. CMV and HSV-2 myeloradiculitis in an HIV infected patient. Rev Inst Med Trop Sao Paulo. 2011;53:173–5.
53. Whiteman ML, Dandapani BK, Shebert RT, et al. MRI of AIDS-related polyradiculomyelitis. J Comput Assist Tomogr. 1994;18:7–11.
54. Willison HJ, Jacobs BC, van Doorn PA. Guillain-Barré syndrome. Lancet. 2016;388:717–27.
55. Duffy MR, Chen T-H, Hancock WT, et al. Zika virus outbreak on Yap Island, Federated States of Micronesia. N Engl J Med. 2009;360:2536–43.
56. Cao-Lormeau V-M, Blake A, Mons S, et al. Guillain-Barré syndrome outbreak associated with Zika virus infection in French Polynesia: a case-control study. Lancet. 2016;387:1531–9.
57. Oehler E, Watrin L, Larre P, et al. Zika virus infection complicated by Guillain-Barre syndrome – case report, French Polynesia, December 2013. Euro Surveill. 2014;19.
58. Stübgen J-P. Immune-mediated myelitis associated with hepatitis virus infections. J Neuroimmunol. 2011;239:21–7.
59. Suzuki K, Takao M, Katayama Y, et al. Acute myelitis associated with HCV infection. BMJ Case Rep. 2013:bcr2013008934. https://doi.org/10.1136/bcr-2013-008934.
60. Bigi S, Aebi C, Nauer C, et al. Acute transverse myelitis in Lyme neuroborreliosis. Infection. 2010;38:413–6.
61. Goh C, Desmond PM, Phal PM. MRI in transverse myelitis. J Magn Reson Imaging. 2014;40:1267–79.
62. Alper G, Petropoulou KA, Fitz CR, et al. Idiopathic acute transverse myelitis in children: an analysis and discussion of MRI findings. Res Pap Mult Scler J. 2011;17:74–80.
63. Harzheim M, Schlegel U, Urbach H, et al. Discriminatory features of acute transverse myelitis: a retrospective analysis of 45 patients. J Neurol Sci. 2004;217:217–23.
64. de Seze J, Stojkovic T, Breteau G, et al. Acute myelopathies: clinical, laboratory and outcome profiles in 79 cases. Brain. 2001;124:1509–21.
65. Beh SC, Greenberg BM, Frohman T, et al. Transverse Myelitis. Neurol Clin. 2013;31:79–138.
66. Gilden DH, Beinlich BR, Rubinstien EM, et al. Varicella-zoster virus myelitis: an expanding spectrum. Neurology. 1994;44:1818.
67. Gilden D, Nagel MA, Cohrs RJ. Varicella-zoster. Handb Clin Neurol. 2014;123:265–83.
68. Friedman DP, Tartaglino LM, Fisher AR, et al. MR imaging in the diagnosis of intramedullary spinal cord diseases that involve specific neural pathways or vascular territories. AJR. 1995;165:515–23.
69. Berth S, Carbunar O, Yang NS, et al. Varicella-zoster virus encephalomyelitis with a prominent demyelinating component. Neuropathology. 2015;35:587–91.
70. Jubelt B, Lipton HL. Enterovirus/picornavirus infections. In: Handbook of clinical neurology; 2014. p. 379–416.
71. Lee H, Chi C. Enterovirus 71 infection-associated acute flaccid paralysis: a case series of long-term neurologic follow-up. J Child Neurol. 2014;29:1283–90.
72. Messacar K, Schreiner TL, Maloney JA, et al. A cluster of acute flaccid paralysis and cranial nerve dysfunction temporally associated with an outbreak of enterovirus D68 in children in Colorado, USA. Lancet. 2015;385:1662–71.
73. Nelson GR, Bonkowsky JL, Doll E, et al. Recognition and management of acute flaccid myelitis in children. Pediatr Neurol. 2016;55:17–21.
74. Kraushaar G, Patel R, Stoneham GW. West Nile virus: a case report with flaccid paralysis and cervi-

cal spinal cord: MR imaging findings. AJNR Am J Neuroradiol. 2005;26:26–9.
75. Ali M, Safriel Y, Sohi J, et al. West Nile Virus Infection: MR Imaging Findings in the Nervous System. Am J Neuroradiol. 2005;20:1281–3.
76. Friess HM, Wasenko JJ. MR of staphylococcal myelitis of the cervical spinal cord. AJNR Am J Neuroradiol. 1997;18:455–8.
77. Hood B, Wolfe SQ, Trivedi RA, et al. Intramedullary abscess of the cervical spinal cord in an otherwise healthy man. World Neurosurg. 2011;76:361.e15–9.
78. Ferrari TCA, Moreira PRR. Neuroschistosomiasis: clinical symptoms and pathogenesis. Lancet Neurol. 2011;10:853–64.
79. Longo DL, Reich DS, Lucchinetti CF, et al. Multiple sclerosis. N Engl J Med. 2018;378:169–80.
80. Honig LS, Sherematat WA. Magnetic resonance imaging of spinal cord lesions in multiple sclerosis. J Neurol Neurosurg Psychiatry. 1989;52:459–66.
81. Tartaglino LM, Friedman DP, Flanders AE, et al. Multiple sclerosis in the spinal cord: MR appearance and correlation with clinical parameters. Radiology. 1995;195:725–32.
82. Bot JCJ, Barkhof F, Polman CH, et al. Spinal cord abnormalities in recently diagnosed MS patients: added value of spinal MRI examination. Neurology. 2004;62:226–33.
83. Klawiter EC, Benzinger T, Roy A, et al. Spinal cord ring enhancement in multiple sclerosis. Arch Neurol. 2010;67:1395–8.
84. Tenembaum S, Chamoles N, Fejerman N. Acute disseminated encephalomyelitis: a long-term follow-up study of 84 pediatric patients. Neurology. 2002;59:1224–31.
85. Pohl D, Alper G, Van Haren K, et al. Acute disseminated encephalomyelitis updates on an inflammatory CNS syndrome. Neurology. 2016;87:S39–45.
86. Ketelslegers I, Visser I, Neuteboom R, et al. Disease course and outcome of acute disseminated encephalomyelitis is more severe in adults than in children. Mult Scler J. 2011;17:441–8.
87. Singh S, Alexander M, Korah IP. Acute disseminated encephalomyelitis: MR imaging features. Am J Roentgenol. 1999;173:1101–7.
88. Jain RS, Kumar S, Mathur T, et al. Longitudinally extensive transverse myelitis: a retrospective analysis of sixty-four patients at tertiary care center of North-West India. Clin Neurol Neurosurg. 2016;148:5–12.
89. Tobin WO, Weinshenker BG, Lucchinetti CF. Longitudinally extensive transverse myelitis. Curr Opin Neurol. 2014;27:279–89.
90. Dutra BG, José A, Rocha D, et al. Neuromyelitis optica spectrum disorders: spectrum of MR imaging findings and their differential diagnosis. Radiographics. 2018;38:169–93.
91. Kitley JL, Leite MI, George JS, et al. The differential diagnosis of longitudinally extensive transverse myelitis. Mult Scler J. 2012;18:271–85.
92. Kister I, Johnson E, Raz E, et al. Specific MRI findings help distinguish acute transverse myelitis of Neuromyelitis Optica from spinal cord infarction. Mult Scler Relat Disord. 2016;9:62–7.
93. Ibitoye RT, Wilkins A, Scolding NJ. Neurosarcoidosis: a clinical approach to diagnosis and management. J Neurol. 2017;264:1023–8.
94. Smith JK, Matheus MG, Castillo M. Imaging manifestations of neurosarcoidosis. Am J Roentgenol. 2004;182:289–95.
95. Kumar N, Frohman EM. Spinal neurosarcoidosis mimicking an idiopathic inflammatory demyelinating syndrome. Arch Neurol. 2004;61:586.
96. Soni N, Bathla G, Pillenahalli MR. Imaging findings in spinal sarcoidosis: a report of 18 cases and review of the current literature. Neuroradiol J. 2019;32:17–28.
97. Kasliwal MK, Harbhajanka A, Nag S, et al. Isolated spinal neurosarcoidosis: an enigmatic intramedullary spinal cord pathology-case report and review of the literature. J Craniovertebral Junction Spine. 2013;4:76–81.
98. Junger SS, Stern BJ, Levine SR, et al. Intramedullary spinal sarcoidosis: clinical and magnetic resonance imaging characteristics. Neurology. 1993;43:333–7.
99. Saadi A, Rajashekara S. Intramedullary spinal neurosarcoidosis. Radiol Case Rep. 2012;7:739.
100. Koçer N, Islak C, Siva A, et al. CNS Involvement in Neuro-Behçet Syndrome: an MR study. AJNR Am J Neuroradiol. 1999;20:1015–24.
101. Liu H-M, Dong C, Zhang Y-Z, et al. Clinical and imaging features of spinal cord type of neuro Behçet disease: a case report and systematic review. Medicine. 2017;96:1–4.
102. Vargas M, Gariani J, Sztajzel R, et al. Spinal cord ischemia: practical imaging tips, pearls, and pitfalls. Am J Neuroradiol. 2015;36:825–30.
103. Novy J, Carruzzo A, Maeder P, et al. Spinal cord ischemia. Arch Neurol. 2006;63:1113.
104. Yuh WT, Marsh EE, Wang AK, et al. MR imaging of spinal cord and vertebral body infarction. AJNR Am J Neuroradiol. 2015;13:145–54.
105. Masson C, Pruvo JP, Meder JF, et al. Spinal cord infarction: clinical and magnetic resonance imaging findings and short term outcome. J Neurol Neurosurg Psychiatry. 2004;75:1431–5.
106. Mawad ME, Rivera V, Ramirez A, et al. Spinal cord ischemia after resection of thoracoabdominal aortic aneurysms: MR findings in 24 patients. Am J Roentgenol. 1990;155:1303–7.
107. Kumral E, Polat F, Güllüoglu H, et al. Spinal ischaemic stroke: clinical and radiological findings and short-term outcome. Eur J Neurol. 2011;18:232–9.
108. Spetzler R, Detwiler P, Riina H, et al. Modified classification of spinal cord vascular lesions. J Neurosurg. 2002;96:145–56.
109. Labauge P, Bouly S, Parker F, et al. Outcome in 53 patients with spinal cord cavernomas. Surg Neurol. 2008;70:176–81.
110. Sulochana S, Sundaram M. Cavernous hemangioma of the spinal cord: a rare case. J Clin Diagn Res. 2012;6:1781.

111. Ogilvy CS, Louis DN, Ojemann RG. Intramedullary cavernous angiomas of the spinal cord. Neurosurgery. 1992;31:219–30.
112. Singh R, Lucke-Wold B, Gyure K, et al. A review of vascular abnormalities of the spine. Ann Vasc Med Res. 2016;3:1045.
113. Jeon I, Jung WS, Suh SH, et al. MR imaging features that distinguish spinal cavernous angioma from hemorrhagic ependymoma and serial MRI changes in cavernous angioma. J Neuro-Oncol. 2016;130:229–36.
114. Marsh WR. Vascular lesions of the spinal cord: history and classification. Neurosurg Clin N Am. 1999;10:1–8.
115. Morris JM. Imaging of dural arteriovenous fistula. Radiol Clin N Am. 2012;50:823–39.
116. Gilbertson JR, Miller GM, Goldman MS, et al. Spinal dural arteriovenous fistulas: MR and myelographic findings. AJNR Am J Neuroradiol. 1995;16:2049–57.
117. Hurst RW, Grossman RI. Peripheral spinal cord hypointensity on T2-weighted MR images: a reliable imaging sign of venous hypertensive myelopathy. AJNR Am J Neuroradiol. 2000;21:781–6.
118. Gupta P, Kumar A, Kumar A, et al. Congenital spinal cord anomalies: a pictorial review. Curr Probl Diagn Radiol. 2013;42:57–66.
119. Rufener SL, Ibrahim M, Raybaud CA, et al. Congenital spine and spinal cord malformations-pictorial review. Am J Roentgenol. 2010;194:S26–37.
120. Breningstall GN, Marker SM, Tubman DE. Hydrosyringomyelia and diastematomyelia detected by MRI in myelomeningocele. Pediatr Neurol. 1992;8:267–71.
121. Sattar MT, Bannister CM, Turnbull IW. Occult spinal dysraphism – the common combination of lesions and the clinical manifestations in 50 patients. Eur J Pediatr Surg. 1996;6(Suppl 1):10–4.
122. Koen JL, McLendon RE, George TM. Intradural spinal teratoma: evidence for a dysembryogenic origin. J Neurosurg. 1998;89:844–51.
123. Huang SL, He XJ, Xiang L, et al. CT and MRI features of patients with diastematomyelia. Spinal Cord. 2014;52:689–92.
124. Marelli C, Salsano E, Politi LS, et al. Spinal cord involvement in adult-onset metabolic and genetic diseases neurogenetics. J Neurol Neurosurg Psychiatry. 2019;90:211–8.
125. Verrips A, Lycklama À, Nijeholt GJ, Barkhof F, et al. Spinal xanthomatosis: a variant of cerebrotendinous xanthomatosis. Brain. 1999;122:1589–95.
126. Bartholdi D, Zumsteg D, Verrips A, et al. Spinal phenotype of cerebrotendinous xanthomatosis. J Neurol. 2004;251:105–7.
127. Abe R, Sekijima Y, Kinoshita T, et al. Spinal form cerebrotendinous xanthomatosis patient with long spinal cord lesion. J Spinal Cord Med. 2016;39:726–9.
128. Wolf NI, Toro C, Kister I, et al. DARS-associated leukoencephalopathy can mimic a steroid-responsive neuroinflammatory disorder. Neurology. 2015;84:226–30.
129. Labauge P, Dorboz I, Eymard-Pierre E, et al. Clinically asymptomatic adult patient with extensive LBSL MRI pattern and DARS2 mutations. J Neurol. 2011;258:335–7.
130. Labauge P, Roullet E, Boespflug-Tanguy O, et al. Familial, adult onset form of leukoencephalopathy with brain stem and spinal cord involvement: inconstant high brain lactate and very slow disease progression. Eur Neurol. 2007;58:59–61.
131. Finnsson J, Sundblom J, Dahl N, et al. LMNB1-related autosomal-dominant leukodystrophy: clinical and radiological course. Ann Neurol. 2015;78:412–25.
132. van der Knaap MS, Ramesh V, Schiffmann R, et al. Alexander disease: ventricular garlands and abnormalities of the medulla and spinal cord. Neurology. 2006;66:494–8.
133. Girard B, Bonnemains C, Schmitt E, et al. Biotinidase deficiency mimicking neuromyelitis optica beginning at the age of 4: a treatable disease. Mult Scler J. 2017;23:119–22.
134. Pfeffer G, Burke A, Yu-Wai-Man P, et al. Clinical features of MS associated with Leber hereditary optic neuropathy mtDNA mutations. Neurology. 2013;81:2073–81.
135. Yu-Wai-Man P, Spyropoulos A, Duncan HJ, et al. A multiple sclerosis-like disorder in patients with *OPA1* mutations. Ann Clin Transl Neurol. 2016;3:723–9.
136. Yilmaz S, Serin M, Canda E, et al. A treatable cause of myelopathy and vision loss mimicking neuromyelitis optica spectrum disorder: late-onset biotinidase deficiency. Metab Brain Dis. 2017;32:675–8.
137. Bottin L, Prud'hon S, Guey S, et al. Biotinidase deficiency mimicking neuromyelitis optica: initially exhibiting symptoms in adulthood. Mult Scler J. 2015;21:1604–7.
138. Ernst LD, Brock K, Barraza LH, et al. Longitudinally extensive nitrous oxide myelopathy with novel radiographic features. JAMA Neurol. 2015;72:1370.
139. Loes DJ, Fatemi A, Melhem ER, et al. Analysis of MRI patterns aids prediction of progression in X-linked adrenoleukodystrophy. Neurology. 2003;61:369–74.
140. Mochel F, Schiffmann R, Steenweg ME, et al. Adult polyglucosan body disease: natural history and key magnetic resonance imaging findings. Ann Neurol. 2012;72:433–41.
141. Pareyson D, Fancellu R, Mariotti C, et al. Adult-onset Alexander disease: a series of eleven unrelated cases with review of the literature. Brain. 2008;131:2321–31.
142. Farina L, Pareyson D, Minati L, et al. Can MR imaging diagnose adult-onset Alexander disease? Am J Neuroradiol. 2008;29:1190–6.
143. Graff-Radford J, Schwartz K, Gavrilova RH, et al. Neuroimaging and clinical features in type II (late-onset) Alexander disease. Neurology. 2014;82:49–56.

Principles of Postoperative Spine MRI

11

Karthik Krishnan, Sophie C. Queler, and Darryl B. Sneag

Introduction

Postoperative spine magnetic resonance imaging (MRI) has become increasingly prevalent as the volume of spinal procedures has increased. From 2004 to 2015 alone, the number of lumbar fusions performed in the USA increased by over 60% [1]. In 2011, an estimated total of 978,000 laminectomies and fusions were performed in the USA [2]. Retrospective studies report complication rates stemming from posterior lumbar fusion or laminectomies ranging from 11% to 19% [3, 4]. As such, radiologists and managing physicians should be cognizant of potential complications and the role of MRI in guiding subsequent management in patients with new or persistent symptoms following surgery. This chapter will discuss technical considerations in postoperative spine MRI and review and illustrate the most common types of complications encountered.

K. Krishnan · D. B. Sneag (✉)
Weill Medical College of Cornell University, New York, NY, USA

Department of Radiology and Imaging, Hospital for Special Surgery, New York, NY, USA
e-mail: sneagd@hss.edu

S. C. Queler
Department of Radiology and Imaging, Hospital for Special Surgery, New York, NY, USA

Technical Considerations

MRI is the primary modality for evaluating the postoperative spine. Computed tomography (CT) is more routinely used, however, to evaluate the precise location and integrity of hardware, hardware loosening, and for the presence of osseous fusion following arthrodesis [5]. CT myelography is sometimes obtained if susceptibility effect from metal is insurmountable on MRI as well as to detect the presence of a dural tear/pseudomeningocele formation if MRI results are negative and clinical suspicion remains high.

Given the potential complexity of postoperative spine MRI, radiologists have several important decisions regarding imaging acquisition, including magnet field strength. Although 3.0 tesla (T) may provide a higher signal-to-noise ratio (SNR) and facilitate faster imaging, which arguably is important in postoperative patients with potential pain and discomfort, other considerations make 1.5 T more suitable. Increased magnetic susceptibility and motion artifact at 3 T, particularly in the cervical region due to swallowing and breathing, make 1.5 T the default choice for imaging the postoperative spine [6, 7].

Our conventional lumbar spine MRI protocol (Table 11.1) includes axial and sagittal short tau inversion recovery (STIR), T1-weighted, and T2-weighted pulse sequences; an additional coronal T2-weighted sequence is also obtained, which we find helpful to delineate transitional lumbosacral anatomy and to detect extraforaminal

W. B. Morrison et al. (eds.), *MRI of the Spine*, https://doi.org/10.1007/978-3-030-43627-8_11

Table 11.1 Suggested 1.5 T lumbar spine MRI protocol

Parameter	Sagittal T1	Sagittal T2	Sagittal IR	Axial T2[a]	Coronal T2	Axial T1 post[b]	Sagittal T1 post[b]
TR (msec)	*550*	*2300*	*4000*	*2200*	*2200*	*500*	*500*
TE (msec)	*<10*	*100*	*17*	*100*	*100*	*14*	*<10*
Flip angle (degrees)	*160*	*180*	*160*	*180*	*180*	*160*	*160*
ETL	*3*	*12*	*10*	*12*	*12*	*4*	*3*
RBW (kHz)	*31.25*	*20.83*	*31.25*	*20.83*	*20.83*	*31.25*	*31.25*
FOV (cm)	*28*	*28*	*28*	*21*	*26*	*21*	*28*
Matrix (frequency × phase)	*512 × 256*	*512 × 224*	*256 × 192*	*512 × 224*	*256 × 256*	*256 × 256*	*512 × 256*
Slice thickness (mm) – no gap	*3.5*	*3.5*	*3.5*	*3.5*	*3*	*3.5*	*3.5*
NEX	*2*	*2*	*2*	*2*	*2*	*2*	*2*
Approximate scan time (min)[c]	*3–4*	*3–4*	*3–4*	*3–4*	*2–3*	*3–4*	*3–4*

Note: *TR* repetition time, *TE* echo time, *ETL* echo train length, *RBW* receiver bandwidth, *FOV* field of view, *NEX* number of excitations, *post* with gadolinium contrast.
[a]Three axial stacks acquired through the upper, lower and L5-S1 motion segments, parallel to disc space
[b]Optional
[c]Variable, depending on coverage

Table 11.2 Suggested 1.5 T cervical spine MRI protocol

Parameter	Sagittal T1	Sagittal T2	Sagittal IR	Axial T2[a]	Axial 2D gradient recalled echo	Axial T1 post[b]	Sagittal T1 post[b]
TR (msec)	*550*	*5000*	*5000*	*2200*	*1000*	*513*	*463*
TE (msec)	*<10*	*100*	*17*	*112*	*14*	*9.1*	*12*
Flip angle (degrees)	*180*	*180*	*180*	*180*	*20*	*160*	*160*
ETL	*4*	*9*	*10*	*10*	*4*	*4*	*4*
RBW (kHz)	*20.83*	*20.83*	*31.25*	*20.83*	*31.25*	*48.83*	*16.28*
FOV (cm)	*22*	*22*	*22*	*16*	*20*	*22*	*17*
Matrix (frequency × phase)	*320 × 224*	*320 × 192*	*256 × 192*	*256 × 224*	*288 × 192*	*512 × 224*	*320 × 224*
Slice thickness (mm) – no gap	*3*	*3*	*3*	*3*	*3*	*3*	*3*
Number of excitations (NEX)	*2*	*2*	*2*	*3*	*2*	*4*	*4*
Approximate scan time (min)[c]	*3–4*	*2–3*	*3–4*	*3–4*	*5–6*	*3–4*	*3–4*

Note: *TR* repetition time, *TE* echo time, *ETL* echo train length, *RBW* receiver bandwidth, *FOV* field of view, *NEX* number of excitations, *2D* two-dimensional, *post* with gadolinium contrast
[a]Two axial stacks acquired through the upper and lower motion segments, parallel to disc space
[b]Optional
[c]Variable, depending on coverage

disc herniations. In the cervical spine (Table 11.2), no coronal is obtained but instead an axial gradient recalled echo sequence is used to help differentiate between disc material (typically intermediate signal intensity relative to cerebrospinal fluid and bone) and low signal intensity vertebral endplate and/or uncovertebral remodeling/osteophytes. In patients with cervical instrumentation, however, the gradient echo sequence is often omitted due to magnetic susceptibility yielding prominent artifact [8].

General techniques for metal artifact reduction include prescribing higher bandwidth (Fig. 11.1) and smaller voxels; modifying these parameters will reduce the signal-to-noise ratio (SNR) and as such, an increased

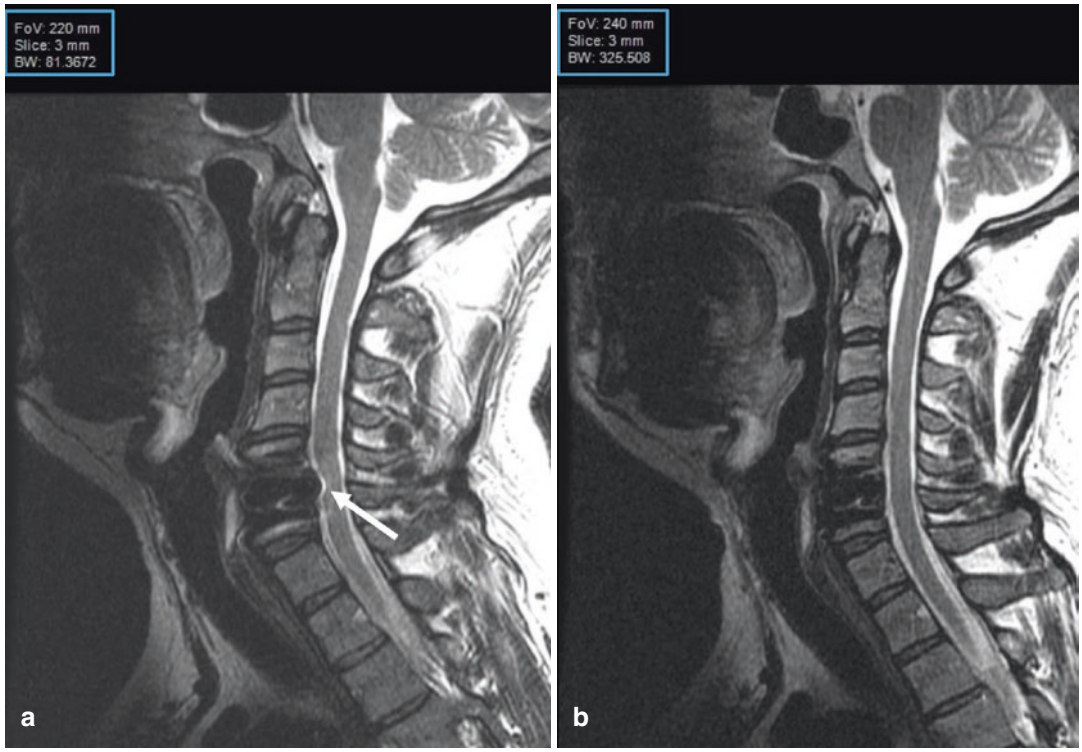

Fig. 11.1 A 36-year-old male with neck pain radiating to the left arm 4 months post anterior cervical discectomy and fusion (ACDF) at C5–6. Sagittal T2-weighted image (**a**) using an 81 kHz bandwidth (blue box) demonstrates susceptibility effect focally obscuring the ventral margin of the spinal cord (arrow). When repeated with a 325 kHz bandwith (blue box) (**b**), the margins of the cord are conspicuous

number of excitations (NEX) is used to compensate. Specialized sequences for metal artifact reduction that may be employed include MAVRIC-SL (multiacquisition variable-resonance image combination selective) (Fig. 11.2) and SEMAC (slice-encoding metal artifact correction) [9], but in our experience they are only sometimes helpful in reducing susceptibility from artificial disc replacements and pedicle screws.

At least one fat suppressed sequence is critical to evaluate for fluid collections and stress fractures (Fig. 11.3) in the postoperative spine. STIR is the most reliable choice for spine imaging, given its insensitivity to B0 and B1 field inhomogeneities [10]. Chemical shift fat suppression should be avoided with metal due to the significant shift in resonance frequency of fat adjacent to metal [11]. Dixon techniques are typically avoided as well due to artifact when evaluating structures immediately adjacent to instrumentation.

Intravenous Gadolinium Contrast

There are several indications for the use of intravenous (IV) gadolinium, used with a T1-weighted pulse sequence, in the postoperative setting. These include differentiating granulation/scar tissue, which will enhance, from residual or recurrent disc, which will not (Fig. 11.4) [12]. Due to the ease with which intravascular contrast can extravasate and permeate the loose extracellular space around developing regions of fibrosis, granulation tissue is expected to enhance consistently; this feature allows for up to 96% accuracy in differentiating disc from scar in the postoperative setting [13]. IV gadolinium is also necessary to determine the presence and extent of fluid

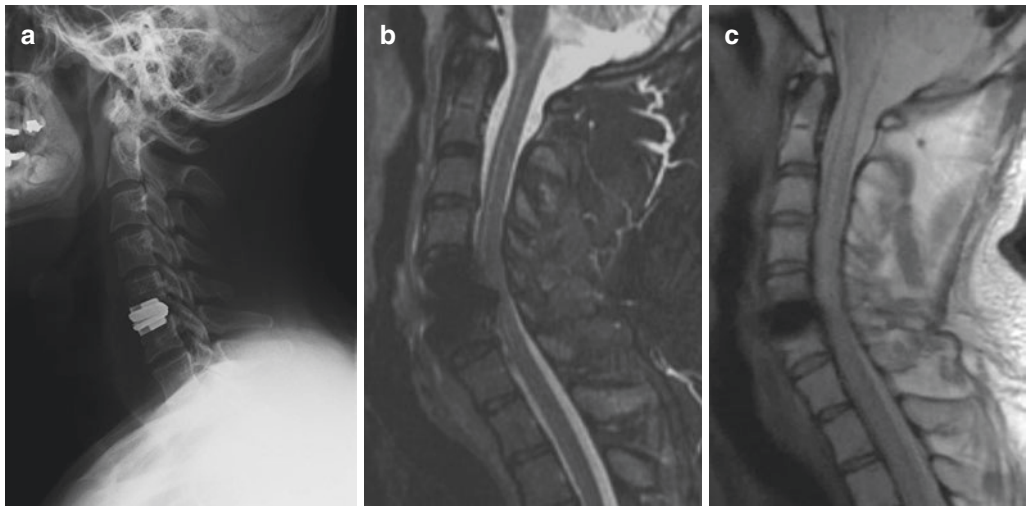

Fig. 11.2 A 36-year-old male with neck pain radiating to the left arm status post C5–6 artificial disc replacement as seen on the lateral radiograph (**a**). Sagittal T2-weighted conventional MR image (**b**) demonstrates susceptibility from the disc replacement obscuring the ventral margin of the spinal cord. Compare with the sagittal MAVRIC sequence (**c**)

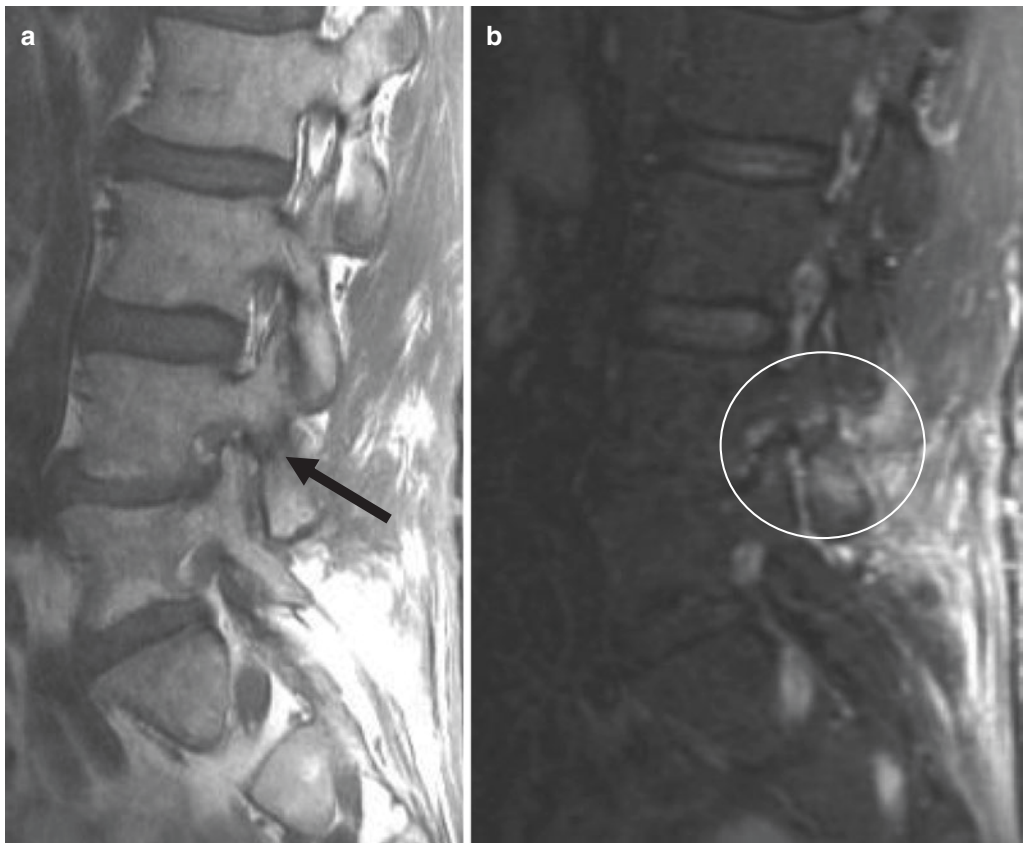

Fig. 11.3 A 49-year-old man with right-sided low back pain following microdiscectomy. Sagittal T1-weighted MR image (**a**) demonstrates a stress fracture of the inferior right articular process (arrow) inciting a severe stress reaction (circle) on the accompanying STIR sequence (**b**)

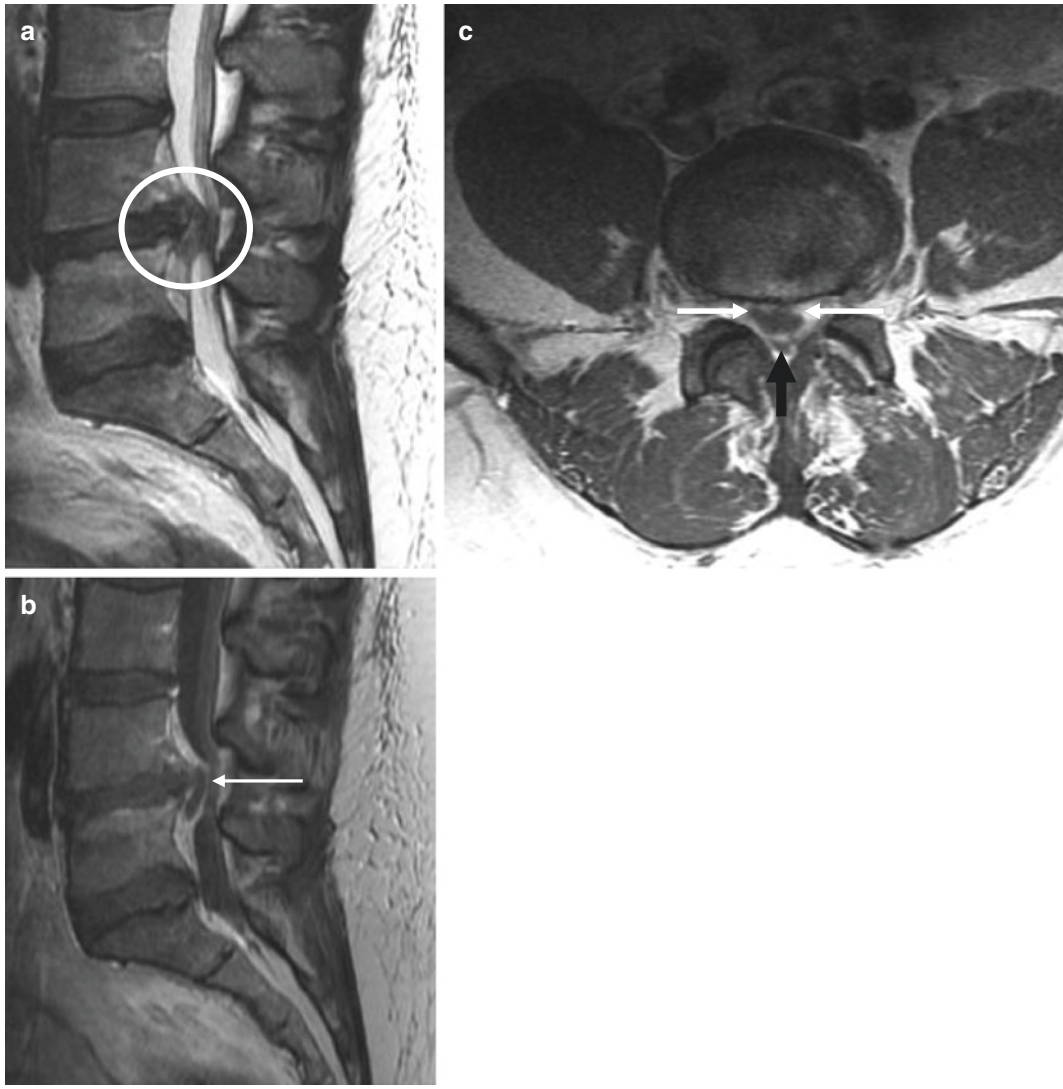

Fig. 11.4 A 37-year-old woman, 7 months status post-microdiscectomy with low back pain radiating down the left leg. Sagittal T2-weighted MR image (**a**) demonstrates a midline mass compressing the thecal sac at L4–5 (circle). Post-contrast sagittal (**b**) and axial (**c**) T1-weighted images demonstrate a large non-enhancing mass compatible with a disc sequestration (white arrows, **b** and **c**) that compresses the thecal sac (black arrow, **c**)

collections. In our experience, contrast is frequently helpful to delineate soft tissue structures adjacent to metallic hardware by resetting of the dynamic contrast range.

Nerve root enhancement after contrast administration is another finding that appears alongside various causes of residual or recurrent postoperative back pain. This enhancement may occur due to disruption of the local blood–nerve barrier [14]. One study of patients undergoing surgery for lumbar disc herniation found that the presence of nerve root enhancement had a positive predictive value of 83.7% for determining clinically significant symptoms [15].

A Few Pearls for Interpretation

Recognizing whether a spine procedure was successful requires understanding how different procedures alter the normal anatomy. A midline laminectomy is typically performed to relieve

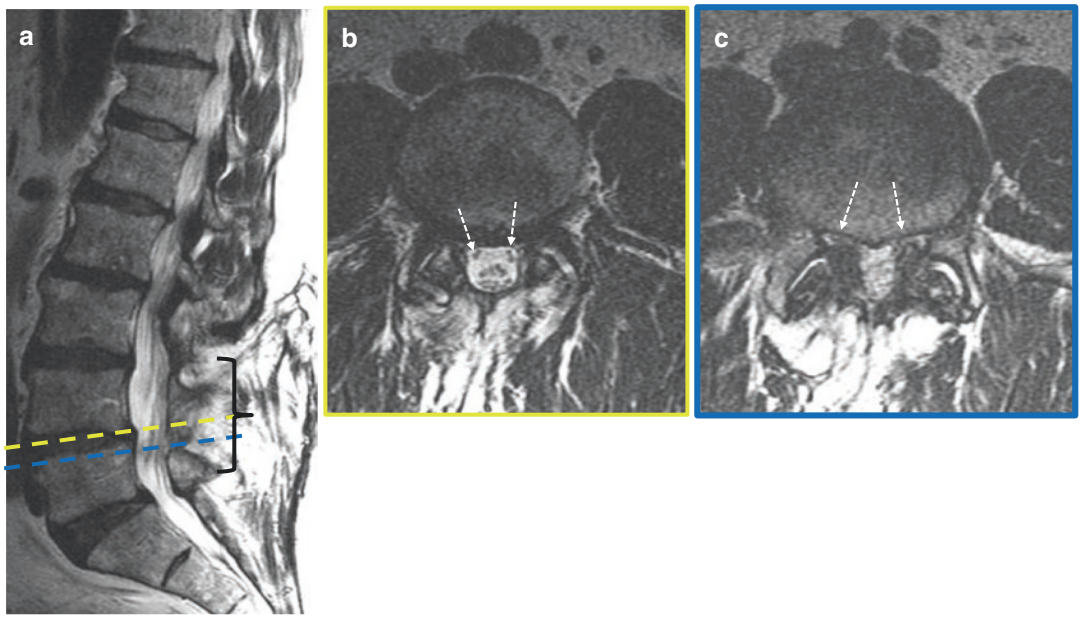

Fig. 11.5 A 69-year-old man status post-L4–5 midline laminectomy (bracket, **a**). Axial T2-weighted MR image (**b**) at the L4–5 disc space (dashed yellow line, sagittal T2-weighted MR image, **a**) demonstrates no impingement on the intrathecal L4 nerve roots (arrows). Axial T2-weighted MR image (**c**) immediately caudal to the disc space (dashed blue line, **a**) demonstrates severe compression of the L5 nerve roots (arrows) within the lateral recess

central stenosis and compression of the spinal cord and/or thecal sac. Degenerative facet arthropathy and ligament flavum thickening, however, may also result in severe subarticular/lateral recess stenosis and compression of the traversing nerve rootlets (Fig. 11.5). Therefore, determining by MRI whether a posterior decompression was successful requires evaluating whether central and subarticular/lateral recess stenosis are present.

Prior laminotomy, typically performed for microdiscectomy, can sometimes be difficult to identify if small, but the most reliable clue (other than reading the operative note!) is partial or complete absence of the ligamentum flavum (Fig. 11.6). Edema in the adjacent paraspinal muscles is another clue and is typically present for at least 6 months, and sometimes longer, following a surgical procedure [16].

Acute and Subacute Complications

In the acute (<4 weeks) to subacute (4–12 weeks) setting, MRI may help identify several postoperative complications. One common issue is identifying the etiology of a postoperative fluid collection. These may include a seroma, hematoma, pseudomeningocele, or abscess, although the latter will typically take several days to weeks to form.

Seromas are the most common fluid collection encountered in the postoperative setting and appear on MRI as well-defined, T1 hypointense/T2 hyperintense fluid collections [5, 17]. Seromas are typically of no clinical significance unless they result in mass effect on the thecal sac or communicate with the skin via a fascial dehiscence, resulting in a draining wound.

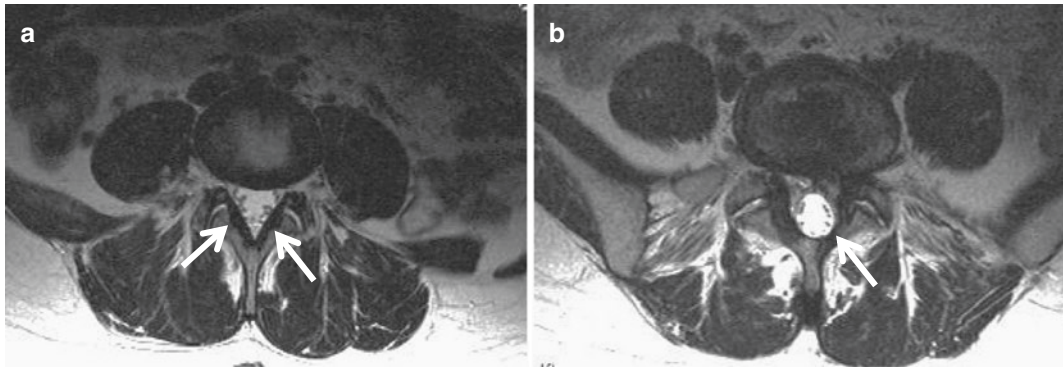

Fig. 11.6 Status-post left L5-S1 laminotomy in a 45-year-old woman. Axial T2-weighted MR image (**a**) at L4–5 demonstrates intact, normal appearance of the ligamenta flava. Axial T2-weighted image (**b**) at L5-S1 demonstrates absence of the left ligamentum flavum (arrow) indicating the site of laminotomy

Abscesses may appear identical to seromas. Other secondary findings, such as the persistence foci of gas within and beyond the margins of a fluid collection following the surgery (Fig. 11.7) and development of fluid collections in tissues outside of the surgical field, particularly within the psoas musculature or prevertebral space, following lumbar and cervical spine surgery, respectively, raise suspicion for infection (Fig. 11.7) [18]. Diffusion weighted imaging can provide additional discrimination, with abscesses demonstrating a low apparent diffusion coefficient (ADC) compared to seromas or pseudomeningoceles [19]. Correlating with clinical signs of infection and trends of serologic inflammatory markers (C-reactive protein and erythrocyte sedimentation rate) may be helpful as well. Infection may manifest with erosive changes of the endplates or with resorptive changes around the hardware, resulting in loosening [5]. Spondylodiscitis may demonstrate T2 hyperintensity of the affected intervertebral disc.

Pseudomeningoceles are extradural cerebrospinal fluid (CSF) collections that develop secondary to a rent in the dura and may complicate up to 6% of discectomies [5]. They are often asymptomatic but may result in headaches, low back pain, and occasionally symptoms of nerve root entrapment. Pseudomeningoceles will demonstrate signal intensity similar to that of cerebrospinal fluid—low T1 and high T2 signal intensity—but may also exhibit some peripheral enhancement [20]. Identifying a dural defect, particularly if small, is frequently difficult on MRI. Communication between an epidural fluid collection and the thecal sac can be confirmed, however, if flow is fast enough to yield a "jet flow" phenomenon secondary to dephasing (Fig. 11.8) [20]. If a dural rent and/or jet phenomenon is not observed and clinical suspicion remains high, then a CT myelogram, as mentioned above, is appropriate or sampling the fluid for beta-transferrin.

Hematomas may present within hours to days postoperatively and are marked by high T1 signal and a potential fluid/hematocrit level. Gradient sequences, although normally useful for recognizing hematomas in other locations due to a "blooming" effect from hemosiderin, may be of limited value when metallic hardware is present due to excessive susceptibility artifact. Like any other collection, hematomas may result in thecal sac compression; this finding was discovered in 58% of epidural hematomas in a study by Sokolowski et al., though no patients exhibited neurological effects from the compression [21].

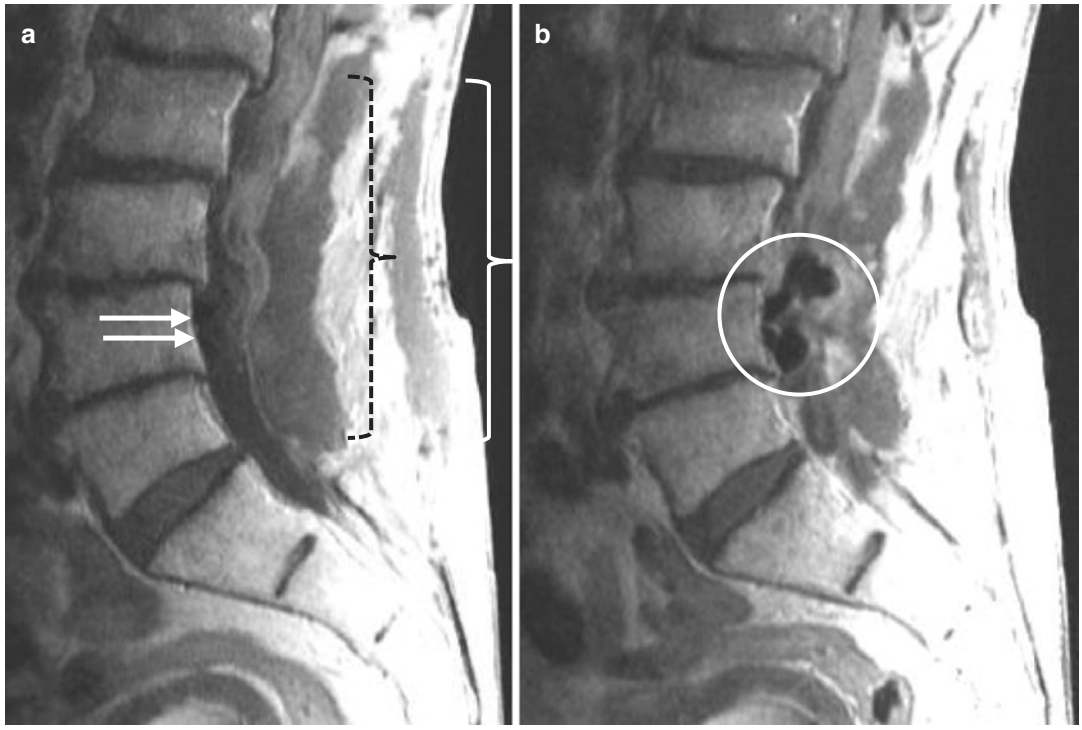

Fig. 11.7 A 82-year-old man with history of prostate cancer and self-catheterization presenting with wound drainage, status post-multilevel laminectomy 1 month prior. Sagittal midline T1-weighted post-contrast MR image (**a**) demonstrates two large dorsal fluid collections, one superficial (white bracket) and one deep (black bracket) that do not communicate with each other and small foci of epidural gas (arrows). Para-sagittal T1 post-contrast image (**b**) demonstrates a large amorphous gas collection (circle) at L3–4 that raises the suspicion for infection; subsequent aspirate grew out *Staphylococcus aureus*

It is sometimes difficult to differentiate between the epidural and subdural location of a hematoma, but some signs are helpful when present (Fig. 11.9). On axial imaging, the combination of centrally clumped nerve roots secondary to subdural hemorrhage (center) and the laterally exiting nerve roots (spokes) may manifest as a "Mercedes Benz" or "Inverted Mercedes Benz" sign (Fig. 11.10) [22, 23]. A "Cap" sign may also be observed, due to the presence of an epidural fat layer as spinal subdural hematomas gravitate and settle dorsally along the dura while the MRI is acquired in a supine position [23].

Hardware malpositioning is another possible cause of postoperative back pain [12]. Screws are generally placed through the pedicle parallel to the vertebral endplate and through the vertebral body without piercing the anterior cortex. However, they may errantly enter the neural foramen or spinal canal. Lumbar screws that extend beyond the pedicle may impinge on nerve roots, causing neuritis. Screws that pass beyond the anterior vertebral cortex are typically of no consequence unless they penetrate the wall of the iliac veins. Screw loosening is best assessed on CT, whereby circumferential lucency is seen about the screw [24]. Hardware fracture is another potential complication; Lonstein found hardware fractures in 2.2% of cases analyzed [25]. Hardware fracture is believed to occur secondary to metal fatigue associated with increased force from spinal movement [12].

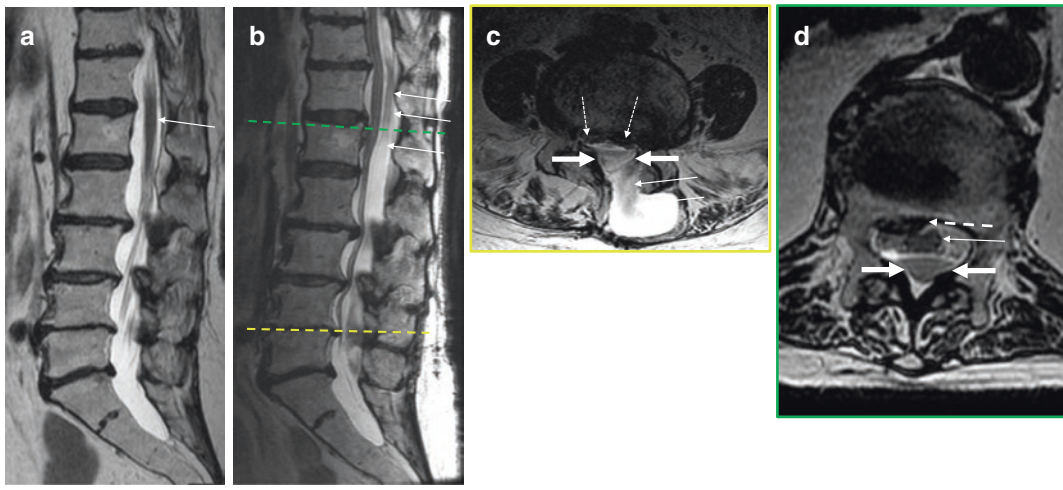

Fig. 11.8 A 79-year-old woman with persistent headache following posterior lower lumbar spine decompression 4 months prior. Preoperative sagittal T2-weighted MR image (**a**) demonstrates the normal position of the spinal cord (arrow). Postoperative MR image (**b**) demonstrates anterior displacement of the cord (arrows) secondary to a dorsal fluid collection. Axial T2-weighted MR image at L4–5 (**c**) demonstrates a "jet flow phenomenon" (thin arrows) indicating pseudomeningocele formation with communication of the epidural fluid collection with the thecal sac. Note ventral displacement of nerve roots of the cauda equina (dashed arrows) secondary to a subdural collection (thick arrows). Axial T2-weighted image (**d**) just caudal to the T12-L1 disc space demonstrates the subdural collection, displacing the cord ventrally, which is also impinged by a disc extrusion (dashed arrow). Axial T2-weighted image (**c**) further demonstrates anterior displacement of nerve roots due to the same collection. Axial sequence at L4–5 level (**d**) demonstrates fluid dephasing jet (red arrows), consistent with pseudomeningocele with additional compression of nerve roots (orange arrows)

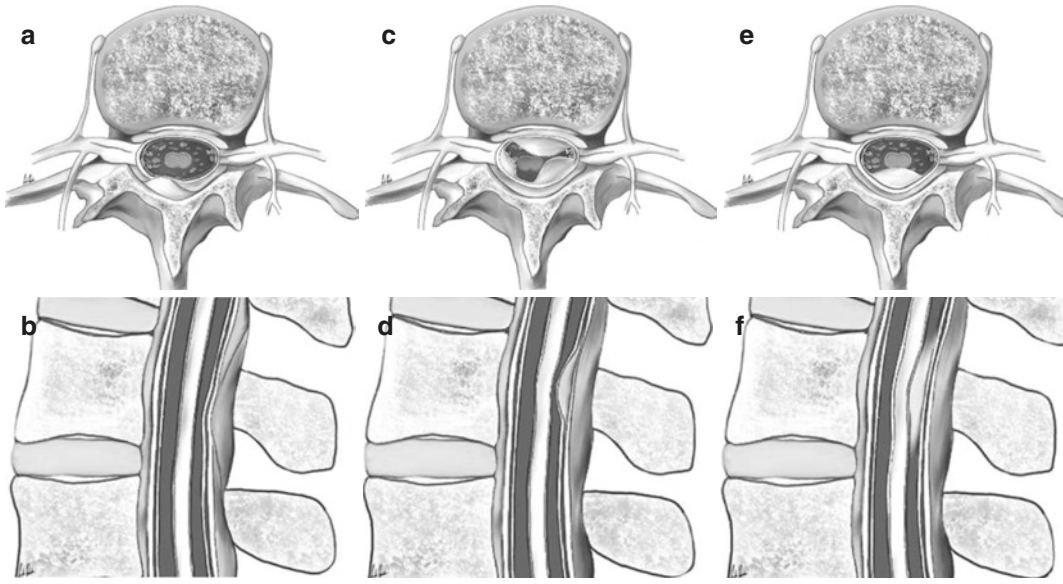

Fig. 11.9 Transverse and sagittal cross-sectional illustrations depicting fluid collections within the epidural (**a**, **b**), subdural (**c**, **d**), and subarachnoid (**e**, **f**) spaces of the lumbar spine

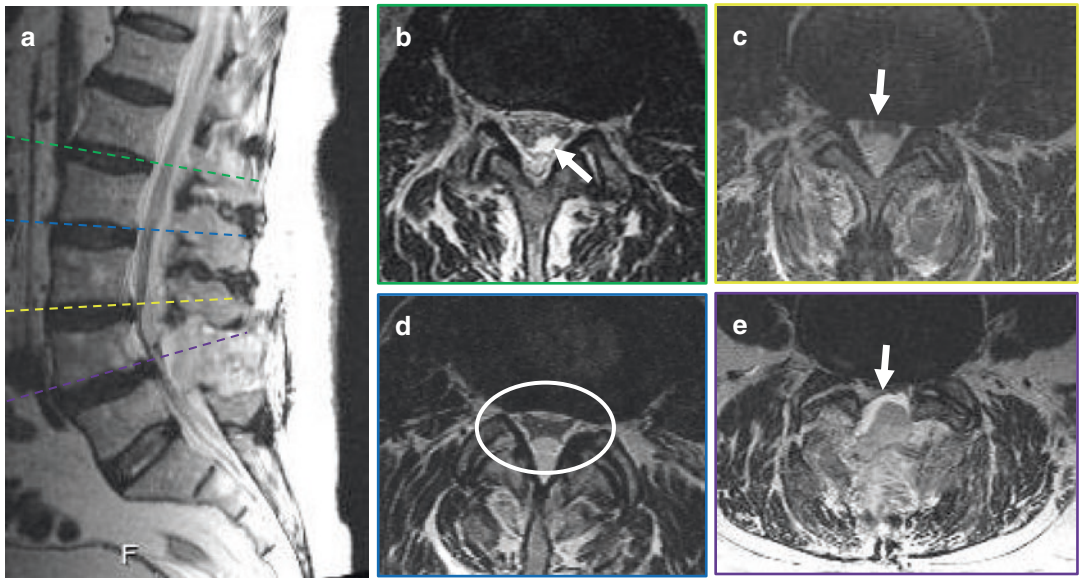

Fig. 11.10 A 76-year-old man presenting with right lower extremity weakness following midline laminectomy at L4–5. Sagittal T2-weighted MR image (**a**) demonstrates a heterogeneous mass-like collection at the laminectomy site compressing the cauda equina. Axial T2-weighted image at L1–2 (**b**) demonstrates a fluid collection of questionable location (arrow), possibly subdural, causing centralization of nerve roots. Axial image at L2–3 (**c**) demonstrates central displacement of nerve roots, strongly suggesting a subdural location for the collection at this level. Axial image at L3–4 (**d**) demonstrates ventral displacement of the cauda equina (arrow), suggesting an epidural location for the fluid collection. Axial image at L4-L5 level (**e**) demonstrating repair of dural rent with DuraGen/DuraSeal; note the bilayer appearance (arrow)

Delayed Complications

Delayed complications of spine surgery, typically manifesting 12 weeks after surgery, include pseudoarthrosis, arachnoiditis, reaction to bone morphogenetic protein (BMP), and junctional failure.

Failure of bony fusion, or pseudoarthrosis, may occur in 5–35% of cases [26], with a higher prevalence in fusions spanning at least 3 motion segments. Patients with pseudoarthrosis are not necessarily symptomatic, though data from Kornblum et al. suggest that patients with a solid arthrodesis report higher satisfaction and improved clinical outcomes (86% with good or excellent clinical outcome) compared to those with pseudoarthrosis (56%) [27]. Although CT is the primary modality for evaluating the integrity of the arthrodesis [26], MRI may suggest a pseudoarthrosis when type 1 Modic changes, which manifest as a bone marrow edema pattern in the subchondral and cancellous bone on fat suppressed sequences [28], persist for more than 1 year [29].

Arachnoiditis, that is, inflammation of the nerve roots of the cauda equina, can result from surgery, infection, hemorrhage, or administration of intrathecal compounds (Pantopaque, steroids, or anesthetics). Mild arachnoiditis may demonstrate nerve root thickening and abnormal "fanning" of nerve roots on sagittal imaging. The "empty sac sign," (Fig. 11.11) secondary to adherence of nerve roots to the periphery of the thecal sac and arachnoid (peripheral clumping), indicates moderate severity. Nerve roots may also adhere to each other and clump centrally (Fig. 11.12). Severe arachnoiditis may manifest as intradural soft tissue "masses" (i.e., clumped, fibrotic nerve roots) or arachnoiditis ossificans. In arachnoiditis ossificans, proliferation of the arachnoid cells and deposition of collagen result in adhesion of the nerve roots to the meninges (Fig. 11.13). Subsequently, osteoblastic metaplasia of arachnoid cells leads to further deposition

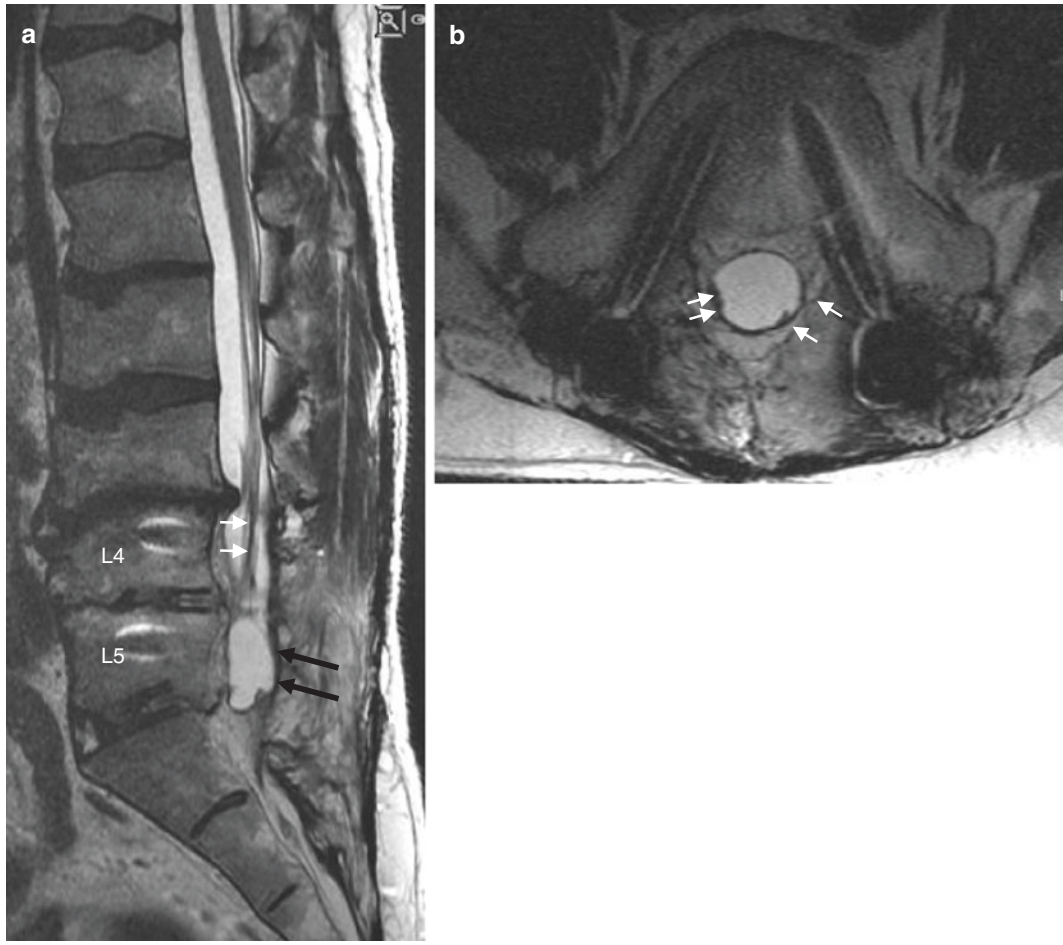

Fig. 11.11 A 70-year-old man with chronic back pain 1 year after lower lumbar midline laminectomy and posterolateral arthodesis. Sagittal T2-weighted MR image (**a**) demonstrates apparent clumping of nerve roots at L4 (white arrows) and an "empty thecal sac sign" (black arrows) at L5, which is confirmed on the corresponding axial T2-weighted MR image (**b**) with nerve roots (arrows) scarred to the periphery of the arachnoid membrane, secondary to arachnoiditis

of osseous material. Domenicucci et al. proposed a classification system of radiologic features of arachnoiditis ossificans [30]. In Type 1, peripheral semicircular ossification is present. In Type 2, the entire circumference of the thecal sac is involved, and in Type 3, the internal contents of the sac are involved with a visible "honeycomb" pattern.

BMP (bone morphogenetic protein), a recombinant growth factor derived from platelets, may be administered by a surgeon to enhance bony fusion [31]. BMP was used in approximately 28% of fusions in 2011 with higher rates of usage in revision surgeries [32]. Its use in cervical spine surgery is limited due to reports (including 2007 FDA public health warning) of postoperative neck swelling leading to dysphagia and difficulty breathing [33]. It continues to be used off-label in selected cervical cases, though at lower rates (9%) compared to other fusions [32]. This reaction to BMP may be seen in up to 27% of patients. In the weeks immediately after surgery, vertebral body endplate resorption can be seen in over 80% of lumbar fusion cases utilizing this factor [34]. At 6–9 months following the operation, changes

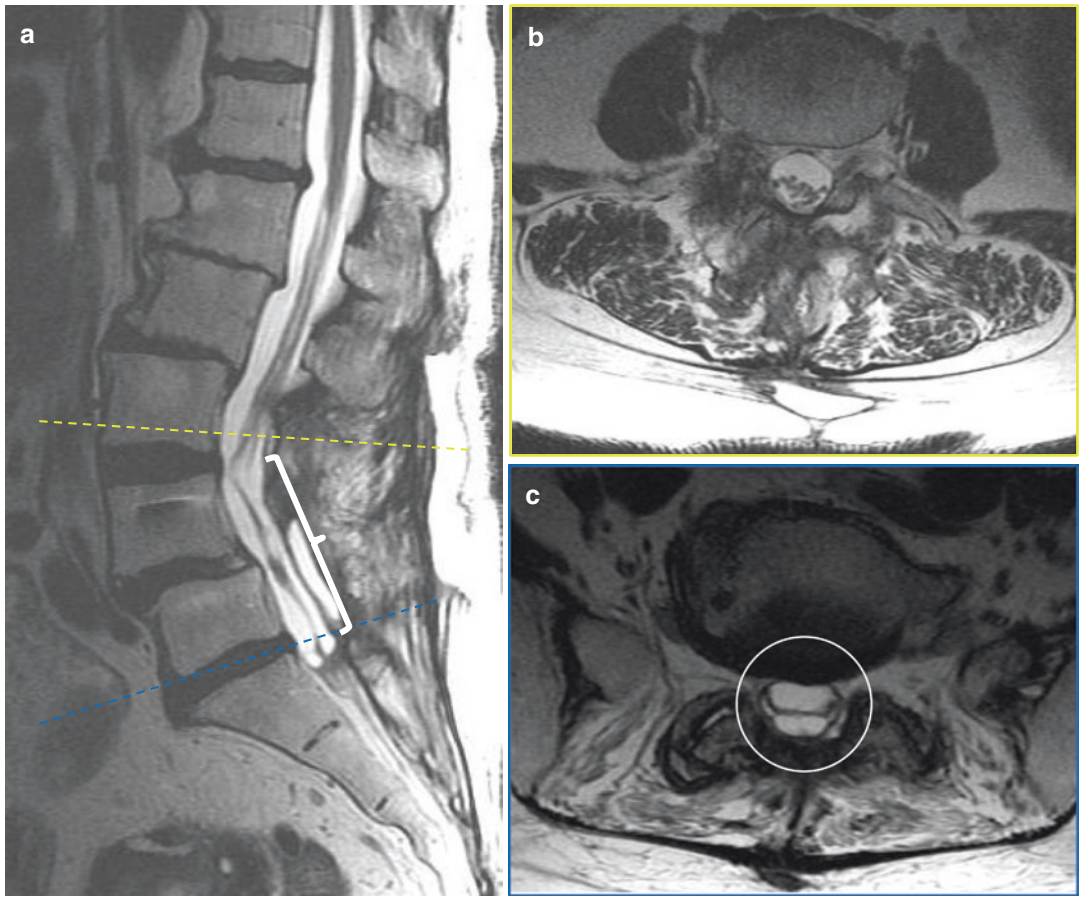

Fig. 11.12 A 58-year-old man 7 months status-post laminectomy and arthrodesis complaining of pain extending from waist to feet. Sagittal T2-weighted MR image (**a**) demonstrates central clumping of nerve roots (bracket). Axial T2-weighted MR image (**b**), just cephalad to the L3–4 disc space (dashed yellow line, **a**) demonstrates normal appearance of "free-floating" nerve roots in the spinal canal. Axial image (**c**), at L5-S1 (dashed blue line, **a**) demonstrates central clumping of nerve roots secondary to arachnoiditis with loss of distinction of individual roots (circle)

secondary to BMP administration may mimic those of discitis-osteomyelitis but may be differentiated by the absence of fever, elevated white blood cell count. Extension of BMP beyond the original site of administration may result in heterotopic bone formation with resultant foraminal stenosis, or ossification along the paraspinal muscles [35].

Proximal junctional failure (PJF), a more severe manifestation of proximal junctional kyphosis (PJK), may present following fusion to correct spinal deformities or instability. The stiffness of the construct used to stabilize spine segments may lead to increased mechanical instability of proximal vertebral junctions following thoracolumbar or lumbar spinal fusion [36]. This may precipitate vertebral body fracture, implant loosening/fracture, or disrupt the posterior ligamentous complex, necessitating revision surgery.

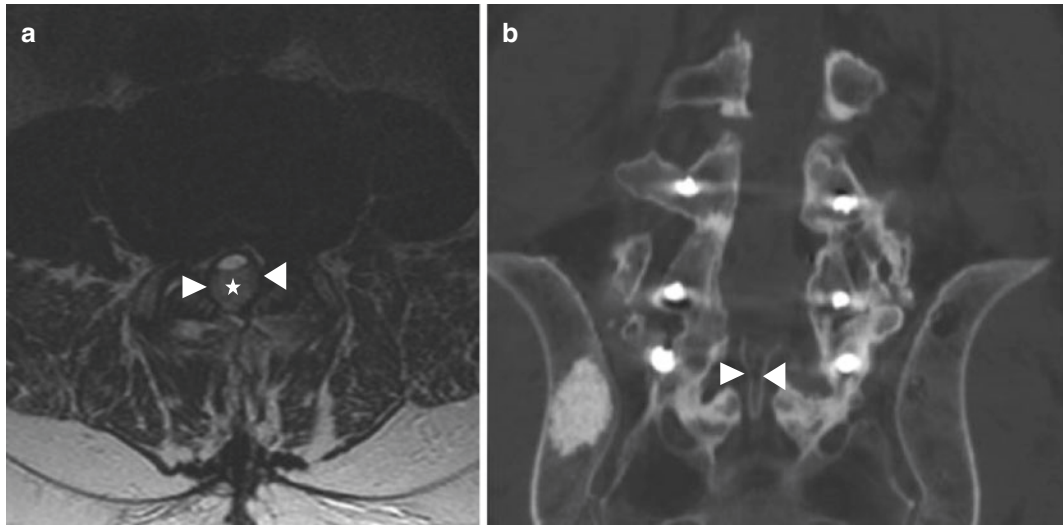

Fig. 11.13 Arachnoiditis ossificans after laminectomy and arthrodesis. Axial T2-weighted MR image (**a**) demonstrates a thick, low signal intensity peripheral rind around the thecal sac (arrows), suggestive of mineralization, with mass-like clumping of nerve roots dorsally (star). Coronal, non-contrast CT image (**b**) confirms this ossification (arrowheads)

Conclusion

This chapter attempts to explain how complications appear on conventional MRI and when another imaging test is more appropriate (e.g., CT scan evaluation for osseous fusion). Future areas of development in postoperative spine imaging will likely include the creation and refinement of pulse sequences to more effectively image around metal. For example, a zero echo time (ZET) MR sequence capable of producing CT-like images has been shown useful in evaluating osseous foraminal stenosis in the cervical spine [37], but its use when imaging around metal is limited. Diffusion weighted imaging may be helpful in evaluating cord pathology, but its use is generally contraindicated in the presence of metal due to severe distortion. Hardware improvements, including surface coil design, will also likely play a major role in advancing spine imaging.

References

1. Martin BI, Mirza SK, Spina N, Spiker WR, Lawrence B, Brodke DS. Trends in lumbar fusion procedure rates and associated hospital costs for degenerative spinal diseases in the United States, 2004 to 2015. Spine. 2019;44:369–76.
2. Weiss AJ, Elixhauser A. Trends in operating room procedures in U.S. Hospitals, 2001—2011. In: Trends in operating room procedures in U.S. Hospitals, 2001–2011 – statistical brief #171. https://www.hcup-us.ahrq.gov/reports/statbriefs/sb171-Operating-Room-Procedure-Trends.jsp. Accessed 15 May 2019.
3. Li G, Patil CG, Lad SP, Ho C, Tian W, Boakye M. Effects of age and comorbidities on complication rates and adverse outcomes after lumbar laminectomy in elderly patients. Spine. 2008;33:1250–5.
4. Kalanithi PS, Patil CG, Boakye M. National complication rates and disposition after posterior lumbar fusion for acquired Spondylolisthesis. Spine. 2009;34:1963–9.
5. Malhotra A, Kalra VB, Wu X, Grant R, Bronen RA, Abbed KM. Imaging of lumbar spinal surgery complications. Insights Imaging. 2015;6(6):579–90. https://doi.org/10.1007/s13244-015-0435-8.

6. Phalke VV, Gujar S, Quint DJ. Comparison of 3.0 T versus 1.5 T MR: imaging of the spine. Neuroimaging Clin N Am. 2006;16:241–8.
7. Hargreaves BA, Worters PW, Pauly KB, Pauly JM, Koch KM, Gold GE. Metal-induced artifacts in MRI. Am J Roentgenol. 2011;197:547–55.
8. Hancock CR, Quencer R, Falcone S. Challenges and pitfalls in postoperative spine imaging. Appl Radiol. 2008;37:23–34.
9. Choi S-J, Koch KM, Hargreaves BA, Stevens KJ, Gold GE. Metal artifact reduction with MAVRIC SL at 3-T MRI in patients with hip arthroplasty. Am J Roentgenol. 2015;204:140–7.
10. Del Grande F, Santini F, Herzka DA, Aro MR, Dean CW, Gold GE, et al. Fat-suppression techniques for 3-T MR imaging of the musculoskeletal system. Radiographics. 2014;34(1):217–33.
11. Talbot BS, Weinberg EP. MR imaging with metal-suppression sequences for evaluation of total joint arthroplasty. Radiographics. 2016;36:209–25.
12. Hayashi D, Roemer FW, Mian A, Gharaibeh M, Müller B, Guermazi A. Imaging features of postoperative complications after spinal surgery and instrumentation. Am J Roentgenol. 2012;199(1):W123. https://doi.org/10.2214/ajr.11.6497.
13. Ross JS, Masaryk TJ, Schrader M, Gentili A, Bohlman H, Modic MT. MR imaging of the postoperative lumbar spine: assessment with gadopentetate dimeglumine. Am J Roentgenol. 1990;155:867–72.
14. Sen K, Singh A. Magnetic resonance imaging in failed Back surgery syndrome. Med J Armed Forces India. 1999;55:133–8.
15. Lee Y, Choi E, Song C. Symptomatic nerve root changes on contrast-enhanced MR imaging after surgery for lumbar disk herniation. Am J Neuroradiol. 2009;30:1062–7.
16. Hyun SJ, Kim YB, Kim YS, Park SW, Nam TK, Hong HJ, Kwon JT. Postoperative changes in Paraspinal muscle volume: comparison between paramedian interfascial and midline approaches for lumbar fusion. J Korean Med Sci. 2007;22:646.
17. Davies A, Hall A, Strouhal P, Evans N, Grimer R. The MR imaging appearances and natural history of seromas following excision of soft tissue tumours. Eur Radiol. 2004;14:1196. https://doi.org/10.1007/s00330-004-2255-y.
18. Acharya J, Gibbs WN. Imaging spinal infection. Radiol Infect Dis. 2016;3:84–91.
19. Moritani T, Kim J, Capizzano AA, Kirby P, Kademian J, Sato Y. Pyogenic and non-pyogenic spinal infections: emphasis on diffusion-weighted imaging for the detection of abscesses and pus collections. Br J Radiol. 2014;87:20140011.
20. Radcliff K, Morrison WB, Kepler C, Moore J, Sidhu GS, Gendelberg D, Miller L, Sonagli MA, Vaccaro AR. Distinguishing pseudomeningocele, epidural hematoma, and postoperative infection on postoperative MRI. Clin Spine Surg. 2016;29:E471. https://doi.org/10.1097/bsd.0b013e31828f9203.
21. Sokolowski MJ, Garvey TA, Perl J, Sokolowski MS, Cho W, Mehbod AA, Dykes DC, Transfeldt EE. Prospective study of postoperative lumbar epidural hematoma. Spine. 2008;33:108–13.
22. Pierce JL, Donahue JH, Nacey NC, Quirk CR, Perry MT, Faulconer N, Falkowski GA, Maldonado MD, Shaeffer CA, Shen FH. Spinal hematomas: what a radiologist needs to know. Radiographics. 2018;38:1516–35.
23. Krishnan P, Banerjee TK. Classical imaging findings in spinal subdural hematoma – "Mercedes-Benz" and "cap" signs. Br J Neurosurg. 2015;30:99–100.
24. Geannette CS, Salomon N. "Pearls and Pitfalls of the Postoperative Lumbar Spine: Anatomy, Lumbar Fusion Techniques, and Postoperative Complications." American Roentgen Ray Society, 2019.
25. Lonstein JE, Denis F, Perra JH, Pinto MR, Smith MD, Winter RB. Complications associated with pedicle screws∗. J Bone Joint Surg. 1999;81:1519–28.
26. Chun DS, Baker KC, Hsu WK. Lumbar pseudarthrosis: a review of current diagnosis and treatment. Neurosurg Focus. 2015;39:E10. https://doi.org/10.3171/2015.7.focus15292.
27. Kornblum MB, Fischgrund JS, Herkowitz HN, Abraham DA, Berkower DL, Ditkoff JS. Degenerative lumbar spondylolisthesis with spinal stenosis. Spine. 2004;29:726–33.
28. Rahme R, Moussa R. The modic vertebral endplate and marrow changes: pathologic significance and relation to low back pain and segmental instability of the lumbar spine. Am J Neuroradiol. 2008;29:838–42.
29. Lang P, Chafetz N, Genant HK, Morris JM. Lumbar spinal fusion assessment of functional stability with magnetic resonance imaging. Spine. 1990;15:581–8.
30. Domenicucci M, Ramieri A, Passacantilli E, Russo N, Trasimeni G, Delfini R. Spinal arachnoiditis ossificans: report of three cases. Neurosurgery. 2004;55:E1011. https://doi.org/10.1227/01.neu.0000137281.65551.54.
31. Dimar JR, Glassman SD, Burkus JK, Pryor PW, Hardacker JW, Carreon LY. Clinical and radiographic analysis of an optimized rhBMP-2 formulation as an autograft replacement in Posterolateral lumbar spine arthrodesis. J Bone Joint Surg Am. 2009;91:1377–86.
32. Mckie J, Qureshi S, Iatridis J, Egorova N, Cho S, Hecht A. Trends in bone morphogenetic protein usage since the U.S. Food and Drug Administration advisory in 2008: what happens to physician practices when the food and drug administration issues an advisory? Global Spine J. 2013;4:071–6.
33. Lebl DR. Bone morphogenetic protein in complex cervical spine surgery: a safe biologic adjunct? World J Orthop. 2013;4:53.
34. Sethi A, Craig J, Bartol S, Chen W, Jacobson M, Coe C, Vaidya R. Radiographic and CT evaluation of recombinant human bone morphogenetic protein-2–assisted spinal interbody fusion. Am J Roentgenol. 2011;197:W128. https://doi.org/10.2214/ajr.10.5484.

35. Shah RK, Moncayo VM, Smitson RD, Pierre-Jerome C, Terk MR. Recombinant human bone morphogenetic protein 2-induced heterotopic ossification of the retroperitoneum, psoas muscle, pelvis and abdominal wall following lumbar spinal fusion. Skelet Radiol. 2010;39:501–4.
36. Nguyen N-LM, Kong CY, Hart RA. Proximal junctional kyphosis and failure—diagnosis, prevention, and treatment. Curr Rev Musculoskelet Med. 2016;9:299–308.
37. Argentieri EC, Koff MF, Breighner RE, Endo Y, Shah PH, Sneag DB. Diagnostic accuracy of zero-echo time MRI for the evaluation of cervical neural foraminal stenosis. Spine. 2018;43:928–33.

12 Identification of Complications Using Postoperative Spine MRI

Prabath Kumar Mondel

Introduction

The prevalence of spine surgery in the United States is the highest in the world. However, there are a wide geographical variation and poor consensus regarding the indications [1]. The commonest indication for which patients undergo spine surgery is low back pain not responding to conservative management with radiological evidence of nerve root compromise [2]. Low back pain affects up to 80% of the population and 1–2% of US population is disabled by low back pain [1]. Current guidelines recommend consideration for direct surgical decompression for symptomatic spinal stenosis associated with low-grade degenerative lumbar spondylolisthesis in patients not responding to a trial of medical/interventional treatment. Furthermore, decompression with fusion improves clinical outcome compared to decompression alone and provides satisfactory long-term results (4 years or more) [3].

Imaging plays a crucial role in the postoperative management of these patients. It is useful to identify the position and integrity of implants, to exclude complications secondary to surgery, to delineate the fusion/decompression status, to detect surgical complications, and to evaluate the success of the procedure [4]. The overall incidence of major neurologic deficit in the immediate postsurgical period is low and less than 1% and slightly more common after thoracic and cervical spine surgeries compared to lumbar spine surgeries [1].

It is estimated that over time 10–20% of patients will experience complications related to spinal surgery. The underlying mechanism of major spinal injury is related to either direct/indirect traumatic injury to cord and/or nerve roots, compression and/or distraction of the spinal column, vascular compromise, spinal hematoma, infection, and mechanical cord compression by spinal elements like ligamentum flavum, disc, and adjacent bony structures [1].

Role of Imaging in Postoperative Spine

Interpretation of imaging in the postoperative spine is complicated by surgical changes in and around the spine, artifacts from metallic hardware, and the varied but expected appearance of various surgical techniques. The imaging findings vary depending on a number of factors like surgical approach: minimally invasive versus traditional; type of surgery: decompression versus decompression and fusion; hardware: titanium versus steel implants; initial imaging findings: degenerative disc disease versus congenital spinal stenosis; time since the surgery: recent versus remote, treatment goal temporary stabilization versus permanent correction, etc. Despite the myriad surgical techniques and other variables,

P. K. Mondel (✉)
Philadelphia, PA, USA

W. B. Morrison et al. (eds.), *MRI of the Spine*, https://doi.org/10.1007/978-3-030-43627-8_12

the basic principles of postoperative imaging remain the same. In this chapter, we discuss these principles and their application in everyday postoperative spine imaging.

Routine scheduled postoperative imaging is performed in otherwise asymptomatic patients to evaluate the position and appearance of spinal instrumentation with follow-up imaging to assess progression of osseous fusion. Imaging is also performed in symptomatic patients with persistent or worsening symptoms to assess procedural complications. Imaging is also utilized to assess patients with little or no relief of symptoms following spinal surgery in what is sometimes known as "failed back surgery syndrome" (FBSS) [1].

General Imaging Principles in the Postoperative Spine

Radiography ("Plain Films") is low cost and easily accessible and provides implant position information with relatively low radiation exposure. Baseline radiography is useful in evaluating implant position in initial imaging performed in postoperative patients. Serial radiographs are used to assess implant fractures (hardware failure), osseous fractures, vertebral alignment, and changes at the implant–bone interface and are useful in long-term monitoring. Radiography with positional imaging (flexion and extension) is used to assess for radiographic spinal instability. Computed tomography (CT) has the ability of multiplanar reconstruction and depiction in exquisite detail of the bony spinal anatomy and implants. It is the investigation of choice to detect osseous and implant anomalies and is also used to assess osseous fusion, vertebral alignment, implant failure, detecting infection, and pseudoarthrosis. CT is also useful for detecting and grading spinal central canal and neural foraminal stenosis. Contrast-enhanced CT can be useful in differentiating postoperative fibrosis from residual/recurrent disc herniation and in identifying fluid collections, particularly in patients with contraindications to MRI. CT is also better than radiography in evaluation of the status and progression of fusion. CT myelogram is useful to quantify the degree of spinal canal and foraminal stenosis in patients with contraindication for MRI. Postmyelographic CT is useful to depict facet arthrosis and degree of foraminal stenosis. However, a limitation is beam-hardening artifact from the surgical implants. Furthermore, evaluation of intraspinal contents is not optimal on CT scan. The higher radiation dose and cost associated with CT are also a significant drawback, limiting its utilization in serial monitoring and requiring a more targeted approach [5, 6].

Role of MRI in Postoperative Spine

MRI is the modality of choice for imaging in postoperative patients due to its high contrast and spatial resolution. It is particularly helpful in evaluation of soft tissues, bone marrow, spinal canal and neural foraminal narrowing, hemorrhage, infection, and intraspinal contents [5–7]. Although artifacts from hardware can be a substantial problem, the use of titanium rather than stainless steel implants has significantly reduced the artifacts [5, 6]. A few techniques can be used to minimize artifacts from implants on MRI as detailed below:

(a) Fast spin echo sequences are better than conventional spine echo, which are better than gradient echo sequences. Shortest echo time reduces metal artifacts.
(b) Postcontrast imaging with fat saturation allows early and more confident detection of minimal enhancement due to suppression of chemical shift artifact. However, in the presence of metal hardware, STIR sequences are better for fat suppression as selective fat saturation pulses are associated with poor homogeneity.
(c) Increase bandwidth
(d) Decrease voxel size
(e) Adjusting the frequency encoding direction parallel to the pedicle screws so that artifacts are linear and parallel to the metal.

Furthermore, artifacts may arise due to the presence of metal in the image plane (in-plane artifacts) or in an adjacent plane (through-plane artifacts). A variety of techniques are used for reducing these artifacts in MRI. A metal artifact reduction sequence (MARS) decreases the size and intensity of susceptibility artifacts resulting from magnetic field distortion. Multiacquisition variable-reso-

nance image combination (MAVRIC) is a specialized sequence, which relies on three-dimensional (3D) Fast Spin Echo (FSE) sequences. Slice Encoding for Metal Artifact Correction (SEMAC) uses an additional slice-encoding gradient to a standard fast-spin echo sequence [8–10].

Imaging in postoperative spine includes axial and sagittal T2, STIR, and pre- and postcontrast T1. The T2 images are used to evaluate the thecal sac contours, nerve roots, and cord. Pre-contrast T1 images are used to evaluate the epidural fat, hemorrhage, and osseous changes. STIR imaging is sensitive to bone marrow changes. Postcontrast T1 images are particularly useful to evaluate infectious processes like spondylodiscitis, differentiate postoperative scar from residual/recurrent disc herniation, and characterize fluid collections [6, 7]. An important caveat is that postcontrast imaging must be acquired within 3–5 minutes to enable differentiation of postoperative scar from recurrent disc [11].

Expected Postsurgical Changes

In the early postoperative period there is a significant overlap in the imaging findings of postoperative complications and expected findings [6]. Expected postsurgical changes include changes in the bone, discs, nerve roots, and epidural soft tissues. It is challenging to differentiate the expected changes from postoperative complications in the first 6 weeks due to similarity in their imaging appearance. There is removal of bone with added bone grafts and susceptibility related to hardware. The osseous anatomy is well assessed on T1 images. A mild protrusion of the dura and CSF into the laminectomy defect is expected and should not be confused with a pseudomeningocele. Enhancement in the marrow is considered pathological except in patients with preoperative Modic 1 marrow changes. There is shrinkage of the thecal sac that returns to normal by 3 weeks. Cauda equina adhesions are present in the thecal sac at the surgical site, but they gradually resolve [2, 6, 12].

High signal intensity on T2 images is demonstrated in the disc that extends to the site of disruption of the annulus. High signal on T2 in the nucleus pulposus can be seen till 2 months in the postoperative period. At 6 months, the high T2 signal annular disruption is gradually replaced by hypointense fibrosis signaling healing of the defect. Annular enhancement, enhancement of the nucleus pulposus, and loss of disc height are expected findings. However, enhancement of the disc is seen in 86% of patients at 6 months. There is homogenous enhancement of the epidural reaction consisting of granulation tissue with progressive fibrosis. Epidural soft tissue with mass effect can be seen in the immediate postoperative period and is difficult to distinguish from recurrent disc herniation. This is considered to be postoperative edema as it has an intermediate signal on T1 and is slightly hyperintense on T2. The nerve roots may enhance at the operative site for up to 6 months. Late nerve root enhancement at 6–8 months is considered abnormal and indicates continued underlying sterile radiculitis. Facet joint enhancement up to 6 months is also common in the postoperative period and is usually reactionary. Enhancement with disruption, edema, fluid collections, and tract leading to the paraspinal muscles is common up to 6 months in the postoperative period. It is not possible to distinguish between the various postoperative fluid collections on MRI alone. The majority of these soft tissue changes resolve over a period of 3 months [2, 6, 11, 12] (Table 12.1).

Table 12.1 Expected postoperative changes [12]

Bone marrow	Unchanged from before surgery unless manipulated for interbody implant placement. No enhancement except in Type 1 Modic changes.
Nerve roots	Enhancement normal up to first 6–8 months.
Intervertebral discs	Contrast enhancement of posterior annulus and increased T2 signal sometimes for years
Epidural tissues	Early soft tissue with mass effect and enhancement expected in first 6 months. Mass effect decreases thereafter. Persistent mass effect thereafter may cause symptoms of radiculopathy. Contrast enhancement may persist for years.

Postoperative Complications

Postoperative complications are broadly classified into early and late complications as shown in Table 12.2. Early complications include postoperative fluid collections and operative injuries. Late complications include recurrent disc herniation, peridural fibrosis, spondylodiscitis, arachnoiditis, accelerated adjacent segment degenerative disease, instrumentation failure, and fusion failure [4].

Postoperative fluid collections include hematoma, seroma, abscess, and pseudomeningocele. The duration since surgery is an important clue to the underlying cause with hematomas and seromas occurring in hours to days whereas abscesses occur over days to weeks. Diffusion weighted imaging (DWI) is useful to detect an abscess in the spinal canal. However, hemorrhage at various stages can also show restricted diffusion. Also, DWI imaging is distorted by hardware [4, 6].

Table 12.2 Postoperative spinal complications [1, 4]

Early	
Postoperative fluid collections	Hematoma, seroma, pseudomeningocele, abscess
Operative injury	Remote injuries like intracranial hemorrhage, remote cerebellar hemorrhage, esophageal injury, etc. Spinal column injuries include neural, vascular, osseous, etc.
Late	
Inflammation	Arachnoiditis, radiculitis
Infection	Spondylodiscitis
Accelerated degenerative disease	Adjacent level disease
Instrumentation and fusion failure	Fractures, pseudoarthrosis

Fluid Collections

Hematoma is a localized collection of blood within or outside the spinal canal. MRI is more sensitive than CT in the evaluation of hemorrhage due to increased sensitivity of T2∗ images to blood products. However, T2∗ imaging is also more prone to susceptibility artifact from hardware and is nearly nondiagnostic in the presence of hardware. The incidence of hematoma is less than 1% and usually presents hours to days after surgery. The imaging appearance of hematoma varies by the stage of hemoglobin (oxidation state) and location of the hematoma. Large hematomas can cause significant mass effect and compress the cord and nerve roots. Subdural hematomas are rare and have a clumped or lobulated appearance and conform to the dura with preserved epidural fat. Epidural hematomas are caused by rupture of internal vertebral venous plexus of Batson and have a biconvex appearance with obliteration of epidural fat. Peripheral or linear enhancement due to dural hyperemia, epidural septa, or vessels may also be seen. The imaging appearance of epidural hematoma by stage and duration is shown in Table 12.3. Follow-up imaging is also done to evaluate for superinfection of the hematoma [1, 4].

Seroma is a lymphatic fluid collection that is believed to be due to damage to local lymphatics. It is rare and often presents in subcutaneous or paraspinal region and may be surrounded by a fibrotic capsule. They are hyperintense on T2 and DWI and hypointense on T1 with slight peripheral enhancement and fluid levels. Seromas are often treated by compression bandage and drainage [1, 4].

It is not possible to distinguish between a meningocele and pseudomeningocele on MRI. Pseudomeningocele is a collection of CSF

Table 12.3 Imaging appearance of epidural hematoma by stage and duration [1]

Stage	Age	Hemoglobin	T1	T2
Hyperacute	<12 hours	Oxyhemoglobin	Isointense	Hyperintense
Acute	1–3 days	Deoxyhemoglobin	Hypointense	Hypointense
Early subacute	3–7 days	Intracellular methemoglobin	Hyperintense	Hypointense
Late subacute	7–14 days	Extracellular methemoglobin	Hyperintense	Hyperintense
Chronic	>2 weeks	Hemosiderin	Hypointense	Hypointense

extending from the spinal canal to the paraspinal soft tissues. It is rare and reported in 2% of patients undergoing laminectomy in lumbar region. Dural injury or incomplete dural closure during surgery is the underlying cause of pseudomeningocele. Although acute pseudomeningoceles have complex signal characteristics due to evolving blood products, follow-up imaging shows the collection following CSF signal on all sequences. Pseudomeningoceles are cystic lesions that communicate with CSF through the bony defect and may show CSF pulsation artifact best depicted by T2-weighted images and by high-resolution balanced steady state gradient echo sequences like CISS or FIESTA. CT myelogram may be required in complex fluid collections with no demonstrable direct communication with the spinal canal CSF [4, 6, 7, 12].

Abscesses are circumscribed infected fluid collections that can occur as superinfections on preexisting fluid collections or de novo. Perioperative antibiotics have reduced their incidence with abscesses seen in 0.2–20% of postsurgical spine patients. The commonest pathogens are *Staphylococcus aureus*, *Staphylococcus epidermidis*, and *Propionibacterium acnes* in implants. On MRI, abscesses are T2 hyperintense/T1 hypointense with irregular rim enhancement and diffusion restriction. Image-guided aspiration is often done prior to therapy with drainage and antibiotics [4, 6].

Operative Injury

Operative injury could be remote or in the vicinity of spinal canal. Remote injuries include subdiaphragmatic hematoma, intracranial hemorrhage, and remote cerebellar hemorrhage. Injury to the dura, vasculature, and osseous and neural elements in and around the spinal canal is not uncommon. There is regional variation but, generally speaking, anterior approach is more prone to vessel and soft tissue injuries like injuries to the carotid arteries, esophagus, etc., and posterior approach more prone to neural injuries like injuries to the cord, nerve roots, dura, etc. Dural tear has an incidence of 12.5–16% following lumbar spine surgery. However, the majority of tears are repaired intraoperatively. However, when not detected or left unrepaired, patients may develop pseudomeningocele, meningocele with CSF leakage, intracranial hypotension, etc. Osseous and hardware fractures are better evaluated on CT scan [4, 6, 13].

Recurrent/Residual Disc Herniation

Recurrent disc herniation is the commonest complication after discectomy. Recurrent disc herniation is defined as herniation at the same level, either ipsilateral or contralateral to the operated site with an initial pain-free interval of at least 6 months. The incidence varies between 3 and 18% in retrospective studies after lumbar discectomy to up to 23% in prospective studies with at least 50% of prospectively imaged patients being asymptomatic. The accuracy of contrast-enhanced MRI in differentiating disc herniation from peridural fibrosis is as high as 96–100%. Herniated discs appear as ventral epidural soft tissue mass that is isointense on T1 and iso to hyperintense on T2 compared to the disc and iso to hypointense relative to annulus and usually hypointense on T2 compared to peridural fibrosis. However, a large sequestered disc has a central high T2 signal. On contrast enhanced MRI, there is no significant or mild peripheral early enhancement due to granulation tissue or dilated epidural plexus [1, 6].

Peridural Fibrosis

Peridural fibrosis is believed to cause persistent symptoms in up to 24% of patients with failed back syndrome, but this association is controversial. Following the decrease in the ill-defined soft tissue granulation tissue and/or edema along the epidural space at the site of surgery, there is scarring/fibrosis. In the first 6 months, epidural edema/granulation tissue may demonstrate peripheral enhancement and may be impossible to

distinguish from recurrent disc herniation. However, after 6 months peridural fibrosis/scarring is seen as an iso to hypointense T1/hyperintense T2 tissue relative to annulus lesion with diffuse early enhancement. Additional features include irregular margin, lack of continuity with disc, and retraction of the dural sac. However, peridural fibrosis can appear mass like with effacement of normal nerve root size or enlargement secondary to cicatrization. In the majority of patients, the mass-like appearance decreases by 6 months [1, 2, 6, 11, 12].

Spondylodiscitis

Spondylodiscitis is infection of the discovertebral complex. It has an estimated incidence of 0.2–2.75% and can be caused either by direct inoculation at the surgical site or by hematogenous seeding. The commonest organisms isolated are *S. aureus* and *S. epidermidis*. The imaging features include decreased disc height, decreased T1 signal and increased T2 signal in the vertebral body and disc, and loss of endplate definition. Furthermore, rim-enhancing collections, ascending epidural collections, bony destruction, and progressive marrow changes suggest underlying infection. Peripheral enhancement of the remaining disc without endplate changes is suggestive of infection. A central linear or curvilinear pattern of enhancement is likely a postsurgical reactive change. Presence of enhancing epidural, subligamentous, or paraspinal enhancing soft tissue at the affected level is highly suggestive of infectious spondylodiscitis. An absence of marrow changes in the peridiscal space and a lack of enhancement of the disc make a diagnosis of spondylodiscitis less likely [7, 14].

Arachnoiditis

Arachnoiditis is inflammation of cauda equina nerve roots. About 6–16% of patients with persistent symptoms after surgery are attributed to arachnoiditis. On imaging, T2-weighted images show abnormal morphology of the nerve roots. There are three distinct patterns described: type 1: centrally clumped nerve roots into one or more cords, type 2: nerve roots are located peripherally (empty thecal sac sign), and type 3: intermediate signal intensity mass obliterating the subarachnoid space below the conus. Surgery is contraindicated in the presence of arachnoiditis [1, 6, 11].

Accelerated Adjacent Segment Degeneration

Following spinal fusion surgeries, there is accelerated degenerative disease in the spinal segments both cranial and caudal to the fused level due to shift in the weight-bearing and decreased flexibility of the fused segment. This may progress to single or multilevel spinal stenosis requiring reintervention. It is most commonly seen in the lumbar spine and if the initial fusion does not incorporate the L5–S1 segment [4, 6, 13].

Conclusion

Imaging of postoperative spine is complex and requires interpretation of the MRI features with regard to multiple factors namely, the type of surgery performed, materials used at the time of surgery, time elapsed since surgery, temporal and anatomical evolution of MRI findings, an understanding of the expected postoperative changes, and correct interpretation of MRI changes that depict postoperative complications. This interpretation needs to be tempered by the patient's clinical picture, oftentimes discussion with the treating physician/surgeon, laboratory values, temporal evolution of the clinical picture, biopsy of the affected level, and sometimes surgical reexploration to optimize and tailor-made therapy to the particular patient.

References

1. Willson MC, Ross JS. Postoperative spine complications. Neuroimaging Clin N Am. 2014;24(2):305–26. https://doi.org/10.1016/j.nic.2014.01.002.
2. Van Goethem JW, Parizel PM, Jinkins JR. Review article: MRI of the postoperative lumbar spine. Neuroradiology. 2002;44(9):723–39. https://doi.org/10.1007/s00234-002-0790-2.
3. Matz PG, Meagher RJ, Lamer T, Tontz WL Jr, Annaswamy TM, Cassidy RC, et al. Guideline summary review: an evidence-based clinical guideline for the diagnosis and treatment of degenerative lumbar spondylolisthesis. Spine J. 2016;16(3):439–48. https://doi.org/10.1016/j.spinee.2015.11.055.
4. Bittane RM, de Moura AB, Lien RJ. The postoperative spine: what the spine surgeon needs to know. Neuroimaging Clin N Am. 2014;24(2):295–303. https://doi.org/10.1016/j.nic.2014.01.006.
5. Thakkar RS, Malloy JP, Thakkar SC, Carrino JA, Khanna AJ. Imaging the postoperative spine. Radiol Clin N Am. 2012;50(4):731–47. https://doi.org/10.1016/j.rcl.2012.04.006.
6. Eisenmenger L, Clark AJ, Shah VN. Postoperative spine: what the surgeon wants to know. Radiol Clin N Am. 2019;57(2):415–38. https://doi.org/10.1016/j.rcl.2018.10.003.
7. Bellini M, Ferrara M, Grazzini I, Cerase A. Neuroimaging of the postoperative spine. Magn Reson Imaging Clin N Am. 2016;24(3):601–20. https://doi.org/10.1016/j.mric.2016.04.006.
8. Hargreaves BA, Worters PW, Pauly KB, Pauly JM, Koch KM, Gold GE. Metal-induced artifacts in MRI. AJR Am J Roentgenol. 2011;197(3):547–55. https://doi.org/10.2214/ajr.11.7364.
9. Hartley KG, Damon BM, Patterson GT, Long JH, Holt GE. MRI techniques: a review and update for the orthopaedic surgeon. J Am Acad Orthop Surg. 2012;20(12):775–87. https://doi.org/10.5435/jaaos-20-12-775.
10. Sutter R, Ulbrich EJ, Jellus V, Nittka M, Pfirrmann CW. Reduction of metal artifacts in patients with total hip arthroplasty with slice-encoding metal artifact correction and view-angle tilting MR imaging. Radiology. 2012;265(1):204–14. https://doi.org/10.1148/radiol.12112408.
11. Babar S, Saifuddin A. MRI of the post-discectomy lumbar spine. Clin Radiol. 2002;57(11):969–81.
12. Helms CA, Major NA, Anderson MW, Kaplan P, Dussault R. Musculoskeletal MRI. 2nd ed. Philadelphia: Saunders/Elsevier; 2009.
13. Borg B, Federle MP, Hamilton BE, Jeffrey RB, LaBarge III DV, Moore KR, et al. Failed back surgery syndrome. In: Imaging in spine. Philadelphia: Elsevier; 2017. p. 348.
14. Van Goethem JW, Parizel PM, van den Hauwe L, Van de Kelft E, Verlooy J, De Schepper AM. The value of MRI in the diagnosis of postoperative spondylodiscitis. Neuroradiology. 2000;42(8):580–5.

Index

W. B. Morrison et al. (eds.), *MRI of the Spine*, https://doi.org/10.1007/978-3-030-43627-8